

Thermal Ignition

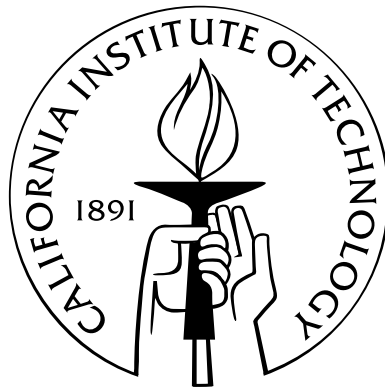
Thesis by

Philipp Andreas Boettcher

In Partial Fulfillment of the Requirements

for the Degree of

Doctor of Philosophy



California Institute of Technology

Pasadena, California

2012

(Defended May 2nd 2012)

© 2012

Philipp Andreas Boettcher

All Rights Reserved

To Leslie, Juliane, Jane, Helmut, Frank, & Trey

Acknowledgments

I would like to acknowledge my advisor, Joseph Shepherd, first. It has been a great pleasure to work with him. He has put a tremendous amount of trust in me and his other students, as we perform combustion experiments. I am very grateful for the opportunity to work for him and very much enjoyed our discussions about science, engineering, history, and philosophy. Guillaume Blanquart has been my *de facto* co-advisor since joining the mechanical engineering faculty. His expertise in combustion and numerical simulation have been a great resource during my time. I am also very grateful to the other members of my thesis committee, Beverly McKeon and John Dabiri, for their help and insightful discussions.

I would also like to thank the other faculty members of GALCIT, particularly Tony Leonard, Dale Pullin, Dan Meiron, and of course Ravi and Hans Hornung for their help on my candidacy committee as well as their general encouragement.

None of this work would have been possible without the other group members of the Explosion Dynamics Laboratory and T5. Jim Karnesky taught me everything I know about electronics, building experiments (and making them work), and lab safety. Sally Bane and I worked closely under the funding provided by Boeing, which Stephanie Coronel is now continuing. An extra big thanks goes to Jason Damazo, “the smart one”, whose collaboration is invaluable. We worked closely on several projects, which are not part of this thesis, but made my graduate school experience much more enjoyable mainly because I got to work with Jason. His expertise in experiments, math, and coding have been a great help. Rémy Mével and Vaughan Thomas are the reason that the auto-ignition work has the current level of detail and made it publication. Both of them have been in the office during the final stages of the thesis writing process and helped me talk through a host of problems. Brian Ventura deserves a lot of credit for his help with the puffing flame investigation. He started with me as a SURF student and I convinced him to stay on and do a senior thesis. Our collaboration in the lab made the rather tedious experiments go by much more quickly. Kliulai Chow-Yee also did a SURF project in the lab and helped with the color schlieren pictures. Aurelien Demenay helped

with the very tedious manual digitization of the flame speeds from schlieren videos. Nick Parziale, who works in T5, is close friend and has kept me going for the past few year. Bahram Valiferdowski has been an excellent resource for all engineering design questions and group morale. Thanks also to Joe Jewell for taking over the 150 seminar and general group entertainment. Alexandra Katsas was a great help and support throughout the years. I would also like to thank Shannon Kao, and Neil Bitter and Bryan Schmidt for setting the stage and continuing the legacy respectively. Shyam Menon, who I would like to nominate as a honorary EDL member, performed all of the simulations for the puffing flame project and helped me try to unravel the phenomenon.

A special thanks goes to the Aeroshop, Brad St John, Ali Kiani, and Joe Haggerty. All of my experimental work was possible by the parts they fabricated, as well as the design help and encouragement I received.

My friends and roommates kept me sane during my time here: Chris, Angie, Pablo, Tony, Paco, Jason R., Travis, Olive, Veronica, and Dr. Jay.

Several members of the staff here at Caltech were exceptional during my stay here with help and opportunities to help others – a big thank you to Felicia, Natalie, Icy, and Kevin. Special thanks also to Dennis Kwon, Adam Savage, and Jamie Hyneman for the opportunity to work on Mythbusters. Jason and I had a wonderful time.

This work was made possible by The Boeing Company through the Strategic Research and Development Relationship Agreement CT-BA-GTA-1. In particular I would like to thank, Eddie Kwon and Art Day at Boeing with whom we worked closely, as well as Mike Grant, Debbie Raddash, and Matt Ganz for their support.

I would like to thank my family for all their support: my parents — Juliane and Helmut; my host family — Jane, Frank, and Trey; my grandparents — Margret and Ludwig; as well as all my aunts, uncles, and cousins. Thank you for cheering me on.

The final thanks is reserved for Leslie Lamberson, who made all of this worth while. I am looking forward to our future together.

Abstract

Accidental ignition of flammable gases is a critical safety concern in many industrial applications. Particularly in the aviation industry, the main areas of concern on an aircraft are the fuel tank and adjoining regions, where spilled fuel has a high likelihood of creating a flammable mixture. To this end, a fundamental understanding of the ignition phenomenon is necessary in order to develop more accurate test methods and standards as a means of designing safer air vehicles. The focus of this work is thermal ignition, particularly auto-ignition with emphasis on the effect of heating rate, hot surface ignition and flame propagation, and puffing flames.

Combustion of hydrocarbon fuels is traditionally separated into slow reaction, cool flame, and ignition regimes based on pressure and temperature. Standard tests, such as the ASTM E659, are used to determine the lowest temperature required to ignite a specific fuel mixed with air at atmospheric pressure. It is expected that the initial pressure and the rate at which the mixture is heated also influences the limiting temperature and the type of combustion. This study investigates the effect of heating rate, between 4 and 15 K/min, and initial pressure, in the range of 25 to 100 kPa, on ignition of *n*-hexane air mixtures. Mixtures with equivalence ratio ranging from $\phi = 0.6$ to $\phi = 1.2$ were investigated. The problem is also modeled computationally using an extension of Semenov's classical auto-ignition theory with a detailed chemical mechanism. Experiments and simulations both show that in the same reactor either a slow reaction or an ignition event can take place depending on the heating rate. Analysis of the detailed chemistry demonstrates that a mixture which approaches the ignition region slowly undergoes a significant modification of its composition. This change in composition induces a progressive shift of the explosion limit until the mixture is no longer flammable. A mixture that approaches the ignition region sufficiently rapidly undergoes only a moderate amount of thermal decomposition and explodes quite violently. This behavior can also be captured and analyzed using a one-step reaction model, where the heat release is in competition with the depletion of reactants.

Hot surface ignition is examined using a glow plug or heated nickel element in a series of premixed

n-hexane air mixtures. High-speed schlieren photography, a thermocouple, and a fast response pressure transducer are used to record flame characteristics such as ignition temperature, flame speed, pressure rises, and combustion mode. The ignition event is captured by considering the dominant balance of diffusion and chemical reaction that occurs near a hot surface. Experiments and models show a dependence of ignition temperature on mixture composition, initial pressure, and hot surface size. The mixtures exhibit the known lower flammability limit where the maximum temperature of the hot surface was insufficient at igniting the mixture. Away from the lower flammability limit, the ignition temperature drops to an almost constant value over a wide range of equivalence ratios ($0.7 < \phi < 2.8$) with large variations as the upper flammability limit is approached. Variations in the initial pressure and equivalence ratio also give rise to different modes of combustion: single flame, re-ignition, and puffing flames. These results are successfully compared to computational results obtained using a flamelet model and a detailed chemical mechanism for *n*-heptane. These different regimes can be delineated by considering the competition between inertia, i.e., flame propagation, and buoyancy, which can be expressed in the Richardson number.

In experiments of hot surface ignition and subsequent flame propagation a ~ 10 Hz “puffing” flame instability is visible in mixtures that are stagnant and premixed prior to the ignition sequence. By varying the size of the hot surface, power input, and combustion vessel volume, we determined that the instability is a function of the interaction of the flame with the fluid flow induced by the combustion products rather than the initial plume established by the hot surface. The phenomenon is accurately reproduced in numerical simulations and a detailed flow field analysis revealed a competition between the inflow velocity at the base of the flame and the flame propagation speed. The increasing inflow velocity, which exceeds the flame propagation speed, is ultimately responsible for creating a puff. The puff is then accelerated upward, allowing for the creation of the subsequent instabilities. The frequency of the puffing is proportional to the gravitational acceleration and inversely proportional to the flame speed. We propose a relation describing the dependence of the frequency on gravitational acceleration, hot surface diameter, and flame speed. This relation shows good agreement for lean and rich *n*-hexane-air as well as lean hydrogen-air flames.

Contents

Abstract	vi
List of Figures	xxv
List of Tables	xxvii
1 Introduction	1
1.1 Motivation	1
1.2 Background	3
1.2.1 Thermal Ignition in a Heated Vessel — Auto-Ignition	5
1.2.2 Thermal Ignition from a Concentrated Hot Surface	8
1.2.3 Hot Surface Ignition of Liquid Fuels	10
1.2.4 Cyclic Flame Propagation in Premixed Combustion	10
1.3 Thesis Outline	12
2 Thermal Ignition of Gaseous Fuel-Air Mixtures Within a Slowly Heated Vessel	13
2.1 Introduction	13
2.2 Experiments	14
2.2.1 Experimental Setup	14
2.2.2 Experimental Results	16
2.2.3 Simultaneous Measurements of Oxygen and Fuel	19
2.2.3.1 Experimental Setup and Calibration Procedure	20
2.2.3.2 Application of Oxygen Measurements	20
2.3 Modeling	21
2.3.1 Modeling with a Detailed Chemical Mechanism	21
2.3.1.1 Kinetic Scheme Validation	24
2.3.1.2 Fast and Slow Combustion Modeling	26

2.3.1.3	Heat Production and Losses	26
2.3.1.4	Radicals and Atoms Rate of Production	28
2.3.1.5	Reaction Pathway Diagrams	31
2.3.1.6	Explosion Limits	35
2.3.1.7	Parametric Study in α , ϕ , and P_0	37
2.3.2	Modeling with a One-Step Mechanism	42
2.4	Theoretical Considerations	46
2.4.1	Ignition With Negligible Consumption	47
2.4.1.1	Dominant Chemical Energy Release	47
2.4.1.2	Effect of Ramp Rate on Induction Time	48
2.4.1.3	Critical Heat Transfer	50
2.4.1.4	Critical Time For Wall Temperature Ramp	51
2.4.2	Ignition With Consumption	54
2.4.2.1	Induction Time With Consumption	54
2.4.2.2	Thermal Ignition with heat-loss, Consumption, and Wall Temperature Ramp	56
2.5	Conclusion	61
3	Thermal Ignition and Flame Propagation from a Concentrated Hot Surface	63
3.1	Introduction	63
3.2	Experimental Setup	64
3.2.1	Composition Uncertainties	68
3.2.2	Peak Pressure	69
3.2.3	Hot Surface I — High-Temperature Glow Plug (Bosch)	71
3.2.4	Hot Surface II — Standard Glow Plug (Autolite 1110)	72
3.3	Ignition Temperature	73
3.3.1	Hot Surface Ignition Temperature as a Function of Composition	74
3.4	Ignition Modeling	75
3.4.1	Modeling Background	75
3.4.2	Simplified Analytical Approach	75
3.4.3	Boundary Layer Modeling Approach	78
3.4.3.1	Thermal Ignition Using Tabulated and Detailed Chemistry Modeling	90
3.4.4	Hot Surface Ignition Temperature as a Function of Pressure	93

3.4.5	Hot Surface Ignition Temperature as a Function of Surface Area	94
3.5	Flame Propagation	97
3.5.1	Experiments	97
3.5.2	Flame Propagation Speed as a Function of Composition	99
3.5.3	Computational Modeling of Flame Propagation	102
3.5.3.1	Chemistry Tabulation	102
3.5.3.2	Reaction Mechanism	103
3.5.4	Effect of the Thermal Plume on the Flame Propagation Speed	105
3.5.5	Combustion Modes	109
3.5.5.1	Single Flames	109
3.5.5.2	Multiple Flames	110
3.5.5.3	Puffing Flames	110
3.5.5.4	Combustion Mode as a Function of Richardson Number	111
3.6	Conclusion	113
4	Cyclic Flame Propagation in a Fully Premixed Initially Stagnant Mixture	115
4.1	Introduction	115
4.2	Experiments	116
4.2.1	Experimental Setup and Procedure	116
4.2.2	Experimental Observations	117
4.2.3	Numerical Simulations	118
4.3	Results — Puffing Frequency	119
4.3.1	Glow Plug Size and Vessel Size	120
4.3.2	Scaling Laws	121
4.3.2.1	Cetegen and Ahmed (1993)	121
4.3.2.2	Durox et al. (1996)	123
4.3.3	Effect of Gravity	124
4.3.4	Effect of Flame Speed	125
4.3.5	Lean Hexane Puffing Flames	127
4.4	Physics of Puffing	129
4.4.1	Flow Field Analysis	129
4.4.2	Onset of Puffing — Flow Velocity vs. Flame Velocity	139
4.5	Conclusions	142

5 Conclusions	143
Bibliography	157
A Absorption Measurements for Hydrocarbon Fuel	159
A.1 Direct Absorption Measurements	159
A.2 Absorption Cross Sections	165
B Second Harmonic Detection of Oxygen with Tunable Diode Lasers	167
B.1 Experimental Setup Addendum	170
C Heated Vessel Theory	173
C.1 Governing Equation and Nomenclature	173
C.2 Induction Time	175
C.2.1 Alternative Derivation	176
C.2.2 Frank-Kamenetskii Approximation	178
C.2.3 Wall Temperature Ramp Without Chemistry	179
C.2.4 Ramp Rate Reduced Induction Time	179
C.2.5 Critical Heat-Loss Rate With Constant Wall Temperature	181
C.3 Full Nondimensional Equations	181
D Collision Limit Calculation for Pre-Exponential	183
E Correlation of Hot Surface Ignition Temperature with Surface Area	185
F Flame Propagation	191
F.1 Introduction	191
F.2 Flame Propagation Speed as a Function of Composition	192
F.3 Tabular Flame Speed Data	195
F.4 Tabular Expansion Ratio Data	196
G Thermal Plume Scaling	197
H Refitting Thermodynamic Data	201
I Experimental Data	207
I.1 Heated Vessel Ignition	207

I.2 Hot Surface Ignition	219
J Ignition Location	227
K Schlieren Sequences	231
L Selected Color Schlieren Images	341
M Hot Surface Temperature and Pressure Traces	347

List of Figures

1.1	ASTM E 659 auto-ignition temperature apparatus (ASTM, 2005)	4
1.2	Ignition as a function of hot surface size (reproduced from Kuchta et al., 1965)	5
1.3	Regions of ignition as a function of temperature and pressure for <i>n</i> -hexane (Townend et al., 1934)	6
2.1	Schematic of the experimental setup (all dimensions are in cm)	15
2.2	Pictures of the heated experimental vessel setup	16
2.3	Slow reaction of a fuel-rich ($\phi = 1.2$) <i>n</i> -hexane/air mixture at an initial pressure of 101 kPa heated at 4.25 K per minute	17
2.4	Ignition of a fuel-rich ($\phi = 1.2$) <i>n</i> -hexane/air mixture at an initial pressure of 101 kPa heated at 11 K per minute	18
2.5	Experimental results as a function of total pressure, temperature ramp rate, and equivalence ratio	19
2.6	Schematic of the experimental setup for molecular oxygen measurements	21
2.7	Calibration curve, second harmonic peak height as a function of molecular oxygen partial pressure with $\pm \sigma$ uncertainty bars (O_2 only and O_2 with 67 kPa N_2 dilution)	22
2.8	Measurement of the molecular oxygen and fuel concentration during a slow reaction for a <i>n</i> -hexane/air mixture. Conditions: $P_0 = 26.67$ kPa, $\phi = 1.2$, $\alpha = 11.2$ K/min	22
2.9	Comparison of shock tube experimental data to the predictions of the Ramirez model for <i>n</i> -hexane-oxygen-argon mixture	25
2.10	Comparison of flow and jet-stirred reactor experimental data to the predictions of the Ramirez model for <i>n</i> -heptane-oxygen-nitrogen mixtures	25
2.11	Simulated temperature and pressure profiles for a <i>n</i> -hexane-air mixture for two different heating rates. Conditions: $\phi = 1.2$ (a) $\alpha = 5$ K/min (b) $\alpha = 10$ K/min	27
2.12	Simulated species profiles for a <i>n</i> -hexane-air mixture for two different heating rates. Conditions: $\phi = 1.2$ (a) $\alpha = 5$ K/min (b) $\alpha = 10$ K/min	27

2.13	Chemical heat production and heat-loss rates for a <i>n</i> -hexane-air mixture for two different heating rates. Conditions: $\Phi = 1.2$; $\alpha = 5$ K/min and $\alpha = 10$ K/min (Ignition — Ign, Slow Reaction — SR)	28
2.14	Net energy release rate during (a) slow reaction and (b) ignition	29
2.15	Rate of production of H atoms and OH radicals for a $\Phi = 1.2$ <i>n</i> -hexane-air mixture and two different heating rates: (a) and (b), $\alpha = 5$ K/min; (c) and (d), $\alpha = 10$ K/min	30
2.16	Carbon reaction pathways during the first phase of a <i>n</i> -hexane-air mixture oxidation for two heating rates. Conditions: $\Phi = 1.2$; $\alpha = 5$ and 10 K/min. Black arrows: common pathways. Blue arrows: additional pathways observed during the slow reaction. The first phase extends from 2350 to 2850 s for the slow reaction and from 1220 to 1430 s for the fast reaction.	33
2.17	Carbon reaction pathways during the second phase of a <i>n</i> -hexane-air mixture oxidation for two heating rates. The second phase extends from 2850 to 3100 s for the slow reaction and from from 1430 to 1495 s for the fast reaction.	34
2.18	Thermodynamic state trajectories along with the explosion limits (Kane et al., 1937) for a <i>n</i> -hexane-air mixture with different heating rates. Conditions: $\phi = 1.2$; $\alpha = 5$ and 10 K/min; (a): temporal evolution (500 s elapsed time between points). (b): <i>n</i> -hexane percentage consumed in the boxed region of (a)	36
2.19	Peak overpressure as a function of initial pressure	37
2.20	Peak overpressure as a function of heating rate	39
2.21	Peak overpressure as a function of equivalence ratio	39
2.22	Fast reaction and slow reaction cases as a function of equivalence ratio and heating rate at an initial pressure of one atmosphere	40
2.23	Fast reaction and slow reaction cases as a function of equivalence ratio and heating rate at an initial pressure of one atmosphere (fine grid)	41
2.24	Transition limits from slow reaction case to ignition cases as function of the initial pressure, equivalence ration, and heating rate	41
2.25	Ignition delay time as a function of reciprocal temperature for a stoichiometric hexane-air mixture at atmospheric pressure. The activation energy at low temperatures is estimated by the slope indicated.	44
2.26	Simulated slow reaction for a heating rate of $\alpha = 5$ K/min using one-step chemistry; (a) reaction progress, (b) temperature	45

2.27	Simulated ignition for a heating rate of $\alpha = 10$ K/min using one-step chemistry; (a) reaction progress, (b) temperature	45
2.28	Ramp rate reduced induction time	50
2.29	Absolute values of heat release and heat-loss components of the energy equation (after Law, 2006)	51
2.30	Heat release and heat-loss with a wall temperature ramp	53
2.31	Temperature (a) and reaction progress (b) for a slow reaction case and (8 K/min) and an ignition case (10 K/min)	57
2.32	Temperature with varying heating rate, α	57
2.33	Reaction progress with varying heating rate, α	58
2.34	Temperature vs. reaction progress with varying heating rate, α	58
2.35	Temperature evolution about the transition point as a function of heating rate	61
3.1	Diagram of the vessel, flow plug mounting fixture with stagnation surface, field of view (FOV), and glow plug (in red), with dimensions in mm	65
3.2	Photograph of the hot surface ignition vessel with an array of thermocouples above the hot surface	65
3.3	Schlieren setup schematic	66
3.4	Example of color schlieren picture	67
3.5	Dark background schlieren visualization of the flame propagation	67
3.6	Temperature measurement at the top of the combustion vessel during the ignition of a hexane-air mixture ($\phi = 1.2$)	68
3.7	Hot surface experiment plumbing diagram	69
3.8	Pressure during the ignition of a hexane-air mixture ($\phi = 1.2$)	70
3.9	Peak pressure as a function of equivalence ratios at atmospheric pressure	70
3.10	High-temperature glow plug schematic	71
3.11	High-temperature glow plug temperature distribution	71
3.12	Autolite glow plug schematic	72
3.13	Autolite glow plug temperature distribution	72
3.14	Temperature of the glow plug during the ignition of a hexane-air mixture ($\phi = 1.2$) .	73
3.15	Hot surface ignition temperature as a function of equivalence ratio at atmospheric pressure for different hot surface sizes	74
3.16	Thermal boundary layer along a vertical hot plate	79

3.17	Temperature profile in a thermal boundary layer along a vertical hot plate	83
3.18	Ignition times for n-heptane and air mixtures computed with the detailed chemical mechanism of Curran et al. (1998)	85
3.19	Energy release rate and energy loss rate along a fluid trajectory	89
3.20	Trajectories and ignition location along a vertical hot surface	89
3.21	Nondimensional temperature profile and velocity profile for a constant and variable density boundary layer along a vertical hot plate (from Cairnie and Harrison, 1982) .	90
3.22	Comparison of ignition locations for different hot surface temperatures	92
3.23	Hot surface ignition temperature from tabulated chemistry simulations and experiments	92
3.24	Ignition delay times for n-heptane and air mixtures computed with the detailed chemical mechanism of Curran et al. (1998)	93
3.25	Simulated ignition temperatures and ignition times as function of pressure	94
3.26	Ignition as a function of hot surface size	95
3.27	Flame position grid	98
3.28	Representative digitization of the flame location and fitting from shot 33	98
3.29	Spherical flame schematic	99
3.30	Flame propagation speed for n-hexane air mixtures as a function of equivalence ratio atmospheric pressure	101
3.31	Flame propagation speed at room temperature and atmospheric pressure	104
3.32	Dark background schlieren visualization of the flame propagation for a hexane-air mixture (Bosch glow plug, $\phi = 1.2$)	105
3.33	Simulation results for flame propagation phenomena (Bosch glow plug, $\phi = 1.2$) . . .	105
3.34	Laminar burning speed as function of equivalence ratio at different temperatures as calculated using the CaltechMech	106
3.35	Comparison between laminar burning speeds calculated using n-heptane-air reaction mechanism and experiments	106
3.36	Laminar burning velocity of <i>n</i> -heptane vs. temperature	106
3.37	(a) Photograph of the thermocouple array in the vessel used to determine the plume temperature; (b) schlieren image during shot 61 with the thermocouple array in place	107
3.38	(a) Temperature distribution above the glow plug without ignition; (b) temperature distribution above the glow plug	108

3.39	Temperature distribution in air above the glow plug comparing simulations and thermocouple measurements	108
3.40	Schlieren visualization of a single flame ignited at the glow plug	109
3.41	Schlieren visualization of a sequence of two flames ignited at the glow plug	110
3.42	Schlieren visualization of puffing behavior	111
3.43	Ignition behavior as function of Richardson number for varying initial pressure and equivalence ratio	112
4.1	Schlieren images of ignition and subsequent flame propagation in a mixture of hexane in air at atmospheric pressure ($\phi = 3.0$)	116
4.2	Direct imaging of CH* molecules through a bandpass filter ($\lambda_c = 460$ nm with FWHM 40 nm) and a short-pass filter (transmittance $> 75\%$ in the range of $\lambda = 430$ – 500 nm), $\phi = 3.0$	117
4.3	Transmission curve of the combined filter and CH* spectrum	119
4.4	Simulation results (density contours) for flame propagation phenomena at an equivalence ratio of $\phi = 2.5$. The black line represents the location of the flame front as marked by the iso-contour of the progress variable, $C = 0.15$	120
4.5	Diagrams of pool fire diameter and premixed flame diameter	122
4.6	Puffing frequency as a function of gravitational acceleration and pressure	124
4.7	Puffing period vs. horizontal flame propagation speed for n-hexane air mixtures from $\phi = 2.15$ – 3.0 , 7% and 8% hydrogen in air and hexane/hydrogen/air mixtures at atmospheric pressure	127
4.8	Flame propagation speeds of hydrogen-air, n-hexane-air, and hydrogen-n-hexane-air mixtures at atmospheric pressure	128
4.9	Radial velocity profile at 50 ms	130
4.10	Flow field and axial velocity	132
4.11	The vorticity production terms along the flame front and resulting vorticity at $t = 50$ ms	133
4.12	Gradients of density, pressure and the resulting baroclinic torque and overall vorticity along the flamefront at $t = 50$ ms associated with the incipient puff	135
4.13	Detailed vorticity distribution	135
4.14	Density as a function of radial location at different locations in the flame	136
4.15	Vorticity as a function of radial location at different locations in the flame	136
4.16	Axial velocity as a function of radial location at different locations in the flame	137

4.17	Radial velocity as a function of radial location at different locations in the flame	137
4.18	Flame propagation speed along the the flame front as a function of time	140
4.19	Inflow velocity along the the flame front as a function of time. Positive velocities mean flow going from unburned to burned side.	141
4.20	Inflow velocity and flame propagation velocity along the the flame front as a function of time showing the 10 Hz frequency observed in experiments and simulations	141
A.1	Beer's law diagram	160
A.2	Fuel detection experimental setup	162
A.3	Judson detector	162
A.4	Detector circuit	163
A.5	Raw fuel data from shot 19	164
B.1	Raw oxygen 2f data from shot 19	171
E.1	Ignition as a function of hot surface size.	189
F.1	Laminar burning velocity at room temperature and atmospheric pressure	192
F.2	Laminar burning velocity at 353 K and atmospheric pressure	193
F.3	Experimental flame propagation speed	193
F.4	Flame propagation speed at room temperature and atmospheric pressure	194
G.1	Plume temperature scaling and thermocouple measurements	199
H.1	Original thermodynamic data - c_p/R	201
H.2	New thermodynamic data - c_p/R	203
I.1	Experimental data from shot 13	210
I.2	Experimental data from shot 14	210
I.3	Experimental data from shot 16	211
I.4	Experimental data from shot 17	211
I.5	Experimental data from shot 19	212
I.6	Experimental data during the ignition event from shot 19	212
I.7	Experimental data from shot 20	213
I.8	Experimental data during the ignition event from shot 20	213
I.9	Experimental data from shot 21	214

I.10	Experimental data from shot 22	214
I.11	Experimental data from shot 23	215
I.12	Experimental data during the ignition event from shot 23	215
I.13	Experimental data from shot 24	216
I.14	Experimental data from shot 25	216
I.15	Experimental data from shot 26	217
I.16	Experimental data from shot 37	218
I.17	Experimental data from shot 40	218
I.18	Experimental data during the ignition event from shot 40	218
I.19	Picture of the hot surface ignition vessel experimental setup	219
J.1	Ignition locations observed in schlieren videos	227
J.2	Ignition locations observed in schlieren videos (continued)	228
J.3	Ignition locations observed in schlieren videos (continued)	229
K.1	Shot 6	231
K.2	Shot 7	232
K.3	Shot 8	233
K.4	Shot 9	234
K.5	Shot 10	235
K.6	Shot 15	236
K.7	Shot 17	237
K.8	Shot 17 montage	238
K.9	Shot 20	239
K.10	Shot 21	240
K.11	Shot 22	241
K.12	Shot 24	242
K.13	Shot 25	243
K.14	Shot 26	244
K.15	Shot 27	245
K.16	Shot 28	246
K.17	Shot 29	247
K.18	Shot 30	248

K.19	Shot 31	249
K.20	Shot 32	250
K.21	Shot 33	251
K.22	Shot 34	252
K.23	Shot 36	253
K.24	Shot 37	254
K.25	Shot 38	255
K.26	Shot 40	256
K.27	Shot 41	257
K.28	Shot 41 montage	258
K.29	Shot 42	259
K.30	Shot 42 montage	260
K.31	Shot 43	261
K.32	Shot 44	262
K.33	Shot 44 montage	263
K.34	Shot 45	264
K.35	Shot 45 montage	265
K.36	Shot 46	266
K.37	Shot 47	267
K.38	Shot 48	268
K.39	Shot 48 montage	269
K.40	Shot 49	270
K.41	Shot 49 montage	271
K.42	Shot 50	272
K.43	Shot 50 montage	273
K.44	Shot 51	274
K.45	Shot 52	275
K.46	Shot 54	276
K.47	Shot 54 montage	277
K.48	Shot 55	278
K.49	Shot 57	279
K.50	Shot 58	280

K.51	Shot 58 montage	281
K.52	Shot 60	282
K.53	Shot 60 montage	283
K.54	Shot 61	284
K.55	Shot 64	285
K.56	Shot 65	286
K.57	Shot 66	287
K.58	Shot 68	288
K.59	Shot 69	289
K.60	Shot 69 montage	290
K.61	Shot 70	291
K.62	Shot 73	292
K.63	Shot 76	293
K.64	Shot 76 montage	294
K.65	Shot 77	295
K.66	Shot 77 montage	296
K.67	Shot 80	297
K.68	Shot 80 montage	298
K.69	Shot 81	299
K.70	Shot 81 montage	300
K.71	Shot 85 (Note the drop of molten copper visible below the hot surface holder in the last two frames)	301
K.72	Shot 86	302
K.73	Shot 86 montage	303
K.74	Shot 87	304
K.75	Shot 87 montage	305
K.76	Shot 90	306
K.77	Shot 90 montage	307
K.78	Shot 91	308
K.79	Shot 91 montage	309
K.80	Shot 92	310
K.81	Shot 93	311

K.82	Shot 94	312
K.83	Shot 97	313
K.84	Shot 98	314
K.85	Shot 98 montage	315
K.86	Shot 100	316
K.87	Shot 100 montage	317
K.88	Shot 101	318
K.89	Shot 101 montage	319
K.90	Shot 102	320
K.91	Shot 103	321
K.92	Shot 103 montage	322
K.93	Shot 104	323
K.94	Shot 104 montage	324
K.95	Shot 110	325
K.96	Shot 110 montage	326
K.97	Shot 112	327
K.98	Shot 112 montage	328
K.99	Shot 115	329
K.100	Shot 116	330
K.101	Shot 117	331
K.102	Shot 118	332
K.103	Shot 118 montage	333
K.104	Shot 119	334
K.105	Shot 119 montage	335
K.106	Shot 121	336
K.107	Shot 122	337
K.108	Shot 123	338
K.109	Shot 123 montage	339
L.1	Color schlieren images from shot 28	342
L.2	Color schlieren images from shot 30	342
L.3	Color schlieren images from shot 33	342
L.4	Color schlieren images from shot 34	343

L.5	Color schlieren images from shot 36	343
L.6	Color schlieren images from shot 41	343
L.7	Color schlieren images from shot 42	344
L.8	Color schlieren images from shot 45	345
M.1	Experimental data from shot 7	348
M.2	Experimental data from shot 8	348
M.3	Experimental data from shot 9	349
M.4	Experimental data from shot 10	349
M.5	Experimental data from shot 11	350
M.6	Experimental data from shot 12	350
M.7	Experimental data from shot 15	351
M.8	Experimental data from shot 17	351
M.9	Experimental data from shot 20	352
M.10	Experimental data from shot 21	352
M.11	Experimental data from shot 22	353
M.12	Experimental data from shot 23	353
M.13	Experimental data from shot 24	354
M.14	Experimental data from shot 25	354
M.15	Experimental data from shot 26	355
M.16	Experimental data from shot 28	355
M.17	Experimental data from shot 28	356
M.18	Experimental data from shot 29	356
M.19	Experimental data from shot 30	357
M.20	Experimental data from shot 31	357
M.21	Experimental data from shot 32	358
M.22	Experimental data from shot 33	358
M.23	Experimental data from shot 34	359
M.24	Experimental data from shot 36	359
M.25	Experimental data from shot 37	360
M.26	Experimental data from shot 38	360
M.27	Experimental data from shot 40	361
M.28	Experimental data from shot 41	361

M.29	Experimental data from shot 42	362
M.30	Experimental data from shot 43	362
M.31	Experimental data from shot 44	363
M.32	Experimental data from shot 45	363
M.33	Experimental data from shot 46	364
M.34	Experimental data from shot 47	364
M.35	Experimental data from shot 49	365
M.36	Experimental data from shot 50	365
M.37	Experimental data from shot 51	366
M.38	Experimental data from shot 54	366
M.39	Experimental data from shot 55	367
M.40	Experimental data from shot 57	367
M.41	Experimental data from shot 58	368
M.42	Experimental data from shot 61	368
M.43	Experimental data from shot 64	369
M.44	Experimental data from shot 65	369
M.45	Experimental data from shot 68	370
M.46	Experimental data from shot 69	370
M.47	Experimental data from shot 70	371
M.48	Experimental data from shot 85	371
M.49	Experimental data from shot 86	372
M.50	Experimental data from shot 87	372
M.51	Experimental data from shot 90	373
M.52	Experimental data from shot 91	373
M.53	Experimental data from shot 92	374
M.54	Experimental data from shot 93	374
M.55	Experimental data from shot 94	375
M.56	Experimental data from shot 95	375
M.57	Experimental data from shot 96	376
M.58	Experimental data from shot 97	376
M.59	Experimental data from shot 98	377
M.60	Experimental data from shot 100	377

M.61	Experimental data from shot 101	378
M.62	Experimental data from shot 102	378
M.63	Experimental data from shot 103	379
M.64	Experimental data from shot 104	379
M.65	Experimental data from shot 115	380
M.66	Experimental data from shot 116	380
M.67	Experimental data from shot 117	381
M.68	Experimental data from shot 118	381
M.69	Experimental data from shot 119	382
M.70	Experimental data from shot 121	382
M.71	Experimental data from shot 122	383
M.72	Experimental data from shot 123	383

List of Tables

1.1	Selected minimum auto-ignition temperatures (AIT) at one atmosphere from Kuchta (1985) and CRC (1983)	7
2.1	Nomenclature	42
2.2	Parameters used in modeling of hexane-air auto-ignition	44
3.1	Parameters used in modeling of hexane-air hot surface ignition	86
4.1	Puffing behavior for fuel-rich hexane air mixture ($\phi = 3.0$)	121
A.1	Uncertainty in fuel concentration measurements	161
A.2	Absorption cross sections	165
C.1	Nomenclature	173
C.2	Additional nomenclature	174
F.1	Laminar burning velocity (S_l) for n -hexane and n -heptane at atmospheric pressure ($P_0 = 101$ kPa)	195
F.2	Expansion ratio for n -hexane and n -heptane at atmospheric pressure ($P_0 = 101$ kPa), room temperature ($T_u = 300$ K) computed using the thermodynamic data from the Ramirez mechanism (Ramirez et al., 2011)	196
I.1	Heated vessel experiments	209
I.2	Hot surface experiments (n -hexane, Bosch glow plug)	220
I.3	Hot surface experiments (n -hexane, Bosch glow plug, continued)	221
I.4	Hot surface experiments (n -hexane, Autolite glow plug)	222
I.5	Hot surface experiments (n -heptane, Autolite glow plug)	223
I.6	Spark ignition experiments (n -hexane)	223
I.7	Hot surface experiments (n -hexane, Autolite glow plug, large vessel)	224

I.8	Hot surface experiments (<i>n</i> -hexane, varying hot surface, 2 liter vessel)	224
I.9	Hot surface experiments (hydrogen, Autolite glow plug, small vessel)	225
I.10	Hot surface experiments (hydrogen-hexane-air mixtures, Autolite glow plug, small vessel)	225

This page intentionally left blank.

Chapter 1

Introduction

1.1 Motivation

Accidental ignition of flammable gases is a critical safety concern in many industrial applications. Particularly in the aviation industry, the main areas of concern on an aircraft are the fuel tank and adjoining regions, where spilled fuel has a high likelihood of creating a flammable mixture. To this end, a fundamental understanding of the ignition phenomenon is necessary in order to develop more accurate test methods and standards as a means of designing safer air vehicles.

Following the TWA 800 accident on July 17, 1996, the National Transportation Safety Board (NTSB) investigated the fuel tank flammability and fuel tank ignition sources (NTSB, 2000). The results of investigation led the NTSB to recommend that the FAA find a means to eliminate flammable mixtures in the fuel tanks. In 2008, the FAA created a requirement to install an inerting system to eliminate flammability, particularly for heated center fuel tanks by reducing the oxygen content below 12%. As part of the NTSB investigation, several research projects were carried out at the Explosion Dynamics Laboratory at California Institute of Technology including: “Flash Point and Chemical Composition of Aviation Kerosene (Jet A)” (Shepherd et al., 1999), Spark Ignition Energy Measurements in Jet A (Shepherd et al., 1997). While not directly addressed in the final FAA rule-making, the reduction or elimination of possible ignition sources is an essential part of engineering design practices for aircraft and industries with flammability hazards. In this regard, Shepherd et al. (1997) investigated the required ignition energy for Jet A, while Bane et al. (2011) showed that kerosene mixtures have comparable minimum ignition energy to the lean hydrogen mixtures used for certification. The lean hydrogen mixtures were assumed to have lower ignition energies and thus using them as test mixtures would have an inherent safety margin. In light of the findings by Bane et al. (2011) we were motivated to investigate the test standards currently in use for thermal

ignition, i.e., in heated vessel or by hot surfaces. There are of course other potential ignition sources such as open flames, electrical streamer discharges, hot and burning particles, but these were not the focus of this study.

For safety aspects, several different temperatures are important for the characterization of a particular fuel. Colwell and Reza (2005) describe how the temperature required for ignition increases given the situation. For example, the flash point is the temperature above which a pool of liquid fuel has sufficient vapor pressure to be ignited by a pilot flame (ASTM, 2010). The flash point of Jet A lies in the range of 43–66 °C (Colwell and Reza, 2005, CRC, 1983, NFPA 325, 1994). If we were to take the flash point as a general upper bound for any design temperature, we would be unable to boil water for coffee or tea on an aircraft. This, of course, is not the case since no open flame is present near the fuel tank, by design.

For ignition from hot elements, the particular quantity of interest is the temperature that leads to ignition of a flammable atmosphere without a flame present. A measure of this temperature is defined as the auto-ignition temperature. The auto-ignition temperature standard test is to inject a fuel into a heated vessel and determine by visual inspection if ignition has occurred within 10 minutes (ASTM, 2005). For many applications, the auto-ignition temperature determined from this standard test is what is then used to define limiting (highest) temperature of hot surfaces in region where flammable vapor may be present. However, this test has many limitations, which are explored in the following chapters. The flame propagation resulting from an ignition of a premixed fuel-air mixture determines the pressure rise and thus potential structural damage resulting from an accidental ignition, and must also be considered. The ignition process is a complicated interaction of chemical heat release, encompassing the competition between chain branching and terminating reactions, heat transfer into and out of the system, and fluid mechanics. To mitigate the risk of accidental explosions in industrial facilities and on aircraft in the aviation industry, the mechanisms and parameters leading to ignition must be investigated. The ultimate goal is to use our better understanding of the thermal ignition process and auto-ignition tests to further improve the safety of aviation and other industrial systems operating with flammable mixtures.

1.2 Background

Seminal work in the area of ignition by hot surfaces was done by Davy (1817) while investigating explosions in coal mines (Babrauskas, 2003). Davy describes a common way of lighting the mines as:

“a steel wheel, which, being made to revolve in contact with flint, affords a succession of sparks: but this apparatus always requires a person to work it; and, though much less liable to explode the fire-damp than a common candle, yet it is said to be not entirely free from danger.”

In his experiments, Davy was unable to ignite a combustible coal gas (firedamp) mixture with a hot iron rod, unless the iron rod itself is burning. The first explanation of this effect (Babrauskas, 2003) was given by Mallard and Le Chatelier in 1880. They concluded that a sufficiently long time is necessary for the gas to stay in contact with the hot surface in order for the mixture to ignite.

Thornton (1919) was among the first to perform experiments on the current required to ignite various gaseous mixtures by electrical wire, with particular focus on the hazard that arises from broken light bulbs in coal mines. In this work, measurements were performed at elevated pressures using water to compress the gas, and it was concluded that ignition by hot wires is independent of pressure, but changes with wire diameter. These experiments, however, are incomparable to the atmospheric tests since the absorption into the water and water vapor content are not accounted for.

In 1927, Coward and Guest investigated the ignition of natural gas and air mixtures by heated nickel bars of varying size, composition, hot surface material, and flow velocity above the hot surface. The work concluded that the ignition temperature depends on the mixture composition, but an explanation was not provided. Coward and Guest observed that wider heated bars reduce the temperature required for ignition, and that flow over hot surface, created by a fan, could either decrease or increase the ignition temperature depending on the speed.

Scott et al. (1948) used an early version of the auto-ignition test apparatus, which would later become the ASTM E 659 test shown in Figure 1.1. Experimental auto-ignition temperatures are given for a multitude of compounds as part of the experiments at the Bureau of Mines in Pittsburgh, PA.

The Bureau of Mines continued their work, which was published in part in Zabetakis et al. (1954) and Kuchta et al. (1965), performing a wide range of experiments on auto-ignition and hot surfaces using a variety of fuels. In these investigations, experiments were conducted to test the effect


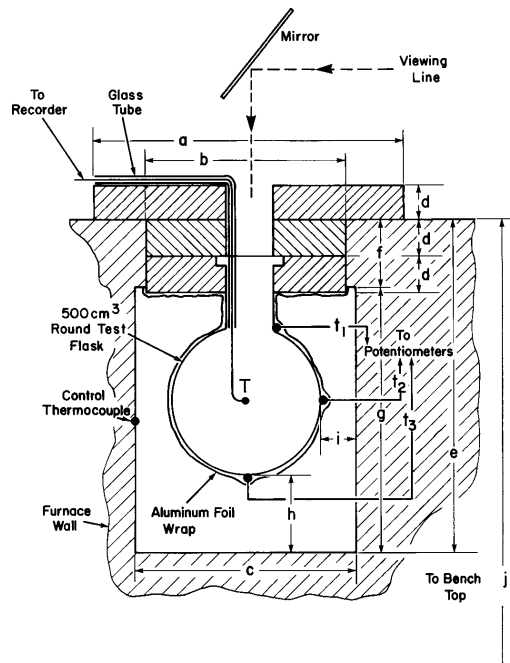

E 659 – 78 (2005)


Figure 1.1: ASTM E 659 auto-ignition temperature apparatus (reprinted, with permission, from ASTM (2005), copyright ASTM International)

of surface area and volume on auto-ignition in quiescent mixtures, with the work on hot surfaces performed in a slow flowing reactor. The results of these efforts included a scaling relationship for the ignition temperature as a function of the natural logarithm of the (hot) surface area as shown in Figure 1.2. However, the effects of the surface geometry or orientation are not considered, and consequently the scaling laws extrapolated from theory developed by Semenov (1940) only hold for a limited range of hot surface areas.

The graph reproduced in Figure 1.2 is also found in Babrauskas (2003) without the data points. While the trends developed by Semenov (1940) are supported by this data, the broad application of this work should be taken very cautiously as the control over composition and flow velocity are very limited.

We separate the investigation of thermal ignition into the goal of finding the lowest possible temperature at which a gaseous mixture will ignite, i.e., auto-ignition, and the required temperature for less favorable geometries such as isolated hot surfaces.

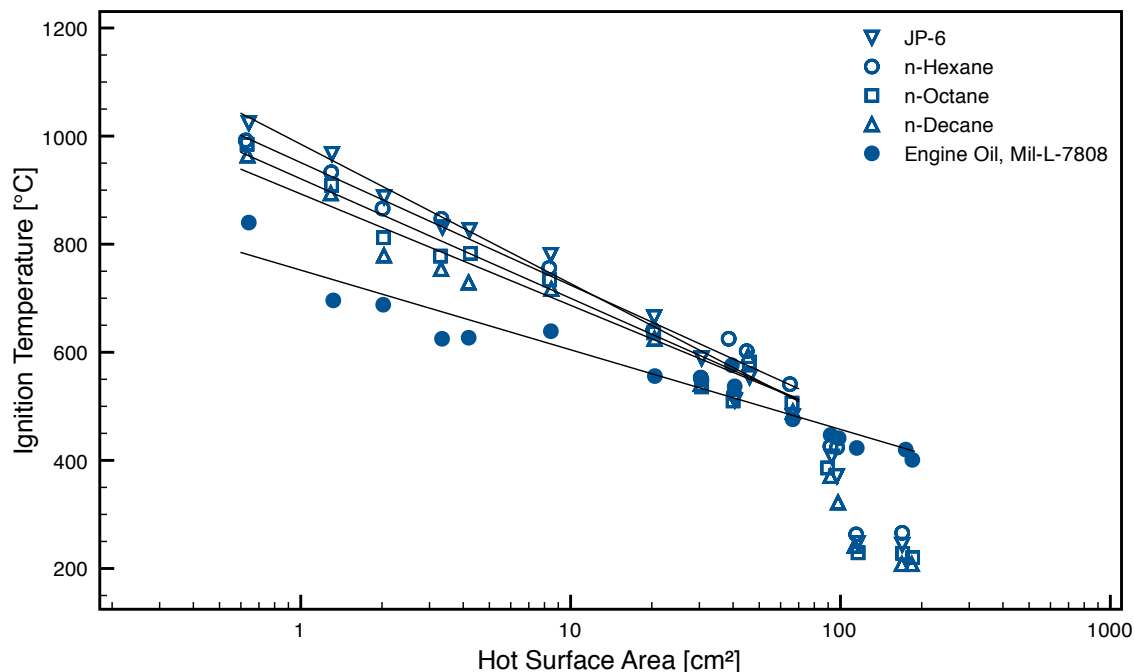


Figure 1.2: Ignition as a function of hot surface size (reproduced from Kuchta et al., 1965)

1.2.1 Thermal Ignition in a Heated Vessel — Auto-Ignition

Ignition is the process of initializing an exothermic chemical reaction that can lead to a propagating flame or detonation. Ignition can occur through the generation of highly reactive species (radicals), whose production rate is in competition with their destruction rate, as well as the competition of chemical heat release and heat loss to walls, which determines the mixture temperature and thus the reaction rates. In general, combustion of hydrocarbon fuels is separated into slow reaction, cool flames, and ignition regimes based on pressure and temperature (Glassman, 2008, Pilling, 1997).

Slow reactions occur when fuel is in contact with an oxidizer at temperatures below the ignition temperature (Babrauskas, 2003). The fuel and oxidizer react, but do so without a rapid increase in pressure, and the heat released by the oxidation is lost to the environment. Since the reaction rate is a strong function of temperature, these reactions will not take place at a temperature far below the ignition temperature (Babrauskas, 2003).

Cool flames occur at temperatures higher than slow reaction and below the ignition temperatures (Babrauskas, 2003). This lower temperature leads the reaction down a different path, creating peroxides as reaction products, which are only partially oxidized and thus release less energy than if the reaction had gone to completion (e.g., CO_2 and H_2O for hydrocarbon oxygen reac-

tions) (Babrauskas, 2003). The resulting flames have a pale blue color, and can exhibit oscillatory behavior (Yang and Gray, 1969). Townend et al. (1934) were the first to map at what temperatures and pressures ignition and cool flames of hexane air mixtures occur.

From a chemical reaction perspective, ignition is characterized by a “rate of chain carrier generation exceeding the chain termination reaction” - or in other words, a runaway reaction (Glassman, 2008). In this case, the reaction releases energy and thus speeds up the reaction rate if that energy cannot be lost to environment at a sufficiently fast rate. The reaction then leads to a pressure and temperature rise until the reactants are consumed.

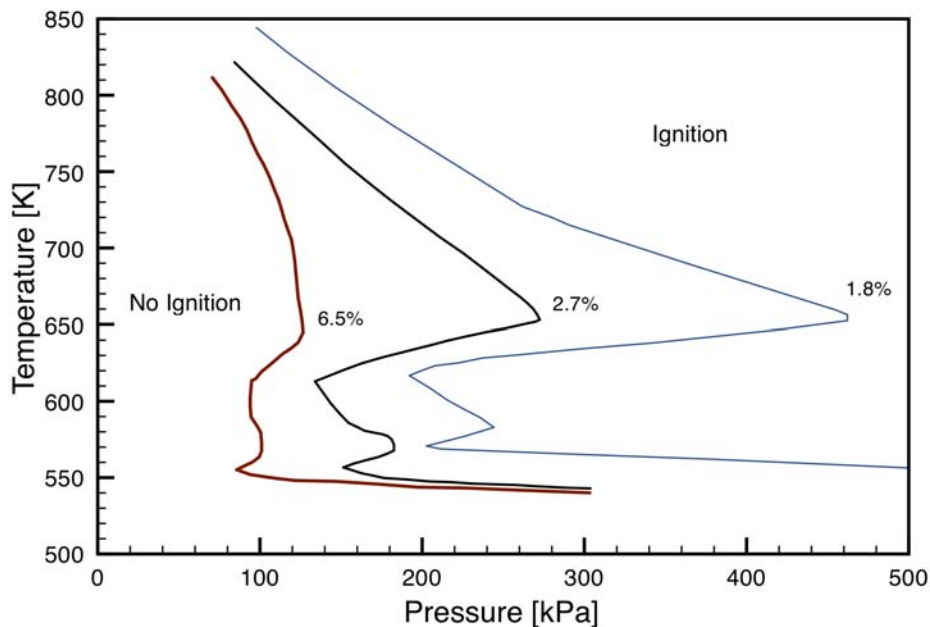


Figure 1.3: Regions of ignition as a function of temperature and pressure for *n*-hexane for several molar concentrations of *n*-hexane in air (Townend et al., 1934) (Figure adapted from Babrauskas, 2003)

A classical view of how ignition, nonignition and cool flames are separated as function of temperature and pressure is given for *n*-hexane as shown in Figure 1.3 (Townend et al., 1934). At low temperature and low pressure some radical species may be formed. Due to the low pressure, the diffusivity is high and they recombine into stable species at wall, which means that testing vessels of different material can have different explosion limits (Warnatz et al., 2006).

The auto-ignition temperature is not a universal quantity and depends on the substance and molecular structure of the fuel as well as the oxidizer and whether or not any diluent are present, e.g., the nitrogen in air. For this investigation, we are interested in fuels like hexane that have comparable auto-ignition temperatures to aviation kerosene (see Table 1.1). The combustion characteristics

and path of pure substances are far more easy to characterize than those of complex hydrocarbon fuels such as Jet A, which consists of many different species of paraffins, iso-paraffins, aromatics, naphthenes, and olefins (Shepherd et al., 1999).

Table 1.1: Selected minimum auto-ignition temperatures (AIT) at one atmosphere from Kuchta (1985) and CRC (1983)

Fuel	AIT [°C]	
	in air	in oxygen
Hydrogen	520	~400
Methane	630	500
Propane	450	N/A
<i>n</i> -Hexane	225	220
Gasoline (100/130)	440	315
Kerosene	230	215
Turbine Fuel	238	N/A

While the ASTM E659 is a standard test for the auto-ignition temperature, only the minimum temperature for ignition at atmospheric pressure is investigated (ASTM, 2005, Colwell and Reza, 2005, Pilling, 1997). The specific mixture composition is not controlled because liquid test fuel is injected directly into an open heated vessel. The contents are not actively mixed, and it is presumed that “a considerable range of composition exist within pockets of gas in the vessel as evaporation of liquid fuel, or mixing of the injected gaseous fuel, occurs” (Pilling, 1997).

In prior laboratory research, the combustion products have either been condensed and the liquid analyzed later (Bailey and Norrish, 1952), or a gas chromatograph was used to analyze a small sample at a maximum frequency of about 0.1 Hz (Wilk et al., 1986). Additional work was done in rapid compression machines at higher temperatures, 600–800 K (Griffiths et al., 1993), and gas sampling techniques (Ribaucour et al., 1992, Vanhove et al., 2006). While pressure transients are easily captured in these experiments, fast and accurate fuel concentration measurements requiring optical techniques have never previously been applied to the auto-ignition phenomenon.

The present work includes tests conducted using hexane as a surrogate for kerosene, with the experimental setup addressing problem of the control over gas composition, allowing for testing at varying pressures, and precise control over the heating rate, which has been identified as an important factor (Mason and Wheeler, 1922). Additionally, the current study allows for continuous measurements of the fuel concentration.

1.2.2 Thermal Ignition from a Concentrated Hot Surface

Isolated hot surfaces surrounded by a flammable mixture such as a pipe carrying hot gas in a flammable leakage zone in an aircraft or the overheating of a failing device, are potential ignition sources. For design purposes, it is important to understand the dependence of the ignition temperature on hot surface size and geometry since limiting space restrictions may lead to unfeasible design solutions. While, standardized tests exist to evaluate various properties of fuels, including the ASTM E659 (ASTM, 2005) for auto-ignition temperature of fuels, and the ASTM D56 (ASTM, 2010) for flash point, no standard test exists for hot surface ignition (Smyth and Bryner, 1997).

As mentioned before, Coward and Guest (1927) investigated hot surface ignition of natural gas-air mixture by various heated metal surfaces, but the control over the flow velocity at the hot surface and visual observations were limited. Platinum surfaces were found to be catalytic, but the ignition temperatures were higher than those of noncatalytic nickel. Kuchta et al. (1965) extended the work at the Bureau of Mines, varying the size and geometry of the hot surfaces, but with limited control over the composition and flow over the hot surface. The hot surface of interest is heated to a given temperature inside a flow reactor and then a mixture of fuel and air is passed over it at a specified flow rate. However, the exact mixture composition is unknown and the flow velocity at the hot surface can only be roughly estimated based on the overall flow rate and vessel size.

Gray (1970) analytically investigated the effect of surface area to volume ratio. The work follows the work of Kuchta et al. (1965) and White (1967) who concluded from experimental data that increasing the surface area in a fuel tank, e.g., by inserting metal honeycomb, increases the safety. Gray pointed to the negative temperature coefficient behavior of larger hydrocarbon as an alternate source for the behavior.

Ono et al. (1976) studied the ignition of stoichiometric mixtures of methane, propane, ethyl-alcohol, and diethylether in air by a vertical hot plate inside a combustion vessel. Measurements of the flow velocity were performed by particle image velocimetry. The choice of geometry is quite useful in comparisons with simulations and analytical models for flow along a heated vertical plate (Tritton, 1988). The temperature of the hot surface is initially kept at a temperature just below the ignition temperature and then raised to initiate ignition. As mentioned earlier, slow reactions can take place at temperatures just below the ignition temperature and change the composition of the mixture.

Laurendeau (1982) performed a wide literature review of available hot surface ignition data for various hydrocarbon fuels, particularly methane. The data collected was used to derive a simple correlation relating the ignition temperature to various parameters. Also taken into account in

the model is the flow outside the hot surface, such as stagnant, free, and forced convection. The value of this model is to give general trends of the ignition temperature, but does not provide accurate numerical values. Laurendeau points out that detailed information about the experiments and application are necessary to make accurate comparisons, including the surface size, orientation, geometry, mixture composition, and temperature history leading to ignition.

Kumar (1989) focused his experiments on hydrogen-oxygen-diluent mixtures. The combustion of hydrogen differs from that of hydrocarbon fuel. In addition, its high diffusivity will change the hot surface ignition characteristics relative to hydrocarbon fuels, which must be kept in mind when comparing the results of ignition experiments and simulations. It is still very relevant for many applications including loss-of-cooling events in nuclear power plant like Fukushima–Daiichi on March 11, 2011.

Kumar also developed a model of solving the transport and energy conservation equation using an explicit scheme, that requires very small time steps down to 1 ns for accurate solutions. The equations describe the ignition from a hot surface in one dimensional unsteady condition with the gas at temperature below the hot surface temperature and the chemistry uses a reduced mechanism for hydrogen-oxygen-diluent combustion. In the experiments and simulations, the effects of pressure, mixture concentration, diluent, and initial gas temperature were investigated with relatively good agreement for most parameters.

In an effort to create a standardized test for hot surface ignition, Smyth and Bryner (1997) at the National Institute of Standards and Technology (NIST) performed a large number of experiments testing the temperature required for ignition of a gas mixture flowing over a heated metal foil. In this work, the foil was placed at 45° for a constant residence time of 150 ms, and a wide variety of fuels and hot surface materials were examined. From the results given in their study, the temperature are higher than even those of Kuchta et al. (1965) at comparable surface size, which would indicate that the residence time was too short to activate any low temperature chemistry. Additionally, the geometry chosen for the experiment is very difficult to reproduce computationally (Shepherd, 2012).

Babrauskas (2003) points out that hot surface ignition can be investigated in a similar manner to the auto-ignition tests, where no uniform heating eliminates convection. For hot surfaces, this could be achieved by placing the hot surface at the top of the vessel and thus stably stratifying the mixture, however, no such experiments have been performed.

1.2.3 Hot Surface Ignition of Liquid Fuels

A special type of hot surface ignition is ignition of liquid fuel droplet by hot surfaces. This process is significantly more complex due to the breakup of droplet, evaporation of the fuel and mixing with the air necessary to create a flammable mixture. However, the connection to the work presented here is clear and thus worth mentioning. In 2005, Colwell and Reza performed a large number of tests using droplets of fuel impinging a hot surface and evaluating the ignition probability as a function of temperature. While the work included a thorough review of thermal ignition testing on available data, an extrapolation of their results to the fundamental physical and chemical processes leading to hot surface ignition is difficult. The complexity of the experiments performed is too great to use analytical models or even perform simulations and a statistical approach is taken to characterize the likelihood of ignition as a function of temperature. A thorough literature review of ignition of liquid droplets was done by Bennett (2001).

In this study, we explore the conditions leading to ignition and compare these to high quality computational results. Our goal is to develop sufficiently realistic and detailed models so that these ignition thresholds and ignition transients can be accurately predicted.

1.2.4 Cyclic Flame Propagation in Premixed Combustion

The process of thermal ignition of a flammable mixture by a hot-surface and the subsequent flame propagation is important to the fundamental understanding of combustion, as well as industrial safety applications. Flame instabilities are of particular interest since they can affect the flame propagation speed and increasing the flame surface area and accelerating the flame speed. This chapter focuses on a global flame instability, i.e., a flickering or puffing flame, rather than small scale instabilities at the flame front.

Flames propagating with a flickering or puffing behavior with frequencies around 10 Hz have been discussed since the First International Symposium on Combustion in September 1928 (Chamberlin and Rose, 1948). Chamberlin and Rose were among the first to make quantitative measurements of the oscillation frequencies observed in Bunsen burners. For a range of gases (e.g., natural gas, hydrogen, carbon monoxide, butane, and ethane), the rate of flame oscillations was observed to be “on the order of 10 per second”. The oscillations were quantified by tracking the tip location of the flame. Chamberlin and Rose observed that frequency changed with the size of the injection nozzle, and the origin of the flicker was attributed to an alternating rate of diffusion of oxygen into the flame

The oscillation of non-premixed gaseous flames have since then been investigated experimentally by Kimura (1965), Toong et al. (1965), Durao and Whitelaw (1974), Grant and Jones (1975), Strawa and Cantwell (1989) and Durox et al. (1996).

Kimura (1965) investigated propane jet flames, which exhibited periodic oscillations (10–15 Hz) above a critical injection velocity. Premixing the propane with air suppressed these oscillations. After investigating the temperature and velocity profile, he concludes that the oscillations are caused by the instability of the laminar jet flow.

Toong et al. (1965) observed these instabilities for flames created by burning liquid fuel at the end of a probe in air to simulate droplet combustion. They postulate that “it is quite likely that the onset of the self-sustained flame oscillations is due to the amplification of the Tollmien-Schlichting waves, in the region where the Reynolds Number is greater than the critical value.” However, Grant and Jones (1975) argue that based on their experiments and those of Durao and Whitelaw (1974), linear stability theory is insufficient in explaining how the frequency is invariant over a large range of parameters.

The jet injection velocity was substantially reduced in the experiments conducted by Durox et al. (1996). In fact, in their theoretical analysis the injection velocity is assumed to be negligible and the flame instability is attributed to a shear layer created by the buoyancy induced velocity on the flow behind the flame front. In their study, the effect of pressure and gravitational acceleration were tested by performing the experiment on parabolic flights that created microgravity as well as maximum accelerations of 1.8 *g*.

Buckmaster and Peters (1988) have carried a theoretical analysis of the oscillations associated with a infinite candle. Similar oscillations have also been observed in fires above pools of liquid fuels (Cetegen and Ahmed, 1993) and in room fires (Zukoski, 1986).

These oscillations are not limited to non-premixed flames, but also occur in premixed flames as shown by Durox et al. (1990), Cheng et al. (1999), Shepherd et al. (2005), Guahk et al. (2009), and Tanoue et al. (2010). In these studies, the frequency of the instability is again on the order of 10 Hz. In all of these previous experiments of premixed flames, the gaseous mixture was injected into the burner at a specific injection velocity.

Durox et al. (1990) also performed experiments on parabolic flights of premixed flames to study the effect of varying gravitational acceleration. Additional data is given for the variation of the oscillation frequency as a function of injection velocity (1.45–2.4 m/s), pressure, and equivalence ratio.

Cheng et al. (1999) studied the effects of buoyancy on premixed “V-flames” by considering both gravitation acceleration in the direction of injection and opposed to it. The results were considered as a function of Richardson number, the ratio of inertia to buoyancy force, but “findings point to the need to include both upstream and downstream contributions in theoretical analysis of flame turbulence interactions.”

Guahk et al. (2009) investigated the oscillations of conical flames and inverted conical flames. They describe the oscillations as a flame-intrinsic Kelvin-Helmholtz instability.

A combined experimental and numerical approach was taken by Shepherd et al. (2005), who injected a methane-air mixture at 0.73 m/s. The analysis showed that the “flame tip oscillation is caused by a competition between the pressure fields associated with the predominantly radial motion of the burnt gases near the flame front and the rotating vortex motion.”

Tanoue et al. (2010) measured the temperature distribution of a premixed methane flame injected at 2 m/s and attribute the instability to a Kelvin-Helmholtz instability.

The experiments and simulations investigated in the present study use a very different configuration than the previous work. Instead of studying jets, a combustible mixture, which is quiescent prior to ignition is examined. The puffing phenomenon occurs in a closed vessel that is filled entirely with a homogeneous combustible mixture and then ignited by a hot surface.

1.3 Thesis Outline

Results from studies on heated vessels subjected to ramp heating are presented in Chapter 2, hot surface ignition in Chapter 3, and premixed puffing flames in Chapter 4. Chapter 2 describes the experimental setup, with additional background for the diagnostic techniques presented in Appendix A and B. Experimental results are presented and discussed here with a complete list of experiments performed given in Appendix I. Additional detail of the theoretical analysis is given in Appendix C and D. Some of the thermodynamic data used in the chemical mechanism was treated for discontinuities as described in Appendix H. Chapter 3 details the dependence of ignition temperature with mixture composition and resulting flame propagation with additional literature and tabular data available in Appendix F. Experimental data and still images are available in Appendix I.2, with color images shown in Appendix L. The puffing phenomenon is described in detail in Chapter 4 with some additional scaling arguments given in Appendix G.

Chapter 2

Thermal Ignition of Gaseous Fuel-Air Mixtures Within a Slowly Heated Vessel ¹

2.1 Introduction

As discussed in Chapter 1, a better understanding of thermal ignition, specifically auto-ignition, is important for safety regulations and engineering design. While a standard test for the auto-ignition temperature, the ASTM (2005), exists, only the minimum temperature for ignition at atmospheric pressure is investigated for a given geometry and size. Additionally, the specific mixture composition is neither controlled nor measured as the liquid test fuel is injected into a heated open vessel. The contents are not actively mixed and it is presumed that a considerable range of composition exists within pockets of gas in the vessel as evaporation of liquid fuel occurs (Pilling, 1997).

Our approach in this study was to precisely control the composition of the gas mixture allowing for comparison with numerical models, while monitoring the temperature and pressure as well as the fuel concentration. Through accurate control of the heating rate, its effect on the combustion can also be studied. Hexane was selected as a test fuel. It has a similar auto-ignition temperature of 498 K (Kuchta et al., 1965, Kuchta, 1985) to kerosene and is comparable to jet fuel or turbine fuel (CRC, 1983, Colwell and Reza, 2005) at 511 K. Additionally, Hexane is easy to handle in liquid form but vaporizes readily, and detailed chemical reaction mechanisms are available.

An extension of the classical Semenov theory (Semenov, 1940), described later in this chapter, can be used to model the auto-ignition process in a closed vessel that is slowly heated from ambient

¹The work in this chapter has been published in large part in Boettcher, P. A., Mével, R., Thomas, V. and Shepherd, J. E. The effect of heating rates on low temperature hexane air combustion. *Fuel* (2012), doi:10.1016/j.fuel.2011.12.044

conditions. This model of the reactor can be used with either a detailed chemical mechanism that fully represents the complex chemistry of *n*-hexane or with a one-step model that is more easily understood analytically. Both approaches are presented in this chapter. The experimental and computational results are compared and a detailed analysis is given of the role of heat transfer and reactant consumption on the progress of the explosion.

2.2 Experiments

2.2.1 Experimental Setup

The test vessel (Figure 2.1) is a closed 400 mL Pyrex cell (surface to volume ratio $\approx 0.85 \text{ cm}^{-1}$). Prior to each experiment, the test cell is evacuated to less than 10 Pa. The vessel is then filled with *n*-hexane, nitrogen, and oxygen using the partial pressure method, then thoroughly mixed by a circulation pump. Hexane is injected as a liquid through a septum at a partial pressure below its vapor pressure. This ensures complete vaporization. The uncertainty in composition is due to the accuracy $\pm 0.01 \text{ kPa}$ of the pressure measurement. Two sapphire windows are spaced 9 cm apart, providing optical access for the laser measurement. The vessel is suspended inside an aluminum shell with an air gap of approximately 3 mm, and the shell is heated by two band heaters rated at a total of 800 W. The temperature inside the vessel is measured by a K-type thermocouple that has been coated with silica in order to avoid catalytic effects. During the experiment, transient pressure is measured with a separate fast-response static pressure gage ($\geq 10 \text{ kHz}$). The final heating rate is computed from the pressure measurements using the values before the onset of the reaction. Assuming no change in moles, using the ideal gas law, the heating rate can be computed from the pressure trace using

$$\frac{dT}{dt} = \frac{V}{n\tilde{R}} \frac{dP}{dt} . \quad (2.1)$$

This method is preferred over measurements using thermocouples because the response time of the pressure transducer is much shorter than that of the thermocouple. The data is directly analyzed and averaged giving an effective sampling rate of 8 Hz. When a specified drop in fuel concentration is detected, a second data acquisition board is triggered that stores data at 150 kHz during a rapid ignition event.

Experiments were performed at three total pressures: 26, 67, and 101 kPa, three equivalence ratios, ϕ : 0.6, 1, and 1.2, and heating rates between 4 K/min and 14 K/min.

The fuel concentration is measured by direct absorption (Klingbeil et al., 2006, Drallmeier, 2003).

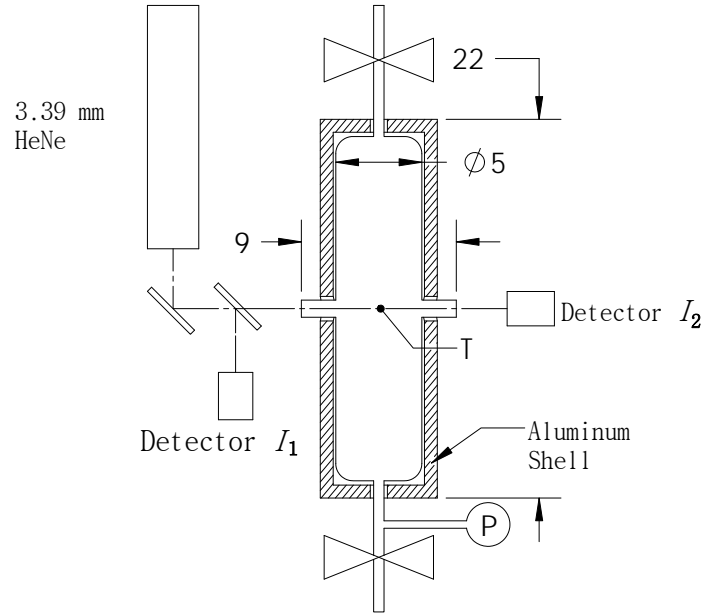


Figure 2.1: Schematic of the experimental setup (all dimensions are in cm)

A commercially available $3.39 \mu\text{m}$ HeNe laser is passed through a chopper running at 300 Hz. The beam is split two ways before entering the test cell through a 0.5 mm thin sapphire window. The main beam passes through the test cell and is measured by a detector on the other side, while the second beam is sent to a reference detector to correct for variations in the initial laser intensity. High angles of incidence ($\sim 10^\circ$) were used to avoid intensity changes due to interference effects from the windows caused by thermal expansion since internal reflections are scattered through a wider angle.

The n -hexane mole fraction is calculated from the detected laser transmission using Beer's law. The C-H bond in any hydrocarbon molecule absorbs at the $3.39 \mu\text{m}$ wavelength; changes from n -hexane into other hydrocarbon molecules other than C_1 species cannot be detected Mével et al. (2012). Thus, an equivalent n -hexane mole fraction, $X_{\text{C}_6\text{H}_{14}}^*$, is calculated based on the absorption cross section of n -hexane, which is found through separate calibration experiments to be $\sigma_\nu = 38 \pm 1 \text{ m}^2/\text{mole}$. This value is in agreement with values from the literature (Jaynes and Beam found $45 \text{ m}^2/\text{mole}$ (Jaynes and Beam, 1969), Drallmeier $38.5 \pm 2 \text{ m}^2/\text{mole}$ (Drallmeier, 2003, Klingbeil et al., 2006), Tsuboi et al. $36.2 \pm 7 \text{ m}^2/\text{mole}$ (Tsuboi et al., 1985, Klingbeil et al., 2006)). Further measurements have been performed by Mével et al. (2012) that show that the absorption cross section is constant for hexane from 303–413 K and the value can thus be assumed to be constant. The intensity changes are related to the equivalent partial pressure of fuel, P_{fuel}^* , via Beer's Law,

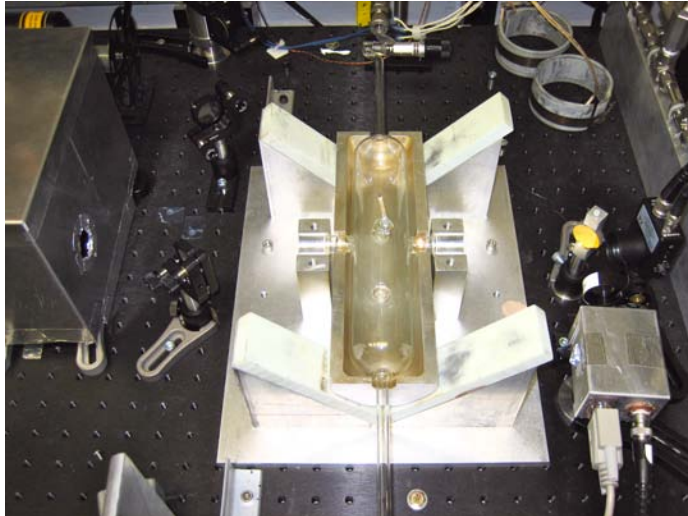


Figure 2.2: Pictures of the heated experimental vessel setup

$$\frac{I}{I_0} = \exp\left(-\frac{\sigma_\nu P_{fuel}^* L}{\tilde{R}T}\right), \quad (2.2)$$

where I is the laser intensity signal, I_0 is the signal intensity without any absorbing species present, σ_ν is the absorption cross section, L is the path length, \tilde{R} is the universal gas constant, and T is the temperature.

As described above only an equivalent partial pressure of fuel or equivalent hexane mole fraction can be measured with this technique. The final equivalent mole fraction of n -hexane is given by

$$X_{C_6H_{14}}^* = \frac{P_{fuel}^*}{P_{total}} = \frac{\tilde{R}T}{\sigma_\nu L P_{total}} \left[\ln\left(\frac{I_1(t)}{I_2(t)}\right) - \ln\left(\frac{I_1^0}{I_2^0}\right) \right], \quad (2.3)$$

where I_1 is the reference detector, and I_2 is the signal detector on the other side of the absorption path, and the superscript 0 represent their values before fuel is added. Additional details are given in Appendix A.

2.2.2 Experimental Results

Experiments were performed varying the composition, initial pressure, and heating rate applied to the vessel walls. Figures 2.3 and 2.4 show the temperature, pressure, and fuel mole fraction during two representative experiments performed with a slightly fuel-rich mixture ($\phi = 1.2$, 2.6 % n -hexane in air) and at a initial pressure of 101 kPa. The mixture of Fig. 2.3 was heated at a rate of 4.25 K/min and underwent a slow reaction. A slow reaction case is characterized by a slow consumption of the

fuel with a minimal pressure rise. The mixture of Fig. 2.4 was heated at 11 K/min and underwent ignition. In this context, an event characterized by rapid consumption of the fuel accompanied by a large pressure rise will be referred to as either an ignition case or fast reaction case.

The slow reaction case (Fig. 2.3) has several features that make it significantly different from the ignition case. As the temperature increases from room temperature, we observe a slow consumption of the fuel (reduction in concentration of C-H bonds) starting at 500 K (2500 s), which reduces the fuel concentration from 2.6% to 0.45% over 250 s until the heating system is turned off at 540 K. During this time neither the pressure nor the temperature rise significantly above the trajectory prescribed by the input heating rate.

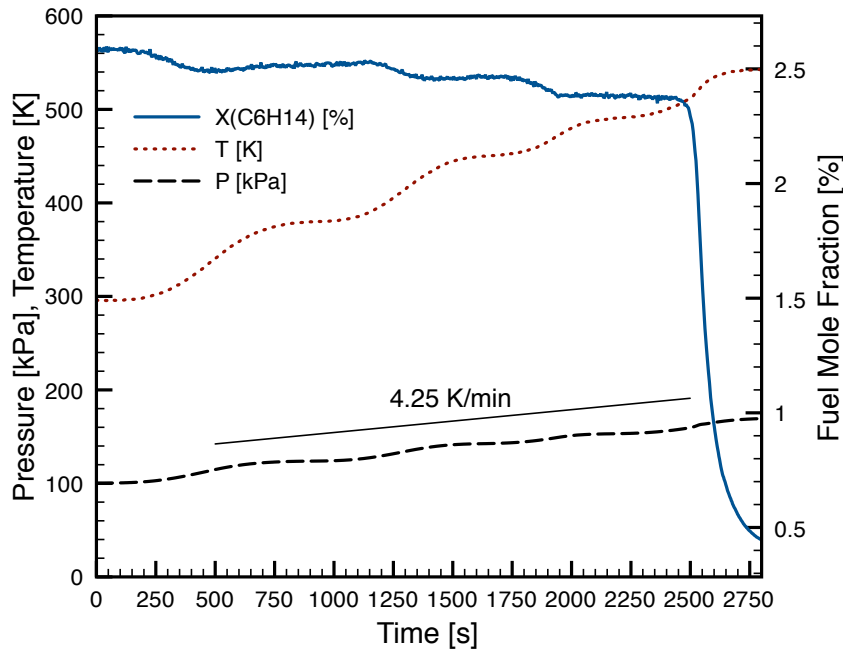


Figure 2.3: Slow reaction of a fuel-rich ($\phi = 1.2$) *n*-hexane/air mixture at an initial pressure of 101 kPa heated at 4.25 K per minute (note that the heating rate is computed from the pressure signal)

The temperature and pressure plot show small steps in the ramp from room temperature to 540 K. These steps are due to the response time of the controller and the aluminum shell to the overall heating rate and temperature change during the initial fuel consumption is 4.25 K/min.

Heating the same mixture ($\phi = 1.2$) at roughly twice the heating rate, 11 K/min, results in a fast reaction (Fig. 2.4). Upon ignition, we observe a spike in pressure, reaching a peak of 330 kPa with elevated pressure for 0.5 seconds. The temperature peak is visible but substantially smaller due to the much slower response time of the thermocouple as compared to the pressure transducer.

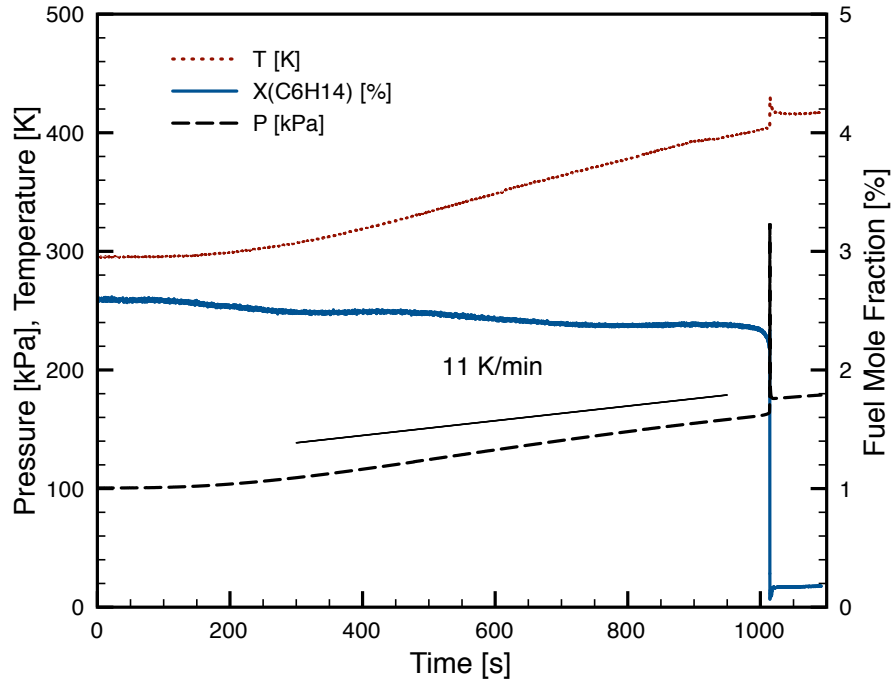


Figure 2.4: Ignition of a fuel-rich ($\phi = 1.2$) *n*-hexane/air mixture at an initial pressure of 101 kPa heated at 11 K per minute (note that the heating rate is computed from the pressure signal)

From the changes in the fuel concentration, temperature, and pressure measurements, we observe that the fast reaction occurs at 1010 s. At this time, we estimate the temperature in the vessel to be 473 K (200 °C), whereas the thermocouple reads 400 K. Due to the limited response rate of the thermocouple, discussed earlier, the actual gas temperature must be inferred from the pressure measurements, using the assumption that the mixture is an ideal gas and negligible changes in the number of moles. At 1000 s we see an initial decrease in fuel concentration followed by a rapid consumption of the fuel during the ignition transient at ~ 1010 s. Unlike the slow reaction, in this case, the response of the measurement system is limited by signal contamination from light emission during the ignition.

The effect of initial pressure and composition was examined for 14 conditions and the outcomes are shown in Figure 2.5. The following changes in the experimental conditions transition the system from a slow reaction to an ignition: (1) increasing the pressure (26–100 kPa), (2) increasing the heating rate (4–12 K/min), (3) increasing the equivalence ratio in the region investigated ($\phi = 0.6 - 1.25$). Each of these factors is confirmed experimentally, while keeping the other two parameters constant.

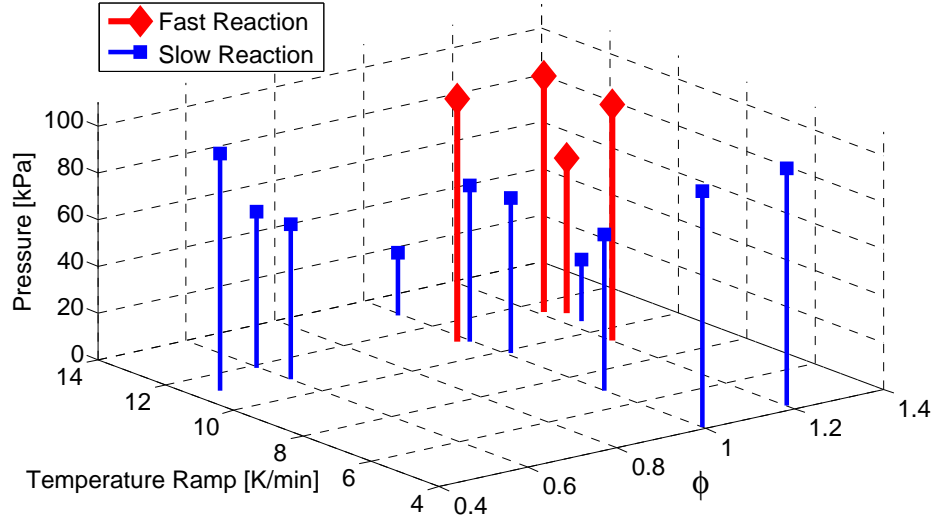


Figure 2.5: Experimental results as a function of total pressure, temperature ramp rate, and equivalence ratio

2.2.3 Simultaneous Measurements of Oxygen and Fuel ²

In addition to the fuel concentration measurements, an attempt has been made to spectroscopically monitor the molecular oxygen concentration during the heating rate experiments. Since transitions in the A band near 760 nm are spin forbidden, direct absorption measurements of O_2 are complicated by the very weak absorption cross sections (Philippe and Hanson, 1993). One method for overcoming this limitation is the use of a derivative technique of spectroscopy with second harmonic (2f) detection as demonstrated by Kroll et al. (1987), Philippe and Hanson (1993), and Rieker et al. (2009). This technique consists of modulating, at a high frequency, the output wavelength of the laser diode, by modulating the diode's current input, allowing a fast scanning across the absorption line. Assuming a perfect gas the second derivative of the signal intensity can be linked to the oxygen partial pressure by the following:

$$\left. \frac{d^2 I}{d\nu^2} \right|_{\nu=\nu_0=\bar{\nu}} = c_0 + c_1 P_{O_2} \quad (2.4)$$

where σ_ν is the absorption cross section, c_0 and c_1 are constants obtained through a calibration procedure. Further details are given in Appendix B.

²The author would like to thank Raza Akbar, Greg Rieker, Adrianus Indrat Aria, Bryan Hires, and David Gutschick for their help with the 2f detection.

2.2.3.1 Experimental Setup and Calibration Procedure

The experimental arrangement is shown in Figure 2.6³. It consists of a signal generator, a summing amplifier, a laser diode with current and temperature controllers, a lock-in amplifier, a low noise preamplifier with bandpass filter, and a waveform recorder. The signal generator is used to create a sawtooth-like carrier signal with a frequency of 80 Hz and an amplitude of ~ 100 mA. This signal scans across the absorption line. The second signal, the sine wave, is generated by the lock-in amplifier's internal signal generator with a frequency of 23.5 kHz and an amplitude of 4 mA. These signals are summed and then sent to the laser diode current controller. Both the sine wave signal and the transmitted laser diode beam are collected by the lock-in detector. The resulting signal is then filtered and recorded by the waveform recorder.

The height of the 2f peak is calibrated against the partial pressure of oxygen. Figure 2.7 shows that the peak height varies linearly with the amount of oxygen as predicted from Equation 2.4 for the range of oxygen concentrations investigated. For calibration, the vessel is first evacuated to below 10 Pa and then filled with increasing amounts of oxygen. The second calibration was performed by first filling the vessel 67 kPa of N₂ and then mixing the oxygen with the nitrogen in increasing steps. The linear constant is reduced when nitrogen is added, which is expected due to the effect of pressure broadening. Also indicated in Figure 2.7 is the uncertainty in the calibration measurement. This uncertainty is strictly based on the evaluation of the standard deviation of the time series data acquired over the measurement interval, typically 30 seconds. The uncertainty in the pressure is less than the indicated symbol size. The calibration was performed at room temperature.

2.2.3.2 Application of Oxygen Measurements

The measurement of oxygen concentration was only implemented successfully once during the course of this investigation. The experimental technique has proven to be extremely sensitive to the variations in the optical path. The experimental procedure of heating the vessel from room temperature to the auto-ignition temperature causes the glass vessel to expand substantially. This produces both an etalon effect and beam steering, which we were only able to correct for by using a nonreactive mixture for one data set. Figure 2.8 shows the consumption of the oxygen and fuel for a fuel-rich mixture ($\phi = 1.2$) at a low initial pressure ($P_0 = 26.67$ kPa) heated at a 11.2 K/min. The measurements show consumption of the fuel and oxygen at the same time, which agrees with the simulation results of the slow reaction shown in Figure 2.12 (a). This result agrees with the overall trends shown

³This figure was adapted from a figure created by Adrianus Indrat Aria, Bryan Hires, and David Gutschick.

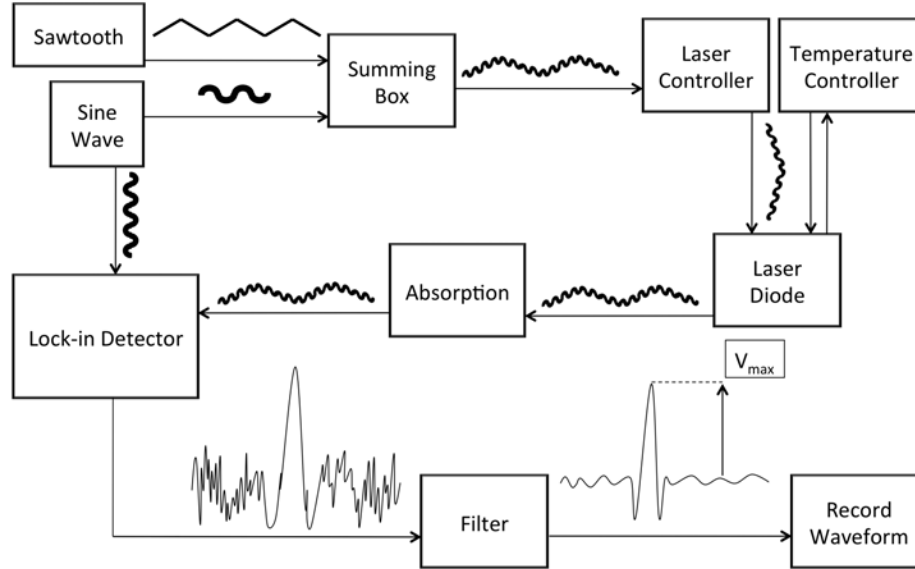


Figure 2.6: Schematic of the experimental setup for molecular oxygen measurements

in Figure 2.5, which show that reducing pressure, heating rate, or equivalence ratio sufficiently in the range investigated leads to a slow reaction of the mixture instead of ignition.

For future experiments, the limitations shown here could be addressed in several ways. First, the impact of the optical path variations could be reduced by increasing the test cell dimension or isolating the windows mechanically from the test cell. Additionally, the sensitivity of the measurements could be increased by evacuating or nitrogen flushing the laser beam path outside the test cell, avoiding perturbations due to the oxygen contained in air. Finally, the overall experimental procedure could be adapted to start the temperature ramp at a higher temperature, reducing the total temperature change.

2.3 Modeling

2.3.1 Modeling with a Detailed Chemical Mechanism

The experiment is modeled using Semenov's theory (Semenov, 1940) for thermal ignition, assuming a well stirred constant volume reactor filled with a uniform mixture of *n*-hexane in air. The wall temperature is increased from room temperature at a constant rate, α , which is included in the energy equation as: $T_w = T_w^0 + \alpha t$. The temperature variation with time is computed from the

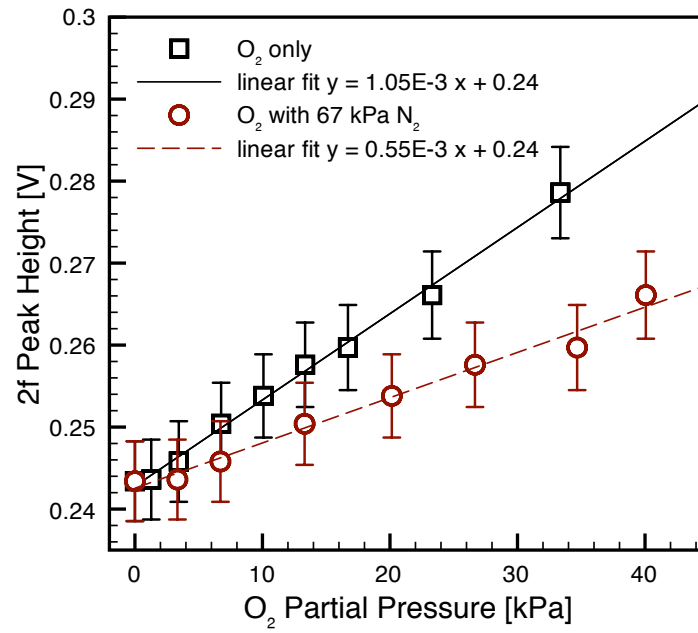


Figure 2.7: Calibration curve, second harmonic peak height as a function of molecular oxygen partial pressure with $\pm \sigma$ uncertainty bars (O₂ only and O₂ with 67 kPa N₂ dilution)

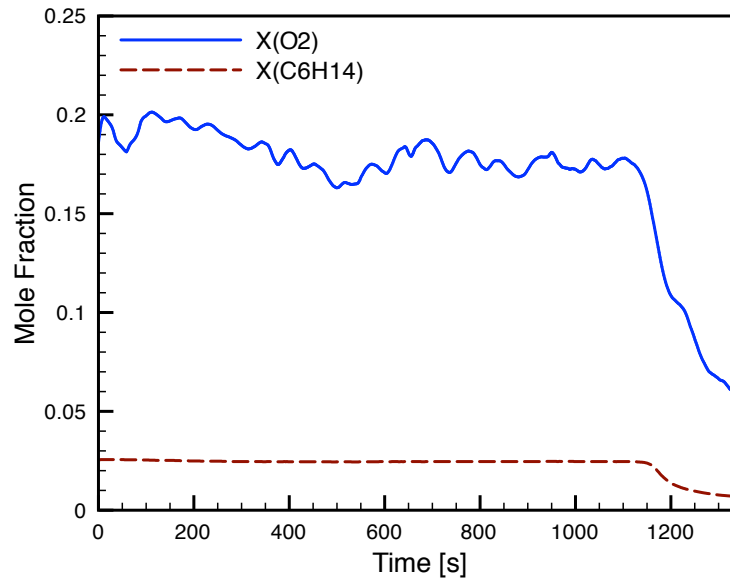


Figure 2.8: Measurement of the molecular oxygen and fuel concentration during a slow reaction for a *n*-hexane/air mixture. Conditions: $P_0 = 26.67$ kPa, $\phi = 1.2$, $\alpha = 11.2$ K/min

energy conservation equation for a well-stirred closed volume:

$$V\rho c_v \frac{dT}{dt} = V \sum_{i=1}^k \dot{\omega}_i u_i + Sh(T_w^0 + \alpha t - T) = \dot{q}_r + \dot{q}_w. \quad (2.5)$$

The species variation with time is computed with the mass conservation equation for a closed volume

$$\frac{dY_i}{dt} = \frac{W_i \dot{\omega}_i}{\rho} \quad i = 1, 2, \dots, k \quad (2.6)$$

where k is the total number of species. The vessel volume, V , and surface area, S , are constant while the density, ρ , and specific heat at constant volume, c_v , are calculated at each solver time step. The heat transfer is modeled with Newton's law of cooling using a lumped parameter, h , to approximate free convection inside the vessel. The change in temperature is determined by the competition between the chemical heat release, \dot{q}_r , and the heat-loss rate, \dot{q}_w , into which the terms of the energy equation have been grouped. Cantera (Goodwin, 2003) is used to compute the net chemical production rate, $\dot{\omega}_i$, utilizing a detailed chemistry mechanism, as well as all thermodynamic properties for both individual species and the gas mixture as a whole. A variable-coefficient ODE solver (VODE) is used to integrate the system of equations (Brown et al., 1989).

The basis for our reaction mechanism is the detailed model of Ramirez et al. (2011). This kinetic scheme was developed to model decane and biofuel chemistry. Further validation for n -hexane was necessary for the present study; this is presented along with the modeling results. The mixture is initialized at a given pressure, temperature, and equivalence ratio, and then the energy equation is integrated forward in time with the wall temperature rising at a specified rate, α .

In order to model this system, a detailed kinetic scheme had to be identified and validated against appropriate low temperature data. Although hydrocarbons have been widely studied, there exists little data concerning n -hexane oxidation (Simmie, 2003). Curran et al. (1995) studied hexane isomer chemistry through the modeling and measurement of exhaust gases from an engine. Shock tube experiments have been performed by Burcat et al. (1996) and Zhukov et al. (2004). Kelley et al. (2011) recently reported laminar flame speeds for C-5 to C-8 n-alkanes. To our knowledge, no low temperature experimental data exists for n -hexane-oxygen mixtures. It should also be noted that no single detailed kinetic scheme is available to model n -hexane combustion chemistry from low to high temperature. In order to describe the kinetics of n -hexane-air mixtures, we employed the C-7 basis of the detailed model published by Ramirez et al. (2011) which includes n -hexane.

2.3.1.1 Kinetic Scheme Validation

For validation at high temperature, we used the experimental data of Burcat et al. (1996) and Zhukov et al. (2004). For validation at intermediate and low temperature, we used *n*-heptane flow reactor and jet stirred reactor data from Held et al. (1997) and Dagaut et al. (1995), respectively.

The experimental *n*-hexane-oxygen-diluent mixture auto-ignition delay times from (Burcat et al., 1996) and (Zhukov et al., 2004) are compared in Fig. 2.9 to the predictions of the Ramirez model. The computed delay times are in reasonable agreement with the experimental results. Although the model typically underestimates the results of Burcat in the high-temperature range, the mean relative error does not exceed 30%. The mean error with respect to the data of Zhukov is around 25%. Considering the usual uncertainty of 20% associated with shock-tube delay times, the model reproduces the experimental data adequately for the purpose of the present study.

The flow reactor experimental data from Held et al. (1997) are compared in Fig. 2.10 (a) to the model predictions for a lean *n*-heptane-oxygen-nitrogen mixture. The temporal mole fraction profiles of the main species are relatively well predicted. The consumption of both reactants, C_7H_{16} and O_2 , are satisfactorily predicted throughout the experiment, whereas the production of CH_4 and C_2H_4 are overestimated early in the oxidation process, and CO mole fraction is underestimated. It should also be noted that the temperature profiles (not shown) are in good agreement with experiments.

The jet-stirred reactor experimental data from Dagaut et al. and the model predictions are compared in Fig. 2.10 (b) for a stoichiometric *n*-heptane-oxygen-nitrogen mixture. The CO mole fraction is well predicted everywhere except within the negative temperature coefficient region (NTC), where an increase in temperature leads to longer induction times (700–800 K). Figure 2.10 (b) shows that the CO_2 mole fraction is underestimated in the low temperature range, but is in close agreement in the high-temperature range. The CH_4 mole fraction is overestimated throughout most of the temperature range. Finally, it can be noted that the NTC region position is correctly predicted.

The last experimental datum to be modeled in testing the validity of the detailed kinetic scheme is the auto-ignition temperature. The experimental value is near 500 K for a stoichiometric *n*-hexane-air mixture at atmospheric pressure. The predicted temperature, based on a constant-volume reactor simulation, is 540 K.

Although the model is not able to reproduce the whole set of selected experimental data with good accuracy, the general trends of *n*-hexane-oxygen mixture reactivity are predicted. A better agreement might be obtained by adjusting the dominant kinetic parameters. However, this would require additional experimental data and is beyond the scope of the present study.

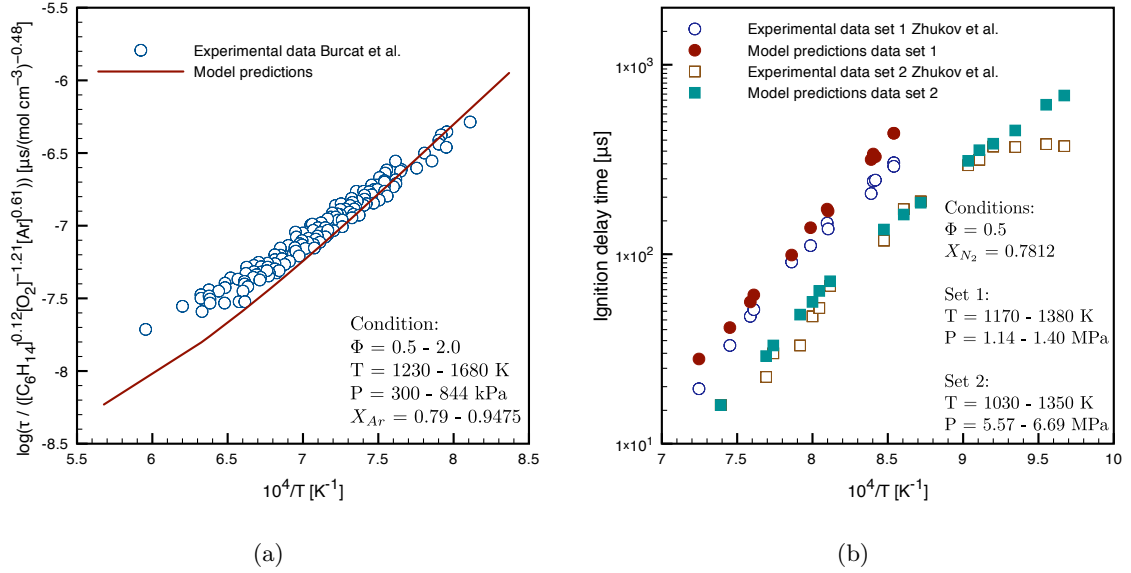


Figure 2.9: Comparison of shock tube experimental data to the predictions of the Ramirez model for *n*-hexane-oxygen-argon mixture. (a) data of Burcat et al. (1996) (b) data of Zhukov et al. (2004)

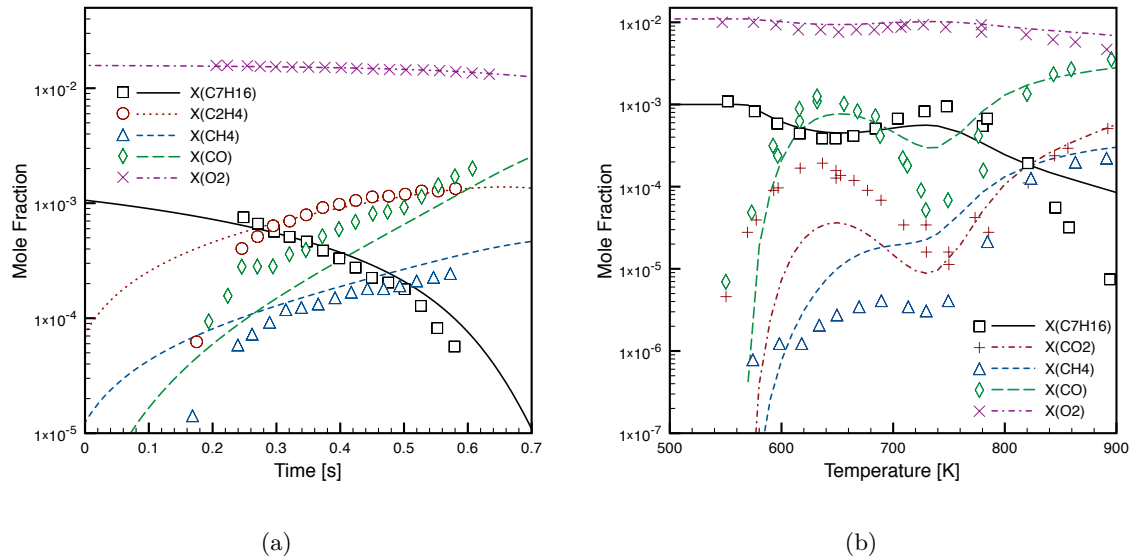


Figure 2.10: Comparison of flow and jet-stirred reactor experimental data to the predictions of the Ramirez model for *n*-heptane-oxygen-nitrogen mixtures. (a) flow reactor data from Held et al. (1997). Conditions: $\phi = 0.79$; $T = 930$ K; $P = 303$ kPa; $X_{N_2} = 0.9831$. (b) jet-stirred reactor data from Dagaut et al. (1995), Conditions: $\phi = 1$; Residence time = 1 s; $P = 1010$ kPa; $X_{N_2} = 0.988$

2.3.1.2 Fast and Slow Combustion Modeling

The purpose of the modeling study was to determine if an existing reaction mechanism could qualitatively reproduce the observed trends using a simple reactor model that simulates the key features of the present experimental setup. The reactor was modeled as a homogenous mixture in a closed, fixed volume with a specified, time-varying wall temperature. Heat transfer from the vessel wall to the contents is characterized through the wall heat transfer coefficient, h , with a value of $15 \text{ W/m}^2\text{-K}$. The value of the heat transfer coefficient was determined iteratively until the switch between the slow and fast reaction was observed for heating rates of 5 and 10 K/min and is consistent with heat transfer from free convection of gases (White, 1984).

Figures 2.11–2.12 present the simulation results for a slow reaction and an ignition event corresponding to a rich mixture, $\phi = 1.2$, with heating rates of 5 and 10 K/min, respectively. In the case of the slow reaction, a slight increase in temperature and pressure can be seen around 2900 s. This time corresponds to the maximum rate of *n*-hexane and oxygen consumption. Reactant consumption extends over a long period of time, several hundred seconds. Although the mixture is rich, only 75% of the oxygen is consumed after 3100 s. In the case of the ignition event, a sharp increase in temperature and pressure is observed at about 1500 s. At this time, reactants are consumed and products are formed over a short period of time, on the order of tens of milliseconds. Figures 2.11 and 2.12 demonstrate that reactant consumption proceeds at essentially constant temperature and pressure in the case of a slow reaction event, and tends towards a constant volume explosion in the case of a fast combustion event.

It is remarkable that a variation of a factor of two in the heating rate results in a completely different mode of combustion in these two cases. Further the temperature at which strong reactant consumption occurs is actually lower in the higher heating rate case (473 K) than in the lower heating case (500 K).

2.3.1.3 Heat Production and Losses

In order to help understand the differences between the slow reaction and ignition cases, the heat production and loss rates have been calculated, along with the energy release rate for each elementary reaction (Figures 2.13 and 2.14).

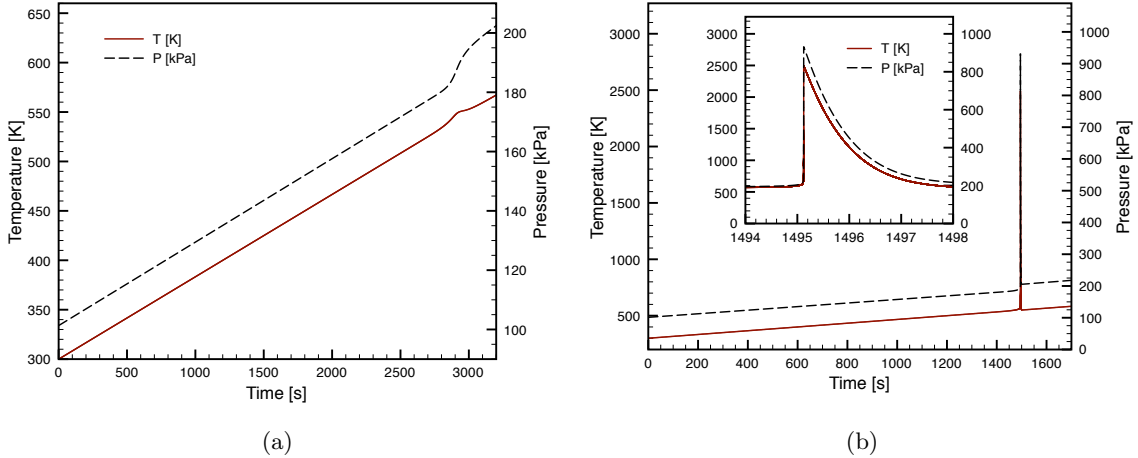


Figure 2.11: Simulated temperature and pressure profiles for a *n*-hexane-air mixture for two different heating rates. Conditions: $\phi = 1.2$ (a) $\alpha = 5$ K/min (b) $\alpha = 10$ K/min

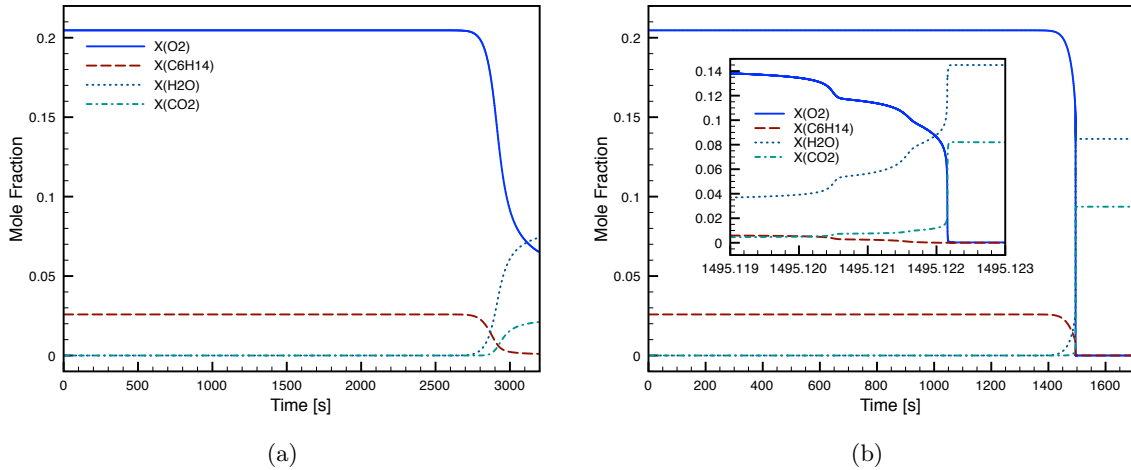


Figure 2.12: Simulated species profiles for a *n*-hexane-air mixture for two different heating rates. Conditions: $\phi = 1.2$ (a) $\alpha = 5$ K/min (b) $\alpha = 10$ K/min

The heat release term, \dot{q}_r , and the magnitude of the heat-loss term, $|\dot{q}_w|$, from Equation 2.5, are shown in Figure 2.13 (note that the time axes are scaled so that temperature history will coincide in the absence of chemical reactions). The initial value of the heat-loss term corresponds directly to the heating rate to the reactor. The inset shows the slight lag of the heat-loss term in comparison to the heat release term. For the slow reaction case, the difference diminishes as the reaction becomes less exothermic, while for the ignition case the difference increases as mixture move towards the ignition point. In the slow reaction case, the chemical heat release is balanced by heat-loss at the wall. In the ignition case, the energy release exceeds the heat-loss at the wall by several orders of magnitude when ignition occurs. The energy release by the chemical reactions is $\sim 10^7$ times greater during an ignition case than during the slow reaction case. The difference in chemical reaction pathways is

shown by the fact that the slow reaction heat release peaks before the ignition case does.

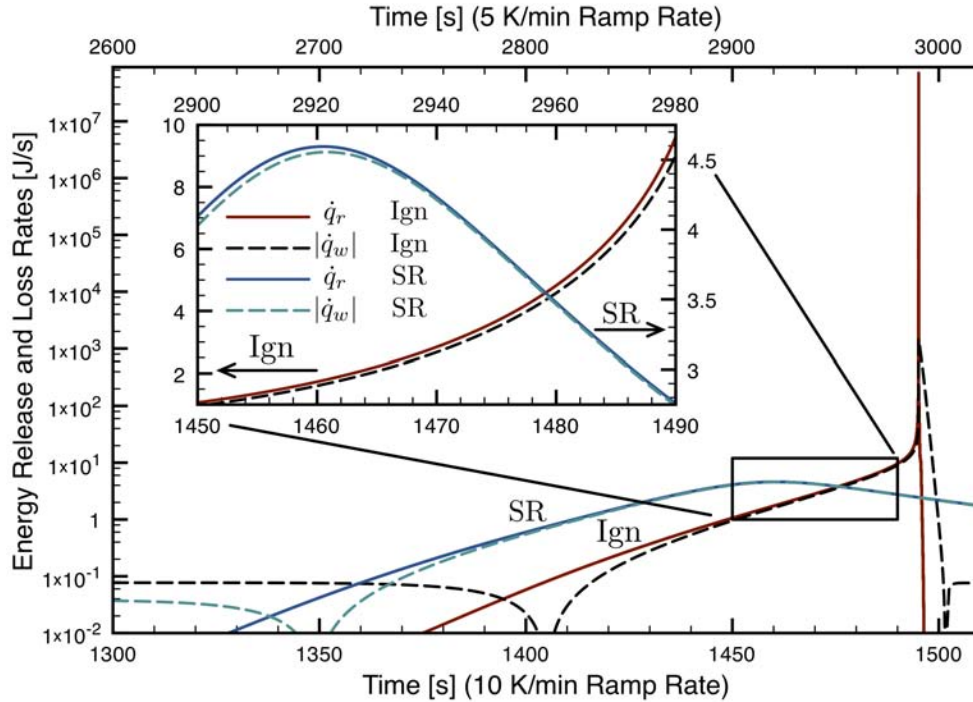


Figure 2.13: Chemical heat production and heat-loss rates for a *n*-hexane-air mixture for two different heating rates. Conditions: $\Phi = 1.2$; $\alpha = 5$ K/min and $\alpha = 10$ K/min (Ignition — Ign, Slow Reaction — SR)

The chemical reactions producing and consuming heat are very different (Fig. 2.14) for the slow and fast reaction cases. In the slow reaction case, the reactions that release energy involve weakly reactive species such as HO_2 , H_2O_2 , and alkylperoxides. Although most of these reactions are highly exothermic, they proceed at a slow rate, keeping the energy release rate low. In the ignition case, the energy release is driven by two reactions: $\text{H} + \text{OH} + \text{M} \rightleftharpoons \text{H}_2\text{O} + \text{M}$ and $\text{CO} + \text{OH} \rightleftharpoons \text{CO}_2 + \text{H}$. These reactions produce the two main reaction products, H_2O and CO_2 , and are very exothermic.

2.3.1.4 Radicals and Atoms Rate of Production

The previous analyses demonstrates that the heating rate of the reactor controls the thermodynamic conditions which in turn control the chemical pathways. The dominant chemical pathways for each case are analyzed via detailed species rate of production and reaction pathway diagrams.

Rate of production analysis have been performed for O and H atoms, as well as, OH and HO_2

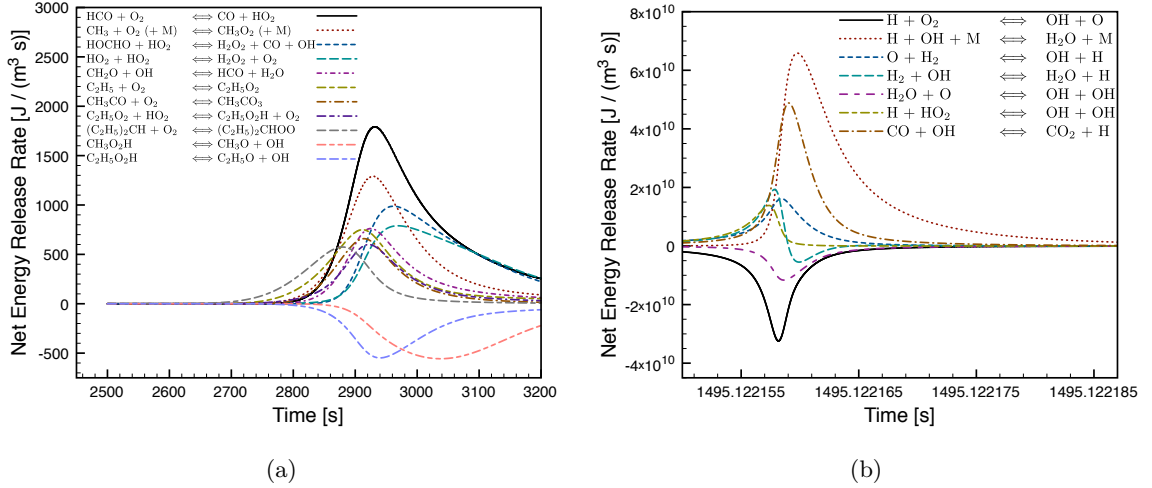


Figure 2.14: Net energy release rate during (a) slow reaction and (b) ignition

radicals. Figure 2.15 presents the results obtained for both the slow reaction and the ignition cases for H and OH. The dominant reaction responsible for the consumption of the H atoms during the slow reaction process is: $\text{H} + \text{O}_2 (+\text{M}) \rightleftharpoons \text{HO}_2 (+\text{M})$, forming less reactive HO_2 radicals. Conversely, during the ignition process, H atoms are primarily consumed through the $\text{H} + \text{O}_2 \rightleftharpoons \text{OH} + \text{O}$ reaction, producing OH radicals. In the slow reaction case, OH radicals are produced by OH elimination reactions and are mainly consumed by the following reactions:

1. $\text{CH}_2\text{O} + \text{OH} \rightleftharpoons \text{HCO} + \text{H}_2\text{O}$
2. $\text{H}_2\text{O}_2 + \text{CO} + \text{OH} \rightleftharpoons \text{HOCHO} + \text{HO}_2$
3. $\text{CH}_3\text{HCO} + \text{OH} \rightleftharpoons \text{CH}_3\text{CO} + \text{H}_2\text{O}$
4. $\text{C}_6\text{H}_{14} + \text{OH} \rightleftharpoons \text{cC}_6\text{H}_{13} + \text{H}_2\text{O}$.

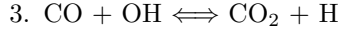
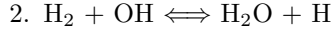
where cC_6H_{13} corresponds to the 3-hexyl radical. The analysis shows that no branching process occurs.

In the ignition case, OH radicals are rapidly produced by the following branching reactions:

1. $\text{H} + \text{O}_2 \rightleftharpoons \text{OH} + \text{O}$
2. $\text{O} + \text{H}_2 \rightleftharpoons \text{OH} + \text{H}$
3. $\text{H}_2\text{O} + \text{O} \rightleftharpoons \text{OH} + \text{OH}$

and are consumed by the following exothermic reactions:

1. $\text{H} + \text{OH} (+\text{M}) \rightleftharpoons \text{H}_2\text{O} (+\text{M})$



The last two reactions also regenerate H atoms.

The consumption of HO_2 radicals is driven by reactions which produce nonreactive species, mainly H_2O_2 . In the fast reaction case, their consumption is driven by the $\text{H} + \text{HO}_2 \rightleftharpoons \text{OH} + \text{OH}$ reaction, which produces the very reactive OH radicals. Finally the O atoms take part in the chain branching process: $\text{H} + \text{O}_2 \rightleftharpoons \text{OH} + \text{O}$ and $\text{O} + \text{H}_2 \rightleftharpoons \text{OH} + \text{H}$, but only during the ignition event and not during the slow reaction.

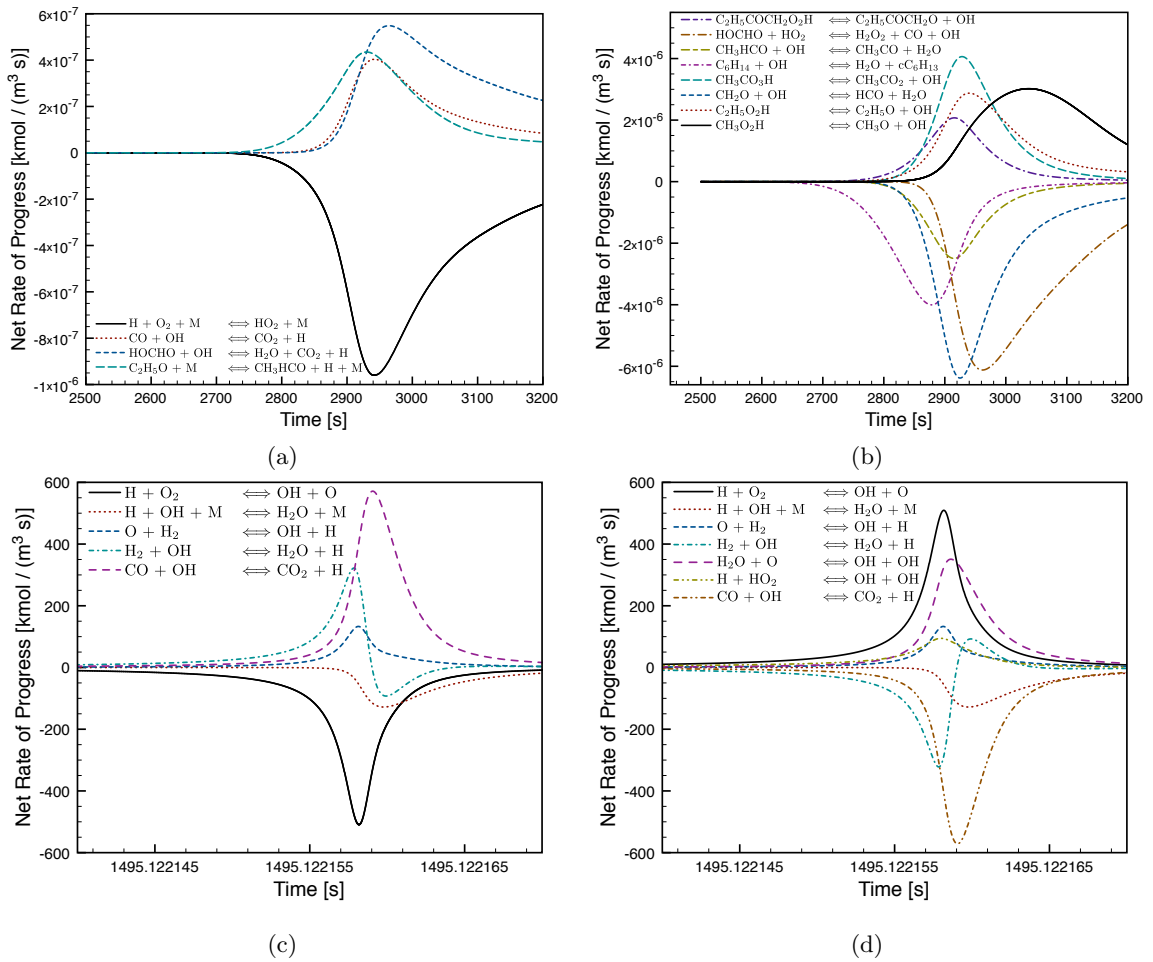


Figure 2.15: Rate of production of H atoms and OH radicals for a $\Phi = 1.2$ *n*-hexane-air mixture and two different heating rates: (a) and (b), $\alpha = 5 \text{ K/min}$; (c) and (d), $\alpha = 10 \text{ K/min}$

2.3.1.5 Reaction Pathway Diagrams

A 10% threshold is used for the element flux pathway diagrams in order to underline the most important pathways for both cases. The carbon element pathways for the two phases in the oxidation process are summarized in Figures 2.16 and 2.17. The first phase corresponds to the period where the temperature increases from 500 to 540 K. In the slow reaction case, this period extends from 2350 to 2850 s; for the fast reaction case, it extends from 1220 to 1430 s. As shown in Figure 2.16, the main path for *n*-hexane consumption in both cases is the following:

1. H abstraction by OH from the third carbon atom (C3),
2. O₂ addition on carbon C3,
3. intramolecular H abstraction by O₂ from the fifth carbon atom (C5),
4. second O₂ addition on carbon C5,
5. OH elimination-intramolecular H abstraction by O₂ on carbon C3-cetone formation on carbon C3.

During the slow reaction, a significant amount of the 5-hydroperoxy-hexan-3-one is decomposed into OH, CH₃HCO, and C₂H₅COCH₂. The last species is further converted through a series of reactions ultimately leading to CH₂O and C₂H₅O. During the first phase, these reaction rates are almost an order of magnitude higher in the slow reaction case as compared to the ignition case. This is explained by the significantly longer time the mixture spends under these conditions, allowing for an increase in OH concentration, and thus increasing the initiation rate.

During the second phase, additional pathways appear to be important. These are presented in Figure 2.17. For the slow reaction case, this phase extends from 2870 and 3100 s with an increase of temperature of 20 K to reach 560 K. This phase is mainly characterized by successive:

1. CO or CO₂ elimination
2. O₂ addition
3. H addition
4. OH elimination

The overall reaction rate remains the same throughout the entire process ($\sim 10^{-5}$ kmol m⁻³ s⁻¹) and, at 3100 s, 95% of the initial *n*-hexane content is consumed. For the fast reaction case, the second

phase extends from 1430 to 1495 s, at which point ignition occurs, with an increase of temperature until 790 K and reaction rates of the order of 100 times higher than the reaction rates of the slow reaction case in this phase. In this phase, C-C bond rupture is favored over O₂ addition. This process rapidly forms CO which then reacts with OH radicals to form CO₂ and H atoms. This fast production of H atoms, further sustained by the temperature increase, induces an increase in the overall reaction rate through the chain branching reaction $\text{H} + \text{O}_2 \rightleftharpoons \text{OH} + \text{O}$, and drives the ignition of the mixture. A large amount of O₂ is consumed through addition reactions during the slow reaction. During the fast reaction case, O₂ is still available in the gas phase for the branching process.

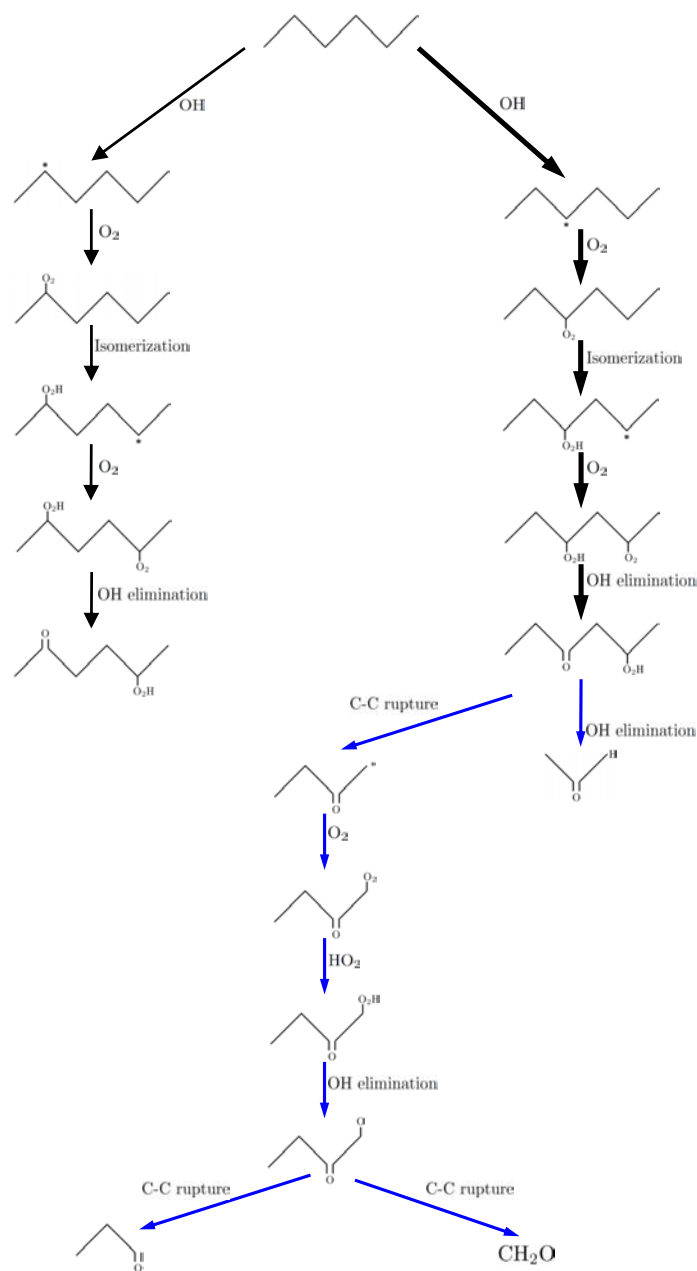


Figure 2.16: Carbon reaction pathways during the first phase of a *n*-hexane-air mixture oxidation for two heating rates. Conditions: $\Phi = 1.2$; $\alpha = 5$ and 10 K/min. Black arrows: common pathways. Blue arrows: additional pathways observed during the slow reaction. The first phase extends from 2350 to 2850 s for the slow reaction and from 1220 to 1430 s for the fast reaction.

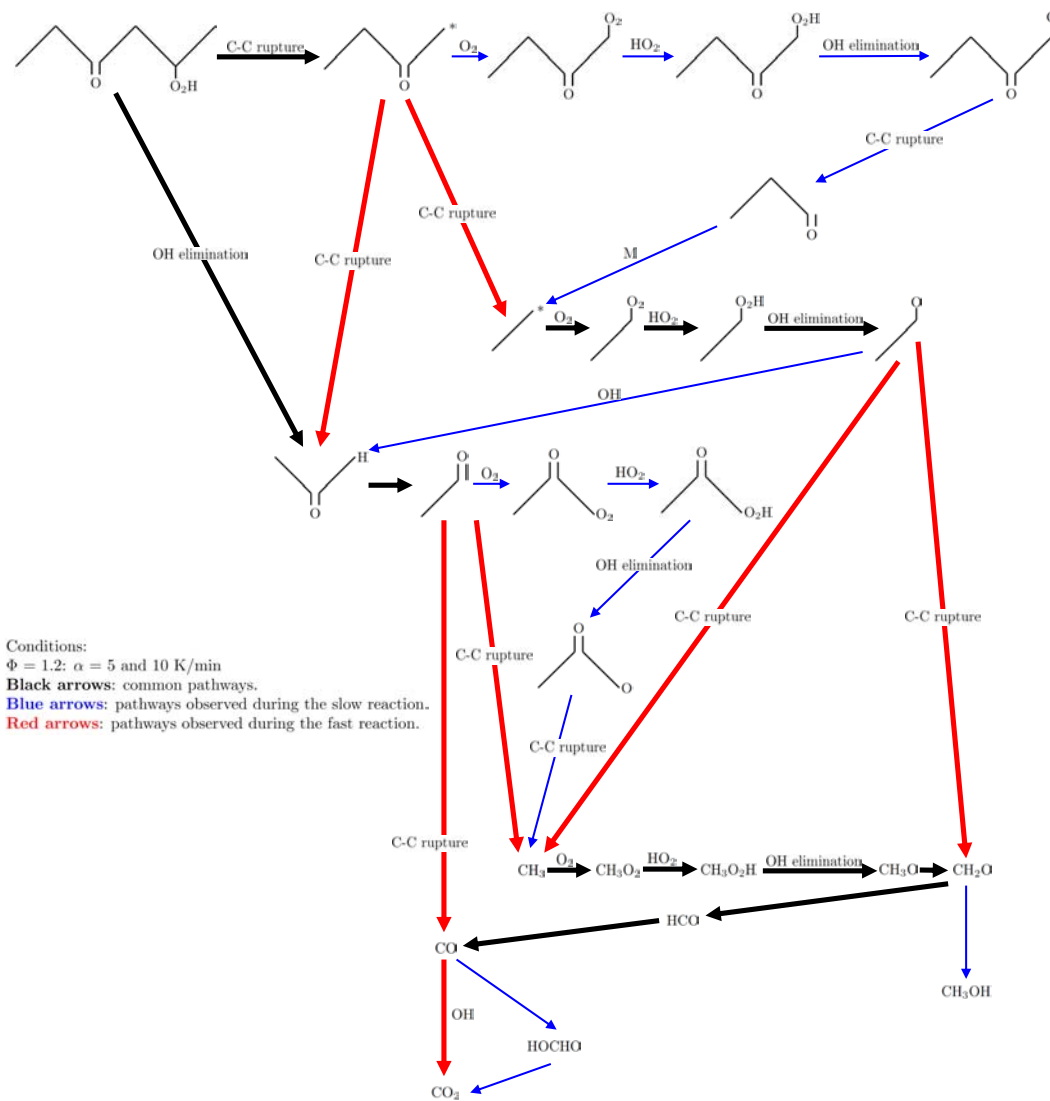


Figure 2.17: Carbon reaction pathways during the second phase of a *n*-hexane-air mixture oxidation for two heating rates. The second phase extends from 2850 to 3100 s for the slow reaction and from 1430 to 1495 s for the fast reaction.

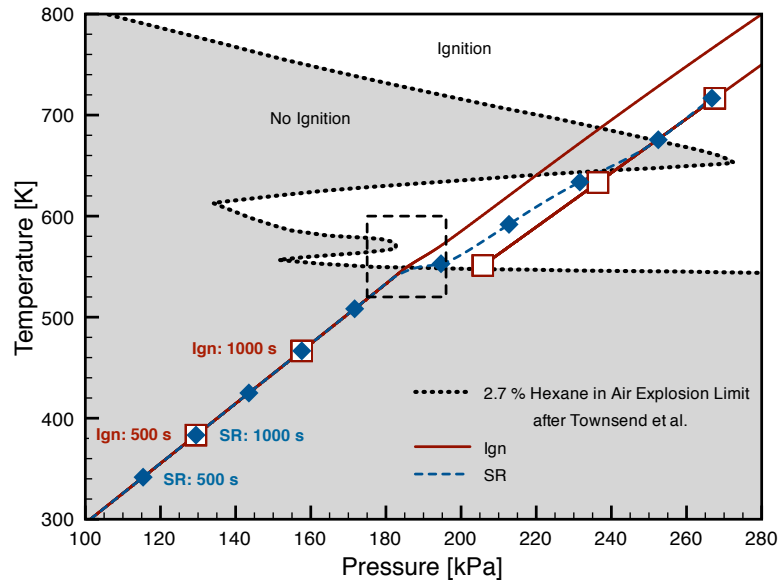
2.3.1.6 Explosion Limits

Figure 2.18 shows the simulated thermodynamic state trajectories, for the case with $\phi = 1.2$, along with the experimental explosion limits obtained for a 2.7% *n*-hexane in air by Kane et al. (1937). Figure 2.18 (a) illustrates the temporal evolution whereas Figure 2.18 (b) emphasizes the *n*-hexane concentration evolution. As shown in Figure 2.18 (a), in the slow reaction case the mixture spends a proportionally long time, several hundred seconds, at a temperature slightly below the auto-ignition temperature 498 K. Due to the extended period the mixture spends at a temperature close to the auto-ignition temperature, more than 50% of reactants are consumed before entering the explosion region. This is shown in Figure 2.18 (b). Both figures together show the importance of considering the evolution, in time and reaction progress, of a particular mixture rather than a simplified threshold point of view.

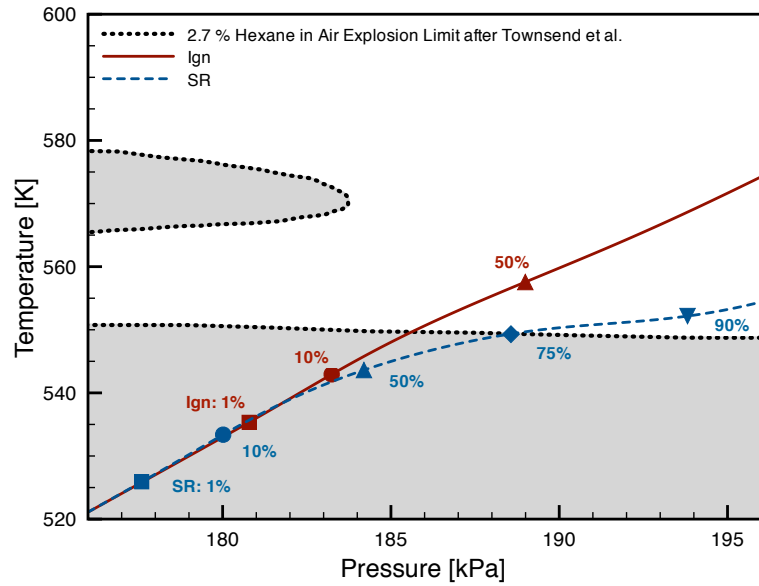
Analysis of the chemical composition during the slow reaction case shows that mixtures changes significantly from the original $\phi = 1.2$ (2.6%) *n*-hexane air mixtures into a mix of other hydrocarbons, mainly oxygenated hydrocarbons. The ignition behavior of this mixture is no longer characterized by the explosion limit of the 2.7% *n*-hexane air mixtures and no ignition is observed as the mixtures enters this ignition region. A slight acceleration of the reaction rate is observed just at the entrance of the explosion region. However, the energy release rate remains too low for ignition to occur and is balanced by the heat-losses at the wall.

Conversely, the fast reaction case progresses much more rapidly, and the mixture quickly enters into the explosion region. In the fast reaction case, although a significant fraction of the reactants, around 10%, is consumed before the mixture enters the explosion region, the composition is not modified enough to avoid explosion and the reactants consumption occurs according to a fast reaction driven by chain branching reactions.

Given the configuration of the experiment, the system has an intrinsic thermochemical feedback loop. By that, we mean the dynamics of the system are controlled by the coupling of the thermodynamic state and the chemical kinetics. Depending on the heating rate, diverging chemical paths occur and in turn influence the evolution of the thermodynamic state.



(a)



(b)

Figure 2.18: Thermodynamic state trajectories along with the explosion limits (Kane et al., 1937) for a *n*-hexane-air mixture with different heating rates. Conditions: $\phi = 1.2$; $\alpha = 5$ and 10 K/min; (a): temporal evolution (500 s elapsed time between points). (b): *n*-hexane percentage consumed in the boxed region of (a)

2.3.1.7 Parametric Study in α , ϕ , and P_0

Through computational simulation of the heated vessel, it is possible to perform a more complete investigation of the behavior as a function of equivalence ratio, initial pressure, and heating rate. The goal is to study the boundary and transformation between a slow reaction and ignition. The simulation is run holding two of the parameters constant and changing the third variable in small increments, with results given in Figures 2.19–2.21. The overpressure created by the reaction is the indicator of ignition and is calculated based on the pressure change relative to the pressure at the time of ignition. Each simulation is run for 3500 seconds, which is sufficient to heat mixtures with heating rates above 5 K/min to temperature higher than 550 K.

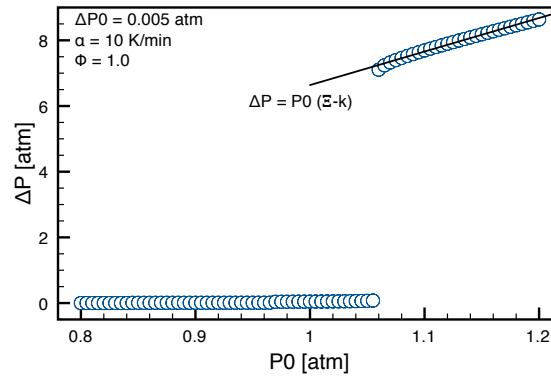


Figure 2.19: Peak overpressure as a function of initial pressure for a stoichiometric mixture of *n*-hexane in air heated at 10 K/min

The first parameter investigated is the pressure, which was shown experimentally to change the behavior from slow reaction to ignition as it is increased (see, for example, shots 4 and 7 in Appendix I). The overpressure is approximately zero until it reaches a critical value and then sharply transitions to large values consistent with an equilibrium calculation for an adiabatic reactor.

For an adiabatic constant volume process at a fixed composition, the ratio of the pressure jump to the initial pressure is basically constant.

$$\frac{\Delta P}{P_0} \cong \text{constant} \quad (2.7)$$

Equivalently, the ratio between the peak pressure, P_p , and pressure at the time of ignition, P_i , is very insensitive to the initial pressure P_0 .

$$\Xi = \frac{P_p}{P_0} \quad (2.8)$$

In these simulations, the mixture is heated from room temperature until reaction occurs. The overpressure is the peak pressure minus the pressure at the time of ignition. In the case of slow reactions the peak pressure is the maximum overpressure beyond that of the prescribed ramp.

$$\Delta P = P_p - P_i \quad (2.9)$$

And the pressure just before ignition is also very insensitive to the initial pressure, because the ignition temperature, T_i , is basically constant and the change in the number of moles before ignition can be neglected for this argument. Using the ideal gas assumption, P_i , is given by

$$P_i = P_0 \frac{T_i}{T_0} = kP_0, \quad (2.10)$$

where T_0 is the initial temperature that is held constant. The increasing over pressure with increasing initial pressure for the ignition cases in Figure 2.19 is thus described by

$$\Delta P = P_p - P_i = P_p - kP_0 = P_0 (\Xi - k). \quad (2.11)$$

In the equation above, for the system we have investigated the constants are $k = 1.83$ and $\Xi = 9.5$ for a stoichiometric mixture.

The next parameter investigated is the heating rate at atmospheric pressure for a stoichiometric mixture ($\phi = 1$). This behavior was the focus of the earlier part of this chapter with experimental results shown in Figures 2.3 and 2.4 for slightly fuel rich mixture ($\phi = 1.2$). The transition point is shifted to a higher transition heating rate than in the fuel-rich case, which is substantiated by the next investigation testing the dependence on equivalence ratio. The overpressure shows a sharp transition from slow reaction cases to ignition cases with increasing α . We see a slight dependence of the overpressure on the heating rate for the ignition cases, which can be attributed to the fact that the heat-loss is reduced with increasing heating rate.

The final parameter that was varied is the equivalence ratio while holding the heating rate and initial pressure constant. The region investigated is between fuel lean to slightly fuel rich mixtures. As with the other two parameters a sharp jump in overpressure is observed with increasing ϕ . The large jump in overpressure for a small change in the equivalence ratio can be attributed to the fact that the mixture energy increases with increasing fuel percentage in this regime and thus the reaction rates, which are highly dependent on the temperature increase drastically. As the equivalence ratio is

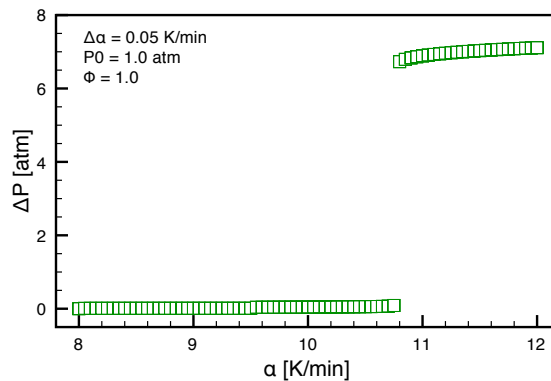


Figure 2.20: Peak overpressure as a function of heating rate for a stoichiometric mixture of *n*-hexane in air at an initial pressure of one atmosphere

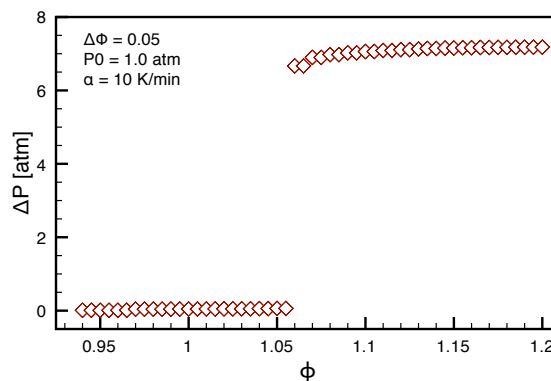


Figure 2.21: Peak overpressure as a function of equivalence ratio for a mixture of *n*-hexane in air at one atmosphere heated at 10 K/min

increased further, the chemistry changes its pathway away from creating CO_2 and H_2O , which have large heats of formation, to creating CO , breakup of the hydrocarbons and internal H-abstraction resulting in smaller heat release. No experimental data are available that could be compared to simulations run at higher equivalence ratio in an experiment with controlled heating rate.

The final goal of this parametric study is to show the behavior for a range of combinations of all three parameters. Simulations were performed for heating rates between 5 and 15 K/min, in increments of 1 K/min, equivalence ratios from 0.7 to 1.4, in increments of 0.05, and for pressures ranging from 0.5 to 1.2 atmospheres, in increments of 0.1 atm. The results from the atmospheric pressure case in Figure 2.22 show the interdependence between the influence of composition and heating rate. The dashed line indicated the crossover points, i.e., the transition from slow reaction to ignition, extrapolated from the data points, which was performed at each pressure to create Figure 2.24. To check the validity of this extrapolation we performed calculations with a finer grid,

increments of 0.2 K/min for the heating rate and 0.2 for equivalence ratio, at atmospheric pressure only (Figure 2.23). The agreement between the extrapolation from the coarse grid and the fine grid calculations is good, so we have confidence in the final results.

One can note the gaps in the results in Figure 2.23, which are simulations that “crashed”, i.e., failed to converge, when calculating the cooling of the system after the temperature spike from the ignition. While there is not question that these points represent ignition cases, they were left in place to stress the difficulty of performing these calculations. For all coarse grid calculations, any missing points were run again with a limited time step size during the cooling phase.

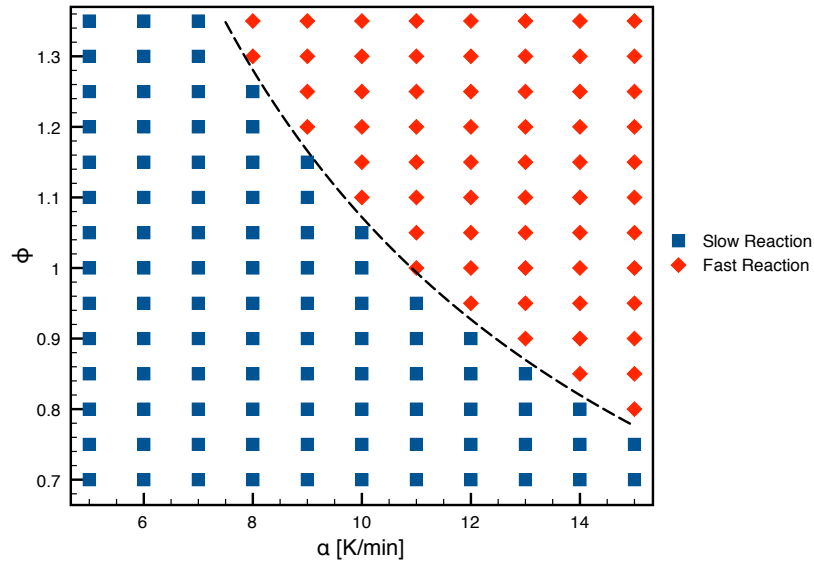


Figure 2.22: Fast reaction and slow reaction cases as a function of equivalence ratio and heating rate at an initial pressure of one atmosphere

The trends shown in the experiments (see Section 2.2.2) for the range we have investigated are confirmed by the calculations presented in Figure 2.24: transition from a slow reaction to ignition occurs by (1) increasing the heating rate, (2) increasing the pressure, and (3) increasing the equivalence ratio (limited to the region shown).

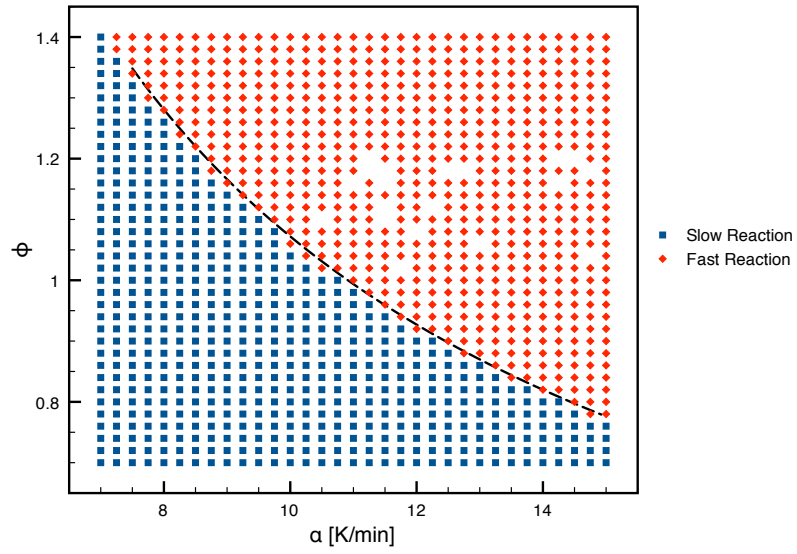


Figure 2.23: Fast reaction and slow reaction cases as a function of equivalence ratio and heating rate at an initial pressure of one atmosphere (fine grid)

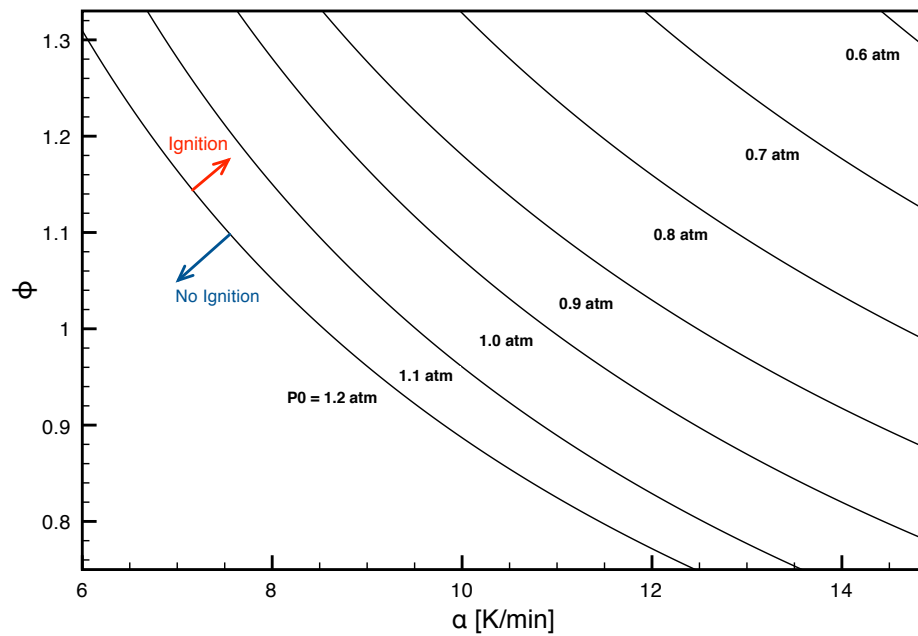


Figure 2.24: Transition limits from slow reaction case to ignition cases as function of the initial pressure, equivalence ratio, and heating rate

2.3.2 Modeling with a One-Step Mechanism

The change in behavior from a slow reaction case to an ignition case observed in the experiment and in the detailed chemical analysis is also present when the chemistry is treated with a simple one-step mechanism. However, only the effect of the heating rate is explored here as the inclusion of effect of pressure and chemical composition are very limited in a one-step model and can be accounted for much more readily in the detailed model.

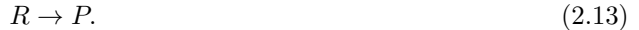
We follow Semenov's theory (Semenov, 1940) for thermal ignition again assuming a uniform mixture with chemically bound energy. The temperature variation with time is computed from the energy conservation equation, using the nomenclature in Table 2.1,

$$V\rho c_v \frac{dT}{dt} = \dot{q}_r + Sh(T_w^0 + \alpha t - T) = \dot{q}_r + \dot{q}_w . \quad (2.12)$$

Table 2.1: Nomenclature

Parameter	Units	Description
T	K	gas temperature
V	m ³	volume
ρ	kg m ⁻³	density
c_v	J kg ⁻¹ K ⁻¹	specific heat at constant volume
q_c	J kg ⁻¹	stored chemical energy (heat of combustion)
$\dot{\omega}_i$	kg m ⁻³ sec ⁻¹	net production rate per unit volume
u_i	J kg ⁻¹	internal energy
S	m ²	surface area
h	J sec ⁻¹ m ⁻² K ⁻¹	heat transfer coefficient
T_w^0	K	initial wall temperature
α	K sec ⁻¹	wall temperature heating rate
\dot{q}_r	J sec ⁻¹	energy release rate
\dot{q}_w	J sec ⁻¹	energy wall loss rate
\dot{T}_r	K sec ⁻¹	reaction-based temperature change rate
\dot{T}_w	K sec ⁻¹	wall-based temperature change rate
T_w	K	wall temperature
Q	J m ⁻³	energy density
λ		progress variable
A	sec ⁻¹	pre-exponential
E_a	J kmol ⁻¹	activation energy
\tilde{R}	J kmol ⁻¹ K ⁻¹	universal gas constant

We assume that the reaction progresses in one step from reactants (R) to products (P):



The rate at which this reaction progresses depends to first order on the temperature and to second order on the amount of reactants still present. This dependence is thus governed by an Arrhenius rate law (Glassman, 2008) with depletion,

$$\frac{d\lambda}{dt} = A(1 - \lambda) \exp\left(-\frac{E_a}{\tilde{R}T}\right) \quad (2.14)$$

where λ is the reaction progress variable such that $\lambda = 0$ represents reactants and $\lambda = 1$ represents products. The reaction progress can also be interpreted as the relative mass fraction of the deficient reactant; for lean mixtures the deficient reactant is the fuel, and for rich mixtures the deficient reactant is the oxidizer. In the Arrhenius rate, E_a is the activation energy and A is the pre-exponential coefficient.

The heat release rate into the reactor is thereby the total energy contained in the system times the consumption rate

$$\dot{q}_r = \rho V q_c \frac{d\lambda}{dt} = V Q \frac{d\lambda}{dt}. \quad (2.15)$$

The chemical energy released per unit mass of reactant, q_c , can be estimated from an equilibrium calculation of a given mixture at constant internal energy and volume.

Table 2.2 shows the parameters chosen for the simulation. The first set is chosen to directly reflect the experimental setup. The heat release and specific heat are calculated using Cantera using the equilibrium calculations for a constant volume explosion (Goodwin, 2003). The specific heat is averaged between the initial and final conditions. The activation energy is estimated from the slope of the ignition delay time at low temperatures in the Arrhenius plot (Figure 2.25) and is consistent with literature values (Burcat et al., 1996). Finally, the pre-exponential is selected empirically so that a transition occurs from a slow reaction case to an ignition case when changing the heating rate from 5 K/min to 10 K/min.

While an upper bound for the pre-exponential can be estimated for an elementary reaction by calculating the collision frequency between molecules (see Appendix D), this estimate does not necessarily hold for a global reaction. Nevertheless, the value found here for the pre-exponential, A , is consistent with values from the literature. Westbrook and Dryer (1984) find $A = 5.7 \times 10^{11} \text{ s}^{-1}$, but consider a lower activation energy of $E_a = 30 \text{ kcal/mol}$.

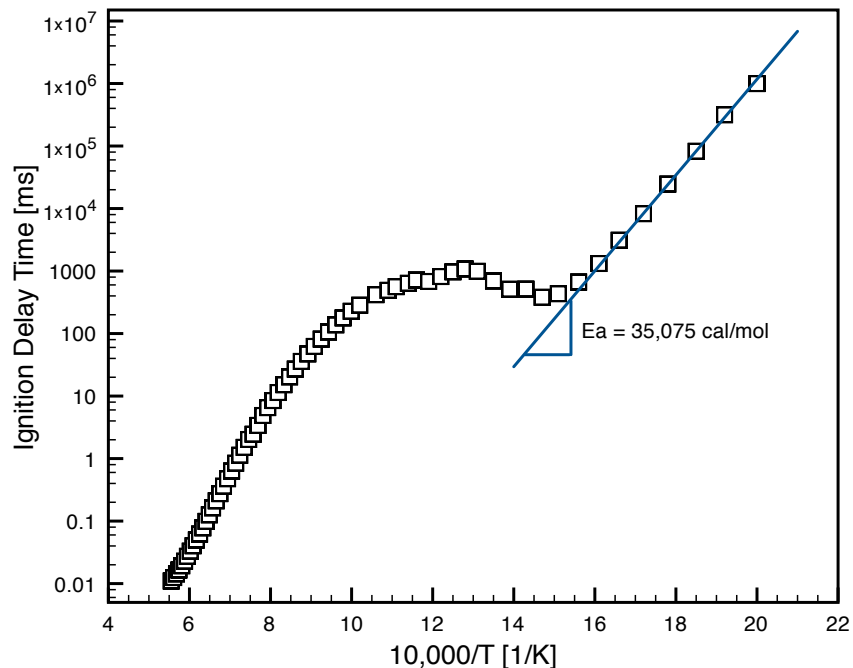


Figure 2.25: Ignition delay time as a function of reciprocal temperature for a stoichiometric hexane-air mixture at atmospheric pressure. The activation energy at low temperatures is estimated by the slope indicated.

Table 2.2: Parameters used in modeling of hexane-air auto-ignition

Parameter		Units	Description
ρ_0	1.24	kg m^{-3}	unburnt gas density
T^0	298	K	initial temperature
T_w^0	298	K	initial wall temperature
V	427	cm^3	gas volume
S	0.05	m^2	surface area of the vessel
q_c	2.3×10^6	J kg^{-1}	stored chemical energy
c_v	930	$\text{J kg}^{-1} \text{K}^{-1}$	average specific heat of the gas mixture at constant volume
E_a	35075	cal kmol^{-1}	activation energy
	146754	J kmol^{-1}	activation energy
A	3.3×10^{14}	s^{-1}	pre-exponential

The results from the simulation using the same heating rates as in the experiments and detailed chemistry modeling are given in Figures 2.27 and 2.26. The values used are given in Table 2.2. The slow reaction case shows the gradual progress of the reaction along with the slight increase of the temperature above the ramp rate. The 10 K/min heating rate case shows the sharp jump in consumption after has reached approximately 60% products, which is accompanied with the large increase in temperature above the prescribed ramp rate. These results are in good agreement with those using the detailed chemical mechanism shown in Figure 2.11.

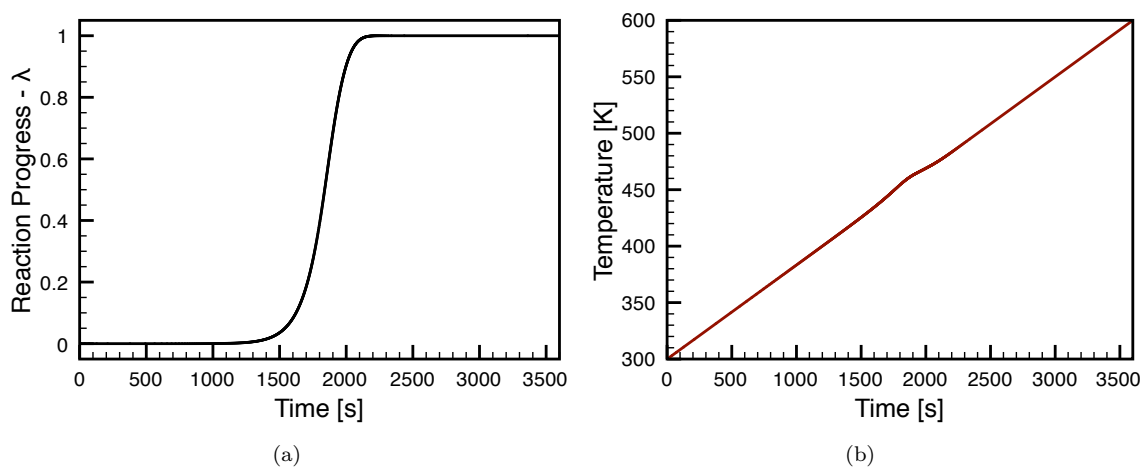


Figure 2.26: Simulated slow reaction for a heating rate of $\alpha = 5$ K/min using one-step chemistry; (a) reaction progress, (b) temperature

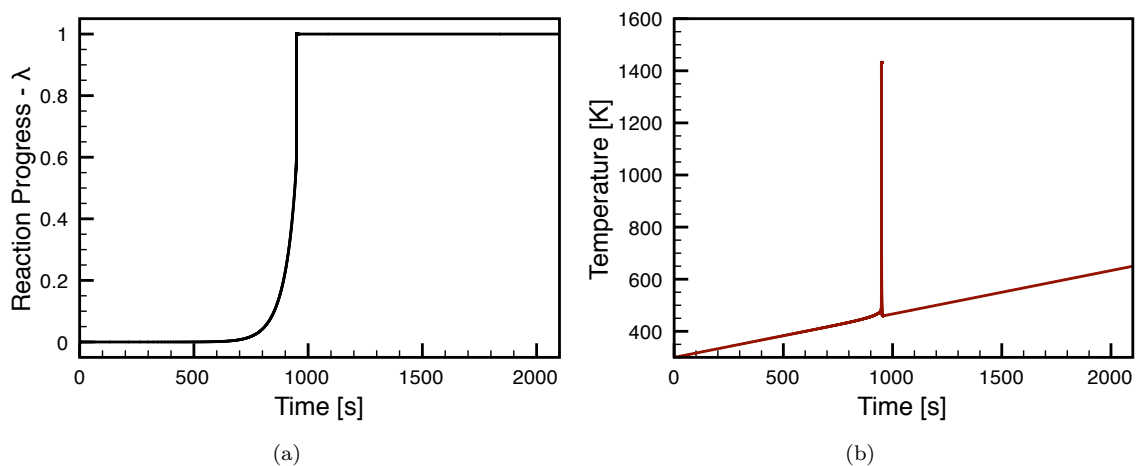


Figure 2.27: Simulated ignition for a heating rate of $\alpha = 10$ K/min using one-step chemistry; (a) reaction progress, (b) temperature

This analysis using the one-step model for the reaction progress demonstrates that slow reactions are not dependent on the the specific chemical processes that occur, which were explored earlier,

but rather the combination of the thermodynamic state and the extent to which the reaction has progressed.

2.4 Theoretical Considerations

Thermal ignition has been analyzed by many authors like Semenov (1940) and Frank-Kamenetskii (1969) and is described in many text books such as “Combustion” by Glassman (2008). However, these studies did not include the effect of ramp heating or include the transition between slow and fast explosions. Our objective is to extend previous work to include the effect of heating rate and examine the role of the heating rate in the transition from slow to ignition events. The energy equation, given in Equation 2.16, and the one-step reaction progress equation, given in Equation 2.17, form the basic set for our theoretical analysis of the ramp-heated vessel.

$$\frac{dT}{dt} = \frac{QA}{\rho c_v} (1 - \lambda) \exp\left(-\frac{E_a}{\tilde{R}T}\right) + \frac{Sh}{\rho V c_v} (T_w^0 + \alpha t - T) \quad (2.16)$$

$$\frac{d\lambda}{dt} = A (1 - \lambda) \exp\left(-\frac{E_a}{\tilde{R}T}\right) \quad (2.17)$$

The nomenclature is the same as for the one-step model given in Table 2.1. Equation 2.16 can be rewritten to reveal several time scales that are in competition,

$$\frac{dT}{dt} = \frac{T_{ref}}{t_r} (1 - \lambda) \exp\left(-\frac{E_a}{\tilde{R}T}\right) - \frac{1}{t_w} (T - T_w^0) + \frac{t T_{ref}}{t_w t_\alpha}, \quad (2.18)$$

which are the chemical energy release time,

$$t_r = \frac{\rho c_v T_{ref}}{QA}, \quad (2.19)$$

the wall heat transfer time,

$$t_w = \frac{\rho V c_v}{Sh}, \quad (2.20)$$

and ramp heating time,

$$t_\alpha = \frac{T_{ref}}{\alpha}. \quad (2.21)$$

T_{ref} is a reference temperature, such as the ignition temperature. In the following sections, we will explore the competition between the physical processes represented by these time scales and the effect of reaction consumption.

2.4.1 Ignition With Negligible Consumption

As a first approximation, we can consider a volume of flammable gas where the consumption of fuel can be neglected. While interesting solutions can be found by neglecting consumption, we subsequently have to revisit this assumption in order to address the transition between slow and fast reactions. The set of governing equations in this case reduces to the energy equation with $\lambda = 0$,

$$\frac{dT}{dt} = \frac{QA}{\rho c_v} \exp\left(-\frac{E_a}{RT}\right) + \frac{Sh}{\rho V c_v} (T_w^0 + \alpha t - T) . \quad (2.22)$$

We can investigate the extensions of two classical theories of ignition, the adiabatic explosion and the explosion with heat-loss and examine how including a wall heating rate changes the results.

2.4.1.1 Dominant Chemical Energy Release

In the limit when the heat release time scale, t_r , is much shorter the heat transfer time scale, t_w , the first term Equation 2.18 dominates and the energy equation reduces to the following form:

$$\frac{dT}{dt} = \frac{QA}{\rho c_v} \exp\left(-\frac{E_a}{RT}\right) . \quad (2.23)$$

This situation is the classical adiabatic thermal explosion, in which a mixture is suddenly increased to a temperature T_0 and after a certain induction time, τ_c , the mixture ignites with a large temperature spike. The induction time is also called the ignition delay time, as it often studied by elevating the temperature of a mixture by, for example, a shock wave, and then measuring the delay between the sudden temperature rise and the ignition event.

The ignition delay time can be found readily by simplifying the analysis one step further and assuming large activation energy as done by Frank-Kamenetskii (1969) (see C.2.2). The temperature is expanded for small perturbations about the initial temperature, $T = T_0 + T'$, resulting in

$$\frac{d\theta}{d\tau} = e^\theta , \quad (2.24)$$

where

$$\tau = \frac{t}{\tau_c} , \quad (2.25)$$

$$\theta = \frac{E_a T'}{RT_0^2} . \quad (2.26)$$

Equation 2.24 can now be integrated directly.

$$\int_0^\tau d\tau' = \int_0^\theta e^{-\theta'} d\theta' \quad (2.27)$$

$$\theta = -\ln(1 - \tau) \quad (2.28)$$

We can now see that the temperature will tend to $+\infty$ when $\tau = 1$, which is the induction time $t = \tau_c$. The infinite temperature is clearly nonphysical and a consequence of neglecting reaction consumption.

Two derivations are given Appendix C.2 that build on the one given above and those found in text books (Law, 2006, Glassman, 2008) leading to the final equation for the ignition delay time, τ_c ,

$$\tau_c = \frac{\rho c_v}{QA} \frac{T_0^2 \tilde{R}}{E_a} \exp\left(\frac{E_a}{\tilde{R}T_0}\right). \quad (2.29)$$

The equation shows that the ignition delay time has a very strong temperature dependence (Law, 2006) and the results of an ignition delay time study are usually plotted as shown earlier in Figure 2.25. It is an important design parameter for many combustion applications as it describes the explosion time for a homogeneous adiabatic reactor, but the ignition delay time is not an appropriate quantity to estimate the ignition time in low temperature safety situations. In these situations, such as ignition time of fuel spilled in an engine compartment or leaked to a compartment adjacent to a fuel tank that is kept at relatively low temperatures, the loss terms and reaction consumption cannot be neglected.

2.4.1.2 Effect of Ramp Rate on Induction Time

Now that we have established the ignition delay time for an adiabatic system, we now consider the effect of heating the walls and investigate the effect of the heating rate, α , on the ignition delay time.

The temperature evolution of a system with a wall temperature ramp and heat transfer is given in Appendix C.2.3. At late times, the temperature ramp inside follows the prescribed ramp rate outside

$$\frac{dT}{dt} = \alpha. \quad (2.30)$$

Neglecting reactant consumption, the chemical energy release can now be considered as an ad-

dition to the temperature ramp:

$$\frac{dT}{dt} = \frac{QA}{\rho c_v} \exp\left(-\frac{E_a}{\tilde{R}T}\right) + \alpha. \quad (2.31)$$

Since the equation is separable, direct integration is possible,

$$\int_0^t dt' = \int_{T_0}^T \frac{1}{k \exp\left(-\frac{E_a}{\tilde{R}T'}\right) + \alpha} dT', \quad (2.32)$$

where $k = QA/\rho c_v$. However, we must make an approximation to find an analytic solution.

$$\int_0^t dt' = \int_{T_0}^T \frac{1}{k} \exp\left(\frac{E_a}{\tilde{R}T'}\right) \left(1 - \frac{\alpha}{k \exp\left(-\frac{E_a}{\tilde{R}T'}\right)} + \left(\frac{\alpha}{k \exp\left(-\frac{E_a}{\tilde{R}T'}\right)}\right)^2 - \dots\right) dT' \quad (2.33)$$

This series converges only for

$$\frac{\alpha}{k \exp\left(-\frac{E_a}{\tilde{R}T'}\right)} < 1 \quad (2.34)$$

which is a reasonable assumption, holding true for $T' > 410$ K given the values in Table 2.2 at a heating rate of 10 K/min. Thus it is possible to determine, by inspecting the integrals, that the time until ignition, t_{ign} is shorter when the external wall temperature is ramped up.

$$t_{ign} = \int_{T_0}^T \frac{1}{k} \exp\left(\frac{E_a}{\tilde{R}T'}\right) \left(1 - \frac{\alpha}{k \exp\left(-\frac{E_a}{\tilde{R}T'}\right)}\right) dT' \quad (2.35)$$

The detailed behavior, of course depends on the different parameters, such as the activation temperature, $T_a = E_a/\tilde{R}$, or k . Varying the initial temperature, T_0 , and numerically integrating both Equation 2.23 and Equation 2.32 gives the ratio, r , between the delay time with and without wall heating in Figure 2.28. The results show how the addition of a wall temperature ramp decreases the ignition delay time and its influence is increased the longer the initial ignition delay time is.

$$r = \int_{T_0}^T \frac{1}{k \exp\left(-\frac{E_a}{\tilde{R}T'}\right)} dT' \Bigg/ \int_{T_0}^T \frac{1}{k \exp\left(-\frac{E_a}{\tilde{R}T'}\right) + \alpha} dT' \quad (2.36)$$

Equation 2.31 does not describe the system accurately because the ramp heating rate is directly coupled to the heat transfer (see Equation 2.22). The derivation described here is therefore more a thought experiment of what would happen to the induction time if the mixture temperature were to increase at a given rate. The main observation from Figure 2.28 is that ratio of induction times is less

than one, i.e., an added temperature increase will shorten the induction time. For the overall system, this implies that system which ignite will even ignite faster if the temperature is increased from the outside or inside. A possibility for this internal temperature ramp could be nuclear reactions not captured in the chemical energy.

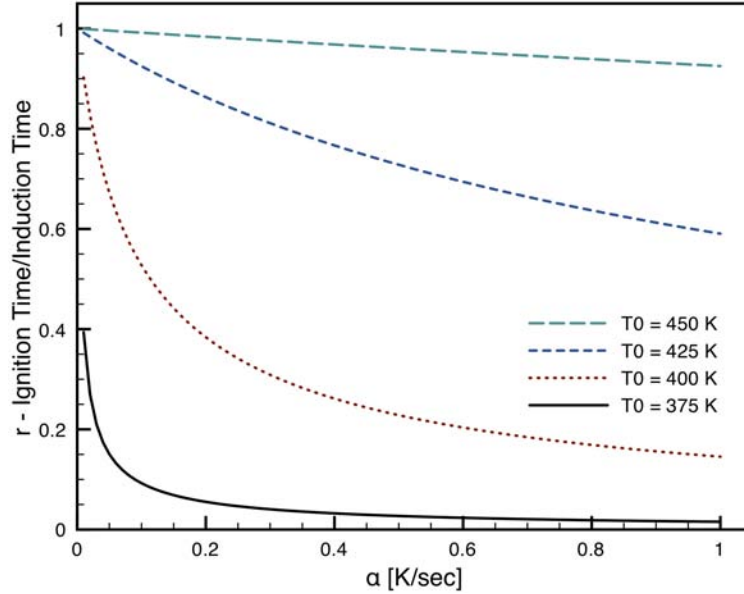


Figure 2.28: Ramp rate reduced induction time

2.4.1.3 Critical Heat Transfer

If we include heat transfer to the wall, but omit the wall temperature ramp ($\alpha = 0$), we can reach solutions which depend on the initial temperature of the mixture. This classical scenario is often called the Semenov problem since he first considered it (Semenov, 1940), and it is discussed in text books (Glassman, 2008, Law, 2006). The energy conservation equation now becomes

$$\frac{dT}{dt} = \frac{QA}{\rho c_v} \exp\left(-\frac{E_a}{RT}\right) - \frac{Sh}{\rho V c_v} (T - T_w^0) , \quad (2.37)$$

which can be reduced to the following form with similar approximations as in the previous section (see Appendix C.2.5 for details)

$$\frac{d\theta}{d\tau} = e^\theta - \hat{h}\theta = \dot{T}_r + \dot{T}_w . \quad (2.38)$$

The equation shows the direct competition between the energy release rate and the heat-loss rate. This competition can be visualized by plotting the reaction-based temperature change rate, \dot{T}_r , and the wall-based temperature change rate, \dot{T}_w , as a function temperature, θ , as shown in Figure 2.29. If

the heat transfer coefficient is below the critical value, $\hat{h} = e$, the chemical energy release rate exceeds the heat-loss rate for all temperature values. At the critical heat transfer value, $\dot{T}_w = -e \cdot \theta$, we can reach an unstable equilibrium point, point “a”, where the heat-loss rate equals the release rate, but any increase in temperature leads to ignition. For higher values of the heat transfer coefficient, a stable equilibrium point, point “b”, and a unstable equilibrium point, point “c”, can be reached depending on the initial temperature. At point “b”, an increase in temperature lead the heat-loss to exceed the chemical heat release and system will return back to “b”. At point “c” increasing the temperature creates a runaway reaction, where the heat-loss can never catch up with the heat release again.

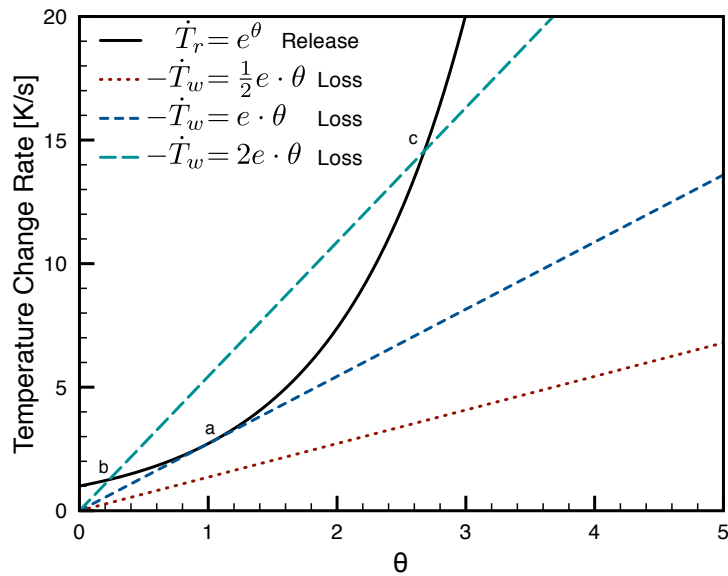


Figure 2.29: Absolute values of heat release and heat-loss components of the energy equation (after Law, 2006)

2.4.1.4 Critical Time For Wall Temperature Ramp

Now, we consider the competition between the chemical energy release and heat-loss with an increasing wall temperature. This means we are considering the full energy equation, but are still neglecting species consumption

$$\frac{dT}{dt} = \frac{QA}{\rho c_v} \exp\left(-\frac{E_a}{\tilde{R}T}\right) + \frac{Sh}{\rho V c_v} (T_0 + \alpha t - T) . \quad (2.39)$$

Here, the initial temperature is the wall temperature since we assume to start far away from the activation temperature, $T_a = E_a/\tilde{R}$, implying that the initial consumption is small. The evolution

of the temperature is considered to be a small deviation, T' , from the initial temperature, T_0 ,

$$T = T_0 + T' . \quad (2.40)$$

The energy equation can then be simplified using the large activation energy assumption (see C.2.2),

$$\frac{dT'}{dt} = \frac{1}{\tau_c} \frac{\tilde{R}T_0^2}{E_a} \exp\left(\frac{E_a T'}{\tilde{R}T_0^2}\right) + \frac{1}{t_w} (\alpha t - T') , \quad (2.41)$$

using the previously defined the wall heat transfer time

$$t_w = \frac{\rho V c_v}{Sh} , \quad (2.42)$$

and the ignition delay time

$$\tau_c = \frac{\rho c_v}{QA} \frac{T_0^2 \tilde{R}}{E_a} \exp\left(\frac{E_a}{\tilde{R}T_0}\right) . \quad (2.43)$$

The temperature, time and other parameters can be nondimensionalized as follows:

$$\tau = \frac{t}{\tau_c} \quad (2.44)$$

$$\theta = \frac{E_a T'}{\tilde{R}T_0^2} \quad (2.45)$$

$$\hat{h} = \frac{\tau_c}{t_w} \quad (2.46)$$

$$\tilde{\alpha} = \frac{\alpha T_0 \tau_c}{T_0^2} . \quad (2.47)$$

The nondimensional energy equation now is

$$\frac{d\theta}{d\tau} = e^\theta + \hat{h} (\tilde{\alpha}\tau - \theta) = \dot{\Theta}_r + \dot{\Theta}_w , \quad (2.48)$$

where the nondimensional reaction-based and wall-based temperature change rates are

$$\dot{\Theta}_r = e^\theta \quad (2.49)$$

and

$$\dot{\Theta}_w = -\hat{h}\theta + \hat{h}\tilde{\alpha}\tau . \quad (2.50)$$

As discussed in the previous section, critical solutions can be observed when the right hand side of the energy equation sums to zero, $d\theta/d\tau = 0$, when the heat transfer coefficient is sufficiently large, $\hat{h} \geq e$. This is observed initially, $\tau = 0$, in a system where the wall temperature is undergoing a ramp heating (see Figure 2.30).

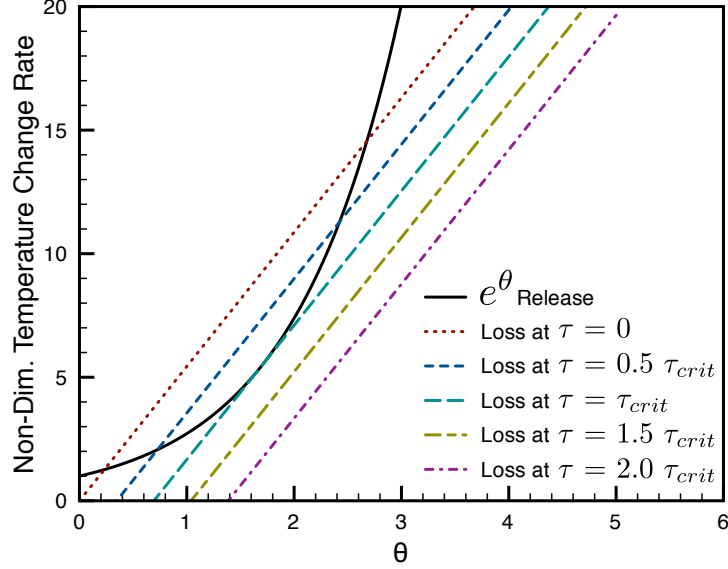


Figure 2.30: Heat release and heat-loss with a wall temperature ramp ($\hat{h} = 2e$)

In system with wall temperature ramp, however, the heat release will eventually always exceed the heat-loss. This point is characterized by not only having the right hand side of the energy equation summing to zero $d\theta/d\tau = 0$,

$$\dot{\Theta}_r = -\dot{\Theta}_w \iff e^\theta = \hat{h}\theta - \hat{h}\tilde{\alpha}\tau \quad (2.51)$$

and also the heat release term, $\dot{\Theta}_r$, and heat-loss term, $\dot{\Theta}_w$, being tangent as shown in Figure 2.30 which can be represented as

$$\frac{d\dot{\Theta}_r}{d\theta} = -\frac{d\dot{\Theta}_w}{d\theta} \iff e^\theta = \hat{h} \quad (2.52)$$

Note that the temperature ramp rate, $\tilde{\alpha}$, is not a function of the temperature. Solving Equation 2.52 for θ and substituting back Equation 2.51 allows us to solve for the critical time τ_{crit}

$$\hat{h} - \hat{h} \ln(\hat{h}) + \hat{h}\tilde{\alpha}\tau_{crit} = 0 \quad (2.53)$$

$$\tau_{crit} = \frac{\ln \hat{h} - 1}{\tilde{\alpha}} . \quad (2.54)$$

This is only of interest for values of $\hat{h} \geq e$, smaller values of \hat{h} yield solutions that always explode faster than τ_{crit} .

Figure 2.30 gives a graphical representation of how the wall heat-loss term, $\dot{\Theta}_w$, evolves in time when a heating ramp is applied. For time less than the critical time, τ_{crit} , the behavior of the system depends on the temperature of the system, i.e., at low temperatures the heat-loss term is greater than the heat release and at large temperature the heat release is always greater than the heat-loss. However, at later times, τ_{crit} and above, the heat release will always exceed the heat-loss. This means that a system that is heated externally will always undergo ignition, as long as consumption can be neglected.

2.4.2 Ignition With Consumption

Treating thermal ignition without consumption is insufficient to explain slow reaction behavior. In this final section of the theoretical treatment consumption is included in the analysis; first without any heat-loss and then considering the full set of equations assuming a one-step model for the chemical reaction. An example of including reaction consumption in a one-step model can be found in Radulescu and Maxwell (2010).

2.4.2.1 Induction Time With Consumption

As a first step we consider how the consumption of reactants changes the induction time, or ignition delay time, explored earlier. Consumption can be reinstated and in the adiabatic case where there is no heat transfer to the wall, the chemical energy is completely converted to thermal energy. This allows us to eliminate the consumption equation. A solution of this problem is discussed in Adler and Enig (1964). The set of equations governing this scenario are the temperature equation from the energy equation

$$\frac{dT}{dt} = \frac{QA}{\rho c_v} (1 - \lambda) \exp\left(-\frac{E_a}{RT}\right) \quad (2.55)$$

and one-step reaction progress equation

$$\frac{d\lambda}{dt} = A (1 - \lambda) \exp\left(-\frac{E_a}{RT}\right), \quad (2.56)$$

where $\lambda = 0$ represents only reactants and $\lambda = 1$ only products. The coupled equations can be simplified to

$$\rho c_v \frac{dT}{dt} = Q \frac{d\lambda}{dt}. \quad (2.57)$$

Multiplying through by dt and assuming constant specific heat we can integrate the equation from the initial condition $T = T_0$, $\lambda = 0$,

$$\int_{T_0}^T \rho c_v dT^* = \int_0^\lambda Q d\lambda^* . \quad (2.58)$$

For adiabatic, constant-volume conditions the relationship between chemical and thermal energy can be obtained from the conservation of energy:

$$\rho c_v (T - T_0) = \lambda Q . \quad (2.59)$$

The final temperature can be calculated at the time when all fuel is consumed ($\lambda = 1$)

$$T_f = T_0 + \frac{Q}{\rho c_v} . \quad (2.60)$$

At any time during the explosion, the progress of the reaction, λ , can then be expressed solely in terms of the fractional temperature rise

$$\lambda(T_f - T_0) = (T - T_0) , \quad (2.61)$$

and the energy equation expressed in terms of temperature alone becomes independent of the progress variable

$$\frac{dT}{dt} = \frac{QA}{\rho c_v} \left(\frac{T_f - T}{T_f - T_0} \right) \exp \left(-\frac{E_a}{RT} \right) . \quad (2.62)$$

This equation can be integrated for as shown by Hermance (1975) and Parang and Jischke (1975):

$$\int_0^t \frac{QA}{\rho c_v (T_f - T_0)} dt^* = \int_{T_0}^T \frac{e^{\frac{E_a}{RT^*}}}{T_f - T^*} dT^* . \quad (2.63)$$

The final answer can be expressed in terms of the exponential integral, $Ei(x)$, which is defined as

$$Ei(x) = - \int_x^\infty \frac{e^{-t}}{t} dt . \quad (2.64)$$

The solution to Equation 2.63 can be written as

$$t(T) = \frac{\rho c_v (T_f - T_0)}{QA} \times \left[Ei \left(\frac{T_a}{T} \right) - Ei \left(\frac{T_a}{T_0} \right) + e^{\frac{T_a}{T_f}} \left[Ei \left(\frac{T_a}{T_0} - \frac{T_a}{T_f} \right) - Ei \left(\frac{T_a}{T} - \frac{T_a}{T_f} \right) \right] \right] . \quad (2.65)$$

where $T_a = E_a/\tilde{R}$ and the solution is only valid for large values of T_a/T_f . To find the induction time the upper limit should be chosen at $T_f - \epsilon$ as it will take an infinite amount of time to reach T_f yielding a non-physical solution.

As Equation 2.65 shows, the inclusion of consumption results in an analytical solution that is substantially more complex than when consumption is neglected. Further discussion of the solution with consumption is discussed in Adler and Enig (1964), Hermance (1975), and Parang and Jischke (1975).

2.4.2.2 Thermal Ignition with heat-loss, Consumption, and Wall Temperature Ramp

Now, we consider the full set of equations for the ramp heated vessel describing the experimental setup using a one-step model for the chemical reaction progress. Our final goal is to describe how the heating rate changes the behavior from a slow reaction case to an ignition case. Again, the equations describing the system are

$$\frac{dT}{dt} = \frac{Q}{\rho c_v} \frac{d\lambda}{dt} + \frac{Sh}{\rho V c_v} (T_w^0 + \alpha t - T) , \quad (2.66)$$

$$\frac{d\lambda}{dt} = A(1 - \lambda) e^{-\frac{E_a}{RT}} . \quad (2.67)$$

The numerical solutions, using the values from Table 2.2, show that the transition from an ignition case to a slow reaction case occurs in a small region of temperature, reaction progress, and time. Figure 2.31 shows an ignition case and a slow reaction case with the transition region indicated in the dashed box.

Taking a closer look at the the indicated transition region, we can observe large changes in temperature, and reaction progress with small changes in time. Computing solutions close to the transition as shown in Figures 2.32 and 2.33, we can see that the transition behavior occur near a specific time, t^* . The transition behavior also occurs near a specific temperature, T^* , and reaction progress, λ^* , most clearly seen Figure 2.34 that shows the numerical results of considering temperature as a function of reaction progress

We can compute an approximate solution of the equations by neglecting chemical reactions, which can serve as a reference case as plotted in Figure 2.34. When setting the heat of reaction to zero, $Q = 0$, the temperature will only increase due to the externally imposed by the wall heating rate (see Appendix C.2.3) and the reaction progress is still governed by the one-step reaction model.

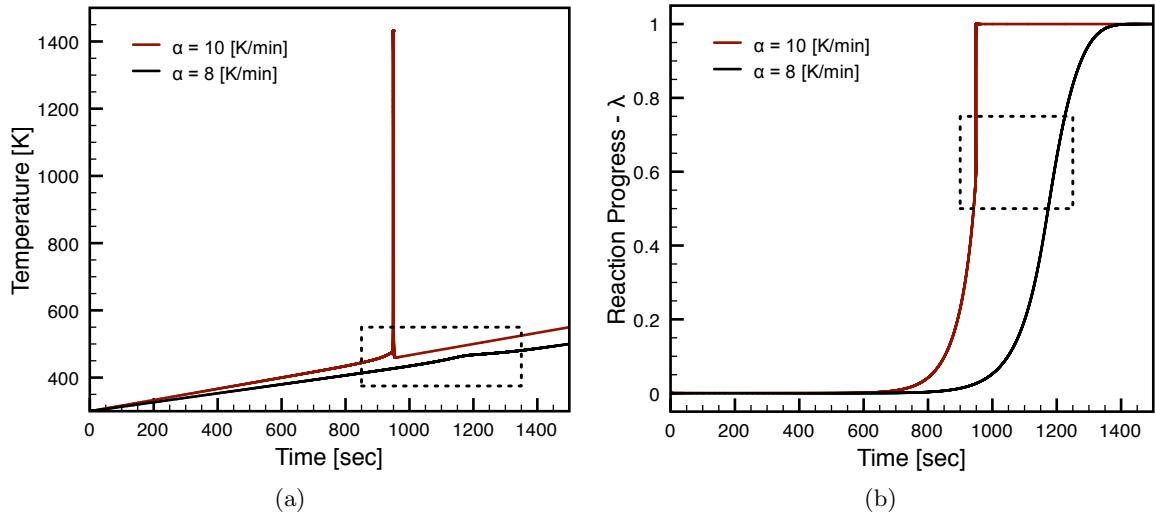


Figure 2.31: Temperature (a) and reaction progress (b) for a slow reaction case and (8 K/min) and an ignition case (10 K/min). The highlighted region indicates the region where the transition point lies.

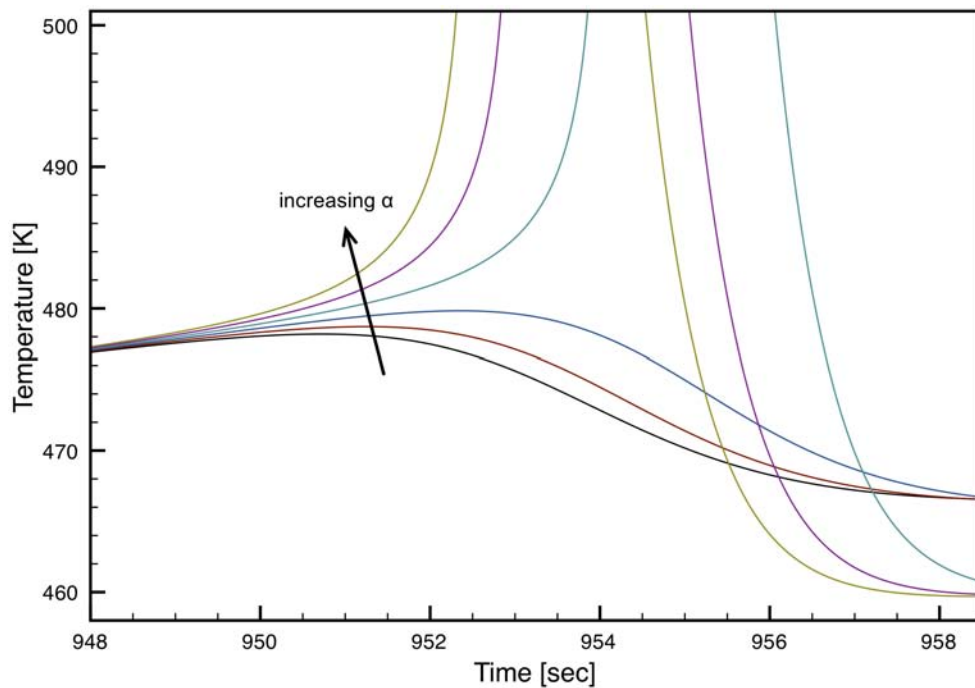


Figure 2.32: Temperature with varying heating rate, α . The curves are spaced equally with increasing heating rates, with a step size of 1.2×10^{-4} K/min (for the lowest curve $\alpha = 9.99546$ K/min).

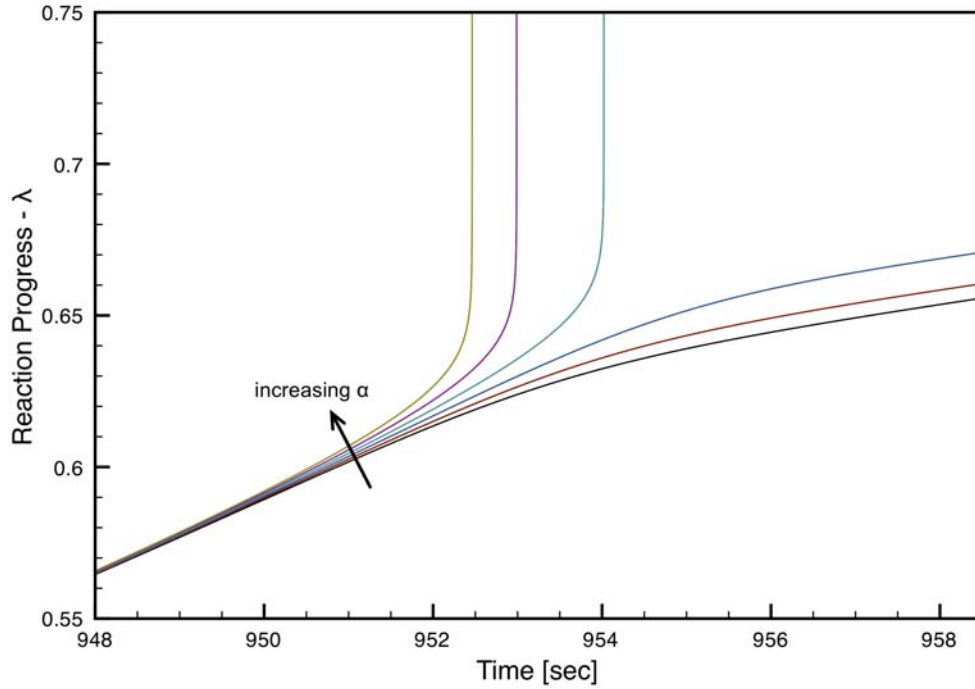


Figure 2.33: Reaction progress with varying heating rate, α . The curves are spaced equally with increasing heating rates, with a step size of 1.2×10^{-4} K/min (for the lowest curve $\alpha = 9.99546$ K/min).

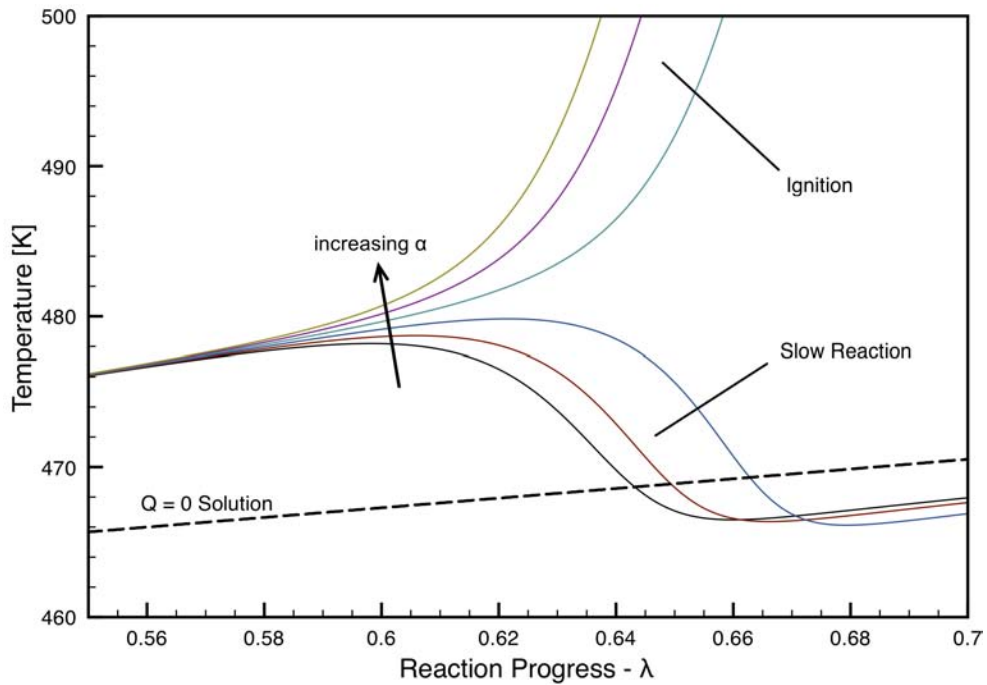


Figure 2.34: Temperature vs. reaction progress with varying heating rate, α . The curves are spaced equally with increasing heating rates, with a step size of 1.2×10^{-4} K/min (for the lowest curve $\alpha = 9.99546$ K/min). The $Q = 0$ solution is computed for the average heating rate value.

$$\frac{dT}{dt} = \alpha \quad (2.68)$$

$$\frac{d\lambda}{dt} = A(1 - \lambda) \exp\left(-\frac{E_a}{\tilde{R}T}\right) \quad (2.69)$$

These two equations can be combined and rearranged to separate the variables,

$$\frac{d\lambda}{1 - \lambda} = A \exp\left(-\frac{E_a}{\tilde{R}T}\right) \frac{dt}{dT} dT = A \exp\left(-\frac{E_a}{\tilde{R}T}\right) \frac{1}{\alpha} dT. \quad (2.70)$$

This equation can be integrated numerically to yield the approximate solution shown in Figure 2.34

$$\int_0^\lambda \frac{d\tilde{\lambda}}{1 - \tilde{\lambda}} = \int_{T_0}^T A \exp\left(-\frac{E_a}{\tilde{R}\tilde{T}}\right) \frac{1}{\alpha} d\tilde{T}. \quad (2.71)$$

The $Q = 0$ solution initially lies below the actual solution because it does not include any heat release from the chemical reaction. Later, the $Q = 0$ solution lies above the full solution for the heat transfer out of the system is sustained as the reaction progresses.

The numerical solutions show that the transition from an ignition case to a slow reaction case occurs over a narrow range of temperature, reaction progress, and time near the transition point (*). The differential equations can be linearized about this transition point (T^* , λ^* , t^*).

$$\lambda = \lambda^* + \lambda' \quad (2.72)$$

$$T = T^* + T' \quad (2.73)$$

$$t = t^* + t' \quad (2.74)$$

We now examine how small changes in the heating rate alter the behavior of the system. To this end it is useful to examine the behavior of the temperature directly as a function of reaction progress, $dT'/d\lambda'$, and then evaluating this dependence at the transition point. Substituting the perturbation into the temperature equation gives:

$$\frac{dT}{dt} = \frac{dT^*}{dt} + \frac{dT'}{dt} = \frac{dT'}{dt} = \frac{Q}{\rho c_v} \frac{d\lambda}{dt} + \frac{Sh}{\rho V c_v} (T_w^0 + \alpha(t^* + t') - T^* - T') . \quad (2.75)$$

The reaction progress equation becomes:

$$\frac{d\lambda}{dt} = \frac{d\lambda^*}{dt} + \frac{d\lambda'}{dt} = \frac{d\lambda'}{dt} = A(1 - \lambda^* - \lambda') \exp\left(-\frac{E_a}{\tilde{R}(T^* + T')}\right) \quad (2.76)$$

Dividing Equation 2.75 by Equation 2.76 gives:

$$\frac{dT'}{d\lambda'} = \frac{Q}{\rho c_v} + \frac{Sh}{A\rho V c_v} \exp\left(\frac{E_a}{\tilde{R}(T^* + T')}\right) \frac{T_w^0 + \alpha(t^* + t') - T^* - T'}{1 - \lambda^* - \lambda'}. \quad (2.77)$$

Now, we can evaluate Equation 2.77 at the the transition point (T^*, λ^*, t^*)

$$\left.\frac{dT'}{d\lambda'}\right|_{T^*, \lambda^*, t^*} = \frac{Q}{\rho c_v} + \frac{Sh}{A\rho V c_v} \exp\left(\frac{E_a}{\tilde{R}T^*}\right) \frac{T_w^0 + \alpha t^* - T^*}{1 - \lambda^*} \quad (2.78)$$

$$\left.\frac{dT'}{d\lambda'}\right|_{T^*, \lambda^*, t^*} = \frac{q_c}{c_v} + \frac{Sh}{A\rho V c_v} \exp\left(\frac{E_a}{\tilde{R}T^*}\right) \frac{T_w^0 + \alpha t^* - T^*}{1 - \lambda^*}. \quad (2.79)$$

Equation 2.79 gives the trajectory of the solution from the transition point forward. Positive values indicate ignition, while negative values indicate slow reactions. The switch between the two is an explicit function of the heating rate, α . The high sensitivity to the heating rate can be shown by evaluating the derivative over a range of heating rates using the parameters given in Table 2.2. From the detailed simulations, we can identify roughly where the transition point (T^*, λ^*, t^*) lies, the values for which are given in Figure 2.35. From these values, an approximate value for the transition heating rate, $\alpha^* = 8.1$ K/min, can be computed by setting the left-hand side of Equation 2.79, which is comparable to the critical value found by inspecting the full solutions, $\alpha_c \approx 9.995$ K/min. The switch in sign of the right-hand side of Equation 2.79 is calculated as indicated in Figure 2.35, showing the zero crossing as well as the very large slope indicating the strong dependence on the heating rate.

At the transition point, the sign of $dT'/d\lambda'$ changes based on the value of the heating rate α . While the heating rate is not the only parameter, changing it while keeping all other parameters constant can change the behavior.

The result of the theoretical analysis shows that a switch from slow reaction to ignition can be controlled by a wall temperature ramping, regardless of the chemical mechanism. This is precisely the behavior observed experimentally as well as in the simulations using the detailed chemical mechanism. It underlines the importance of considering the heating rate as one of the parameters controlling the ignition behavior of a mixtures and thus must be taken into account when making assessments regarding ignition safety.

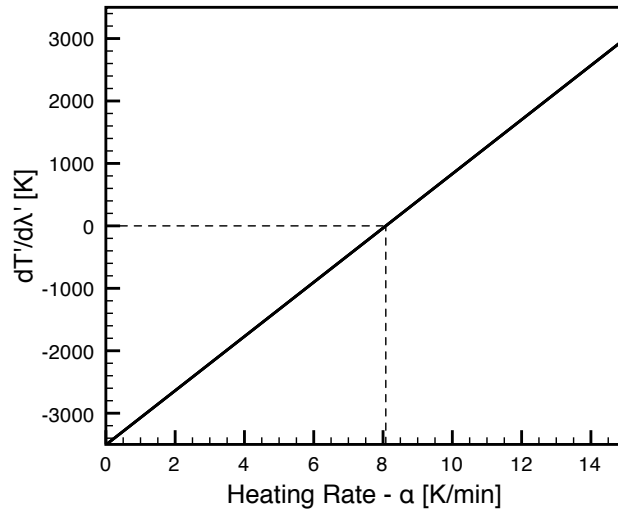


Figure 2.35: Temperature evolution about the transition point as a function of heating rate ($T^* = 480$ K, $\lambda^* = 0.6$, $t^* = 950$ s)

2.5 Conclusion

In the classical view of auto-ignition, a minimum temperature exists that leads to the ignition of a given fuel under specified conditions. It is known that the auto-ignition temperature depends on many parameters and the present study demonstrates that one of these, the rate at which the mixture is heated, greatly influences how the reaction progresses, and consequently whether the mixture ignites. Further, in contrast to a violent ignition event, we have found slow reaction cases, where it is possible to consume all the fuel without an ignition event at a well-defined temperature.

For instance, increasing the heating rate of the vessel by a factor of 2, from 4.25 to 11 K/min, produces an ignition event with a rapid pressure rise in a mixture that otherwise would have generated a slow reaction with no significant pressure rise. The same transition in behavior is shown for an increase in equivalence ratio from 1 to 1.2. In the range investigated, the minimum heating rate required for fast reactions decreases with increasing equivalence ratios.

The computations demonstrate that a model based on Semenov theory is capable of capturing the qualitative behavior of the explosion event. By adding the heating rate, α , to the classical Semenov model, we are able to reproduce the observed transition from a slow reaction case to an ignition case with increasing heating rate; with the necessity of determining the lumped heat transfer coefficient empirically.

The simulation results are not limited to detailed chemical mechanisms, but also hold when the chemistry is approximated by a one-step model. Through the theoretical treatment, we can clearly

determine that the heating rate switches the mixture evolution from slow reactions to ignitions.

The type of reaction that the mixture undergoes is a complex function of the mixture composition, thermochemical feedback loop, residence time, and heat transfer. Consequently, for sufficiently slow heating rates, it is possible for the fuel to be completely consumed without any rapid pressure transient at temperatures above the classical auto-ignition value. The experimental results also indicate that the transitional heating rate is a function of the initial pressure and composition.

The results presented here show that an assessment of safety should include factors such as the temperature, pressure, mixture composition, and heating rate rather than just a threshold temperature when considering auto-ignition. For instance, the temperatures at which the reactions occur are near the listed auto-ignition temperatures for the slow reaction case, but slightly below for the ignition case. These factors come into play both when designing a standard test procedure to determine fuel properties as well as assessing the safety of a particular engineering design.

The simulations show that the slow reaction and ignition behavior can be modeled correctly, however due to the complex chemical pathways and limited data on fuels like *n*-hexane at low temperatures it is difficult to predict the temperature at the onset of reaction to an accuracy better than 50 K.

Chapter 3

Thermal Ignition and Flame Propagation from a Concentrated Hot Surface

3.1 Introduction

Hot surface ignition includes ignition by hot wires, pipes carrying hot gases, or malfunctioning equipment generating heat. One area of particular concern is the aviation industry where flammable mixtures can be ignited by sufficiently hot surface in the fuel tank or surrounding flammable leakage zones. For aviation applications ignition may occur at any altitude, and therefore a range of pressures and fuel-air mixtures should be investigated.

Ignition of a gaseous mixture from a rapidly-heated hot surface of small spatial extent occurs in an inhomogeneous atmosphere in contrast to the homogeneous situation examined in Chapter 2. There are very significant gradients of temperature next to the ignition surface that play an essential role in the ignition process. We showed in the previous chapter that homogeneously heated mixtures can be modeled as a zero-dimensional problem and reasonable results obtained for ignition behavior considering only species and energy balances for the entire volume. Ignition by a hot surface requires multidimensional calculations of the fluid mechanics, heat transfer, species transport, and chemical reactions. It is necessary to perform experiments that test specific conditions of interest in order to obtain reliable results for ignition limits of hydrocarbon fuels like Jet A. Experiments also provide valuable data for testing numerical simulations of ignition based on approximate reaction mechanisms.

The approach taken in this study is to control the composition and pressure of the mixture and power input to the hot surface in order to control the peak surface temperature and determine

ignition thresholds.

Key measured properties include the temperature of the hot surface leading to ignition, the subsequent flame propagation speed and shape, and finally the resulting peak pressure.

3.2 Experimental Setup

The experiment uses a closed 2 liter combustion vessel. For each experiment the vessel is evacuated and filled with hexane, oxygen, and nitrogen using the method of partial pressures to create a specified mixture (accurate to 0.01 kPa). The mixture is then mixed using a circulation pump for 2 minutes, and left to settle for 2 minutes before increasing the temperature of the hot surface. Several different hot surfaces are used in the study, but the majority of the ignition temperature data are obtained from a Bosch high-temperature glow plug (noncommercial) and an Autolite 1110 glow plug (commercially available).

The schematic in Figure 3.1 shows a cross section view of the combustion vessel used in the experiment. The inside of the vessel is a rectangular prism with inner dimensions of 11.4 cm \times 11.4 cm \times 17.1 cm (width \times depth \times height) giving an internal volume of approximately 2 liters. Four access ports, including two windows, as shown in Figure 3.2 allow for schlieren visualization and simultaneous access for temperature measurements.

The hot surface is mounted inside the field of view of the schlieren system with a reference-stagnation surface visible at the lower edge (see Figures 3.1 and 3.4). The diameter of the surface is 58 mm, slightly smaller than the window diameter. The mounting fixture is made of aluminum and the stagnation surface limits the gas motion and helps facilitate the comparison with simulations, which do not consider the volume beneath the stagnation surface.

During an experiment, the temperatures at glow plug as well as at the top of the vessel are measured with K-type thermocouples, with response times of 0.5 s and approximately 1 s, respectively. The pressure is measured with a fast-response (≥ 10 kHz) pressure gage (Endevco Model 8530B-200) at the top of the vessel.

A schlieren technique is used to visualize the plume of hot gas generated from the hot surface and the flame front. Settles (2001) has a detailed description of many different schlieren techniques. We usually used a typical schlieren system with a vertical and horizontal knife edge or dark background schlieren system (see Figure 3.5). A schematic of the setup used is given in Figure 3.3. Figure 3.4 shows an example of a color schlieren image that is obtained by placing a four color slide at the focus of the schlieren mirror. In all cases, we exploit the fact that the sharp density gradient across the

flame front changes the index of refraction of the gas and deflects the collimated light beam passed through the test section, creating the schlieren effect.

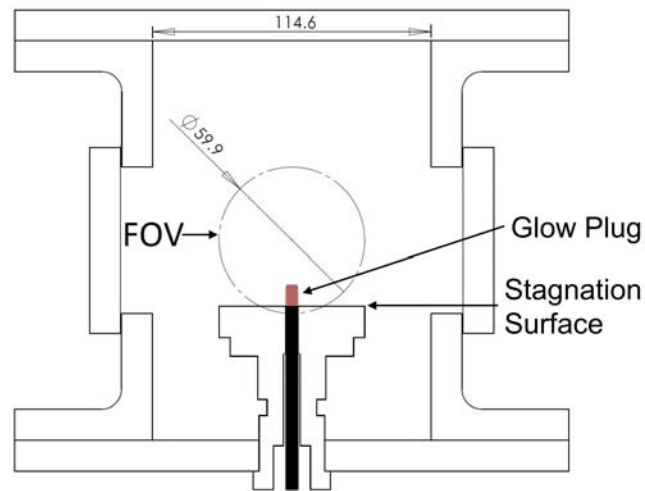


Figure 3.1: Diagram of the vessel, flow plug mounting fixture with stagnation surface, field of view (FOV), and glow plug (in red), with dimensions in mm

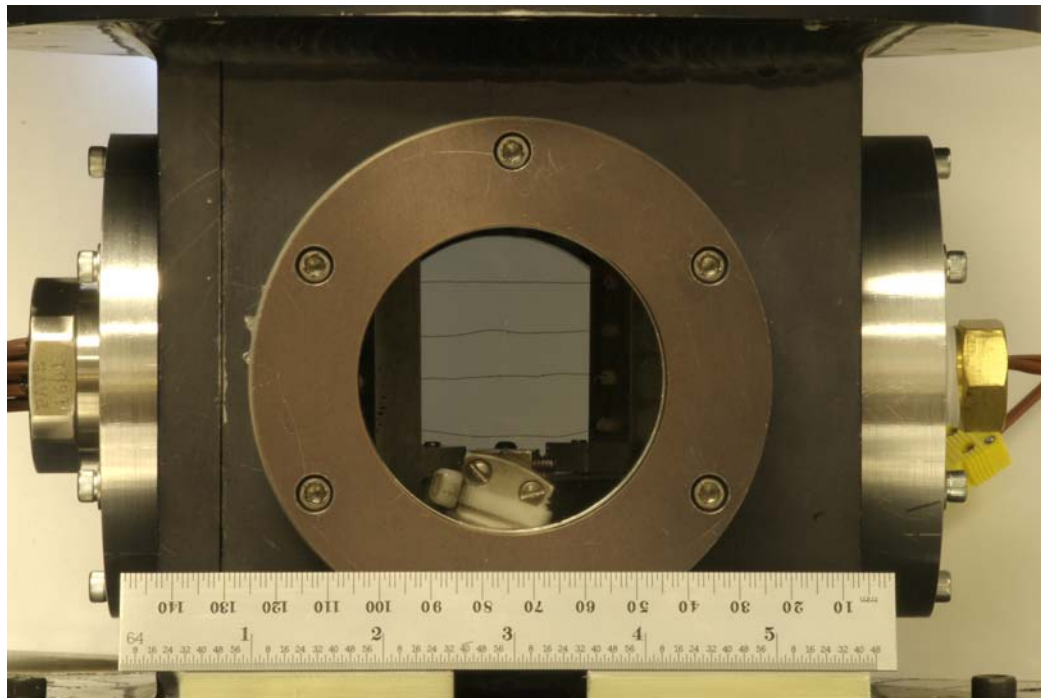


Figure 3.2: Photograph of the hot surface ignition vessel with an array of thermocouples above the hot surface. The flange on the left side shows a feedthrough for array of thermocouples and the feedthrough on the right is used for the thermocouple measuring the temperature of the hot surface.

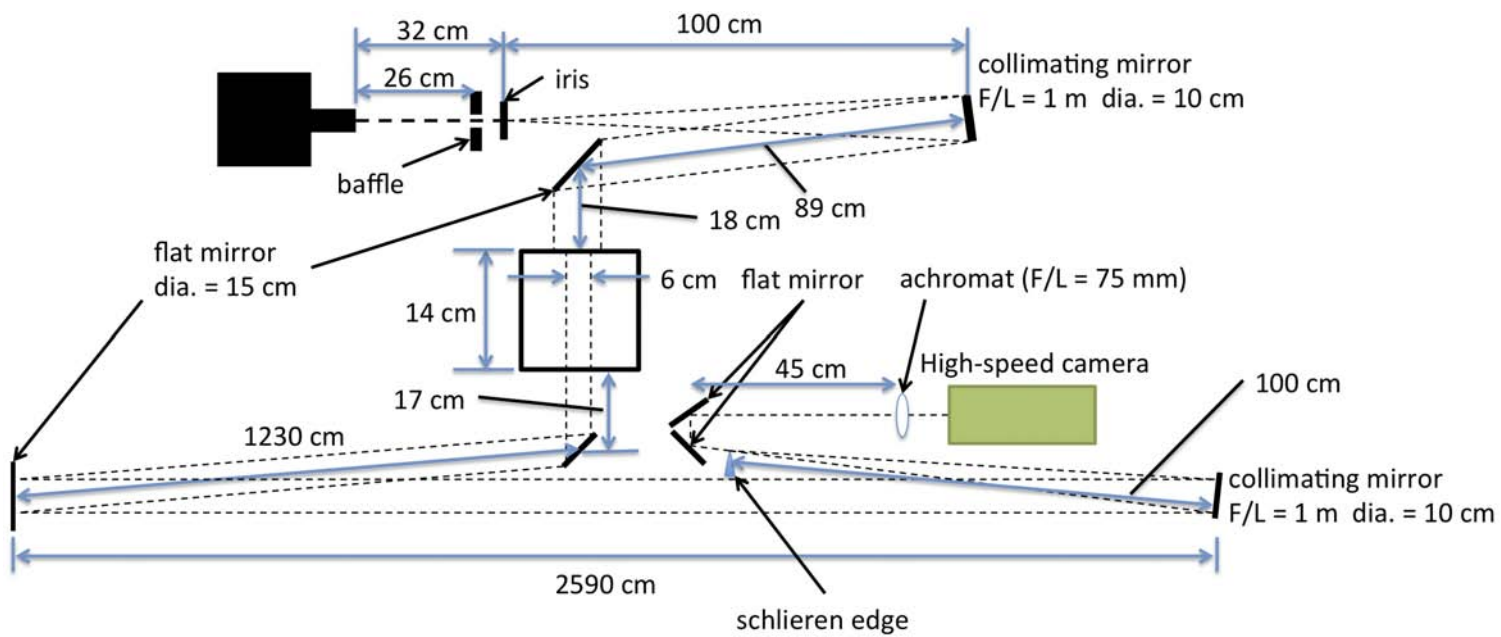


Figure 3.3: Schlieren setup schematic (the camera is used without a compound lens attached to the camera - the image is focused directly onto the CMOS with the 75 mm F/L lens)

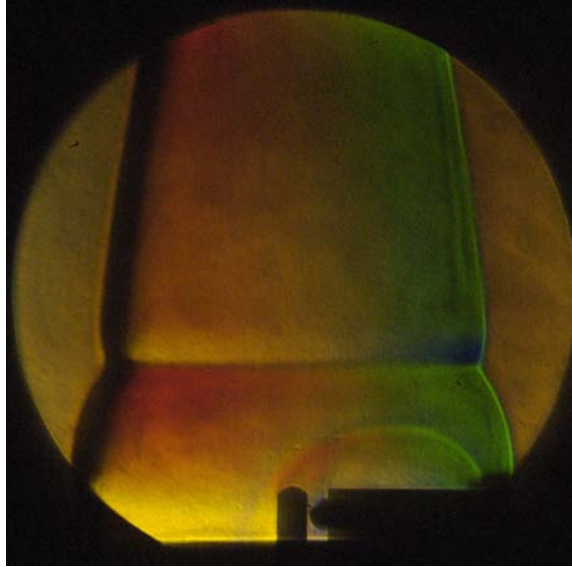


Figure 3.4: Example of color schlieren picture taken during the flame propagation of a hexane-air mixture at an equivalence ratio of $\phi = 1.9$, and initial pressure of $P_0 = 101$ kPa

Figure 3.5 shows a few frames from the high-speed schlieren video. From the video, we can confirm that the mixture ignited and at what time. The video is synchronized with the temperature and pressure measurements so that the ignition temperature can be identified. Additionally, the flame propagation speed is inferred from the video and the size of the window ($\varnothing = 59.9$ mm/2.36 in) is used as the reference scale.

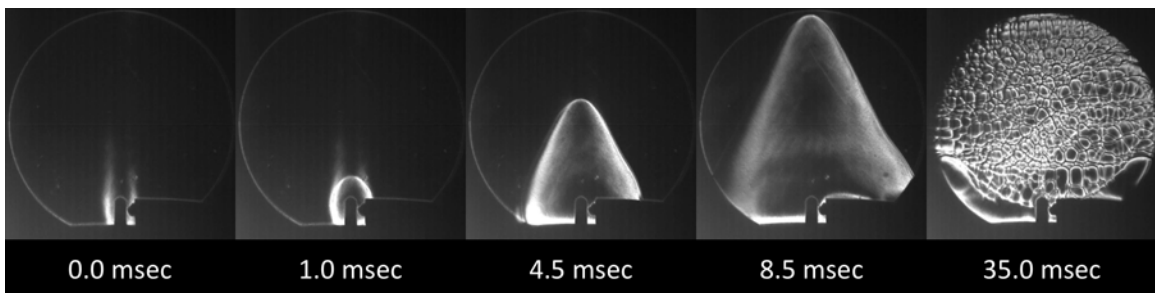


Figure 3.5: Dark background schlieren visualization of the flame propagation of shot 24 for a hexane-air mixture ($\phi = 1.2$). Typical frame rates were 1000–2000 frames per second (fps) using a 800×800 pixel resolution

The temperature measurement taken at the top of the vessel (Figure 3.6) gives an indication of the gas temperature before and after ignition. This measurement is mostly used for the initial temperature of the gas and to confirm whether or not ignition occurred in case other measurements should fail.

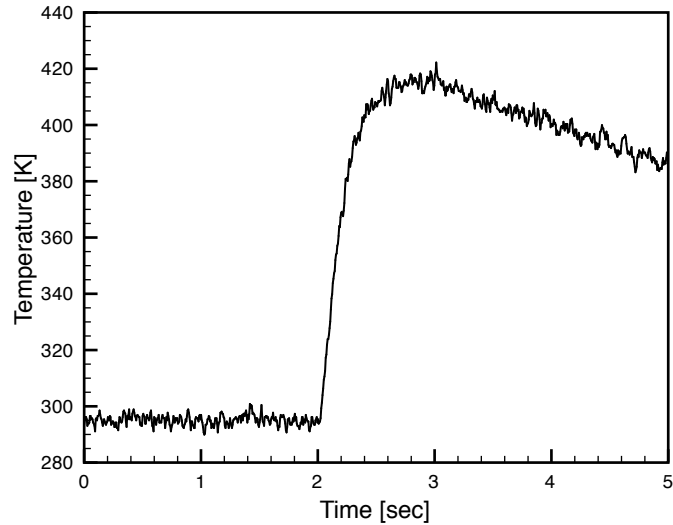


Figure 3.6: Temperature measurement at the top of the combustion vessel during the ignition of a hexane-air mixture ($\phi = 1.2$) initially at atmospheric pressure

The choice of hexane as the fuel for the experiments was motivated by its strong similarities to aviation and industrial hydrocarbon fuels while remaining simpler to handle experimentally. The hexane sample used in the experiments was characterized by the manufacturer as 89% *n*-hexane and 11% other hexane isomers. Mixtures of *n*-hexane/air are of interest at atmospheric pressure and lower, with equivalence ratios varying from the lower flammability limit at $\phi = 0.56$ to $\phi = 3.0$, corresponding to fuel concentrations from 1.2 to 6.48% (Zabetakis, 1965). At atmospheric and room temperature, the maximum partial pressure of hexane used was 6.5 kPa, which is well below the hexane room temperature vapor pressure of 15.6 kPa (Reid et al., 1977), and thus none of the fuel is expected to condense.

3.2.1 Composition Uncertainties

As described in the experimental procedure, the composition of the fuel-air mixture is controlled by filling the initially evacuated vessel using the method of partial pressures. The main uncertainty in the composition can be attributed to the accuracy of the pressure readings of 0.1 Torr (0.01 kPa). As part of the experimental procedure, deviations from the targeted pressure of 0.2 Torr were deemed acceptable. Some uncertainty in the composition is also created by the possibility of dissolving oxygen in the fuel.

However, additional uncertainty is created by the experimental setup, whose schematic is depicted in Figure 3.7. In the mixture preparation process, *n*-hexane is injected first to vaporize the liquid fuel,

and then oxygen and nitrogen are added in turn to create a fuel-air mixture. When the circulation pump is turned on next, the space between valve V3 and the tee to its right in the plumbing system (highlighted in Figure 3.7) will not be fully mixed with the rest of the system. While the exact mixture trapped in this dead space is not known, it is reasonable to assume that the fuel will be compressed into this volume until the amount of oxygen is sufficient to reach the junction to the right of V3. This leads to a reduction in the amount of hexane injected by 1.7 % from the values reported in Appendix I.2. In this chapter, the composition has been adjusted to account for the shift in equivalence ratio just described. The maximum uncertainty is even greater ($\sim 10\%$) considering that more of the fuel could be pushed into the dead space mentioned. Combining this uncertainty with the others gives an overall uncertainty of $+3\%/-13\%$ in terms of ϕ , which is either given as part of the error bars on the equivalence ratio or mentioned in the caption below each figure.

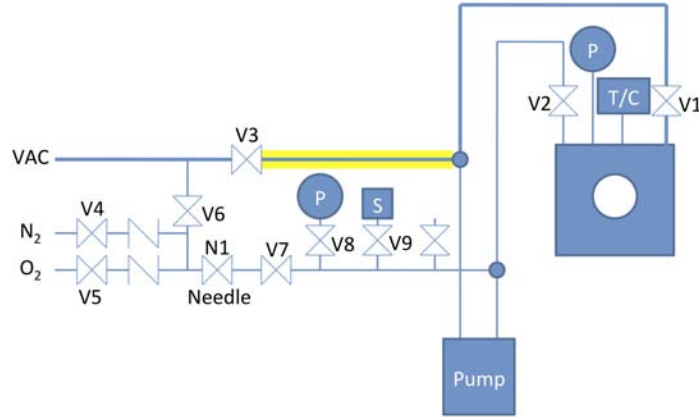


Figure 3.7: Hot surface experiment plumbing diagram (V–ball valve, VAC–vacuum pump, P–pressure transducer, T/C–thermocouple, S–Septum, Needle–needle valve for metering input)

3.2.2 Peak Pressure

The pressure during combustion is recorded with a fast-response pressure transducer at the top of the vessel. Pressure measurements such as the one shown in Figure 3.8 are important in assessing the potential structural damage that could be caused by an explosion. These measurements can be compared to constant-volume adiabatic equilibrium calculation performed with Cantera (Goodwin, 2003) as shown in Figure 3.9. Heat transfer during the combustion results in the experimental pressure being lower than those predicted by a constant-volume equilibrium calculation (Shepherd and Ratzel, 1985). At higher equivalence ratios, $\phi > \sim 2$, the flame speed is reduced, increasing the time for losses to occur and increasing the effect of buoyancy thus consuming a decreasing fraction

the mixture and reducing the peak pressure significantly below that predicted by the equilibrium calculation.

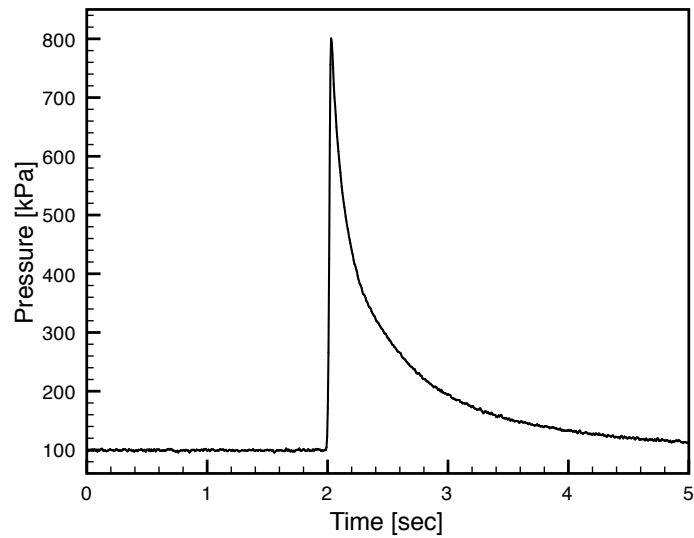


Figure 3.8: Pressure during the ignition of a hexane-air mixture ($\phi = 1.2$) initially at atmospheric pressure. The pressure is measured at the top of the combustion vessel. The peak pressure measured is 802.2 kPa.

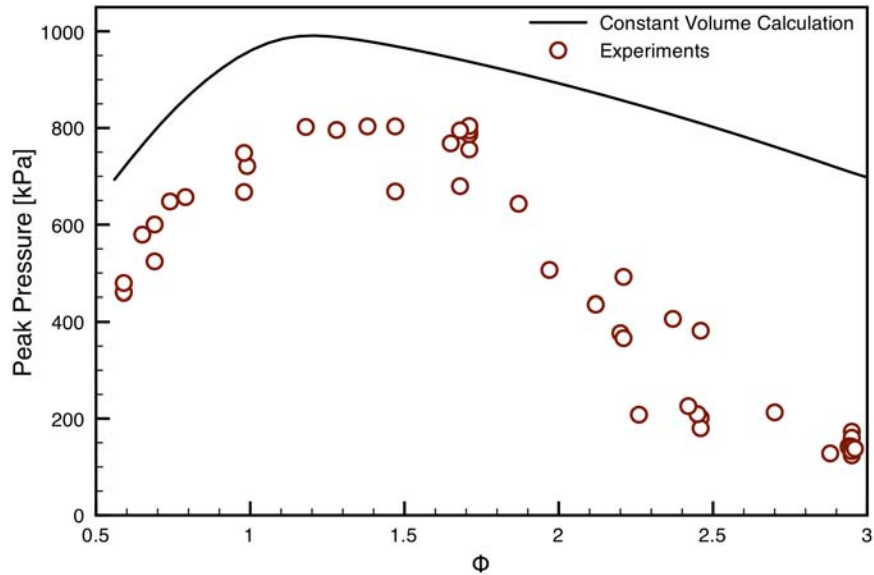


Figure 3.9: Peak pressure as a function of equivalence ratios at $P_0 = 101$ kPa. Experimental results and equilibrium calculations performed using Cantera (Goodwin, 2003). All mixture compositions have the associated uncertainty in ϕ of +3%/-13%, not shown here.

3.2.3 Hot Surface I — High-Temperature Glow Plug (Bosch)

One of the hot surfaces used in this study is a specialized high-temperature glow plug (Bosch Part number: 978801-0485). The geometry of the glow plug is shown in Figure 3.10, and typical temperature traces as a function of time are shown in Figure 3.11. This glow plug reaches temperatures in excess of 1000 K in 10 seconds and temperatures of above 1500 K after 30 seconds. During typical operation the glow plug was not powered for more than 30 seconds to prolong its lifetime. This glow plug was used for a large number of experiments. After these experiments, temperature measurements along the glow plug were taken to characterize its temperature distribution and during this the glow plug failed. Unfortunately only one such glow plug was available. Most of the remaining experiments were performed with a commercially available glow plug.

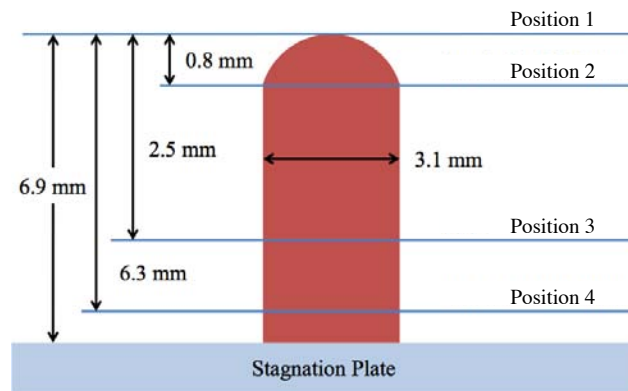


Figure 3.10: High-temperature glow plug schematic

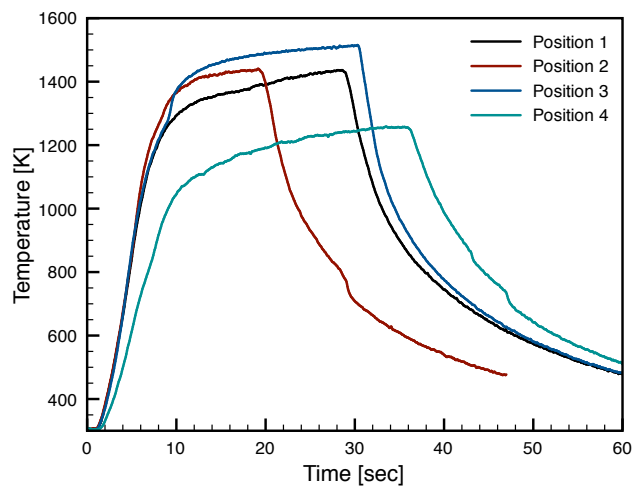


Figure 3.11: High-temperature glow plug temperature distribution

3.2.4 Hot Surface II — Standard Glow Plug (Autolite 1110)

The other standard hot surface that was used in this test series is a commercial automobile (diesel) glow plug (Autolite 1110). It is placed inside the stagnation plate in a similar fashion to the high-temperature glow plug. The geometry is shown in Figure 3.12 and the temperature profile is shown in Figure 3.13. It can reach a maximum temperature of 1453 K which fixed the upper limit of ignition temperature we were able to test.

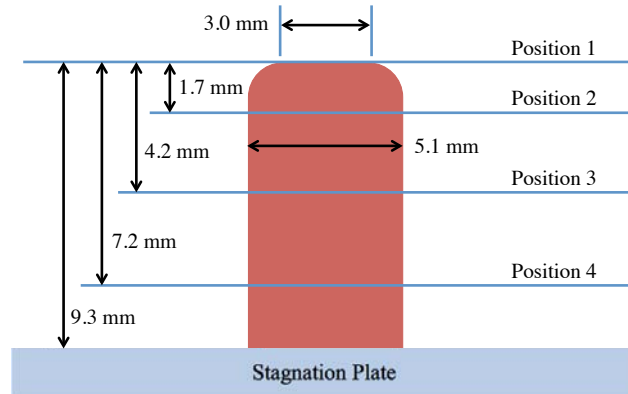


Figure 3.12: Autolite glow plug schematic

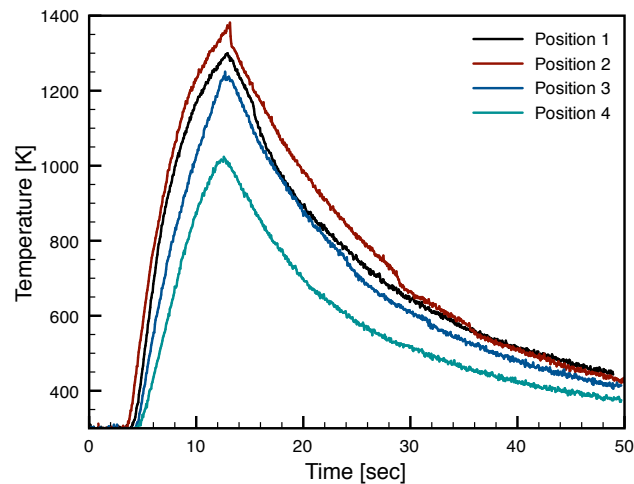


Figure 3.13: Autolite glow plug temperature distribution

3.3 Ignition Temperature

In this section, we investigate how the ignition temperature changes as a function of the fuel-air mixture, the initial pressure, and surface area of the hot surface. The hot surface temperature monitored during the experiment at the hottest part of the glow plug by a K-type thermocouple (bead size: $\varnothing = 0.3$ mm). The glow plug has an approximately 5 second temperature ramp before ignition. Figure 3.14 shows example of the measured glow plug temperature, beginning at the latter half of the temperature ramp. The ignition temperature of the gas mixture is defined as the temperature of the glow plug at the time ignition occurs. Ignition occurs at around 2 seconds as seen in the sharp increase in temperature slope. The exact time of ignition is inferred from the accompanying schlieren video. This confirms that the ignition coincides with the change in slope seen in the temperature reading. However, because the thermocouple has a response time of 0.5 seconds and the temperature of the glow plug is ramped up at ≈ 220 K/s, the ignition temperature has an uncertainty of +110 K from the measured value.

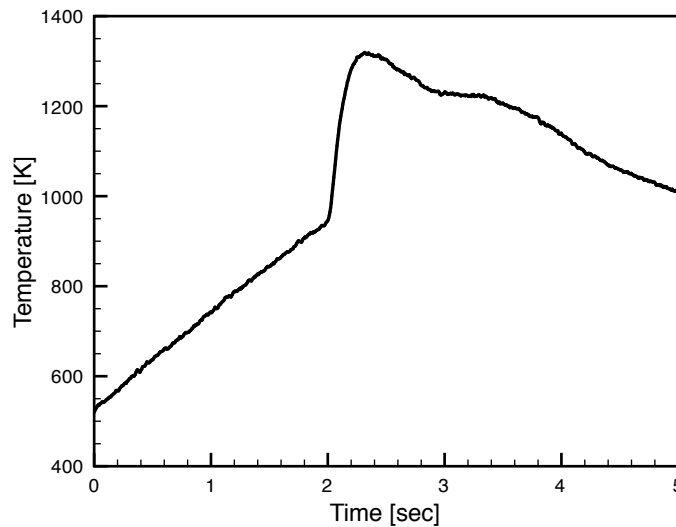


Figure 3.14: Temperature of the glow plug during the ignition of a hexane-air mixture ($\phi = 1.2$) initially at atmospheric pressure

Experiments with and without a thermocouple on the glow plug were performed to check if the presence of the thermocouple has an effect on the glow plug performance. Schlieren images show that the ignition location, which occurs on the top of the glow plug or its side, is not affected by the presence of the thermocouple (see Appendix J). From these images we conclude that the effect of the thermocouple is negligible as the substantial variability in ignition location is unbiased.

3.3.1 Hot Surface Ignition Temperature as a Function of Composition

A systematic study has been performed using the Bosch glow plug investigating the ignition temperature as a function of composition expressed by the equivalence ratio, ϕ , at atmospheric pressure. Additional experiments have been performed using the Autolite glow plug and a small strip of electrically heated nickel foil. The minimum ignition temperature is observed to be essentially constant at $920 \text{ K} \pm 20 \text{ K}$ for equivalence ratios in the range of $\phi = 0.75 - 3.0$ as shown in Figure 3.15. Large increase and variability in the ignition temperature is observed at the extreme lean ($\phi \sim 0.6$) and rich ($\phi \sim 3.0$) conditions. Consistent with the literature (Zabetakis, 1965), the lower flammability limit is observed to be less than $\phi = 0.6$ with a mixture at $\phi = 0.5$ not igniting after heating for 30 seconds and the glow plug reaching 1520 K . In the literature the upper flammability limit of *n*-hexane in air is given as 7.4% , $\phi = 3.4$ (Zabetakis, 1965). We saw significant variability in ignition temperature at $\phi = 3.0$, but did not explore richer mixtures to confirm the flammability limit. The source of the variability in ignition temperature near $\phi = 3.0$ when using the Autolite glow plug is not clearly understood and should be considered for future study.

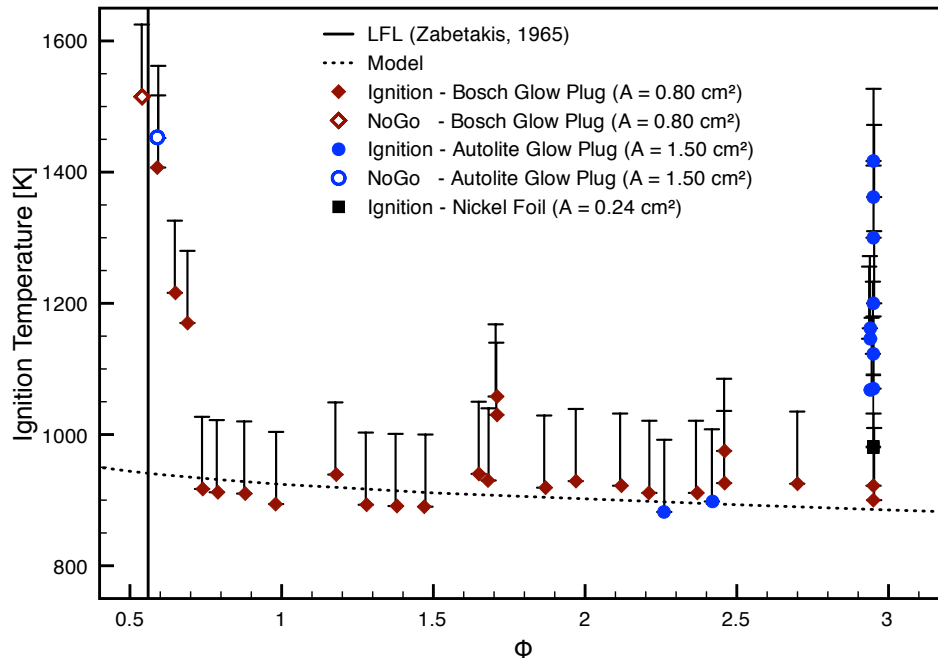


Figure 3.15: Hot surface ignition temperature as a function of equivalence ratio at atmospheric pressure for different hot surface sizes. The uncertainty associated with the ignition temperature stems from the ramp rate of the glow plug of $\approx 220 \text{ K/sec}$ and the response time of the thermocouple of 0.5 seconds. All mixture compositions have the associated uncertainty of $+3\%/-13\%$ in ϕ , not shown here.

In addition to the experiments, we present in Figure 3.15 the results of a simple model for ignition (discussed in the next section). The model captures the minimum ignition temperature and shows a weak dependence on composition, but does not describe the lower or upper flammability limit.

3.4 Ignition Modeling

3.4.1 Modeling Background

Modeling and predicting the ignition process near a hot surface requires considering the spatial and temporal evolution of the species and temperature of the gas. Simplified approaches are possible, but for an accurate prediction it is necessary to solve the fluid mechanical and chemical equations simultaneously on a grid sufficiently small to resolve the thermal and fluid dynamical boundary layer around the hot surface as well as including the low-temperature chemistry that has a critical influence on the ignition process as detailed in Chapter 2. An additional feature of nonhomogeneous ignition is the differential diffusion of species, a large range of molecular weights exists in the gas mixtures, which is challenging to accurately simulate.

The main approaches to modeling hot surface ignition have been to use one-dimensional conduction equation with heat-release from the chemical reactions. Extensions of this are 2-dimensional steady simulations as done by Adler (1999) and unsteady simulations like the ones performed by Kumar (1989).

Adler (1999) modeled the problem of a circular hot spot, e.g., from a laser, in contact with a combustible mixture. In his model one of the main assumptions is that the heated layer of gas is stagnant and thus the problem is governed by the energy equation including heat conduction and energy release from the chemical reactions, which in its steady form is usually referred to as the Frank-Kamenetskii problem (Glassman, 2008).

3.4.2 Simplified Analytical Approach

The minimum ignition temperature may be estimated using a simple analytical model such as that proposed by Laurendeau (1982). An additional discussion of hot surface ignition as developed by Semenov (1940) and Kuchta et al. (1965) are given in Appendix E.

The Laurendeau model proposes that ignition occurs when the rate of heat-loss from the reacting mixture just balance the energy release by chemical reactions. The steady one-dimensional energy

conservation equation with chemical energy release is modeled as

$$Qr_f = -k \frac{d^2T}{dx^2}, \quad (3.1)$$

where k is the thermal conductivity coefficient, Q is the chemical energy release, and r_f is the reaction rate given by an empirical model that is slightly more sophisticated than the ones presented in the previous chapter and includes a dependency on composition and density, but without reactant consumption

$$r_f = -X_F^{m_f} X_O^{m_o} \rho^n A \exp \left[-\frac{E_a}{\tilde{R}T} \right]. \quad (3.2)$$

X_F and X_O are the initial mole fraction of the fuel and oxidizer, respectively; ρ is the density and $n = m_f + m_o$ is the reaction order. Equation 3.1 is integrated across a stagnant thermal boundary layer subject to the following boundary conditions:

$$x = 0, \quad T = T_w, \quad (3.3)$$

$$x = \delta, \quad T = T_e, \quad (3.4)$$

where the wall at $x = 0$ is at the wall temperature, T_w , and outside the boundary layer ($x = \delta$), the temperature relaxes back to the ambient temperature, T_e . Laurendeau (1982) evaluates the density at a geometric mean temperature given by

$$\rho = \frac{P}{\tilde{R}\sqrt{T_w T_e}} \quad (3.5)$$

Prior to integrating Equation 3.1, it is multiplied by $(dT/dx)dx = dT$

$$k \frac{d^2T}{dx^2} \frac{dT}{dx} dx = QX_F^{m_f} X_O^{m_o} \rho^n A \exp \left[-\frac{E_a}{\tilde{R}T} \right] dT \quad (3.6)$$

making the integration of the left-hand side into a spatial integral and the right-hand side into a temperature integral.

$$k \int_0^\delta \left(\frac{d^2T}{dx^2} \right) \left(\frac{dT}{dx} \right) dx = AQX_F^{m_f} X_O^{m_o} \rho_e^n \left(\frac{T_e}{T_w} \right)^{n/2} \int_{T_w}^{T_e} \exp \left[-\frac{E_a}{\tilde{R}T} \right] dT \quad (3.7)$$

Using the chain rule, the left-hand side can be simplified and integrated.

$$k \int_0^\delta \left(\frac{d^2 T}{dx^2} \right) \left(\frac{dT}{dx} \right) dx = k \int_0^\delta \frac{1}{2} \frac{d}{dx} \left(\frac{dT}{dx} \right)^2 dx = \frac{k}{2} \left[\left(\frac{dT}{dx} \right)^2 \right]_0^\delta \quad (3.8)$$

The spatial derivative of the temperature is zero as we leave the boundary layer, i.e., at $x = \delta$. Absorbing the minus sign into the integration order of the right-hand side the energy equation becomes

$$k \left(\frac{dT}{dx} \right)_w^2 = 2AQX_F^{m_f} X_O^{m_o} \rho_e^n \left(\frac{T_e}{T_w} \right)^{n/2} \int_{T_e}^{T_w} \exp \left[-\frac{E_a}{\tilde{R}T} \right] dT. \quad (3.9)$$

In order to evaluate the integral, the standard large activation energy approximation as discussed in previous chapter and Appendix C.2.2 can be made:

$$T = T_w + T', \quad (T' < 0) \quad (3.10)$$

$$\exp \left[-\frac{E_a}{\tilde{R}T} \right] \cong \exp \left[-\frac{E_a}{\tilde{R}T_w} + \frac{E_a}{\tilde{R}T_w^2} T' \right] \quad (3.11)$$

Using this approximation, the energy equation simplifies to

$$k \left(\frac{dT}{dx} \right)_w^2 = 2AQX_F^{m_f} X_O^{m_o} \rho_e^n \left(\frac{T_e}{T_w} \right)^{n/2} \exp \left[-\frac{E_a}{\tilde{R}T_w} \right] \int_{T_e - T_w}^0 \exp \left[\frac{E_a}{\tilde{R}T_w^2} T' \right] dT', \quad (3.12)$$

where by noting that $(T_e - T_w)$ is negative, the integral becomes

$$\int_{-(T_w - T_e)}^0 \exp \left[\frac{E_a}{\tilde{R}T_w^2} T' \right] dT' = \left(\frac{\tilde{R}T_w^2}{E_a} \right) \left(1 - \exp \left[-\frac{E_a}{\tilde{R}T_w^2} (T_w - T_e) \right] \right) \approx \left(\frac{\tilde{R}T_w^2}{E_a} \right). \quad (3.13)$$

Recall that the upper integration limit refers to the wall temperature (see Equation 3.9), which dominates the energy release due to the high-activation energy assumption. Finally, the energy equation is

$$k \left(\frac{dT}{dx} \right)_w^2 \approx 2AQX_F^{m_f} X_O^{m_o} \rho_e^n \left(\frac{T_e}{T_w} \right)^{n/2} \exp \left[-\frac{E_a}{\tilde{R}T_w} \right] \left(\frac{\tilde{R}T_w^2}{E_a} \right), \quad (3.14)$$

so that for steady-state conditions, the heat flux from the gas to the wall due to chemistry is

$$q_{\text{chem}} = k \left(\frac{dT}{dx} \right)_w = \sqrt{2kAQX_F^{m_f} X_O^{m_o} \rho_e^n \left(\frac{T_e}{T_w} \right)^{n/2} \exp \left[-\frac{E_a}{\tilde{R}T_w} \right] \left(\frac{\tilde{R}T_w^2}{E_a} \right)}. \quad (3.15)$$

Laurendeau proposes that this must be equal to the heat flux from the wall to the gas as modeled

by an engineering correlation

$$q_{\text{loss}} = \frac{kNu}{L} (T_{\text{wall}} - T_e) . \quad (3.16)$$

The condition for ignition is given as (Laurendeau, 1982)

$$q_{\text{chem}} = q_{\text{loss}} . \quad (3.17)$$

Depending on the flow condition (stagnant, free or forced convection) the expression for the Nusselt number, Nu , changes. For example, for stagnant mixtures, the Nusselt number is constant and thus the wall temperature scales inversely with the natural log of the length scale (Laurendeau, 1982, Semenov, 1940).

$$\ln L \propto \frac{E_a}{2\bar{R}T_{\text{wall}}} \quad (3.18)$$

This dependence on surface size and the obvious limitations will be discussed further in subsequent sections (see Figure 3.26).

Law and Law (1979) discuss the problem of ignition in a steady boundary layer flow for mixtures with large activation energies. Their analysis shows that a locally similar region of balanced reaction and diffusion is present next to the wall, and a nonsimilar diffusion and convection balance outside this region. The problem is solved using the method of matched asymptotics, and the ignition behavior is presented as a function of the Damköhler number, the ratio of the fluid time scale to the chemical reaction time scale. The Damköhler number defined is the ratio of the heat-loss and chemical release described in Laurendeau (1982). Ignition is predicted to occur as the Damköhler number reaches unity.

3.4.3 Boundary Layer Modeling Approach ¹

The temperature at which the mixture ignites corresponds to a balance between heat-release due to chemical reactions and heat-loss due to diffusion and convection. An estimate of the ignition temperature may be determined by comparing the time scales of these processes. As the glow plug heats up the surrounding mixture, natural convection begins and a boundary layer develops on the surface of the glow plug. A fluid element passing through the boundary layer is heated up initiating chemical reaction, whose energy release is in competition with heat conduction and convection away

¹A preliminary version of this work was presented at the Eighth International Symposium on Hazards, Prevention, and Mitigation of Industrial Explosions (8th ISHPMIE) in Yokohama, Japan: “Hot Surface Ignition of Hydrocarbons in Air — A Comparison of Experimental and Computational Results” (Philipp A. Boettcher, Brian Ventura, Guillaume Blanquart, and Joseph E. Shepherd).

from the fluid element.

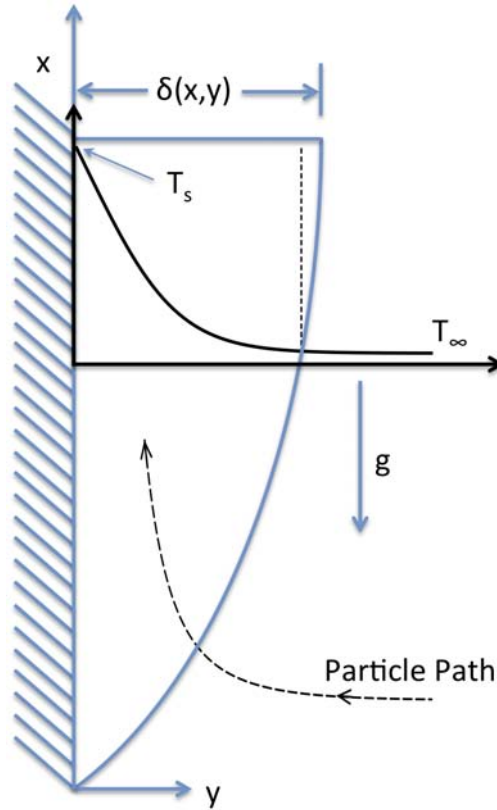


Figure 3.16: Thermal boundary layer along a vertical hot plate

The full governing equations are adapted from Kee et al. (2003) for Cartesian coordinates.

Continuity:

$$\frac{\partial \rho}{\partial t} + \frac{\partial}{\partial x}(\rho u) + \frac{\partial}{\partial y}(\rho v) = 0 \quad (3.19)$$

x - Momentum:

$$\rho \frac{\partial u}{\partial t} + \rho u \frac{\partial u}{\partial x} + \rho v \frac{\partial u}{\partial y} = -\frac{\partial P}{\partial x} + \mu \left(\frac{\partial^2 u}{\partial x^2} + \frac{\partial^2 u}{\partial y^2} \right) + \rho g \beta (T - T_\infty) \quad (3.20)$$

y - Momentum:

$$\rho \frac{\partial v}{\partial t} + \rho u \frac{\partial v}{\partial x} + \rho v \frac{\partial v}{\partial y} = -\frac{\partial P}{\partial y} + \mu \left(\frac{\partial^2 v}{\partial x^2} + \frac{\partial^2 v}{\partial y^2} \right) \quad (3.21)$$

Energy:

$$\rho c_p \frac{\partial T}{\partial t} + \rho u c_p \frac{\partial T}{\partial x} + \rho v c_p \frac{\partial T}{\partial y} = u \frac{\partial P}{\partial x} + \frac{\partial}{\partial y} \left(k \frac{\partial T}{\partial y} \right) - \sum_{k=1}^{K_g} \rho c_{pk} Y_k V_{k_y} \frac{\partial T}{\partial y} - \sum_{k=1}^{K_g} \dot{\omega}_k W_k h_k \quad (3.22)$$

In general, these equation have to solved by numerical methods. To make analytical progress, a number of simplifying assumptions will be made. We will assume that density gradients are only important when multiplied by gravity (Boussinesq approximation). The volumetric expansion coefficient, β , will be evaluated at an average temperature value. We assume the gas is composed of only one species, which does not undergo any chemical composition change following Kaviany (2002). Additionally, we assume the boundary layer is laminar and steady and neglect pressure gradients along the x-axis. The boundary layer is also assumed to be thin, such that gradients in the y-direction are much greater than those in the x-direction, and that $u \gg v$. To estimate the time scales for energy release and energy loss, we consider the development of the boundary layer separately from the chemical energy release. This assumption simplifies our analysis and is somewhat justified by the Arrhenius rate dependence of the reaction rate on temperature, which implies that most of the chemical reaction occurs at elevated temperatures close to ignition. The resulting equations for a steady, non-reacting thermal boundary layer driven by buoyancy are:

Continuity:

$$\frac{\partial u}{\partial x} + \frac{\partial v}{\partial y} = 0 \quad (3.23)$$

x-Momentum:

$$\rho \left(u \frac{\partial u}{\partial x} + v \frac{\partial u}{\partial y} \right) = \rho g \beta (T - T_\infty) + \mu \frac{\partial^2 u}{\partial y^2} \quad (3.24)$$

y-Momentum:

$$\frac{\partial p}{\partial y} = 0 \quad (3.25)$$

Energy:

$$\rho c_p \left(u \frac{\partial T}{\partial x} + v \frac{\partial T}{\partial y} \right) = k \frac{\partial^2 T}{\partial y^2} \quad (3.26)$$

The boundary conditions are:

$$u(x, 0) = v(x, 0) = u(x, \infty) = 0 \quad (3.27)$$

$$T(x, 0) = T_s \text{ and } T(x, \infty) = T_\infty \quad (3.28)$$

The most significant approximation, other than neglecting chemical reactions, is the assumption of constant density. This assumption introduces some error, but greatly simplifies the calculations, while still clearly illustrating the concept. Cairnie and Harrison (1982) present the variable density equations, which are more appropriate for large surface-to-ambient temperature differences. While the pressure remains constant the large temperature at the wall has a significant impact on the specific volume of the fluid close to the wall, which leads to a shift of the velocity and temperature away from the wall. This shift can be expressed by using Howarth-Dorodnitsyn (Stewartson, 1964) transformed coordinate

$$\bar{y} = \int_0^y \frac{\rho}{\rho_\infty} dy . \quad (3.29)$$

While this transformation is needed for accurate solutions, we do not consider this approach and only treat the $\rho = \text{constant}$ case. Following the derivation given by Gebhart et al. (1988) a similarity solution for Equations 3.23-3.28 can be obtained by combining the spatial variable into a single nondimensional coordinate $\eta(x, y)$ described below

$$\eta = b(x)y , \quad (3.30)$$

where $b(x)$ is the function that links the scaling

$$b(x) = \frac{1}{x} \left[\frac{gx^3}{4\nu^2} \beta (T_s - T_\infty) \right]^{1/4} . \quad (3.31)$$

The velocities are expressed through a stream function, ψ

$$u = \psi_y \quad v = -\psi_x \quad \psi(x, y) = \nu c(x) f(x, y), \quad (3.32)$$

where $f(x, y)$ and $c(x)$ are nondimensional functions

$$c(x) = 4 \left[\frac{gx^3}{4\nu^2} \beta (T_s - T_\infty) \right]^{1/4} . \quad (3.33)$$

The temperature is nondimensionalized via

$$T^* = \frac{T - T_\infty}{T_s - T_\infty} . \quad (3.34)$$

The functions $b(x)$ and $c(x)$ are found such that T^* and f are only functions of η while also satisfying

all of the boundary conditions (Gebhart et al., 1988).

The new non-dimensionalized momentum and energy equations are

$$f''' + 3ff'' - 2f'^2 + T^* = 0 \quad (3.35)$$

$$(T^*)'' + 3Prf(T^*)' = 0 \quad (3.36)$$

where $'$ denotes differentiation with respect to η . Pr is the Prandtl number

$$Pr = \frac{\nu}{\alpha}, \quad (3.37)$$

where α is the thermal diffusivity and ν is the kinematic viscosity. The stream function ψ is expressed as a function of the Grashof number based on x ,

$$\psi(x, y) = 4\nu \left(\frac{Gr_x}{4} \right)^{1/4} f(x, y), \quad (3.38)$$

$$Gr_x = \frac{g\beta(T_s - T_\infty)x^3}{\nu^2}, \quad (3.39)$$

and the similarity parameter η is

$$\eta = \frac{y}{x} \left(\frac{Gr_x}{4} \right)^{1/4} = \frac{y}{x^{1/4}} \left[\frac{g\beta(T_s - T_\infty)}{4\nu^2} \right]^{1/4} \quad (3.40)$$

The momentum and energy equations can be solved to give the velocity and temperature distribution as well as the boundary layer thickness along the plate. The temperature distribution is computed using the similarity solution as a function of the similarity parameter, η , as using the methods described in text books by Kaviany (2002) and Gebhart et al. (1988).

Figure 3.17 shows the temperature distribution away from the hot surface and indicates the edge of the laminar, viscous boundary layer at $\eta_{0.01} = 4.423$ defined as the point where $T^* = 0.01$. Equation 3.40 can be rearranged to solve for the boundary layer thickness, $y = \delta$, a given length, $x = L$, away from the start of the plate

$$\delta = \frac{\eta_\delta L}{(Gr_L/4)^{1/4}}. \quad (3.41)$$

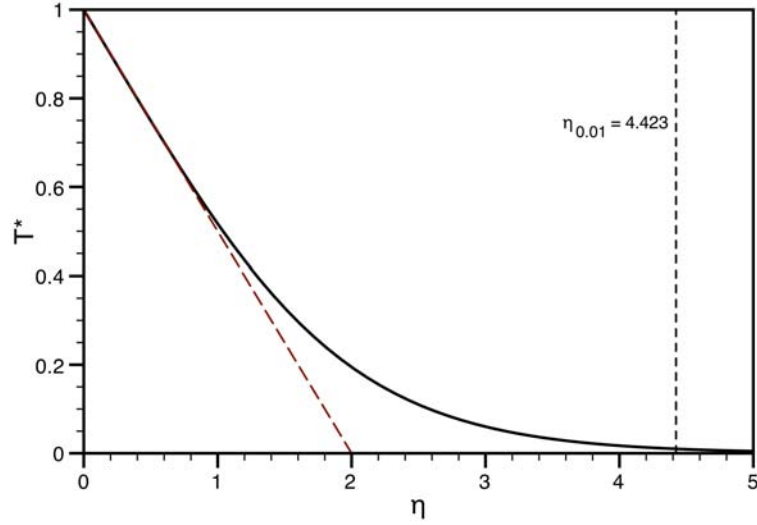


Figure 3.17: Temperature profile in a thermal boundary layer along a vertical hot plate ($Pr = 0.72$)

Using a simple dimensional analysis, we can extract an approximate time scale for heat conduction through the boundary layer. Squaring both sides of Equation 3.41 and multiplying by the Prandtl number allows for the following simplification.

$$\frac{\delta^2 \nu}{\alpha} = Pr \frac{\eta_\delta^2 L^2}{(Gr_L/4)^{1/2}} \quad (3.42)$$

$$\frac{\delta^2}{\alpha} = Pr \sqrt{\frac{4\eta_\delta^4 L^4}{Gr_L \nu^2}} \quad (3.43)$$

$$\frac{\delta^2}{\alpha} = Pr \sqrt{\frac{4\eta_\delta^4 L^4}{\nu^2} \frac{\nu^2}{g\beta(T_s - T_\infty)L^3}} \quad (3.44)$$

$$\frac{\delta^2}{\alpha} = Pr \sqrt{\frac{4\eta_\delta^4 L}{g\beta(T_s - T_\infty)}} \quad (3.45)$$

The characteristic time scale for heat conduction through the layer then becomes

$$\tau_{diff} = \frac{\delta^2}{\alpha} = Pr \sqrt{\frac{4\eta_\delta^4 L}{g\beta(T_s - T_\infty)}} \quad (3.46)$$

Figure 3.17 shows that an approximation of the temperature profile as a linear function of η , which is consistent with defining $\eta_\delta = 2$, gives the diffusion time scale,

$$\tau_{diff} = 8 Pr \sqrt{\frac{L}{\beta \Delta T g}} \quad (3.47)$$

where L is the height of the glow plug, β is the thermal expansion ratio, and ΔT is the temperature difference across the boundary layer ($T_s - T_\infty$). For a mixture with a Prandtl number of $Pr = 0.72$, we obtain $\tau_{diff} \approx 250$ ms.

The chemical time scale is found by computing the time to ignition of mixture of n-heptane and air at a given temperature assuming a constant pressure, adiabatic reactor. A mixture is initialized at a given temperature and the chemical heat-release is allowed to evolve, which leads to a temperature increase that can be captured by the energy equation

$$\frac{dT}{dt} = \frac{\dot{q}_r}{V \rho c_p} \quad (3.48)$$

and the ignition time, τ_{ign} , is defined as time elapsed until the maximum temperature increase rate is reached

$$t = \tau_{ign} \text{ when } \frac{dT}{dt} = \text{maximum} . \quad (3.49)$$

The computations were obtained using the detailed chemical mechanism of Curran et al. (1998) with the FlameMaster code (Pitsch and Bollig, 1994). Heptane was used in place of hexane since the chemistry of heptane is better understood, and previous studies have shown that normal alkanes share very similar ignition properties, such as the shock tube ignition delay time (Shen et al., 2009, Westbrook et al., 2009).

The ignition temperature is then defined as the initial temperature for which the ignition time, τ_{ign} , is equal to the diffusion time, τ_{diff} . For instance, as shown on Figure 3.18, a mixture with equivalence ratio $\phi = 1.0$ is predicted to ignite within 250 ms if the initial temperature is around 905 K. This analysis is repeated for several different equivalence ratios, and the predicted ignition temperatures are compared to the temperatures measured experimentally. As shown on Figure 3.15, both the experiments and the simple model predict a weak dependence of the ignition temperature on the equivalence ratio. This result is due to the weak dependence of ignition time on equivalence ratio. However, the model fails to predict the sudden rise in ignition temperature below $\phi = 0.7$. There could be multiple sources of discrepancies; for instance, the model accounts only for thermal diffusion and neglects diffusion of key combustion intermediates such as radicals.

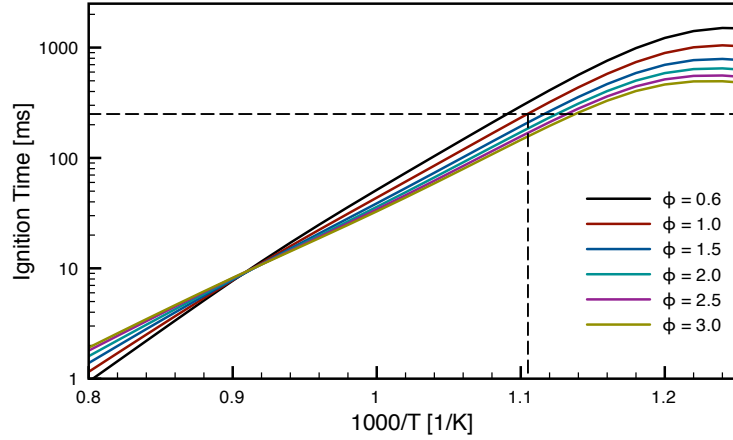


Figure 3.18: Ignition times for n-heptane and air mixtures at atmospheric pressure computed with the detailed chemical mechanism of Curran et al. (1998) ($\tau_{diff} = 250$ ms, $T = 905$ K indicated)

Temperature Profile Along Particle Trajectories While the scaling arguments just described give a simple model for estimating the ignition temperature, a more realistic model for the ignition event may be investigated by following an individual fluid element through the boundary layer. Using the similarity solution, we can obtain the trajectory of the fluid element. Recall the nondimensional equations for x-momentum, energy and the stream function, ψ , from Gebhart et al. (1988), which can be solved numerically.

$$f''' + 3ff'' - 2f'^2 + T^* = 0 \quad (3.50)$$

$$(T^*)'' + 3Prf(T^*)' = 0 \quad (3.51)$$

$$\psi(x, y) = 4\nu \left(\frac{Gr_x}{4} \right)^{1/4} f(x, y) \quad (3.52)$$

The viscosity and thermal conductivity are taken at the mean temperature, $(T_s + T_\infty)/2 - 650$ K in this example, using the data from Kadoya et al. (1985) and Stephan and Laesecke (1985), respectively.

Table 3.1: Parameters used in modeling of hexane-air hot surface ignition

Parameter		Units	Description
g	9.81	m s^{-2}	gravitational acceleration
T_s	1000	K	surface temperature
T_∞	300	K	gas temperature away from the wall
μ	3.257×10^{-5}	Pa s	dynamic air viscosity at 650 K
ρ_0	0.57	kg m^{-3}	unburnt gas density at 650 K
ν	5.71×10^{-5}	$\text{m}^2 \text{s}$	kinematic air viscosity at 650 K
β	1.54×10^{-3}	K^{-1}	volumetric thermal expansion coefficient
k	4.862×10^{-2}	$\text{W m}^{-1} \text{K}^{-1}$	thermal conductivity of air at 650 K
q_c	2.3×10^6	J kg^{-1}	stored chemical energy
c_p	1357	$\text{J kg}^{-1} \text{K}^{-1}$	average specific heat of the gas mixture at constant pressure
E_a	35075	cal kmol^{-1}	activation energy
	146754	J kmol^{-1}	activation energy
A	3.3×10^{14}	s^{-1}	pre-exponential

We can follow a given fluid element with an initial position (x_0, y_0) by computing the local velocity $(u(x, y), v(x, y))$ and integrating the path.

$$x = x_0 + \int_0^t u(x, y) dt' \quad (3.53)$$

$$y = y_0 + \int_0^t v(x, y) dt' \quad (3.54)$$

From the definition of the stream function the velocities are computed

$$u = \frac{\partial \psi}{\partial y} = 4\nu \left(\frac{Gr_x}{4} \right)^{1/4} \frac{\partial f}{\partial \eta} \frac{\partial \eta}{\partial y} \quad (3.55)$$

$$v = -\frac{\partial \psi}{\partial x} = -\frac{4\nu}{4^{1/4}} \frac{\partial (Gr_x)^{1/4}}{\partial x} f - 4\nu \left(\frac{Gr_x}{4} \right)^{1/4} \frac{\partial f}{\partial \eta} \frac{\partial \eta}{\partial x} \quad (3.56)$$

where f , and $\partial f/\partial \eta$ are computed as part of the numerical solution. Away from the wall, in the outer layer, the temperature is low and the contribution of chemical energy release is negligible and the equations above correctly predict the temperature and flow path of a fluid element.

The chemical energy release becomes important at high-temperatures, which are found in a small inner layer next to the wall. If the chemical energy release is included in the energy equation, for

example, using a one-step model, the equation becomes

$$\rho c_p \left(u \frac{\partial T}{\partial x} + v \frac{\partial T}{\partial y} \right) - k \frac{\partial^2 T}{\partial y^2} = -q_c A \exp \left[-\frac{E_a}{\tilde{R}T} \right]. \quad (3.57)$$

The chemical energy release increases the fluid element temperature. This energy release is small until very high-temperatures due to the large activation energy, E_a . Before ignition occurs the energy release can be lost through either conduction or convection. At the wall, we can establish the dominant balance to find whether conduction or convection is responsible for the energy loss. A version of this calculation is given by Law and Law (1979).²

Near the wall both temperature and wall velocity are small, which can be expressed in the nondimensional parameters T^* and f .

$$T^* = T_w^* + \epsilon_1 \tilde{T}^* \quad (3.58)$$

$$f = f_w + \epsilon_2 \tilde{f} \quad (3.59)$$

Making the substitution above in the x-momentum equation, while noting that $f_w = 0$ due to the boundary conditions (nonporous wall and nonslip condition), gives

$$\epsilon_1 \tilde{f}''' + 3\epsilon_1^2 \tilde{f} \tilde{f}'' - 2\epsilon_1^2 \tilde{f}'^2 + T_w^* + \epsilon_1 \tilde{T}^* = 0 \quad (3.60)$$

which implies that the deviations are of the same magnitude $\epsilon_1 = \epsilon_2 = \epsilon$. Via the same substitution the energy becomes

$$\epsilon (\tilde{T}^*)'' + 3\epsilon^2 Pr \tilde{f} (\tilde{T}^*)' = -\tilde{q} \quad (3.61)$$

where \tilde{q} is the nondimensional chemical energy release. From Equation 3.61 we can see that the dominant balance at the wall is between the chemical energy release rate and the thermal diffusion, with the convection an order of magnitude smaller.

Along the path we can now compute the heat transfer as well as the heat-release from a one-step model as well as the heat diffusion. As a simplifying assumption, we treat the heat-loss as the dominant in the y-direction so the heat transfer term of the energy equation is

$$k \frac{\partial^2 T}{\partial y^2} = k(T_s - T_\infty) \frac{\partial^2 T^*}{\partial \eta^2} \left(\frac{\eta}{y} \right)^2. \quad (3.62)$$

²The author would like to thank Jason S. Damazo for his significant contribution in unraveling this argument.

The one-step energy release rate is given by

$$\rho q_c A \exp \left[-\frac{E_a}{RT} \right]. \quad (3.63)$$

Figure 3.19 shows the heat-loss rate, the heat-release rate, and temperature as a fluid element, initially outside the boundary layer ($x_0 = 0.01$ m, $y_0 = 0.01$ m, Trajectory 1 in Figure 3.20), is entrained by the boundary and heated. The point of ignition is defined as the point where the heat-release rate and heat-loss rate are equal. Several of these trajectories are shown in Figure 3.20, which demonstrate how the ignition location changes with the initial location. For Trajectory 3, for example, the temperature gradients in the boundary layer are higher and thus the heat diffusion is higher, which leads to the fluid element ignition closer to the hot surface.

If we consider the case where the density is variable the effect will be a stretching of the solution as described in Equation 3.29, the detailed calculation has been done by Cairnie and Harrison (1982). For the trajectories considered, this implies that the paths are shifted away from the wall. However, since both the temperature and velocity profile are shifted away from the wall, the final dominant balance arguments laid forth are still valid and the qualitative features of ignition should be predicted correctly in the same manner as presented above, although the precise ignition location will be incorrect. A more realistic simulation would require considering the full two-dimensional solution and a detailed chemical reaction mechanism, but this is outside the scope of this thesis.

It should be noted that ignition occurs fairly far away from the wall in Figure 3.20. This is due to the fact that the wall temperature was too high in this example. A more rigorous study would require varying the temperature and using non-averaged fluid properties. However, this is also outside the scope of this thesis.

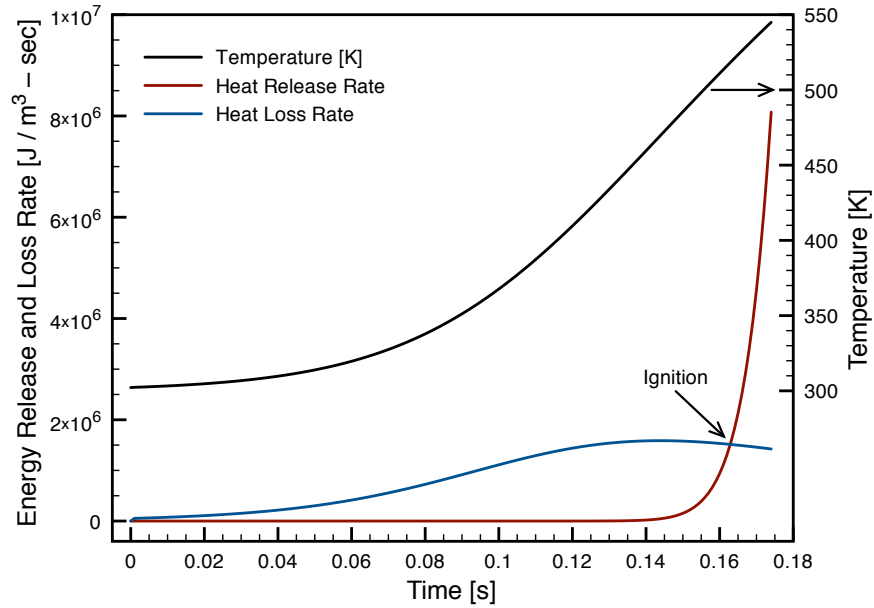


Figure 3.19: Energy release rate, energy loss rate, and temperature along a fluid trajectory ($x_0 = 0.01$ m, $y_0 = 0.01$ m); the ignition location is indicated as the point where energy loss rate equals the energy release rate

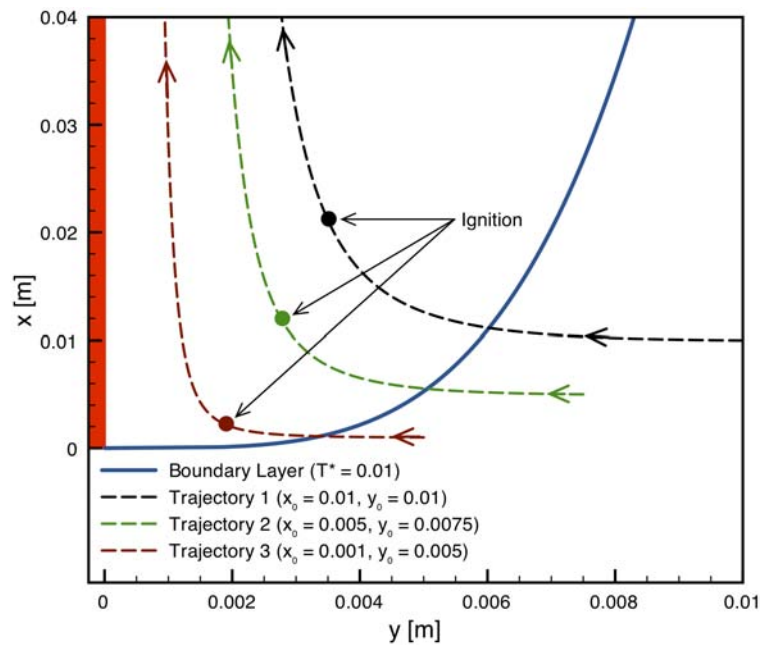


Figure 3.20: Trajectories of fluid elements into a boundary layer created by a hot surface at the left edge; the ignition location is defined as the point where energy release rate equals the energy loss rate

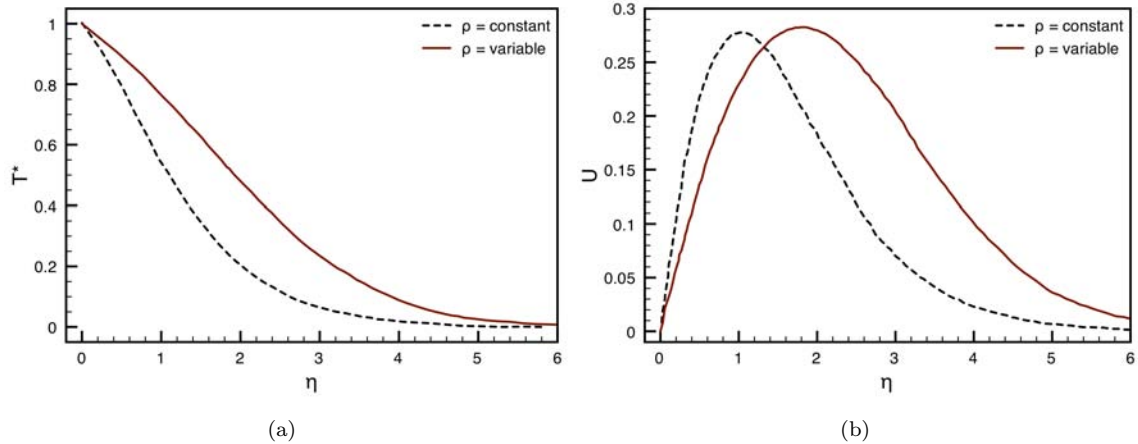


Figure 3.21: Nondimensional (a) temperature profile and (b) velocity profile for a constant and variable density boundary layer along a vertical hot plate (from Cairnie and Harrison, 1982) ($T_w/T_\infty \sim 2.3 - T_w \sim 690$ K, $T_\infty \sim 300$ K)

3.4.3.1 Thermal Ignition Using Tabulated and Detailed Chemistry Modeling ³

The final approach taken in investigating hot surface ignition is the numerical simulations of the fluid dynamic processes (convection and diffusion) in conjunction with finite rate chemistry. The hot surface temperature leading to ignition of various flammable mixtures is investigated.

This work utilizes a detailed reaction mechanism for heavy hydrocarbon fuels which has been validated extensively over a wide range of temperatures, pressures, and equivalence ratios (Blanquart et al., 2009, Narayanaswamy et al., 2010). Although the fuel used in the experiments is hexane, the simulations were performed using *n*-heptane. This is because the chemistry of heptane at low temperatures is better understood than that of hexane; more experimental data exist for heptane to validate the chemical model; and previous studies have shown that normal alkanes have very similar ignition and flame propagation characteristics (Davis and Law, 1998a, Shen et al., 2009, Westbrook et al., 2009).

Simulation Details Simulations are carried out in a 2D axisymmetric domain with the symmetry plane established at the center line of the cylinder, which is assigned a Neumann boundary condition, while all the other surfaces except the glow plug are modeled as closed adiabatic walls.

The experimental observations indicated that the surface temperature of the glow plug is almost uniform. As a result, in the simulations, the glow plug is initialized spatially with a uniform tem-

³Portions of the following work were submitted but not accepted to 34th Combustion Symposium in the paper “Investigation of hot surface ignition of a flammable mixture” by S. Menon, P. Boettcher, B. Ventura, J. Shepherd, G. Blanquart.

perature. Furthermore, the temperature of the glow plug is kept fixed in time, rather than being increased up to a final value as in the experiments.

The progress variable at the glow plug surface is set to zero. A zero value for the progress variable at the wall can be understood in two different ways. First, it means that no increase in temperature is allowed above the imposed, unburned temperature (T_u). Second, it is representative of the destruction of radicals at the wall through their recombination into stable species. The surface itself is inert having no chemical reactions with the mixture. The sensitivity of the simulation results to this boundary condition is checked by using a Neumann boundary condition at the glow plug surface. The results indicates no change in the ignition location or delay time.

The solution is obtained on a mesh consisting of 256 grid points in the vertical direction and 128 points in the radial (horizontal) direction. The grid is clustered closer to the glow plug with 128 points for one glow plug height and 32 points for one glow plug diameter. Simulations are performed using the NGA code (Desjardins et al., 2008). The code relies on high order conservative finite difference schemes developed for the simulation of variable density flows. A third order WENO scheme is used to compute scalar transport (Liu et al., 1994).

Figure 3.22 shows contours of the progress variable at the time of ignition corresponding to different hot surface temperatures. Figure 3.22 (a) and (b) correspond to simulations performed with the full chemical model, including low temperature reaction pathways. Figure 3.22 and (d) correspond to simulations performed without the low temperature reaction pathways. The ignition kernel is illustrated by the black iso-contour.

The numerical simulations predict that ignition occurs above the glow plug surface, consistent with experimental observations. The location of ignition is found to be insensitive to the surface temperature when only the high-temperature chemistry is considered. However, when the full model is used, the ignition location depends on the surface temperature and decreases in height with increase in surface temperature (Figures 3.22 (a) and (b)). Additionally, the minimum surface temperature required to ignite the mixture decreases when the full model is used.

Figure 3.23 shows the effect of mixture equivalence ratio on the minimum temperature for ignition. The experimental results are the same as presented in Figure 3.15, however, only the minimum value corresponding to a particular equivalence ratio is included. For each equivalence ratio the hot surface temperature is varied until ignition is no longer observed. Lack of ignition is indicated by an asymptotic behavior for the maximum value of the progress variable in the domain.

The ignition temperature (around 920K) obtained from experiments, appears to be fairly inde-

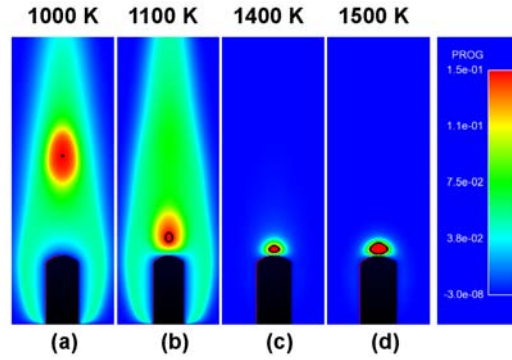


Figure 3.22: Comparison of ignition locations for different hot surface temperatures; the full chemical reaction mechanism is considered in (a) and (b), while the low temperature reaction pathways are neglected in (c) and (d)

pendent of the equivalence ratio. A similar behavior, at higher temperature ($T \approx 1400\text{K}$) is observed for the simulation where low temperature (LT) chemistry is excluded. However, when the full chemical model is used, the simulation results in Figure 3.23 show a considerable effect of equivalence ratio on minimum hot surface temperature for ignition and lead to values that are smaller than that measured experimentally.

While the chemical model gives very good results for low temperature ignition under high pressures, it remains unvalidated for atmospheric pressures. The present results may suggest that the low temperature chemistry is too fast for rich conditions. Despite uncertainties in the low temperature pathways, the simulations confirm that a mixture with an equivalence ratio less than 0.5 should not ignite.

The deviation from experimental results seem to be in part due to our incomplete understanding of the low temperature reaction kinetics and indicates an area of future research.

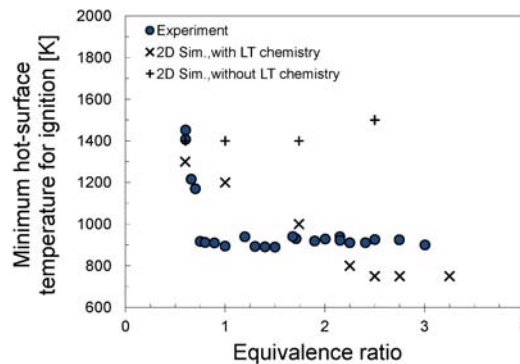


Figure 3.23: Hot surface ignition temperature from tabulated chemistry simulations (with and without low temperature, LT, chemistry) and experiments

3.4.4 Hot Surface Ignition Temperature as a Function of Pressure

The pressure dependence of the ignition temperature is investigated for two cases while holding the equivalence ratio constant in the range of total pressure from 25 kPa to 100 kPa. Experimental results in Figure 3.24 show that the required ignition temperature increases as the pressure is decreased.

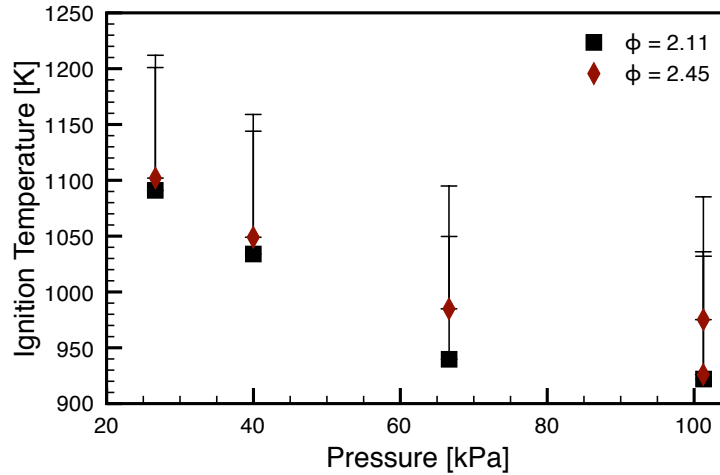


Figure 3.24: Ignition delay times for n-heptane and air mixtures computed with the detailed chemical mechanism of Curran et al. (1998)

We can apply the model of equating the thermal diffusion time scale to the ignition time scale to estimate the pressure dependence by calculating the ignition time as a function of pressure. The thermal diffusion time computed from Equation 3.47 remains basically unchanged as the pressure is changed from 100 kPa to 25 kPa. Figure 3.25 shows both the temperature calculated leading to ignition in 250 ms, the ignition temperature, as well as the ignition time at a constant temperature, 1000 K, computed using the chemical mechanism from Curran et al. (1998) in a isobaric calculation with varying initial pressure⁴. At both equivalence ratios tested an increase in ignition temperature with a decrease in pressure is observed.

As in the previous section, the results presented here depend on the size of the hot surface element. The particular fluid element trajectory as well as the time spend near the hot surface greatly influence the temperature and reaction history. For a quantitative prediction of the ignition temperature, it is necessary to solve the nonsteady evolution of the hot surface temperature, the detailed chemical processes, thermal and species diffusion along with the fluid mechanics, and surface reactions. As shown in the previous chapter, this is a difficult task even in zero-dimensional calculation.

⁴The author would like to thank Guillaume Blanquart for performing these simulations.

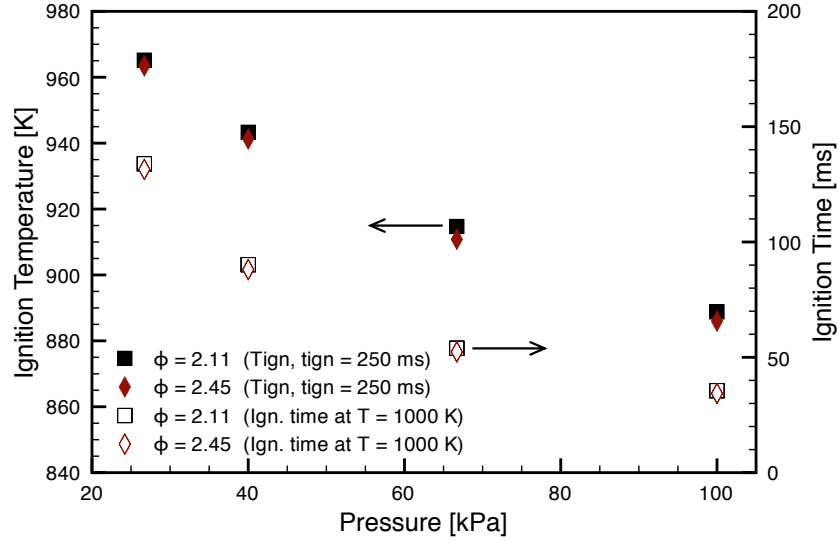


Figure 3.25: Simulated ignition temperatures and ignition times as function of pressure

3.4.5 Hot Surface Ignition Temperature as a Function of Surface Area

The ignition temperature is observed to be correlated with the the hot surface size and shape (Kuchta et al., 1965, Laurendeau, 1982), neglecting any additional effect that catalytic properties of the hot surface that may be present. Semenov (1940) made some analytical progress, described in Appendix E, arriving at the following relationship for the ignition temperature, T_1 as a function of radius for heated wires of radius, r , in a vessel of a specified radius, R_V , kept a constant temperature, T_0 ,

$$r \ln \frac{R_V}{r} = \left(\frac{E_a \lambda (T_1 - T_0)^2}{2R_V T_1^2 Q A \exp[-E_a/(\tilde{R}T_1)]} \right)^{1/2}. \quad (3.64)$$

This is based on a one-step chemical reaction model, where the reaction energy, Q , is released according to Arrhenius rate described by the activation energy, E_a , and pre-exponential, A . Kuchta et al. (1965) simplified this relationship by assuming that the exponential term dominates, expanding the left-hand side, and keeping only the leading order term,

$$r \sim \exp \left[\frac{E_a}{2\tilde{R}T_1} \right]. \quad (3.65)$$

Taking the natural logarithm of both sides yields the approximate $T \sim [\ln r]^{-1}$ dependence of the ignition temperature on surface area:

$$\ln r \sim \frac{1}{T_1}. \quad (3.66)$$

The experimental data presented by Kuchta et al. (1965) support this scaling analysis (see Figure 3.26) over a range of hot surface sizes between 0.6 cm^2 and 70 cm^2 . Based on our experiments we found ignition temperatures of up to $300 \text{ }^\circ\text{C}$ lower at a surface area of about 1.5 cm^2 and thus we strongly caution against extrapolation of the Kuchta et al. (1965) results when making safety assessments.

Kuchta et al. (1965) show ignition temperatures for heat sources of comparable surface area to that of the glow plug (0.63 cm^2) to be 1270 K . When compared using the radius of the glow plug (0.165 cm), temperatures were observed to be 1070 K (Kuchta et al., 1965). These values were obtained using heated wires and rods in a 400 cm^3 vessel maintained at $150 \text{ }^\circ\text{C}$. The test gas was passed through the reactor at 0.35 cm/s calculated from the volumetric flow rate. In contrast, the vessel wall in the current experiment remained at room temperature and the characteristic flow velocity in the plume above the glow plug is 40 cm/s based on simulation results. Smyth and Bryner (1997) performed experiments with a combustible mixture impinging on hot metal surfaces made from nickel, stainless steel, and titanium at 45° at a flow speed of 16 cm/s . The overall average ignition temperature for n-hexane was 1105 K . Both of these previous studies were performed in open combustion vessels, which is similar to the technique employed in the standard for auto-ignition temperature testing (ASTM, 2005), which limits the accuracy of the composition control.

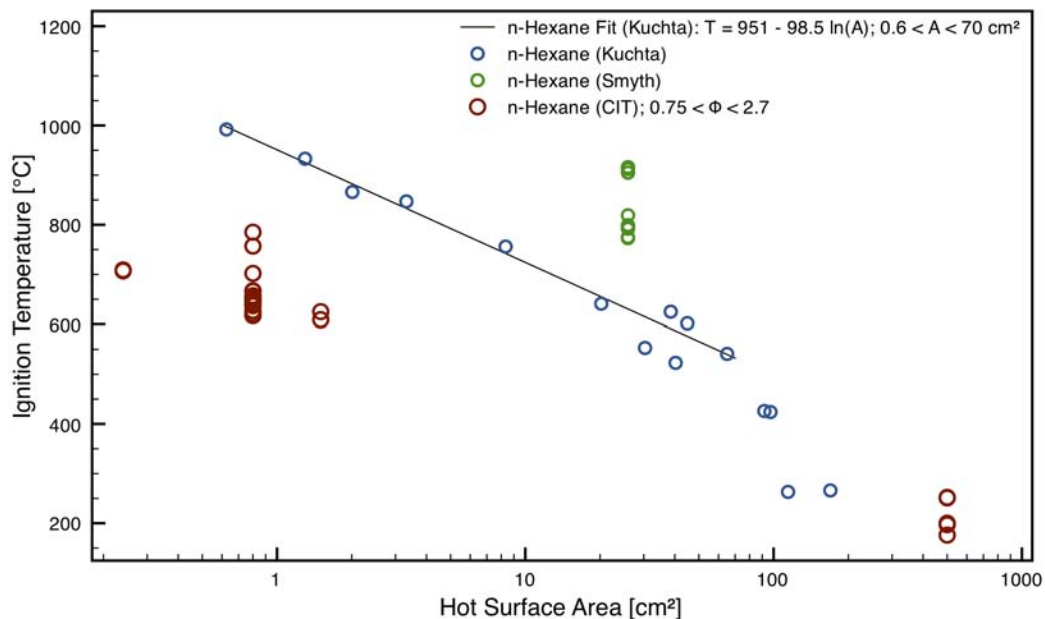


Figure 3.26: Ignition as a function of hot surface size (uncertainty in ignition temperature for CIT measurements is $+110 \text{ K}$). Range in values for CIT measurements is due to a range of compositions and initial pressure.

Figure 3.26 demonstrates the overall trend in which the ignition temperature increases with decreasing hot surface area. The large range in ignition temperatures in the current data are due to the range of equivalence ratios examined examined in the present study. The higher flow velocity of Smyth and Bryner (1997) leads to an increase in the ignition temperature relative to the Kuchta et al. (1965) data. The logarithmic curve fit of the historical data greatly underestimates the minimum ignition temperatures observed in the current study.

The ignition temperature data includes the auto-ignition experiments presented in the previous chapter on the far right of Figure 3.26. These ignition temperatures also fall below the historical values because they were performed in a closed vessel initially at room temperature and heated to the ignition temperature, rather than introducing the fuel at atmospheric pressure.

3.5 Flame Propagation

In our studies, we found three different flame regimes, single, multiple ignitions, and puffing flames, which are continuous flames with large scale instabilities. The flame propagation is discussed in this section and puffing flames are detailed in the next chapter. A schlieren system was used in order to confirm that ignition of the mixture occurred. In addition to determining if and where ignition had taken place, the schlieren movie can be used to observe the flame propagation, determine the flame speed, and observe instabilities. While the experiment is not specifically designed to determine laminar flame speeds, the observations can be compared to literature data and simulations by making reasonable assumptions about the gas motion.

3.5.1 Experiments

The schlieren system records gradients in image intensity corresponding to density gradients, which are very prominent across the flame front ($\rho_{\text{unburnt}}/\rho_{\text{burnt}} \sim 5.5\text{--}8$). Experiments used a 150 W Oriel Arc Light Source (P/N 66907), which is focused on a pinhole and then collimated using a 1.5 m focusing mirror. Best results were obtained when using a transparency with a small circular black spot as the schlieren stop (dark background schlieren). Figure 3.27 shows a dark background schlieren image, which has clear outlines of the flame shape for all flame orientations. The image was captured using a Phantom v710 high-speed camera using a resolution of 800×800 pixels with frame rates of 1000–2000 fps and exposure times of 5–50 μs .

The flame position is digitized using a Matlab digitizing routine⁵, which manually measures the position of the flame relative to the top of the glow plug (origin). For the left and right flame positions, the horizontal distance between the left most edge and right most edge and origin are used. The diameter of the window visible in the image is used as the reference length scale.

Representative results of the digitized flame position as a function of time are shown in Figure 3.28. The initial slope is higher than the final value due to the increased gas temperature in the plume as well as the curvature effects on the flame propagation. The start of the linear regime is found by inspection of the raw data and the final propagation speed is computed by linear least squares regression of the data in the linear regime.

⁵The digitizing routine used here is based on the digitize.m program written by J. D. Cogdell and the digitize2.m program written by A. Prasad, both available from the Mathworks File Exchange with edits from M. Rubel and J. S. Damazo. Both programs have been invaluable tools in preparing this thesis.

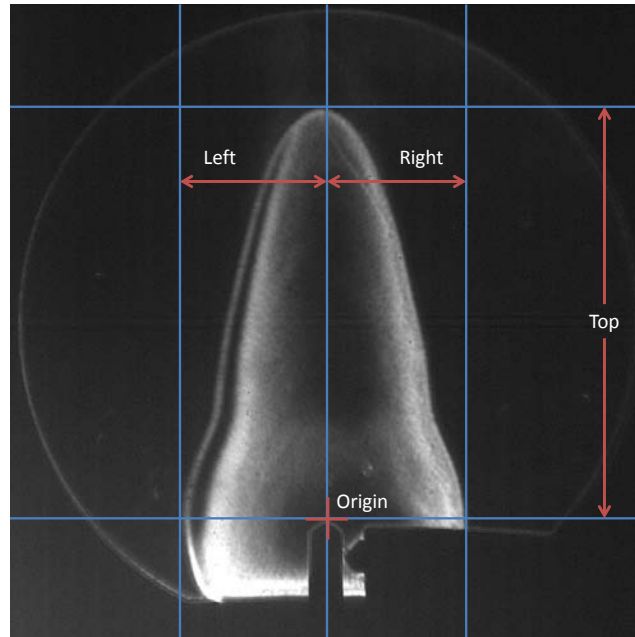


Figure 3.27: Definition of flame outside and origin location

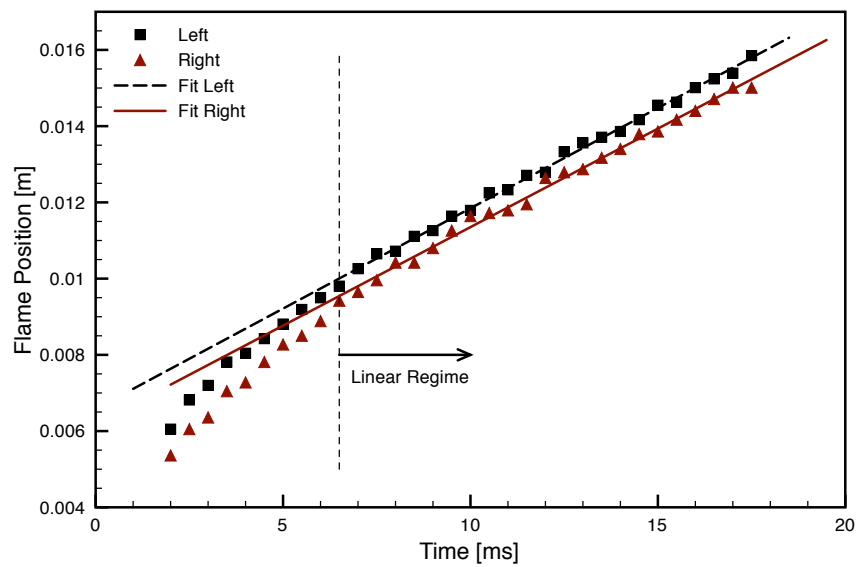


Figure 3.28: Representative digitization of the flame location and fit flame speed from shot 33

3.5.2 Flame Propagation Speed as a Function of Composition

The composition, initial pressure and temperature of the flammable mixture are significant factors in determining the propagation speed of the flame (Glassman, 2008). Several methods are available to measure this dependence, including closed combustion vessels (Kelley et al., 2011), and counterflow burners (Ji et al., 2010), and the laminar unstretched burning velocity S_L is reported. Detailed data from the literature for n -hexane and n -heptane is given in Appendix F and compared to the present experimental results. Due to the less than ideal conditions of the current setup for measuring flame speed, we can only make an approximate comparison to the literature value as the effects of flame stretch and strain, flow out in front of the flame, and heat transfer during the flame propagation are not taken into account.

As a first idea, we idealize the flame as sphere, and compute the propagation speed, \dot{R} , as the sum of the flame propagation speed and the flow speed, u , established by the expansion of the hot gas inside the flame. In order to carry out this computation, we assume that the gas inside the flame is stationary. Detailed simulations, discussed later, show that this is not the case, but that the error introduced is acceptable.

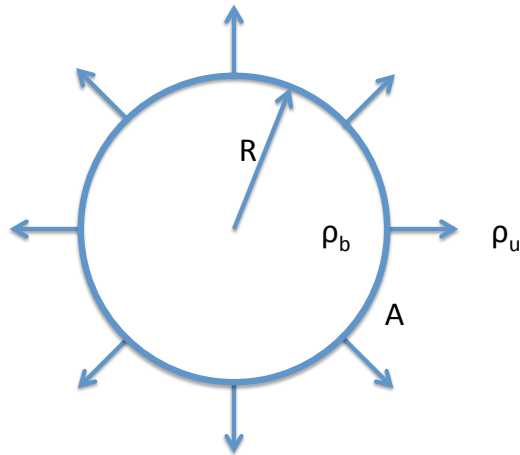


Figure 3.29: Spherical flame schematic

Another method is to use conservation of mass. The mass flux of burned gas into the flame, \dot{m}_b , is equal to the mass flux of unburned gas through the flame front, \dot{m}_u ,

$$\dot{m}_b = \rho_b \dot{V} = \rho_b 4\pi R^2 \dot{R} \quad (3.67)$$

$$\dot{m}_u = \rho_u S_L A = \rho_u S_L 4\pi R^2 \quad (3.68)$$

$$\dot{m}_u = \dot{m}_b \implies \dot{R} = \frac{\rho_u}{\rho_b} S_L = \epsilon S_L \quad (3.69)$$

where ϵ is the expansion ratio, ρ_u/ρ_b , Equation 3.69 gives an approximate flame propagation speed as laminar burning velocity given in the literature times the expansion ration, which can be computed from a constant pressure equilibrium calculation.

Alternatively, we can approximate the lower part of the flame as an expanding cylindrical flame with inflow at the top. This is can be accomplished by considering the incompressible flow just inside the flame.

$$\nabla \cdot \vec{u} = 0 \quad (3.70)$$

From simulations of stoichiometric fuel-air mixtures, the mass inflow at the top can be approximated by a top hat profile with an inflow velocity, u_z , of 2 m/s over a radius of 2 cm, R_1 . At a point in time where the flame is about 6 cm, R_2 , in diameter and 2 cm high, h , the outflow velocity, u_r^- just behind the flame front can be calculated

$$\int \vec{u} \cdot \hat{n} dA = 0 \quad (3.71)$$

$$\int_0^{R_1} u_z 2\pi r dr = \int_0^h u_r^- 2\pi R_2 dz \quad (3.72)$$

$$u_r^- = \frac{u_z R_1}{2R_2 h} \quad (3.73)$$

The outflow at the flame front, u_r^- , is about 10 cm/s, which is small relative to the measured flame velocities, V_f . The flame propagation velocity is the sum burning speed and the underlying flow velocity,

$$V_f = S_l + u_r \quad (3.74)$$

The effect of the outflow is small except at very large equivalence ratios, where the shape of the flame is drastically influenced by the fluid motion. Consequently, for comparisons of the flame propagation speed with literature values the spherical approximation is reasonable.

The experimental flame propagation speed at the left side, right side, and top are given in Figure 3.30. The vertical burning velocity is clearly influenced by both the flow in the plume

above the glow plug and the increased temperature in this region, which is discussed in detail in Section 3.5.4.

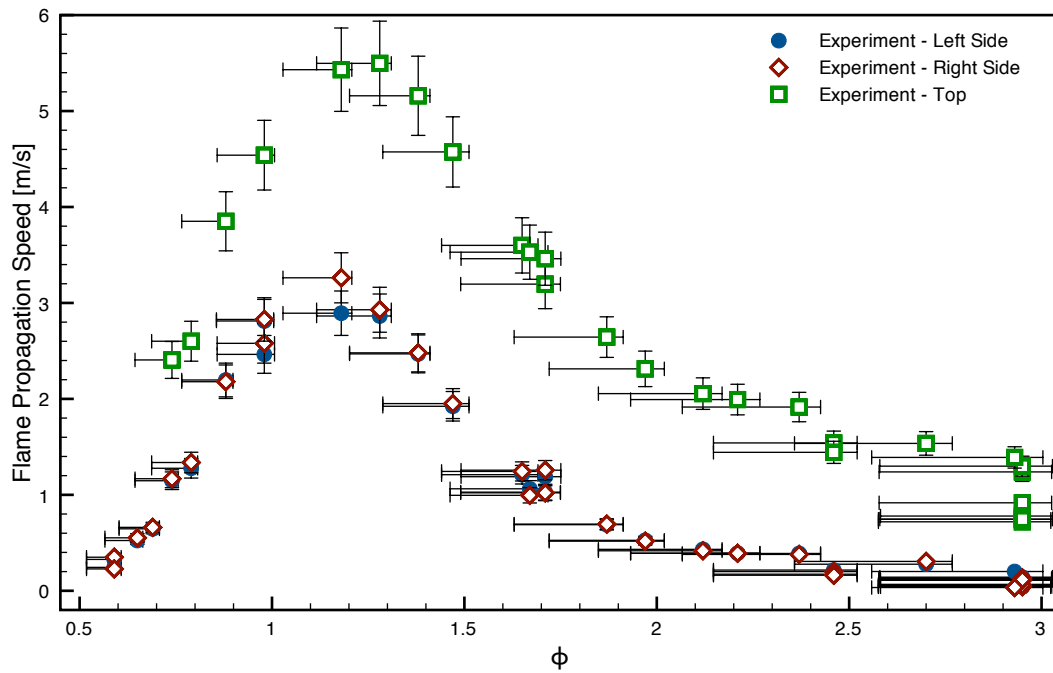


Figure 3.30: Flame propagation speed for n-hexane air mixtures as a function of equivalence ratio at atmospheric pressure

The measurement uncertainty that arises include the measurements of the reference scale, the window size, aberrations due collimation errors, and uncertainty in the position of the flame front . All of these errors result in a total of 8% uncertainty in the flame propagation speed. More rigorous experiments have been performed by Mével et al. (2009) to determine flame speeds in spherical pressure vessels and found uncertainties of 6%. Given the complicated flame shape arising from plume temperature distribution the larger uncertainties in our experiment are not unreasonable.

3.5.3 Computational Modeling of Flame Propagation ⁶

The governing equations of fluid motion for the simulations performed here are the variable density, low-Mach, number Navier-Stokes equations.

$$\partial_t \rho + \nabla \cdot (\rho u) = 0 \quad (3.75)$$

$$\partial_t(\rho u) + \nabla \cdot (\rho u u) = -\nabla p + \nabla \cdot \tau + \rho g \quad (3.76)$$

where τ is the viscous shear stress tensor and g represents the gravity vector.

The simulations are performed using the NGA code (Desjardins et al., 2008). The code relies on high order conservative finite difference schemes developed for the simulation of variable density turbulent flows.

The closed vessel is modeled as a sufficiently large volume. The symmetry of the problem allows the computation to be performed on a 2D axisymmetric structured mesh. The mesh is locally refined in the vicinity of the glow plug in the horizontal and vertical directions. A Dirichlet boundary condition consisting of a temperature profile is assigned to the glow plug surface. The temperature at any location on the glow plug is constant in time but it varies in space along the surface of the glow plug to match experimentally determined values. The walls of the vessel are modeled as adiabatic boundaries.

The code utilizes a lookup table procedure to acquire species and mixture properties during the course of the simulation. Two elements critical in reproducing the experimental results are the chemistry tabulation and the reaction mechanism.

3.5.3.1 Chemistry Tabulation

Reaction chemistry is incorporated using a lookup table procedure where species and mixture properties are tabulated as a function of the unburned gas temperature (T_u) and the progress variable (C). The code utilizes the flamelet progress variable (FPV) approach, which requires the solution of transport equations for additional scalar variables, namely, the progress variable,

$$\partial_t(\rho C) + \nabla \cdot (\rho u C) = \nabla \cdot (\rho D \nabla C) + \dot{\omega}_C \quad (3.77)$$

⁶The numerical simulations were performed by Shyam K. Menon and Guillaume Blanquart using geometries and temperature distribution from the experimental setup.

and the transport of the unburned gas temperature

$$C_{p,u} [\partial_t(\rho T_u) + \nabla \cdot (\rho u T_u)] = \nabla \cdot [\lambda \nabla T_u] \quad (3.78)$$

The progress variable is defined to be the sum of mass fractions of major product species — CO, CO₂, H₂ and H₂O, and is used to represent the extent (or progress) of the reaction.

The transport equation for temperature relates to the unburned gas and hence it does not have any chemical source terms in it. The approach pursued here currently uses unburned gas temperature in-lieu of enthalpy. Since there are no other energy loss or source terms being considered in the current simulation, the two variables (temperature and enthalpy) are equivalent. Species mass fractions, production rates, mixture transport properties, flame speeds etc., are tabulated as a function of the unburned gas temperature and reaction progress variable. Prior to tabulation, these properties are obtained from calculations for freely propagating laminar premixed flames conducted with full detailed chemistry using the FlameMaster software (Pitsch and Bollig, 1994).

3.5.3.2 Reaction Mechanism

For 1-D flat flames at constant unburned gas temperature (T_u), the model reproduces the laminar flame speeds from kinetic models. Hence, the accuracy of the 2-D axisymmetric simulations is limited by the accuracy of the kinetic model.

The reaction mechanism used in this work is one for heavy hydrocarbon fuels which been extensively validated over a wide range of temperatures, pressures, and equivalence ratios (Blanquart et al., 2009, Narayanaswamy et al., 2010). Heptane is used as the fuel in all simulations since the reaction model is calibrated against numerous heptane experiments. Previous studies have shown that normal alkanes show very similar ignition and flame propagation characteristics (Davis and Law, 1998a, Shen et al., 2009, Westbrook et al., 2009) so we expect that the results will be comparable to hexane.

The detailed mechanism is used to estimate flame speeds for *n*-heptane-air mixtures at different equivalence ratios and unburned gas temperatures at which experimental data are available from literature Davis and Law (1998b); Huang et al. (2004); Kumar et al. (2007); Ji et al. (2010); Kelley et al. (2011); and Van Lipzig et al. (2011). The calculations are carried out using FlameMaster and results are shown in Figure 3.34. The detailed chemical model is able to predict the effects of unburned temperatures and equivalence ratios on the burning velocity. The agreement between simulation and experimental results give us confidence in the model.

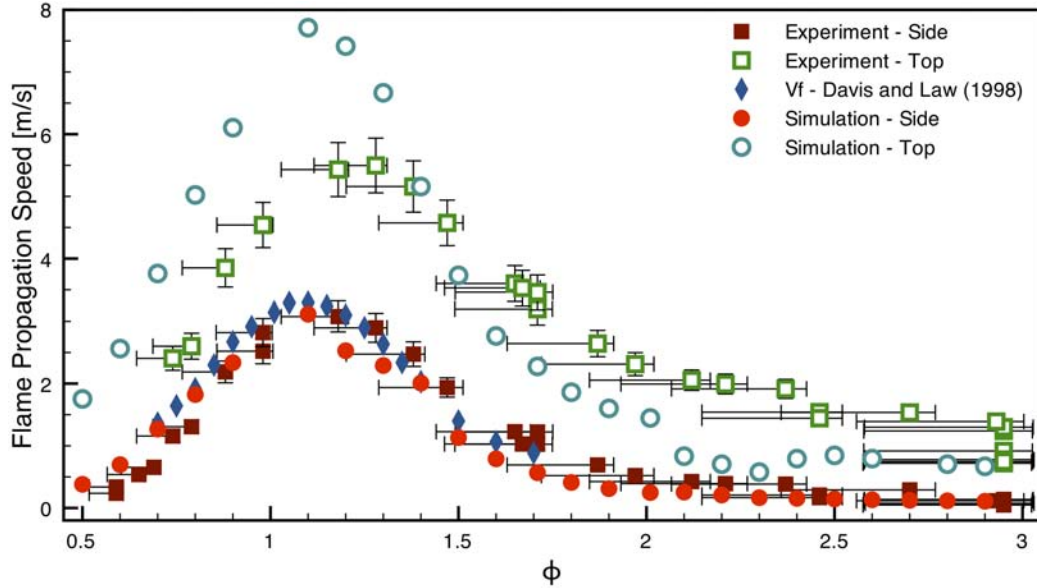


Figure 3.31: Flame propagation speed at room temperature and atmospheric pressure including the estimated flame propagation speed from Davis and Law (1998b) calculated by multiplying the the laminar burning velocity by the expansion ratio obtained by equilibrating the mixture at constant pressure using the reduced Ramirez mechanism (Ramirez et al., 2011)

The overall shape of the flame is well captured in the numerical simulation as shown in Figures 3.32 and 3.33. As for the experiment, the flame propagation speed in the simulation is determined by tracking the flame edges as shown in Figure 3.27. Figure 3.31 gives a detailed comparison of the flame propagation speed obtained in the simulation and the experiments. The agreement is reasonable and consistent with the estimated uncertainties in the measure flame speed and composition. The discrepancy between the simulation and experiments ranges from 0.15 to 0.8 m/s with an average of 0.46 m/s. The flame propagation speeds at the top have a larger discrepancy between the experiments and simulations, which may be attributed to the uncertainties in the plume temperature, and the fact that the plume temperature is transient in the experiment and steady-state in the simulations.

The simulation results have several sources of uncertainty and error including a lack of validation of the chemical mechanism for $\phi > 1.7$, for no laminar flame speed data is available. Additionally, the flamelet model introduces unquantified uncertainties and the location of the flame is a function of the progress variable value chosen.

The shape of the plume as indicated by the density of the gas mixture in the (first frame of Figure 3.33) is in qualitative agreement with that shown in the schlieren images taken in the experiments (first frame of Figure 3.32).

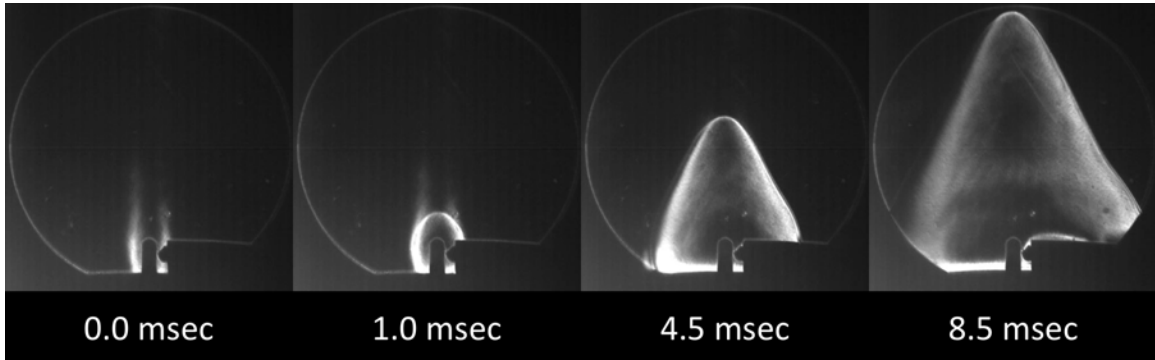


Figure 3.32: Dark background schlieren visualization of the flame propagation for a hexane-air mixture (Bosch glow plug, $\phi = 1.2$)

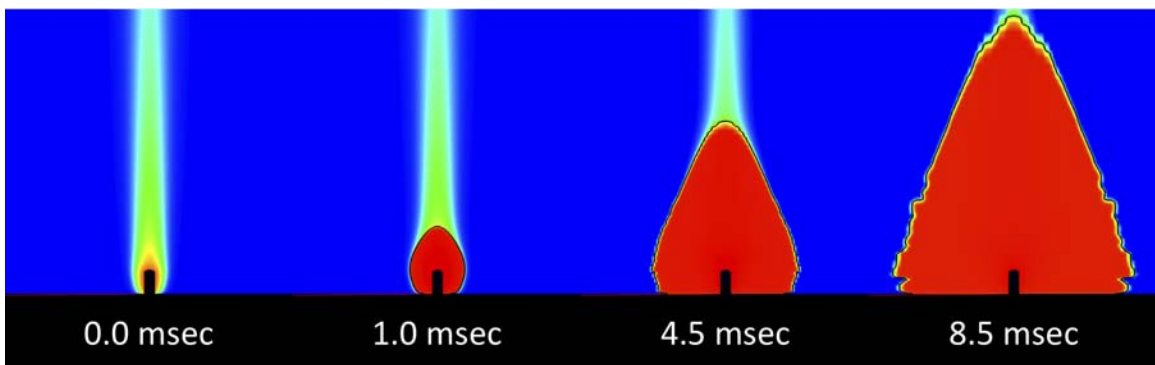


Figure 3.33: Simulation results for flame propagation phenomena (Bosch glow plug, $\phi = 1.2$)

3.5.4 Effect of the Thermal Plume on the Flame Propagation Speed

As seen above the the flame propagation speed is different at the top of the flame and on the sides. The major contributing factor to this phenomenon is the elevated temperature in the plume above the glow plug. Some scaling arguments about the size and temperature in the plume are given in Appendix G.

The effect of temperature on flame propagation speed has been investigated by experimentally by Davis and Law (1998b), Huang et al. (2004), Kumar et al. (2007), Ji et al. (2010), Kelley et al. (2011), and Van Lipzig et al. (2011). Results of simulations based on Blanquart's CaltechMech reaction mechanism (Blanquart, 2011) are shown in Figure 3.34. The simulation reproduces the observed temperature dependence and experimental data. Figure 3.35 illustrates that even a temperature increase of 100 K can raise the laminar flame speed by over 50%. Although data are not available at the highest temperatures observed in the plume, the extrapolation of the flame speed shown in Figure 3.36 indicates that the flame speeds could be as high as 200-300 cm/s immediately above the glow plug (Gaydon and Wolfhard, 1979).

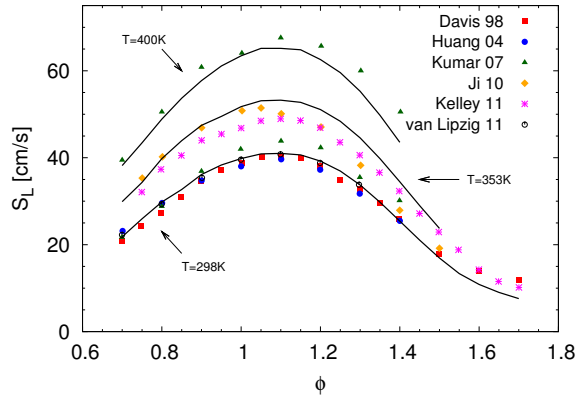


Figure 3.34: Laminar burning speed as function of equivalence ratio at different temperatures as calculated using the CaltechMech

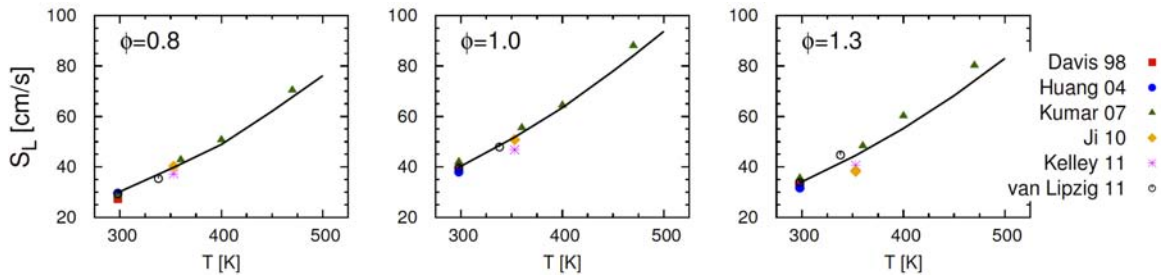


Figure 3.35: Comparison between laminar burning speeds calculated using n-heptane-air reaction mechanism and experimental data by Davis and Law (1998b), Huang et al. (2004), Kumar et al. (2007), Ji et al. (2010), Kelley et al. (2011), and Van Lipzig et al. (2011)

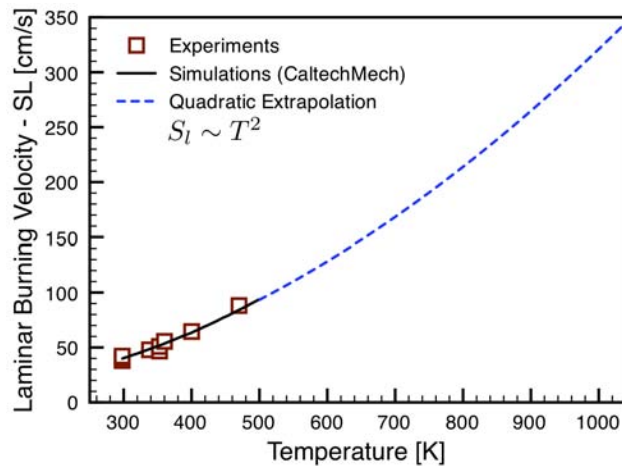


Figure 3.36: Laminar burning velocity of stoichiometric *n*-heptane as a function of temperature as found in experiments, predicted by the CaltechMech (Blanquart, 2011), and quadratic extrapolation of the simulation results ($\phi = 1.0$)

In order to make accurate comparisons with simulations, it is necessary to make measurements of the temperature in the plume in order to calibrate the nonreactive plume model. An array of thermocouples⁷ was placed directly above the glow plug as shown in Figure 3.37. The thermocouples are spaced vertically approximately 1 cm apart along the centerline.

For comparisons of the initial conditions of the experiment with the simulations, the temperature in the plume is measured with air in the vessel as shown in Figure 3.38 (a). The glow plug is powered on at ~ 1 second raising its temperature as well as the plume temperature and then turned off at ~ 10.5 seconds allowing it cool off. The array was also in place during an ignition and flame propagation experiment shown in Figure 3.38 (b), but due to the limited time response it is not possible to use these results to estimate the flame speed or temperature.

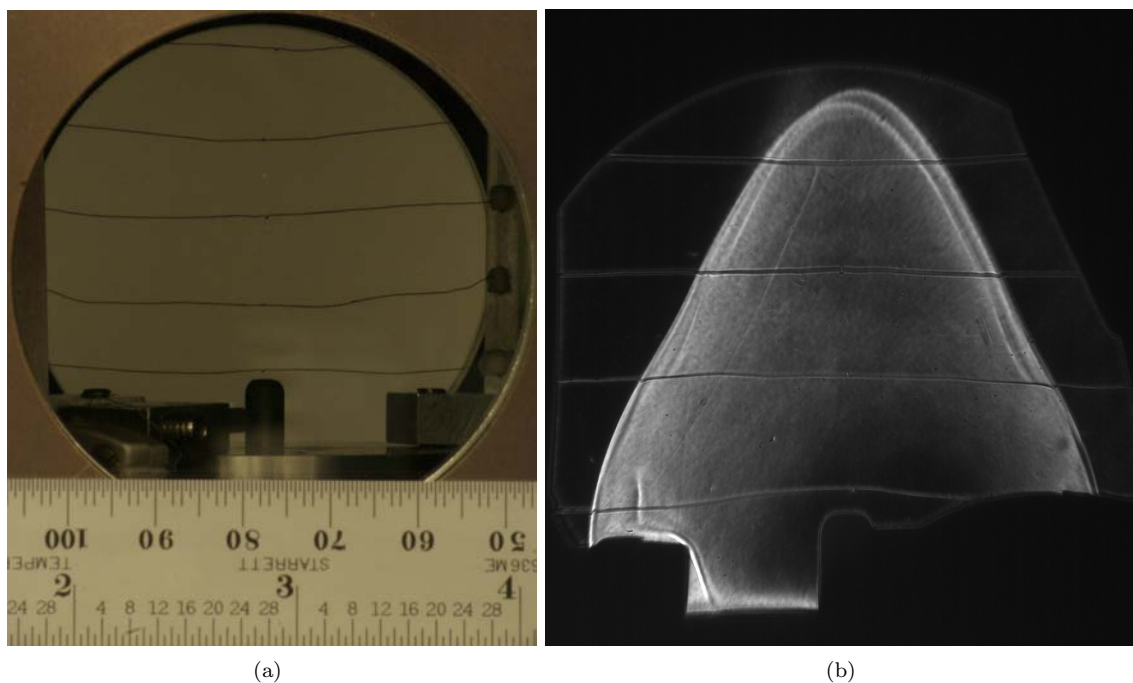


Figure 3.37: (a) Picture of the thermocouple array in the vessel used to determine the plume temperature; (b) schlieren image during shot 61 with the thermocouple array in place

The simulation of the plume temperature is performed for the Autolite glow plug at 1320 K, which corresponds to the peak temperatures in Figure 3.38 (a). The simulation, like the experiment, is performed without chemical heat-release. The results, given in Figure 3.39, indicate reasonable agreement between the simulation and experiment.

It should be noted that the maximum temperatures observed by the thermocouple in Figure 3.38 (b) are significantly below the adiabatic flame temperature, which is around 2200 K for hydrocarbon

⁷The thermocouple array was designed and implemented by Brian Ventura.

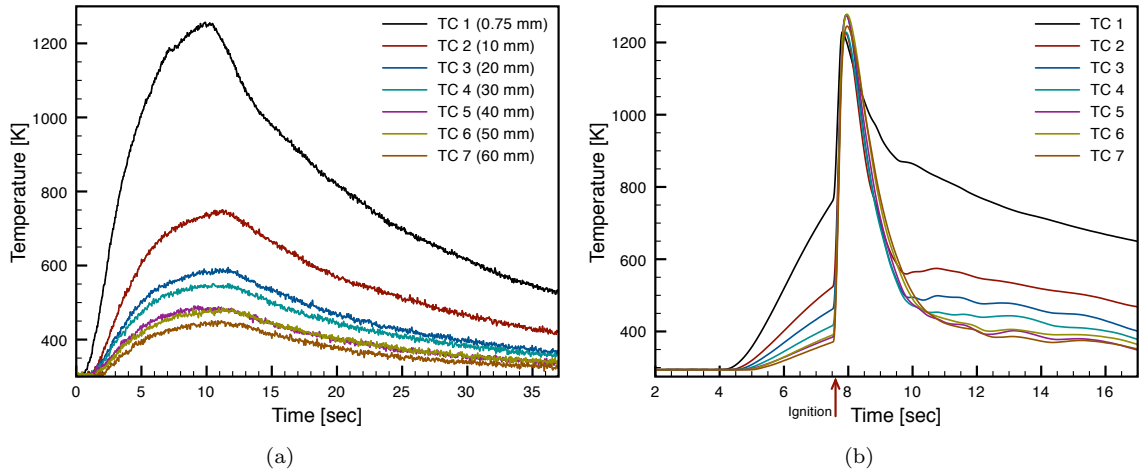


Figure 3.38: (a) Temperature distribution above the glow plug without ignition from thermocouple array; (b) temperature distribution above the glow plug with ignition during shot 61 ($\phi = 1.0$ hexane-air mixture, ignition occurred at 7.0645 s as indicated on the x-axis)

combustion in air (Glassman, 2008). This experiment was not designed to measure adiabatic flame temperatures. As the flame passes over the thermocouples, the response time of the thermocouple creates a lag during which the temperature decreases and additionally the thermocouple loses heat to conduction along the wires as well as radiation.

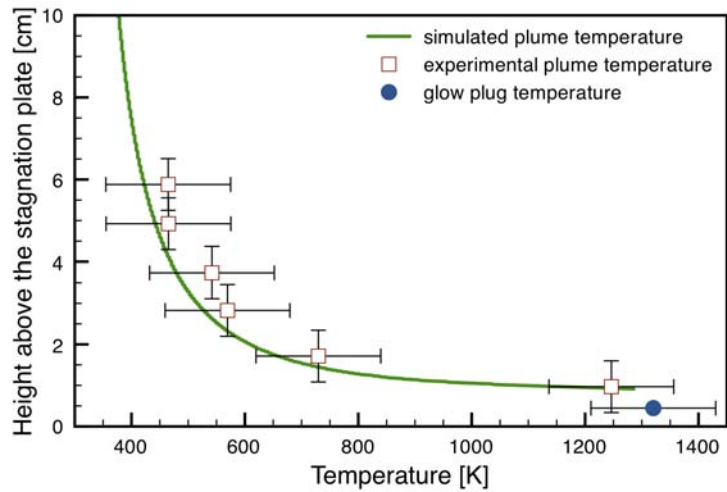


Figure 3.39: Temperature distribution in air above the glow plug comparing simulations and thermocouple measurements

3.5.5 Combustion Modes

The experiments show three different combustion modes depending on the composition and initial pressure. The first mode involves a single flame propagating until it reaches the vessel walls as shown in the sequence of images from a schlieren video in Figure 3.40. In the second mode, two to three flames ignite sequentially, as shown in Figure 3.41. The final mode corresponds to a continuously puffing flame, as shown in Figure 3.42.

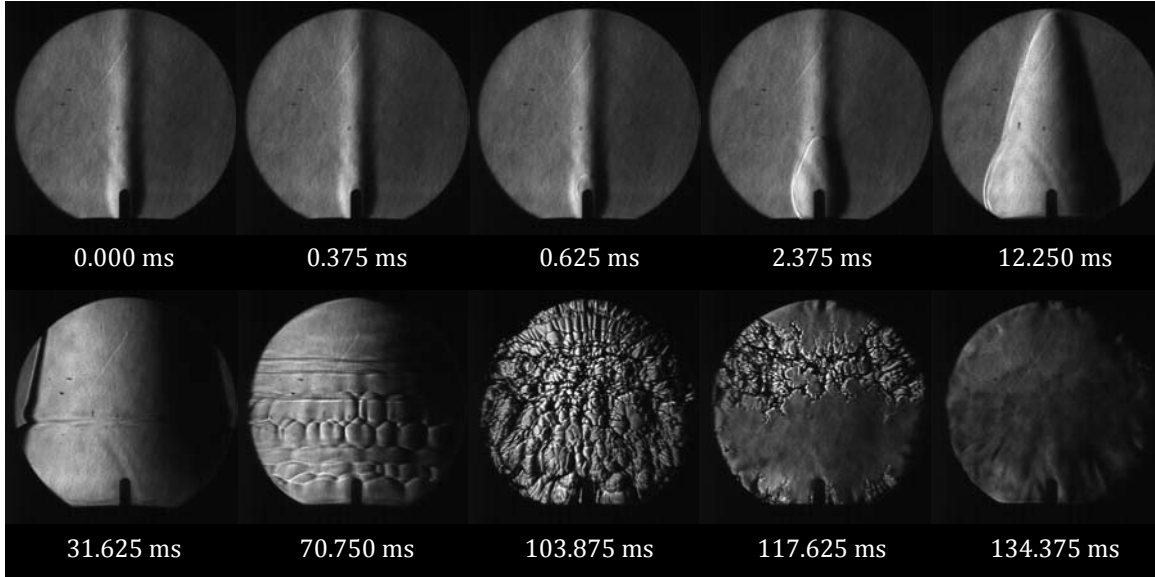


Figure 3.40: Schlieren visualization of a single flame ignited at the glow plug at 0.125 ms ($P_0 = 101$ kPa, $\phi = 1.74$)

3.5.5.1 Single Flames

Figure 3.40 shows schlieren images obtained using a vertical knife edge of a fuel-rich hexane air-mixture, $\phi = 1.74$, igniting at the top of the glow plug and propagating at different speeds in the horizontal and vertical direction. The high flame speed causes the flame to consume the entire vessel before any buoyancy effects change the shape of the flame. In most of the cases, ignition occurs at the top of the glow plug (see Appendix J for ignition locations from various experiments), with some experiments igniting on the side of the glow plug where the temperature is slightly higher than at the top (see Sections 3.2.3 and 3.2.4) and very lean mixtures igniting in the plume above the glow plug. Additionally, the region of reverse curvature (frame 5 of Figure 3.40) develops the initial instability leading to a highly wrinkled flame before the flame front reaches the windows. The growth of these instabilities is a function of the composition and curvature of the flame, which will be elaborated in

the next section. The initial region of curvature change is due to the flame propagating out of the plume produced before ignition, which would not be present in typical spark ignition experiments.

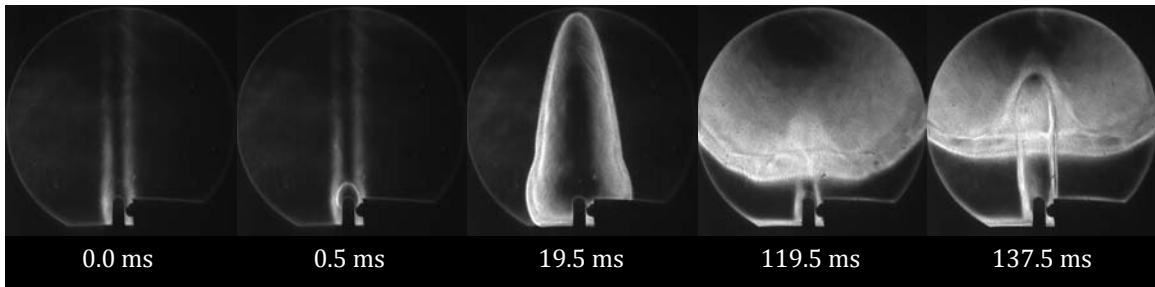


Figure 3.41: Schlieren visualization of a sequence of two flames ignited at the glow plug at $t < 0.5$ ms and 119.5 ms ($P_0 = 101$ kPa, $\phi = 2.25$)

3.5.5.2 Multiple Flames

As the equivalence ratio is increased for rich mixtures, the flame propagation speed is reduced and we observe that the flame is lifted away from the glow plug by buoyancy and the second flame ignites in its wake. Visualization of the flame is crucial to observe multiple ignitions and their timing. Figure 3.41 shows the established plume above the glow plug in a dark background schlieren image and the two successive ignitions at $t < 0.5$ ms and 119.5 ms. Depending on the flame speed, the re-ignition can occur again with the inflow from the second flame extinguishing the flame at the glow plug, or the flame transitions to a puffing flame. Multiple flames are a special case of the puffing flames and like those, a characteristic frequency can be assigned. When investigating the dependence of the frequency on various parameters, they are considered together with continuously puffing flames.

3.5.5.3 Puffing Flames

For even richer mixtures, continuously puffing flames are observed as shown in Figure 3.42. The flame ignited at the glow plug and propagates outward, slowly on the sides and quickly on the top due to the different temperature. The puffing flame is created by the interaction of the flame propagation and the flow field. Three different effects contribute the flow field outside the flame. The volumetric expansion across the flame front creates a dilatation flow that pushes the unburnt gas outside the flame outward. Second, the burnt gas has a lower density and buoyancy accelerates the flame upward creating an entrainment flow at the bottom of the flame. Finally, the density gradient across the flame front is misaligned with the hydrostatic pressure gradient, which leads to

the creation of vorticity from baroclinic torque. All of these effects combined create an inflow that exceeds the outward flame propagation leading to an instability of the flame front. The process, which is discussed in detail in the next chapter, repeats itself periodically until the temperature of the glow plug decreases sufficiently or the hot products, which fill the vessel from the top, reach the ignition source. The interface between burned and unburned gases is visible in the last four frames of Figure 3.42 and reaches the glow plug after 8 seconds.

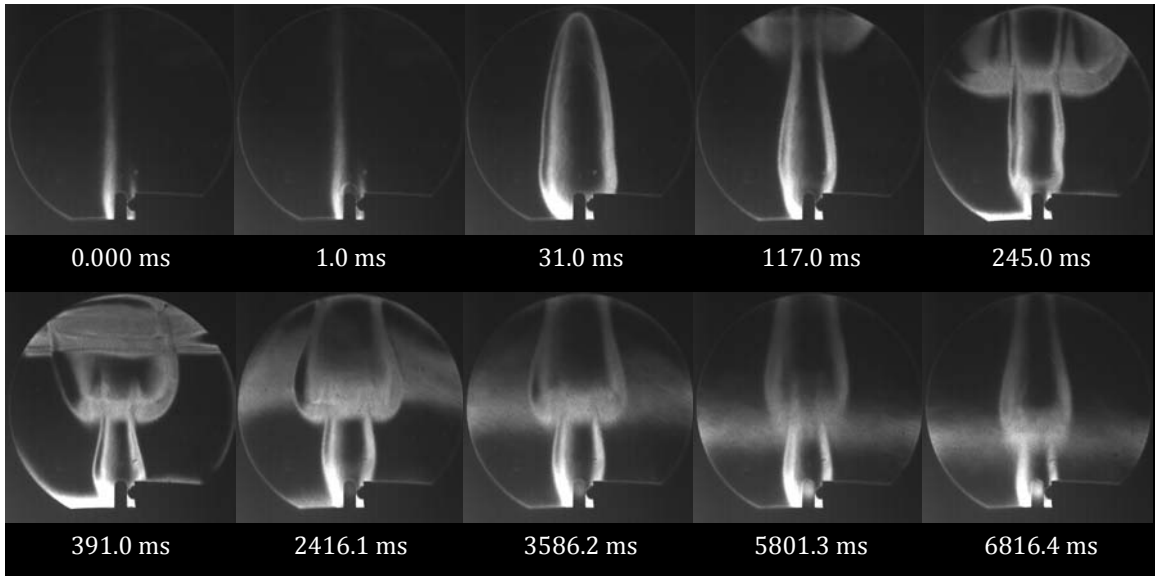


Figure 3.42: Schlieren visualization of puffing behavior (ignition at 1 ms, $P_0 = 101$ kPa, $\phi = 3.0$, shot 42)

3.5.5.4 Combustion Mode as a Function of Richardson Number

The different modes of combustion are a function of the flame propagation speed and the buoyancy of the burned gases. The buoyancy effect depends on the densities of the burned and unburned gas and the gravitational acceleration. We suggest that the different regimes can be characterized by the Richardson number, Ri , which represents the ratio of buoyancy to inertial effects in gas motion

$$Ri = \frac{AgL}{U^2} = \left(\frac{\rho_u - \rho_b}{\rho_u + \rho_b} \right) \frac{gL}{V_f^2} \quad (3.79)$$

$$Ri = \frac{\text{buoyancy}}{\text{inertia}} = \frac{\Delta\rho gL}{\bar{\rho}V_f^2} \quad (3.80)$$

where A is the Atwood number based on the unburned and burned gas densities (ρ_u and ρ_b , respectively), g is gravitational acceleration, L is the height of the glow plug, and U is the measured

horizontal flame propagation velocity (V_f). Figure 3.43 shows how the Richardson number changes with the mixture composition. We observe a single flame when the Richardson number is below 0.4 (see region II in Figure 3.43) with the exception of the 4 lowest equivalence ratios (region I).

In region I near the lean limit, we observe a different ignition and flame propagation phenomenon. As we approach the lean limit the ignition temperature is raised to above 1170 K, which increases the size of the plume and ignition is not observed in a small kernel, but in the plume. The flames propagate quickly in the hot plume and consume the entire volume. This phenomenon is observed in shots 28, 30, 36, and 37 with mixtures ranging from $\phi = 0.59$ to 0.69. Images showing the ignition location are available in Appendix J and schlieren sequences in Appendix K. By adding hydrogen and lowering the ignition temperature it is possible to obtain puffing behavior as discussed in Section 4.3.5.

For Richardson numbers between 0.4 and 2.5 re-ignition occurs (see region III) and for value above 3.5 puffing flames are observed (see region IV). This suggests that when the buoyancy and inertia are of the same magnitude the flame transitions to re-ignition and further decrease in the inertia leads to puffing flames.

Although the correlation of behavior with Richardson number is reasonable, other explanation are possible, that are explained in more detail in the next chapter.

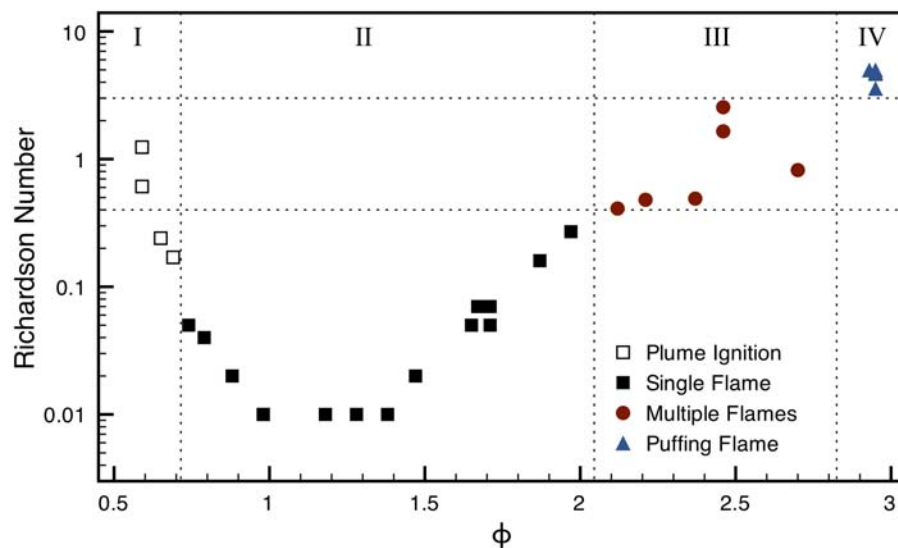


Figure 3.43: Ignition behavior as function of Richardson number for varying equivalence ratio at atmospheric pressure in the 2 liter combustion vessel

3.6 Conclusion

The ignition of gaseous *n*-hexane-air mixtures and subsequent flame propagation have been investigated by varying the mixture composition, initial pressure, and hot surface used to ignite the mixture. Consistent with the known lower flammability limit, the maximum temperature of the hot surface was insufficient at igniting the mixture. Away from the lower flammability limit, the ignition temperature is an almost constant value over a wide range of equivalence ratios ($0.75 < \phi < 2.7$) with large variations as the upper flammability limit is approached.

A simple model to investigate hot surface ignition is proposed based on the buoyancy driven flow along a vertical hot plate. In this situation, the fluid elements are entrained into the hot boundary layer, where the temperature increases as the elements move closer to the hot surface. Considering a large activation energy assumption, the dominant balance occurs between the diffusion and convection in the outer region of the boundary layer. In the inner layer, diffusion balances with the chemical reactions until ignition occurs. The effects of changing composition and initial pressure can be captured using this dominant balance approach. Further modeling of the ignition temperature has been done using tabulated detailed chemistry, which improved on capturing the lower flammability limit, but is still limited by the available low temperature reaction mechanisms, which are particularly sparse for *n*-hexane, and indicate an opportunity for future research. A limited study of the effect of hot surface area also indicates an area of future research. However, the limited experiments performed show that some historical data indicates ignition temperatures that are significantly higher than observed in the current study.

The flame propagation that follows the ignition has been studied and compared to simulation results and literature values. Over the range of equivalence ratios investigated three distinct modes of combustion are observed: single flame, multiple flames, and puffing. These regimes are captured by considering the competition between inertia, i.e., flame propagation, and buoyancy, which can be expressed in the Richardson number. The various regimes are clearly delineated by the Richardson number and give a direction for studying the puffing phenomenon in detail in the next chapter.

This page intentionally left blank.

Chapter 4

Cyclic Flame Propagation in a Fully Premixed Initially Stagnant Mixture

4.1 Introduction

This chapter focuses on the periodic flame motion, the puffing flame described in Chapter 3, that was discovered during the investigation of flame propagation subsequent thermal ignition.

Flames exhibiting a flickering or puffing behavior with frequencies around 10 Hz have been discussed since the First International Symposium on Combustion in September 1928 (Chamberlin and Rose, 1948). The oscillation of non-premixed gaseous flames were investigated experimentally by Kimura (1965), Toong et al. (1965), Grant and Jones (1975), Durao and Whitelaw (1974), and later by and Tanoue et al. (2010). Theoretical work has been carried out by Buckmaster and Peters (1988), who investigated oscillations associated with the model problem of an infinite candle. Similar oscillations have also been observed in fires above pools of liquid fuels (Cetegen and Ahmed, 1993) and in room fires (Zukoski, 1986).

These oscillations are not limited to non-premixed flames, but can also occur in premixed flames as shown by Strawa and Cantwell (1989), Durox et al. (1990), Kostiuk and Cheng (1995), Cheng et al. (1999), Shepherd et al. (2005), and Guahk et al. (2009). In these studies, the frequency of the motion is also on the order of 10 Hz. In all of the previous experiments of premixed flames, the gaseous mixture was injected into the burner at a specific injection velocity. In contrast, the experiments and simulations presented here are performed in a combustible mixture, which is quiescent prior to the ignition sequence. The following investigation of the cyclic flame propagation in a premixed environment is conducted using a combined experimental and numerical approach.

4.2 Experiments

4.2.1 Experimental Setup and Procedure

The experimental setup and procedure for the cyclic flame propagation are the same as used in the study of hot surface ignition detailed in Chapter 3, with a few additions. Experiments are performed using a standard diesel glow plug (Autolite 1110), a high-temperature glow plug (noncommercial Bosch 978801-0485), as well as a nickel foil, and a chromel wire in order to investigate the effect of the hot surface size. The characteristic dimensions of the different hot surfaces, as well as their power consumptions are given in Table 4.1. Similarly, two vessels of different sizes, the 2 liter vessel shown in Figure 3.1 and a 22 liter cylindrical vessel, are used to test the effects of vessel size and recirculation. The cyclic or puffing flame is visualized using either a regular z-type schlieren system showing the density gradients (Figure 4.1), or by observing the excited CH radical, CH* (Figure 4.2), which is created in the combustion of hydrocarbon fuels at the flame front.

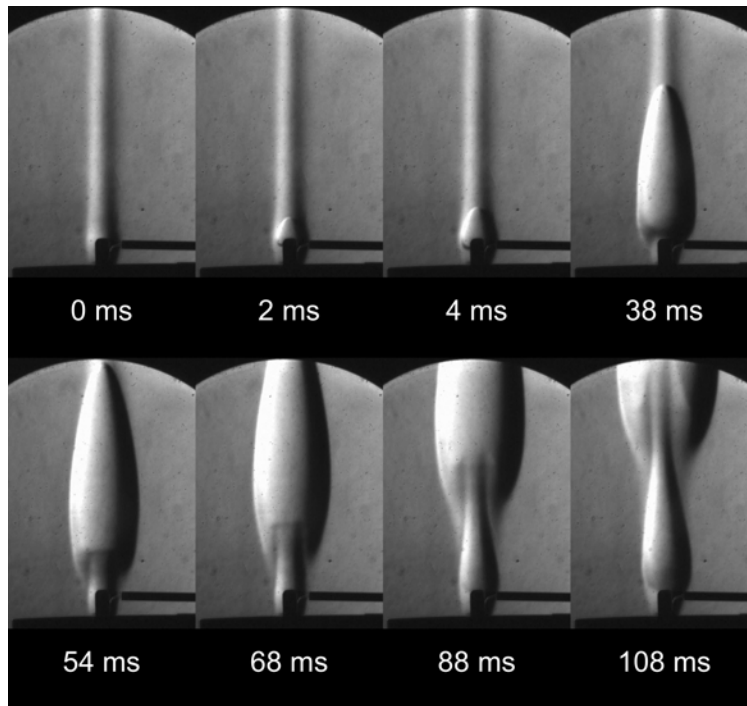


Figure 4.1: Schlieren images of ignition and subsequent flame propagation in a mixture of hexane in air at atmospheric pressure ($\phi = 3.0$). The hot surface is an Autolite 1110 glow plug, mounted in a 60-mm-diameter aluminum cylinder in a closed 22 liter combustion vessel. The hot surface temperature is measured by a fine wire K-type thermocouple at the hottest point on the glow plug.

The images of CH*, which emit light between 420 and 440 nm, are acquired by observing the flame directly through a narrow bandpass filter (center wavelength $\lambda_c = 450 \pm 10$ nm, 70 ± 30 nm

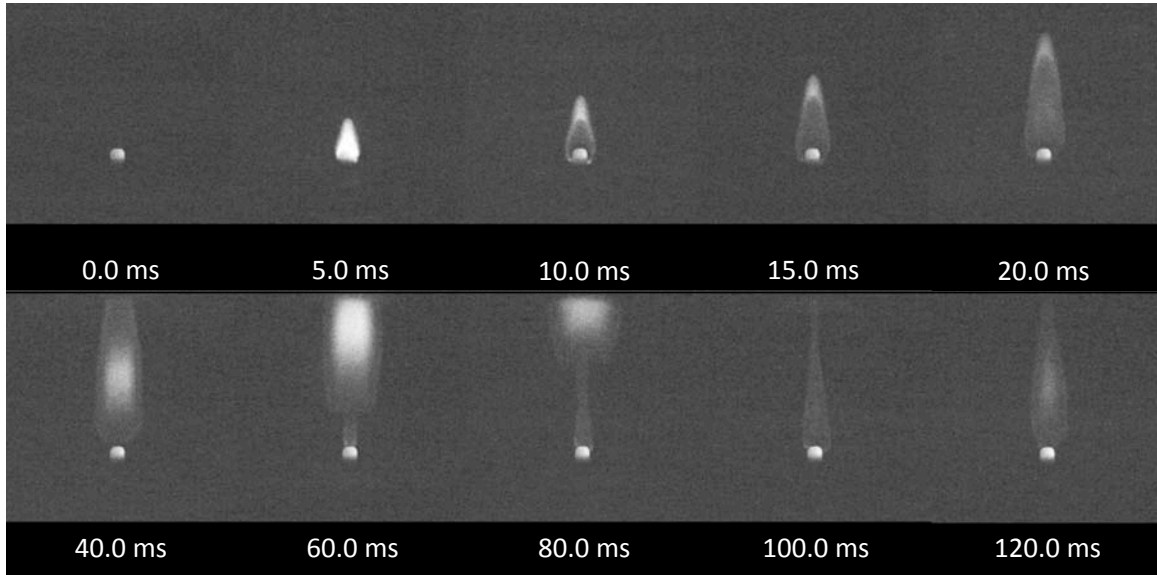


Figure 4.2: Direct imaging of CH^* molecules through a bandpass filter ($\lambda_c = 460$ nm with FWHM 40 nm) and a short-pass filter (transmittance $> 75\%$ in the range of $\lambda = 430\text{--}500$ nm), $\phi = 3.0$

FWHM) and a short-pass filter (transmittance $> 75\%$ in the range of $\lambda = 430\text{--}500$ nm). Figure 4.3 gives the transmittance curve of the combined optical filter and the CH^* emission spectrum. Due to the low light level, the exposure time is increased to 5 ms and the frame rate is reduced to 200 frames per second. Afterwards, the contrast of the images is enhanced in order to make the flames more easily visible.

4.2.2 Experimental Observations

The usual combustion mode following ignition in a closed vessel is a single quasi-spherical flame that spreads in all directions, and is distorted by buoyancy at low propagation velocities (i.e., very lean or rich mixtures). As described in Chapter 3, the hot surface establishes a thermal buoyant plume in the vessel, which induces an initial flow field prior to ignition. This thermal plume is shown in the first schlieren image in Figure 4.1 for a rich *n*-hexane-air mixture ($\phi = 3.0$). Then, the mixture ignites near the tip of the glow plug and propagates quickly upward along the thermal plume. At this equivalence ratio, the laminar burning velocity is very low – around 20 cm/s (see Figure 3.31). Due to the temperature increase within the plume and the buoyancy-induced flow, the upward flame propagation velocity is significantly higher than the flame propagation velocity on the sides. In the schlieren images, the flame appears not to propagate downward after ignition due to the upward flow velocity at the glow plug base. As subsequently shown by numerical simulations, the upward

velocity is induced initially by the thermal plume of the glow plug and subsequently by buoyancy and vorticity produced by the combustion products.

Once ignition has occurred, the temperature in the region above the hot surface is determined by combustion products. The upward motion of the buoyant hot products entrains cold premixed, but unreacted, gas. The entrainment velocity limits the horizontal spreading of the flame. The puffing behavior appears to be a result of the instability of the flow and the flame sheet due to the interaction between the entrainment, buoyancy-induced flow, and flame dynamics. Following the initial ignition transient, the temperature distribution and flow field is determined by the continuous, but periodically varying, cylindrical flame extending upward from the thermal ignition source. Radial entrainment provides a continuous source of fresh reactants. The resulting configuration appears to be an axisymmetric “V-flame” anchored by the ignition source.

The sequence of images showing the CH^* luminescence in Figure 4.2 further illustrates the puffing phenomenon. In the images three different sources of light are visible: CH^* radiation, which is produced at the flame front; second the tip of glow plug, which radiates over a broad spectrum; and finally soot, visible in the middle of the flame at later times, which also radiates over a broad spectrum. This technique is not sensitive to density gradients, so the initial plume is not visible. In the second image, ignition at the top of the glow plug is clearly visible. The flame propagates outward, more quickly within the hot plume above the glow plug, but remains a continuously connected flame and anchored at the top of the glow plug.

The puffing process occurs at a consistent frequency of about 6-15 Hz depending on the initial composition. The scaling of the puffing frequency and the physics of the puffing phenomenon are examined in detail in the following sections.

4.2.3 Numerical Simulations ¹

Two-dimensional unsteady simulations are performed using the same flamelet model as described in Chapter 3. Ignition is simulated by creating a small spherical flame sheet at the top of the glow plug inside the established thermal plume. The initial thermal plume created while the glow plug heats up to ignition temperature (as discussed previously) was simulated in order to have a realistic comparison of experimental and computational results.

Simulations are performed for both glow plug geometries (Bosch and Autolite - see Sections 3.2.3 and 3.2.4), resulting in puffing flames over a range of *n*-heptane-air mixtures from $\phi = 2.5$ –3.0 with

¹All numerical simulations were performed by Shyam Menon and Guillaume Blanquart

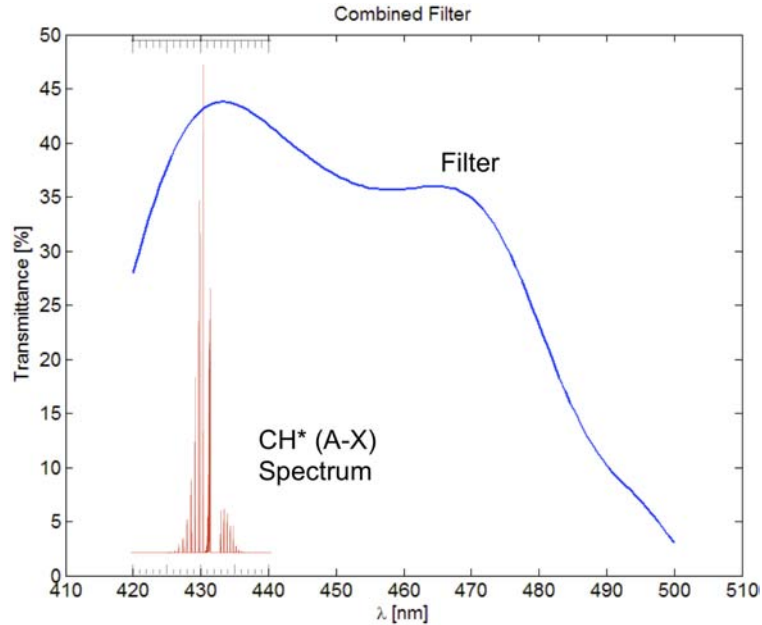


Figure 4.3: Transmission curve of the combined filter and CH^* spectrum calculated with Lif-Base (Luque and Crosley, 1999) superposed on the filter transmission function

small variations in the puffing frequency. The simulations, such as the one in Figure 4.4, show the flame propagating outward initially before the deformation of the flame front develops as observed in the experiments. Once it was demonstrated that the simplified numerical model gave realistic results, it was used to explore the effect of a variety of parameters as well as the details of the flow field.

4.3 Results — Puffing Frequency

As seen in the previous chapter, the combustion mode depends on the exact composition of the mixture and possibly other factors such as size of the hot surface. The effect of total vessel volume is of special interest because for very small vessel sizes the combustion products could force the flow into a large-scale recirculation or result in coupling to the acoustic modes with the flame motion. The following section provides details on the effects of these parameters and gives dimensional arguments on how the frequency changes as function of the flame propagation speed and gravity.

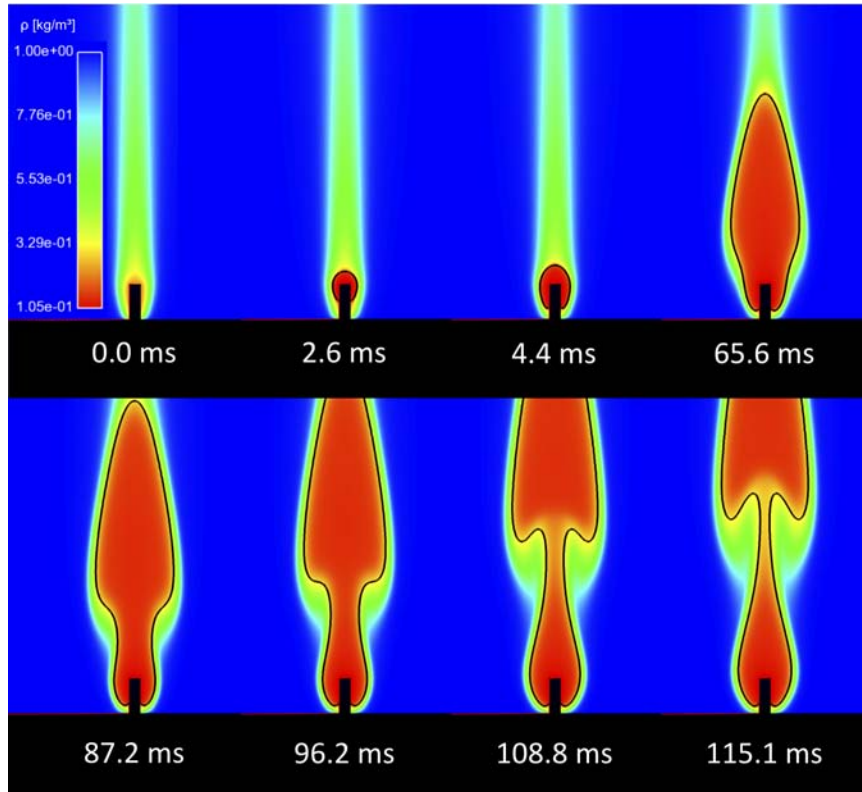


Figure 4.4: Simulation results (density contours) for flame propagation phenomena at an equivalence ratio of $\phi = 2.5$. The black line represents the location of the flame front as marked by the iso-contour of the progress variable, $C = 0.15$.

4.3.1 Glow Plug Size and Vessel Size

The experiments were performed with 4 different heat sources as listed in Table 4.1. The measurements show that there is a very limited dependence of the puffing frequency on igniter size, as well as power input. Similarly, changing the vessel volume from 2 to 22 liters did not change the puffing frequency noticeably. Similar analysis is performed with numerical simulations by changing the size of the modeled glow plug by a factor of 0.5 and 2 and the size of the vessel from 1 liter to 5 liters². These observations suggest that the frequency is a function of the flame dynamics and the flow induced by the flame, and is independent of the igniter and vessel sizes. This rules out that the periodic motion is caused by a recirculation created by the flame pushing the unburned gas upward stagnating at the top, pushing fluid down the side and back into the flame. The independence of frequency from vessel size also rules out acoustic interactions with the enclosure as a possible puffing mechanism.

²The numerical simulation only models the vessel above the stagnation surface, which is roughly in the middle of the vessel giving a volume of 1 liter for small vessel. The large vessel is only modeled to a size of 5 liters to limit the number of grid points and the computational time required.

Table 4.1: Puffing behavior for fuel-rich hexane air mixture ($\phi = 3.0$)

Hot Surface	Power [W]	Area [m ²]	V _{vessel} [m ³]	T _{ign} [K]	Freq. [Hz]
Bosch Glow Plug [†]	≈100	8×10 ⁻⁵	2×10 ⁻³	920-975	12-13 (+1/-1)
Autolite 1110 Glow Plug	96	1.5×10 ⁻⁴	2×10 ⁻³	775-825	12-13 (+1/-2)
			22×10 ⁻³	1120	14-15 (+1/-1)
Nickel Foil 0.05 mm	≈400	2.4×10 ⁻⁵	2×10 ⁻³	980	20 (+8/-2)
Chromel Wire ∅ 0.13 mm	≈10	2.4×10 ⁻⁶	2×10 ⁻³	n/a	14 (+3/-2)

[†] non-commercial Bosch (961) 64 978801-0485 Duraterm

n/a - not available

4.3.2 Scaling Laws

4.3.2.1 Cetegen and Ahmed (1993)

Buoyant plumes and pool fires have instabilities and periodic motions that are very similar to those observed in the present premixed puffing flames. As a first approximation, the frequency behavior of plumes and pool fires can be estimated using dimensional analysis. The observed frequency is a function of the buoyancy-induced flow, with no puffing was observed in zero-g conditions³, making gravity, g , one of the parameters of interest. The main length scale parameter is the diameter of the burner, D , through which either a buoyant plume of light gas, such as helium, combustion products from a preburner, or a pool of evaporating fuel is introduced. Cetegen and Ahmed (1993) suggest that the following nondimensional ratio

$$\frac{f^2 D}{g} \quad (4.1)$$

has a universal value. This implies that at a constant gravitational acceleration,

$$f \sim D^{-1/2} . \quad (4.2)$$

Cetegen and Ahmed (1993) compiled data for many different gaseous and liquid fuels as well as light gases and showed good agreement using this scaling argument for burner sizes of approximately 10^{-2} to 10^1 m.

For pool fires, the size of the pool determines the size of the flame. The fuel from the liquid or gaseous pool has to mix with the air outside to create a combustible mixture. This mixing interface originates near the edge of the fuel pool. The diameter of the flame, d_f , is therefore fixed and proportional to the pool diameter as shown in Figure 4.5.

³Simulations of the configuration shown in Figure 4.4 were performed without gravity (Menon, 2011).

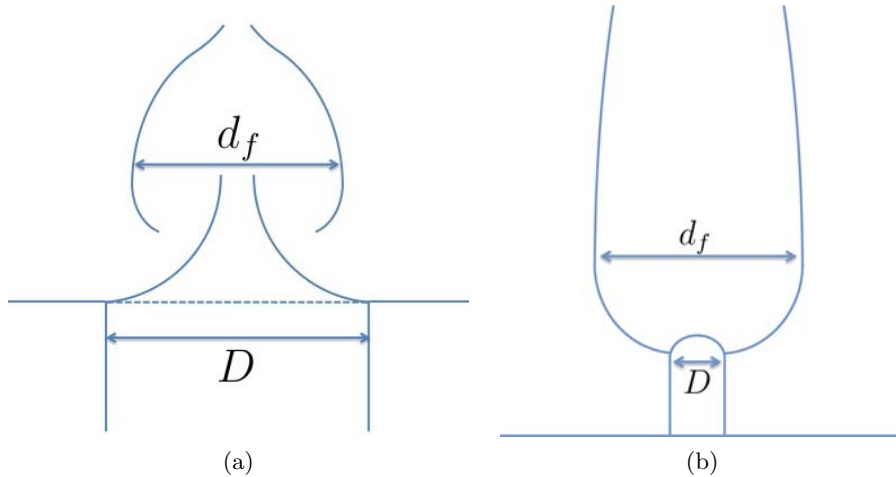


Figure 4.5: (a) Flame diameter, d_f and pool diameter, D , based on Cetegen and Ahmed (1993). (b) Flame diameter, d_f and hot surface, D , for premixed puffing flames

$$d_f \propto D \quad (4.3)$$

The puffing flames described here, however, are premixed flames. The diameter of the flame significantly exceeds that of the hot surface since the flame starts at the hot surface and propagates outward until the flame front becomes unstable and the upward flow sweeps it away. The flame initially propagates outward spherically so that the radius scales as $\epsilon S_{l,u} t$, where ϵ is the density ratio across the flame front and $S_{l,u}$ is the laminar flame speed relative to the unburned gas⁴. The flame diameter increases until the instability takes over, giving the time scale of $T \sim 1/f$. We propose that the characteristic diameter of the flame can be modeled as the sum of the two terms,

$$d_f = 2 \frac{\epsilon S_{l,u}}{f} + D. \quad (4.4)$$

The first term represents the diameter of the flame at the peak of the puffing cycle and the second term represents the diameter of the hot surface, D , the initial position from which the flame starts.

In the present experimental study, hot surfaces with different diameters, ranging from $D = 0.1$ mm to $D = 5$ mm were considered. The puffing period, T , is about 0.1 s for flame propagation speeds of about 0.2 m/s. Under these conditions, the flame diameter changes by only 12.5% for a change in hot surface size of almost 2 orders of magnitude. If as an initial approximation the diameter of the hot surface is neglected, a new nondimensional ratio can be formulated similar to

⁴In this thesis $S_{l,u}$ and S_l are used interchangeably to mean the laminar flame speed relative to the unburned gas.

the one proposed by Cetegen and Ahmed (1993) in Equation 4.1

$$N_B = \frac{f\epsilon S_{l,u}}{g} = \frac{\epsilon S_{l,u}}{gT}, \quad (4.5)$$

has a value of 0.2-0.3, which is comparable 0.23 found by Cetegen and Ahmed (1993) ⁵.

$$f \propto g \text{ for fixed } \epsilon S_{l,u} \quad (4.6)$$

and

$$f \propto (\epsilon S_{l,u})^{-1} \text{ for fixed } g. \quad (4.7)$$

These scaling results are compared with experimental data in the subsequent sections.

4.3.2.2 Durox et al. (1996)

Durox et al. (1996) investigated the the flickering of jet diffusion flames and arrived at a different set of scaling relations. Fuel is introduced through a small nozzle (2–4 mm in diameter) at low velocities (2 mm/s). Tests were performed at varying pressure and at varying gravitational acceleration, which was achieved during parabolic flight tests. In these experiments, the mean diameter of the flame is greater than the nozzle diameter. In contrast, in pool fire experiments, the mean flame diameter is smaller than the pool diameter.

Through dimensional analysis the frequency, f , is scaled with the gravitational acceleration, g , and the viscous diffusion, ν ,

$$f^3 \sim \frac{g^2}{\nu}. \quad (4.8)$$

Durox et al. (1996) perform a more detailed theoretical analysis of the flame instability, where the flame creates a constant inflow of hot gases in the middle and thus a shear layer is formed across the flame front. Durox et al. argue that the most amplified frequencies, f , in this flow are given by

$$f = c \left[\left(\frac{\rho_u - \rho_b}{\rho_b} \right)^2 \frac{g^2}{\nu_b} \right]^{2/3} \quad (4.9)$$

where c is a constant, ρ_u and ρ_b are the unburned and unburned density, g is the gravitational acceleration, and ν_b is the viscosity of the burned gas. This scaling is based on the developments of the instabilities at a certain height above the nozzle exit, but can also be obtained by dimensional

⁵Cetegen and Ahmed (1993) give the scaling for pool fires at normal gravity as $f = 1.5D^{-1/2}$. Squaring both sides and dividing through by g gives $(f^2D)/g = 0.23$.

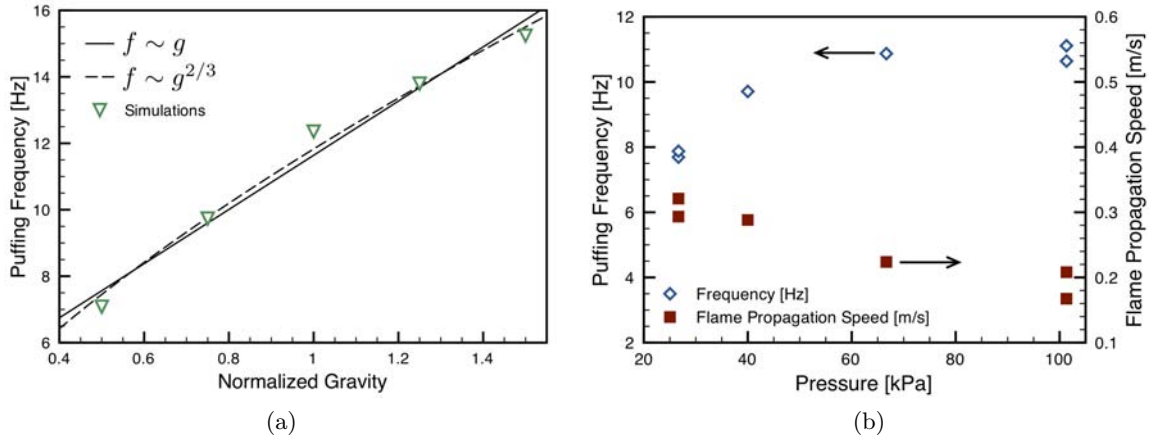


Figure 4.6: (a) Simulation results for the puffing frequency as a function of gravitational acceleration. (b) Experimental results for puffing frequency and flame propagation speed as function of initial pressure at $\phi = 2.5$

analysis when considering only the effects of buoyancy acceleration [m/s^2] and kinematic viscosity [m^2/s]. As the viscosity varies with pressure as $\nu_b \sim P^{-1}$ (Durox et al., 1996) the frequency can be written as

$$f \propto g^{2/3} \text{ and } f \propto P^{1/3}. \quad (4.10)$$

Note that this model predicts that the frequency is dependent on viscosity rather than burning speed because the combustion is not premixed. This scaling will be compared to the experimental data and the ideas of the previous section in the next section.

4.3.3 Effect of Gravity

In the puffing flames described here, the flame front initially spreads out from the hot surface almost spherically, with a propagation speed equal, V_f , that is close to the product of the expansion ratio, ϵ , and the laminar burning speed relative to the unburned gas, $S_{l,u}$. Gravity creates a buoyancy force on the burned gas, which is less dense than the surrounding gas, and lifts the flame upward once it has reached a critical size. The burned gas moves upward more rapidly than it is replenished by combustion of inward flowing combusted gas. This process appears to be responsible for the puffing behavior and gives rise to the characteristic frequency. Experiments and simulations confirm that the frequency of the puffing changes with the flame propagation speed and magnitude of gravitational acceleration.

Figure 4.6 (a) shows the results of a computational study of changing the acceleration of gravity. With increasing values of g , the puffing frequency increases. This is consistent with the flame puff being lifted by the acceleration of gravity and the hydrostatic pressure, creating an entrainment flow pinching the flame together. Both of these effects are increased as the acceleration due to gravity is increased.

Over the range investigated both the linear relation, $f \sim g$, as well as the nonlinear relation, $f \sim g^{2/3}$ are both consistent with the simulation results. The nonlinear scaling gives a zero puffing frequency at zero gravitational acceleration, which is expected from the postulated mechanism and simulations. The y-intercept of the linear scaling is not zero, which can be attributed to the initial diameter of the flame being neglected. This indicates that a more general relationship for scaling should be considered, which is done in the next section.

4.3.4 Effect of Flame Speed

The flame propagation speed can be varied in the experiments by either changing the initial pressure of the mixture or changing the composition. In Figure 4.6 (b), experimental results are shown for varying the initial pressure from 25 to 100 kPa for a $\phi = 2.5$ *n*-hexane/air mixture. As the pressure is decreased from ambient, the measured flame propagation speed increases, which is consistent with other data on slow burning flames Lewis (1954), Gaydon and Wolfhard (1979), Kelley et al. (2011), and the puffing frequency decreases.

A re-analysis of the relationship above is shown in Figure 4.7. The puffing period, $T = 1/f$, is plotted versus the flame propagation speed for both experiments and simulations. The experimental mixtures shown are *n*-hexane in air from $\phi = 2.15-3.0$ and at initial pressures varying from 25 kPa to 100 kPa, 7% and 8 % hydrogen in air, as well as lean and rich hexane mixtures doped with hydrogen (see the following section). In agreement with the proposed scaling relationship, the puffing period increases approximately linearly with flame speed for all experimental and computational results. The deviation from a linear relationship can be rationalized as being due to neglecting the initial hot surface diameter (D) in Equation 4.4. The zero flame speed intercept has a finite puffing frequency that is consistent with the plume and pool fire scaling proposed by Cetegen and Ahmed (1993).

A more general expression may be derived by using the full form of Equation 4.4. Following the arguments from Cetegen and Ahmed (1993), and assuming that the important length scale is the

diameter of the hot products, we propose that the following expression must be a constant:

$$\frac{f^2 d_f}{g} = \frac{2\epsilon S_{l,u} f}{g} + \frac{f^2 D}{g} = \text{constant} = C . \quad (4.11)$$

We can rearrange this equation to give

$$\epsilon S_{l,u} = \frac{gC}{2} T - \frac{kD}{2} \frac{1}{T} \quad (4.12)$$

where the flame propagation speed is a function of the puffing period as plotted in Figure 4.7 which can be written as a quadratic equation for the puffing period

$$\frac{gC}{2} T^2 - \epsilon S_{l,u} T - \frac{kD}{2} = 0 . \quad (4.13)$$

An additional constant k has been introduced to provide a better fit to the experimental data and account for the fact that the initial flame diameter may not be exactly D . Using all experimental and numerical results, the coefficients C and k were found using a least squares minimization ($C = 0.64$ and $k = 3.35$).

Figure 4.7 shows both the experimental data and simulation results. The linear relation, ($k = 0$) is also shown; while in general agreement with the observations, the nonlinear correlation (4.12) is a definite improvement.

A direct comparison with the scaling proposed by Cetegen and Ahmed (1993) is also possible by setting the flame speed to zero. In dimensional form, the frequency in Hz as function of diameter in meters at 1 g is given by Cetegen and Ahmed (1993) as

$$f = 1.5 D^{-1/2} . \quad (4.14)$$

Setting $S_{l,u} = 0$ in Equation 4.12 results in expression

$$T = \sqrt{\frac{gC}{k}} D^{-1/2} \quad (4.15)$$

Using the results obtained for the coefficients C and k , the constant of proportionality is $\sqrt{gC/k} = 1.4 \text{ Hz m}^{1/2}$, which is within 10% of the Cetegen and Ahmed value.

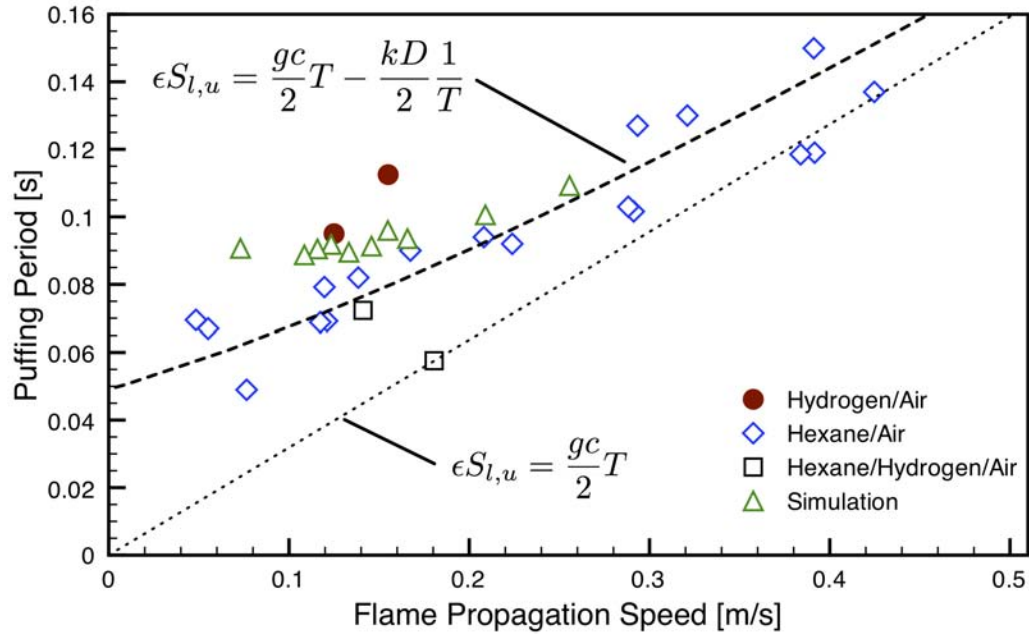


Figure 4.7: Puffing period vs. horizontal flame propagation speed for n-hexane air mixtures from $\phi = 2.15$ –3.0, 7% and 8% hydrogen in air and hexane/hydrogen/air mixtures at atmospheric pressure

4.3.5 Lean Hexane Puffing Flames ⁶

Based on the scaling ideas presented above, the phenomenon of puffing flames should not be limited to rich hydrocarbon mixtures, but should also occur in lean hydrocarbon mixtures if the flame speed is sufficiently slow. However, tests using lean hexane-air mixtures did not show puffing, apparently because the lower flammability limit is reached in the experiments before the flame propagation speed is sufficiently slow.

We were able to show that the puffing phenomenon does occur in lean hydrogen flames. In hydrogen flames, much lower flame speeds can be obtained with lean mixtures than in *n*-hexane-air cases. For lean H₂-air mixtures, the flame speed gradually increases as hydrogen concentration is increased, and for rich mixtures, the flame speed changes quickly with increasing concentration until the upper flammability limit is reached. Hydrogen-air mixtures have a very wide range of flammability from 4% to 75% (Zabetakis, 1965). Lean puffing hydrogen flames were observed for 7% and 8% hydrogen in air at frequencies of 10.5 and 8.9 Hz, respectively. For a 5% mixture only a single puff is visible, which propagates upward and the flame extinguishes. Figure 4.8 shows the flame speed as a function of hydrogen mole fraction from current experiments and simulations performed by Bane (2011).

⁶This work was presented by Brian Ventura in his senior thesis in May 2011

We can take advantage of the wide flammability range and slow flame speed of lean hydrogen-air mixtures by adding small amounts of hydrogen to hexane-air mixtures just below the flammability limit. Adding hydrogen to a mixture of *n*-hexane-air, which is below the flammability limit makes it possible to ignite the mixture and obtain slow flame speeds. Figure 4.8 shows flame speeds from experiments and simulation of *n*-hexane-air mixtures whose lowest propagation speed is just above 30 cm/s. Initially this increases the propagation speed as shown by the mixtures of 1.1% *n*-hexane and 2% hydrogen in Figure 4.8. However, decreasing the amount of hydrogen and *n*-hexane reduces the flame propagation speed to 25 cm/s, which leads to a series of puffing flames. The mixture of 1.05 % *n*-hexane and 1.5 % hydrogen (highlighted in Figure 4.8) has sufficiently a slow flame propagation speed that and shows a puffing flame at ~ 17 Hz (see shot 123).

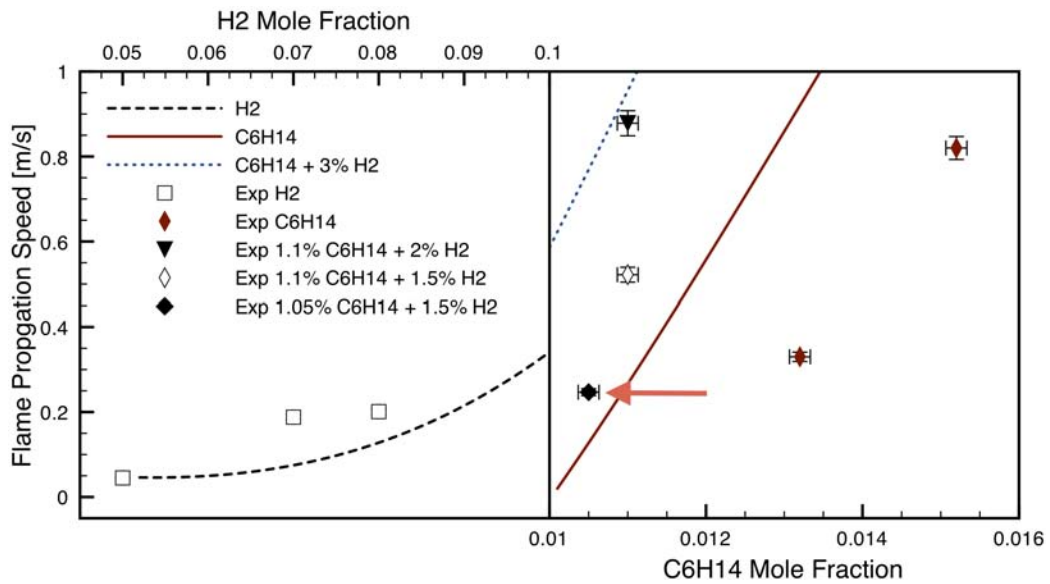


Figure 4.8: Flame propagation speeds of hydrogen-air, *n*-hexane-air, and hydrogen-*n*-hexane-air mixtures at atmospheric pressure

4.4 Physics of Puffing

Experiments and simulations have both demonstrated a periodic motion associated with flame propagation in rich premixed hydrocarbon-air mixtures (and lean hydrogen flames). We have also verified that the frequency of this periodic motion is linked to the flame propagation speed and acceleration due to gravity. The instability of the flow and flame front leading to the periodic motion apparently arises from a competition between flame propagation and buoyancy-induced entrainment flow with additional effects from volumetric expansion and vorticity. In order to get more insight into the puffing mechanism, the simulation results are used to analyze the instantaneous flow field associated with the combustion-induced flow as well as the generation of vorticity by the flame and boundaries.

4.4.1 Flow Field Analysis

The flow field is created by three different effects resulting from the combustion process. Across the flame, the temperature is increased, which lowers the density inside the flame. This volumetric expansion across the flame front induces a dilatation flow field ahead of the flame front because the flow is subsonic. The lighter gas inside the flame is also accelerated upward by buoyancy, creating an entrainment flow at the bottom of the flame. At the flame front, vorticity is created, predominantly from baroclinic torque arising from the misalignment of the density gradient across the flame front and the hydrostatic pressure gradient. The inflow created by the motion of the flame and the hot products opposes the flame propagation at the bottom of the flame.

Part of the effect of the dilation produced by combustion can be estimated by treating the flame as an ideal cylindrical flame. In Section 3.5.2 the flame propagation speed of a spherically expanding flame is estimated using a mass balance across the flame front. The result for a cylindrical flame or radius R with stationary combustion products is

$$\dot{R} = \epsilon S_l \quad (4.16)$$

where \dot{R} is the expansion rate of the flame, ϵ is the density ratio across the flame front, and S_l is the laminar burning speed. The definition of the burning speed is the speed at the which the flame propagates relative to the underlying flow velocity u ,

$$S_l = \dot{R} - u(R) . \quad (4.17)$$

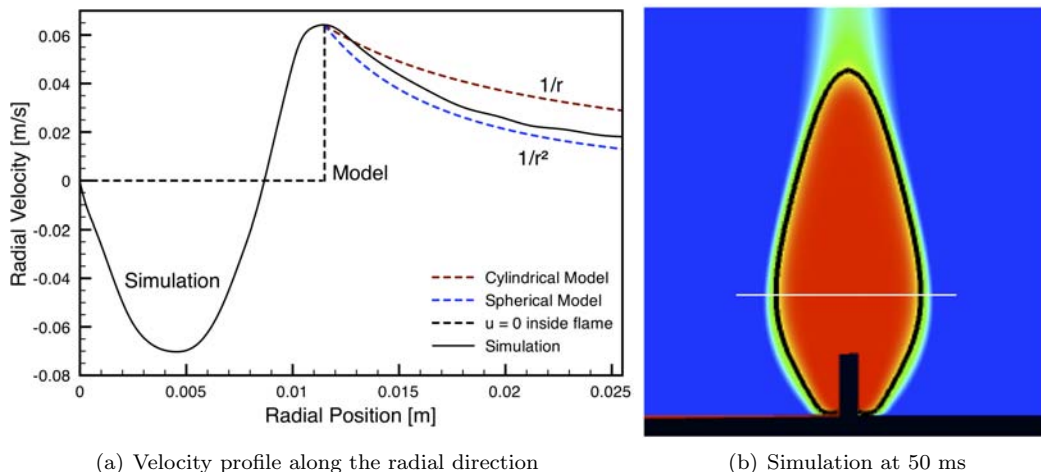
For incompressible, cylindrical flow the mass conservation outside the flame gives the velocity at any location $r > R$ in terms of the velocity $u(R)$ just ahead of the flame

$$\rho_u U(R) 2\pi R(t) = \rho_u u(r) 2\pi r \quad (4.18)$$

$$u(r) = U(R) \frac{R(t)}{r} = (\epsilon - 1) S_l \frac{R(t)}{r} \quad \text{for } r \geq R \quad (4.19)$$

with the assumption that the flow inside the flame is stationary, $u = 0$ for $0 \leq r < R$. For spherical flames, a similar derivation gives

$$u(r) = (\epsilon - 1) S_l \frac{R^2(t)}{r^2} \quad \text{for } r \geq R. \quad (4.20)$$



(a) Velocity profile along the radial direction

(b) Simulation at 50 ms

Figure 4.9: Radial velocity profile

Figure 4.9 (a) shows the radial velocity as a function of radial position from simulation at the widest part of the flame at 50 ms as indicated in Figure 4.9 (b). The simulations show that inside the flame, we have nonzero flow towards the center. This is not captured by the simple model and is due to the upward accelerating flow due to buoyancy and vorticity. Outside the flame, the flow is outward and the variation with radius is between r^{-1} and r^{-2} depending on the distance from the flame. The induced outward flow opposes the inflow leading to the formation of a puff, as discussed in the next section. Since the flow is nonzero inside the flame, we cannot use the simple models to achieve a good estimate of the flow velocity produced by the volumetric expansion across the flame front.

An alternative estimate of the influence of the volumetric expansion can be obtained by comput-

ing the pressure jump across the flame. In the reference frame of the flame, the unburned gases flow into the flame at a speed, w_1 , the laminar burning speed, and exit the flame at the flame propagation speed, w_2 , the product of laminar burning speed and the expansion ratio.

$$w_1 = S_l \quad (4.21)$$

$$w_2 = \epsilon S_l \quad (4.22)$$

The jump relation across the flame front is

$$P_2 + \rho_2 w_2^2 = P_1 + \rho_1 w_1^2, \quad (4.23)$$

where the subscript 1 represents unburned gas and subscript 2 represents burned gas. Substituting in for the velocities and densities gives

$$P_2 - P_1 = \rho_u \left(S_l^2 - \frac{\rho_b}{\rho_u} \epsilon^2 S_l^2 \right), \quad (4.24)$$

with $\epsilon = \rho_u/\rho_b$ this results in the pressure jump being

$$\Delta P = -\rho_u S_l^2 (\epsilon - 1). \quad (4.25)$$

For a rich *n*-hexane-air ($\phi = 3.0$) flame that exhibits puffing behavior, the initial density is about 1.2 kg/m³, the laminar flame speed is roughly 0.04 m/s, and the expansion ratio is around 5.5. From Equation 4.25 the pressure jump across the flame front is about 1×10^{-2} Pa.

In the quasi-steady flow outside the flame, the flow-induced pressure, $(\Delta P)_f$, can also be estimated by considering the maximum velocity ahead of the flame from (4.20)

$$(\Delta P)_f \sim \frac{1}{2} \rho u^2 \sim \frac{1}{2} \rho_u (\epsilon - 1)^2 S_l^2 \quad (4.26)$$

which using the values from above is ~ 0.02 Pa.

In comparison to the pressure jump across the flame front and the flow induced pressure, the pressure difference due to gravity across a 10-cm-diameter flame is

$$\Delta P = \rho g d = 1.2 \frac{\text{kg}}{\text{m}^3} \cdot 9.81 \frac{\text{m}}{\text{s}^2} \cdot 0.1 \text{m} = 1.2 \text{ Pa} . \quad (4.27)$$

The fact that the hydrostatic pressure head dominates the flame and flow-induced pressure gradients is very relevant to the subsequent discussion on the sources of vorticity at the flame front. It also points out the very substantial role the buoyancy-driven flow will play in the flow field, which supports the scaling arguments advanced earlier.

The simulation results provide the instantaneous velocity vectors created by the expanding flame front. In the lab frame, as shown in Figure 4.10 (a), the flow outside the flame appears to rotate about a point that translates as the puffing cycle progresses⁷. The appearance of rotation and the location of this point is a function of the reference frame chosen. A more detailed analysis of the flow field shows that the trajectory of the fluid elements outside the flame result in complex trajectories due to the competing effects of displacement and entrainment.

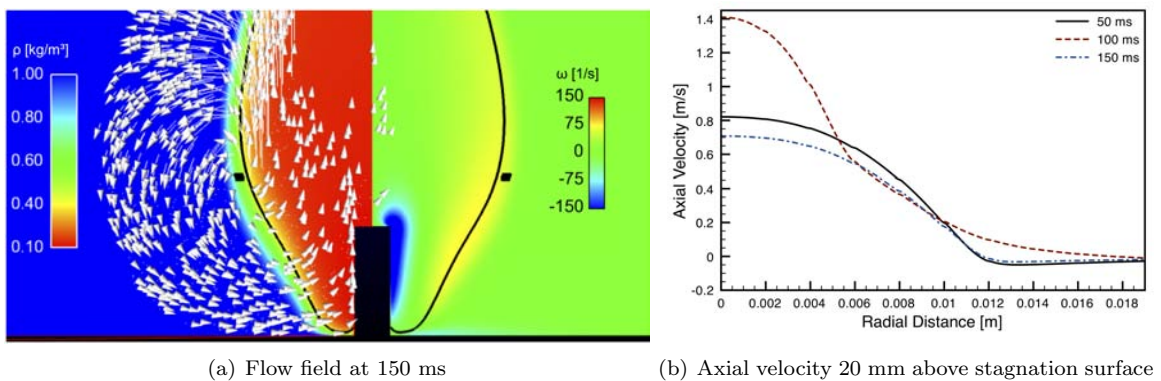


Figure 4.10: Flow field and axial velocity at 150 ms (height of glow plug is 11 mm)

Buoyancy accelerates the burned gases upward. If we estimate the resulting velocity, V , after one puffing cycle ($T = 0.1$ seconds)

$$V \sim gT \sim 9.81 \frac{\text{m}}{\text{s}^2} \cdot 0.1\text{s} \sim 1 \frac{\text{m}}{\text{s}} . \quad (4.28)$$

This velocity is on the same order of magnitude as the velocities observed in the center of the flame, Figure 4.10 (b).

The vorticity equation is derived by taking the curl of the Navier-Stokes equation and can be expressed as follows:

$$\frac{\partial \omega}{\partial t} + (\mathbf{u} \cdot \nabla) \omega = (\omega \cdot \nabla) \mathbf{u} - \omega (\nabla \cdot \mathbf{u}) + \frac{1}{\rho^2} [\nabla \rho \times \nabla p] + \nu \nabla^2 \omega . \quad (4.29)$$

⁷The location of the center of apparent rotation is identified using a technique similar to Graftieaux et al. (2001).

The first term on the right hand side corresponds to vorticity production due to vortex stretching; the second term arises due to volumetric expansion; the third term is vorticity generation due to baroclinic torque; and the final term is viscous diffusion. The source term due to diffusion gives a length scale outside of the flame that is small, on the order of the flame thickness. The pressure field in Equation 4.29 is obtained from simulation results includes hydrodynamic and hydrostatic effects and can be expressed as

$$\nabla p = \nabla p' + \rho_a g . \quad (4.30)$$

We now compute the magnitude of the different source terms in Equation 4.29 using the simulation results for a “puffing” flame at an equivalence ratio of $\phi = 2.5$. It is to be noted that, since the simulations are axisymmetric, only one component of vorticity (which points out of the plane of the paper) is generated.

Figure 4.11 shows a time-instance of the puffing motion with contours for the following terms from left to right: source term due to vortex stretching, source term due to volumetric expansion, source term due to baroclinic torque, sum of all the source terms, and the magnitude of induced vorticity. As before, the flame location is indicated by a black line corresponding to an iso-contour of the progress variable. The contour plot for vorticity includes velocity vectors illustrating the direction of the flow. The source term due to diffusion is small and not plotted here.

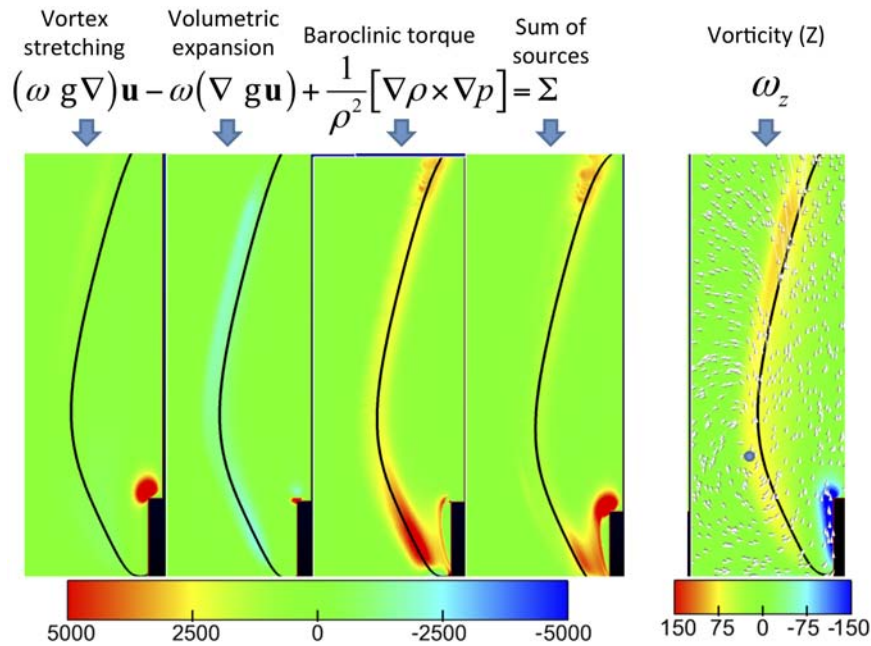


Figure 4.11: The vorticity production terms along the flame front and resulting vorticity at $t = 50$ ms

The vorticity is primarily generated along the flame front. The source terms due to vortex stretching and volumetric expansion along the flame front are opposite in direction to that produced by baroclinic torque. In case of baroclinic torque, the source term is seen to be primarily concentrated along the vertical sections of the flame front. The magnitude of this term is also seen to be considerably larger (100 times) than that due to vortex stretching and volumetric expansion. The net result is a positive (counter clockwise) generation of vorticity along the vertical edges of the flame.

Figure 4.12 shows contours of three quantities: density gradient, pressure gradient, and resulting baroclinic torque as well as the vorticity. The directions of the density and pressure gradients are further illustrated by arrows.

The location along the flame front where vorticity is generated (primarily due to baroclinic torque as shown in Fig. 4.11) is coincident with a large density and pressure gradient. These gradients are seen to be almost perpendicular to each other with the density gradient pointing mostly horizontally away from the flame front and the pressure gradient pointing predominantly vertically downwards.

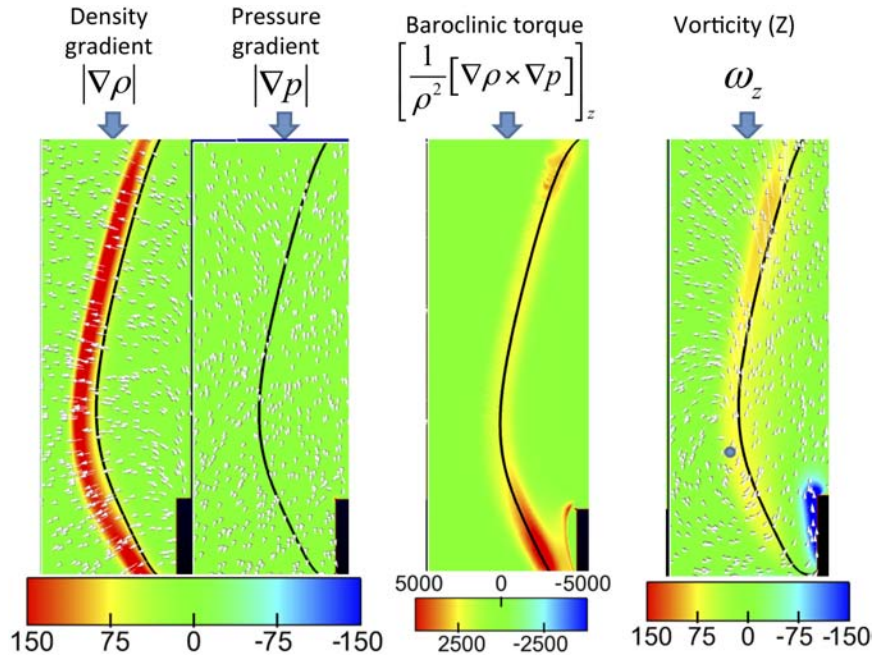


Figure 4.12: Gradients of density, pressure and the resulting baroclinic torque and overall vorticity along the flamefront at $t = 50$ ms associated with the incipient puff

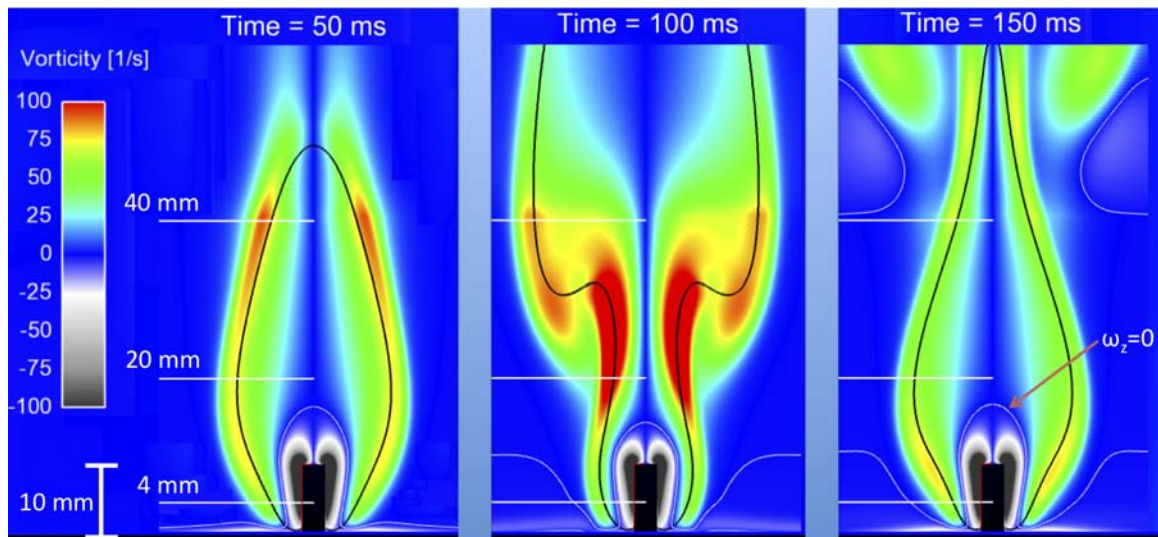
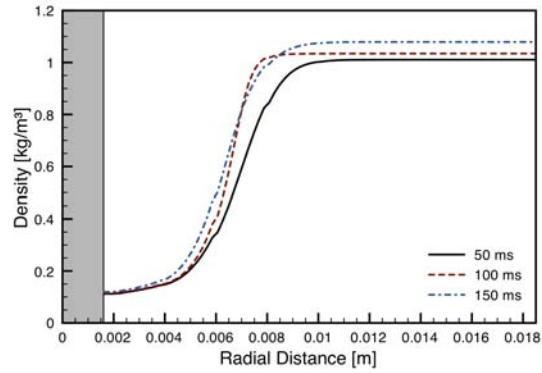
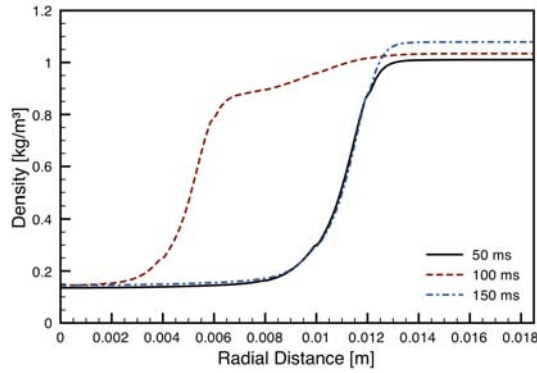


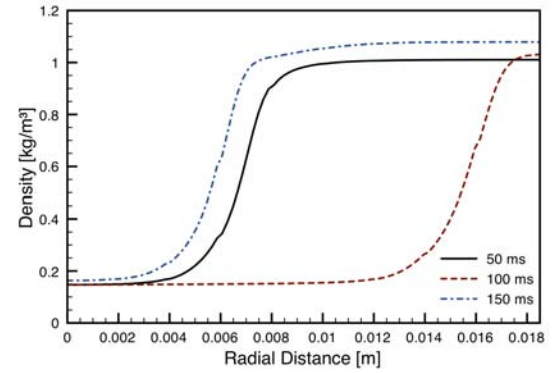
Figure 4.13: Detailed vorticity distribution at simulation time of 50, 100, and 150 ms (zero vorticity contour is indicated by the thin white line); subsequent figures show density, vorticity, and velocity profiles at the indicated locations 4, 20, and 40 mm above the stagnation surface



(a) 4 mm above stagnation surface

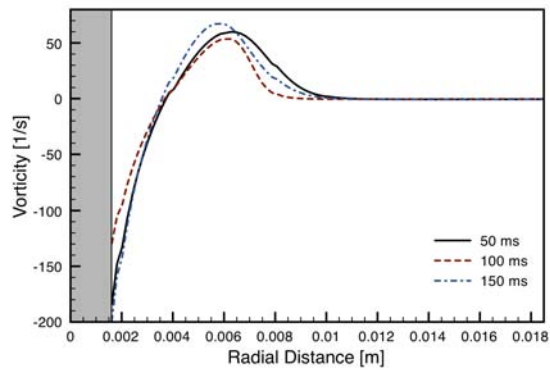


(b) 20 mm above stagnation surface

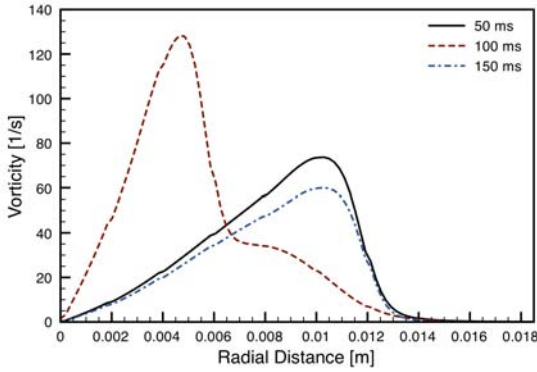


(c) 40 mm above stagnation surface

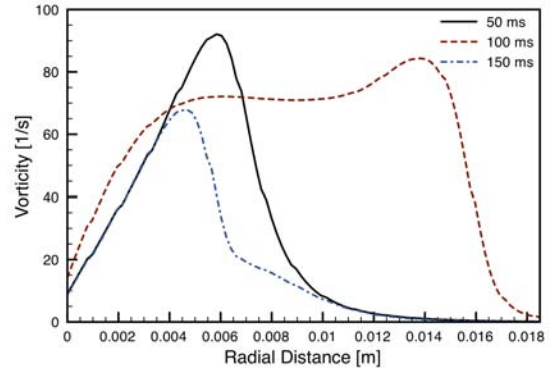
Figure 4.14: Density as a function of radial location at different locations in the flame



(a) 4 mm above stagnation surface

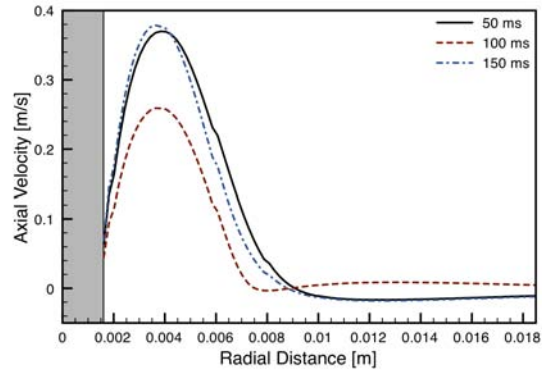


(b) 20 mm above stagnation surface

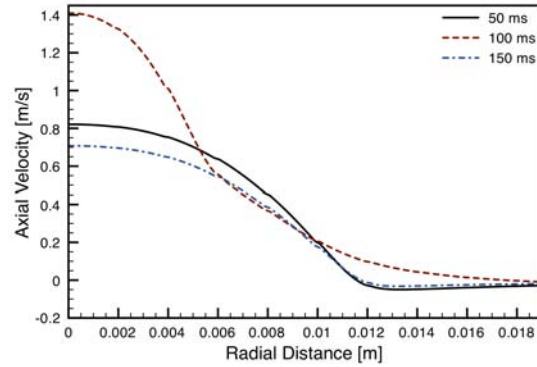


(c) 40 mm above stagnation surface

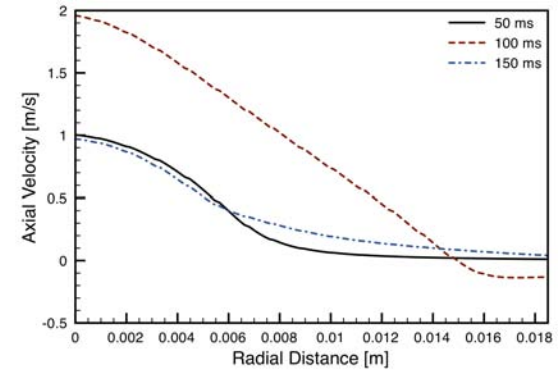
Figure 4.15: Vorticity as a function of radial location at different locations in the flame



(a) 4 mm above stagnation surface

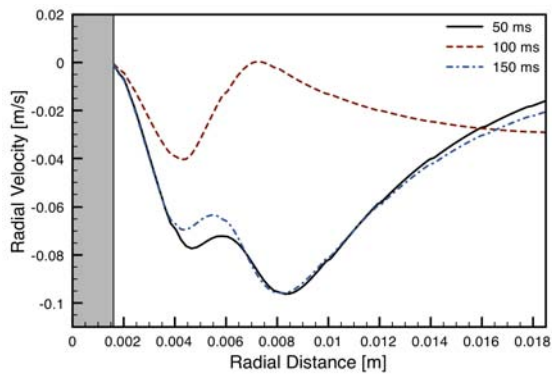


(b) 20 mm above stagnation surface

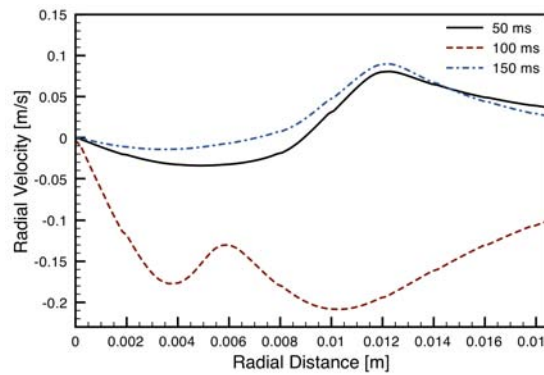


(c) 40 mm above stagnation surface

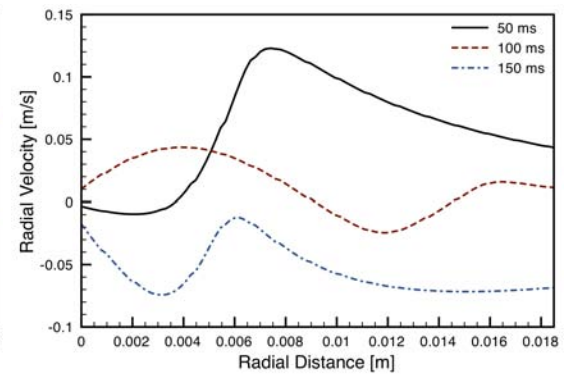
Figure 4.16: Axial velocity as a function of radial location at different locations in the flame



(a) 4 mm above stagnation surface



(b) 20 mm above stagnation surface



(c) 40 mm above stagnation surface

Figure 4.17: Radial velocity as a function of radial location at different locations in the flame

The vorticity generated at the flame front can also be estimated following the work of Uberoi et al. (1958). The analysis of Uberoi et al. (1958) can be extended to include the effect of gravity to obtain the vorticity downstream of an irrotational flow

$$u_n \omega_\theta = -\frac{1}{\rho} \frac{\partial P}{\partial s} - \frac{1}{2} \frac{\partial}{\partial s} (u_n^2 + u_t^2) + g_t \quad (4.31)$$

where u_n is the velocity normal to the flame front, u_t is the velocity tangential to the flame front, ω_θ is vorticity out of the page, s is the coordinate along the flame front, and g_t is the component of gravity tangential to the flame front. Using the momentum and mass balance across the flame front as in Uberoi et al. (1958), the vorticity inside the flame can be shown to be

$$\omega_{\theta f} = \frac{\rho_b - \rho_u}{\rho u_n} \vec{g} \cdot \vec{t} = \frac{\rho_b - \rho_u}{\rho_u S_l} g_t \approx \left(\frac{1}{\epsilon} - 1 \right) \frac{g}{S_l} \approx 200 \text{ s}^{-1} \quad (4.32)$$

This estimate is consistent with the results obtained in the simulations, which can be seen particularly clearly in Figures 4.15 and 4.13 as well as the analysis in Emmons (1958).

The velocity that is then induced by a vorticity distribution can be calculated using the Biot-Savart law (Batchelor, 2007)

$$\vec{u} = -\frac{1}{4\pi} \int \frac{\vec{s} \times \vec{\omega}(\zeta)}{s^3} dV_\zeta . \quad (4.33)$$

For a cylindrical sheet of vorticity $dV_\zeta = 2\pi r dr dz$ and along the centerline $s = \sqrt{r^2 + (z - z_0)^2}$.

If we consider a finite sheet of vorticity of length L , that only extends over the flame front δ_f for a flame or radius R ,

$$u = -\frac{1}{4\pi} \int_{-L/2}^{L/2} \int_R^{R+\delta_f} \frac{\omega_\theta \sin \theta}{s^2} 2\pi r dr dz \quad (4.34)$$

where $\sin \theta = r/s$.

$$u = -\frac{1}{4\pi} \int_{-L/2}^{L/2} \int_R^{R+\delta_f} \frac{\omega_\theta r}{s^3} 2\pi r dr dz \quad (4.35)$$

Since the flame is thin relative to the flame radius, i.e., $\delta_f \ll R$,

$$u = -\frac{1}{4\pi} \int_{-L/2}^{L/2} \int_R^{R+\delta_f} \frac{\omega_\theta r}{(R^2 + (z - z_0^2))^{3/2}} 2\pi r dr dz . \quad (4.36)$$

This allows us to integrate in r

$$u = -\frac{2\pi\omega_\theta}{4\pi} \int_{-L/2}^{L/2} \frac{1}{(R^2 + (z - z_0^2))^{3/2}} dz \int_R^{R+\delta_f} r^2 dr . \quad (4.37)$$

Once again because $\delta_f \ll R$, the second integral can be approximated as $R^2\delta_f$

$$u = -\frac{2\pi\omega_\theta R^2\delta_f}{4\pi} \int_{-L/2}^{L/2} \frac{1}{(R^2 + (z - z_0)^2)^{3/2}} dz, \quad (4.38)$$

which for $z_0 = 0$ becomes

$$u = -\frac{2\pi\omega_\theta\delta_f}{4\pi} \left[\frac{z}{(R^2 + z^2)^{1/2}} \right]_{-L/2}^{L/2} \quad (4.39)$$

$$u = -\frac{2\pi\omega_\theta\delta_f}{4\pi} \frac{L}{(R^2 + L^2/4)^{1/2}}, \quad (4.40)$$

$$u = -\omega_\theta\delta_f \frac{L}{(4R^2 + L^2)^{1/2}}, \quad (4.41)$$

For a flame of 10 mm radius and with a 40 mm height the final inflow velocity using the 200 s^{-1} vorticity is 0.18 m/s, which is about 15 - 20% of the velocity observed inside the flame (see Figure 4.16).

Therefore the main mechanism responsible for creating the inflow ultimately leading to the formation of a ‘‘puff’’ is buoyancy with a lesser contribution from flame-generated vorticity.

4.4.2 Onset of Puffing — Flow Velocity vs. Flame Velocity

The flow velocity and flame velocity can be extracted directly from the simulation. In Figures 4.18 and 4.19, both are presented as a function of the coordinate along the flame front, arclength, starting at the base of the flame at the glow plug and ending at the top of the flame. Figure 4.18 shows the evolution of the flame propagation speed at various instances in time. The flame speed is strongly influenced by the temperature and flow velocity in the hot plume above the glow plug, which increase the flame speed. As the flame propagates out of the plume, the propagation speed asymptotes to a constant value comparable to the product of the laminar burning velocity, S_L , and the expansion ratio across the flame front, ϵ , $V_f = \epsilon S_L$.

The inflow velocity is computed by taking the negative of the normal component of the flow velocity ($-\vec{u} \cdot \hat{n}$) along the flame front. Initially, the flame pushes the gases outward giving a negative inflow velocity as shown in Figure 4.19. The flow then turns inward and gains in magnitude. This increase in inflow velocity is due to the entrainment of the buoyant plume of combustion products and the continuous production of vorticity along the flame front due to the baroclinic torque.

At 50 ms, the inflow velocity exceeds the flame propagation velocity (Fig. 4.20). At this point, the flame moves back towards the centerline. This is because the flame motion is relative to the

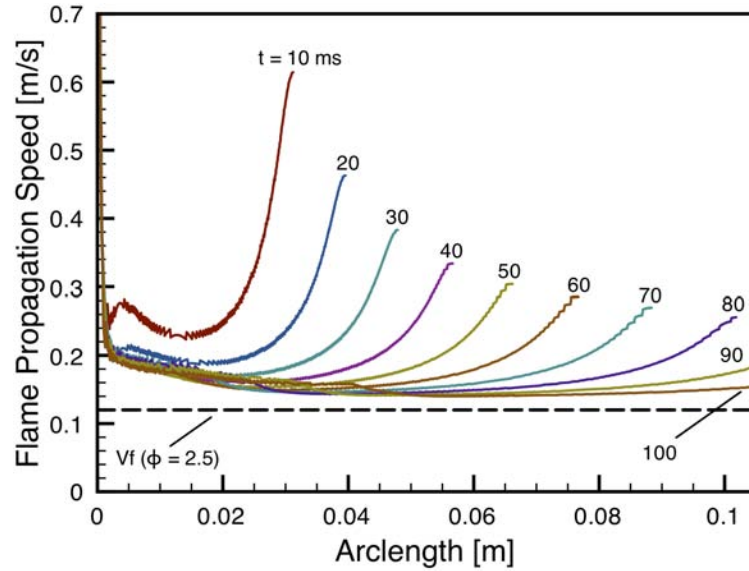


Figure 4.18: Flame propagation speed along the the flame front as a function of time

incoming flow. After this point on in the puffing cycle, the inflow velocity will be greater than the burning speed until the puffing cycle is complete. Figure 4.20 shows a direct comparison of the flame propagation and flow velocity indicating the crossover point between 40 ms and 50 ms and between 140 ms and 150 ms (100 ms later). This analysis also shows the origin of the puffing frequency at 10 Hz. The inflow must be strong enough to exceed flame propagation to generate the periodic motion. The puff is advected sufficiently fast that the subsequent puff is its own independent event where entrainment flow is gathered and not influenced by the previous cycle.

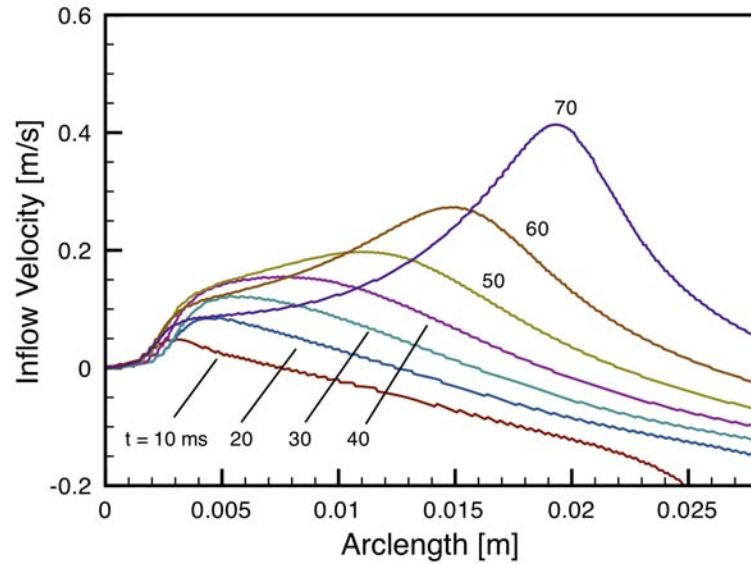


Figure 4.19: Inflow velocity along the the flame front as a function of time. Positive velocities mean flow going from unburned to burned side.

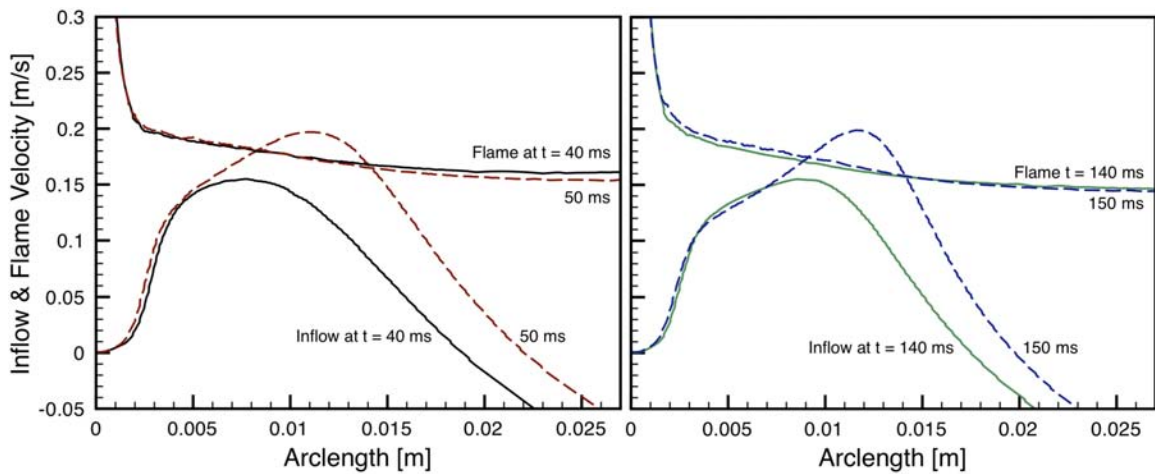


Figure 4.20: Inflow velocity and flame propagation velocity along the the flame front as a function of time showing the 10 Hz frequency observed in experiments and simulations

4.5 Conclusions

In experiments of hot surface ignition and subsequent flame propagation a ~ 10 Hz puffing flame is visible in mixtures that are stagnant and premixed prior to the ignition sequence. This discovery extends the range of observed puffing or flickering flames that were previously observed in non-premixed flame and premixed injection flames. By varying the size of the hot surface, power input, and combustion vessel volume, we determined that the periodic motion is a function of the interaction of the flame with the fluid flow induced by the combustion products rather than the initial plume established by the hot surface. Additionally, the periodic motion is neither caused by acoustic interaction with the vessel nor by a large-scale recirculation zone. The phenomenon is accurately reproduced in numerical simulations and a detailed flow field analysis revealed a competition between the inflow velocity at the base of the flame and the flame propagation speed. The inflow is caused by the entrainment flow due the buoyancy acceleration of the light combustion products and the vorticity generated at the flame front. The increasing inflow velocity, which exceeds the flame propagation speed is ultimately responsible for creating a “puff”, which is the accelerated upward, a process that is then repeated periodically until the combustion vessel is filled with products sufficiently to interrupt the process.

Chapter 5

Conclusions

In this work, thermal ignition has been investigated for homogeneously heated mixtures that expand our knowledge of auto-ignition as well as heterogeneously heated mixtures that show how hot surfaces interact with flammable mixtures as well as the subsequent flame propagation.

The auto-ignition experiment was constructed to allow for precise control of the mixture composition as well as temperature history, while simultaneously allowing for measurements of the fuel concentration in addition to temperature and pressure measurements. The experimental results showed that the rate at which the mixture is heated to the expected auto-ignition temperature played an important role. Mixtures heated sufficiently slowly can undergo a slow reaction that does not lead to a explosion event. Fast heating rates initiate an ignition event that is associated with rapid consumption of the fuel and a substantial pressure rise. The transition between these two events can be produced by varying the heating rate by as little as a factor of 2 in the experiments.

Detailed and simplified chemistry models were used to confirm these observations in the context of the classical Semenov thermal ignition theory. The detailed chemistry showed that the chemical pathways differ depending on the heating rate. During slow heating, peroxides are formed that react slowly, while in fast heating case chain branching occurs that results in rapid energy release. The simplified chemistry model was successfully used to pinpoint the effect the heating rate in transitioning a mixture evolution from a slow reaction to an ignition. While the heating rate is acknowledged as a factor in the literature, this detailed study underlines the importance of considering the heating rate in safety testing and design.

The hot surface ignition experiments highlight the increased temperature necessary to ignite flammable mixtures that are heated by an isolated hot surface. The ignition temperature shows a dependence on mixture composition and initial pressure. The ignition temperature is modeled to varying degrees of sophistication including the balance between diffusion time scale and ignition

time scale, to considering the trajectories of fluid elements and their temperature evolution along a vertical hot plate, and finally using tabulated detailed chemistry in a full fluid mechanics simulation. All models show reasonable agreement with the experiment away from the rich and lean extremes and an increasing level of applicability with increasing sophistication.

The flame propagation that follows the ignition is investigated over a range of mixture compositions leading to a range of flame propagation speeds. The measured propagation speed is consistent with numerical simulations and literature data. As the propagation speed decreases with increasing fuel concentration above slightly more than stoichiometric, the flame is more and more dominated by buoyancy effects. This competition between the flame propagation and buoyancy appears to be characterized appropriately by a Richardson number. As the Richardson number reaches unity, lifting flames and subsequent re-ignition at the glow plug is observed, and further increase in Richardson number results in puffing flames.

The puffing flame phenomenon is investigated by a detailed analysis of the flow field. The flow field is extracted from the simulation results and shows an inflow at the bottom of the flame due to buoyancy and vorticity generated at the flame front. Baroclinic torque is identified as the main source of vorticity, which is due to the misalignment of the density gradient across the flame front and the hydrostatic pressure gradient. The puffing motion is initiated because the inflow velocity exceeds the flame propagation speed. The puff is then accelerated upward leading to a decay in the inflow velocity so that the flame can again expand and the process repeats itself.

In summary the following observations were made in this study:

1. auto-ignition depends on the heating rate and can result in either a slow or fast reaction
2. A dramatic change in explosion behavior occurs with small changes in heating rate
3. Hot surface ignition temperature is insensitive to composition away from the limits
4. A new premixed combustion mode is observed for the first time: premixed puffing flames

Bibliography

- J. Adler. Ignition of a combustible stagnant gas layer by a circular hot-spot. *Combustion Theory and Modelling*, 3(2):359–369, 1999. *Cited on page: 75.*
- J. Adler and J. W. Enig. The critical conditions in thermal explosion theory with reactant consumption. *Combustion and Flame*, 8(2):97–103, 1964. *Cited on pages: 54 and 56.*
- ASTM. ASTM E659-78 (2005) Standard Test Method for Autoignition Temperature of Liquid Chemicals, 2005. *Cited on pages: xiii, 2, 4, 7, 8, 13, and 95.*
- ASTM. ASTM D56-05 (2010) Standard Test Method for Flash Point by Tag Closed Cup Tester, 2010. *Cited on pages: 2 and 8.*
- V. Babrauskas. *Ignition Handbook*. Fire Science Publishers, 2003. *Cited on pages: 3, 4, 5, 6, and 9.*
- H. C. Bailey and R. G. W. Norrish. The oxidation of hexane in the cool-flame region. *Proceedings of the Royal Society of London*, 212(1110):311–330, 1952. *Cited on page: 7.*
- S. P. M. Bane. Personal Communication, 2011. *Cited on page: 127.*
- S. P. M. Bane, J. L. Ziegler, P. A. Boettcher, S. A. Coronel, and J. E. Shepherd. Experimental investigation of spark ignition energy in kerosene, hexane, and hydrogen. *Journal of Loss Prevention in the Process Industries*, 2011. *Cited on page: 1.*
- G. K. Batchelor. *An Introduction to Fluid Dynamics*. Cambridge University Press, 2007. *Cited on page: 138.*
- M. J. Bennett. Ignition of combustible fluids by heated surfaces. *Process safety progress*, 20(1):29–36, 2001. *Cited on page: 10.*
- G. Blanquart. Personal Communication, 2011. *Cited on pages: 105, 106, and 191.*

- G. Blanquart, P. Pepiot-Desjardins, and H. Pitsch. Chemical mechanism for high temperature combustion of engine relevant fuels with emphasis on soot precursors. *Combustion and Flame*, 156(3):588–607, 2009. *Cited on pages: 90 and 103.*
- P. A. Boettcher, R. Mével, V. Thomas, and J. E. Shepherd. The effect of heating rates on low temperature hexane air combustion. *Fuel*, 2011. *Cited on page: 201.*
- P. N. Brown, G. D. Byrne, and A. C. Hindmarsh. Vode, a variable-coefficient ode solver. *The SIAM Journal on Scientific and Statistical Computing*, 10:1038–1051, 1989. *Cited on page: 23.*
- J. Buckmaster and N. Peters. The infinite candle and its stability—a paradigm for flickering diffusion flames. In *Symposium (International) on Combustion*, volume 21, pages 1829–1836. Elsevier, 1988. *Cited on pages: 11 and 115.*
- A. Burcat, E. Olchanski, and C. Sokolinski. Kinetics of hexane combustion in a shock tube. *Israel Journal of Chemistry*, 36:313–320, 1996. *Cited on pages: 23, 24, 25, and 43.*
- L. R. Cairnie and A. J. Harrison. Natural convection adjacent to a vertical isothermal hot plate with a high surface-to-ambient temperature difference. *International Journal of Heat and Mass Transfer*, 25(7):925–934, 1982. *Cited on pages: xvi, 81, 88, and 90.*
- B. M. Cetegen and T. A. Ahmed. Experiments on the periodic instability of buoyant plumes and pool fires. *Combustion and Flame*, 93(1–2):157–184, 1993. *Cited on pages: x, 11, 115, 121, 122, 123, 125, and 126.*
- D. S. Chamberlin and A. Rose. The flicker of luminous flames. *Proceedings of the Symposium on Combustion*, 1:27–32, 1948. *Cited on pages: 10 and 115.*
- R. K. Cheng, B. Bédat, and L. W. Kostiuk. Effects of buoyancy on lean premixed V-flames Part I: laminar and turbulent flame structures. *Combustion and flame*, 116(3):360–375, 1999. *Cited on pages: 11 and 115.*
- J. D. Colwell and A. Reza. Hot Surface Ignition of Automotive and Aviation Fluids. *Fire Technology*, 41:105–123, 2005. *Cited on pages: 2, 7, 10, and 13.*
- H. F. Coward and P. G. Guest. Ignition of natural gas-air mixtures by heated metal bars 1. *Journal of the American Chemical Society*, 49(10):2479–2486, 1927. *Cited on pages: 3 and 8.*
- Coordinating Research Council CRC. *Handbook of Aviation Fuel Properties—CRC Report No. 530*. Society of Automotive Engineers, Warrendale, PA, 1983. *Cited on pages: xxvi, 2, 7, and 13.*

- H. J. Curran, P. Gaffuri, W. J. Pitz, C. K. Westbrook, and W. R. Leppard. Autoignition chemistry of the hexane isomers: an experimental and kinetic modelling study. In *SAE International Fuels and Lubricants Meeting and Exposition*, 1995. *Cited on page: 23.*
- H. J. Curran, P. Gaffuri, W. J. Pitz, and C. K. Westbrook. A comprehensive modeling study of n-heptane oxidation. *Combustion and flame*, 114(1-2):149-177, 1998. *Cited on pages: xvi, 84, 85, and 93.*
- P. Dagaut, M. Reuillon, and M. Cathonnet. Experimental study of the oxidation of n-heptane in a jet stirred reactor from low to high temperature and pressures up to 40 atm. *Combustion and Flame*, 101:132-140, 1995. *Cited on pages: 24 and 25.*
- S. G. Davis and C. K. Law. Laminar flame speeds and oxidation kinetics of iso-octane-air and n-heptane-air flames. *Twenty-Seventh Symposium (International) on Combustion*, 27(1):521-527, 1998a. *Cited on pages: 90 and 103.*
- S. G. Davis and C. K. Law. Determination of and fuel structure effects on laminar flame speeds of C1 to C8 hydrocarbons. *Combustion Science and Technology*, 140(1-6):427-449, 1998b. *Cited on pages: 103, 104, 105, 106, 191, 192, 194, and 195.*
- H. Davy. Some new experiments and observations on the combustion of gaseous mixtures, with an account of a method of preserving a continued light in mixtures of inflammable gases and air without flame. *Philosophical Transactions of the Royal Society of London*, 107:77-85, 1817. *Cited on page: 3.*
- O. Desjardins, G. Blanquart, G. Balarac, and H. Pitsch. High order conservative finite difference scheme for variable density low mach number turbulent flows. *Journal of Computational Physics*, 227(15):7125-7159, 2008. *Cited on pages: 91 and 102.*
- J. A. Drallmeier. Hydrocarbon absorption coefficients at the 3.39- μm He-Ne laser transition. *Applied Optics*, 42(6):979-982, 2003. *Cited on pages: 14, 15, and 165.*
- D. F. G. Durao and J. H. Whitelaw. Instantaneous velocity and temperature measurements in oscillating diffusion flames. *Proceedings of the Royal Society of London. A. Mathematical and Physical Sciences*, 338(1615):479, 1974. *Cited on pages: 11 and 115.*
- D. Durox, F. Baillet, P. Scouffaire, and R. Prud'Homme. Some effects of gravity on the behaviour of premixed flames. *Combustion and Flame*, 82(1):66-74, 1990. *Cited on pages: 11 and 115.*

- D. Durox, T. Yuan, and E. Villermaux. The effect of buoyancy on flickering in diffusion flames. *Combustion Science and Technology*, 124(1–6):277–294, 1996. *Cited on pages: x, 11, 123, and 124.*
- H. W. Emmons. *Fundamentals of Gas Dynamics*, volume 3. Princeton University Press Princeton, 1958. Section G - Gas Dynamics of Combustion and Detonations. Chapter 2 - Flow Discontinuities Associated with Combustion. *Cited on page: 138.*
- D. A. Frank-Kamenetskii. *Diffusion and heat transmission in chemical kinetics*. Plenum, New York, 1969. *Cited on pages: 46, 47, 178, and 187.*
- A. G. Gaydon and H. G. Wolfhard. *Flames*. Chapman and Hall, 4th edition, 1979. *Cited on pages: 105 and 125.*
- B. Gebhart, Y. Jaluria, R.L. Mahajan, and B. Sammakia. *Buoyancy-induced flows and transport*. Hemisphere Publishing, New York, NY, 1988. *Cited on pages: 81, 82, and 85.*
- I. Glassman. *Combustion*. Academic Press, San Diego, 4th edition, 2008. *Cited on pages: 5, 6, 43, 46, 48, 50, 75, 99, and 108.*
- D. G. Goodwin. An open-source, extensible software suite for chemical vapor deposition process simulation. *Chemical Vapor Deposition XVI and EUROCVVD*, 14:2003–08, 2003. *Cited on pages: 23, 43, 69, and 70.*
- S. Gordon and B. J. McBride. Computer program for calculation of complex chemical equilibrium compositions and applications. Technical report, National Aeronautics and Space Administration, Office of Management, Scientific and Technical Information Program, 1994. *Cited on page: 201.*
- L. Graftieaux, M. Michard, and N. Grosjean. Combining piv, pod and vortex identification algorithms for the study of unsteady turbulent swirling flows. *Measurement Science and technology*, 12:1422, 2001. *Cited on page: 132.*
- A. J. Grant and J. M. Jones. Low-frequency diffusion flame oscillations. *Combustion and Flame*, 25:153–160, 1975. *Cited on pages: 11 and 115.*
- B. F. Gray. The dependence of spontaneous ignition temperature on surface to volume ratio in static systems for fuels showing a negative temperature coefficient. *Combustion and Flame*, 14(1):113–115, 1970. *Cited on page: 8.*

- J. F. Griffiths, P. A. Halford-Maw, and D. J. Rose. Fundamental Features of Hydrocarbon Autoignition in a Rapid Compression Machine. *Combustion and Flame*, 95(3):291–306, 1993. *Cited on page: 7.*
- Y. T. Guahk, D. K. Lee, K. C. Oh, and H. D. Shin. Flame-intrinsic kelvin-helmholtz instability of flickering premixed flames. *Energy & Fuels*, 23(8):3875–3884, 2009. *Cited on pages: 11, 12, and 115.*
- T. J. Held, A. J. Marchese, and F. L. Dryer. A semi-empirical reaction mechanism for n-heptane oxidation and pyrolysis. *Combustion Science and Technology*, 123:107–146, 1997. *Cited on pages: 24 and 25.*
- C. E. Hermance. Implications concerning general ignition processes from the analysis of homogeneous, thermal explosions. *Combustion Science and Technology*, 10(5):261–265, 1975. *Cited on pages: 55 and 56.*
- K. M. Hinckley and A. J. Dean. Time resolved measurements of fuelair stoichiometry in pulse detonation engines using a non-intrusive laser sensor. *43rd AIAA Aerospace Sciences Meeting and Exhibition paper number AIAA 2005-0628*, 2005. *Cited on page: 165.*
- Y. Huang, C. J. Sung, and J. A. Eng. Laminar flame speeds of primary reference fuels and reformer gas mixtures. *Combustion and Flame*, 139(3):239–251, 2004. *Cited on pages: 103, 105, and 106.*
- D. N. Jaynes and B. H. Beam. Hydrocarbon gas absorption by a He-Ne laser beam at a 3.39 μm wavelength. *Applied Optics*, 8(8):1741–1742, 1969. *Cited on pages: 15 and 165.*
- C. Ji, E. Dames, Y. L. Wang, H. Wang, and F. N. Egolfopoulos. Propagation and extinction of premixed C_5 – C_{12} n-alkane flames. *Combustion and Flame*, 157(2):277–287, 2010. *Cited on pages: 99, 103, 105, 106, 193, and 195.*
- K. Kadoya, N. Matsunaga, and A. Nagashima. *Viscosity and thermal conductivity of dry air in the gaseous phase*. American Chemical Society and the American Institute of Physics for the National Bureau of Standards, 1985. *Cited on page: 85.*
- G. P. Kane, E. A. C. Chamberlain, and D. T. A. Townend. The Spontaneous Ignition under Pressure of the Simpler Aliphatic Hydrocarbons, Alcohols, and Aldehydes. *Journal of Chemical Society*, pages 436–443, 1937. *Cited on pages: xiv, 35, and 36.*
- M. Kaviany. *Principles of heat transfer*. Wiley, New York, NY, 2002. *Cited on pages: 80 and 82.*

- R. J. Kee, M. E. Coltrin, and P. Glarborg. *Chemically reacting flow: theory and practice*. John Wiley and Sons, 2003. *Cited on page: 79.*
- A. P. Kelley, A. J. Smallbone, D. L. Zhu, and C. K. Law. Laminar flame speeds of C5 to C8 n-alkanes at elevated pressures: Experimental determination, fuel similarity, and stretch sensitivity. *Proceedings of the Combustion Institute*, 33:963–970, 2011. *Cited on pages: 23, 99, 103, 105, 106, 125, 191, 193, and 195.*
- I. Kimura. Stability of Laminar Jet Flames. *Tenth Symposium (International) on Combustion*, pages 1295–1300, 1965. *Cited on pages: 11 and 115.*
- A. E. Klingbeil, J. B. Jeffries, and R. K. Hanson. Temperature- and pressure-dependent absorption cross sections of gaseous hydrocarbons at $3.39\ \mu\text{m}$. *Measurements Science and Technology*, 17: 1950–1957, 2006. *Cited on pages: 14, 15, and 165.*
- L. W. Kostiuk and R. K. Cheng. The coupling of conical wrinkled laminar flames with gravity. *Combustion and flame*, 103(1–2):27–40, 1995. *Cited on page: 115.*
- M. Kroll, J. A. McClintock, and O. Ollinger. Measurement of gaseous oxygen using diode laser spectroscopy. *Applied Physics Letters*, 51:1465–1467, 1987. *Cited on page: 19.*
- J. M. Kuchta. Investigation of Fire and Explosion Accidents in the Chemical, Mining, and Fuel-Related Industries. Bulletin 680, Bureau of Mines, 1985. *Cited on pages: xxvi, 7, and 13.*
- J. M. Kuchta, A. Bartkowiak, and M. G. Zabetakis. Hot surface ignition temperatures of hydrocarbon fuel vapor-air mixtures. *Journal of Chemical and Engineering Data*, 10(3):282–288, 1965. *Cited on pages: xiii, 3, 5, 8, 9, 13, 75, 94, 95, 96, 185, 187, and 188.*
- K. Kumar, J. E. Freeh, C. J. Sung, and Y. Huang. Laminar flame speeds of preheated iso-octane/O₂/N₂ and n-heptane/O₂/N₂ mixtures. *Journal of propulsion and power*, 23(2):428–436, 2007. *Cited on pages: 103, 105, and 106.*
- R. K. Kumar. Ignition of hydrogen-oxygen-diluent mixtures adjacent to a hot, nonreactive surface. *Combustion and flame*, 75(2):197–215, 1989. *Cited on pages: 9 and 75.*
- N. M. Laurendeau. Thermal ignition of methane-air mixtures by hot surfaces: A critical examination. *Combustion and Flame*, 46:29–49, 1982. *Cited on pages: 8, 9, 75, 76, 78, 94, and 186.*
- C. K. Law. *Combustion physics*. Cambridge University Press, 2006. *Cited on pages: xv, 48, 50, 51, and 181.*

- C. K. Law and H. K. Law. Thermal-ignition analysis in boundary-layer flows. *Journal of Fluid Mechanics*, 92(01):97–108, 1979. *Cited on pages: 78 and 87.*
- B. Lewis. *Selected Combustion Problems*, page 177. Butterworths Scientific Publications, 1954. *Cited on page: 125.*
- X. D. Liu, S. Osher, and T. Chan. Weighted essentially non-oscillatory schemes. *Journal of Computational Physics*, 115(1):200–212, 1994. *Cited on page: 91.*
- J. Luque and D. R. Crosley. Lifbase: Database and spectral simulation (version 2.0. 60, 2008). Technical report, Tech. rep., SRI International, 1999. *Cited on page: 119.*
- W. Mason and R. V. Wheeler. CCXLIX—The ignition of gases. Part II. Ignition by a heated surface. Mixtures of methane and air. *J. Chem. Soc., Trans.*, 121:2079–2091, 1922. *Cited on page: 7.*
- MATLAB. *version 7.9.0.529 (R2009b)*. The MathWorks Inc., Natick, Massachusetts, 2010. *Cited on page: 203.*
- S. K. Menon. Personal Communication, 2011. *Cited on page: 121.*
- R. Mével, F. Lafosse, N. Chaumeix, G. Dupré, and C.-E. Paillard. Spherical expanding flames in H₂-N₂O-Ar mixtures: flame speed measurements and kinetic modeling. *International Journal of Hydrogen Energy*, 34:9007–9018, 2009. *Cited on page: 101.*
- R. Mével, P. A. Boettcher, and J. E. Shepherd. Absorption Cross Section at 3.39 μm of Alkanes, Aromatics and Substituted Hydrocarbons. *Chem Phys Lett*, submitted for publication, 2012. *Cited on pages: 15 and 165.*
- K. Narayanaswamy, G. Blanquart, and H. Pitsch. A consistent chemical mechanism for oxidation of substituted aromatic species. *Combustion and Flame*, 157(10):1879–1898, 2010. *Cited on pages: 90 and 103.*
- NFPA 325. *Guide to Fire Hazard Properties of Flammable Liquids, Gases, and Volatile Solids*. National Fire Protection Association, Quincy, MA, 1994. *Cited on page: 2.*
- NTSB. In-flight Breakup Over The Atlantic Ocean, Trans World Airlines Flight 800, Boeing 747-131, N93119, Near East Moriches, New York, July 17, 1996. Technical report, National Transportation Safety Board, Washington, DC, 2000. *Cited on page: 1.*

- S. Ono, H. Kawano, H. Niho, and G. Fukuyama. Ignition in a Free Convection from Vertical hot Plate. *Bulletin of the JSME-Japan Society of Mechanical Engineers*, 19(132):676–683, 1976. *Cited on page: 8.*
- M. Parang and M. C. Jischke. Adiabatic ignition of homogeneous systems. *AIAA Journal*, 13: 405–408, 1975. *Cited on pages: 55 and 56.*
- M. Y. Perrin and J. M. Hartmann. High-Temperature Absorption of the 3.39 μm He-Ne Laser Line by Methane. *Journal of Quantitative Spectroscopy & Radiative Transfer*, 42(6):459–464, 1989. *Cited on page: 165.*
- L. C. Philippe and R. K. Hanson. Laser diode wavelength-modulation spectroscopy for simultaneous measurement of temperature, pressure, and velocity in shock-heated oxygen flows. *Applied Optics*, 32:6090–6103, 1993. *Cited on page: 19.*
- M. J. Pilling, editor. *Comprehensive Chemical Kinetics*, chapter 6 by J. F. Griffiths and C. Mohamed — Experimental and Numerical Studies of Oxidation Chemistry and Spontaneous Ignition Phenomena, pages 545–650. Elsevier, 1997. *Cited on pages: 5, 7, and 13.*
- H. Pitsch and M. Bollig. Flamemaster, a computer code for homogeneous and one-dimensional laminar flame calculations. *Institut für Technische Mechanik, RWTH Aachen*, 1994. *Cited on pages: 84, 103, and 191.*
- M. I. Radulescu and B. M. Maxwell. Critical ignition in rapidly expanding self-similar flows. *Physics of Fluids*, 22:066101, 2010. *Cited on page: 54.*
- H. P. Ramirez, K. Hadj-Ali, P. Dievart, G. Dayma, C. Togbe, G. Moreac, and P. Dagaut. Oxidation of commercial and surrogate bio-diesel fuels (B30) in a jet-stirred reactor at elevated pressure: Experimental and modeling kinetic study. *Proceedings of the Combustion Institute*, 33:375–382, 2011. *Cited on pages: xxvi, 23, 104, 194, 196, and 201.*
- J. Reid and D. Labrie. Second Harmonic Detection with Tunable Diode Lasers Comparison of Experiment and Theory. *Applied Physics*, 26:203–210, 1981. *Cited on page: 167.*
- R. C. Reid, J. M. Prausnitz, and B. E. Poling. *The properties of gases and liquids*. McGraw Hill Book Co., New York, NY, 3rd edition, 1977. *Cited on page: 68.*

- M. Ribaucour, R. Minetti, M. Carlier, and L. R. Sochet. Autoignition at High-Pressure — Design, Construction and Test of a Rapid Compression Machine. *Journal de Chimie Physique et de Physico-Chimie Biologique*, 89(11–12):2127–2152, 1992. *Cited on page: 7.*
- G. B. Rieker. Personal Communication, 2009. *Cited on page: 171.*
- G. B. Rieker, J. B. Jeffries, and R. K. Hanson. Calibration-free wavelength-modulation spectroscopy for measurements of gas temperature and concentration in harsh environments. *Applied Optics*, 48(29):5546–5560, 2009. *Cited on pages: 19, 171, and 172.*
- L. S. Rothman, D. Jacquemart, A. Barbe, D. C. Benner, M. Birk, L. R. Brown, M. R. Carleer, C. Chackerian, K. Chance, L. H. Coudert, V. Dana, V. M. Devi, J. M. Flaud, R. R. Gamache, A. Goldman, J. M. Hartmann, K. W. Jucks, A. G. Maki, J. Y. Mandin, S. T. Massie, J. Orphal, A. Perrin, C. P. Rinsland, M. A. H. Smith, J. Tennyson, R. N. Tolchenov, R. A. Toth, J. Vander Auwera, P. Varanasi, and G. Wagner. The HITRAN 2004 molecular spectroscopic database. *Journal of Quantitative Spectroscopy & Radiative Transfer*, 96(2):139–204, 2005. *Cited on page: 165.*
- G. S. Scott, G. W. Jones, and F. E. Scott. Determination of Ignition Temperatures of Combustible Liquids and Gases. *Analytical Chemistry*, 20(3):238–241, 1948. *Cited on page: 3.*
- N. N. Semenov. Thermal theory of combustion and explosion. *Progress of Physical Science*, 23, 1940. English Version: Technical Memorandums - National Committee for Aeronautics No.-1024 (NACA 1024). *Cited on pages: 4, 13, 21, 42, 46, 50, 75, 78, 94, 181, 185, 186, 187, and 188.*
- G. S. Settles. *Schlieren and shadowgraph techniques: visualizing phenomena in transparent media*. Springer Verlag, 2001. *Cited on page: 64.*
- S. W. Sharpe, T. J. Johnson, R. L. Sams, P. M. Chu, G. C. Rhoderick, and P. A. Johnson. Gas-phase databases for quantitative infrared spectroscopy. *Applied Spectroscopy*, 58(12):1452–1461, DEC 2004. ISSN 0003-7028. *Cited on page: 165.*
- H. P. S. Shen, J. Steinberg, J. Vanderover, and M. A. Oehlschlaeger. A shock tube study of the ignition of n-heptane, n-decane, n-dodecane, and n-tetradecane at elevated pressures. *Energy & Fuels*, 23(5):2482–2489, 2009. *Cited on pages: 84, 90, and 103.*
- I. G. Shepherd, R. K. Cheng, and M. S. Day. The dynamics of flame flicker in conical premixed flames: An experimental and numerical study. Technical report, Lawrence Berkeley National Laboratory Report LBNL-59249, 2005. *Cited on pages: 11, 12, and 115.*

- J. E. Shepherd. Personal Communication, 2012. *Cited on page: 9.*
- J. E. Shepherd and A. C. Ratzel. Heat transfer resulting from premixed combustion. *Heat Transfer in Fire and Combustion Systems, ASME HTD-45*, pages 191–201, 1985. *Cited on page: 69.*
- J. E. Shepherd, C. J. Krok, and J. J. Lee. Spark Ignition Energy Measurements in Jet A. Technical report, Graduate Aeronautical Laboratories at the California Institute of Technology, Pasadena, CA, 1997. *Cited on page: 1.*
- J. E. Shepherd, C. D. Nuyt, and J. J. Lee. Flash Point and Chemical Composition of Aviation Kerosene (Jet A). Technical report, Graduate Aeronautical Laboratories at the California Institute of Technology, Pasadena, CA, 1999. *Cited on pages: 1 and 7.*
- J. E. Shepherd, S. Browne, and J. Ziegler. Numerical Solution Methods for Shock and Detonation Jump Conditions. Technical report, Aeronautical and Mechanical Engineering California Institute of Technology, Pasadena, CA, 2006. *Cited on page: 201.*
- J. Simmie. Detailed chemical kinetic models for the combustion of hydrocarbon fuels. *Progress in Energy and Combustion Science*, 29:599–634, 2003. *Cited on page: 23.*
- K. C. Smyth and N. P. Bryner. Short-duration autoignition temperature measurements for hydrocarbon fuels near heated metal surfaces. *Combustion Science and Technology*, 126(1–6):225–253, 1997. *Cited on pages: 8, 9, 95, and 96.*
- K. Stephan and A. Laesecke. *The thermal conductivity of fluid air*. American Chemical Society and the American Institute of Physics for the National Bureau of Standards, 1985. *Cited on page: 85.*
- K. Stewartson. *The theory of laminar boundary layers in compressible fluids*. Oxford University Press, 1964. *Cited on page: 81.*
- A. Strawa and B. Cantwell. Investigation of an excited jet diffusion flame at elevated pressure. *Journal of Fluid Mechanics*, 200:309–336, 1989. *Cited on pages: 11 and 115.*
- K. Tanoue, Y. Ogura, M. Takayanagi, and T. Nishimura. Measurement of temperature distribution for the flickering phenomenon around the premixed flame by using laser speckle method. *Journal of visualization*, 13(3):183–185, 2010. *Cited on pages: 11, 12, and 115.*
- Teledyne Judson Technologies. J14 Series Lead Selenide Detectors Product Bulletin, Oct 2000. URL http://www.teledynejudson.com/files/pdf/selenide_PB3326.pdf. *Cited on page: 162.*

- W. M. Thornton. LX. The ignition of gases by hot wires. *Philosophical Magazine Series 6*, 38(227): 613–633, 1919. *Cited on page: 3.*
- E. Tomita, N. Kawahara, M. Shigenaga, A. Nishiyama, and R. W. Dibble. In situ measurement of hydrocarbon fuel concentration near a spark plug in an engine cylinder using the 3.392 μm infrared laser absorption method: discussion of applicability with a homogeneous methane/air mixture. *Measurement Science and Technology*, 14(8):1350, 2003. *Cited on page: 165.*
- T. Toong, R. F. Salant, J. M. Stopford, and G. Y. Anderson. Mechanisms of combustion instability. *Tenth Symposium (International) on Combustion*, pages 1301–1313, 1965. *Cited on pages: 11 and 115.*
- D. T. A. Townend, L. L. Cohen, and M. R. Mandlekar. The influence of pressure on the spontaneous ignition of inflammable gas-air mixtures. iii. hexane-and isobutane-air mixtures. *Proceedings of the Royal Society of London. Series A*, 146(856):113–129, 1934. *Cited on pages: xiii and 6.*
- D. J. Tritton. *Physical Fluid Dynamics*. Oxford University Press, New York, 1988. *Cited on pages: 8 and 197.*
- T. Tsuboi, K. Inomata, Y. Tsunoda, A. Isobe, and K. Nagaya. Light-absorption by hydrocarbon molecules at 3.392 μm of He-Ne Laser. *Japanese Journal of Applied Physics Part 1 - Regular Papers Short Notes & Review Papers*, 24(1):8–13, 1985. *Cited on pages: 15 and 165.*
- M. S. Uberoi, A. M. Kuethe, and H. R. Menkes. Flow field of a bunsen flame. *Physics of Fluids*, 1(2):150–158, 1958. *Cited on page: 138.*
- J. P. J. Van Lipzig, E. J. K. Nilsson, L. P. H. De Goey, and A. A. Konnov. Laminar burning velocities of n-heptane, iso-octane, ethanol and their binary and tertiary mixtures. *Fuel*, 2011. *Cited on pages: 103, 105, and 106.*
- G. Vanhove, G. Petit, and R. Minetti. Experimental study of the kinetic interactions in the low-temperature autoignition of hydrocarbon binary mixtures and a surrogate fuel. *Combustion and Flame*, 145(3):521–532, 2006. *Cited on page: 7.*
- W. G. Vincenti and C. H. Kruger. *Introduction to physical gas dynamics*. Krieger Publishing Company, 1967. *Cited on page: 183.*
- H. Wang, E. Dames, B. Sirjean, D. A. Sheen, R. Tangko, A. Violi, J. Y. W. Lai, F. N. Egolfopoulos, D. F. Davidson, R. K. Hanson, C. T. Bowman, C. K. Law, W. Tsang, N. P. Cernansky, D. L.

- Miller, and R. P. Lindstedt. A high-temperature chemical kinetic model of n-alkane (up to n-dodecane), cyclohexane, and methyl-, ethyl-, n-propyl and n-butyl-cyclohexane oxidation at high temperatures, JetSurF version 2.0, September 19, 2010., 2010. URL (<http://melchior.usc.edu/JetSurF/JetSurF2.0>). *Cited on page: 192.*
- J. Warnatz, U. Maas, and R.W. Dibble. *Combustion: Physical and Chemical Fundamentals, Modeling and Simulation, Experiments, Pollutant Formation*. Springer Verlag, 2006. *Cited on page: 6.*
- C. K. Westbrook and F. L. Dryer. Chemical Kinetics Modeling of Hydrocarbon Combustion. *Progress in Energy and Combustion Science*, 10(1):1–57, 1984. *Cited on page: 43.*
- C. K. Westbrook, W. J. Pitz, O. Herbinet, H. J. Curran, and E. J. Silke. A comprehensive detailed chemical kinetic reaction mechanism for combustion of n-alkane hydrocarbons from n-octane to n-hexadecane. *Combustion and Flame*, 156(1):181–199, 2009. *Cited on pages: 84, 90, and 103.*
- F. M. White. *Heat Transfer*. Addison-Wesley, Boston, MA, 1984. *Cited on page: 26.*
- R. G. White. Spontaneous ignition of kerosene/AVTUR/vapour — the effect of the ratio, vessel surface area to volume (effect of vessel surface area on minimum spontaneous ignition temperature of kerosene). Technical report, Royal Aircraft Establishment 67107, 1967. *Cited on page: 8.*
- R. D. Wilk, N. P. Cernansky, and R. S. Cohen. The Oxidation of Propane at Low and Transition Temperatures. *Comb. Sci. and Tech*, 49:41–78, 1986. *Cited on page: 7.*
- C. H. Yang and B. F. Gray. Slow oxidation of hydrocarbons and cool flames. *The Journal of Physical Chemistry*, 73(10):3395–3406, 1969. *Cited on page: 6.*
- S. Yoshiyama, Y. Hamamoto, E. Tomita, and K. Minami. Measurement of hydrocarbon fuel concentration by means of infrared absorption technique with 3.39 μm He-Ne laser. *JSAE Rev.*, 17: 339–345, 1996. *Cited on page: 165.*
- M. G. Zabetakis. Flammability characteristics of combustible gases and vapors. Technical report, Bureau of Mines, 1965. Bulletin 627. *Cited on pages: 68, 74, and 127.*
- M. G. Zabetakis, A. L. Furno, and G. W. Jones. Minimum spontaneous ignition temperatures of combustibles in air. *Industrial & Engineering Chemistry*, 46(10):2173–2178, 1954. *Cited on page: 3.*

- V. P. Zhukov, V. A. Sechenov, and A. Yu. Starikovskii. Ignition delay times in lean n-hexane-air mixture at high pressures. *Combustion and Flame*, 136:257–259, 2004. *Cited on pages: 23, 24, and 25.*
- E. E. Zukoski. Fluid dynamic aspects of room fires. In *Proc. of First International Symp. Fire Safety Science*, 1986. *Cited on pages: 11 and 115.*

This page intentionally left blank.

Appendix A

Absorption Measurements for Hydrocarbon Fuel

This appendix gives the details of the technique used to measure the direct absorption of laser light at $3.39 \mu\text{m}$ by the C-H bond present in hydrocarbon fuels.

A.1 Direct Absorption Measurements

When a beam of collimated light of a specific wavelength, e.g. from a laser, passes through an absorbing medium, the molecules may absorb photons at that wavelength. Consequently, if the intensity of photons is measured before and after the medium, the change is proportional to the initial intensity of light, I_0 , the path length, dx , and the absorption coefficient of the absorbing species, $\alpha(\nu)$:

$$I + dI = I - \alpha(\nu)I dx \quad (\text{A.1})$$

$$\frac{dI}{I} = -\alpha(\nu) dx . \quad (\text{A.2})$$

Integrating over the entire absorption path gives:

$$I = I_0 \exp[-\alpha(\nu)(x - x_0)] \quad (\text{A.3})$$

The absorption coefficient $\alpha(\nu)$ is equal to the product of the molar density n and the absorption cross section σ_ν :

$$\alpha(\nu) = \sigma_\nu n . \quad (\text{A.4})$$

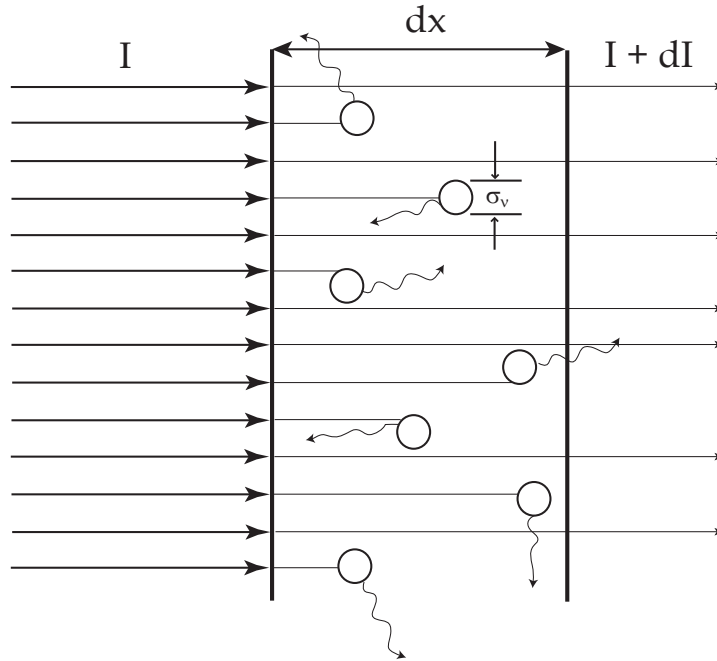


Figure A.1: Beer's law diagram

Assuming the perfect gas law:

$$P = n\tilde{R}T \quad (\text{A.5})$$

$$\alpha(\nu) = \sigma_\nu \frac{P}{\tilde{R}T} . \quad (\text{A.6})$$

Let $L = (x - x_0)$ be the distance the laser light travels through the absorbing medium, giving the following form for Beer's law:

$$\frac{I}{I_0} = \exp\left(-\frac{\sigma_\nu PL}{\tilde{R}T}\right) . \quad (\text{A.7})$$

In order to monitor the power variations of the laser over time the beam is split before it enters the test cell

$$I = I_1 + I_2$$

where I_1 is the reference beam and I_2 passes through the test cell as shown in Figure A.2. Now the necessary expressions can be written for the calibration of the absorption cross section, σ_ν , and calculating the partial pressure of fuel, P_{fuel} , where I_1^0 and I_2^0 are measurements taken when the

cell is evacuated

$$\sigma_\nu = \frac{\tilde{R}T}{P_{fuel}L} \left[\ln \left(\frac{I_1(t)}{I_2(t)} \right) - \ln \left(\frac{I_1^0}{I_2^0} \right) \right] \quad (\text{A.8})$$

$$P_{fuel} = \frac{\tilde{R}T}{\sigma_\nu L} \left[\ln \left(\frac{I_1(t)}{I_2(t)} \right) - \ln \left(\frac{I_1^0}{I_2^0} \right) \right] . \quad (\text{A.9})$$

Using the equations above, we can first estimate to what accuracy the absorption cross section can be measured and then predict the accuracy of the pressure measurement using this technique. The propagation of uncertainties for the absorption cross section is given by the following equation

$$\frac{d\sigma_\nu}{\sigma_\nu} = \frac{dT}{T} + \frac{dP}{P} + \frac{dL}{L} + \frac{d\Upsilon}{\Upsilon} , \quad (\text{A.10})$$

where

$$\Upsilon = \left[\ln \left(\frac{I_1(t)}{I_2(t)} \right) - \ln \left(\frac{I_1^0}{I_2^0} \right) \right] . \quad (\text{A.11})$$

Summing all the uncertainties given in Table A.1 results in a total uncertainty of 2.7%, given the absorption cross section of $38 \pm 1 \text{ m}^2/\text{kmol}$. Using the same scheme we can compute the uncertainty in the fuel pressure, which is 5.2% of the measured value.

Table A.1: Uncertainty in fuel concentration measurements

	(x)	d(x)	units
T	295	1	K
P	10	.01	kPa
L	90	2	mm
Υ	0.373	3.45E-04	-

In this work a $3.39 \mu\text{m}$ wavelength HeNe laser is used to provide the collimated laser light (ThorLabs: [H339P2](#)) and passed through an optical chopper (Stanford Research System: [SRS 540](#)) running at 300 Hz allowing the detectors to relax and avoid saturation. The detectors used in this setup were two PbSe detectors manufactured by Judson Technology (Part Number: PE-0-53) that can be used at room temperature without cooling, and are sensitive in the infrared spectrum as shown in Figure A.3. The detector output was amplified using the circuit shown in Figure A.4

The wavelength of the absorption band is at $3.39 \mu\text{m}$ so that the test cell windows must transmit at this frequency. Sapphire was chosen as the window material, which transmits for wavelengths as long as $5 \mu\text{m}$. The windows were connected to the Pyrex body of the vessel via Schott specialty glass and iridium glass (manufactured by M&M Glassblowing in Nashua, NH and the Caltech Glass

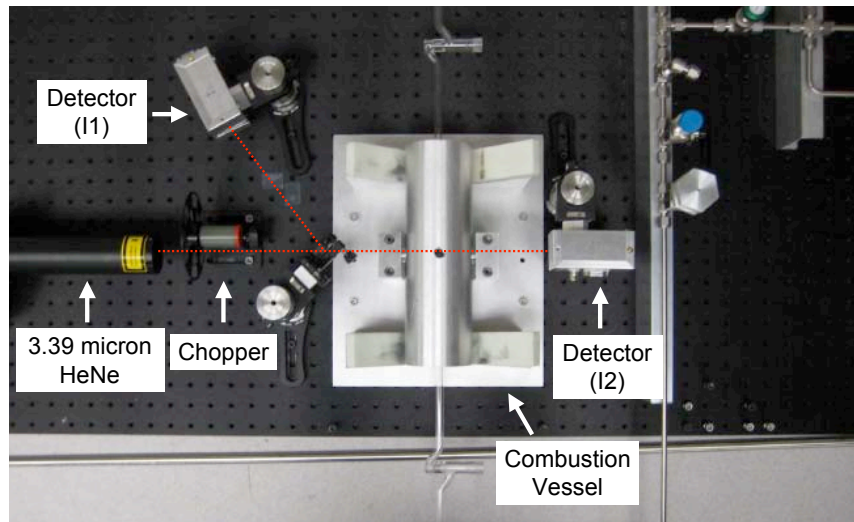


Figure A.2: Fuel detection experimental setup

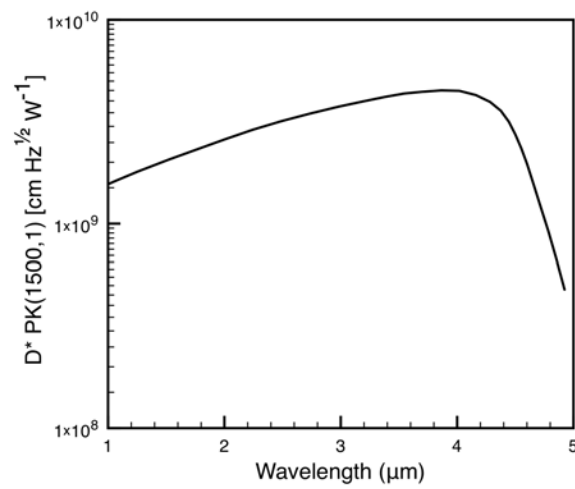


Figure A.3: Judson PE-0-53 detector sensitivity as function of wavelength (Teledyne Judson Technologies, 2000)

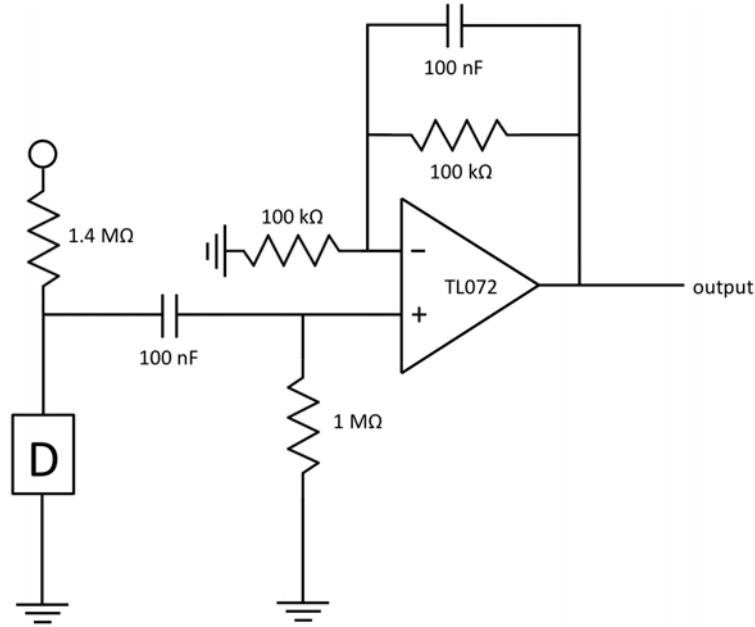


Figure A.4: Circuit used to amplify the signal from the detector (D)

Shop). In addition to using special windows, gold mirrors (ThorLabs: [PF10-03-M01](#)) were used for the beam steering due to their higher reflectance in the infrared.

LabView is used for data data acquisition and the program records continuous sets of 2000 samples at 50 kHz. This data is then directly analyzed and averaged giving an effective rate of 8 Hz during heating and slow reactions generating approximately 15k data points. Further, a second data acquisition board is triggered during an ignition event recording raw data at 150 kHz for a total of 200k data points. The maximum sampling rate for the optical fuel measurement is limited by the chopping frequency.

A sample set of raw data for the fuel measurements is shown in Figure A.5. For the fuel measurement, the intensity of the laser light going through the test cell, I_1 , the intensity of the reference beam, I_2 , and the synchronization output from the optical chopper (SYNC) are sampled at 50 kHz. The SYNC output, which is a 5 V square wave at the same frequency as the chopper, is used the trigger for the LabView script to begin recording 2000 samples. The processed chopper signal (SYNC > 2.5 V) is shown Figure A.5 as “Chopper (logic)”, and then a subset as indicated by “Chopper (adjusted, logic)” is selected. The signals for I_1 and I_2 , and the time are averaged in each selected window and thus give one data point for each window in which the chopper is “on”.

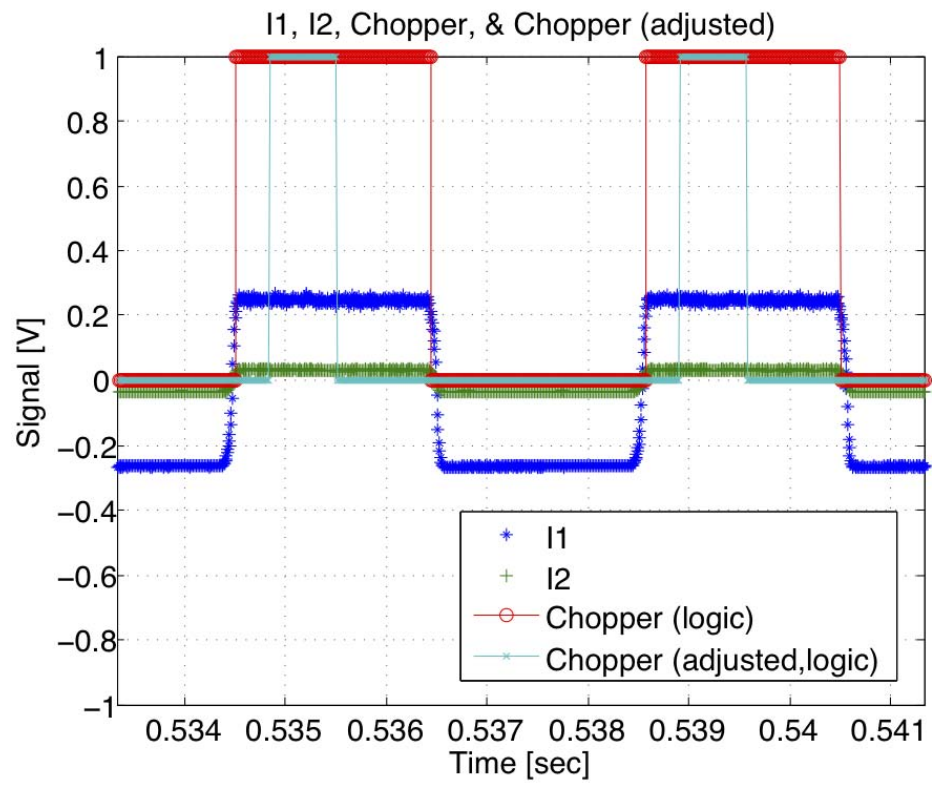


Figure A.5: Raw fuel data from shot 19

A.2 Absorption Cross Sections

As a reference the absorption cross sections at $\lambda = 3.39 \mu\text{m}$ for various hydrocarbons including *n*-hexane are given in Table A.2. Further measurements of absorption cross sections have been performed by Mével et al. (2012).

Table A.2: Absorption cross sections expanded from Klingbeil et al. (2006)

Hydrocarbon	Reference	Total Pressure [Torr]	σ_ν [m ² mole ⁻¹]	Uncertainty [%]	Technique	
Methane	Klingbeil et al. (2006)	760	21.1	3	HeNe	
CH ₄	Yoshiyama et al. (1996)	760	25.3	N/A	HeNe	
	Tomita et al. (2003)	760	21.9	2	HeNe	
	Perrin and Hartmann (1989)	760	22.5	5	HeNe	
	Rothman et al. (2005)	760	21.4	N/A	Calculation	
	Jaynes and Beam (1969)	30.4	36.7	N/A	HeNe	
	Sharpe et al. (2004)	760	19.5	3	FTIR	
	Ethylene	Klingbeil et al. (2006)	760	0.459	3.5	HeNe
C ₂ H ₄	Rothman et al. (2005)	760	0.386	N/A	Calculation	
	Sharpe et al. (2004)	760	0.426	3	FTIR	
	Hinckley and Dean (2005)	760	0.391	2	HeNe	
	Propane	Klingbeil et al. (2006)	760	20.2	3.4	HeNe
C ₃ H ₈	Sharpe et al. (2004)	760	21.2	3	FTIR	
	Tsuboi et al. (1985)	760	20.7	20	HeNe	
	Yoshiyama et al. (1996)	760	23.9	N/A	HeNe	
	Jaynes and Beam (1969)	760	48.9	N/A	HeNe	
	Jaynes and Beam (1969)	23	20.3	N/A	HeNe	
	Hexane	Jaynes and Beam (1969)	11.4	45	N/A	HeNe
	C ₆ H ₁₄	Drallmeier (2003)	650	38.5	5	HeNe
This Work		760	38	2.6	HeNe	

N/A - not available

This page intentionally left blank.

Appendix B

Second Harmonic Detection of Oxygen with Tunable Diode Lasers

The following section gives the details for second harmonic detection of oxygen concentration that lead to Equation 2.4 in Section 2.2.3. The analysis of second harmonic detection described here was derived by Reid and Labrie (1981). In order to detect weak absorption features a tunable diode laser is modulated at a high frequency, while the mean wavelength of the laser is scanned more slowly across the feature. The intensity only drops very slightly as the wavelength reaches the wavelength at which the molecules absorb the photons. The change of the wavelength must be accounted for in the Beer-Lambert law and is written here in terms of the frequency of light $\nu = c/\lambda$, where λ is the wavelength and c is the speed of light:

$$I(\nu) = I_0(\nu) \exp(-\alpha(\nu)L) \quad (\text{B.1})$$

Assuming that the absorption lines are weak $\alpha(\nu)L < 0.05$, the following approximation is valid:

$$I(\nu) \simeq I_0(\nu) [1 - \alpha(\nu)L] \quad (\text{B.2})$$

In order to obtain a harmonic output, the electrical current input to the laser diode is modulated at a specified frequency, ω , which in turn modulates the wavelength of light emitted by the laser diode:

$$\nu(t) = \bar{\nu} + a \cos(\omega t) \quad (\text{B.3})$$

The mean frequency, $\bar{\nu}$, is ramped slowly (80 Hz) relative to the modulation, ω , (23.5 kHz). For small ramping amplitude the incident light intensity is constant:

$$I(\nu) \approx I_0(\nu_0) \approx I_0 \quad (\text{B.4})$$

Now the received intensity at the detector can be written as:

$$I(\nu) = I_0 - I_0 \alpha(\nu) L \quad (\text{B.5})$$

$$= I_0 - I_0 \alpha(\bar{\nu} + a \cos(\omega t)) L \quad (\text{B.6})$$

The time dependent part is then expanded in a Taylor series about $\nu = \bar{\nu}$:

$$\begin{aligned} \alpha(\bar{\nu} + a \cos(\omega t)) &= \alpha(\bar{\nu}) + \frac{d\alpha}{d\nu}_{\nu=\bar{\nu}} (a \cos(\omega t)) + \frac{1}{2!} \frac{d^2\alpha}{d\nu^2}_{\nu=\bar{\nu}} (a \cos(\omega t))^2 \\ &+ \frac{1}{3!} \frac{d^3\alpha}{d\nu^3}_{\nu=\bar{\nu}} (a \cos(\omega t))^3 + \frac{1}{4!} \frac{d^4\alpha}{d\nu^4}_{\nu=\bar{\nu}} (a \cos(\omega t))^4 + \dots \end{aligned} \quad (\text{B.7})$$

Using identities for the powers of cosine gives:

$$\begin{aligned} \alpha(\bar{\nu} + a \cos(\omega t)) &= \alpha(\bar{\nu}) + \frac{d\alpha}{d\nu}_{\nu=\bar{\nu}} (a \cos(\omega t)) + \frac{a^2}{2!} \frac{d^2\alpha}{d\nu^2}_{\nu=\bar{\nu}} \left(\frac{1}{2} + \frac{1}{2} \cos(2\omega t) \right) \\ &+ \frac{a^3}{3!} \frac{d^3\alpha}{d\nu^3}_{\nu=\bar{\nu}} \left(\frac{1}{4} \right) (3 \cos(\omega t) + \cos(3\omega t)) \\ &+ \frac{a^4}{4!} \frac{d^4\alpha}{d\nu^4}_{\nu=\bar{\nu}} \left(\frac{1}{8} \right) (3 + 4 \cos(2\omega t) + \cos(4\omega t)) + \dots \end{aligned} \quad (\text{B.8})$$

Collecting terms with the same frequency gives:

$$\begin{aligned}
\alpha(\bar{\nu} + a \cos(\omega t)) &= \alpha(\bar{\nu}) + \left(\frac{1}{2} \frac{1}{2!} \frac{d^2 \alpha}{d\nu^2} \Big|_{\nu=\bar{\nu}} a^2 + \frac{3}{8} \frac{1}{2!} \frac{d^4 \alpha}{d\nu^4} \Big|_{\nu=\bar{\nu}} a^4 + \dots \right) \\
&+ \left(\frac{d\alpha}{d\nu} \Big|_{\nu=\bar{\nu}} a + \frac{3}{4} \frac{1}{3!} \frac{d^3 \alpha}{d\nu^3} \Big|_{\nu=\bar{\nu}} a^3 + \dots \right) \cos(\omega t) \\
&+ \left(\frac{1}{2} \frac{1}{2!} \frac{d^2 \alpha}{d\nu^2} \Big|_{\nu=\bar{\nu}} a^2 + \frac{1}{2} \frac{1}{4!} \frac{d^4 \alpha}{d\nu^4} \Big|_{\nu=\bar{\nu}} a^4 + \dots \right) \cos(2\omega t) \\
&+ \left(\frac{1}{4} \frac{1}{3!} \frac{d^3 \alpha}{d\nu^3} \Big|_{\nu=\bar{\nu}} a^3 + \dots \right) \cos(3\omega t) \\
&+ \left(\frac{1}{8} \frac{1}{4!} \frac{d^4 \alpha}{d\nu^4} \Big|_{\nu=\bar{\nu}} a^4 + \dots \right) \cos(4\omega t) + \dots
\end{aligned} \tag{B.9}$$

Reid and Labrie write the equation above in the following short-hand notation:

$$\alpha(\bar{\nu} + a \cos(\omega t)) = \sum_{n=0}^{\infty} H_n(\bar{\nu}) \cos(n\omega t) \tag{B.10}$$

where

$$H_n(\bar{\nu}) = \frac{2^{1-n}}{n!} \alpha^n \frac{d^n \alpha(\nu)}{d\nu^n} \Big|_{\nu=\bar{\nu}}, n \geq 1 \tag{B.11}$$

The sinusoidal modulation amplitude is 4 mV, which small relative to the mean scanning amplitude of 100 mV (smallest sinusoidal output from **SR830** is 4 mV). For very small modulations such that $a \ll 1$:

$$\begin{aligned}
\alpha(\bar{\nu} + a \cos(\omega t)) &\approx \alpha(\bar{\nu}) + a \frac{d\alpha}{d\nu} \Big|_{\nu=\bar{\nu}} \cos(\omega t) + \frac{a^2}{2} \frac{1}{2!} \frac{d^2 \alpha}{d\nu^2} \Big|_{\nu=\bar{\nu}} \cos(2\omega t) \\
&+ \frac{a^3}{4} \frac{1}{3!} \frac{d^3 \alpha}{d\nu^3} \Big|_{\nu=\bar{\nu}} \cos(3\omega t) + \frac{a^4}{8} \frac{1}{4!} \frac{d^4 \alpha}{d\nu^4} \Big|_{\nu=\bar{\nu}} \cos(4\omega t) + \dots
\end{aligned} \tag{B.12}$$

A lock-in amplifier is used to selectively amplify the second harmonic term, which is proportional to

$$\frac{a^2}{2} \frac{1}{2!} \frac{d^2 \alpha}{d\nu^2} \Big|_{\nu=\bar{\nu}} \cos(2\omega t) . \tag{B.13}$$

Derivatives of $\alpha(\nu)$, assuming a Lorentzian line shape, are:

$$\alpha(\nu) = \frac{\alpha_0}{1 + \left[\frac{\nu - \nu_0}{\Delta\nu}\right]^2} = \frac{\alpha_0 \Delta\nu^2}{\Delta\nu^2 + (\nu - \nu_0)^2} \quad (\text{B.14})$$

$$\frac{d\alpha(\nu)}{d\nu} = -\frac{2\alpha_0 \Delta\nu^2 (\nu - \nu_0)}{(\nu^2 - 2\nu\nu_0 + \nu_0^2 + \Delta\nu^2)^2} = -\frac{2\alpha_0 \Delta\nu^2 (\nu - \nu_0)}{((\nu - \nu_0)^2 + \Delta\nu^2)^2} \quad (\text{B.15})$$

$$\frac{d^2\alpha(\nu)}{d\nu^2} = \frac{2\alpha_0 \Delta\nu^2 (3\nu^2 - 6\nu\nu_0 + 3\nu_0^2 - \Delta\nu^2)}{(\nu^2 - 2\nu\nu_0 + \nu_0^2 + \Delta\nu^2)^3} = \frac{2\alpha_0 \Delta\nu^2 (3(\nu - \nu_0)^2 - \Delta\nu^2)}{((\nu - \nu_0)^2 + \Delta\nu^2)^3} \quad (\text{B.16})$$

Evaluating at $\nu = \nu_0 = \bar{\nu}$ gives:

$$\left. \frac{d^2\alpha(\nu)}{d\nu^2} \right|_{\nu=\nu_0=\bar{\nu}} = -\frac{2\alpha_0}{\Delta\nu^2} \quad (\text{B.17})$$

$$\left. \frac{d^2 I}{d\nu^2} \right|_{\nu=\nu_0=\bar{\nu}} = \frac{2\alpha_0 I_0 L}{\Delta\nu^2} \exp(-\alpha_0 L) \quad (\text{B.18})$$

Finally the absorption coefficient, α_0 also equal to the product of the absorption cross section, σ_ν , and the number of molecules in the volume, n , as done in the previous section, $\alpha(\nu) = \sigma_\nu n$, giving:

$$\left. \frac{d^2 I}{d\nu^2} \right|_{\nu=\nu_0=\bar{\nu}} = \frac{2I_0 L \sigma_\nu}{\tilde{R}T \Delta\nu^2} P \exp\left(-\frac{\sigma_\nu L}{\tilde{R}T} P\right) \quad (\text{B.19})$$

In the actual application, the exponential term can be expanded in a Taylor series. A constant should be added to account for the air outside the test section and the coefficients of the series are obtained by calibration.

$$\left. \frac{d^2 I}{d\nu^2} \right|_{\nu=\nu_0=\bar{\nu}} = c_0 + c_1 P + c_2 P^2 + \dots \quad (\text{B.20})$$

The constants, c_0 , c_1 , and c_2 , must be calibrated before the experiment and for relatively small amounts of oxygen a linear fit is sufficient.

B.1 Experimental Setup Addendum

The following section gives additional information to the experimental setup for oxygen detector not covered in section 2.2.3.1.

The laser diode used is a ULM763-03-TN-S46FTT, manufactured by Laser Components. The laser is tunable from 760 nm to 766 nm via current and temperature control. This allows for scanning across the absorption line. In our experiments the current is modulated, using a Thorlabs LDC 200 C

producing 20 mA, and temperature held constant by a Thorlabs TED 2002 C temperature controller. The detectors used are large-area, visible-spectrum-amplified Si detectors, Thorlabs PDA100A. The modulation signal is generated by adding the sine wave generated by the lock-in amplifier, Stanford Research System SR830, with a sawtooth wave generated by a function generator, Stanford Research Systems DS345, in a summing amplifier, Stanford Research System SIM980 powered independently without a SIM900 mainframe. The final signal can be amplified and bandpass filtered using a preamplifier like a Stanford Research Systems SR560.

The sweeping frequency can be adjusted from the 80 Hz mentioned to suit the needs of the experiment (Rieker et al., 2009), but was not changed significantly during this study. For the current configuration of 80 Hz sweep and 23.5 kHz modulation frequency a time constant of 100 μ s is found to give good 1f (fundamental harmonic) and 2f (2nd harmonic) signals without excessive noise. The modulation depth of 4 mA can also be changed to maximize the 2f signal (Rieker, 2009). The signal can be amplified and bandpass filtered either before the lock-in amplifier and afterwards. An example of the signal is shown in Figure B.1 including the gate signal extracted from the synchronization signal produced by the signal generator that creates the sawtooth wave.

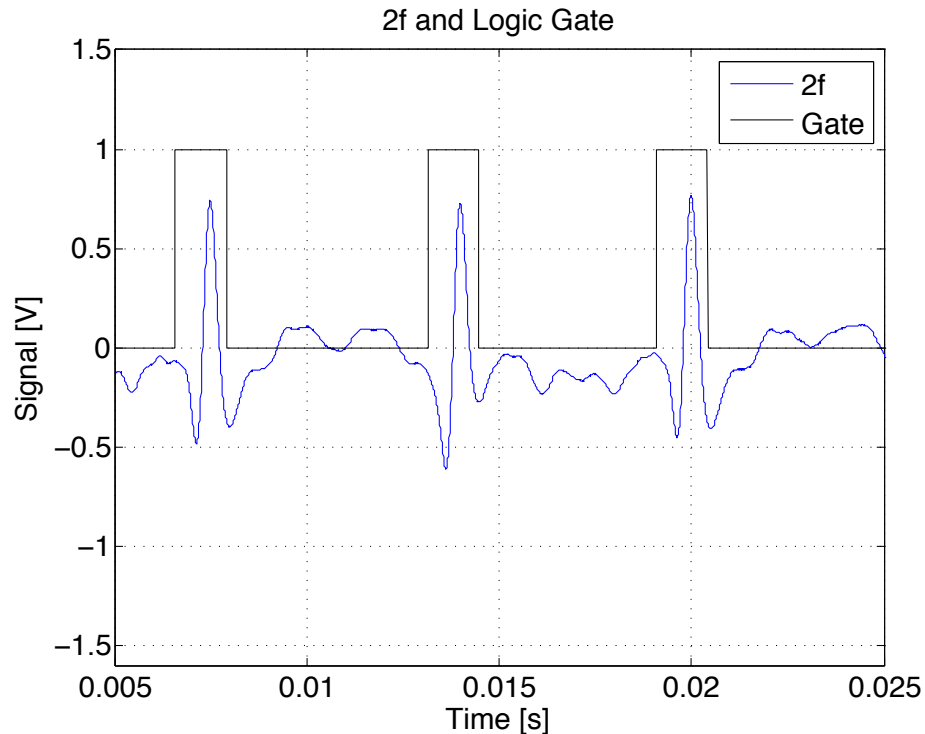


Figure B.1: Raw oxygen 2f data from shot 19

The measurements drifted significantly during the test time due to temperature changes of the

vessel and subsequent beam-steering and internal reflections in the windows (etalon). Some of the drifting can be accounted for by normalizing the 2f signal by the 1f intensity at the time of the 2f peak height (see Rieker et al. (2009)). However, for the large temperature changes imposed during the auto-ignition tests, the effects were generally too large to be compensated for using this method. The only reasonable data set is shown Figure 2.8 in section 2.2.3.2. The data was obtained by normalizing the drift using data obtained during the next experiment where the fuel was replaced by additional nitrogen in the mixture and all other parameters were kept the same.

For experiments with large temperature changes in the optical equipment, such as the windows, the 2f technique is not recommended.

Appendix C

Heated Vessel Theory

C.1 Governing Equation and Nomenclature

Recall Equation 2.5 from the discussion using the detailed chemical mechanism

$$V \rho c_v \frac{dT}{dt} = V \sum_{i=1}^k \dot{\omega}_i u_i + Sh (T_w^0 + \alpha t - T) = \dot{q}_r + \dot{q}_w. \quad (\text{C.1})$$

with the following nomenclature.

Table C.1: Nomenclature

Parameter	Units	Description
T	K	gas temperature
V	m^3	volume
ρ	kg m^{-3}	density
c_v	$\text{J kg}^{-1} \text{K}^{-1}$	specific heat at constant
q_c	J kg^{-1}	chemical heat release (heat of combustion)
$\dot{\omega}_i$	$\text{kg m}^{-3} \text{sec}^{-1}$	net production rate per unit volume
u_i	J kg^{-1}	internal energy
S	m^2	surface area
h	$\text{J sec}^{-1} \text{m}^{-2} \text{K}^{-1}$	heat transfer coefficient
T_w^0	K	initial wall temperature
α	K sec^{-1}	wall temperature heating rate
\dot{q}_r	J sec^{-1}	energy release rate
\dot{q}_l	J sec^{-1}	energy loss rate

We now simplify the model such that we use a first order one-step Arrhenius rate for the consumption of the fuel, the governing equations for the reactor are:

$$V\rho c_v \frac{dT}{dt} = VQ \frac{d\lambda}{dt} - Sh(T - T_w) \quad (\text{C.2})$$

$$\frac{d\lambda}{dt} = A(1 - \lambda) \exp\left(-\frac{E_a}{\tilde{R}T}\right). \quad (\text{C.3})$$

The stored chemical energy per unit mass, q_c , is related to the energy density, Q , through the density, ρ , by

$$Q = \rho q_c. \quad (\text{C.4})$$

Table C.2: Additional nomenclature

Parameter	Units	Description
T_w	K	wall temperature
Q	J m ⁻³	energy density
λ		progress variable
A	sec ⁻¹	pre-exponential
E_a	J kmol ⁻¹	activation energy
\tilde{R}	J kmol ⁻¹ K ⁻¹	universal gas constant

C.2 Induction Time

If we take the energy equation for a spatially homogeneous reactive material and assume a first order one-step Arrhenius rate,

$$\rho c_v \frac{dT}{dt} = QA(1 - \lambda) \exp\left(-\frac{E_a}{\tilde{R}T}\right) - \frac{Sh}{V}(T - T_w) \quad (\text{C.5})$$

$$\frac{d\lambda}{dt} = A(1 - \lambda) \exp\left(-\frac{E_a}{\tilde{R}T}\right) \quad (\text{C.6})$$

and now neglect fuel consumption and heat loss.

$$\frac{dT}{dt} = \frac{QA}{\rho c_v} \exp\left(-\frac{E_a}{\tilde{R}T}\right) \quad (\text{C.7})$$

let $k = (QA)/(\rho c_v)$ and $\zeta = (E_a)/(\tilde{R}T)$ and integrate the equation to find the finite time at which the temperature tends to infinity.

$$\frac{d\zeta}{dT} = -\left(\frac{E_a}{\tilde{R}T}\right)^{-1} = -\frac{\tilde{R}}{E_a} \zeta^2 \implies dT = -\frac{E_a}{\tilde{R}} \frac{d\zeta}{\zeta^2}$$

$$k \int_0^t dt' = -\frac{E_a}{\tilde{R}} \int_{\zeta_0}^{\zeta} \frac{\exp(\zeta)}{\zeta^2} d\zeta$$

$$kt = \frac{E_a}{\tilde{R}} \int_{\zeta}^{\zeta_0} \frac{\exp(\zeta)}{\zeta^2} d\zeta \quad (\text{C.8})$$

Using integration by parts we can proceed until further approximations must be made. $\int u dv = uv - \int v du$ with $v = \exp(\zeta)$ and $u = \zeta^{-n}$

$$\int_{\zeta}^{\zeta_0} \frac{\exp(\zeta)}{\zeta^2} d\zeta = \frac{\exp(\zeta)}{\zeta^2} \Big|_{\zeta}^{\zeta_0} + \int_{\zeta}^{\zeta_0} 2 \frac{\exp(\zeta)}{\zeta^3} d\zeta$$

$$\int_{\zeta}^{\zeta_0} \frac{\exp(\zeta)}{\zeta^2} d\zeta = \frac{\exp(\zeta)}{\zeta^2} \Big|_{\zeta}^{\zeta_0} + 2 \left[\frac{\exp(\zeta)}{\zeta^3} \Big|_{\zeta}^{\zeta_0} + \int_{\zeta}^{\zeta_0} 3 \frac{\exp(\zeta)}{\zeta^4} d\zeta \right]$$

$$\int_{\zeta}^{\zeta_0} \frac{\exp(\zeta)}{\zeta^2} d\zeta = \left[\frac{\exp(\zeta)}{\zeta^2} \left(1 + \frac{2}{\zeta} + \dots + \frac{(n+1)!}{\zeta^n} + \dots \right) \right]_{\zeta}^{\zeta_0}$$

To leading order

$$t = \frac{E_a}{k\tilde{R}} \left(\frac{\exp(\zeta_0)}{\zeta_0^2} - \frac{\exp(\zeta)}{\zeta^2} \right) \quad (\text{C.9})$$

Note: $T \rightarrow \infty$ (i.e., $\zeta \rightarrow 0$) as $t \rightarrow \infty$ because fuel consumption has been neglected. From equation C.7 we see that $dT/dt \rightarrow (QA)/(\rho c_v)$ as $T \rightarrow \infty$. We must thus choose a criterion for the temperature, which classifies ignition. Numerical integration of C.7 shows an inflection point in the temperature, which may be a suitable reference point.

$$\begin{aligned}\frac{dT}{dt} &= \frac{QA}{\rho c_v} \exp\left(-\frac{T_a}{T}\right) \\ \frac{d^2T}{dt^2} &= \left(\frac{QA}{\rho c_v}\right)^2 \frac{T_a}{T^2} \exp\left(-2\frac{T_a}{T}\right) \\ \frac{d^3T}{dt^3} &= 2\left(\frac{QA}{\rho c_v}\right)^3 \frac{T_a(T_a - T)}{T^4} \exp\left(-3\frac{T_a}{T}\right) \\ \frac{d^3T}{dt^3} &= 0 \rightarrow T = T_a\end{aligned}$$

At the inflection point, the temperature has reached the activation temperature, which is corollary to rapid chemical reaction. $T = T_a$ implies $\zeta = 1$, which now allows us to evaluate C.9

$$t = \frac{E_a}{k\tilde{R}} \left(\frac{\exp(\zeta_0)}{\zeta_0^2} - e \right)$$

Recall that $\zeta_0 = T_a/T_0$

$$t = \frac{E_a}{k\tilde{R}} \left(\frac{\exp(T_a/T_0)}{(T_a/T_0)^2} - e \right)$$

Thus for large activation energy (i.e., large activation temperature), the first term completely dominates and we conclude that the induction time, τ_c , is

$$\tau_c = \frac{\rho c_v}{QA} \frac{\tilde{R}T_0^2}{E_a} \exp\left(\frac{E_a}{\tilde{R}T_0}\right) \quad (\text{C.10})$$

C.2.1 Alternative Derivation

We can find the same induction time via a slightly different route. Starting from the heat equation without losses or consumption

$$\frac{dT}{dt} = \frac{QA}{\rho c_v} \exp\left(-\frac{E_a}{\tilde{R}T}\right), \quad (\text{C.11})$$

let $\phi = \tilde{R}T/E_a$, $k = QA/\rho c_v$

$$\frac{d\phi}{dt} = \frac{k\tilde{R}}{E_a} \exp\left(-\frac{1}{\phi}\right) \quad (\text{C.12})$$

$$\frac{k\tilde{R}}{E_a} \int_0^t dt' = \int_{\phi_0}^{\phi} \exp\left(\frac{1}{\phi'}\right) d\phi' \quad (\text{C.13})$$

where $\phi_0 = \tilde{R}T_0/E_a$, and $\phi_{max} = \tilde{R}T_{max}/E_a$, where T_{max} is the maximum temperature reached if fuel consumption was included. The temperatures scale as follows

$$1 < \exp\left(\frac{1}{\phi_{max}}\right) < \exp\left(\frac{1}{\phi}\right) < \exp\left(\frac{1}{\phi_0}\right)$$

as $\phi_0 \ll 1 \implies e^{\frac{1}{\phi_0}} \gg 1$.

The limit of the integrand as T or ϕ tend to ∞ is 1 and thus the integral diverges as $\phi \rightarrow \infty$. Let us separate the integral into 2 components.

$$t \frac{k\tilde{R}}{E_a} = \int_{\phi_0}^{\phi} \exp\left(\frac{1}{\phi'}\right) d\phi' = \int_{\phi_0}^{\phi} \left(\exp\left(\frac{1}{\phi'}\right) - 1\right) d\phi' + \int_{\phi_0}^{\phi} d\phi' = I + II$$

However, within finite time, i.e., as ϕ approaches ϕ_{max} , I dominates the integral, so the induction time can be approximated as follows.

$$\tau_c = \frac{E_a}{k\tilde{R}} \int_{\phi_0}^{\phi_{max}} \left(\exp\left(\frac{1}{\phi'}\right) - 1\right) d\phi' \quad (\text{C.14})$$

Make a change of variables as follows.

$$x = \frac{\phi_0}{\phi'} \quad ; \quad d\phi' = -\frac{\phi_0}{x^2} dx \quad ; \quad \exp\left(\frac{1}{\phi'}\right) = \exp\left(\frac{x}{\phi_0}\right)$$

$$\tau_c = \frac{E_a}{k\tilde{R}} \phi_0 \int_{\epsilon}^1 \frac{\left(\exp\left(\frac{x}{\phi_0}\right) - 1\right)}{x^2} dx \quad (\text{C.15})$$

This integral is dominated by the contribution at $x = 1$ and thus we can integrate the equation and set $x = 1$.

$$\tau_c = \frac{E_a}{k\tilde{R}} \phi_0^2 e^{1/\phi_0} \quad (\text{C.16})$$

Substituting back ϕ_0 and k gives

$$\tau_c = \frac{\rho c_v T_0^2 \tilde{R}}{QA E_a} \exp\left(\frac{E_a}{\tilde{R}T_0}\right). \quad (\text{C.17})$$

C.2.2 Frank-Kamenetskii Approximation

We can follow the linearization by Frank-Kamenetskii (1969) about the initial temperature T_0 , i.e., $T = T_0 + T'$. Using the geometric series

$$\frac{E_a}{\tilde{R}T} = \frac{E_a}{\tilde{R}(T_0 + T')} = \frac{E_a}{\tilde{R}T_0(1 + T'/T_0)} = \frac{E_a}{\tilde{R}T_0} - \frac{E_a}{\tilde{R}T_0^2}T' + \frac{E_a}{\tilde{R}T_0^3}T'^2 - \dots \quad (\text{C.18})$$

and neglecting higher order terms gives us

$$\frac{dT}{dt} = \frac{QA}{\rho c_v} \exp\left(-\frac{E_a}{\tilde{R}T_0}\right) \exp\left(\frac{E_a T'}{\tilde{R}T_0^2}\right) \quad (\text{C.19})$$

which we can now nondimensionalize the temperature as $\theta = (E_a T')/(\tilde{R}T_0^2)$, which will reveal the correct scaling for the time

$$\frac{d\theta}{dt} = \frac{QA}{\rho c_v} \frac{E_a}{\tilde{R}T_0^2} \exp\left(-\frac{E_a}{\tilde{R}T_0}\right) \exp(\theta)$$

$$\tau = t \frac{QA}{\rho c_v} \frac{E_a}{\tilde{R}T_0^2} \exp\left(-\frac{E_a}{\tilde{R}T_0}\right)$$

$$\frac{d\theta}{d\tau} = e^\theta \quad (\text{C.20})$$

$$\int_0^\tau d\tau = \int_0^\theta e^{-\theta} d\theta$$

$$\theta = -\ln(1 - \tau) \quad (\text{C.21})$$

We can now see that the temperature will tend to $+\infty$ when $\tau = 1$, which is the induction time (τ_c).

$$\tau_c = \frac{\rho c_v}{QA} \frac{\tilde{R}T_0^2}{E_a} \exp\left(\frac{E_a}{\tilde{R}T_0}\right) \quad (\text{C.22})$$

C.2.3 Wall Temperature Ramp Without Chemistry

In future section we would like to treat the chemical reaction as a deviation from the underlying behavior induced by the wall temperature ramp. While the final result is obvious, the details are still of interest. Neglecting the chemical reaction gives the following equation:

$$\frac{dT}{dt} = \frac{Sh}{\rho V c_v} (T_w^0 + \alpha t - T) . \quad (\text{C.23})$$

Once cast in the following form the equation can be integrated using the integrating factor,

$$\frac{dT}{dt} + \frac{T}{t_w} = \frac{T_w^0 + \alpha t}{t_w} , \quad (\text{C.24})$$

such that the final solution is found to be

$$T(t) = T_w^0 + \alpha t + \alpha t_w \left(e^{-t/t_w} - 1 \right) , \quad (\text{C.25})$$

where $t_w = (\rho V c_v)/(Sh)$ is the wall heat transfer time. At early time, we can expand the exponential term.

$$T(t) = T_w^0 + \alpha t + \alpha t_w \left(1 - \frac{t}{t_w} + \frac{1}{2} \left(\frac{t}{t_w} \right)^2 - \dots - 1 \right) \quad (\text{C.26})$$

$$= T_w^0 + \alpha t - \alpha t_w \frac{t}{t_w} + \frac{1}{2} \left(\frac{t}{t_w} \right)^2 - \dots \quad (\text{C.27})$$

$$= T_w^0 + \frac{1}{2} \left(\frac{t}{t_w} \right)^2 - \dots \quad (\text{C.28})$$

At later times, as $t/t_w \rightarrow \infty$

$$T(t) = T_w^0 + \alpha (t - t_w) , \quad (\text{C.29})$$

which implies that the temperature follows the outside ramping with a lag.

C.2.4 Ramp Rate Reduced Induction Time

The induction can be reduced when the vessel is heated from the outside. This introduces the heating rate in the energy equation in the following form,

$$\frac{dT}{dt} = \frac{QA}{\rho c_v} \exp\left(-\frac{E_a}{RT}\right) + \alpha . \quad (\text{C.30})$$

The chemical energy release is a perturbation above the rate at which the temperature is increased externally.

Following the high activation energy arguments we can write equation as follows:

$$\frac{d\theta}{dt} = \frac{QA}{\rho c_v} \frac{E_a}{\tilde{R}T_0^2} \exp\left(-\frac{E_a}{\tilde{R}T_0}\right) \exp(\theta) + \frac{\alpha E_a}{\tilde{R}T_0^2} \quad (\text{C.31})$$

where

$$\theta = \frac{E_a T'}{\tilde{R}T_0^2}. \quad (\text{C.32})$$

Now we can substitute

$$\tau = t \frac{QA}{\rho c_v} \frac{E_a}{\tilde{R}T_0^2} \exp\left(-\frac{E_a}{\tilde{R}T_0}\right) = \frac{t}{\tau_c} \quad (\text{C.33})$$

$$a = \frac{\alpha E_a}{\tilde{R}T_0^2} \quad (\text{C.34})$$

which gives

$$\frac{d\theta}{d\tau} = \exp(\theta) + \frac{a}{\tau_c}, \quad (\text{C.35})$$

that can be integrated

$$\int_0^{\tau_{ign}} d\tau = \int_0^{\theta_a} \frac{1}{e^\theta + \frac{a}{\tau_c}} d\theta = \int_0^{\theta_a} \frac{1}{e^\theta + \beta} d\theta, \quad (\text{C.36})$$

where $\beta = a/\tau_c$.

$$\tau = \left[\frac{\theta - \ln(\beta + e^\theta)}{\beta} \right]_0^{\theta} \quad (\text{C.37})$$

$$\tau = \frac{1}{\beta} \left(\theta - \ln \left(\frac{\beta + e^\theta}{\beta + 1} \right) \right) \quad (\text{C.38})$$

$$\tau = \tau_c \frac{\tilde{R}T_0^2}{\alpha E_a} \left(\theta - \ln \left(\frac{\beta + e^\theta}{\beta + 1} \right) \right) \quad (\text{C.39})$$

$$\tau = \tau_c \frac{\tilde{R}T_0^2}{\alpha E_a} \left(\frac{E_a T'}{\tilde{R}T_0^2} - \ln \left(\frac{\beta + e^\theta}{\beta + 1} \right) \right) \quad (\text{C.40})$$

$$\tau = \frac{\tau_c}{\alpha} \left(T' - \frac{\tilde{R}T_0^2}{E_a} \ln \left(\frac{\beta + e^\theta}{\beta + 1} \right) \right) \quad (\text{C.41})$$

C.2.5 Critical Heat-Loss Rate With Constant Wall Temperature

If we take the energy equation with heat loss to the wall, but keep the wall temperature constant and omit fuel consumption we arrive the classical Semenov model (Semenov, 1940). Following Law (2006, Combustion Physics, chapter 8.1.3), we can obtain the critical heat transfer coefficient.

$$\rho c_v \frac{dT}{dt} = QA \exp\left(-\frac{E_a}{\tilde{R}T}\right) - \frac{Sh}{V} (T - T_w) \quad (\text{C.42})$$

T_w is the wall temperature to which the heat is lost, which may or may not be equal to the initial temperature T_0 . Following the earlier perturbation and nondimensionalization we get

$$\frac{d\theta}{d\tau} = e^\theta - \hat{h} \left(\theta + \frac{T_a}{T_0} (T_0 - T_w) \right) \quad (\text{C.43})$$

where $\hat{h} = \tau_c / \tau_l$ with $\tau_l = \rho V c_v / Sh$, which is the characteristic heat-loss time, and as before $\tau_c = \rho c_v \tilde{R} T_0^2 / QA E_a \exp\left(E_a / \tilde{R} T_0\right)$.

For the case where $T_0 = T_w$, there exist solutions for $d\theta/d\tau = 0$ as long as $\hat{h} > e$. $\hat{h} = e$ is the critical heating transfer coefficient with values below e always leading to explosion, while for values of \hat{h} higher than e the initial temperature ultimately determines the stability.

$$\frac{d\theta}{d\tau} = e^\theta - \hat{h}\theta \quad (\text{C.44})$$

$$\frac{d\theta}{d\tau} = 0 \implies e^\theta = \hat{h}\theta \quad (\text{C.45})$$

$$\frac{d}{d\theta} \implies e^\theta = \hat{h} \quad (\text{C.46})$$

critical conditions for $\theta = 1$ and $\hat{h} = e$.

C.3 Full Nondimensional Equations

$$\rho c_v \frac{dT}{dt} = QA(1 - \lambda) \exp\left(-\frac{E_a}{\tilde{R}T}\right) + \frac{Sh}{V} (T_w + \alpha t - T) \quad (\text{C.47})$$

$$\frac{d\lambda}{dt} = A(1 - \lambda) \exp\left(-\frac{E_a}{\tilde{R}T}\right) \quad (\text{C.48})$$

Here we make no assumptions about the activation energy or fuel consumption. Let $T_a = E_a / \tilde{R}$.

$$\frac{dT}{dt} = (1 - \lambda) \frac{1}{\tau_c} \exp\left(\frac{T_a}{T_0} - \frac{T_a}{T}\right) + \frac{1}{\tau_l} (T_w + \alpha t - T) \quad (\text{C.49})$$

$$\frac{d(TT_a/T_0^2)}{d(t/\tau_c)} = (1 - \lambda) \exp\left(\frac{T_a}{T_0} - \frac{T_a}{T_0^2} \left(\frac{T_0^2}{TT_a}\right)\right) - \frac{\tau_c}{\pi} \left(\frac{T_w T_a}{T_0^2} + \alpha t - \left(\frac{TT_a}{T_0^2}\right)\right) \quad (\text{C.50})$$

let $\theta = TT_a/T_0^2$, $\theta_0 = T_a/T_0$, $\theta_w = T_w T_a/T_0^2$, $\tau = t/\tau_c$, $\hat{h} = \tau_c/\pi$, $\tilde{\alpha} = \alpha\tau_c T_a/T_0^2$, $A^* = A\tau_c$

$$\frac{d\theta}{d\tau} = (1 - \lambda) \exp\left(\theta_0 - \frac{\theta_0^2}{\theta}\right) + \hat{h}(\theta_w + \tilde{\alpha}\tau - \theta) \quad (\text{C.51})$$

$$\frac{d\lambda}{d\tau} = A^* (1 - \lambda) \exp\left(-\frac{\theta_0^2}{\theta}\right) \quad (\text{C.52})$$

If we assume that the initial wall temperature is equal to the initial gas temperature, then $\theta_w = \theta_0$, thus slightly simplifying C.51 to:

$$\frac{d\theta}{d\tau} = (1 - \lambda) \exp\left(\theta_0 - \frac{\theta_0^2}{\theta}\right) + \hat{h}(\theta_0 + \tilde{\alpha}\tau - \theta) \quad (\text{C.53})$$

Appendix D

Collision Limit Calculation for Pre-Exponential

For bimolecular reactions,



the reaction rate is limited by the collision limit, i.e., R_1 and R_2 cannot react faster than the rate at which they collide. The collision rate between two unlike molecules per unit volume and time is given in Vincenti and Kruger (1967) as

$$Z_{R_1 R_2} = n_{R_1} n_{R_2} d_{R_1 R_2}^2 \left(\frac{8\pi kT}{m_{R_1 R_2}^*} \right)^{1/2} . \quad (\text{D.2})$$

The reaction rate of R_1 can thus be expressed as

$$-\frac{d[R_1]}{dt} = Z_{R_1 R_2} \frac{1}{N_{AV}} \exp\left(-\frac{E_a}{\tilde{R}T}\right) . \quad (\text{D.3})$$

Assuming that the mixture is slightly off stoichiometric gives

$$[R_1] = [R_1]_0 (1 - \lambda) \quad (\text{D.4})$$

$$[R_2] \approx [R_2]_0 . \quad (\text{D.5})$$

Substituting back into the equation gives

$$\frac{d\lambda}{dt} [R_1]_0 = n_{R_1} n_{R_2} d_{R_1 R_2}^2 \left(\frac{8\pi kT}{m_{R_1 R_2}^*} \right)^{1/2} \frac{1}{N_{AV}} \exp\left(-\frac{E_a}{\tilde{R}T}\right) . \quad (\text{D.6})$$

Noting that $n_{R_1} = [R_1] N_{AV} = [R_1]_0 (1 - \lambda) N_{AV}$ and $n_{R_2} = [R_2] N_{AV} \approx [R_2]_0 N_{AV}$ gives

$$\frac{d\lambda}{dt} [R_1]_0 = [R_1]_0 (1 - \lambda) N_{AV} [R_2]_0 N_{AV} d_{R_1 R_2}^2 \left(\frac{8\pi kT}{m_{R_1 R_2}^*} \right)^{1/2} \frac{1}{N_{AV}} \exp\left(-\frac{E_a}{RT}\right), \quad (\text{D.7})$$

which can be simplified to

$$\frac{d\lambda}{dt} = (1 - \lambda) [R_2]_0 N_{AV} d_{R_1 R_2}^2 \left(\frac{8\pi kT}{m_{R_1 R_2}^*} \right)^{1/2} \exp\left(-\frac{E_a}{RT}\right). \quad (\text{D.8})$$

The simplified one-step model has been cast in the following way

$$\frac{d\lambda}{dt} = A (1 - \lambda) \exp\left(-\frac{E_a}{RT}\right). \quad (\text{D.9})$$

Thus we can find the limit for A using

$$A = [R_2]_0 N_{AV} d_{R_1 R_2}^2 \left(\frac{8\pi kT}{m_{R_1 R_2}^*} \right)^{1/2}. \quad (\text{D.10})$$

As a upper limit we can assume that R_2 is the oxygen concentration, which is

$$[R_2]_0 = \frac{P}{RT} X_{O_2} = 1 \text{ atm} \times \frac{\text{K mol}}{8.205746 \times 10^{-5} \text{ atm m}^3} \times \frac{1}{300 \text{ K}} \times 0.20 = 8.13 \frac{\text{mol}}{\text{m}^3}. \quad (\text{D.11})$$

The collision cross section is

$$d_{R_1 R_2}^2 = \left(\frac{2.92 \times 10^{-10} \text{ m} + 5.87 \times 10^{-10} \text{ m}}{2} \right)^2 = 1.9 \times 10^{-19} \text{ m}^2. \quad (\text{D.12})$$

The reduced mass is

$$m_{R_1 R_2}^* = \frac{m_{R_1} \times m_{R_2}}{m_{R_1} + m_{R_2}} = \frac{32 \text{ amu} \times 86 \text{ amu}}{32 \text{ amu} + 86 \text{ amu}} \times \frac{1.66 \times 10^{-27} \text{ kg}}{\text{amu}} = 5.39 \times 10^{-22} \text{ kg}. \quad (\text{D.13})$$

Then A is

$$A = [R_2]_0 N_{AV} d_{R_1 R_2}^2 \left(\frac{8\pi kT}{m_{R_1 R_2}^*} \right)^{1/2} \quad (\text{D.14})$$

$$A = 8.13 \frac{\text{mol}}{\text{m}^3} \times \frac{6.022 \times 10^{23}}{\text{mol}} \times 1.9 \times 10^{-19} \text{ m}^2 \left(\frac{8\pi \times 1.3806503 \times 10^{-23} \text{ kg m}^2 \times 300 \text{ K}}{5.39 \times 10^{-22} \text{ kg s}^2 \text{ K}} \right)^{1/2}$$

$$A = 1.29 \times 10^7 \text{ sec}^{-1}$$

Appendix E

Correlation of Hot Surface Ignition Temperature with Surface Area

Kuchta et al. (1965) presented their results for hot surface ignition as a function of hot surface size and created empirical correlations for various fuels. The analysis follows the analytical work performed by Semenov (1940) for cases considering conductive heat transfer only. The temperature profile is governed by the energy equation

$$\rho c_p \frac{dT}{dt} = k \frac{d^2T}{dx^2} + \dot{q}_r . \quad (\text{E.1})$$

The heat generated by chemical reaction is given by

$$\dot{q}_r = QA(1 - \lambda) \exp\left(-\frac{E_a}{\tilde{R}T}\right) \quad (\text{E.2})$$

and the spatial temperature distribution at steady state is given by

$$-\lambda \frac{d^2T}{dx^2} = \dot{q}_r . \quad (\text{E.3})$$

Using the linearization as discussed in C.2.2 and neglecting consumption ($\lambda \approx 0$), the steady state equation becomes

$$\lambda \frac{d^2T}{dx^2} = QA \exp\left(-\frac{E_a}{\tilde{R}T_1}\right) \exp\left(-\frac{E_a(T_1 - T)}{\tilde{R}T_1^2}\right) , \quad (\text{E.4})$$

where T_1 is the temperature of the hot surface. The steady state case allows us to find a critical condition for the ignition.

The condition leading to ignition is traced back to van't Hoff and described in 2 different ways.

First, the condition for ignition is given as a zero temperature gradient at the hot surface, r_s ,

$$\left. \frac{dT}{dr} \right|_{r=r_s} = 0. \quad (\text{E.5})$$

Second, as given by Semenov (1940) the point

“at which the plate does not lose heat and all the heat cold plate will be generated by the reaction taking place in a relatively narrow zone, ζ , near the hot plate.”

This can be expressed by considering that the gas temperature at the wall is slightly higher than the wall itself and the heat transfer into the wall is equal to the heat transfer out of the gas

$$-k \left. \frac{dT_{gas}}{dx} \right|_{x=0} = h(T_w - T_{gas}(x=0)) \quad (\text{E.6})$$

where k is the conductivity of the gas and h is the conductivity of the wall.

The energy equation (E.4) can be integrated across the small boundary near the heated wall by first multiplying through by dT/dx and integrating with respect to x :

$$- \int_0^\zeta \frac{dT}{dx} \frac{d^2T}{dx^2} dx = \int_0^\zeta \frac{QA}{k} \exp\left(-\frac{E_a}{\tilde{R}T_1}\right) \exp\left(-\frac{E_a(T_1 - T)}{\tilde{R}T_1^2}\right) \frac{dT}{dx} dx. \quad (\text{E.7})$$

The left-hand side can be simplified and the right-hand side can be reduced to an integration with respect to temperature:

$$- \int_0^\zeta \frac{1}{2} \frac{d}{dx} \left(\frac{dT}{dx} \right)^2 dx = \int_{T_1}^{T_e} \frac{QA}{k} \exp\left(-\frac{E_a}{\tilde{R}T_1}\right) \exp\left(-\frac{E_a(T_1 - T)}{\tilde{R}T_1^2}\right) dT. \quad (\text{E.8})$$

$$\left(\frac{dT}{dx} \right)^2 \Big|_{x=0} - \left(\frac{dT}{dx} \right)^2 \Big|_{x=\zeta} = \frac{2QA\tilde{R}T_1^2}{kE_a} \exp\left(-\frac{E_a}{\tilde{R}T_1}\right) \left(1 - \exp\left(-\frac{E_a(T_1 - T)}{\tilde{R}T_1^2}\right) \right) \quad (\text{E.9})$$

The gradient at $x = \zeta$ is zero and the first term dominates the right-hand side in the regime of interest (Semenov, 1940, Laurendeau, 1982)

$$\left(\frac{dT}{dx} \right) \Big|_{x=0} = \sqrt{\frac{2QA\tilde{R}T_1^2}{kE_a} \exp\left(-\frac{E_a}{\tilde{R}T_1}\right)}. \quad (\text{E.10})$$

Semenov (1940) gives the example of the a flammable gas between two plate, one hot at an elevated temperature T_1 , and one cold at T_0 . Considering only conduction, the temperature gradient is equal

to the temperature difference divided by the distance between the plates, d .

$$\frac{dT}{dx} = \frac{T_1 - T_0}{d} \quad (\text{E.11})$$

So the ignition temperature T_1 can be related to the distance between two plates or equivalently to the size of a heated vessel (Frank-Kamenetskii, 1969, Kuchta et al., 1965).

$$d = \sqrt{\frac{kE_a (T_1 - T_0)^2}{2QA\tilde{R}T_1^2} \exp\left(\frac{E_a}{\tilde{R}T_1}\right)} \quad (\text{E.12})$$

For ignition from hot spheres and wires a similar argument can be made. Consider a small hot sphere of radius R_S , which is inside a large vessel of radius, R_V ($R_V \gg r$), filled with flammable gas.

“By assuming that the zone within which the reaction occurs extends to a distance $[\xi]$ from the surface of the sphere very much less than the radius of the sphere the problem, to an accuracy sufficient for our purposes, is reduced to the parallel plate case just considered.” (Semenov, 1940)

The heat flux due to the chemical energy generated in the reaction zone is given by

$$\tilde{Q}_{\text{chem}} = 4\pi (R_S + \xi) \sqrt{\frac{2QA\tilde{R}T_1^2}{kE_a} \exp\left(-\frac{E_a}{\tilde{R}T_1}\right)}. \quad (\text{E.13})$$

Outside the reaction zone, ξ , the temperature distribution is the same as for a non-reacting mixture, and given as function of the radial distance, r ,

$$T - T_0 = \frac{(T_1 - T_0)(R_S + \xi)}{r}. \quad (\text{E.14})$$

The heat flux through a sphere of radius $R_S + \xi$ is

$$\tilde{Q}_{\text{loss}} = 4\pi k (T_1 - T_0) (R_S + \xi). \quad (\text{E.15})$$

Equating the heat release and loss flux, the relationship for ignition temperature for heated spheres

is given by Semenov (1940) to be

$$R_S = \left(\frac{E_a k (T_1 - T_0)^2}{2R_V T_1^2 Q A \exp(-E_a/(\tilde{R}T_1))} \right)^{1/2}. \quad (\text{E.16})$$

Similarly, Semenov arrives at the following relationship for the ignition temperature as a function of radius for heated wires of radius R_W ,

$$R_W \ln \frac{R_V}{R_W} = \left(\frac{E_a k (T_1 - T_0)^2}{2R_V T_1^2 Q A \exp(-E_a/(\tilde{R}T_1))} \right)^{1/2}. \quad (\text{E.17})$$

Kuchta et al. (1965) simplifies this relationship by assuming that the exponential term dominates and expands the left-hand side and keeping only the leading order term,

$$r \sim \exp\left(\frac{E_a}{2\tilde{R}T_1}\right). \quad (\text{E.18})$$

Taking the natural logarithm of both sides yields

$$\ln r \sim \frac{1}{T_1} \quad (\text{E.19})$$

which Kuchta et al. (1965) used to fit part of their data.

It seems that Kuchta et al. (1965) extended this relationship from the radius of the wire to the surface area by assuming a constant length and thus giving a linear relationship between the surface area and radius.

$$A = 2\pi r L \quad (\text{E.20})$$

The results obtained in the current study are compared to the data and fit in Section 3.4.5 (see Figure 3.26). The data presented in Section 3.4.5 is limited to the lowest temperature observed as the equivalence ratio is varied. The higher ignition temperature near lower and upper flammability limit are not shown. For completeness all ignition data collected at various pressure and equivalence ratios is given in Figure E.1. We can observe some overlap with the historical data, but while the fit shown captures the overall trend of increasing the hot surface temperature required for ignition as the size of the hot surface decreases, it is insufficient in capturing the lowest temperature observed in this study. We would like to stress that control over composition, pressure as well as careful characterization of the hot surface temperature and geometry are necessary to fully assess safety

hazards stemming from hot surfaces in contact with flammable mixtures.

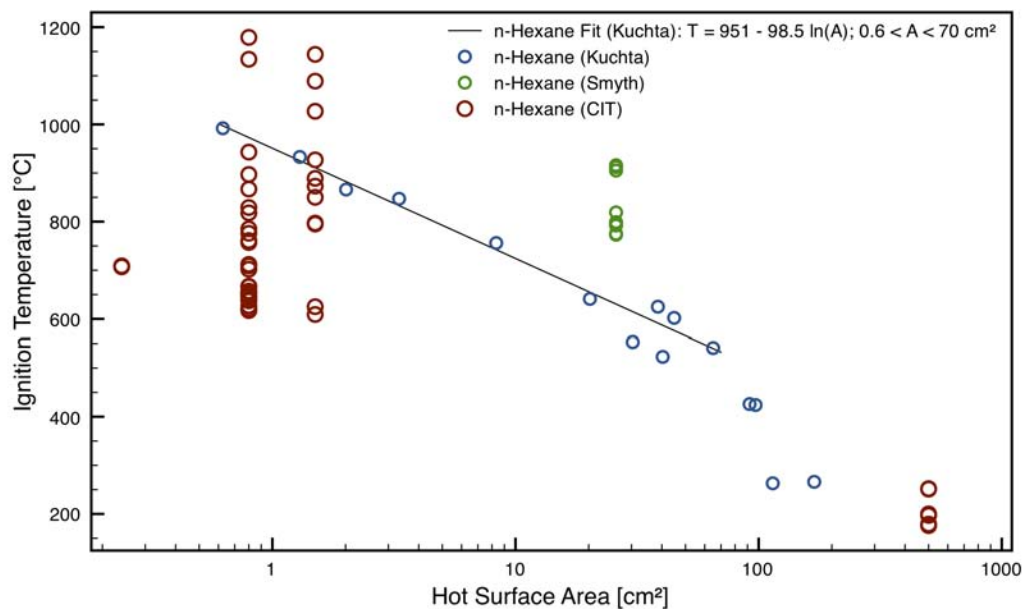


Figure E.1: Ignition as a function of hot surface size (uncertainty in ignition temperature for CIT measurements is +110 K). Range in values for CIT measurements is due to a range of compositions and initial pressure.

This page intentionally left blank.

Appendix F

Flame Propagation

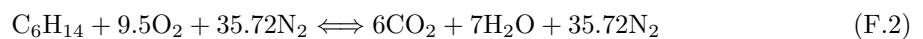
F.1 Introduction

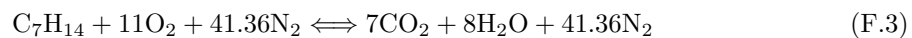
A limited amount of data is available for the flame and burning speed of *n*-hexane-air mixtures. Davis and Law (1998b) used a counterflow twin flame burner to systematically eliminate the effects of flame stretch. Kelley et al. (2011) performed experiments in a double-chambered vessel, basically eliminating the pressure rise during the flame propagation, while using schlieren visualization of the flame propagation and nonlinear extrapolation to the laminar burning speed to account for the effects of flame stretch. The accuracy of the mixture composition is verified using a gas chromatograph and flame ionization detector (Kelley et al., 2011). The range of equivalence ratios that can be investigated using this technique is limited due to the onset of hydrodynamic instabilities and thus at atmospheric pressure no flame speed data is available for equivalence ratios larger than $\phi = 1.7$ (Kelley et al., 2011).

At the current stage, the CaltechMech (Blanquart, 2011) has validated flame speeds for *n*-heptane only. In the simulations performed using the FlameMaster software (Pitsch and Bollig, 1994) *n*-heptane is substituted for *n*-hexane, which creates a slightly different mixture composition for complete oxidation as shown in Equations F.2 and F.3 and thus the results are shown as a function of equivalence ratio ϕ , where

$$\phi = \frac{N_{\text{fuel}}/N_{\text{oxidizer}}}{(N_{\text{fuel}}/N_{\text{oxidizer}})_{\text{stoichiometric}}} . \quad (\text{F.1})$$

The balanced chemical equation give the stoichiometric ratio for *n*-hexane and *n*-heptane oxidation in air.





F.2 Flame Propagation Speed as a Function of Composition

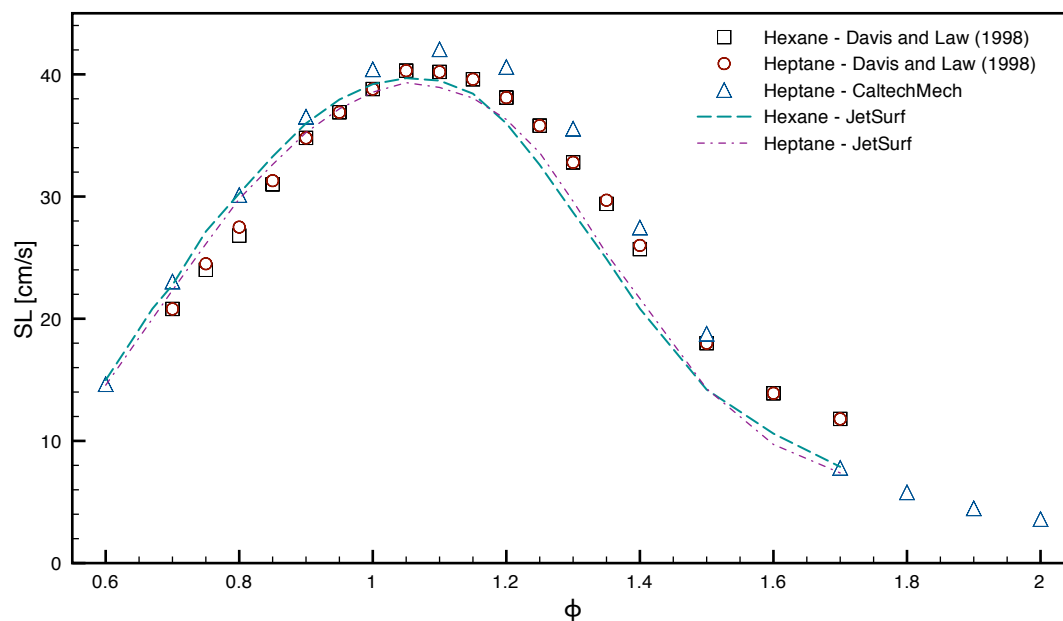


Figure F.1: Laminar burning velocity at room temperature and atmospheric pressure for *n*-hexane and *n*-heptane (Davis and Law (1998b), JetSurF results from Wang et al. (2010))

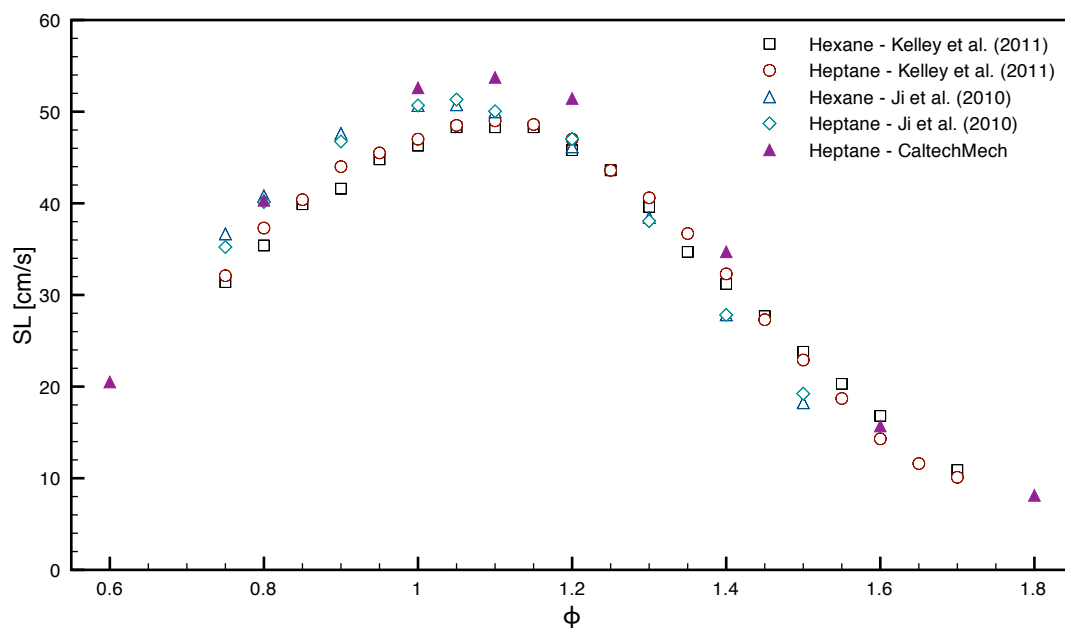


Figure F.2: Laminar burning velocity at 353 K and atmospheric pressure for *n*-hexane and *n*-heptane Kelley et al. (2011), Ji et al. (2010)

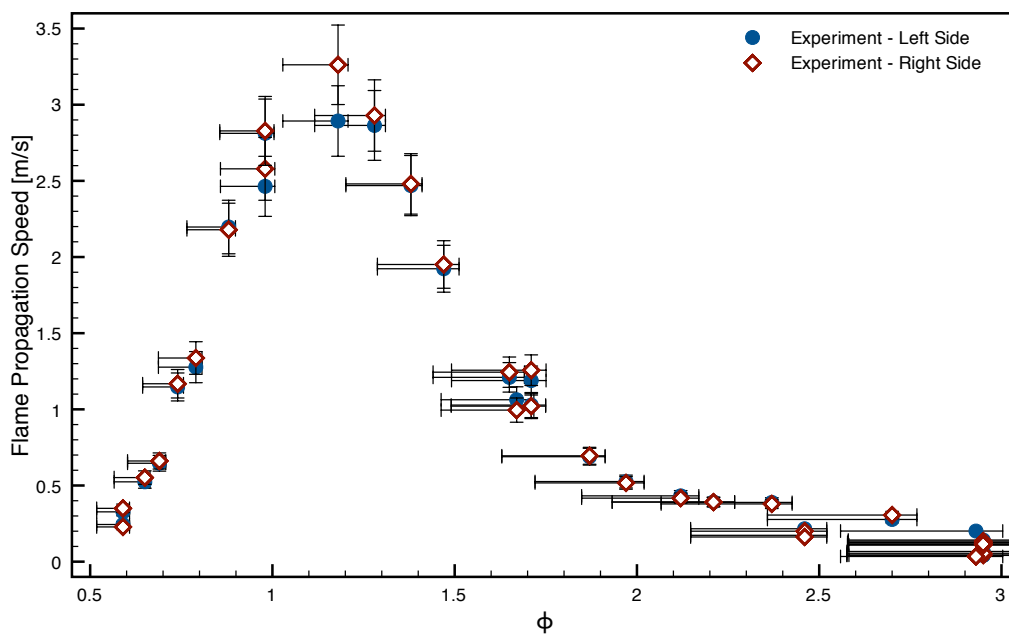


Figure F.3: Experimental flame propagation speed on the left and right side with measurement uncertainties. Initial pressure is one atmosphere with the mixture at room temperature (294 K).

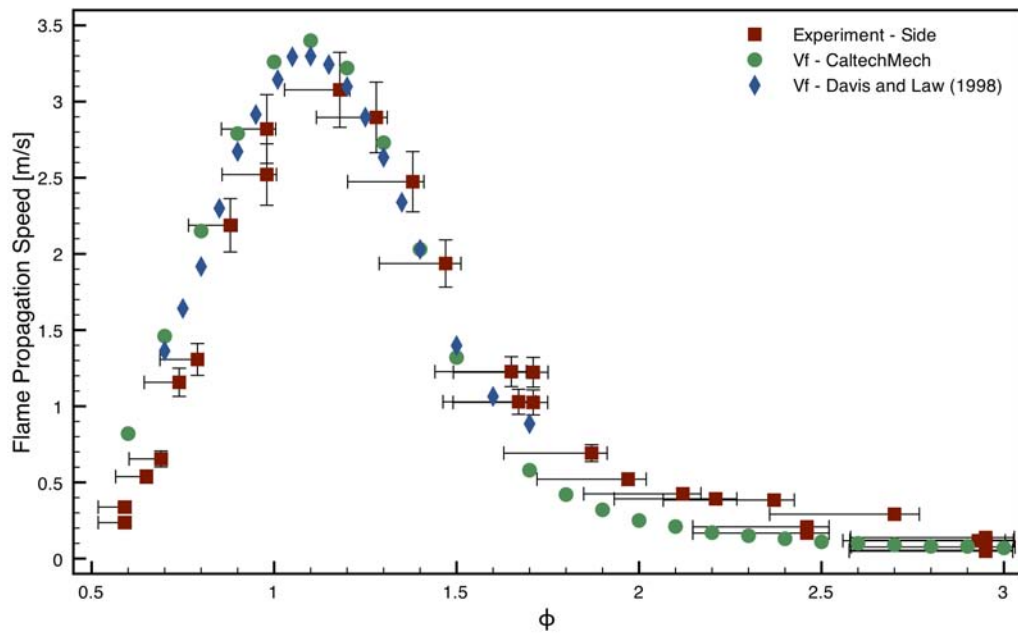


Figure F.4: Flame propagation speed at room temperature and atmospheric pressure including the estimated flame propagation speed from Davis and Law (1998b) calculated by multiplying the the laminar burning velocity by the expansion ratio obtained by equilibrating the mixture at constant pressure using the thermodynamic data from the Ramirez mechanism (Ramirez et al., 2011)

F.3 Tabular Flame Speed Data

Table F.1: Laminar burning velocity (s_L) for n -hexane and n -heptane at atmospheric pressure ($P_0 = 101$ kPa), room temperature ($T_u = 300$ K) digitized from Davis and Law (1998b) and at elevated temperature ($T_u = 353$ K) digitized from Kelley et al. (2011) and Ji et al. (2010)

ϕ	$T_u = 300$ K		$T_u = 353$ K		$T_u = 353$ K	
	Davis and Law (1998b)		Kelley et al. (2011)		Ji et al. (2010)	
	n -hexane S_l (cm/s)	n -heptane S_l (cm/s)	n -hexane S_l (cm/s)	n -heptane S_l (cm/s)	n -hexane S_l (cm/s)	n -heptane S_l (cm/s)
0.75	23.98	24.52	31.44	32.14	36.66	35.23
0.80	26.82	27.54	35.40	37.25	40.81	40.16
0.85	30.96	31.30	39.85	40.43	-	-
0.90	34.79	34.79	41.58	43.95	47.61	46.75
0.95	36.89	36.89	44.80	45.45	-	-
1.00	38.82	38.82	46.29	46.95	50.66	50.68
1.05	40.28	40.28	48.27	48.54	50.75	51.32
1.10	40.18	40.18	48.27	48.99	49.98	50.04
1.15	39.62	39.62	48.27	48.55	-	-
1.20	38.05	38.05	45.79	46.97	46.16	47.02
1.25	35.84	35.84	43.56	43.63	-	-
1.30	32.80	32.80	39.60	40.55	38.44	38.06
1.35	29.35	29.66	34.65	36.69	-	-
1.40	25.67	25.98	31.19	32.29	27.83	27.82
1.45	-	-	27.72	27.28	-	-
1.50	17.97	17.97	23.76	22.88	18.23	19.23
1.55	-	-	20.30	18.75	-	-
1.60	13.91	13.91	16.83	14.26	-	-
1.65	-	-	-	11.62	-	-
1.70	11.78	11.78	10.89	10.13	-	-

F.4 Tabular Expansion Ratio Data

Table F.2: Expansion ratio for *n*-hexane and *n*-heptane at atmospheric pressure ($P_0 = 101$ kPa), room temperature ($T_u = 300$ K) computed using the thermodynamic data from the Ramirez mechanism (Ramirez et al., 2011)

<i>n</i> -hexane			<i>n</i> -heptane		
ϕ	ϵ	ϵ	ϕ	ϵ	ϵ
0.55	5.53	5.55	1.80	7.38	7.46
0.60	5.88	5.90	1.85	7.31	7.39
0.65	6.21	6.24	1.90	7.24	7.32
0.70	6.54	6.57	1.95	7.17	7.25
0.75	6.85	6.88	2.00	7.09	7.18
0.80	7.15	7.18	2.05	7.02	7.11
0.85	7.43	7.46	2.10	6.94	7.03
0.90	7.68	7.72	2.15	6.87	6.96
0.95	7.90	7.94	2.20	6.79	6.88
1.01	8.10	8.14	2.25	6.71	6.81
1.05	8.18	8.22	2.30	6.63	6.73
1.10	8.21	8.25	2.35	6.55	6.65
1.15	8.19	8.23	2.40	6.47	6.57
1.20	8.14	8.19	2.45	6.39	6.49
1.25	8.09	8.14	2.50	6.31	6.41
1.30	8.03	8.09	2.55	6.22	6.33
1.35	7.97	8.03	2.60	6.14	6.24
1.40	7.91	7.97	2.65	6.05	6.16
1.45	7.85	7.91	2.70	5.96	6.07
1.50	7.78	7.85	2.75	5.88	5.99
1.55	7.72	7.79	2.80	5.79	5.90
1.60	7.65	7.72	2.85	5.70	5.81
1.65	7.58	7.66	2.90	5.62	5.73
1.70	7.52	7.59	2.95	5.55	5.66
1.75	7.45	7.52	3.00	5.49	5.60

Appendix G

Thermal Plume Scaling

We follow the arguments by Tritton (1988) to determine the thermal plume properties above the hot surface before ignition occurs. For steady flows without chemical reaction and with changes in density that are negligible except for when they create a buoyancy force (Boussinesq approximation), the following hold true for changes in density, continuity, momentum, and energy balance.

$$\Delta\rho = -\alpha\rho_0\Delta T \quad (\text{G.1})$$

$$\frac{\partial u_i}{\partial x_i} = 0 \quad (\text{G.2})$$

$$u_j \frac{\partial u_i}{\partial x_j} = -\frac{1}{\rho} \frac{\partial P}{\partial x_i} - \nu \frac{\partial^2 u_i}{\partial x_j^2} - g\hat{k}\alpha\Delta T \quad (\text{G.3})$$

$$u_j \frac{\partial T}{\partial x_j} = \kappa \frac{\partial^2 T}{\partial x_j^2} \quad (\text{G.4})$$

Neglecting pressure gradients, the inertial, viscous, and buoyancy terms are of the same magnitude in a laminar plume. In the vertical direction (z, \hat{k}), this gives the following scaling:

$$\frac{w_{max}^2}{z} \sim \frac{\nu w_{max}}{\delta^2} \sim g\alpha\Delta T \quad (\text{G.5})$$

where w_{max} is the maximum vertical velocity in the plume, δ is the width of the plume, and z is the height above the plume. For a plume that is created from a small hot wire the maximum vertical velocity, w_{max} , and the maximum temperature difference, ΔT_{max} , occur along the centerline. From Equation G.5, the scaling of w_{max} and δ can be found as a function of the height above the source, z ,

$$w_{max} \sim [g\alpha\Delta T z]^{1/2} \propto z^{1/2} \quad (\text{G.6})$$

$$\delta \sim \left[\frac{\nu^2 z}{g\alpha\Delta T} \right]^{1/4} \propto z^{1/4} \quad (\text{G.7})$$

The thermal plume behaves similarly to a jet, where vertical momentum is a conserved quantity at any cross section of the jet along its axis. For the thermal plume, the energy flux is conserved and the vertical momentum increases with distance due to buoyancy. Drawing a control volume around the source, \dot{Q} , and plume and applying energy conservation, we find that the quantity

$$\int_{CV} h\rho u_i n_i dA = \dot{Q} \quad (\text{G.8})$$

is constant.

While we have a source of energy, there is not mass source and thus

$$\int_{CV} \rho u_i n_i dA = 0 \quad (\text{G.9})$$

which by multiplying both sides by the the constant h_0 , the enthalpy outside the plume gives

$$\int_{CV} h_0 \rho u_i n_i dA = 0. \quad (\text{G.10})$$

Subtracting equation G.10 from G.8 and applying $h = c_p T$ gives

$$\int_{CV} c_p (T - T_0) \rho u_i n_i dA = \dot{Q} = \text{const.} \quad (\text{G.11})$$

This equation must hold true for any control volume that includes the plume and source and thus

$$\frac{d}{dz} \int_{CV} c_p (T - T_0) \rho u_i n_i dA = 0. \quad (\text{G.12})$$

For the equation above to hold true, the integrand must be constant with respect to z , which implies

$$c_p \Delta T \rho w \delta \sim \text{constant} . \quad (\text{G.13})$$

Using the scalings in Equation G.5

$$w \sim \frac{\nu z}{\delta^2} \quad (\text{G.14})$$

$$\Delta T \sim \frac{\nu^2 z}{\delta^4 g \alpha} \quad (\text{G.15})$$

gives

$$\frac{\nu^2 z}{\delta^4 g \alpha} \frac{\nu z}{\delta^2} \delta = \text{constant} , \quad (\text{G.16})$$

which simplifies to

$$\frac{z^2}{\delta^5} = \text{constant} . \quad (\text{G.17})$$

If we suppose a power scaling for the width, δ , with height, z ,

$$\delta = z^m \quad (\text{G.18})$$

then $m = 2/5$ such that the left-hand side of Equation G.17 is constant. This means that the maximum temperature difference (at the centerline) ΔT_{max} , the maximum velocity w_{max} , and the width δ scale as follows with the height above the source, z .

$$\Delta T_{max} \sim z^{-3/5}, w_{max} \sim z^{1/5}, \delta \sim z^{2/5} \quad (\text{G.19})$$

With the temperature measurements taken using the thermocouple array, we can confirm the scaling of the temperature, ΔT , with height above the glow plug as shown Figure G.1. Due to the fact that the glow plug is an extended source, the scaling holds for the far field readings obtained further away from the glow plug.

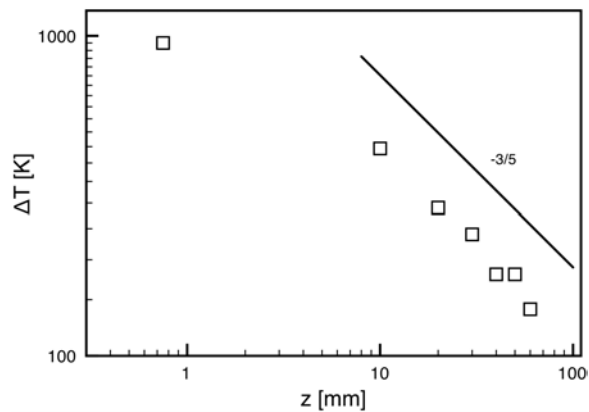


Figure G.1: Plume temperature scaling and thermocouple measurements taken using the thermocouple array.

This page intentionally left blank.

Appendix H

Refitting Thermodynamic Data ¹

Thermodynamic data, including specific heat, enthalpy and entropy for each species, are part of the chemical mechanism used to compute the ignition in the slowly heated vessel in Boettcher et al. (2011). In the thermodynamic data included as part of the mechanism published by Ramirez et al. (2011), many of the species have a discontinuity at the point where the low temperature fit connects to the high-temperature fit as shown in Figure H.1 for $C_2H_5CO_2$. These discontinuities are problematic for some numerical solvers and should be avoided.

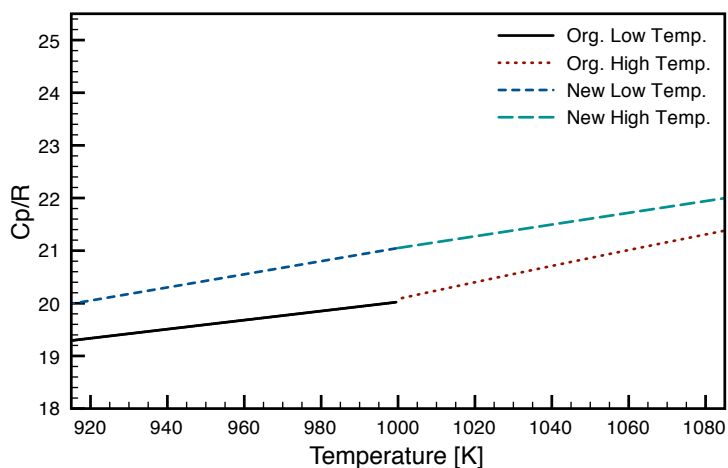


Figure H.1: Original thermodynamic data - c_p/R for $C_2H_5CO_2$

The NASA polynomial representation is used for complex equilibrium calculations as discussed by Gordon and McBride (1994). Further discussion of the polynomials and fitting is given in Shepherd et al. (2006)². For each species the data has two sets of seven coefficients, a_n for the low temperature regime and seven coefficients, b_n for the high-temperature regime. For example, the

¹The following work was based on a routine for fitting thermodynamic data created by Jack Ziegler and was finished with help from Vaughan Thomas, Rémy Mével, Jason Damazo, and Joseph Shepherd.

²<http://www.galcit.caltech.edu/EDL/public/cantera/doc/tex/ShockDetonation/ShockDetonation.pdf>

specific heat at low temperature is given by the following equation

$$\frac{c_p}{R} = \sum_{n=0}^4 a_n T^n . \quad (\text{H.1})$$

In this case we take the available fits and create new ones without discontinuities. The first step is to select the species whose polynomials require refitting and generating a data set based on the original fits. A choice has to be made about the step size in which to create the data set, which creates stable final polynomials. In this case data has been generated every 100 K and at the mid point the average of the high and low temperature is taken. Then a constrained least squares fitting of the data is performed while keeping the enthalpy of formation and formation entropy the same.

The new fit must maintain the original values of the enthalpy of formation, $\Delta_f h^\circ$, and the formation entropy, $s_o(T^\circ)$. Both of these quantities can be computed from the original data. The enthalpy is computed using the first 6 coefficients using the following equation

$$\frac{h}{RT} = \sum_{n=0}^4 \frac{a_n T^n}{n+1} + \frac{a_5}{T} , \quad (\text{H.2})$$

where

$$a_5 = \frac{\Delta_f h^\circ}{R} - \sum_{n=0}^4 \frac{a_n}{n+1} (T^\circ)^{n+1} . \quad (\text{H.3})$$

Thus to maintain the original values of $\Delta_f h^\circ$, it is computed from the initial data and we solve the following equation for the first five constants in the least squares fitting using

$$\left[\frac{h}{RT} - \frac{\Delta_f h^\circ}{RT} \right]_{\text{org}} = \sum_{n=0}^4 \frac{a_n}{n+1} \left[T^n - \frac{(T^\circ)^{n+1}}{T} \right] \quad (\text{H.4})$$

and then Equation H.3 for a_5 .

The entropy is computed from Equations H.5 and H.6.

$$\frac{s_o}{R} = a_0 \ln(T) + \sum_{n=1}^4 \frac{a_n T^n}{n} + a_6 \quad (\text{H.5})$$

$$a_6 = \frac{s_o(T^\circ)}{R} - \left(a_0 \ln(T^\circ) + \sum_{n=1}^4 \frac{a_n (T^\circ)^n}{n} \right) \quad (\text{H.6})$$

Similarly, to maintain the original value of $s_o(T^\circ)$, it is computed from the original data and we solve Equation H.7 in the least squares fitting

$$\left[\frac{s_o}{R} - \frac{s_o(T^\circ)}{R} \right]_{\text{org}} = a_0 \ln \left(\frac{T}{T^\circ} \right) + \sum_{n=1}^4 \frac{a_n (T^n - (T^\circ)^n)}{n}, \quad (\text{H.7})$$

and then solve for a_6 using Equation H.6.

The constrained least squares fitting was carried out with the following constraints applied for the two polynomials:

1. Match lowest and highest value of c_p/R
2. C^0 (continuous) c_p/R at mid point
3. C^1 (1st derivative continuous) c_p/R at mid point
4. Match lowest and highest value of $h/(RT)$
5. C^0 (continuous) $h/(RT)$ at mid point
6. C^0 (continuous) s_o/R at mid point.

The final result of the fitting in Figure H.2 shows the successful refit of the specific heat.

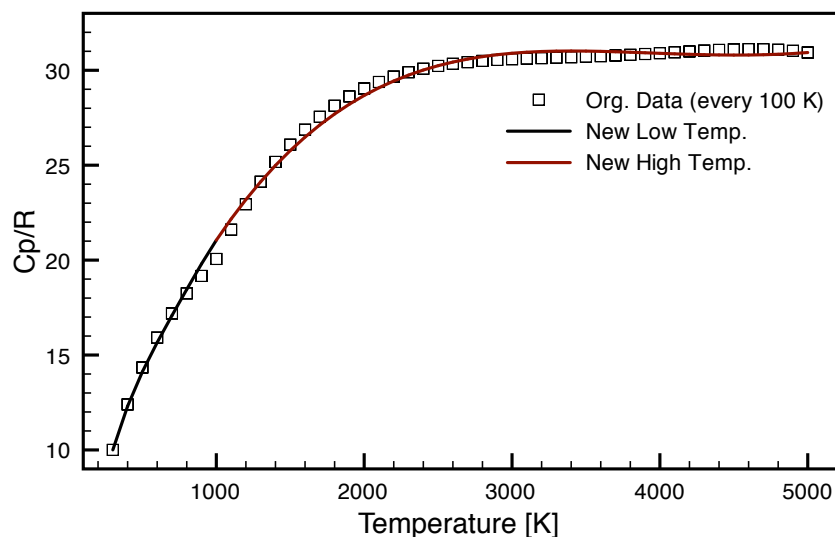


Figure H.2: New thermodynamic data - c_p/R for $\text{C}_2\text{H}_5\text{CO}_2$

In our current version the refitting is performed using MATLAB using the constrained linear least-squares solver `lsqlin` (MATLAB, 2010). The function solves the matrix equation $Ax = b$ using a minimization subject to the constraint equation $A_{eq}x = b_{eq}$. The `lsqlin` function is called in the following way:

`[x] = lsqlin(A, b, [], [], Aeq, beq, lb, ub, x0)`

During the first iteration the starting point is empty, $x_0 = []$. The least squares fitting is then called an additional 50 times in a loop using the previous result as the initial condition for the current iteration. The lower and upper bounds, `lb` and `ub`, are simply set at `-Inf` and `+Inf`.

The least square equation is set up such that x vector contains the new coefficients for the low temperature, a_n , and high temperature, b_n ,

$$x = [a_0, a_1, \dots, a_5, a_6, b_0, b_1, \dots, b_5, b_6] . \quad (\text{H.8})$$

The A matrix is arranged in the following way:

$$A = \begin{bmatrix} c_p/R \text{ in the low temperature range (M rows)} \\ c_p/R \text{ in the high temperature range (N rows)} \\ h/(RT) \text{ in the low temperature range (M rows)} \\ h/(RT) \text{ in the high temperature range (N rows)} \\ s_o/R \text{ in the low temperature range (M rows)} \\ s_o/R \text{ in the high temperature range (N rows)} \end{bmatrix} , \quad (\text{H.9})$$

where M is the number of elements in a vector spanning from the lowest temperature to the mid temperature in increments of 100 K, and N is the number of elements in a vector spanning from the mid temperature to the highest temperature in increments of 100 K.

For example, for the specific heat $Ax = b$ is

$$\begin{bmatrix} T_1^0 & T_1^1 & \cdots & T_1^4 & 0 & 0 & 0 & 0 & \cdots & 0 & 0 & 0 \\ \vdots & & & & & & & & & & & \\ T_{\text{mid}}^0 & T_{\text{mid}}^1 & \cdots & T_{\text{mid}}^4 & 0 & 0 & 0 & 0 & \cdots & 0 & 0 & 0 \\ 0 & 0 & \cdots & 0 & 0 & 0 & T_{\text{mid}}^0 & T_{\text{mid}}^1 & \cdots & T_{\text{mid}}^4 & 0 & 0 \\ \vdots & & & & & & & & & & & \\ 0 & 0 & \cdots & 0 & 0 & 0 & T_{\text{max}}^0 & T_{\text{max}}^1 & \cdots & T_{\text{max}}^4 & 0 & 0 \end{bmatrix} \begin{bmatrix} a_0 \\ a_1 \\ \vdots \\ a_4 \\ a_5 \\ a_6 \\ b_1 \\ b_2 \\ \vdots \\ b_4 \\ b_5 \\ b_6 \end{bmatrix} = \begin{bmatrix} \frac{c_p}{R} |_{\text{org @ } T_1} \\ \vdots \\ \frac{c_p}{R} |_{\text{org @ } T_{\text{mid}}} \\ \frac{c_p}{R} |_{\text{org @ } T_{\text{mid}}} \\ \vdots \\ \frac{c_p}{R} |_{\text{org @ } T_{\text{max}}} \end{bmatrix} . \quad (\text{H.10})$$

For the enthalpy and entropy equation the entries of b are the left-hand sides of Equations H.4 and H.7, respectively, computed from the original data.

The constrain equations are implemented in a similar way. For example, matching the specific heat at the mid point is constraint by the following equation:

$$\begin{bmatrix} T_{\text{mid}}^1 & T_{\text{mid}}^2 & \cdots & T_{\text{mid}}^4 & 0 & 0 & -T_{\text{mid}}^1 & -T_{\text{mid}}^2 & \cdots & -T_{\text{mid}}^4 & 0 & 0 \end{bmatrix} \begin{bmatrix} a_0 \\ \vdots \\ b_6 \end{bmatrix} = 0 . \quad (\text{H.11})$$

The final step is to compute the remaining error in the fit at the mid point, which in our example is 1×10^{-14} and thus sufficient for the solver. If the error is too large more iterations of the least square fitting should be performed.

This page intentionally left blank.

Appendix I

Experimental Data

I.1 Heated Vessel Ignition

A series of about 40 experiments were performed to study the ignition of *n*-hexane in air in a slowly heated vessel. The experimental conditions and results are summarized in Table I.1. Temperature and pressure traces as well as fuel concentration measurements are presented for selected shots.

As discussed in section 2.2 the temperature history was estimated from the pressure measurements. This is because the temperature is either measured with a thermocouple (K-type) at the outside of the glass vessel or internally at the end of a two-bore Pyrex tube with the bead coated. The two-bore Pyrex tube is heated and fused around the thermocouple. In order to avoid catalytic effects of the exposed end with the bead was encased in a thin layer of AREMCO-SEAL 4030, a silicone based high-temperature protective coating. While the layer around the bead is thin, the response time is still affected and the temperature measurements are not accurate for transient events.

The response time of the pressure transducer, however, is 10 μ s and therefore sufficient to capture all transients of the combustion event. For the experiments performed in the closed vessel we have no changes in volume at any time during the experiment. The measurements of the fuel concentration give a good indication of when the reaction starts. Before the reaction starts, we assumed that the number of moles is constant and ideal gas law will give following result.

$$PV = N\tilde{R}T \tag{I.1}$$

$$\frac{P}{T} = \frac{N\tilde{R}}{V} = k \tag{I.2}$$

The constant k can be determined from the initial temperature and pressure. This method can also

be used to find the final number of moles of gas based on the measured pressure and temperature, assuming equilibrium conditions after the reaction has been completed.

Note for shot 14: as it was one of the first shots performed in a new vessel, the target temperature of the heating system was set to around the ignition temperature. Due to the inertia of the system heating slowed down and when the reaction started the temperature oscillated around the ignition temperature. Hence, the effective heating rate is 0 K/min and no pressure rise was observed. The effective residence time that the gas spends above the temperature at which it ignites is 300 seconds (5 min).

Note for shot 17: laser absorption measurements during this test show reaction in two stages. The initial reaction starts at a temperature of 506 K and the partial pressure of fuel decreases linearly from 0.86 kPa to 0.82 kPa over the course of 65 seconds without noticeable pressure rise. The reaction then speeds up and produces a slight overpressure of 0.2 kPa.

Note for shot 18: laser oxygen diagnostic have significant interference in the windows, distorting the concentration measurements. Temperature measurements have error due to wire contact away from the thermocouple junction and can therefore not be used to normalize the etaloning.

Note for shot 20: we observe a fast reaction with overpressure, but only ~ 17 kPa.

Note for shot 26: the pressure transducer is destroyed during the ignition event because the flame is not quenched before it reaches the gage.

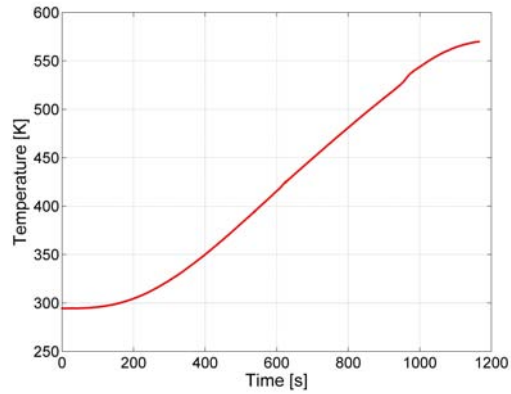
Note for shot 37 & 40: no temperature measurement available.

In the temperature measurements during the ignition events electrical noise from the 60 Hz switching of the AC power can be observed.

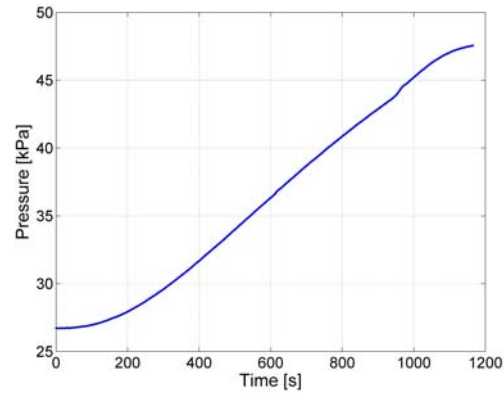
Table I.1: Heated vessel experiments

Shot	Date	$P_{n\text{-hexane}}$ [kPa]	P_{N_2} [kPa]	P_{O_2} [kPa]	P_{total} [kPa]	ϕ	$\Delta T/\Delta t$ [K/min]	Fuel Consumed %	Peak Overpressure [kPa]	Ignition Temperature [K]	Result
1	7/21/08	1.524	78.85	20.96	101.33	0.69	N/A	N/A	N/A	N/A	N/A
2	7/22/08	1.520	78.85	20.96	101.32	0.69	N/A	N/A	N/A	N/A	N/A
3	7/22/08	2.189	78.31	20.82	101.33	1.00	N/A	N/A	N/A	N/A	N/A
4	7/23/08	0.576	20.61	5.48	26.67	1.00	11 (8.3*)	65	0.24	542 (463*)	SR
5	7/23/08	2.189	78.31	20.82	101.32	1.00	N/A	N/A	N/A	N/A	N/A
6	7/24/08	2.176	99.14	0.0	101.31	0.00	N/A	N/A	N/A	N/A	N/A
7	7/25/08	1.440	51.53	13.63	66.66	1.00	14 (8.6*)	85.4	14.6	531 (452*)	FR
8	9/4/08	2.178	78.32	20.82	101.32	0.99	5	N/A	N/A	N/A	N/A
9	9/11/08	2.197	78.31	N/A	N/A	N/A	N/A	N/A	N/A	N/A	N/A
10	9/16/08	2.189	78.20	20.93	101.32	0.99	6	N/A	N/A	N/A	N/A
11	9/16/08	2.190	78.31	20.82	101.33	1.00	10	N/A	N/A	N/A	N/A
12	11/10/08	2.192	78.31	20.82	101.33	1.00	N/A	N/A	N/A	N/A	N/A
13	4/14/09	0.576	20.60	5.50	26.68	1.00	18	77	0.4	523	SR
14	4/19/09	2.189	78.31	20.82	101.32	1.00	0	60	0.0	506	SR
15	4/22/09	1.440	51.54	13.68	66.66	1.00	2	80	0.0	504	SR
16	5/19/09	1.440	51.68	13.56	66.67	1.01	11	N/A	0.7	550	SR
17	5/21/09	0.864	52.00	13.80	66.66	0.59	13	74	0.2	507	SR
18	5/29/09	0.692	20.63	5.35	26.66	1.23	N/A	N/A	0.1	N/A	SR
19	5/29/09	2.626	77.95	20.74	101.32	1.20	14	92	157.2	524	FR
20	6/15/09	1.725	51.30	13.21	66.23	1.24	15	73	16.7	525	FR
21	6/16/09	0.868	52.85	13.81	66.66	0.60	16	75	0.51	521	SR
22	6/22/09	1.013	79.27	21.08	101.36	0.46	11*	85	6.95	472*	SR
23	6/23/09	2.622	77.97	20.65	101.36	1.21	11*	93	329	470*	FR
24	6/24/09	2.618	78.01	20.69	101.36	1.20	5*	84	2.53	464*	SR
25	6/25/09	1.440	51.56	13.75	66.74	1.00	11*	78	1.03	471*	SR
26	6/26/09	2.189	80.30	21.12	103.71	0.98	14*	98	N/A	473*	FR
37	2/17/10	0.680	20.54	5.26	26.67	1.20	11*	74	0.2	470*	SR
40	3/17/10	1.440	51.53	13.69	66.66	1.00	10*	77	20	449*	FR

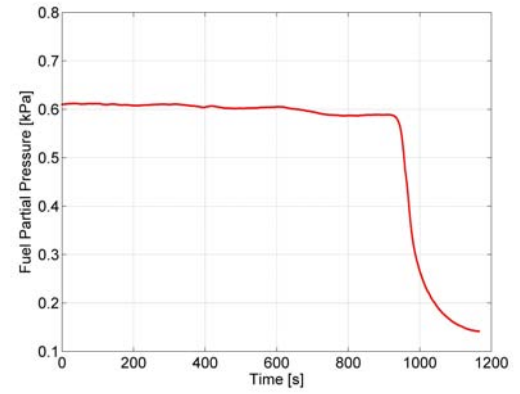
Notes: SR - Slow Reaction, FR - Fast Reaction, N/A - not available, * - estimated from pressure (see text)



(a) Temperature

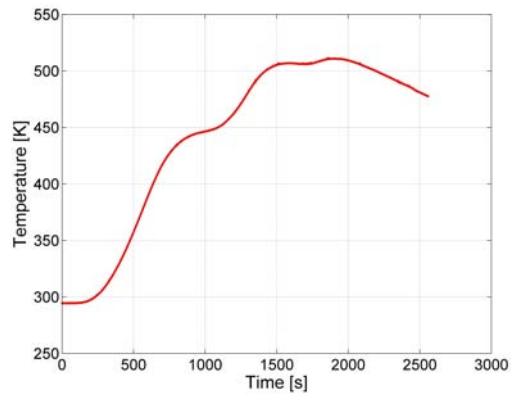


(b) Total pressure

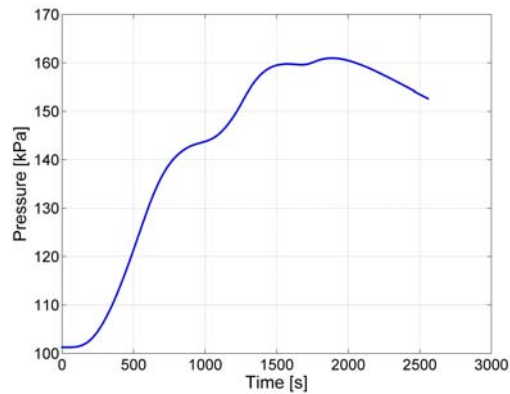


(c) Partial pressure of the fuel

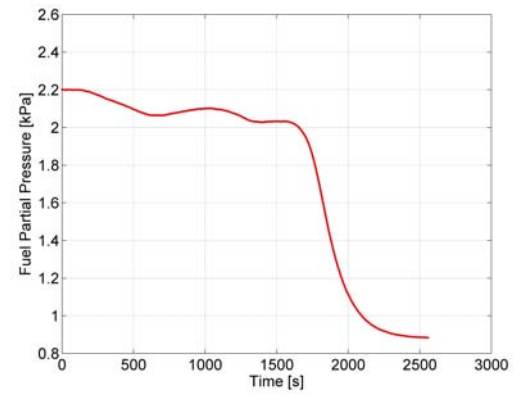
Figure I.1: Experimental data from shot 13



(a) Temperature

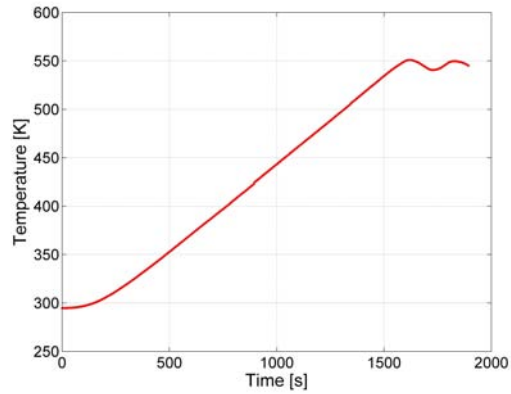


(b) Total pressure

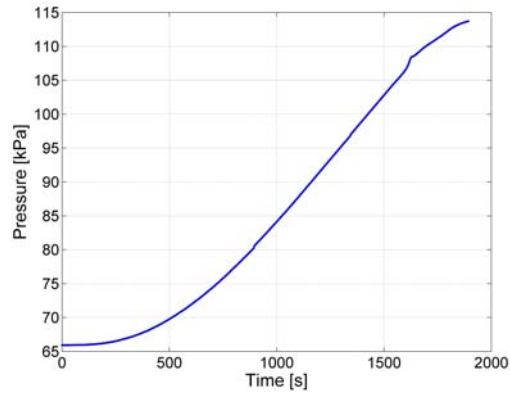


(c) Partial pressure of the fuel

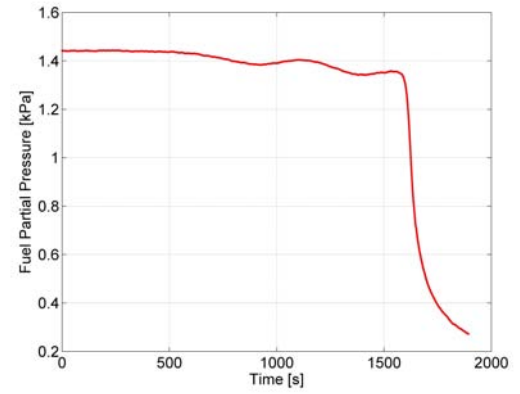
Figure I.2: Experimental data from shot 14



(a) Temperature

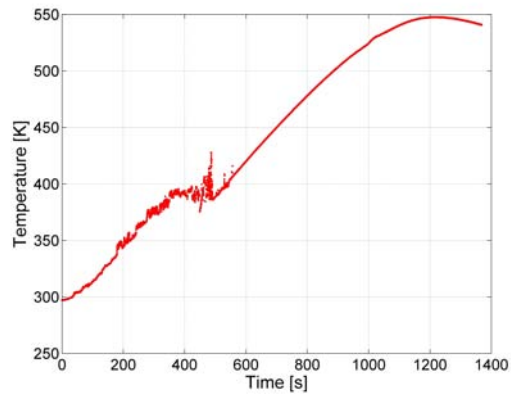


(b) Total pressure

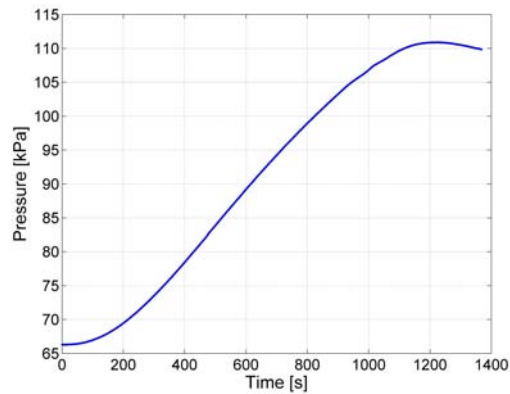


(c) Partial pressure of the fuel

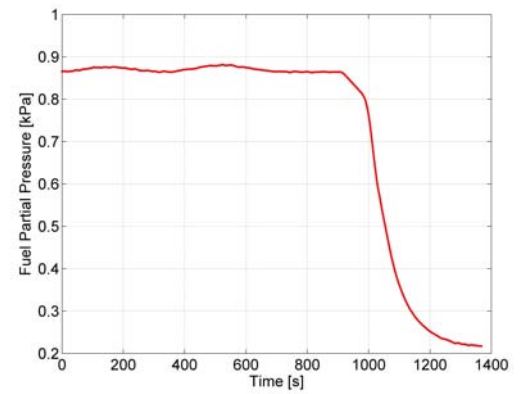
Figure I.3: Experimental data from shot 16



(a) Temperature

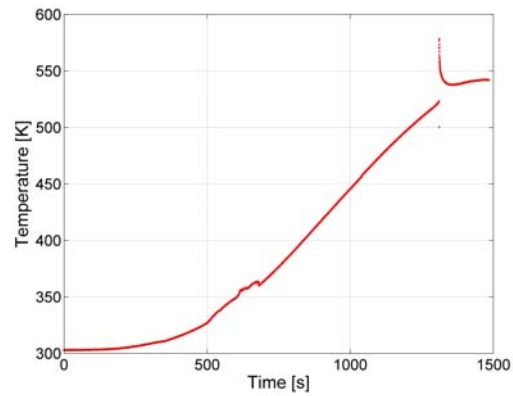


(b) Total pressure

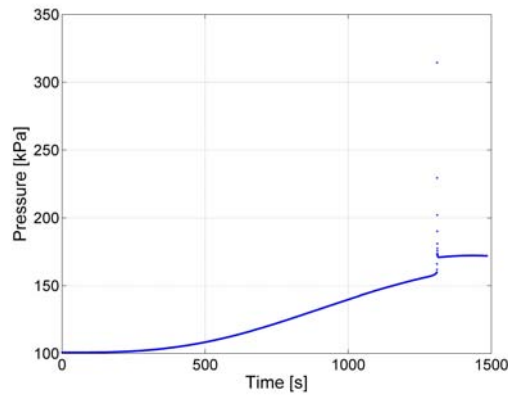


(c) Partial pressure of the fuel

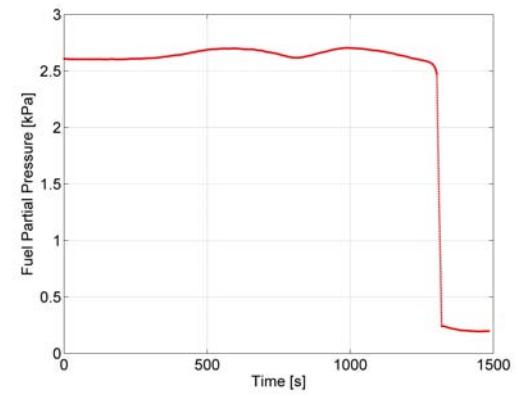
Figure I.4: Experimental data from shot 17



(a) Temperature

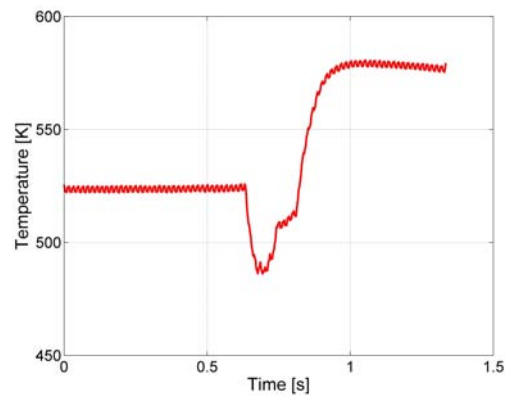


(b) Total pressure

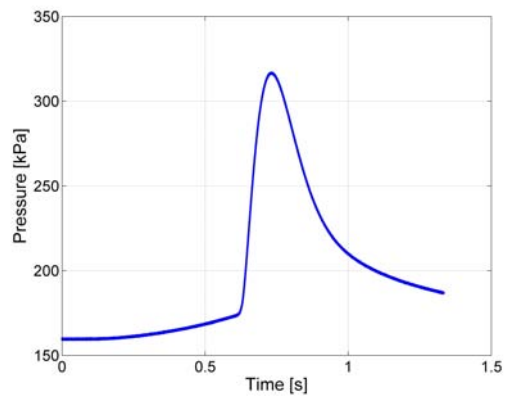


(c) Partial pressure of the fuel

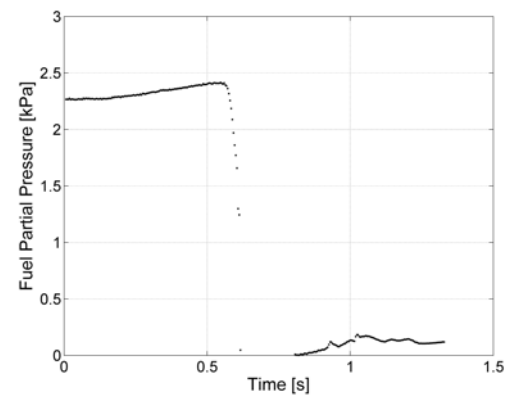
Figure I.5: Experimental data from shot 19



(a) Temperature

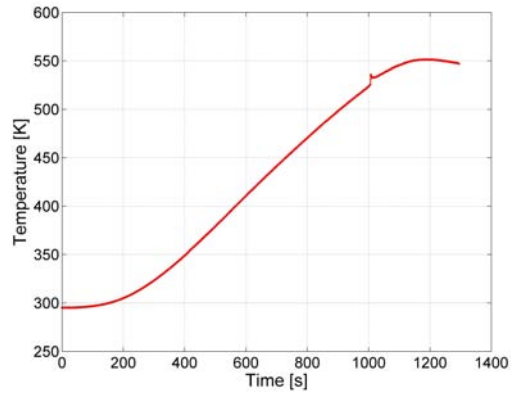


(b) Total pressure

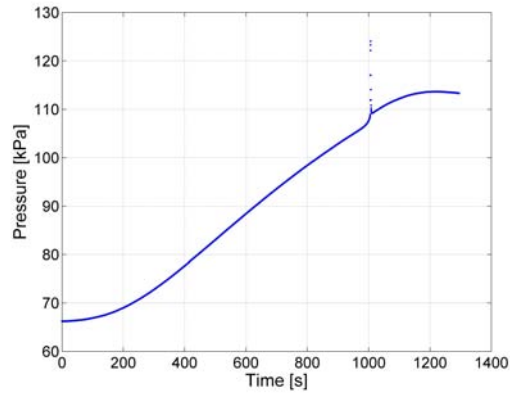


(c) Partial pressure of the fuel

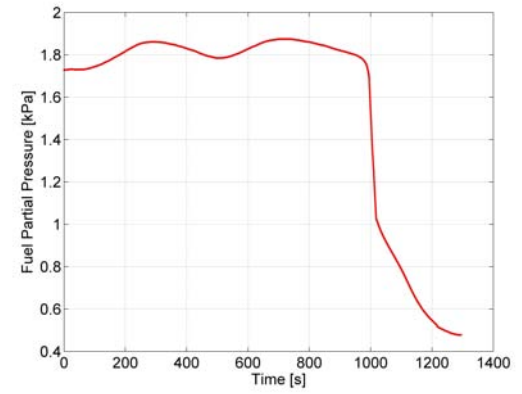
Figure I.6: Experimental data during the ignition event from shot 19



(a) Temperature

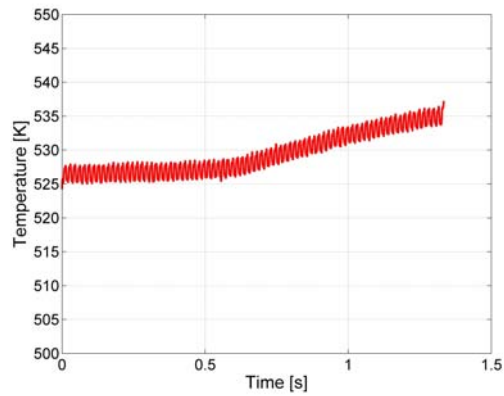


(b) Total pressure

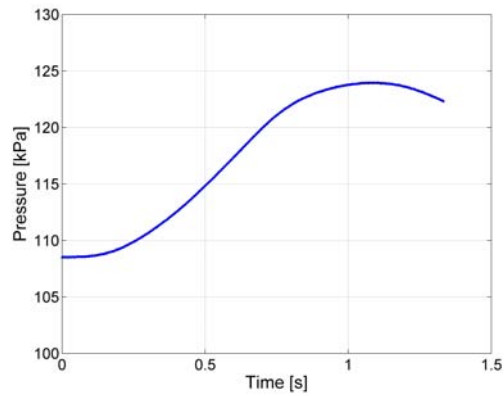


(c) Partial pressure of the fuel

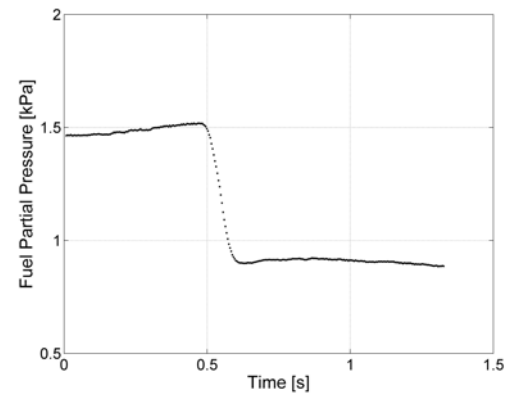
Figure I.7: Experimental data from shot 20



(a) Temperature

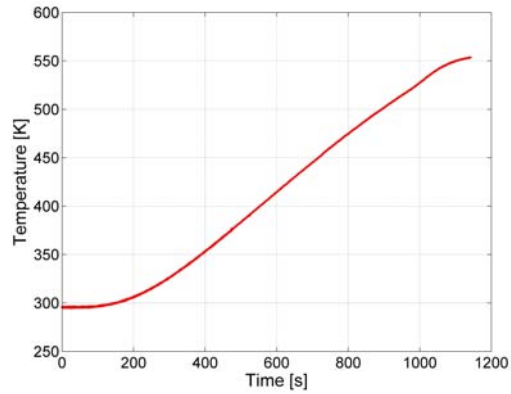


(b) Total pressure

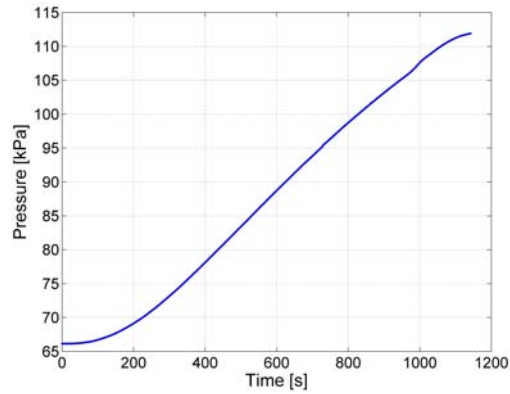


(c) Partial pressure of the fuel

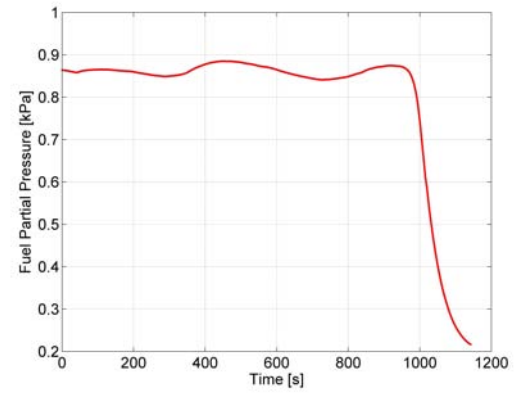
Figure I.8: Experimental data during the ignition event from shot 20



(a) Temperature

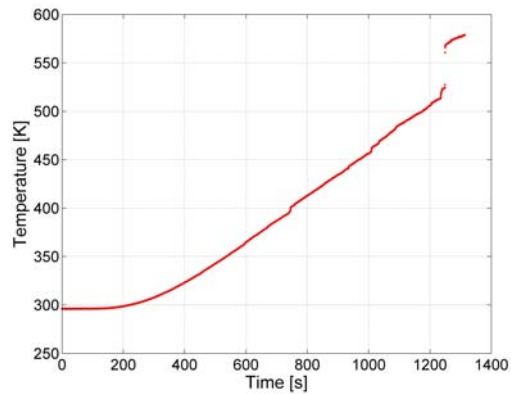


(b) Total pressure

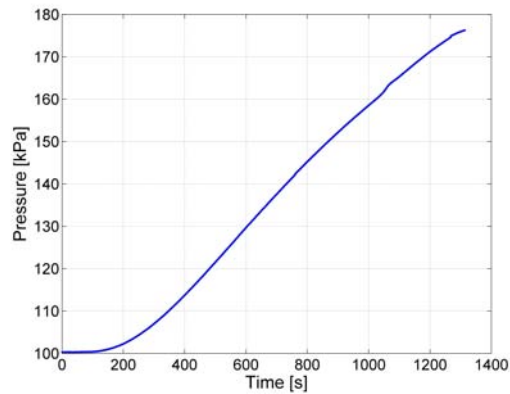


(c) Partial pressure of the fuel

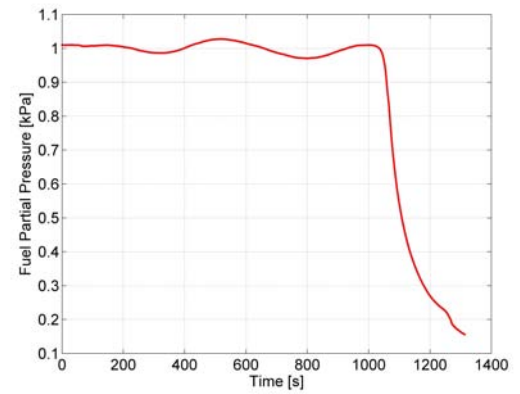
Figure I.9: Experimental data from shot 21



(a) Temperature

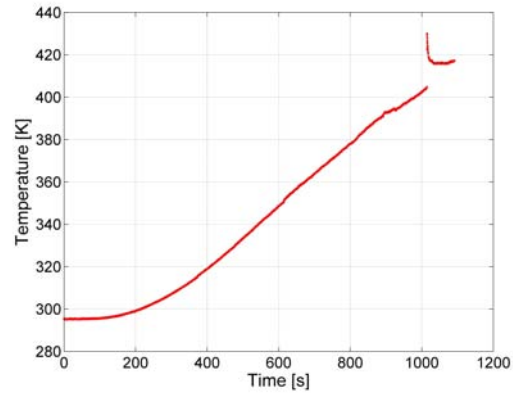


(b) Total pressure

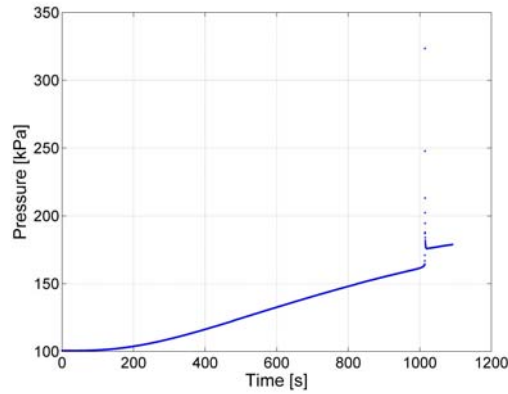


(c) Partial pressure of the fuel

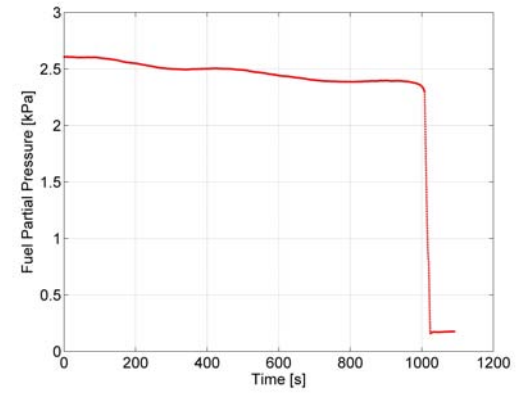
Figure I.10: Experimental data from shot 22



(a) Temperature

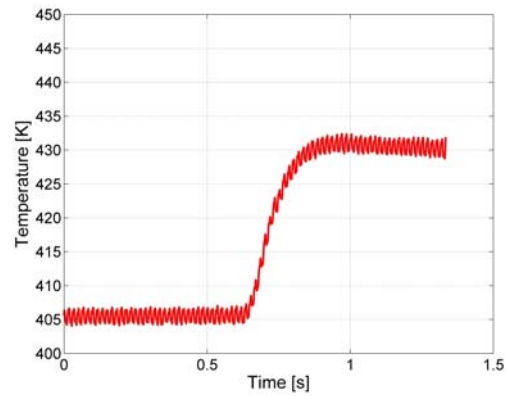


(b) Total pressure

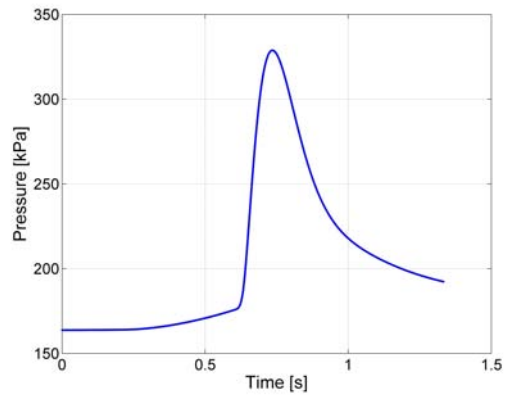


(c) Partial pressure of the fuel

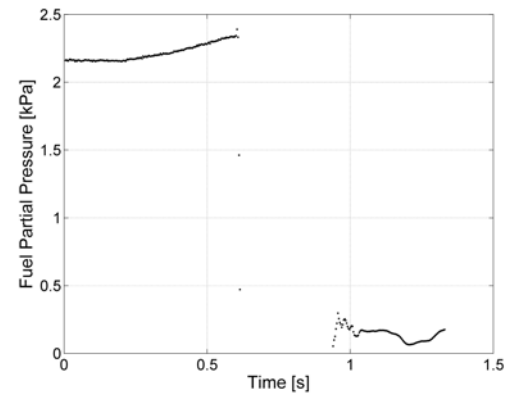
Figure I.11: Experimental data from shot 23



(a) Temperature

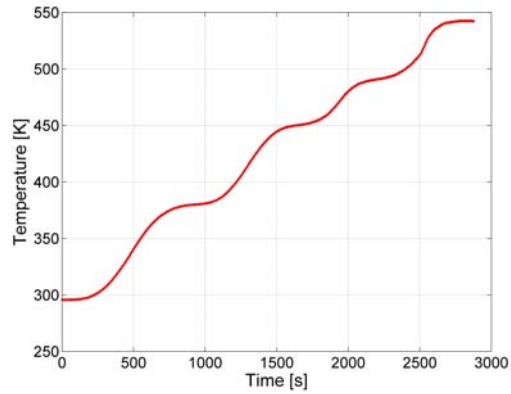


(b) Total pressure

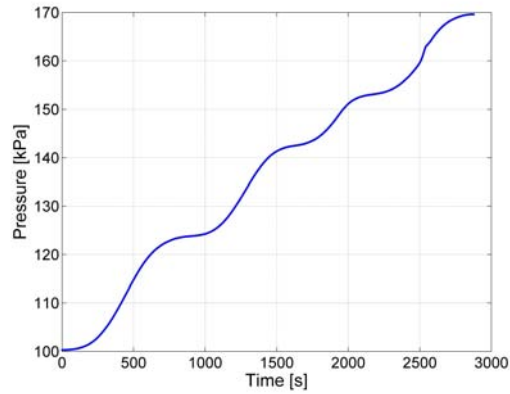


(c) Partial pressure of the fuel

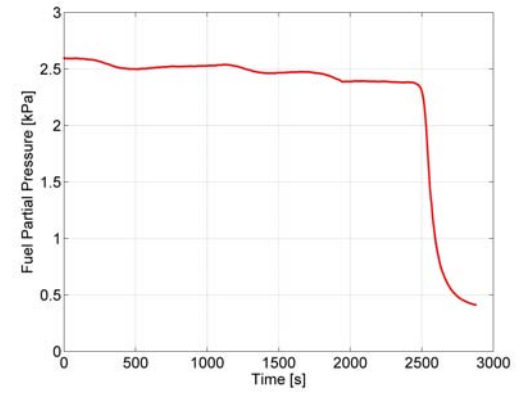
Figure I.12: Experimental data during the ignition from event shot 23



(a) Temperature

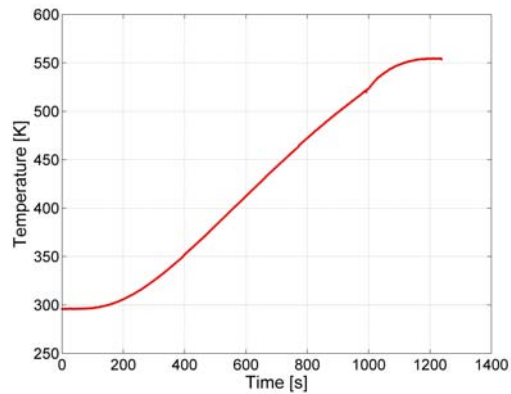


(b) Total pressure

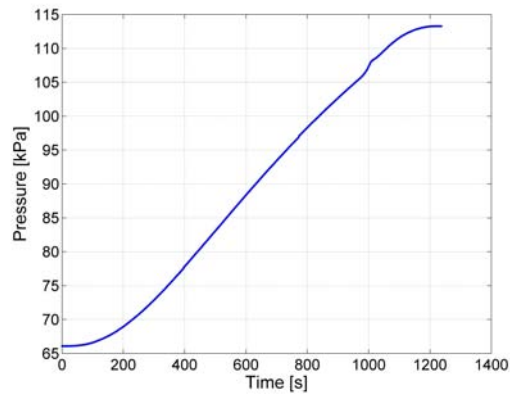


(c) Partial pressure of the fuel

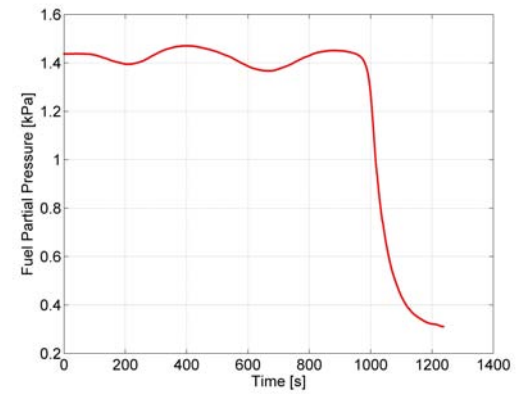
Figure I.13: Experimental data from shot 24



(a) Temperature

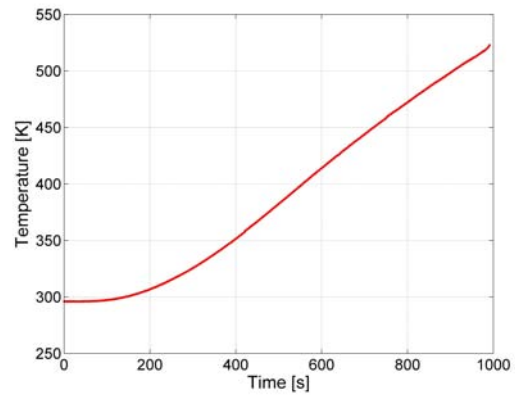


(b) Total pressure

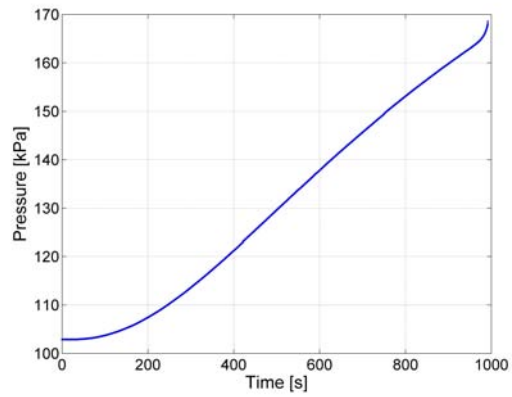


(c) Partial pressure of the fuel

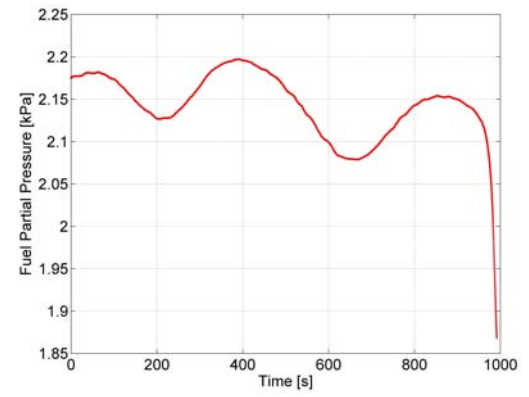
Figure I.14: Experimental data from shot 25



(a) Temperature



(b) Total pressure



(c) Partial pressure of the fuel

Figure I.15: Experimental data from shot 26

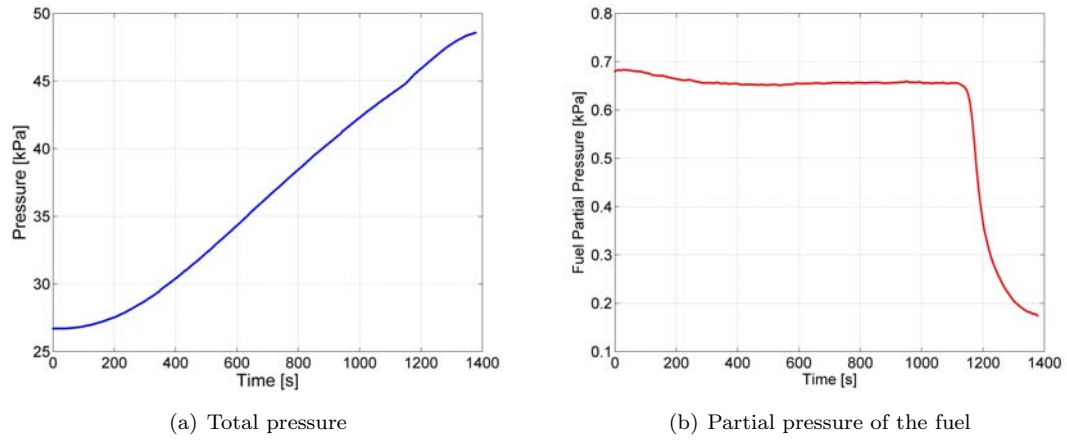


Figure I.16: Experimental data from shot 37

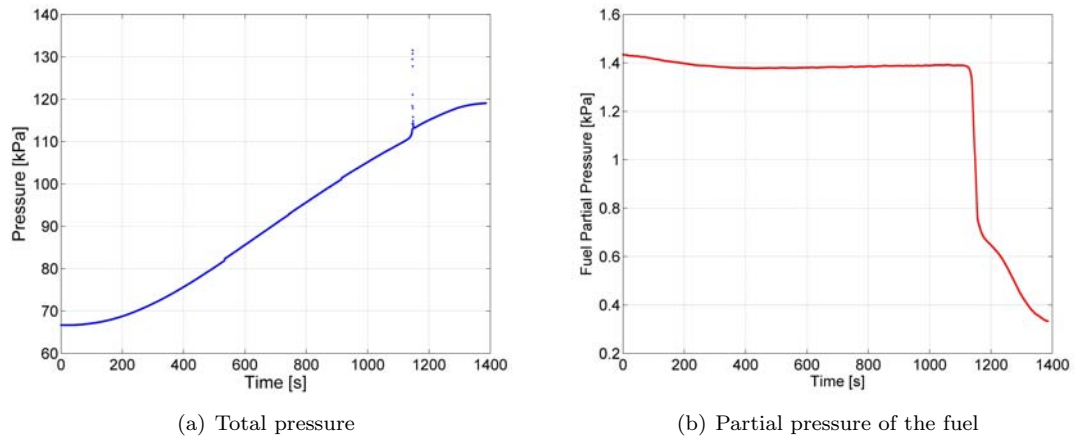


Figure I.17: Experimental data from shot 40

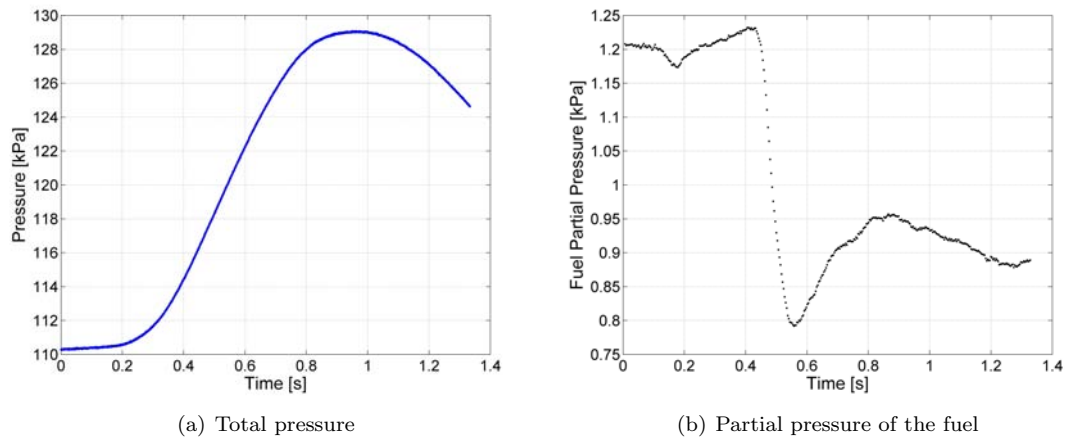


Figure I.18: Experimental data during the ignition event from shot 40

I.2 Hot Surface Ignition

This section includes the conditions for all hot surface experiments performed and also the reference spark ignition tests. In the cases where the vertical propagation velocity, V_F Top, is indicated as “not available”, but the flame propagation velocity on the sides, V_F Left & Right, are given, the top of the flame was not visible in the schlieren image. The accuracy of the pressure transducer used in filling the vessel was 0.1 Torr (0.01 kPa) and thus the composition is given to an accuracy of 2 decimal places. Temperature and pressure traces as well as schlieren images have been included for selected experiments.

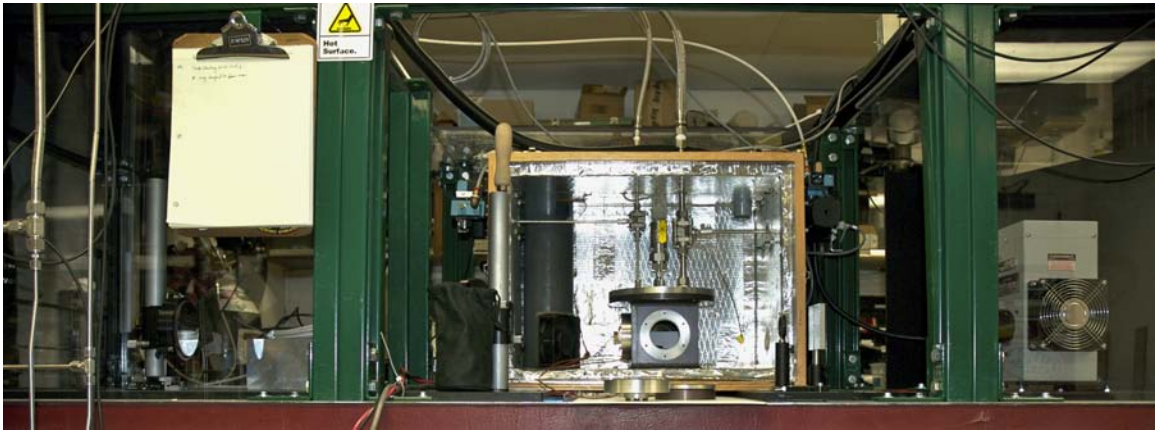


Figure I.19: The hot surface ignition vessel experimental setup.

Table I.2: Hot surface experiments with *n*-hexane using the Bosch glow plug in a 2 liter vessel

Shot	Date	P _{<i>n</i>-hexane} [kPa]	P _{N₂} [kPa]	P _{O₂} [kPa]	P _{total} [kPa]	ϕ	Peak Pressure [kPa]	Ignition Temperature [K]	V _F Left [m/s]	V _F Right [m/s]	V _F Top [m/s]	Note
6	3/24/10	3.75	77.09	20.49	101.32	1.74	N/A	N/A	1.36	1.40	3.67	
7	3/24/10	2.20	78.30	20.82	101.32	1.00	721.20	N/A	1.92	2.00	3.41	
8	3/30/10	3.75	77.07	20.50	101.32	1.74	755.70	N/A	1.03	1.02	3.20	
9	3/30/10	3.75	77.09	20.49	101.32	1.74	786.70	N/A	1.19	1.26	3.46	
10	4/9/10	3.75	77.09	20.49	101.32	1.74	794.81	1030	1.45	1.43	3.70	
11	4/9/10	3.69	77.41	20.22	101.32	1.73	804.03	1058	N/A	N/A	N/A	
12	4/21/10	3.69	77.13	20.50	101.32	1.71	795.00	930	N/A	N/A	N/A	
13	5/12/10	6.32	75.05	19.97	101.34	3.01	-	-	-	-	-	NoGo
14	5/12/10	5.31	75.86	20.16	101.32	2.50	381.91	N/A	N/A	N/A	N/A	$f = 9.19$ Hz
15	5/12/10	5.80	75.46	20.06	101.32	2.75	212.91	925	0.28	0.31	1.54	$f = 9.84$ Hz
16	5/13/10	6.31	75.06	19.96	101.32	3.00	N/A	N/A	N/A	N/A	N/A	
17	5/13/10	6.31	75.05	19.96	101.31	3.00	173.00	922	0.11	0.13	1.24	$f = 12.63$ Hz
18	5/13/10	1.65	78.73	20.93	101.31	0.75	N/A	N/A	N/A	N/A	N/A	
20	6/29/10	4.80	76.26	20.26	101.32	2.25	491.86	911	0.39	0.39	1.99	$f = 8.40$ Hz
21	6/30/10	5.12	75.99	20.21	101.32	2.41	406.30	911	0.39	0.38	1.91	
24	7/9/10	2.61	77.98	20.73	101.32	1.20	802.20	939	2.89	3.26	5.43	
25	7/12/10	1.65	78.73	20.93	101.31	0.75	648.00	917	1.15	1.17	2.41	
26	7/12/10	1.76	78.66	20.90	101.32	0.80	657.00	912	1.28	1.34	2.60	
27	7/12/10	1.96	78.47	20.88	101.31	0.89	N/A	910	2.20	2.18	3.85	
28	7/12/10	1.33	79.03	20.98	101.35	0.60	460.10	1452	0.33	0.35	N/A	
29	7/12/10	2.83	77.82	20.66	101.31	1.30	795.90	893	2.86	2.93	5.50	
30	7/13/10	1.33	77.78	21.00	101.31	0.60	479.30	1407	0.26	0.28	N/A	
31	7/13/10	3.04	77.65	20.64	101.32	1.40	803.30	891	2.47	2.48	5.16	
32	7/13/10	3.25	77.46	20.61	101.32	1.50	803.30	890	1.92	1.95	4.57	
33	7/13/10	4.08	76.87	20.42	101.38	1.90	643.20	919	0.69	0.69	2.64	
34	7/13/10	4.29	76.67	20.36	101.32	2.00	506.30	929	0.53	0.52	2.31	
35	7/14/10	1.21	79.07	21.02	101.32	0.55	-	-	-	-	-	NoGo

Notes: N/A - not available, NoGo - no ignition with the glow plug reaching 1515 K

Table I.3: Hot surface experiments with *n*-hexane using the Bosch glow plug in a 2 liter vessel (continued)

Shot	Date	P _{<i>n</i>-hexane} [kPa]	P _{N₂} [kPa]	P _{O₂} [kPa]	P _{total} [kPa]	ϕ	Peak Pressure [kPa]	Ignition Temperature [K]	V _F Left [m/s]	V _F Right [m/s]	V _F Top [m/s]	Note
36	7/14/10	1.45	78.93	20.94	101.32	0.66	579.31	1216	0.52	0.55	N/A	
37	7/14/10	1.55	78.83	20.94	101.32	0.70	600.35	1170	0.65	0.66	N/A	
38	7/14/10	2.19	78.34	20.80	101.30	1.00	748.31	894	2.46	2.58	4.54	
39	7/15/10	3.67	77.14	20.49	101.32	1.70	-	-	-	-	-	No Trigger
40	7/15/10	3.63	77.15	20.53	101.31	1.68	768.24	940	1.21	1.24	3.60	
41	7/15/10	5.31	75.86	20.16	101.32	2.50	201.47	975	0.22	0.20	1.54	$f = 10.64$ Hz
42	7/15/10	6.31	75.05	19.94	101.30	3.00	160.51	900	0.14	0.14	1.30	$f = 12.20$ Hz
43	7/20/10	3.03	50.29	13.37	66.69	2.15	252.76	940	0.40	0.38	1.71	$f = 6.67$ Hz
44	7/20/10	3.49	49.90	13.27	66.66	2.50	123.24	985	0.24	0.21	1.46	$f = 10.87$ Hz
45	7/20/10	5.31	75.85	20.16	101.31	2.50	180.07	926	0.17	0.16	1.44	$f = 11.11$ Hz
46	7/20/10	4.60	76.45	20.30	101.35	2.15	435.78	922	0.43	0.42	2.05	$f = 7.30$ Hz
47	7/20/10	1.21	20.08	5.36	26.65	2.15	122.65	1091	0.79	0.76	2.08	
48	7/20/10	1.41	19.97	5.28	26.66	2.54	N/A	N/A	0.32	N/A	1.47	$f = 7.69$ Hz
49	7/21/10	1.40	19.94	5.32	26.66	2.50	57.12	1102	0.29	0.29	1.39	$f = 7.87$ Hz
50	7/21/10	2.09	29.93	7.97	40.00	2.49	83.02	1049	0.31	0.27	1.44	$f = 9.71$ Hz
51	7/21/10	1.81	30.17	8.03	40.01	2.15	147.97	1034	0.64	0.60	2.07	

Notes: N/A - not available, NoGo - no ignition with the glow plug reaching 1515 K

Table I.4: Hot surface experiments with *n*-hexane using the Autolite glow plug in a 2 liter vessel

Shot	Date	P _{<i>n</i>-hexane} [kPa]	P _{N₂} [kPa]	P _{O₂} [kPa]	P _{total} [kPa]	ϕ	Peak Pressure [kPa]	Ignition Temperature [K]	V _F Left [m/s]	V _F Right [m/s]	V _F Top [m/s]	Note
52	8/16/10	3.71	76.91	20.68	101.30	1.70	N/A	N/A	1.06	1.00	3.53	
53	8/16/10	3.69	77.37	20.49	101.55	1.71	679.68	N/A	N/A	N/A	N/A	
54	8/27/10	6.23	74.81	20.17	101.20	2.93	128.00	N/A	T/C array trips instabilities		$f = 12.06$ Hz	
55	10/13/10	3.24	77.46	20.61	101.31	1.49	668.61	N/A	T/C array trips instabilities			
56	10/13/10	4.80	76.23	20.33	101.36	2.24	376.74	N/A	N/A	N/A	N/A	
57	10/13/10	4.79	76.26	20.26	101.31	2.24	366.41	N/A	T/C array trips instabilities			
58	10/13/10	5.31	75.83	20.18	101.32	2.50	209.22	N/A	T/C array trips instabilities		$f = 9.48$ Hz	
59	10/20/10	6.19	75.07	20.22	101.48	2.91	N/A	N/A	N/A	N/A	N/A	
60	10/20/10	6.31	75.06	19.96	101.32	3.00	N/A	N/A	T/C array trips instabilities		$f = 12.66$ Hz	
61	10/20/10	2.19	78.31	20.82	101.32	1.00	667.51	N/A	N/A	N/A	N/A	
62	10/20/10	1.33	78.97	21.02	101.32	0.60	-	-	-	-	-	NoGo
63	10/21/10	1.65	78.74	20.93	101.32	0.75	N/A	N/A	N/A	N/A	N/A	
64	10/21/10	1.55	78.83	20.94	101.32	0.70	523.97	N/A	N/A	N/A	N/A	
95	2/15/11	6.28	75.07	19.97	101.32	2.99	142.06	1146	direct imaging		$f = 13.39$ Hz	
96	2/15/11	6.31	75.07	19.94	101.32	3.00	139.48	1200	direct imaging		$f = 14.35$ Hz	
99	2/23/11	6.31	75.06	19.96	101.32	3.00	135.79	1300	N/A	N/A	N/A	No Video
100	2/24/11	6.29	75.03	20.00	101.32	2.99	142.80	1162	direct imaging w/ CH* filter [†]		$f = 13.12$ Hz	
101	2/24/11	6.31	75.06	19.96	101.32	3.00	141.32	1070	direct imaging w/ CH* filter [†]		$f = 12.97$ Hz	
102	2/24/11	6.29	75.07	19.96	101.32	3.00	140.95	1068	direct imaging w/ CH* filter [*]		$f = 12.88$ Hz	
103	3/3/11	6.31	75.06	19.94	101.31	3.00	142.06	1362	direct imaging w/ CH* filter [*]			
104	3/3/11	6.31	75.05	19.96	101.31	3.00	140.95	1417	direct imaging w/ CH* filter [*]		$f = 13.02$ Hz	
113	4/5/11	6.32	75.02	19.98	101.32	3.00	132.84	N/A	direct imaging w/ PI-MAX 3 ICCD		No Images	
114	4/5/11	6.32	75.06	19.94	101.32	3.01	137.63	N/A	direct imaging w/ PI-MAX 3 ICCD		fps too low	
118	5/3/11	4.91	76.15	20.26	101.32	2.30	208.11	881.5	direct imaging w/ CH* filter [‡]		$f = 8.16$ Hz	
119	5/3/11	5.23	75.91	20.18	101.32	2.46	225.82	897.5	direct imaging w/ CH* filter [‡]		$f = 8.33$ Hz	

Notes: N/A - not available, NoGo - no ignition with the glow plug reaching 1453 K, fps - frames per second

[†] Newport Filter 20BPF70-450 (Bandpass Filter, 50.8 × 50.8 mm, 450±10 nm Center, 70±30 nm FWHM)

^{*} Newport Filter 20BPF70-450 (see above) & MellesGriot SPF-500 (Short Pass Filter, Transmittance > 75% 430-500 nm)

[‡] Edmund Optics Filter 43-160 (430 nm Center Wave Length, 10 nm Bandwidth, 50.8 × 50.8 mm)

Table I.5: Hot surface experiments with *n*-heptane using the Autolite glow plug in a 2 liter vessel

Shot	Date	P _{<i>n</i>-heptane}	P _{N₂}	P _{O₂}	P _{total}	ϕ	Peak	Ignition	V _F	V _F	V _F	Note	
		[kPa]	[kPa]	[kPa]	[kPa]		Pressure	Temperature	Left	Right	Top		
							[kPa]	[K]	[m/s]	[m/s]	[m/s]		
65	10/21/10	1.89	78.55	20.88	101.32	1.00	658.28	N/A	2.36	2.46	4.30		
66	10/21/10	3.73	77.10	20.40	101.23	2.01	685.22	N/A	1.46	1.37	4.74		
67	10/26/10	1.19	79.10	21.04	101.32	0.62	-	-	-	-	-	NoGo	
68	10/26/10	4.40	76.39	20.53	101.32	2.36	448.69	N/A	T/C array trips instabilities				
69	10/26/10	5.35	76.81	20.18	102.34	2.91	395.19	N/A	T/C array trips instabilities			$f = 10.72$ Hz	
70	10/28/10	3.54	76.59	21.18	101.32	1.84	396.74	N/A	T/C array trips instabilities			Filling Error [†]	

Notes: N/A - not available, NoGo - no ignition with the glow plug reaching 1453 K

[†] The mixture was filled using the Endevco gage, which is much less accurate. The final pressure before ignition was 603 Torr due to a leak through the vacuum valve.

Table I.6: Spark ignition experiments of *n*-hexane air mixtures in a 22 liter vessel

Shot	Date	P _{<i>n</i>-hexane}	P _{N₂}	P _{O₂}	P _{total}	ϕ	V _F	V _F	V _F	Gap	<i>C</i>	<i>V</i>	Energy	Note	
		[kPa]	[kPa]	[kPa]	[kPa]		Left	Right	Top	Width					
							[m/s]	[m/s]	[m/s]	[mm]	[μ C]	[V]	[J]		
71	1/14/11	6.29	75.08	19.95	101.32	3.00	-	-	-	4	5	300	0.225	No Ignition After 3 Sparks	
72	1/14/11	5.31	75.85	20.16	101.32	2.50	-	-	-	4	5	300	0.225	No Ignition After 3 Sparks	
73	1/14/11	2.19	78.52	20.87	101.58	1.00	2.81	2.83	N/A	4	5	300	0.225		
74	1/18/11	6.30	75.07	19.95	101.32	3.00	-	-	-	6	5	300	0.225	No Ignition After 3 Sparks	
75	1/18/11	5.31	76.05	20.16	101.53	2.50	-	-	-	6	5	300	0.225	No Ignition After 3 Sparks	
76	1/20/11	4.28	76.67	20.39	101.33	1.99	0.40	0.46	0.63	6	5	300	0.225		
77	1/20/11	5.31	75.85	20.16	101.32	2.50	N/A	N/A	N/A	6	5	300	0.225	No Video Available	
78	1/24/11	6.25	75.12	19.96	101.33	2.98	-	-	-	2.4-9.5	10	300	0.450	No Ignition After 3 Sparks	
79	1/24/11	6.28	75.09	19.96	101.33	2.99	-	-	-	2.4-9.5	10	300	0.450	No Ignition After 4 Sparks	

Notes: N/A - not available, energy of the spark is based on the stored energy $E = \frac{1}{2}CV^2$

Table I.7: Hot surface experiments with *n*-hexane using the Autolite glow plug in a 22 liter vessel

Shot	Date	P _{<i>n</i>-hexane} [kPa]	P _{N₂} [kPa]	P _{O₂} [kPa]	P _{total} [kPa]	ϕ	Peak Pressure [kPa]	Ignition Temperature [K]	V _F Left [m/s]	V _F Right [m/s]	V _F Top [m/s]	Note
80	1/31/11	6.30	75.07	19.96	101.33	3.00	124.88	N/A	0.07	0.04	0.72	$f = 14.93$ Hz
81	2/1/11	6.30	75.06	19.96	101.32	3.00	128.14	1123	0.04	0.06	0.75	$f = 14.39$ Hz
82	2/1/11	6.30	75.07	19.95	101.32	3.00	-	-	-	-	-	NoGo at 1453 K
83	2/1/11	6.30	75.08	19.95	101.33	3.00	-	-	-	-	-	NoGo at 1453 K
105	3/3/11	5.30	75.08	19.95	100.33	2.52	-	-	-	-	-	NoGo
106	3/3/11	4.59	76.42	20.32	101.32	2.15	-	-	-	-	-	NoGo
107	3/3/11	5.26	75.90	20.16	101.32	2.48	-	-	-	-	-	NoGo
108	3/3/11	4.60	76.42	20.29	101.30	2.15	-	-	-	-	-	NoGo
109	3/29/11	2.19	78.02	20.82	101.03	1.00	-	-	-	-	-	NoGo
110	3/29/11	2.61	77.97	20.74	101.32	1.20	861.67	N/A	N/A	N/A	N/A	GP Upside Down
111	3/31/11	6.29	75.06	19.97	101.32	2.99	-	-	-	-	-	NoGo
112	3/31/11	6.27	75.05	20.00	101.32	2.98	129.68	N/A	0.20	0.03	1.39	$f = 14.53$ Hz, GP at 24.5° angle

Notes: N/A - not available, NoGo - no ignition

Table I.8: Hot surface experiments with *n*-hexane using varying hot surfaces in a 2 liter vessel

Shot	Date	P _{<i>n</i>-hexane} [kPa]	P _{N₂} [kPa]	P _{O₂} [kPa]	P _{total} [kPa]	ϕ	Peak Pressure [kPa]	Ignition Temp. [K]	V _F Left [m/s]	V _F Right [m/s]	V _F Top [m/s]	Note	Area [m ²]
84	2/2/11	6.31	75.06	19.96	101.32	3.00	-	-	-	-	-	NoGo, Brass Foil	2.4×10^{-5}
85	2/3/11	6.31	75.06	19.96	101.32	3.00	123.98	982	0.13	0.11	0.92	Copper Foil	
86	2/3/11	6.31	75.09	19.93	101.32	3.01	135.05	980	0.04	0.11	0.78	$f = 20.42$ Hz, Nickel Foil	2.4×10^{-5}
87	2/3/11	6.31	75.09	19.94	101.34	3.00	138.37	N/A	0.13	0.12	0.75	$f = 14.45$ Hz, Nickel Wire	2.4×10^{-6}

Notes: N/A - not available, NoGo - no ignition

Table I.9: Hot surface experiments with hydrogen using the Autolite glow plug in a 2 liter vessel

Shot	Date	P _{H₂} [kPa]	P _{N₂} [kPa]	P _{O₂} [kPa]	P _{total} [kPa]	ϕ	Peak Pressure [kPa]	Ignition Temperature [K]	V _F Left [m/s]	V _F Right [m/s]	V _F Top [m/s]	Note
88	2/8/11	7.60	34.02	9.04	50.66	0.42	N/A	N/A	N/A	N/A	N/A	
89	2/8/11	7.09	74.43	19.80	101.32	0.18	-	-	-	-	-	NoGo
90	2/10/11	7.09	74.45	19.78	101.32	0.18	111.4	840	0.12	0.13	1.18	$f = 10.53$ Hz
91	2/10/11	8.11	74.17	19.69	101.96	0.21	125.8	808	0.17	0.14	1.41	$f = 8.89$ Hz
92	2/10/11	5.07	76.05	20.21	101.32	0.13	indiscernible	910	0.07	0.05	0.78	
93	2/10/11	72.95	22.40	5.97	101.32	6.11	384.1	1038	3.00	2.70	4.84	
94	2/10/11	74.97	20.82	5.53	101.32	6.77	361.2	1087	1.66	1.71	2.54	

Notes: N/A - not available, NoGo - no ignition with the glow plug reaching 1453 K

Table I.10: Hot surface experiments with hydrogen-hexane-air mixtures using the Autolite glow plug in a 2 liter vessel

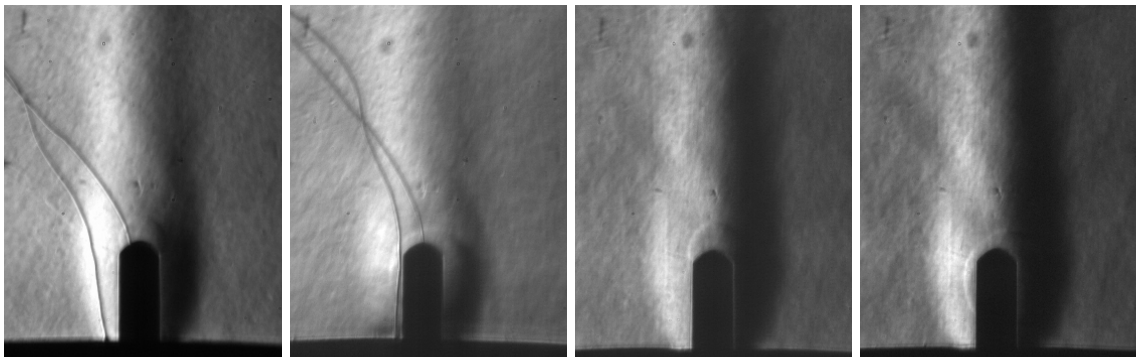
Shot	Date	P _{n-hexane} [kPa]	P _{H₂} [kPa]	P _{N₂} [kPa]	P _{O₂} [kPa]	P _{total} [kPa]	Peak Pressure [kPa]	Ignition Temperature [K]	V _F Left [m/s]	V _F Right [m/s]	V _F Top [m/s]	Note
97	2/15/11	1.47	5.07	74.89	19.90	101.32	649.80	999	1.58	1.44	3.79	
98	2/15/11	5.99	5.07	71.31	18.96	101.32	139.50	1001	0.17	0.12	1.15	$f = 13.83$ Hz
115	4/6/11	1.28	3.05	76.65	20.36	101.34	594.44	935	1.17	1.15	3.68	
116	4/7/11	1.47	3.17	76.31	20.32	101.27	650.90	876.8	2.24	1.90	5.38	
117	4/7/11	1.39	10.15	70.93	18.88	101.34	668.61	865.9	4.89	4.67	11.84	
120	5/26/11	1.09	1.01	78.35	20.82	101.28	-	-	-	-	-	NoGo
121	5/26/11	1.13	2.03	77.54	20.61	101.31	483.01	1158	0.42	0.37	2.01	
122	5/26/11	1.13	1.52	77.94	20.72	101.31	396.30	1180	0.29	0.22	1.60	
123	5/26/11	1.07	1.53	77.98	20.73	101.31	327.66	1205	0.20	0.17	1.39	$f = 17.37$ Hz

Notes: N/A - not available, NoGo - no ignition with the glow plug reaching 1453 K

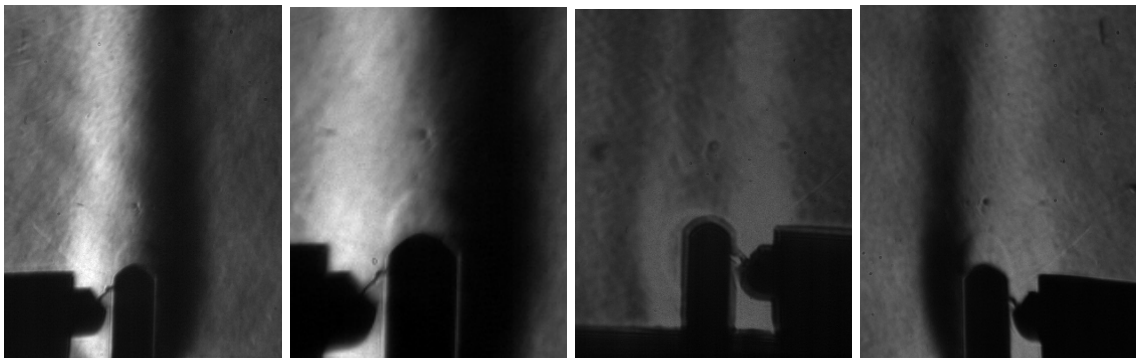
This page intentionally left blank.

Appendix J

Ignition Location



(a) **T**: Shot 6 ($t = 0.375$ ms) (b) **S**: Shot 7 ($t = 1.375$ ms) (c) **T**: Shot 8 ($t = 0.375$ ms) (d) **S**: Shot 9 ($t = 0.2$ ms)



(e) **T**: Shot 10 ($t = 0.2$ ms) (f) **T**: Shot 11 ($t = 0.3$ ms) (g) **S**: Shot 12 ($t = 0.3$ ms) (h) **T**: Shot 15 ($t = 0.2$ ms)

Figure J.1: Ignition locations observed in schlieren videos (**T** - top ignition, **S** - side ignition, **P** - plume ignition, time indicated is elapsed from 1 frame before any flame is visible)

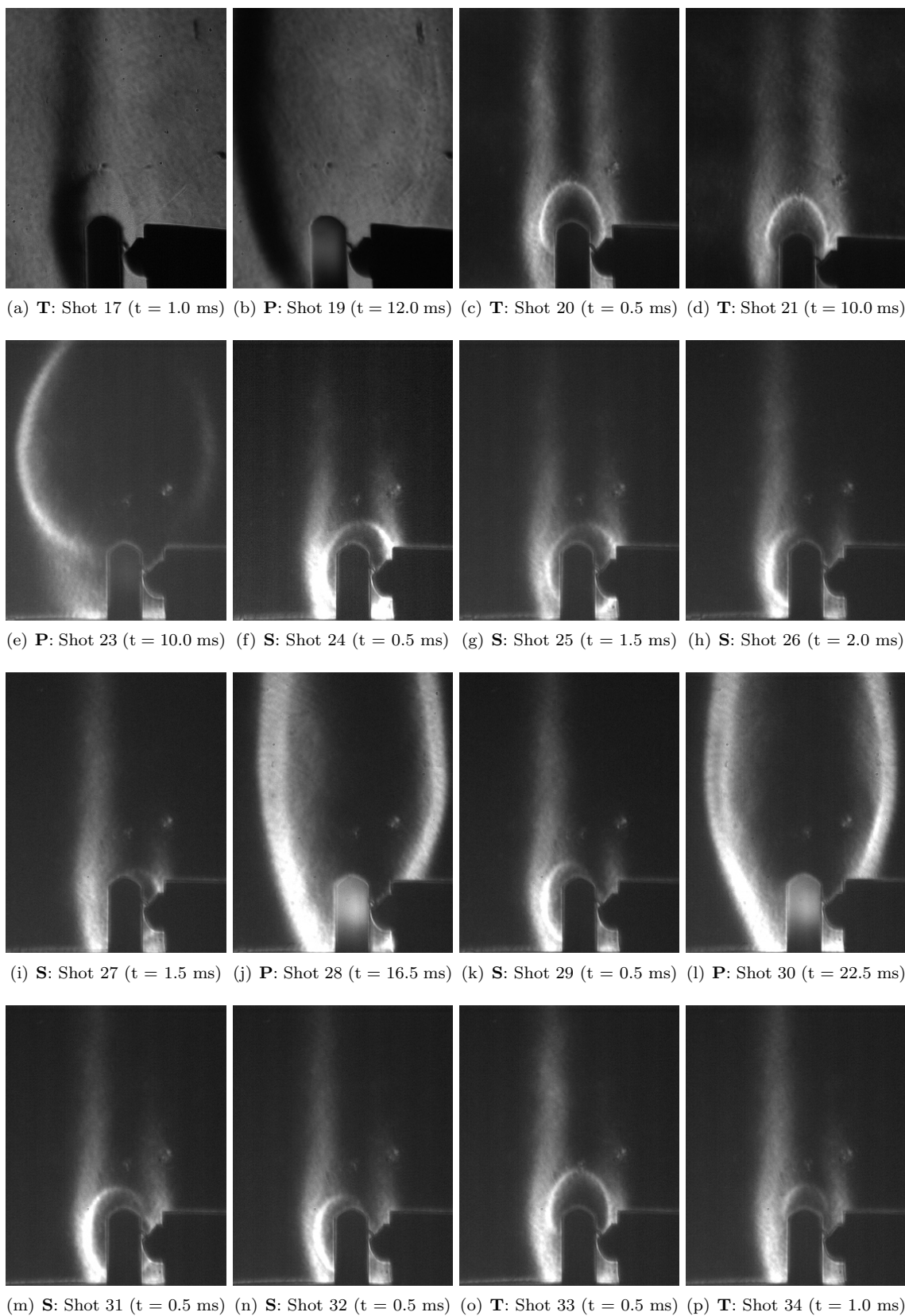
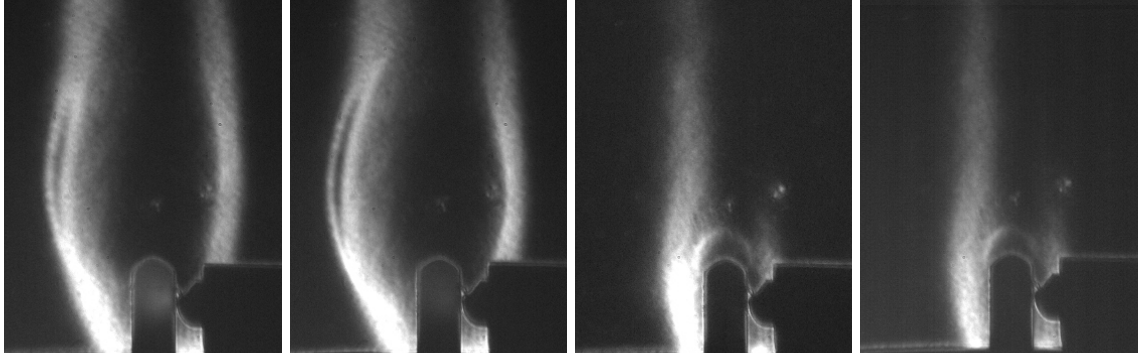
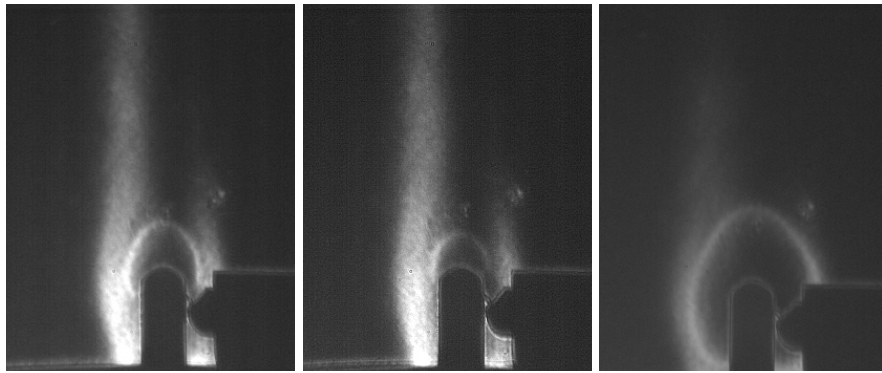


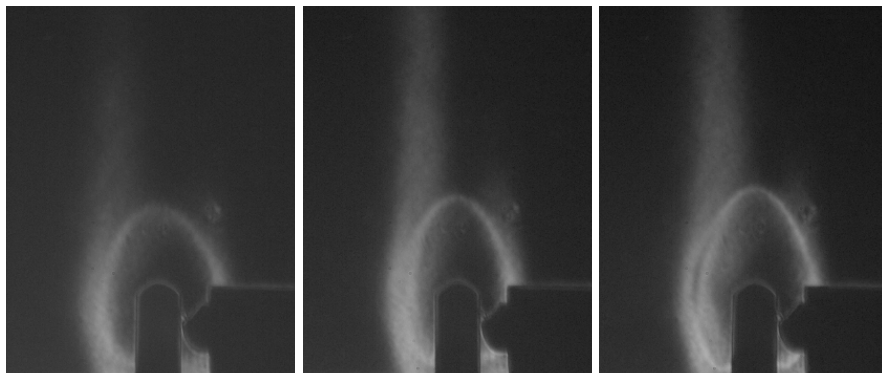
Figure J.2: Ignition locations observed in schlieren videos continued (**T** - top ignition, **S** - side ignition, **P** - plume ignition, time indicated is elapsed from 1 frame before any flame is visible)



(a) **P**: Shot 36 ($t = 13$ ms) (b) **P**: Shot 37 ($t = 11$ ms) (c) **T**: Shot 38 ($t = 1.0$ ms) (d) **T**: Shot 40 ($t = 0.5$ ms)



(e) **T**: Shot 41 ($t = 0.5$ ms) (f) **T**: Shot 42 ($t = 1.0$ ms) (g) **T**: Shot 43 ($t = 1.0$ ms)



(h) **T**: Shot 44 ($t = 1.0$ ms) (i) **T**: Shot 45 ($t = 2.0$ ms) (j) **T**: Shot 46 ($t = 1.0$ ms)

Figure J.3: Ignition locations observed in schlieren videos continued (**T** - top ignition, **S** - side ignition, **P** - plume ignition, time indicated is elapsed from 1 frame before any flame is visible)

This page intentionally left blank.

Appendix K

Schlieren Sequences

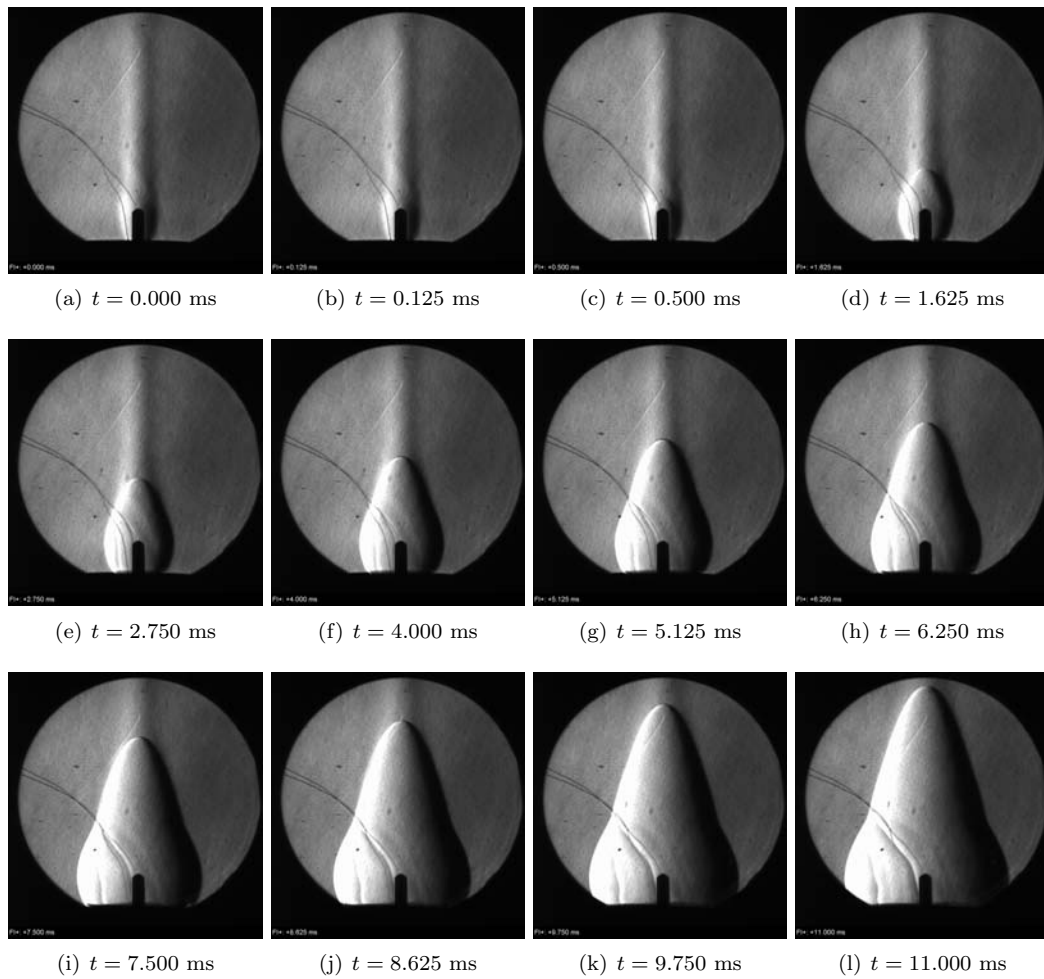


Figure K.1: Shot 6

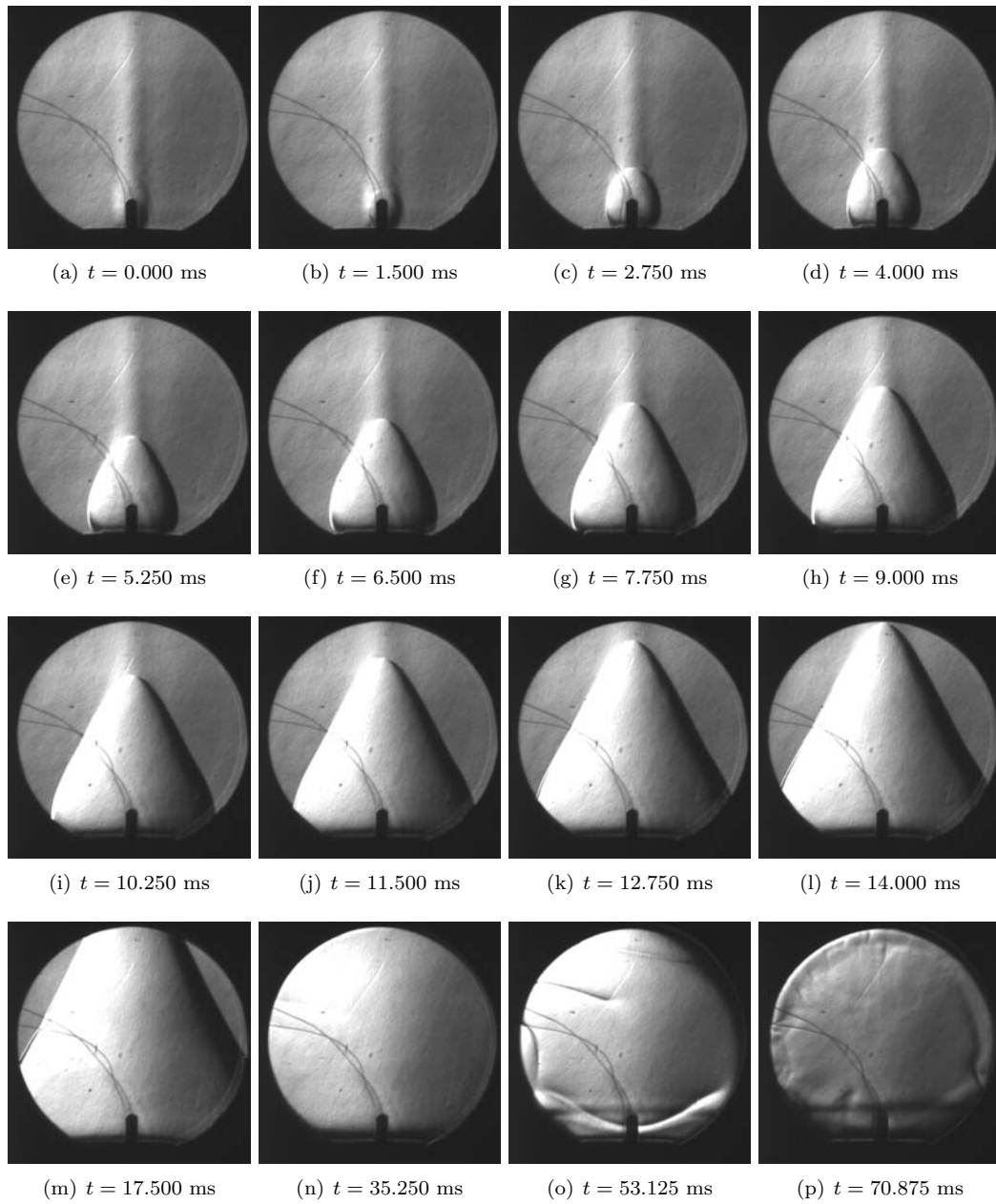


Figure K.2: Shot 7

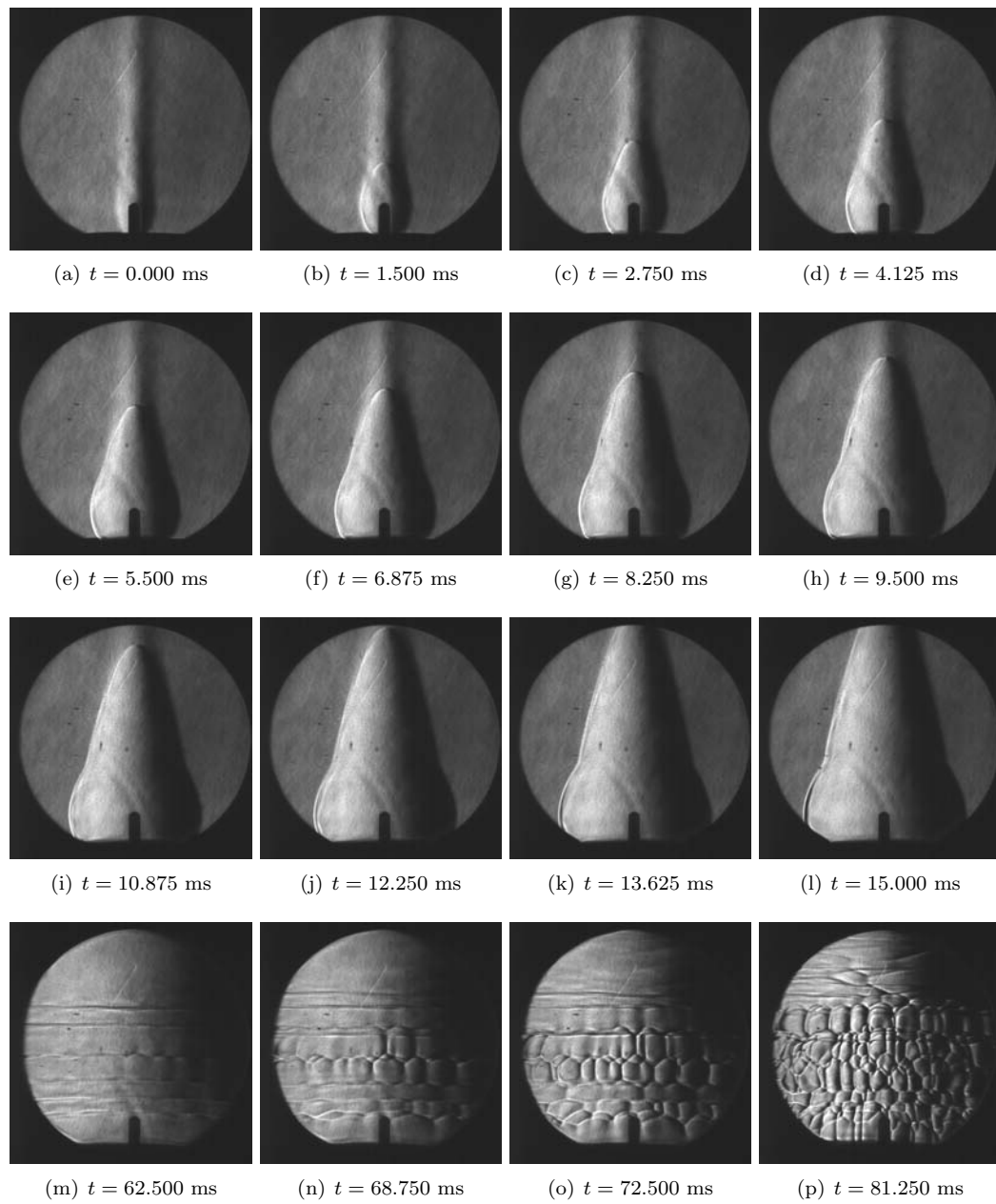


Figure K.3: Shot 8

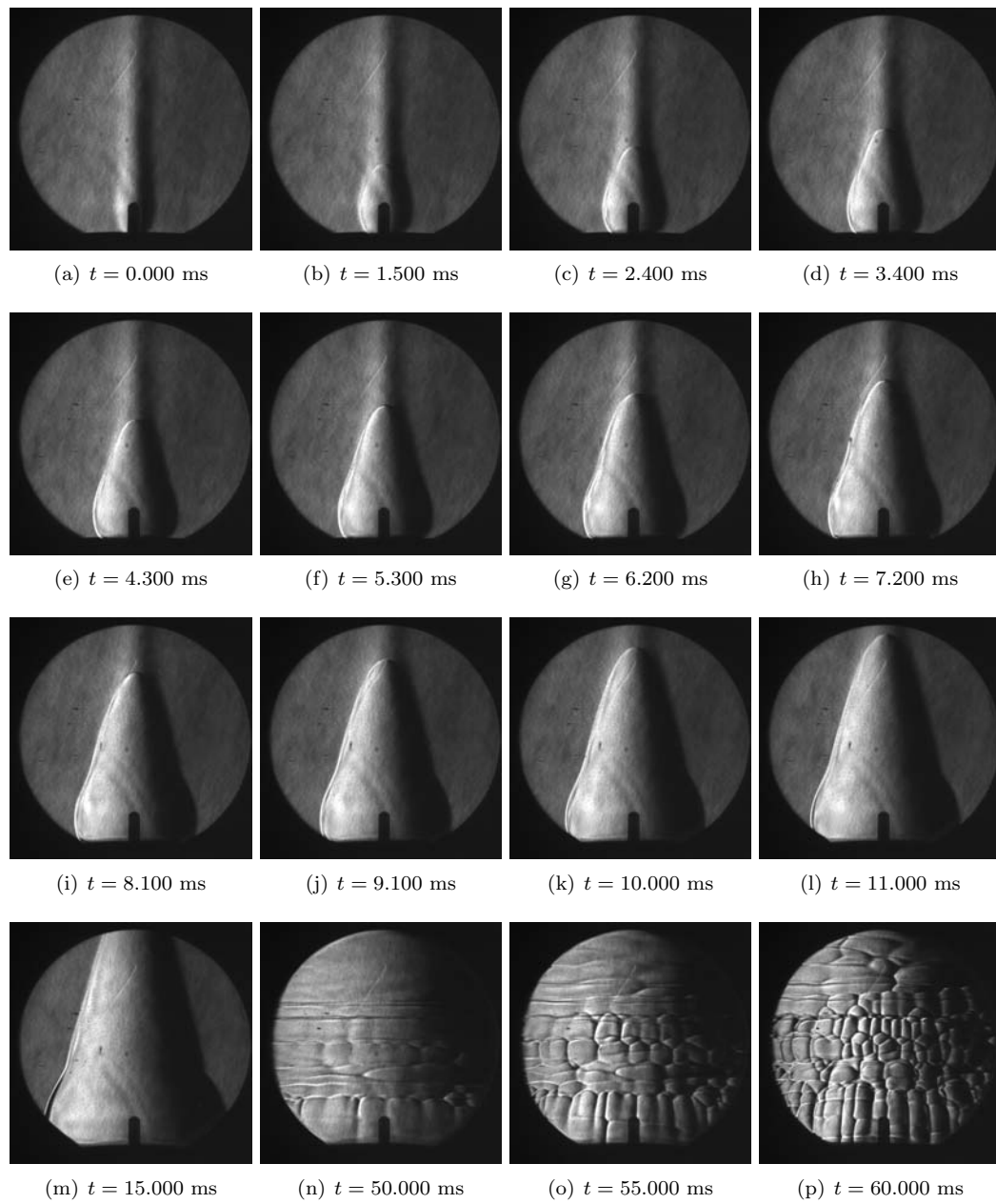


Figure K.4: Shot 9

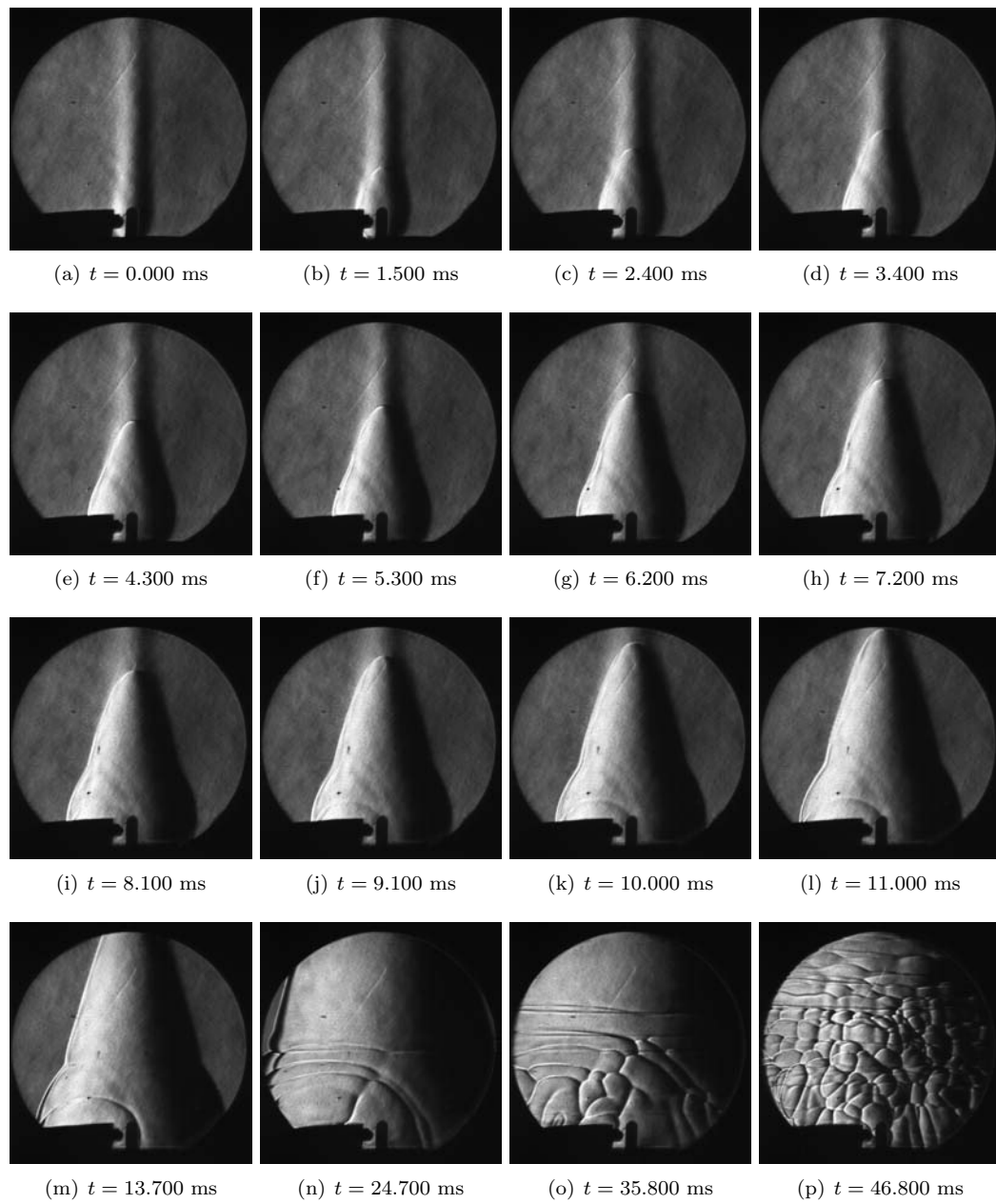


Figure K.5: Shot 10

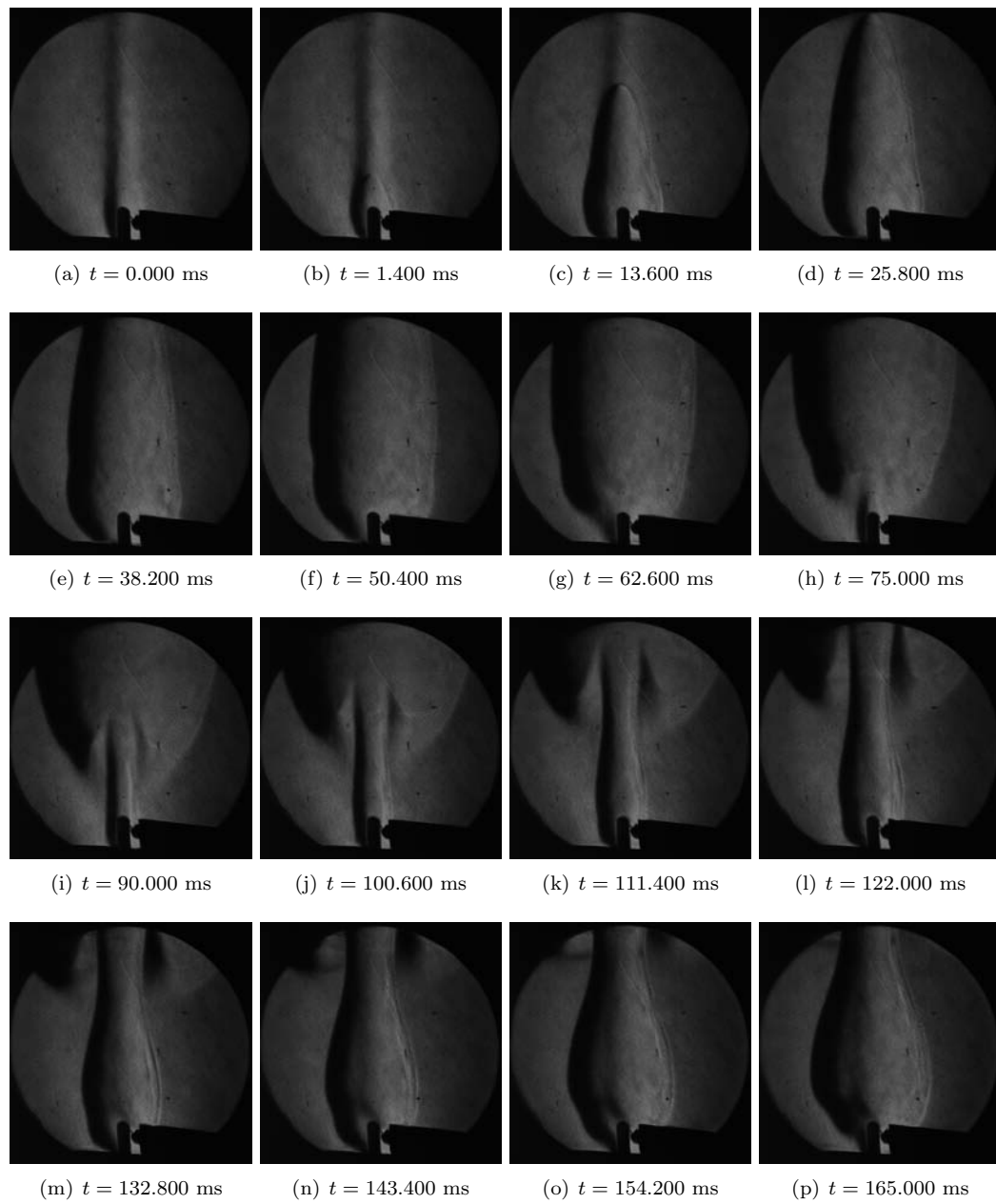


Figure K.6: Shot 15

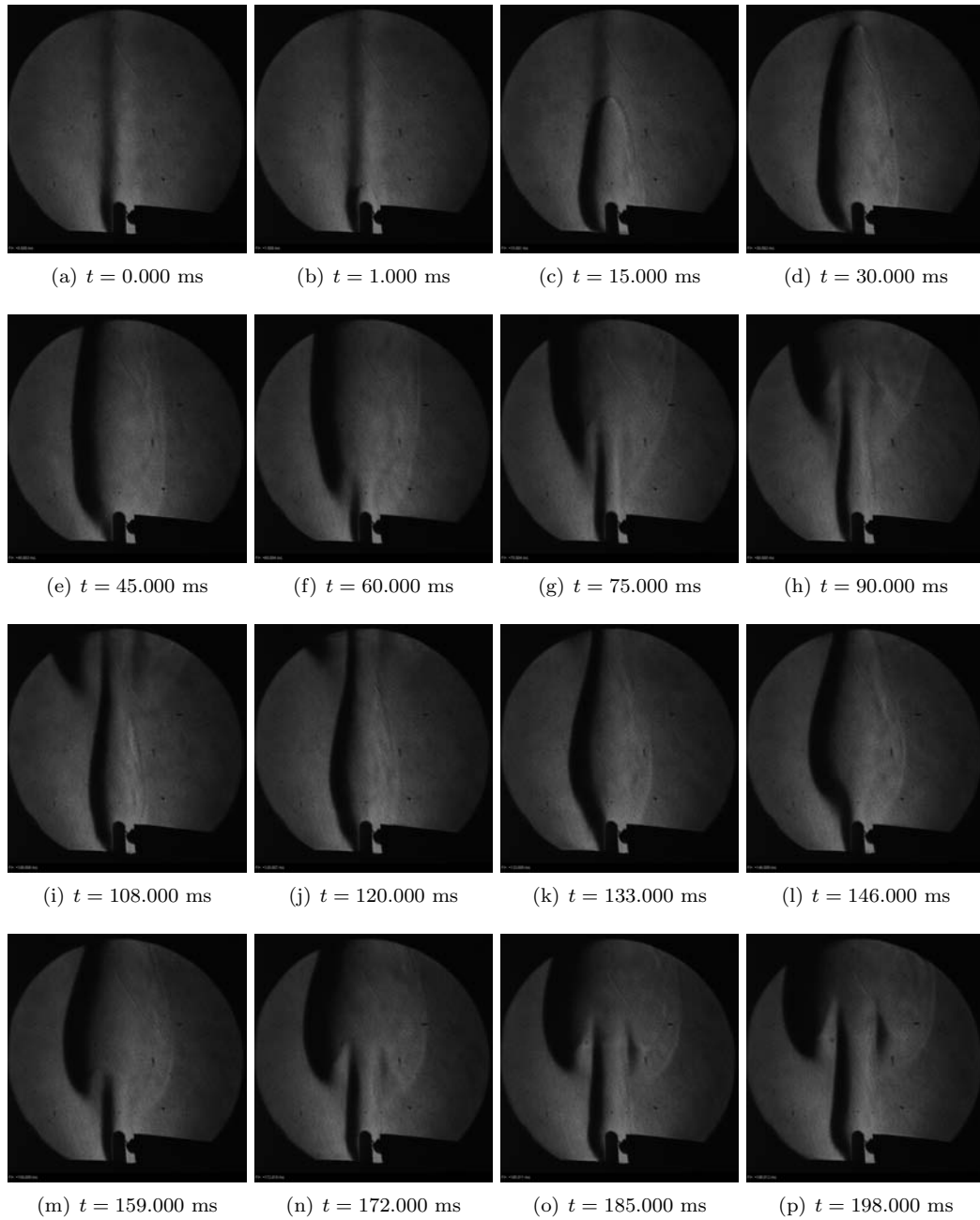


Figure K.7: Shot 17

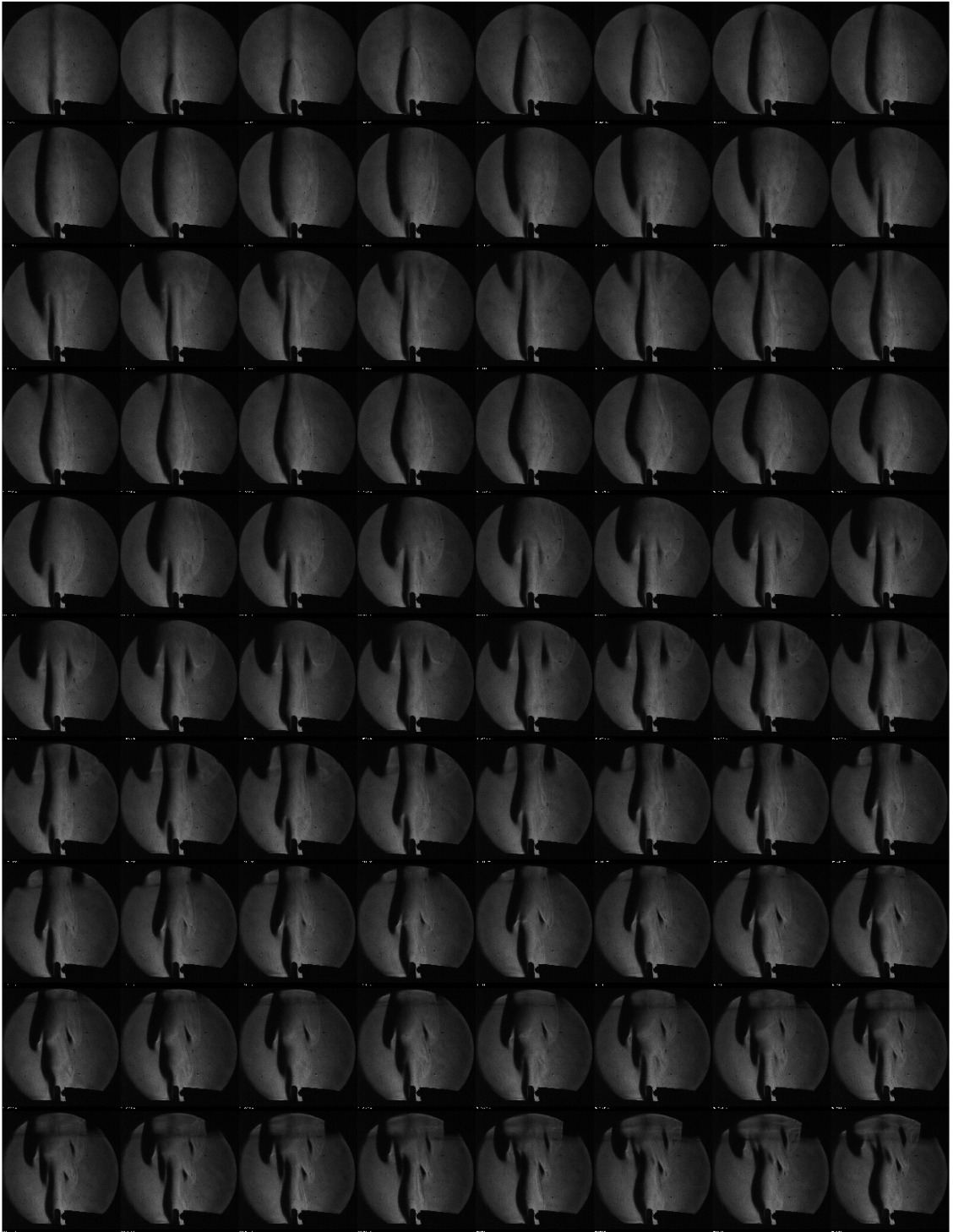


Figure K.8: Shot 17 montage ($\Delta t = 5$ ms between images)

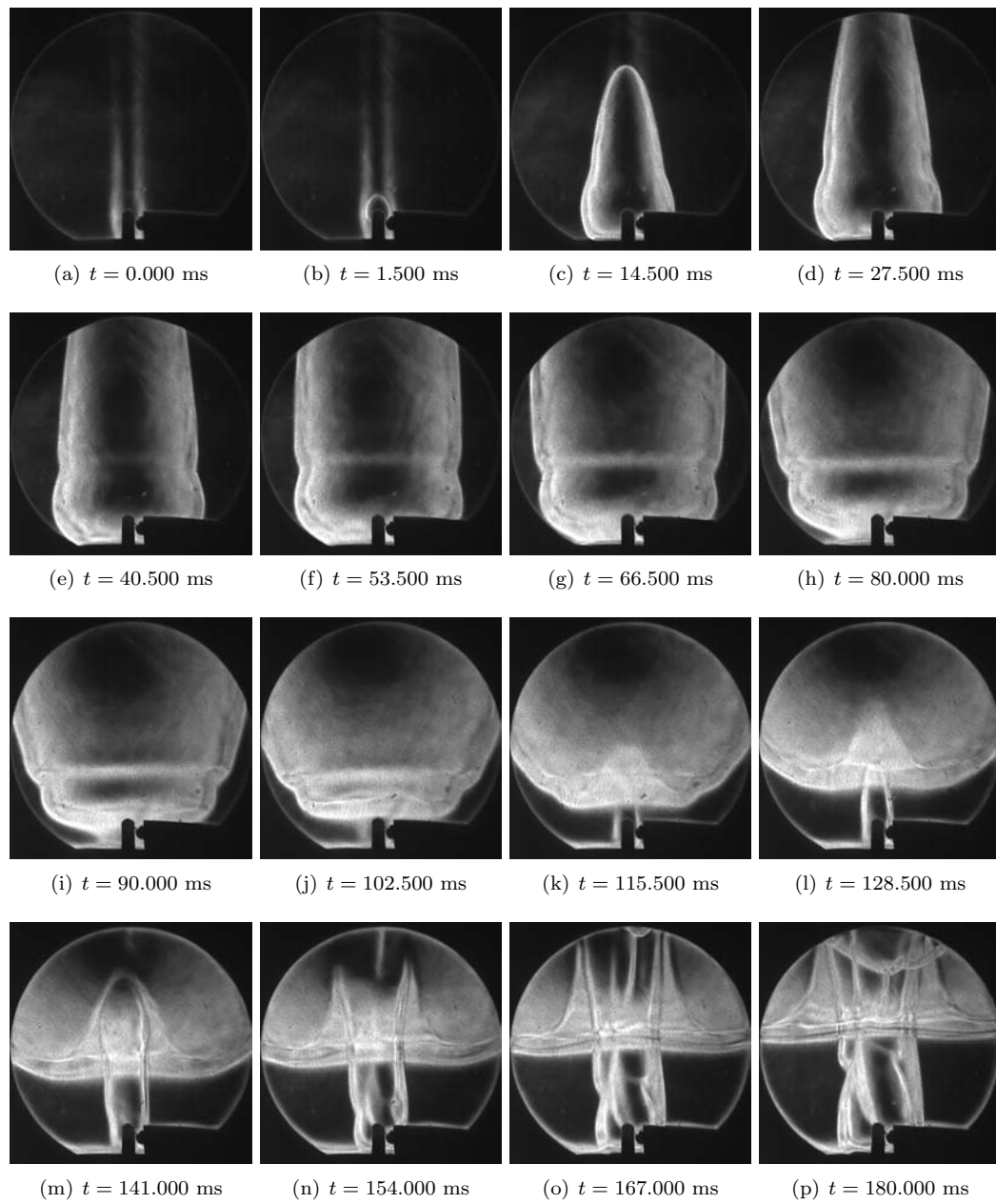


Figure K.9: Shot 20

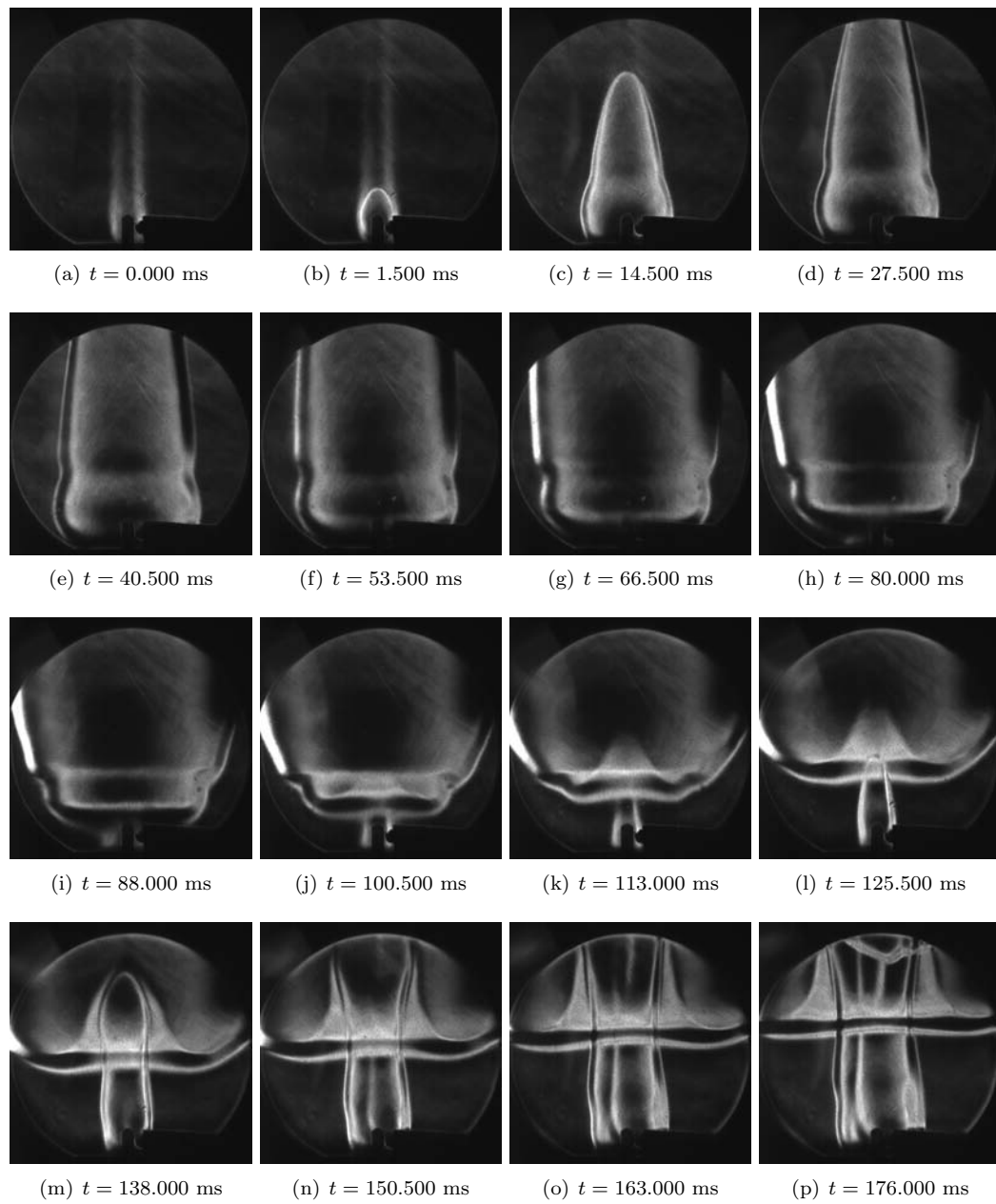


Figure K.10: Shot 21

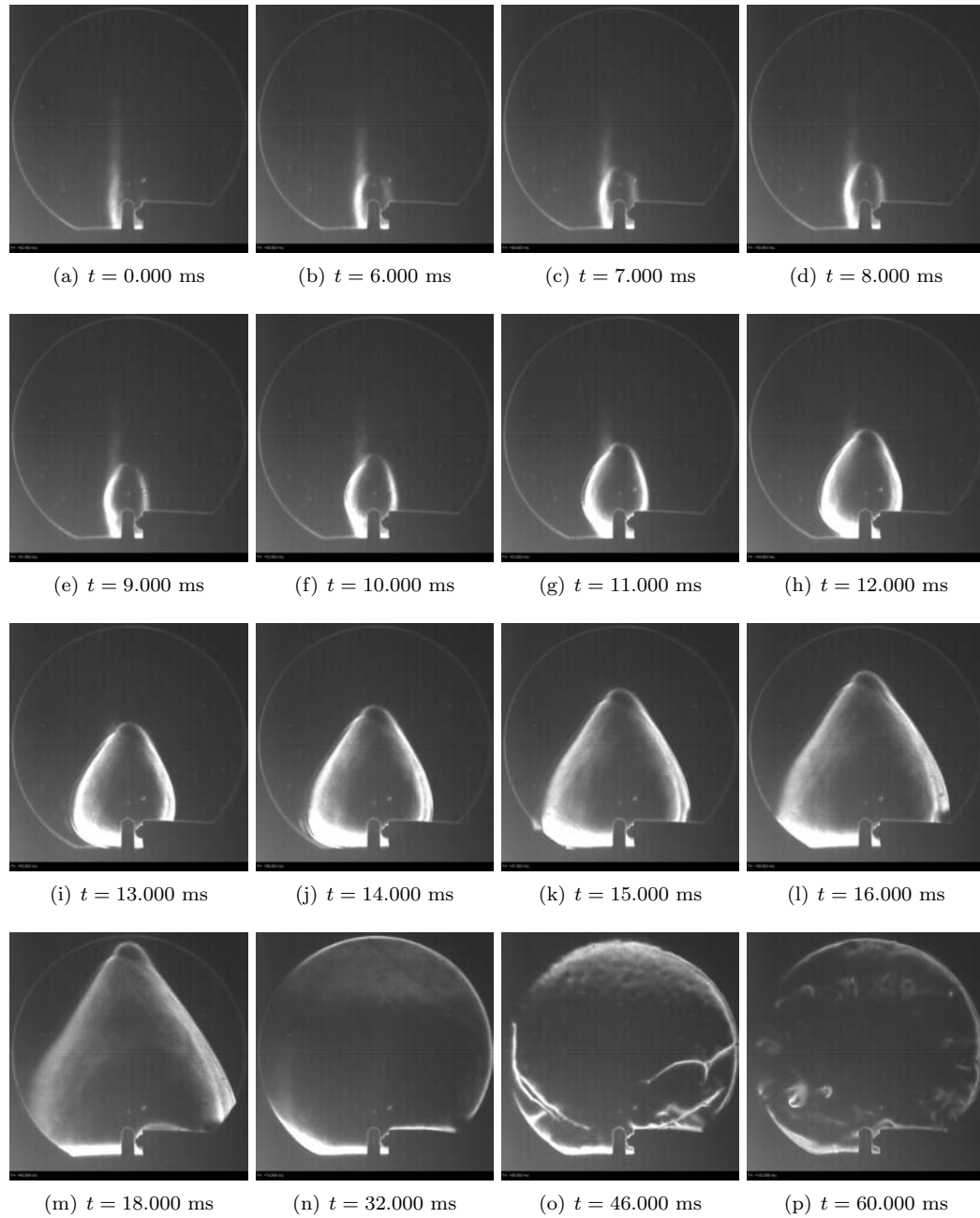


Figure K.11: Shot 22

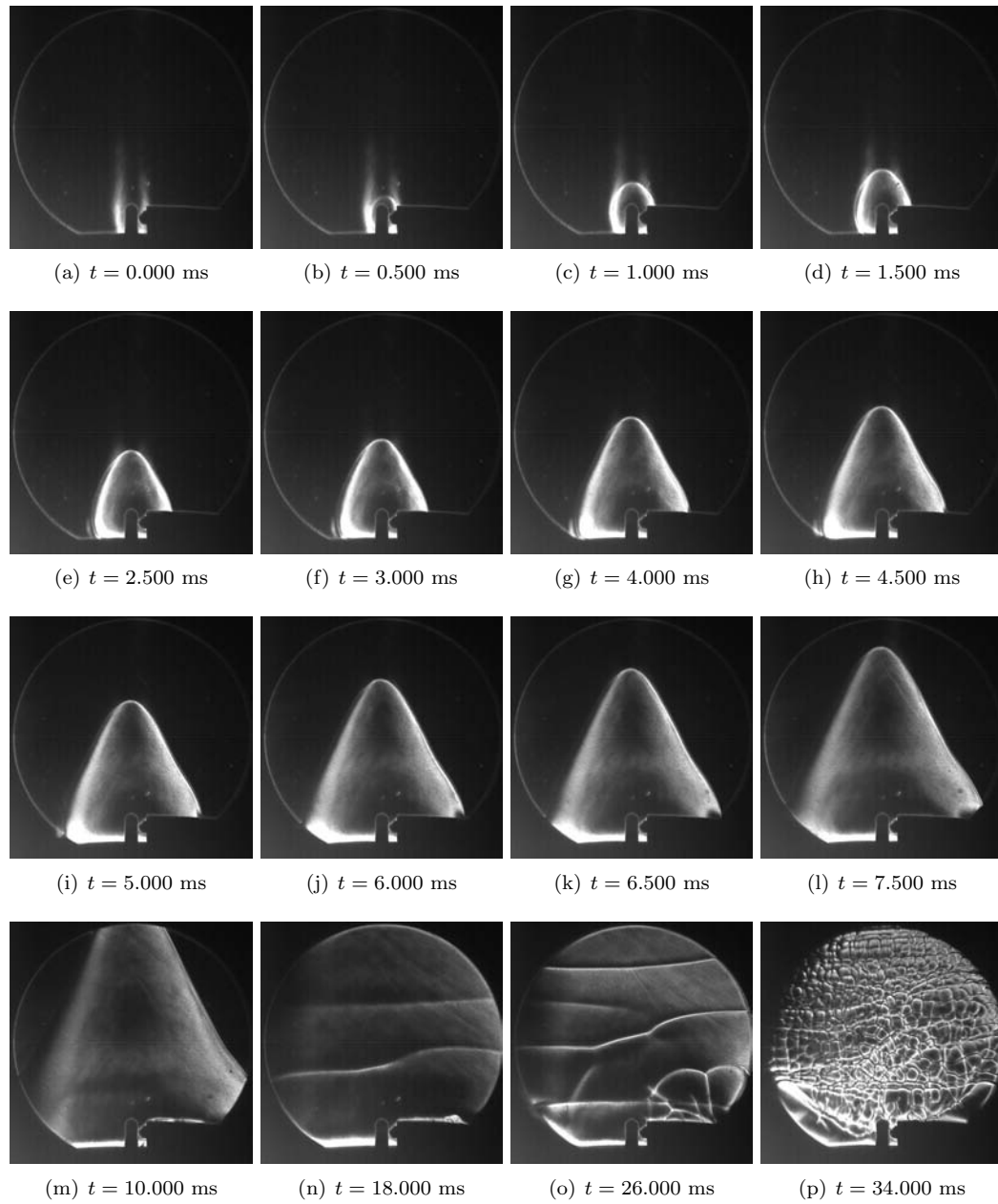


Figure K.12: Shot 24

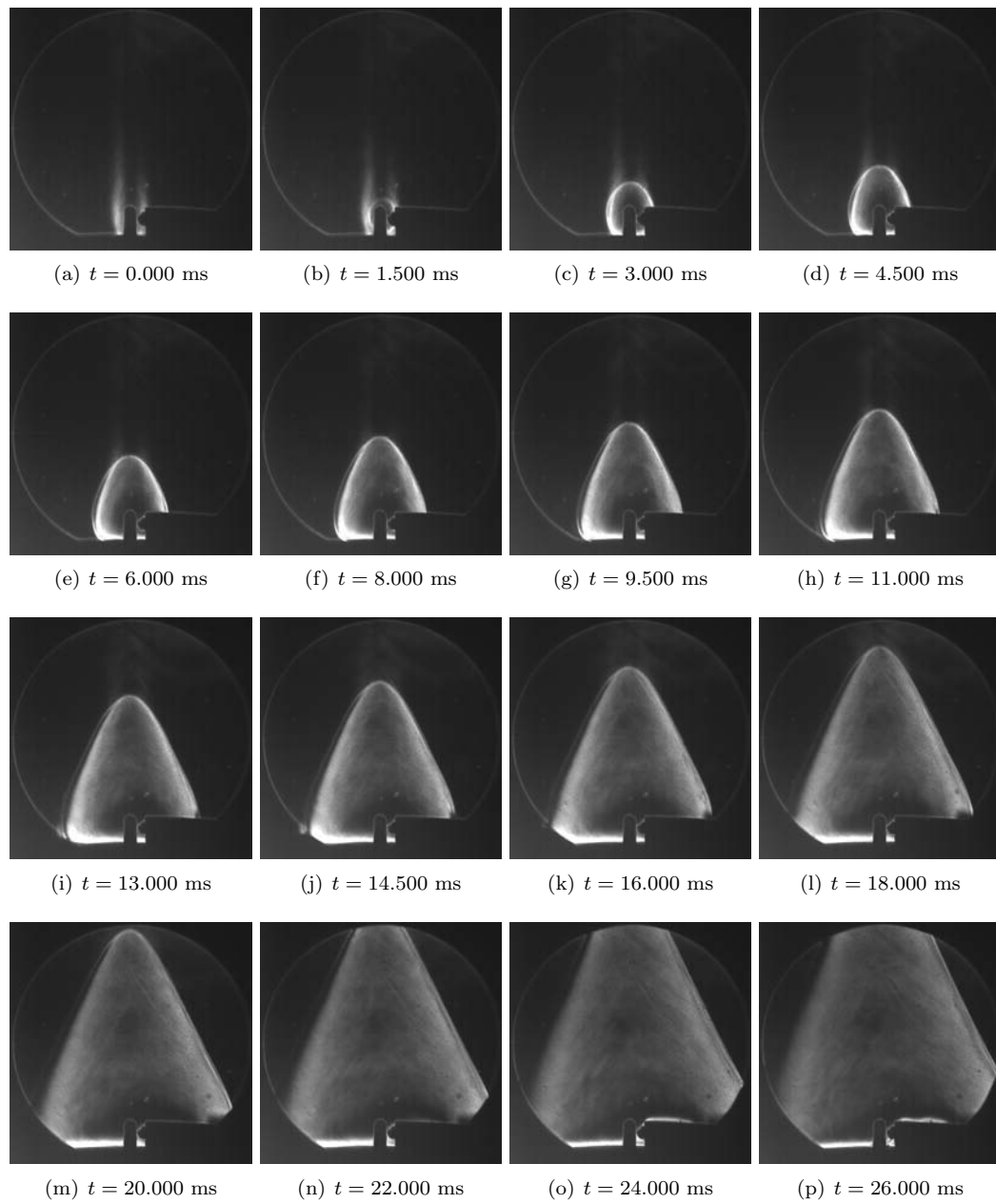


Figure K.13: Shot 25

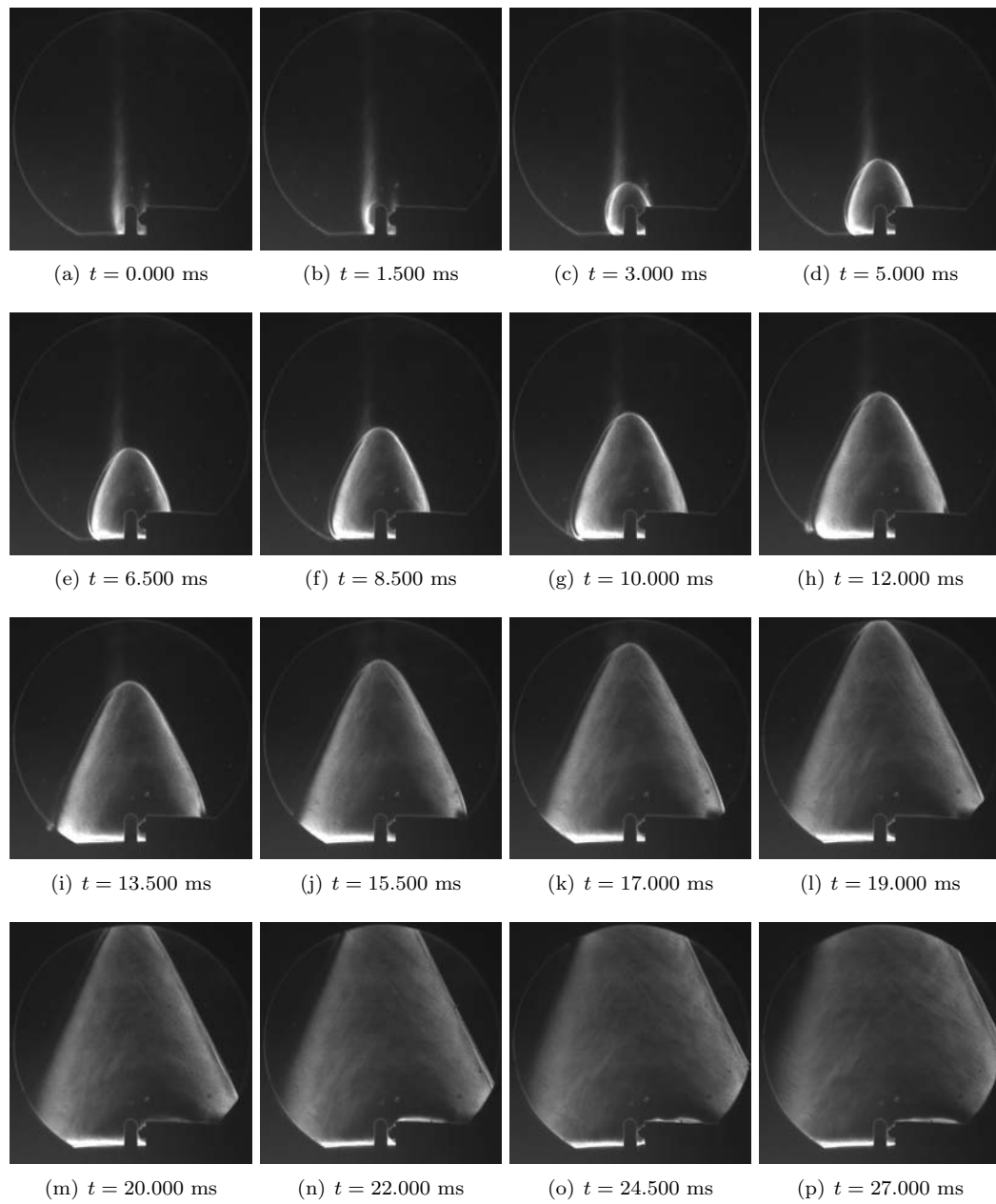


Figure K.14: Shot 26

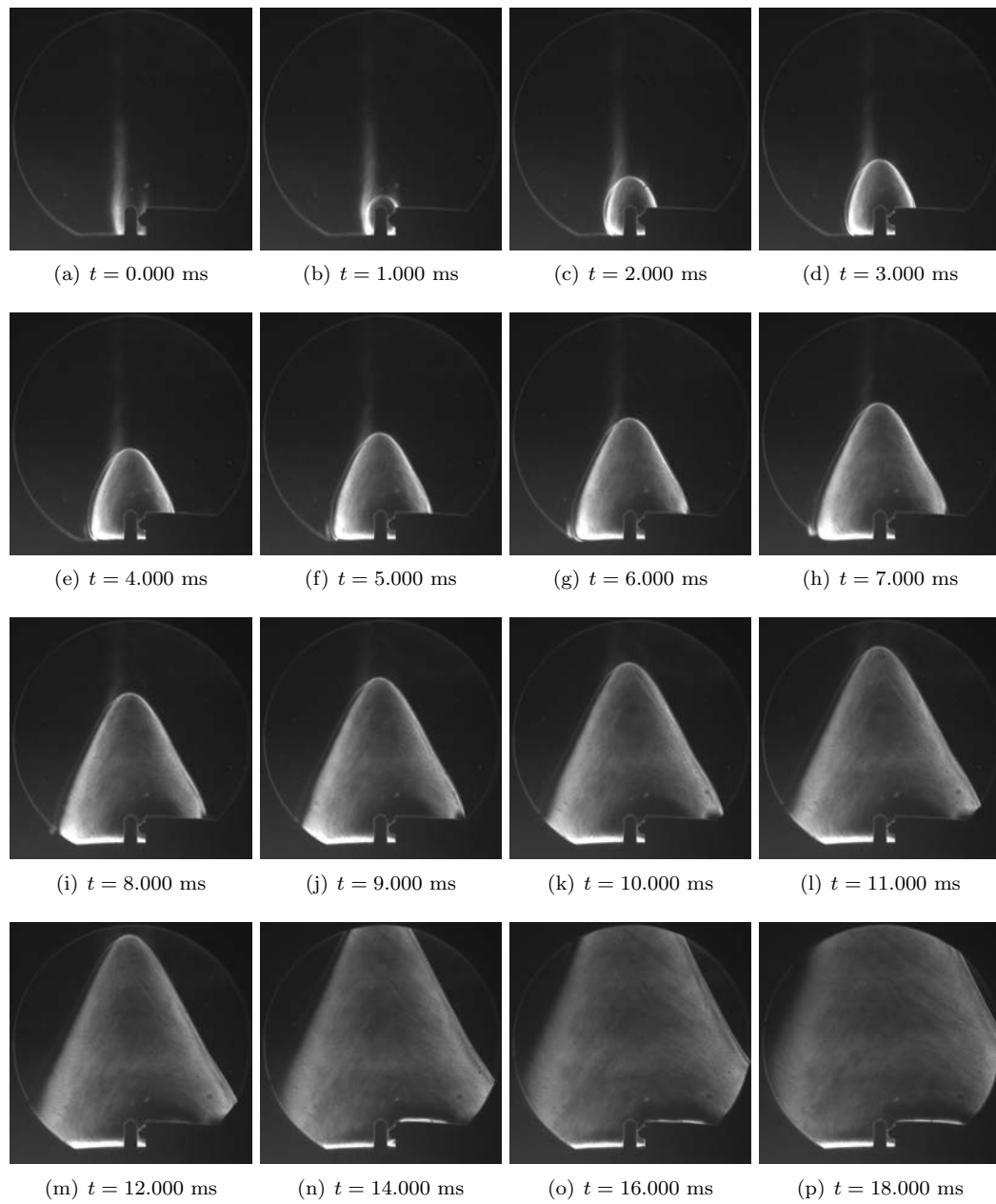


Figure K.15: Shot 27

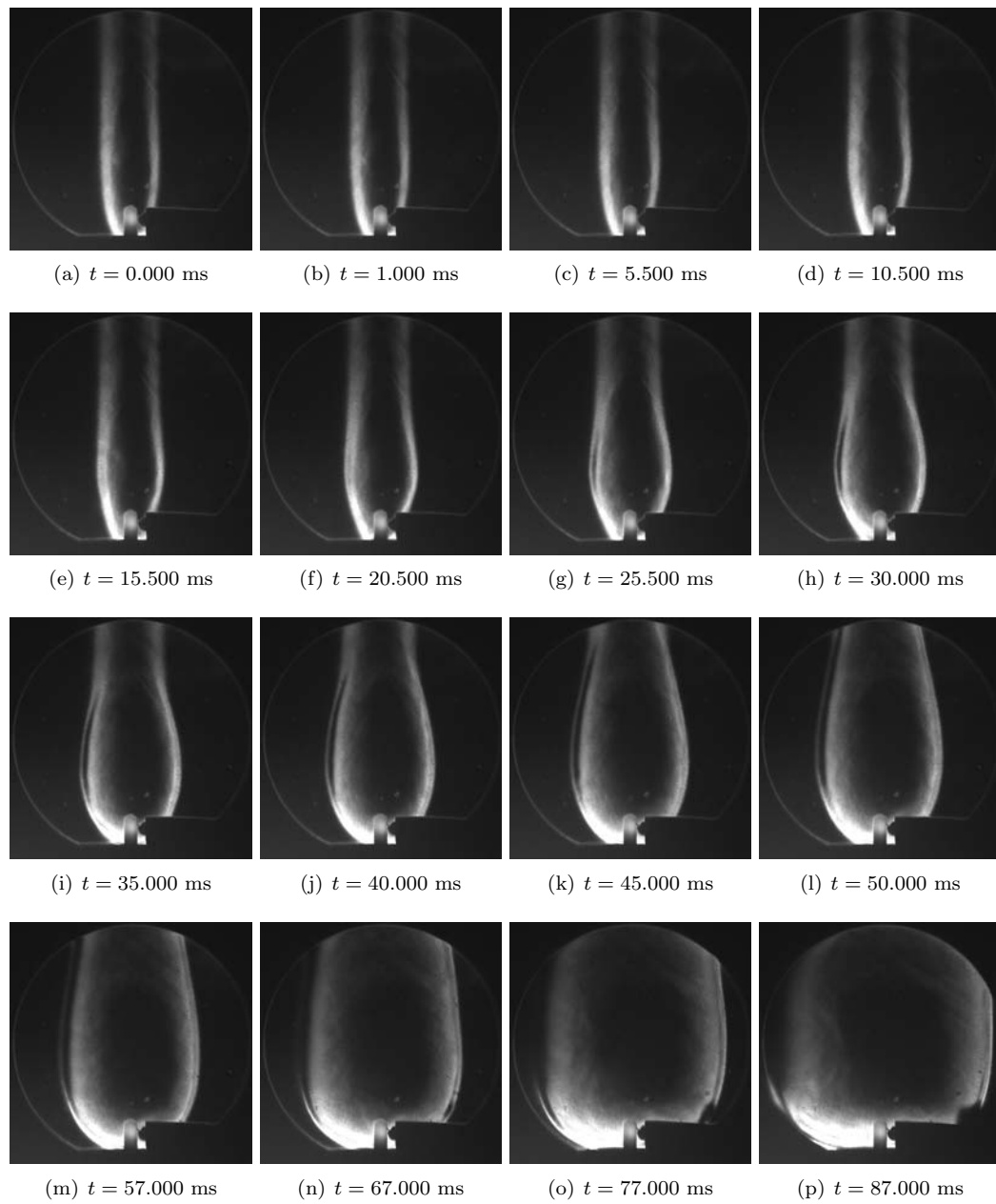


Figure K.16: Shot 28

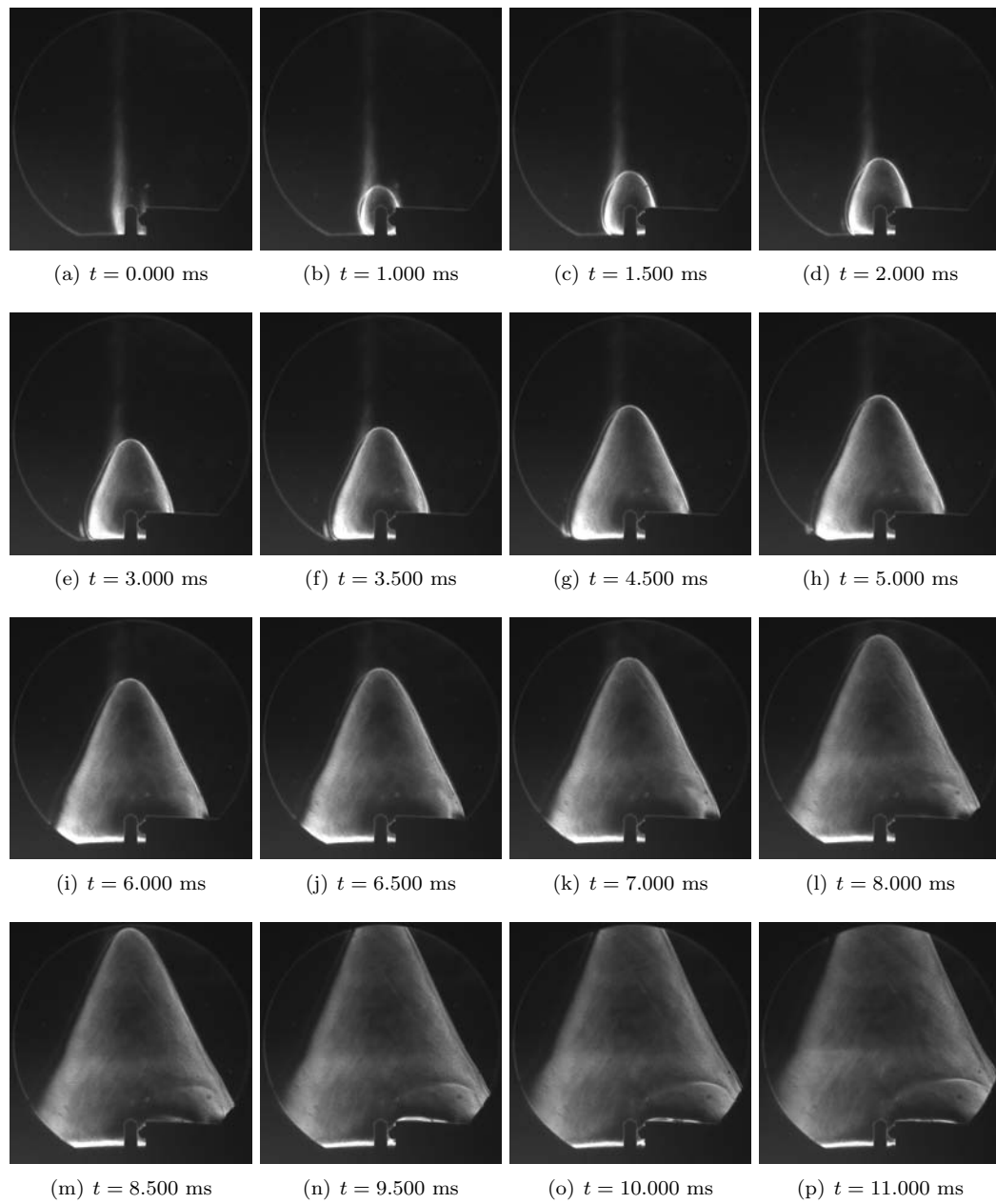


Figure K.17: Shot 29

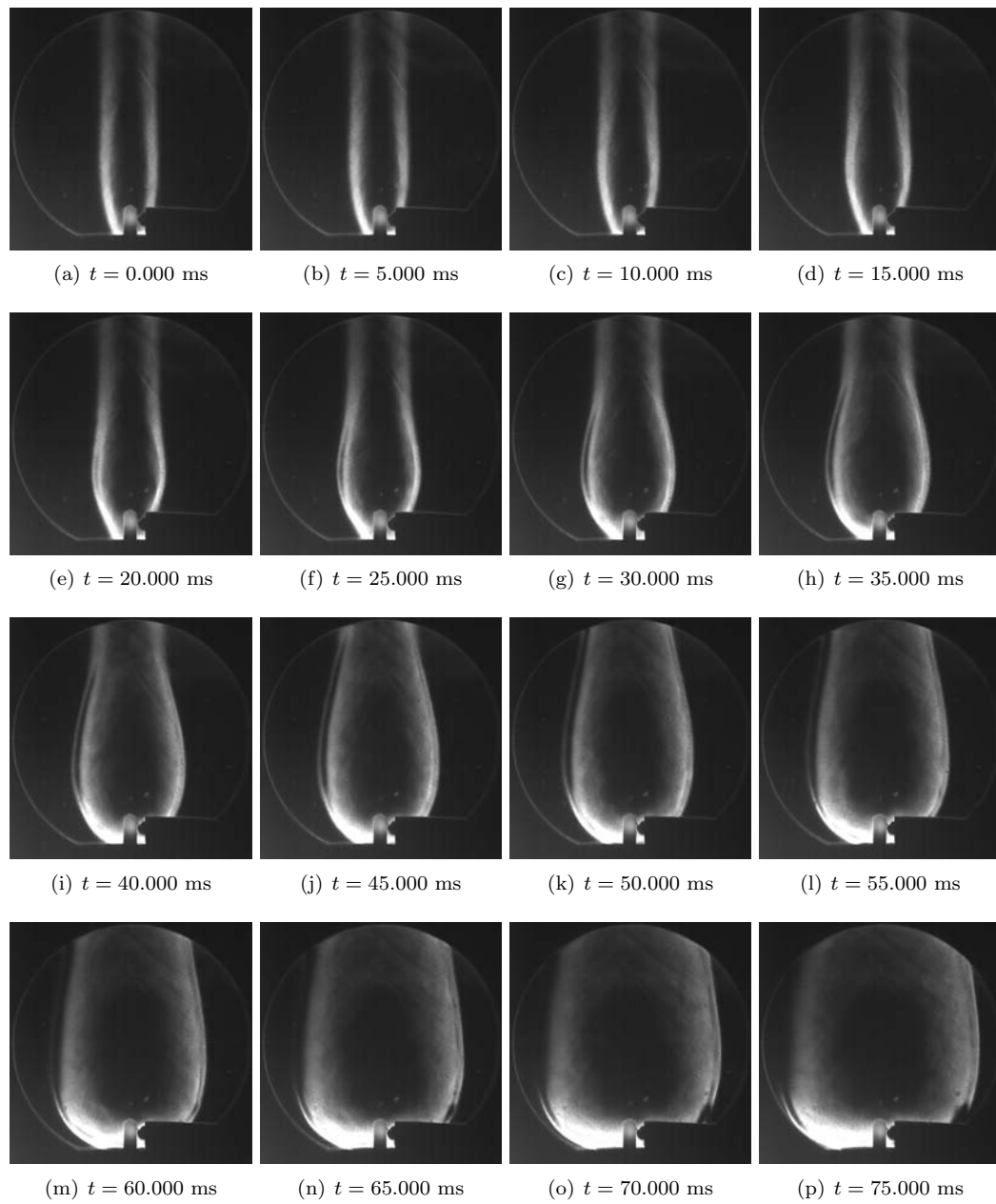


Figure K.18: Shot 30

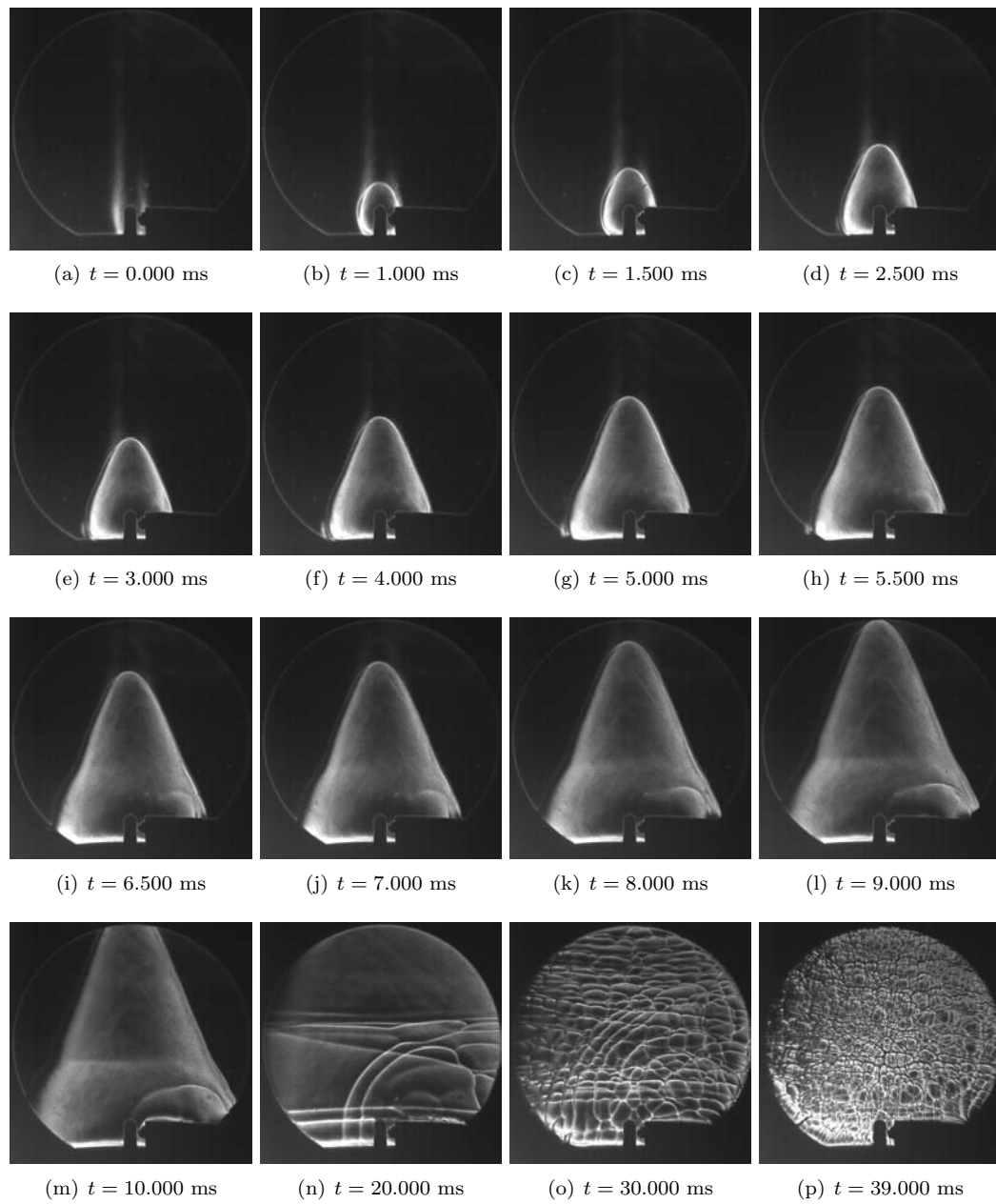


Figure K.19: Shot 31

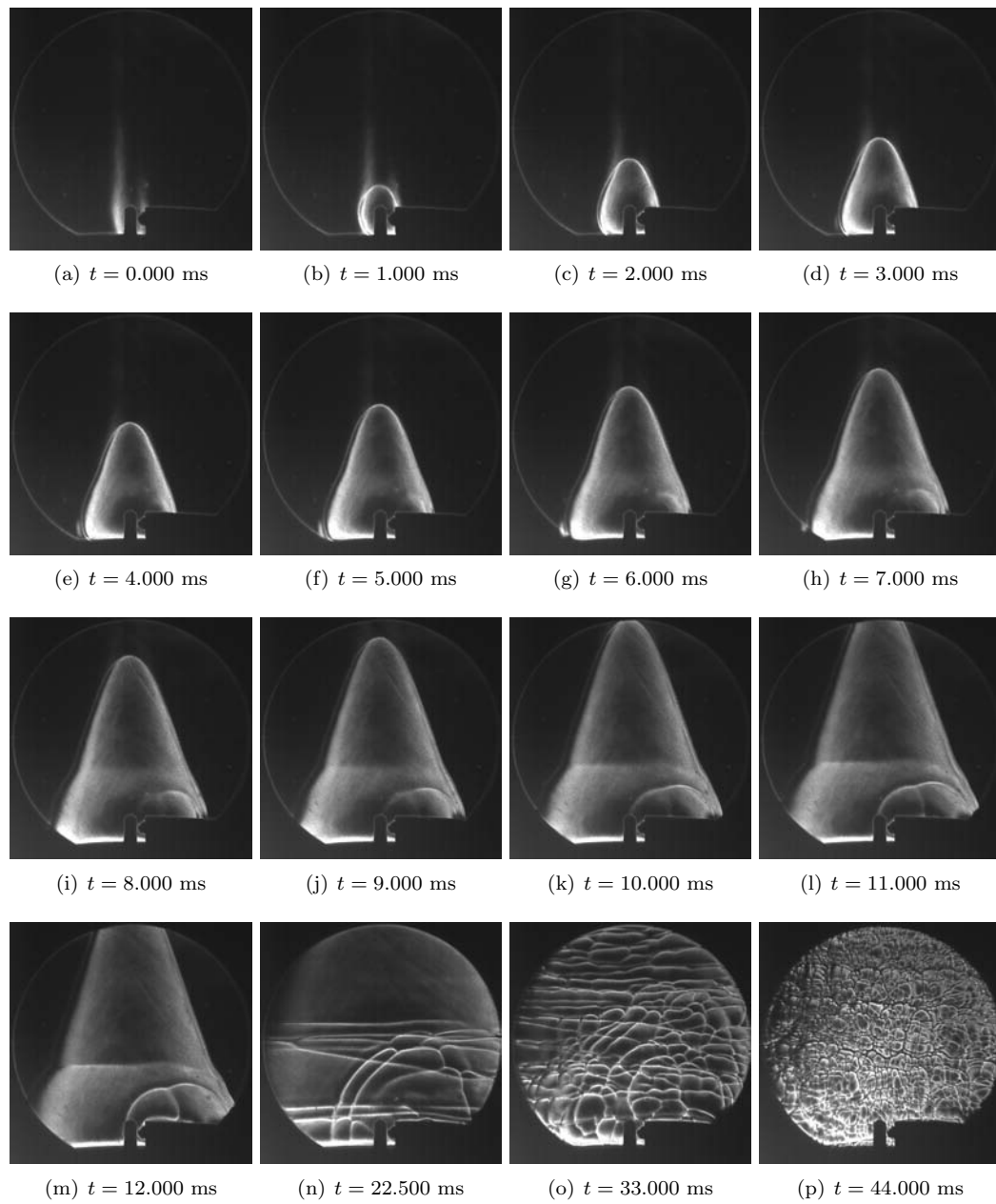


Figure K.20: Shot 32

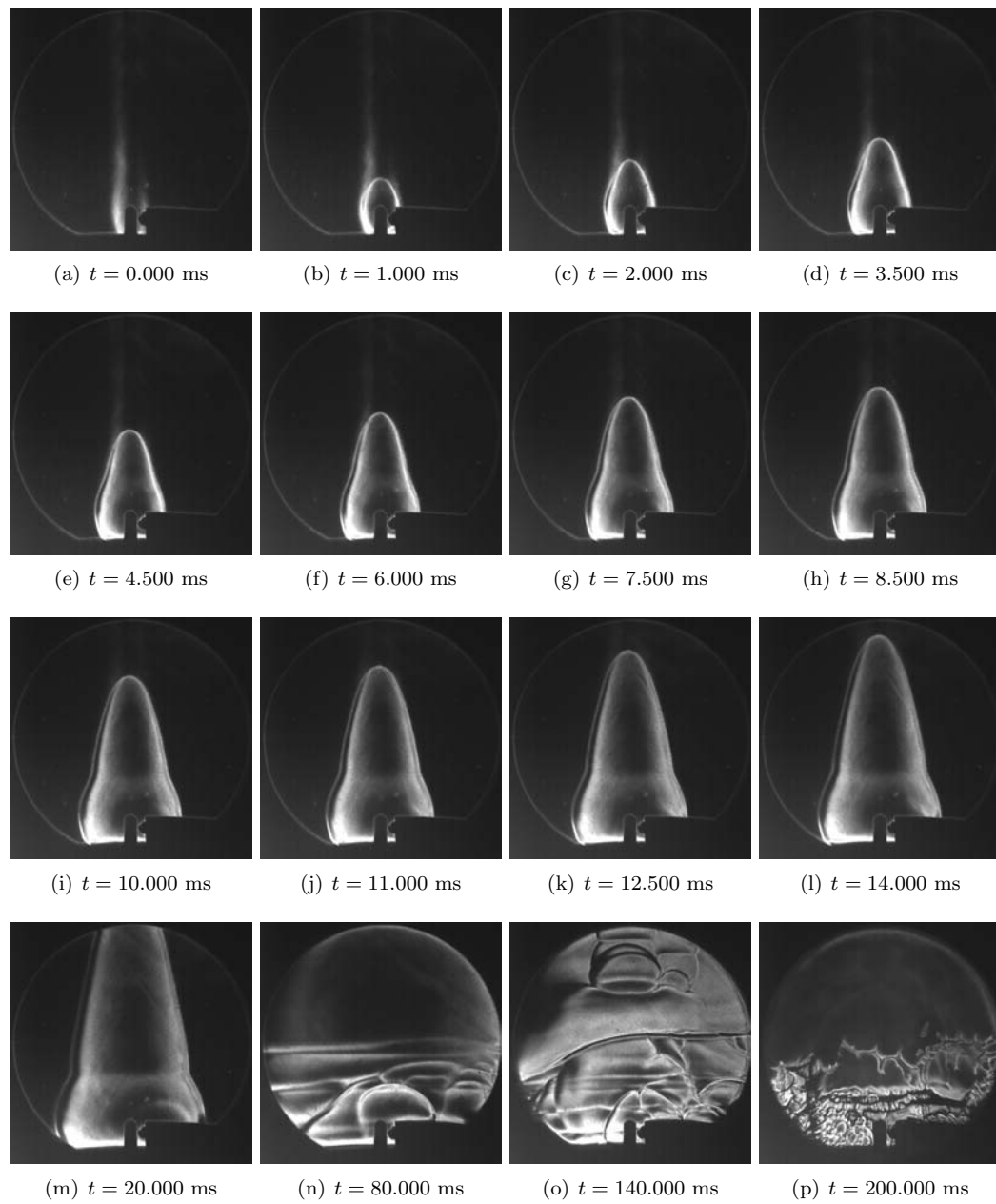


Figure K.21: Shot 33

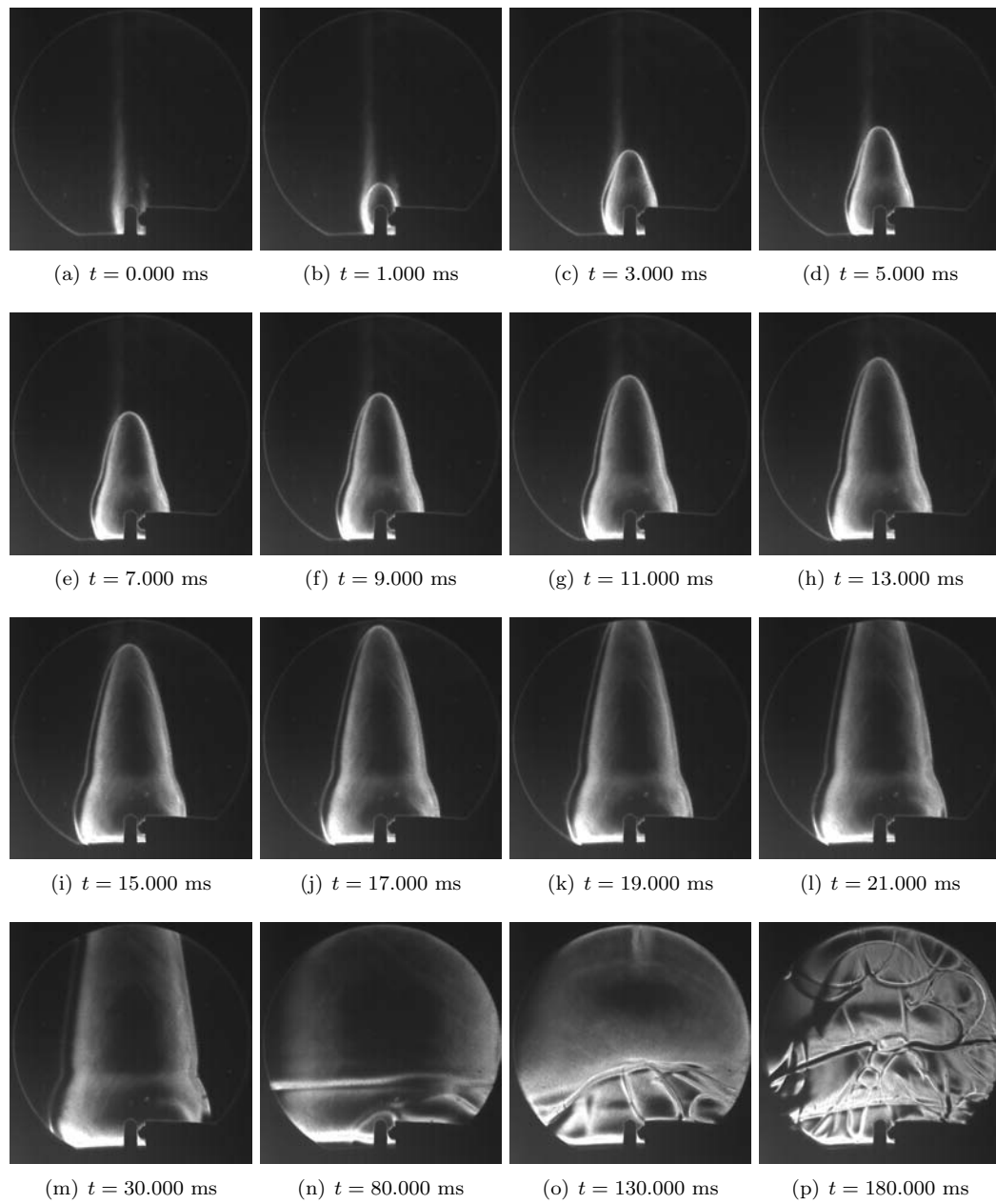


Figure K.22: Shot 34

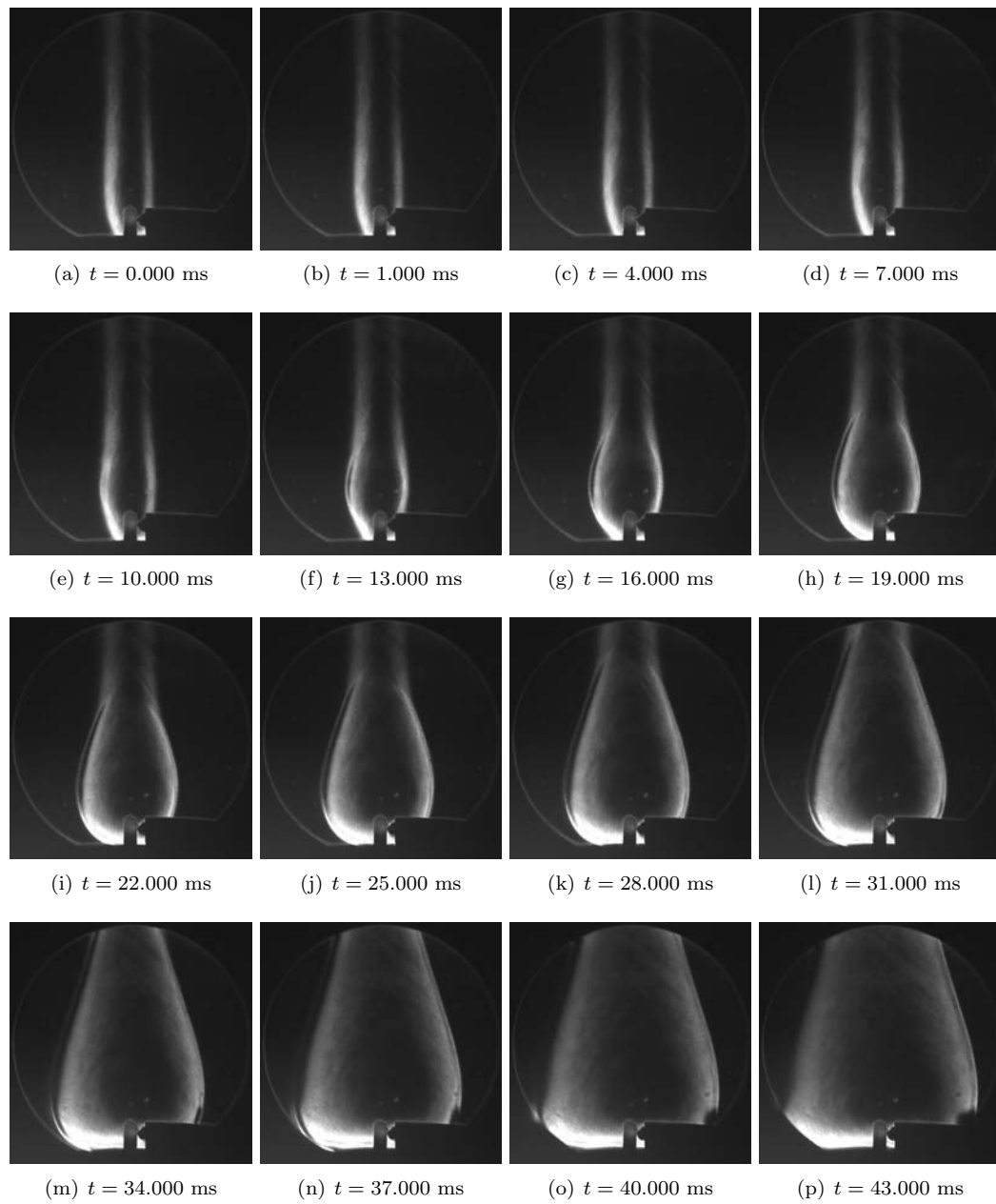


Figure K.23: Shot 36

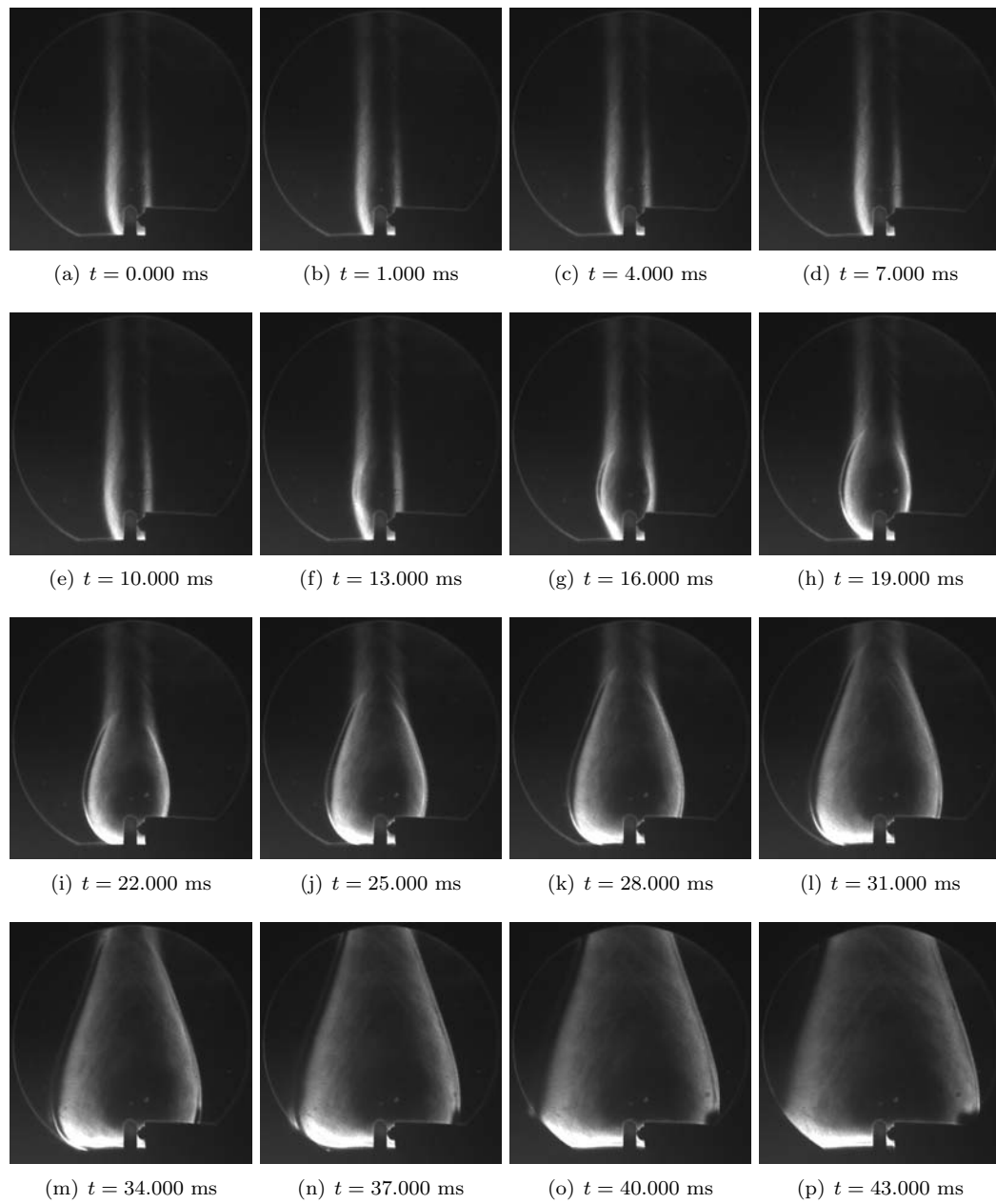


Figure K.24: Shot 37

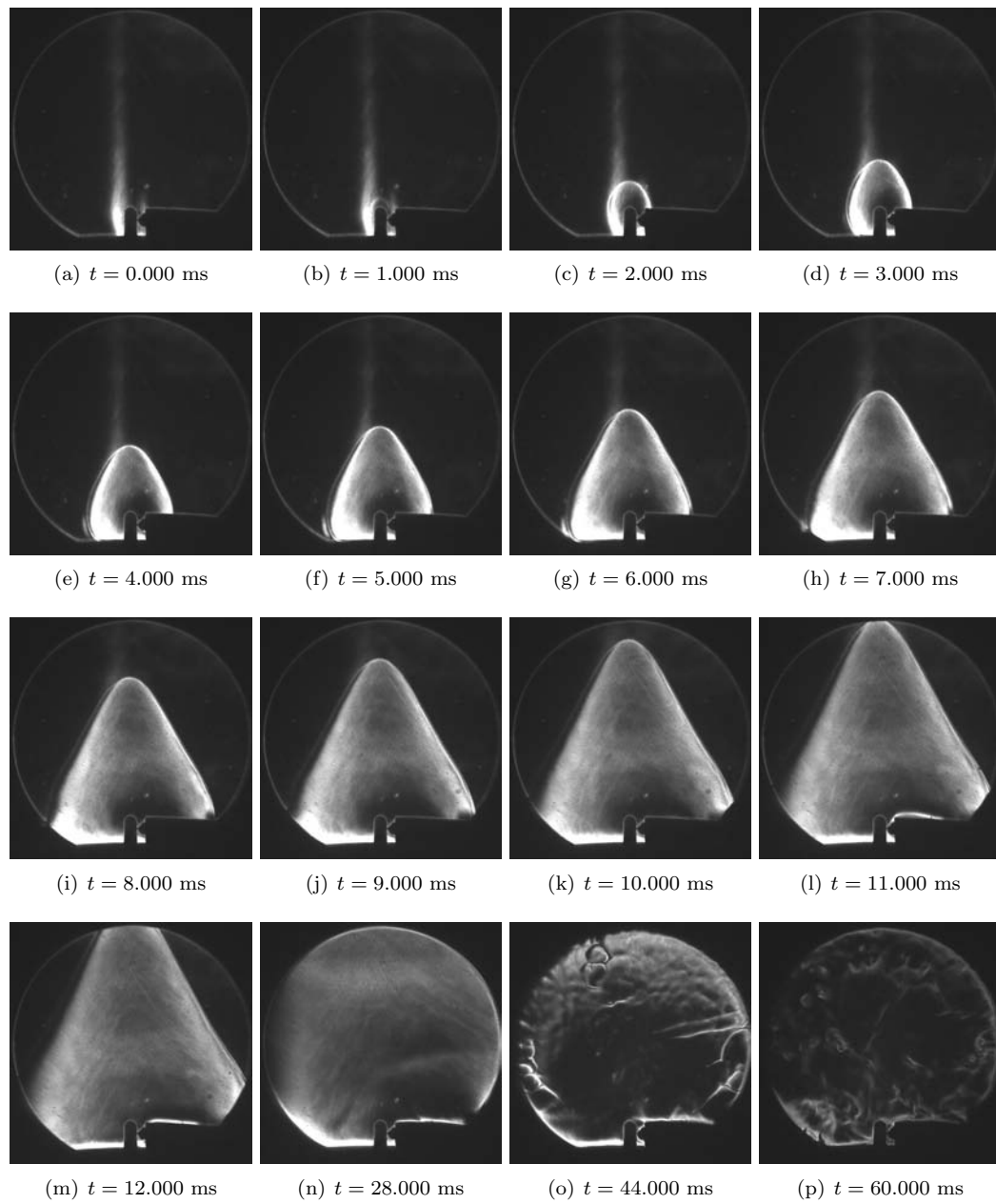


Figure K.25: Shot 38

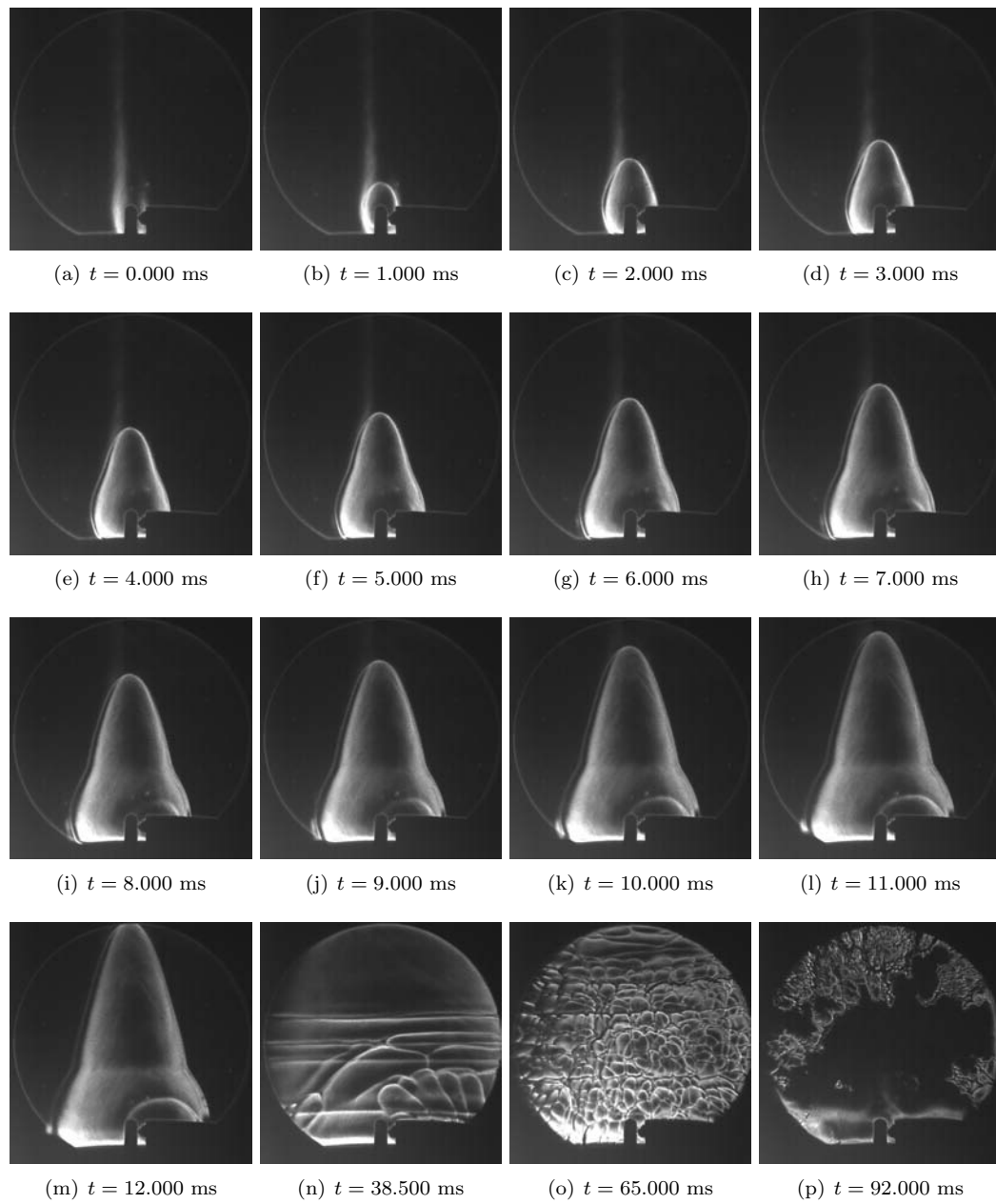


Figure K.26: Shot 40

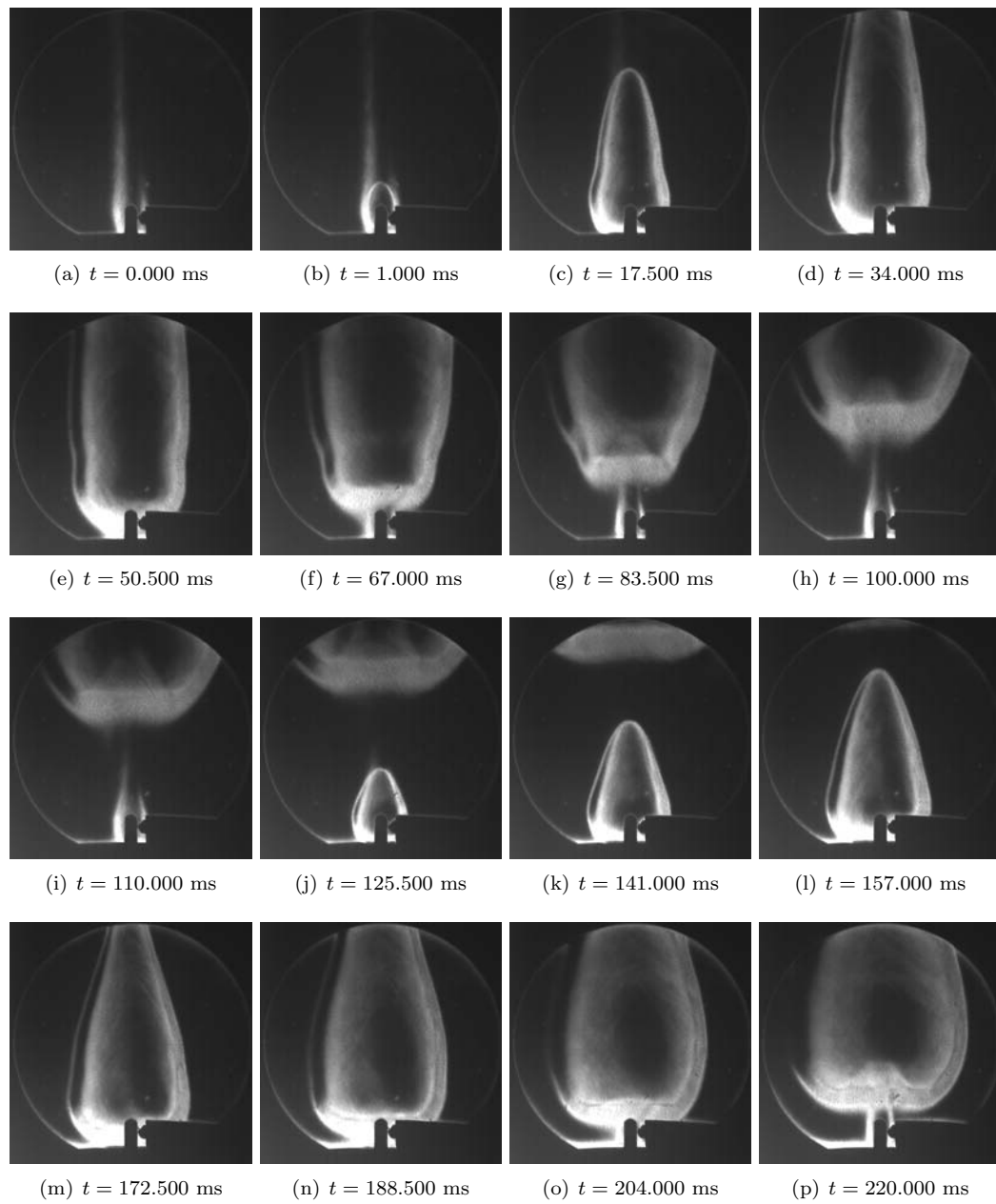


Figure K.27: Shot 41

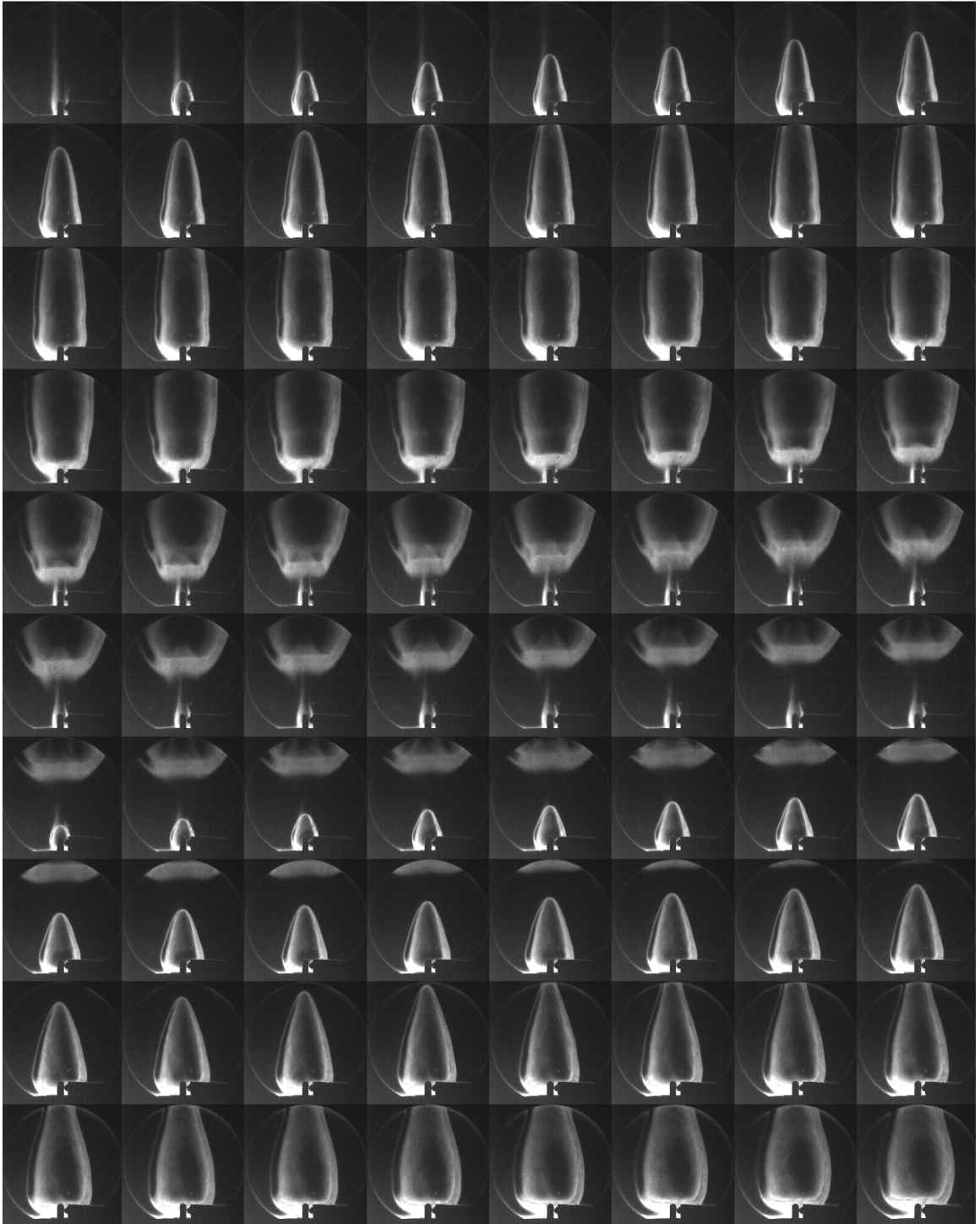


Figure K.28: Shot 41 montage ($\Delta t = 2.5$ ms between images)

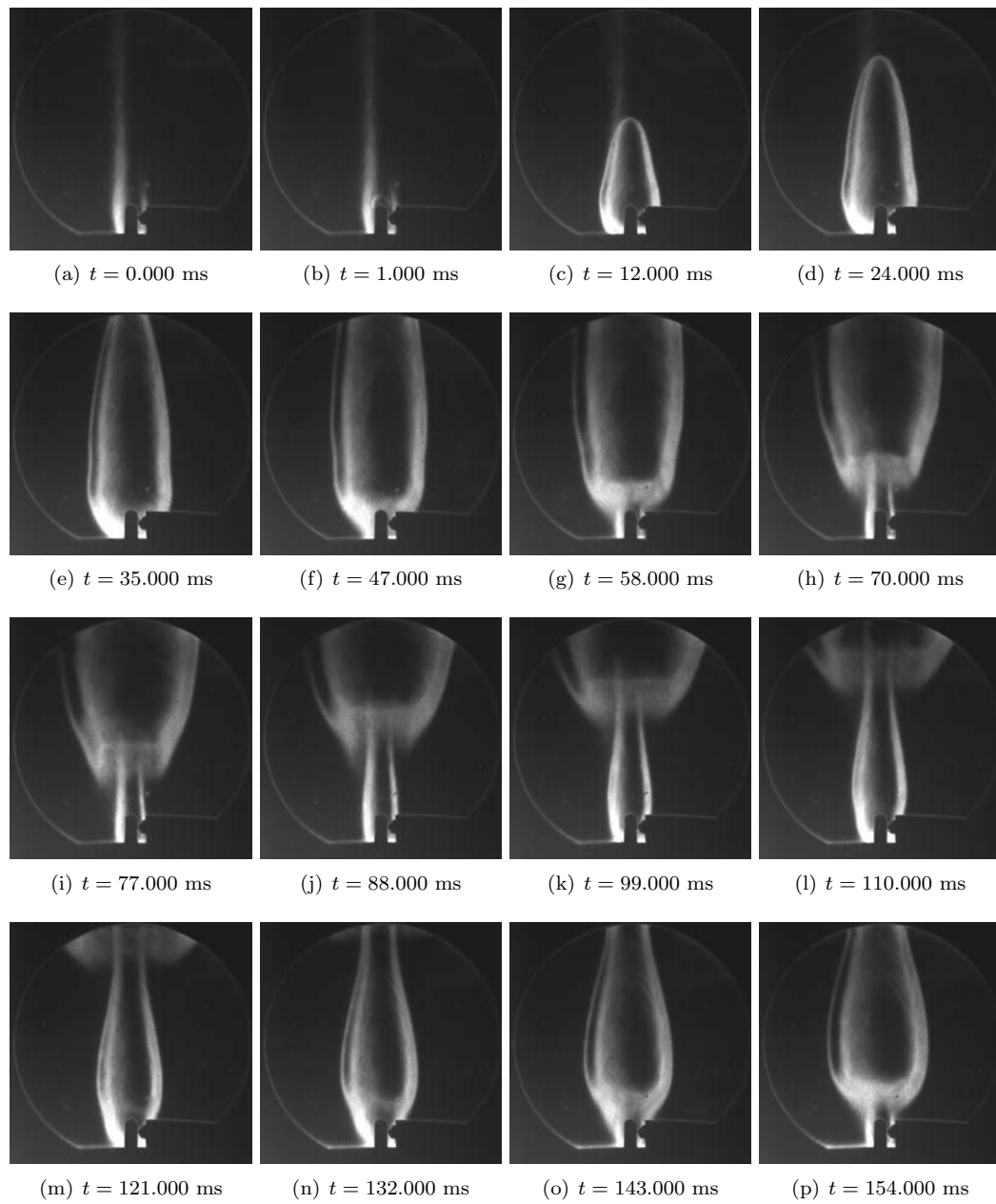


Figure K.29: Shot 42

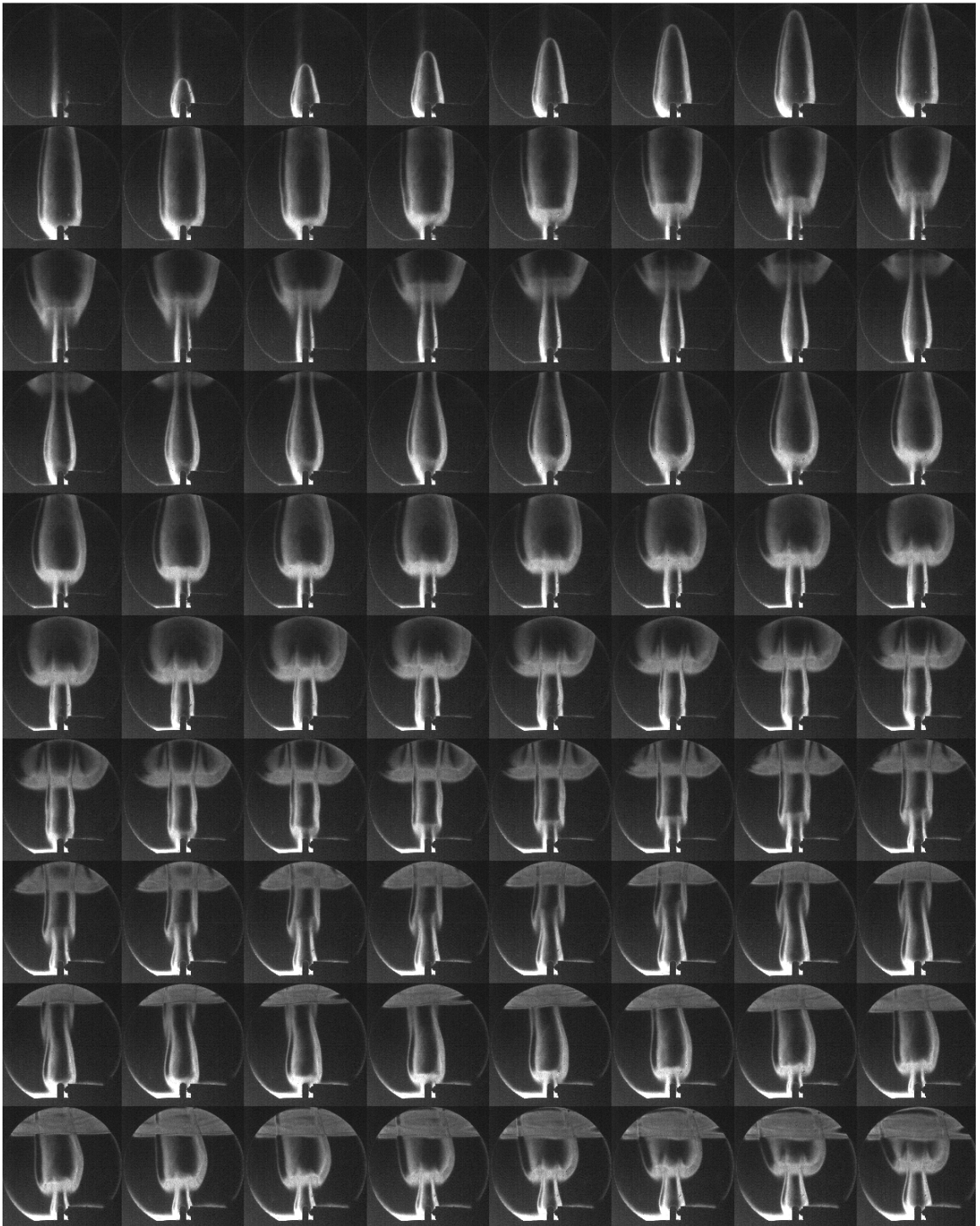


Figure K.30: Shot 42 montage ($\Delta t = 5$ ms between images)

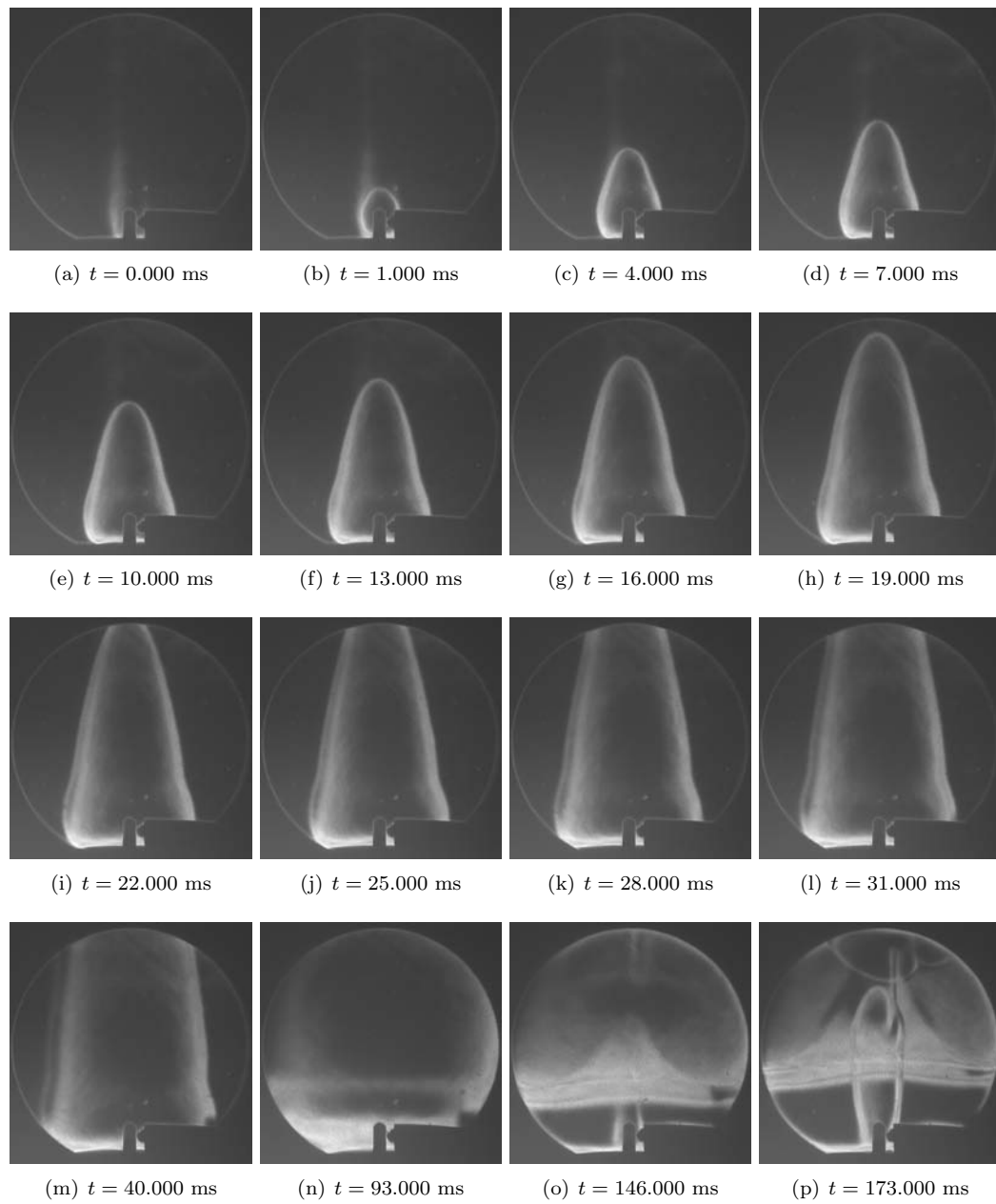


Figure K.31: Shot 43

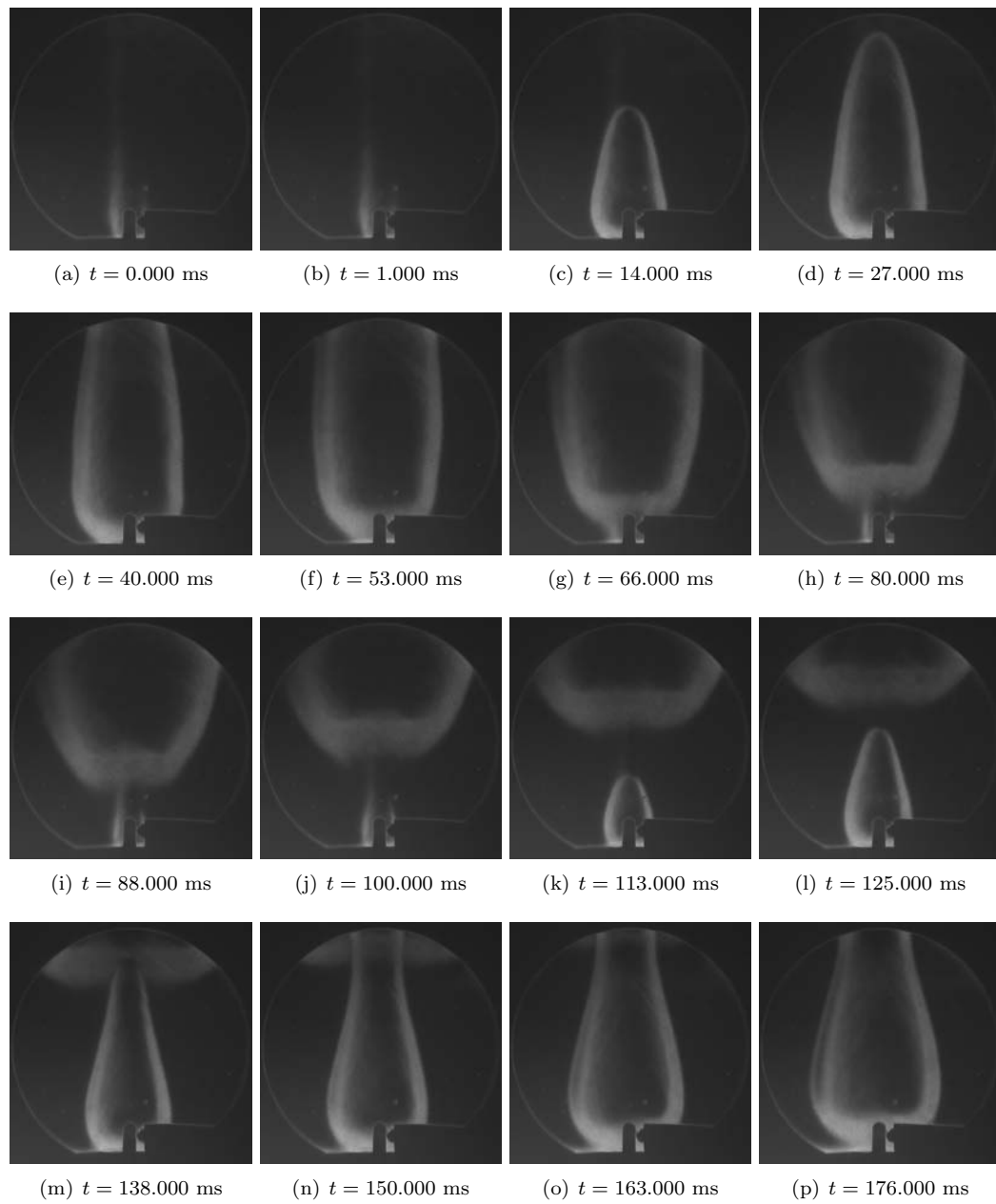


Figure K.32: Shot 44

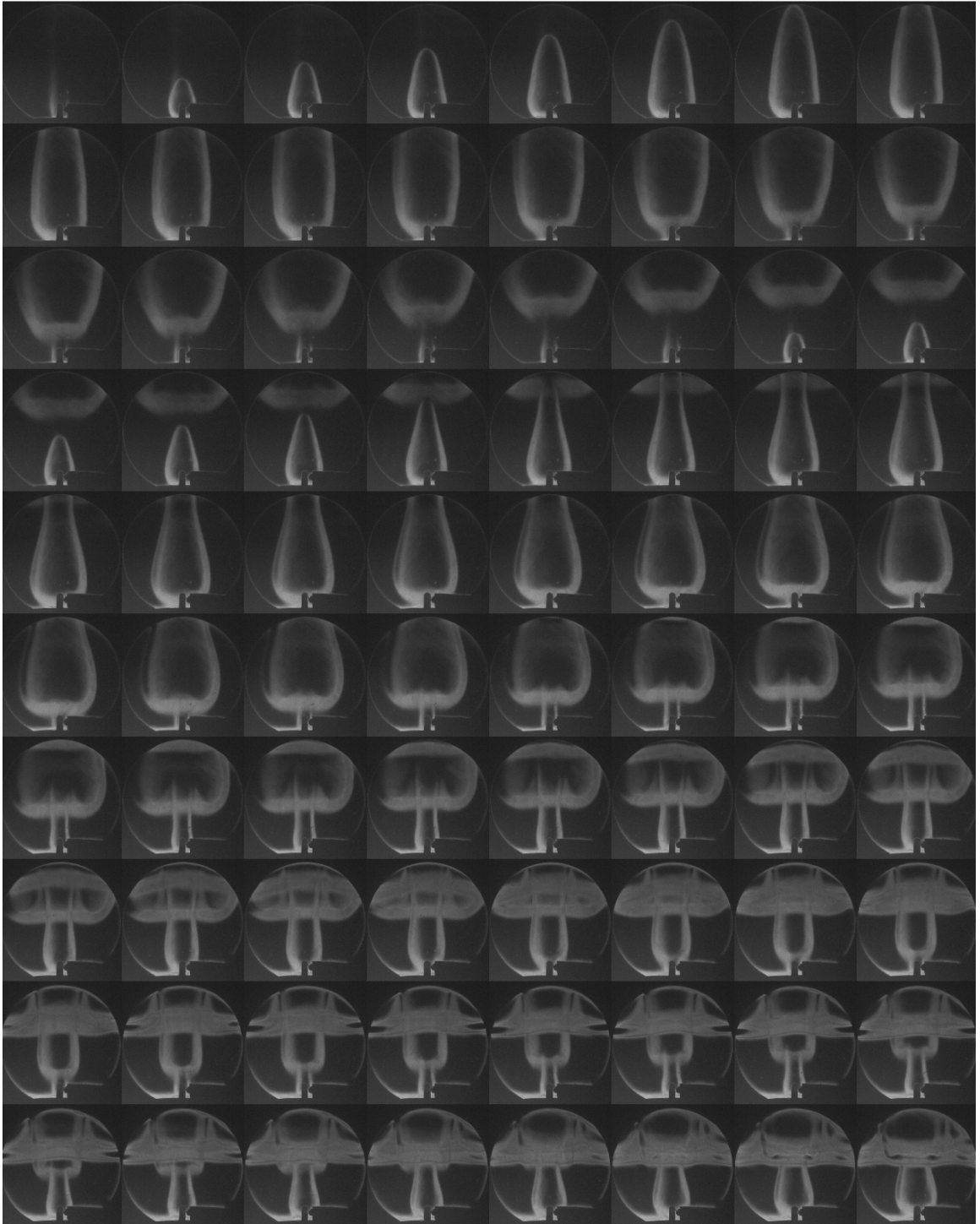


Figure K.33: Shot 44 montage ($\Delta t = 5$ ms between images)

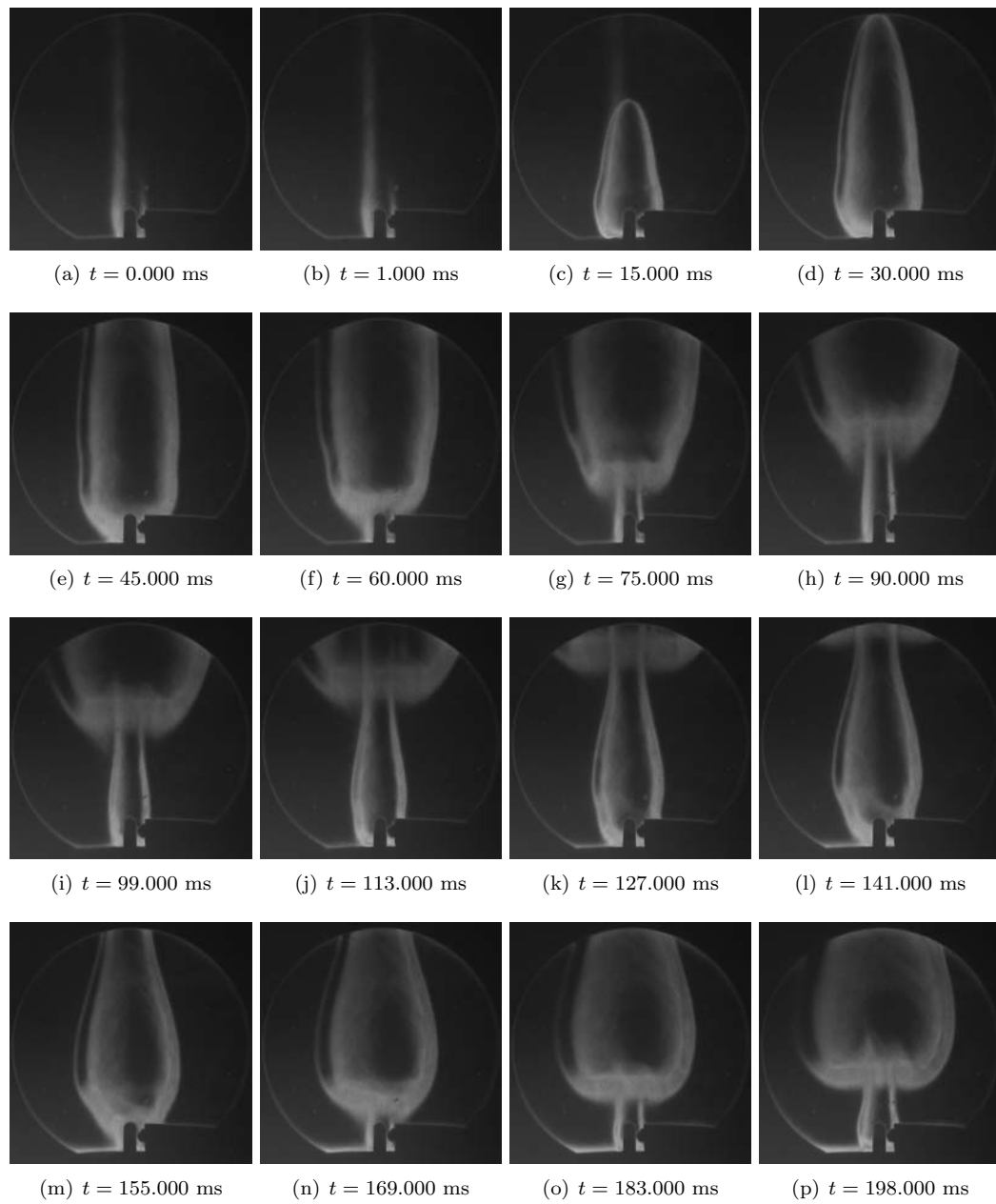


Figure K.34: Shot 45

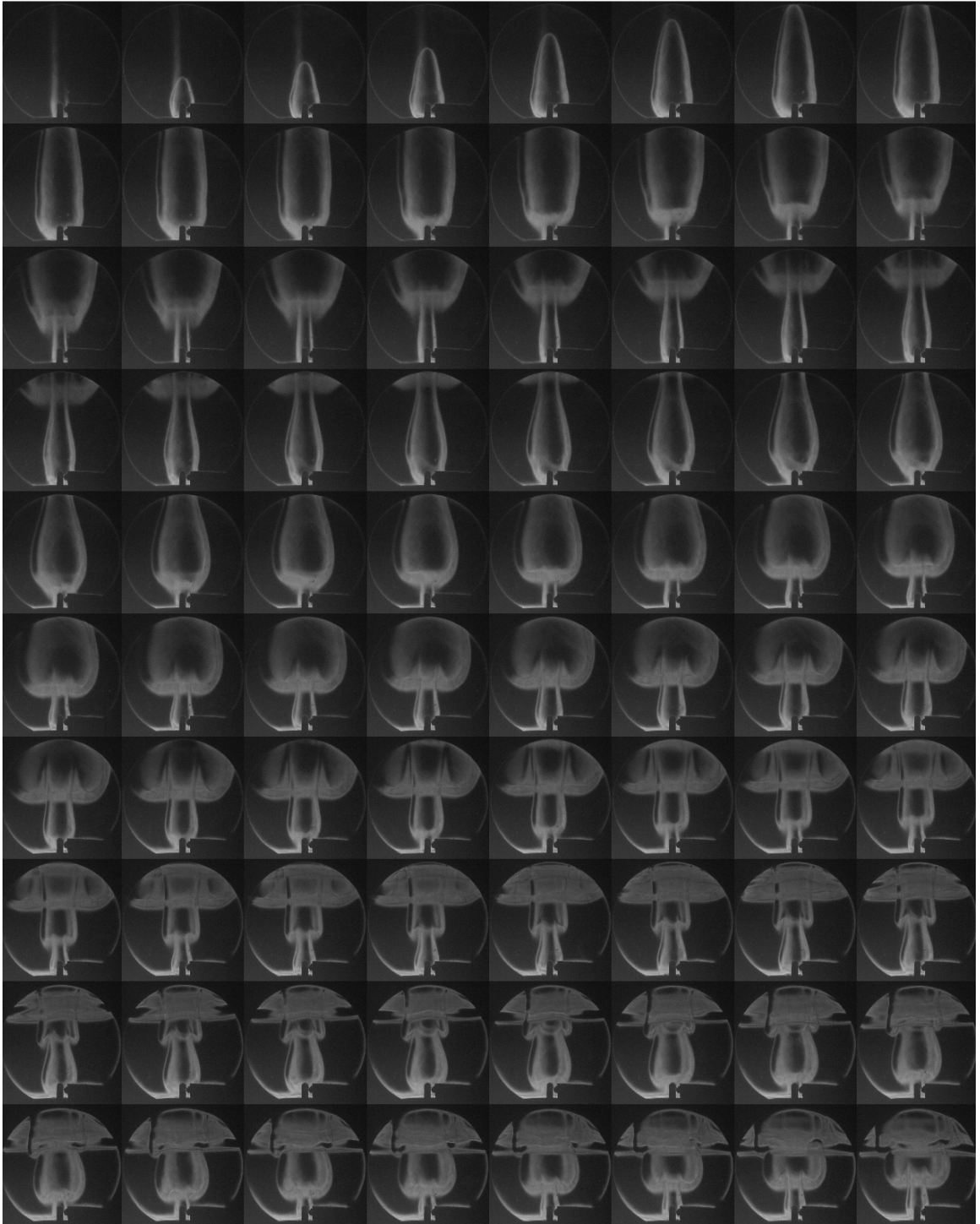


Figure K.35: Shot 45 montage ($\Delta t = 5$ ms between images)

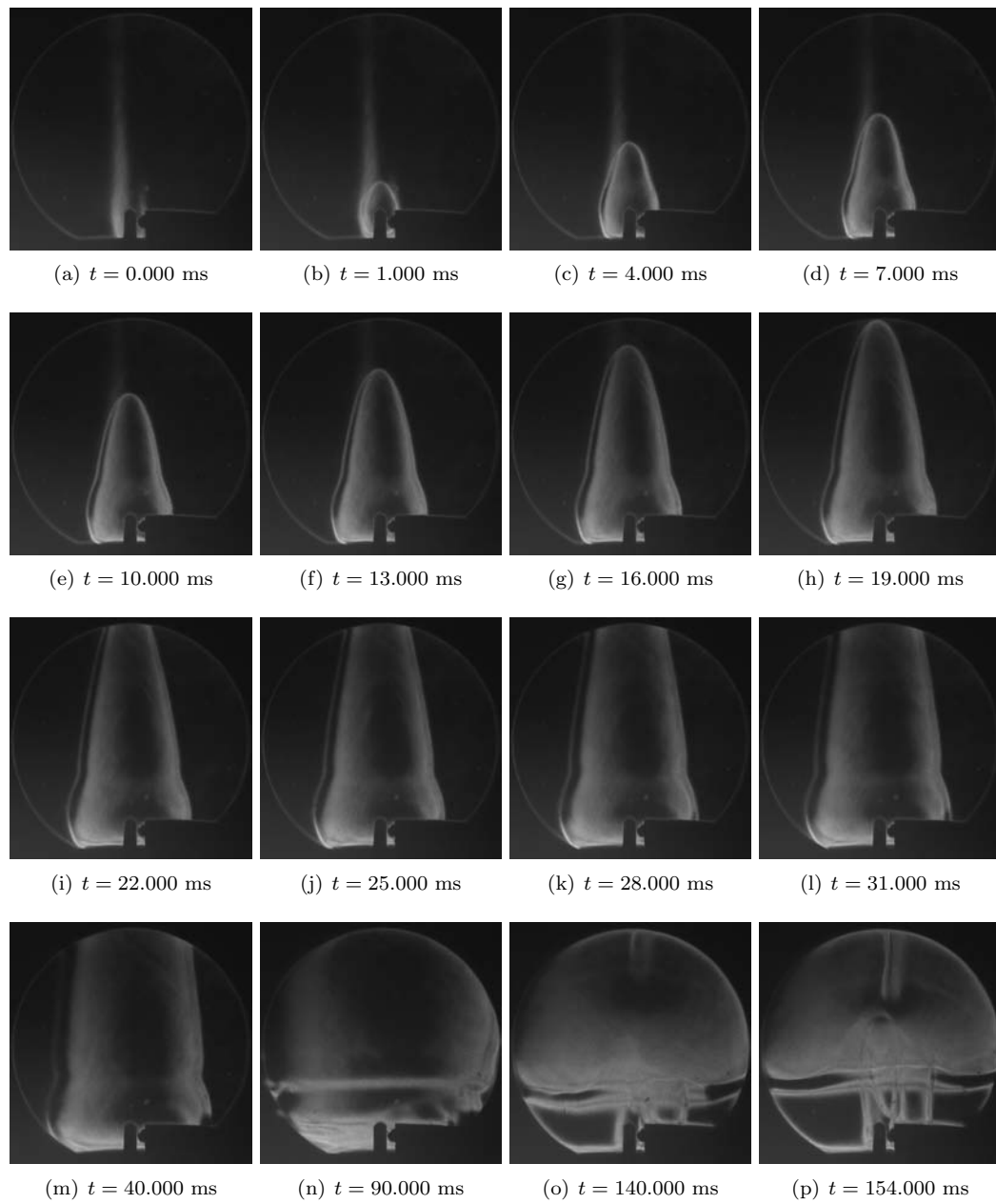


Figure K.36: Shot 46

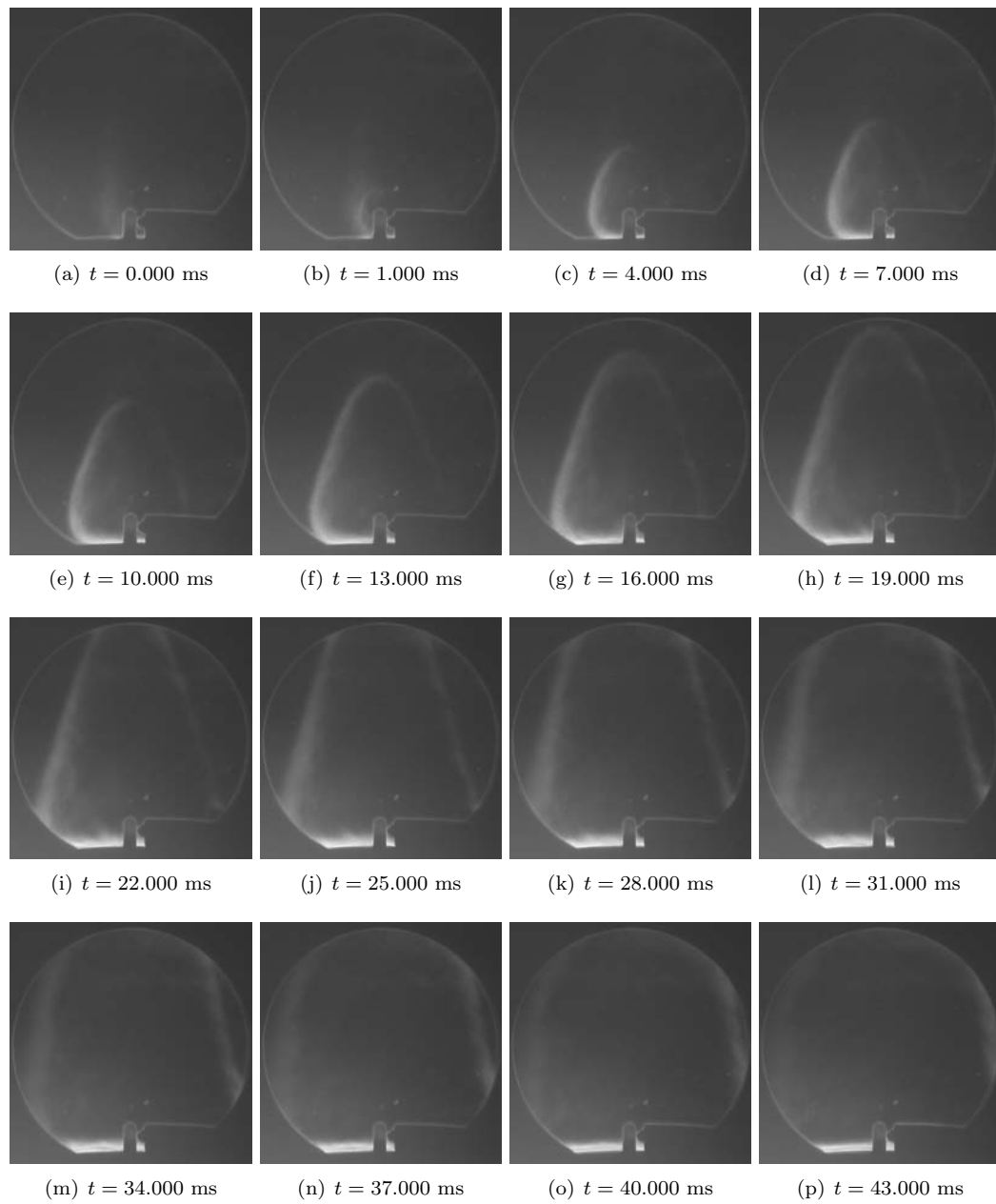


Figure K.37: Shot 47

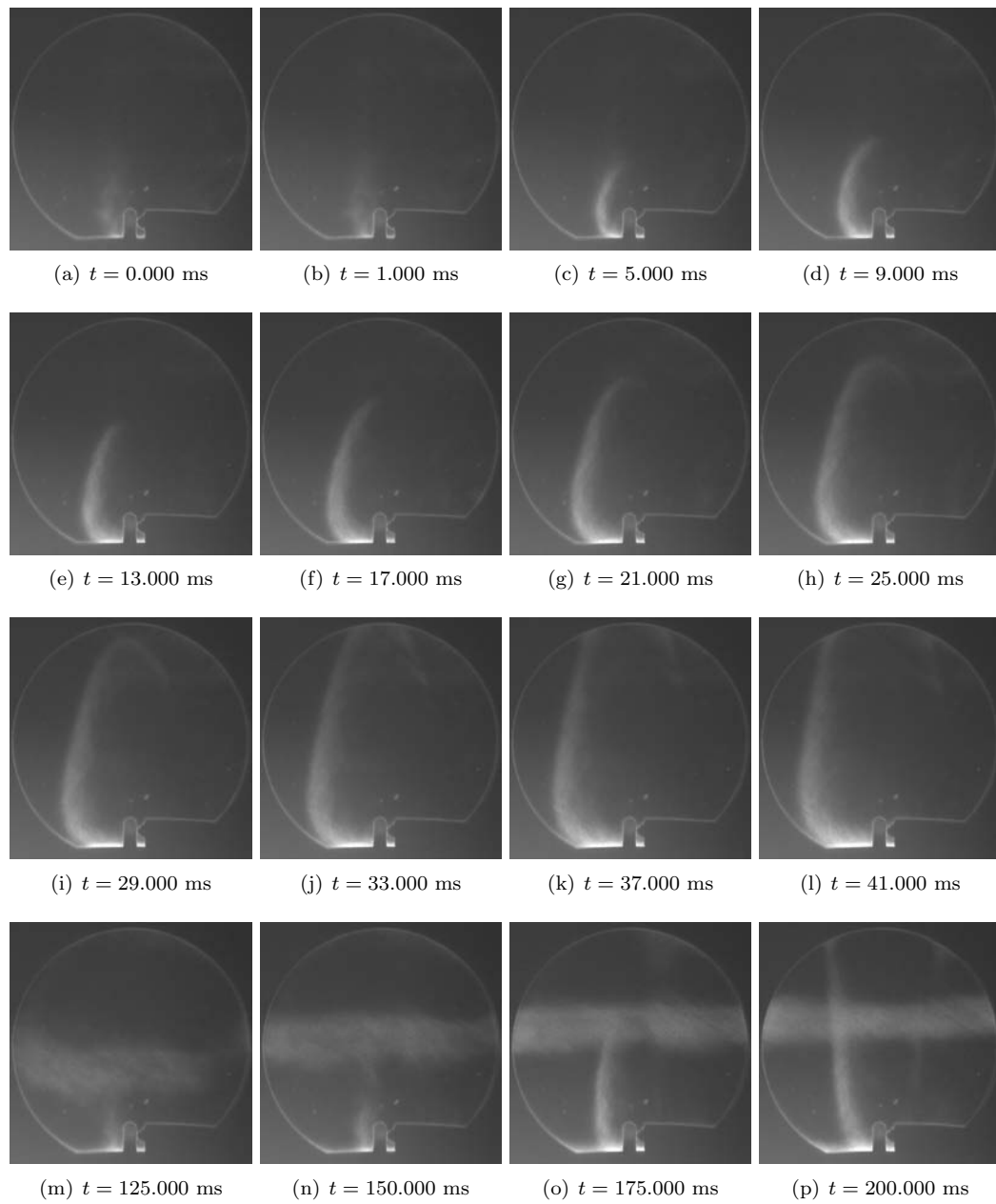


Figure K.38: Shot 48

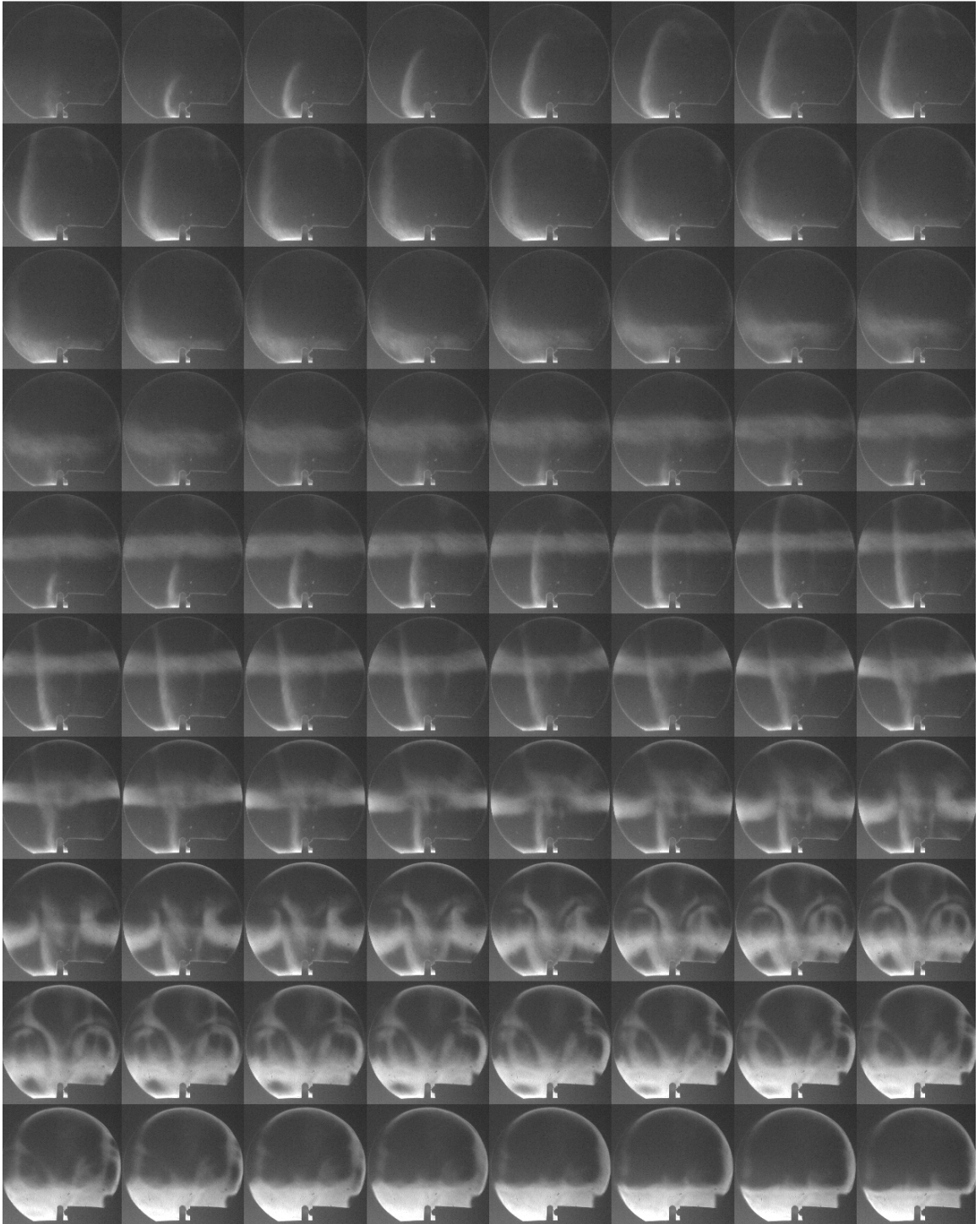


Figure K.39: Shot 48 montage ($\Delta t = 5$ ms between images)

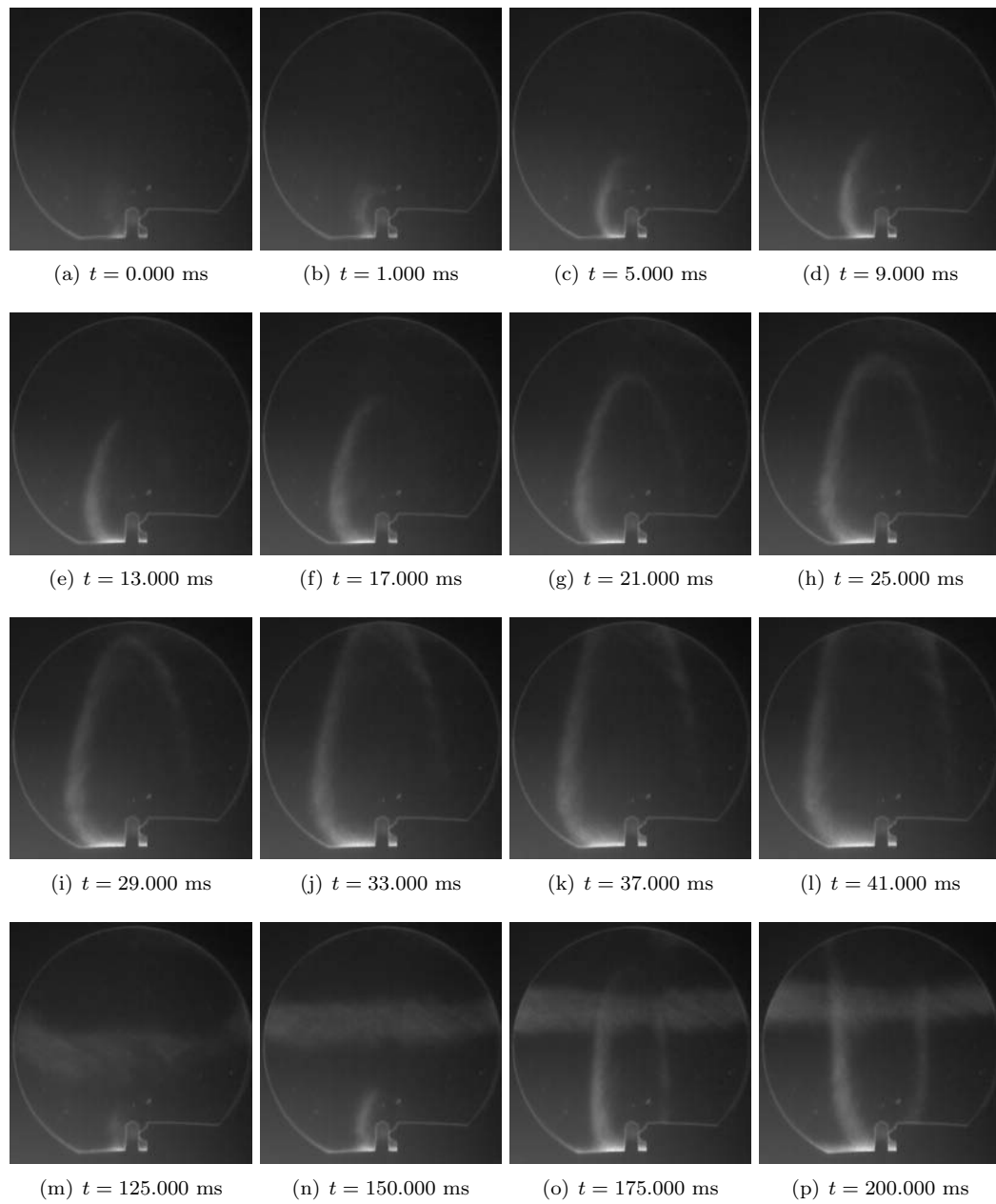


Figure K.40: Shot 49

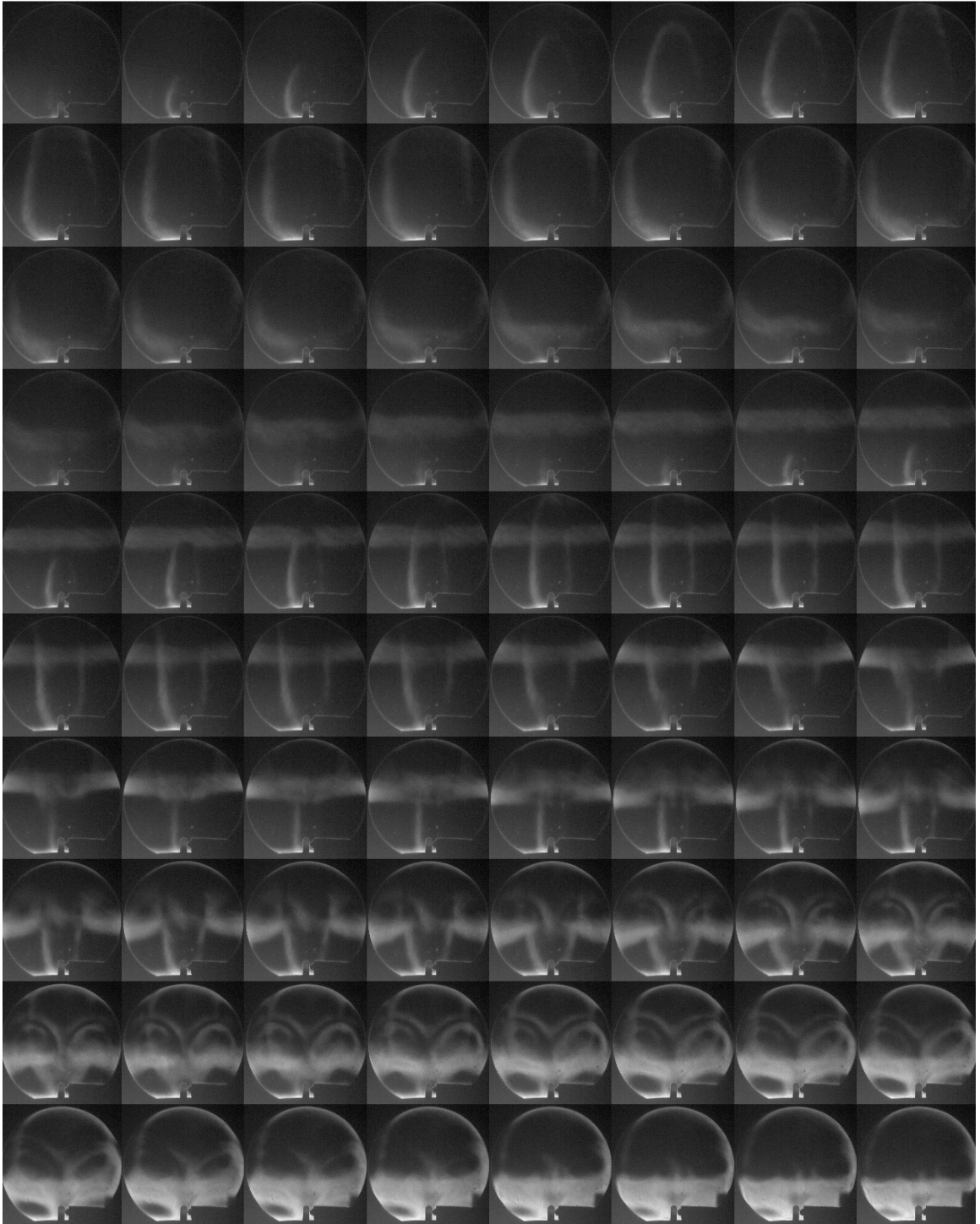


Figure K.41: Shot 49 montage ($\Delta t = 5$ ms between images)

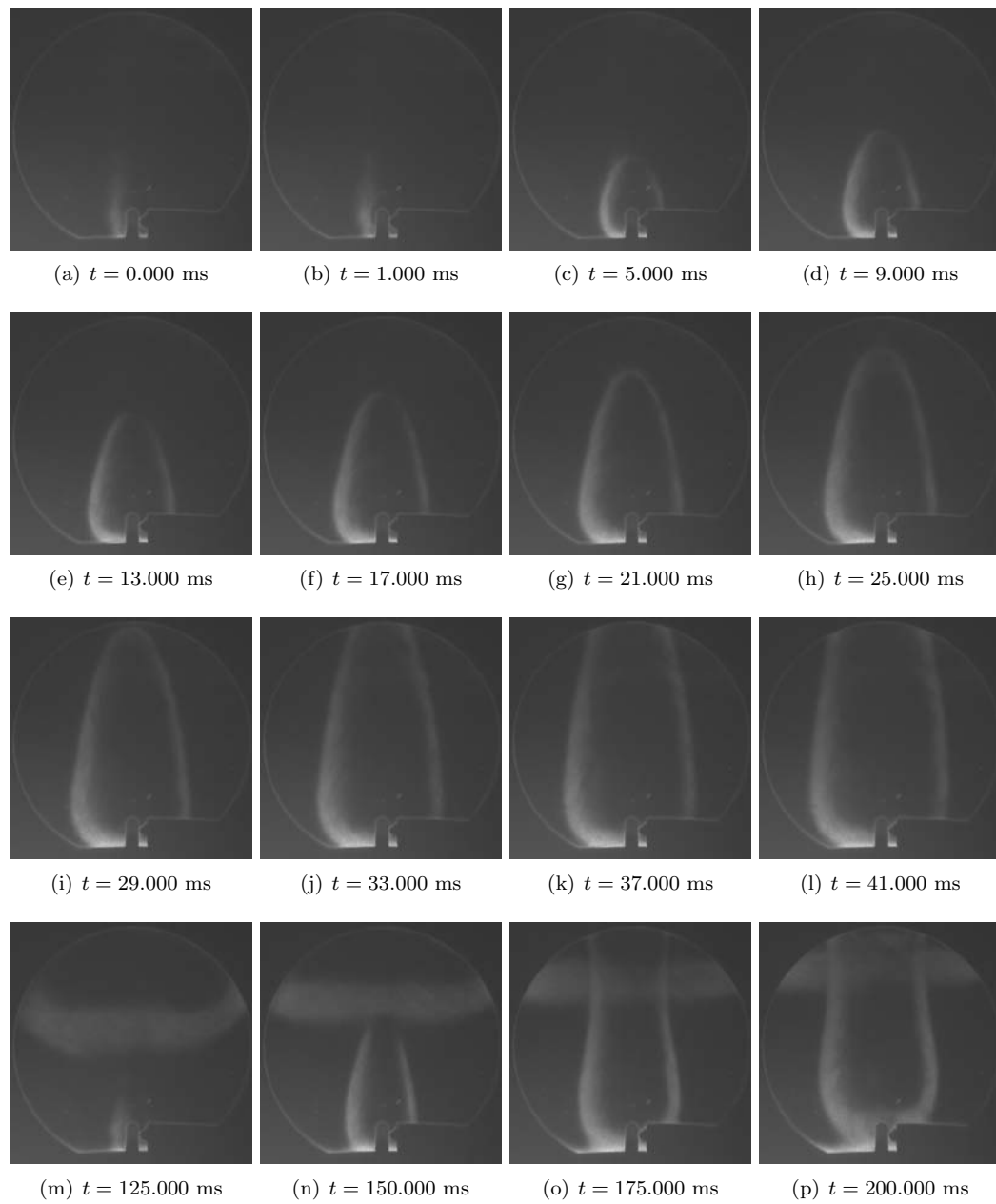


Figure K.42: Shot 50

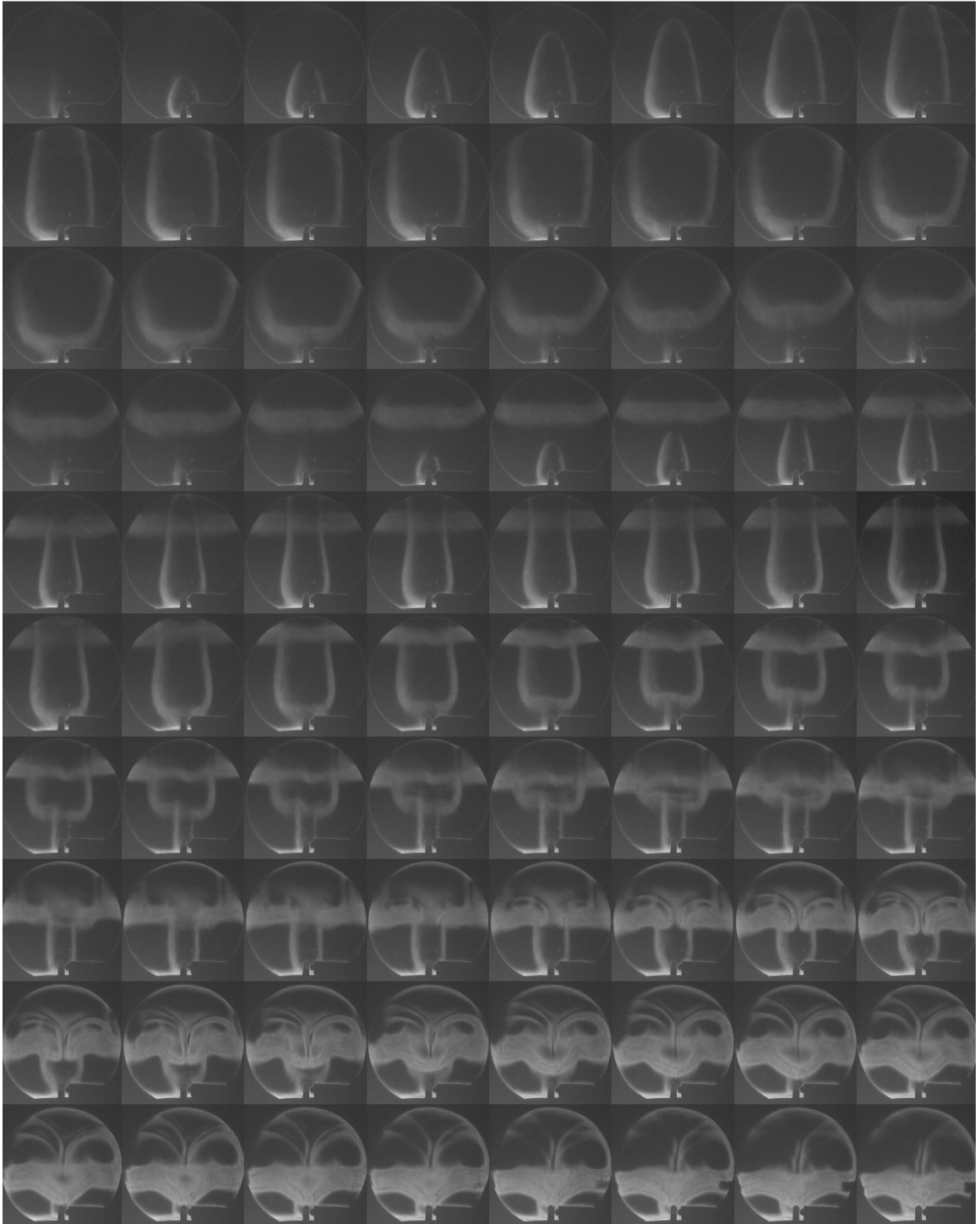


Figure K.43: Shot 50 montage ($\Delta t = 5$ ms between images)

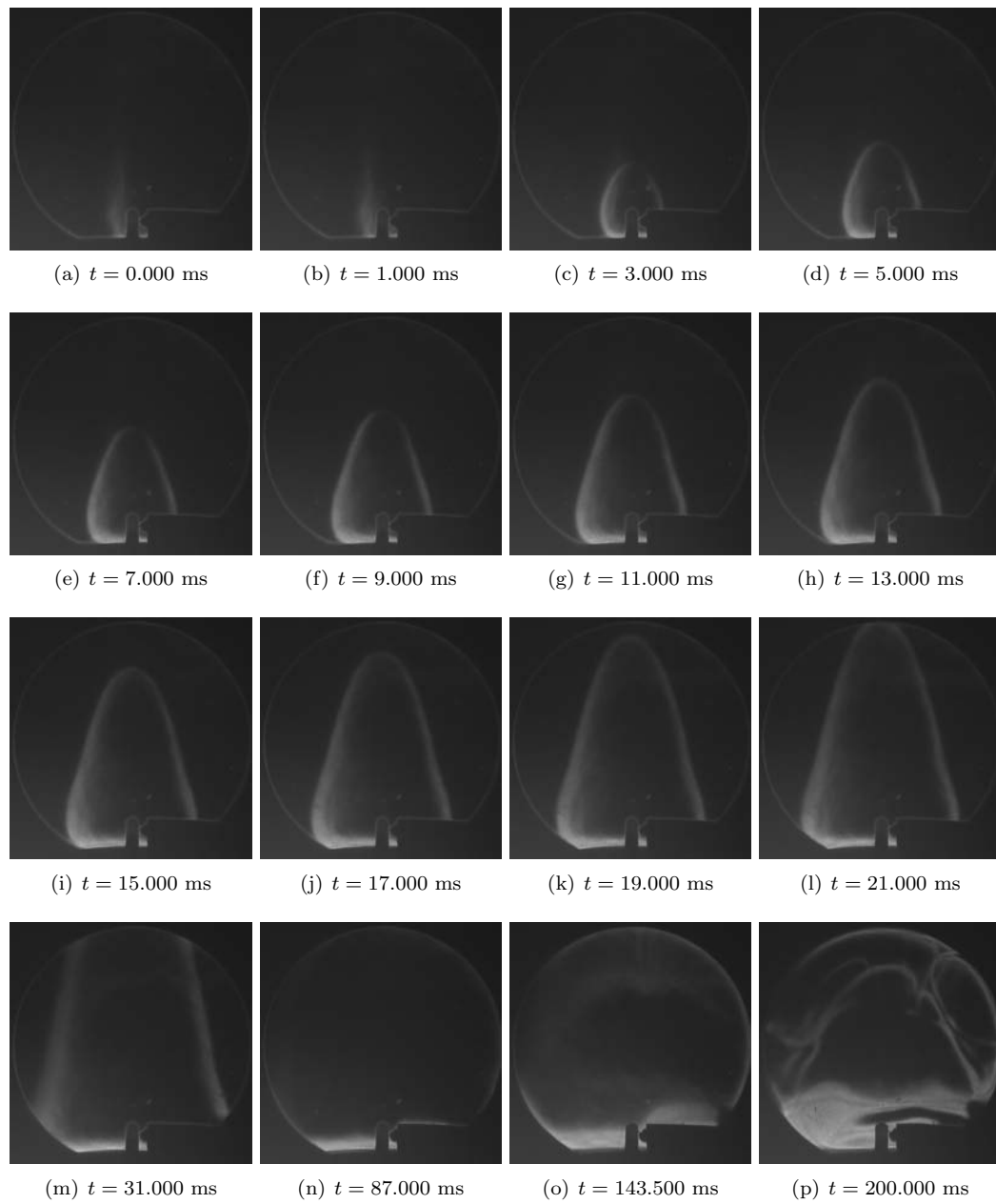


Figure K.44: Shot 51

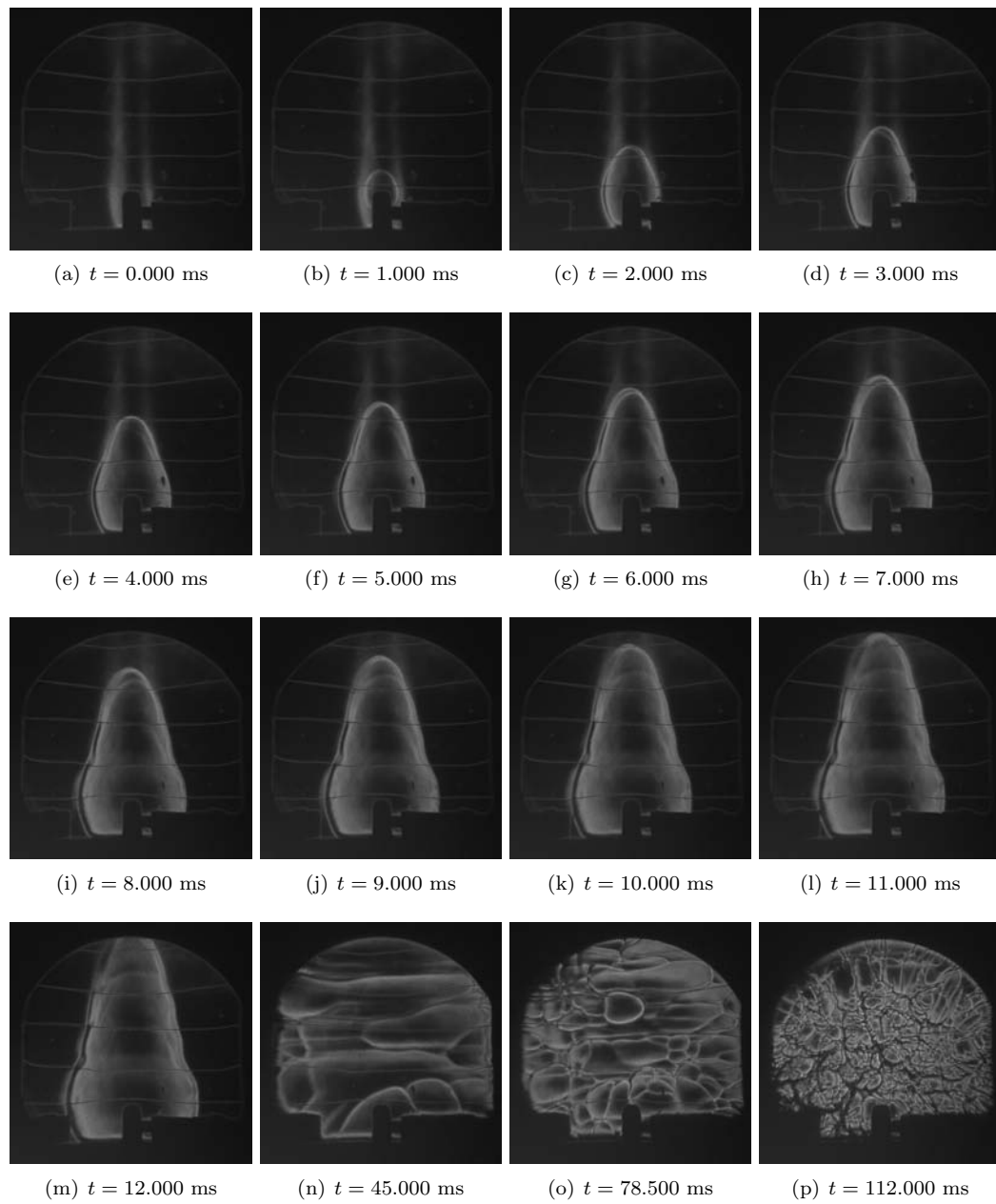


Figure K.45: Shot 52

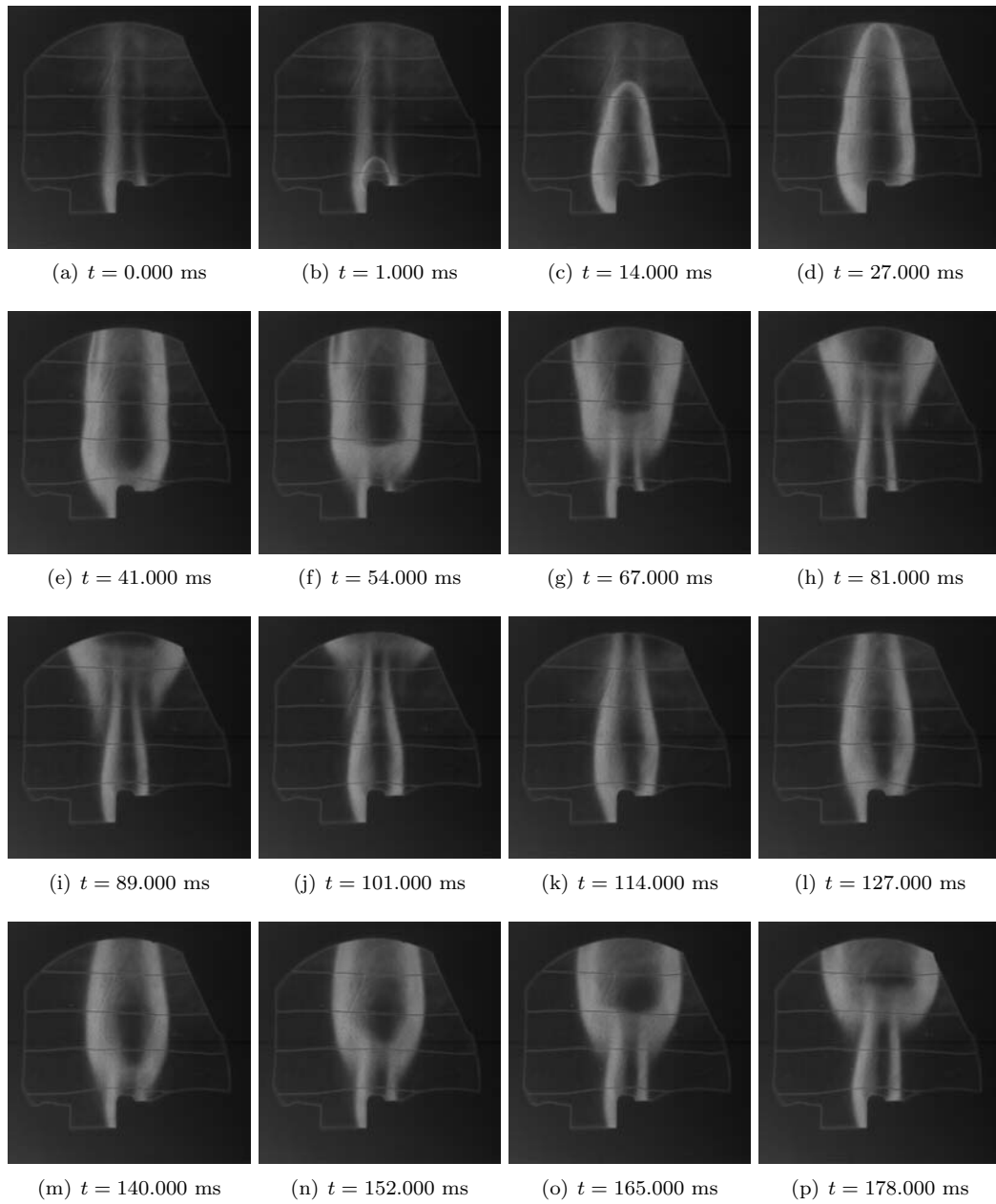


Figure K.46: Shot 54

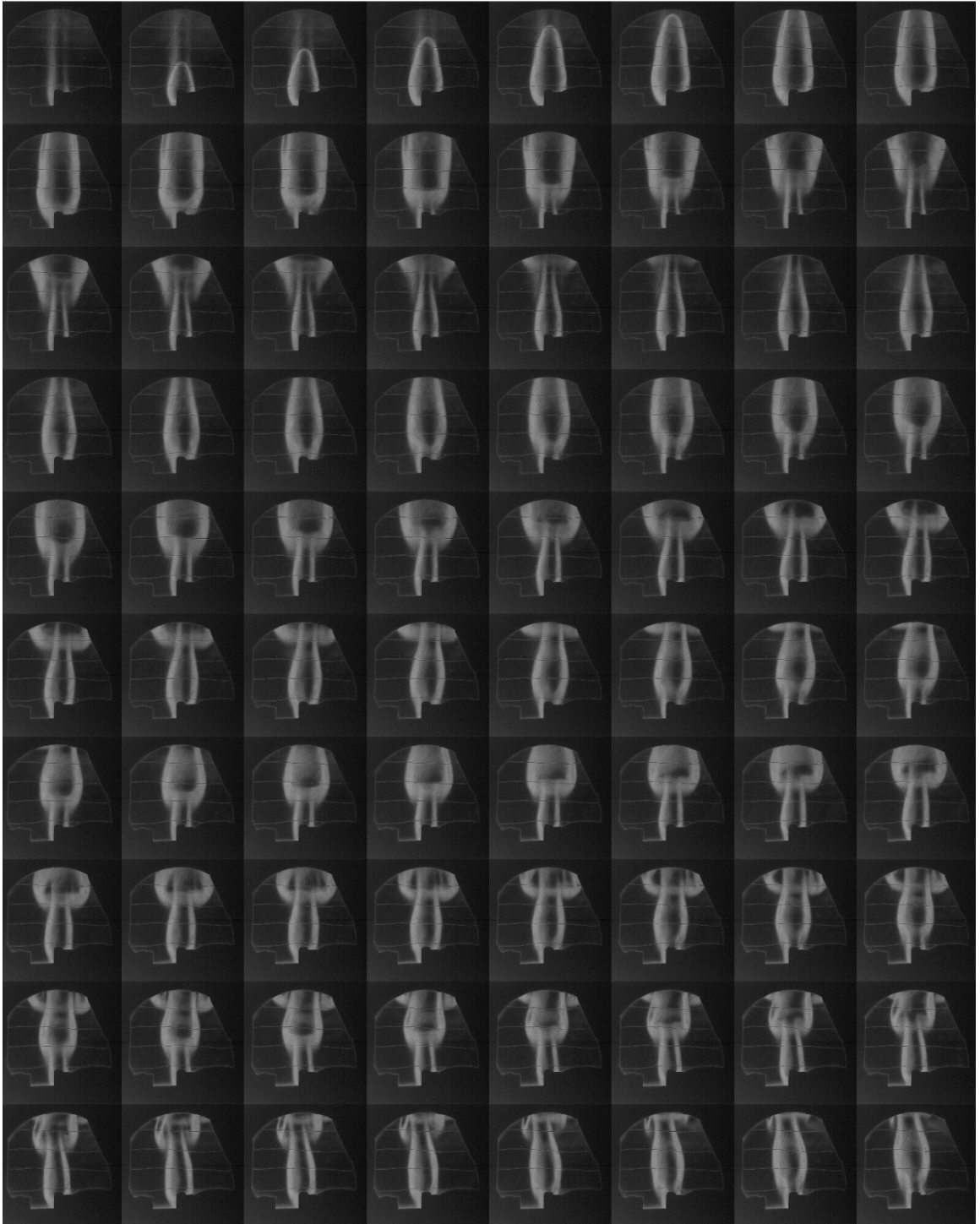


Figure K.47: Shot 54 montage ($\Delta t = 5$ ms between images)

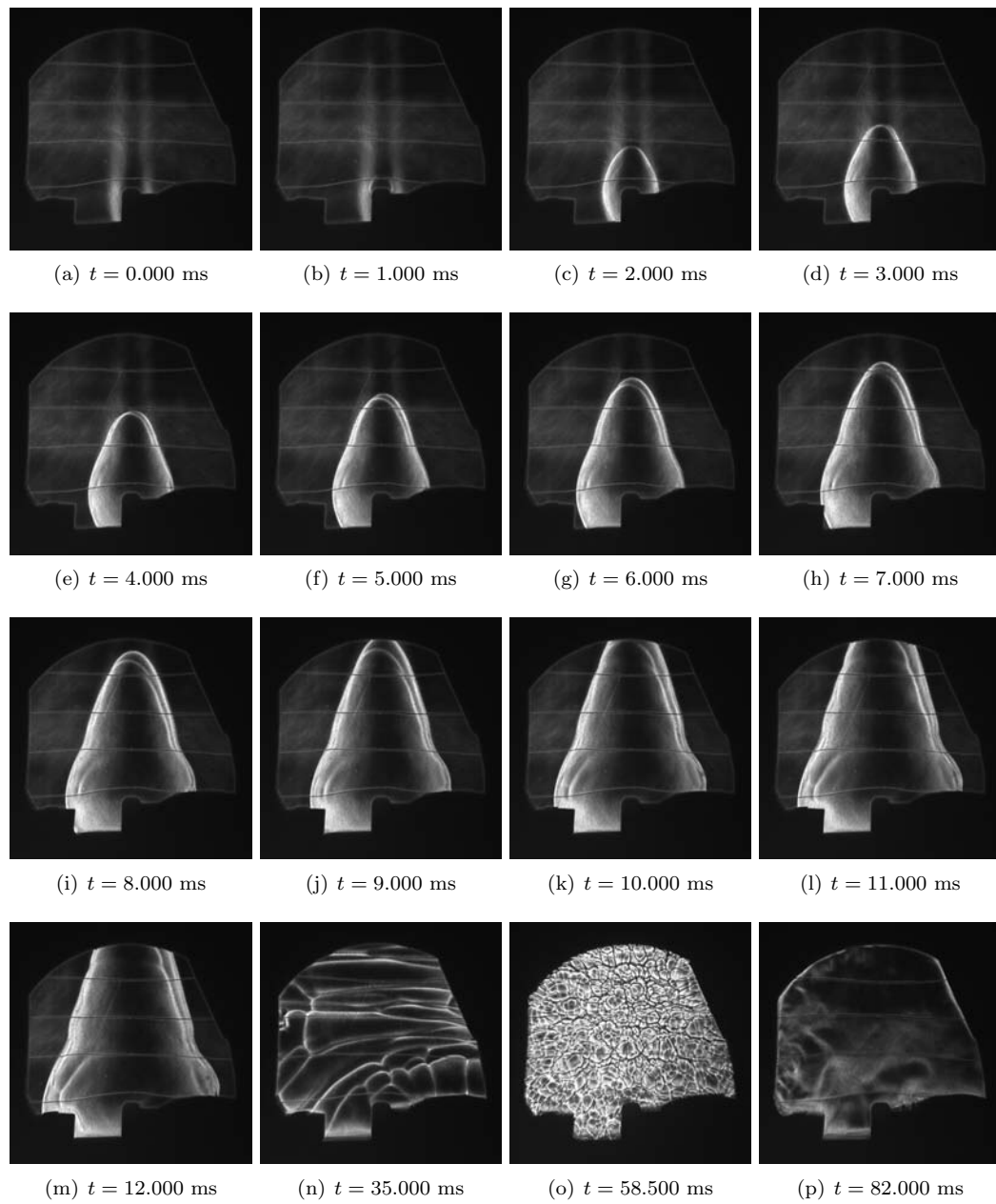


Figure K.48: Shot 55

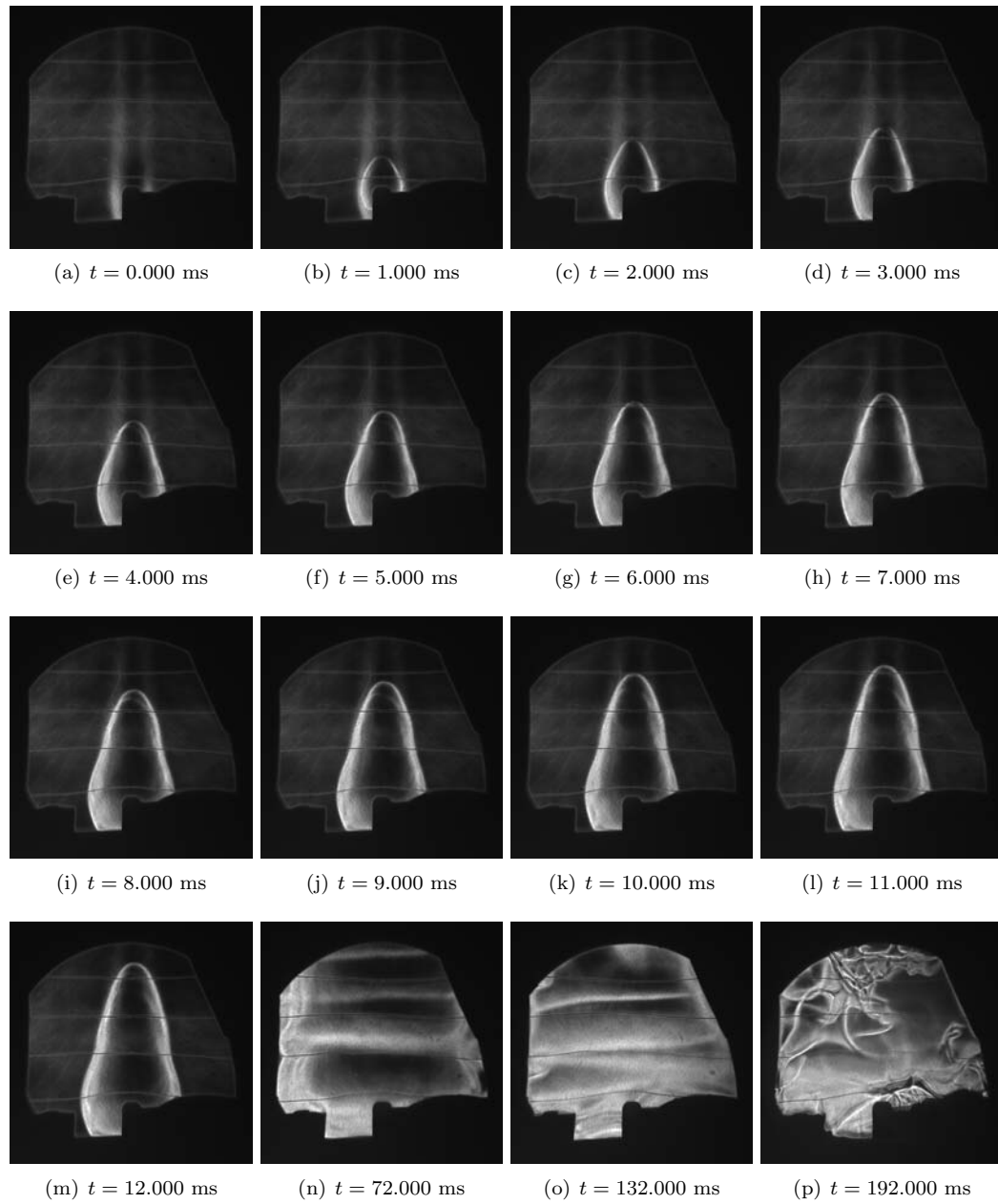


Figure K.49: Shot 57

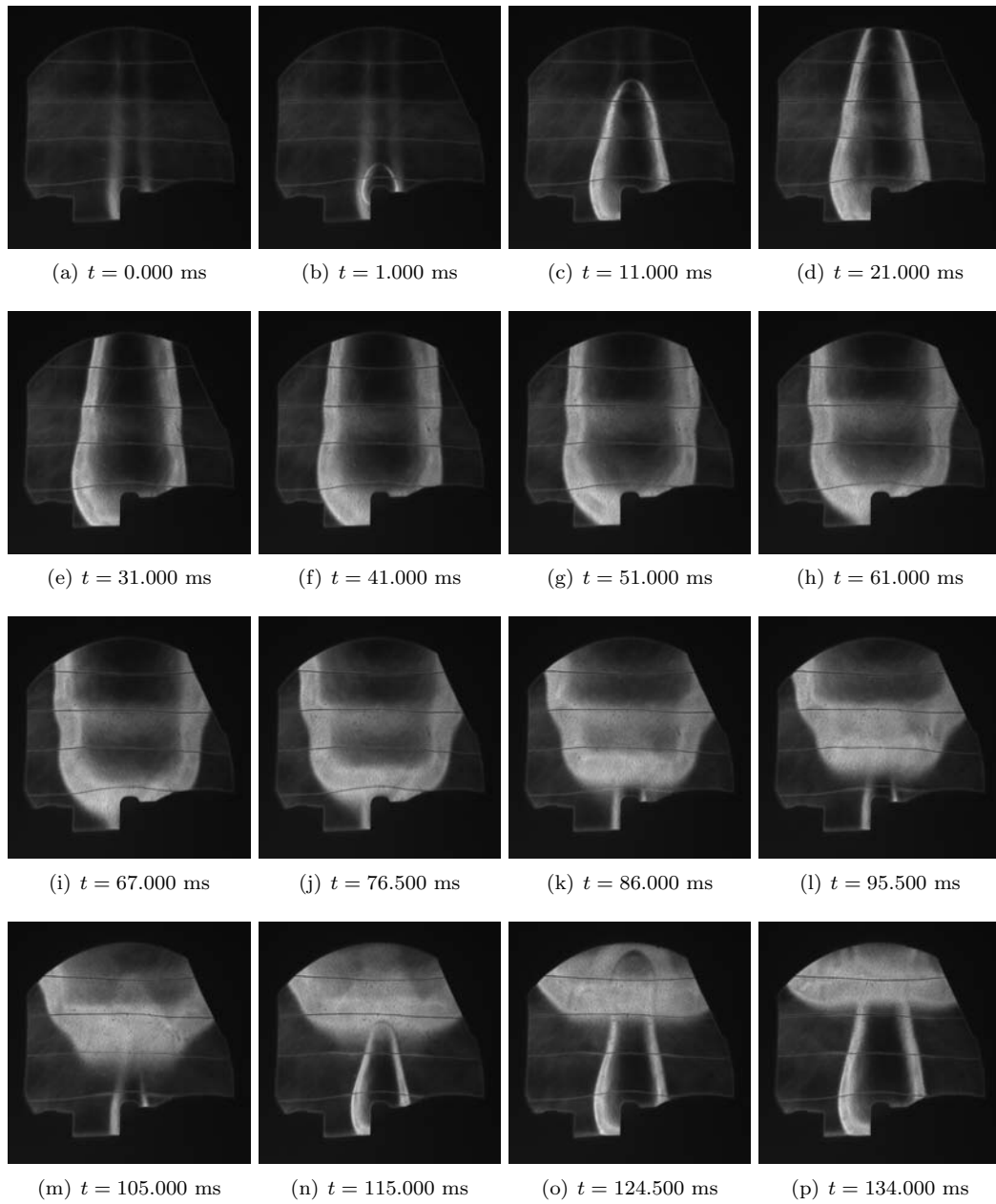


Figure K.50: Shot 58

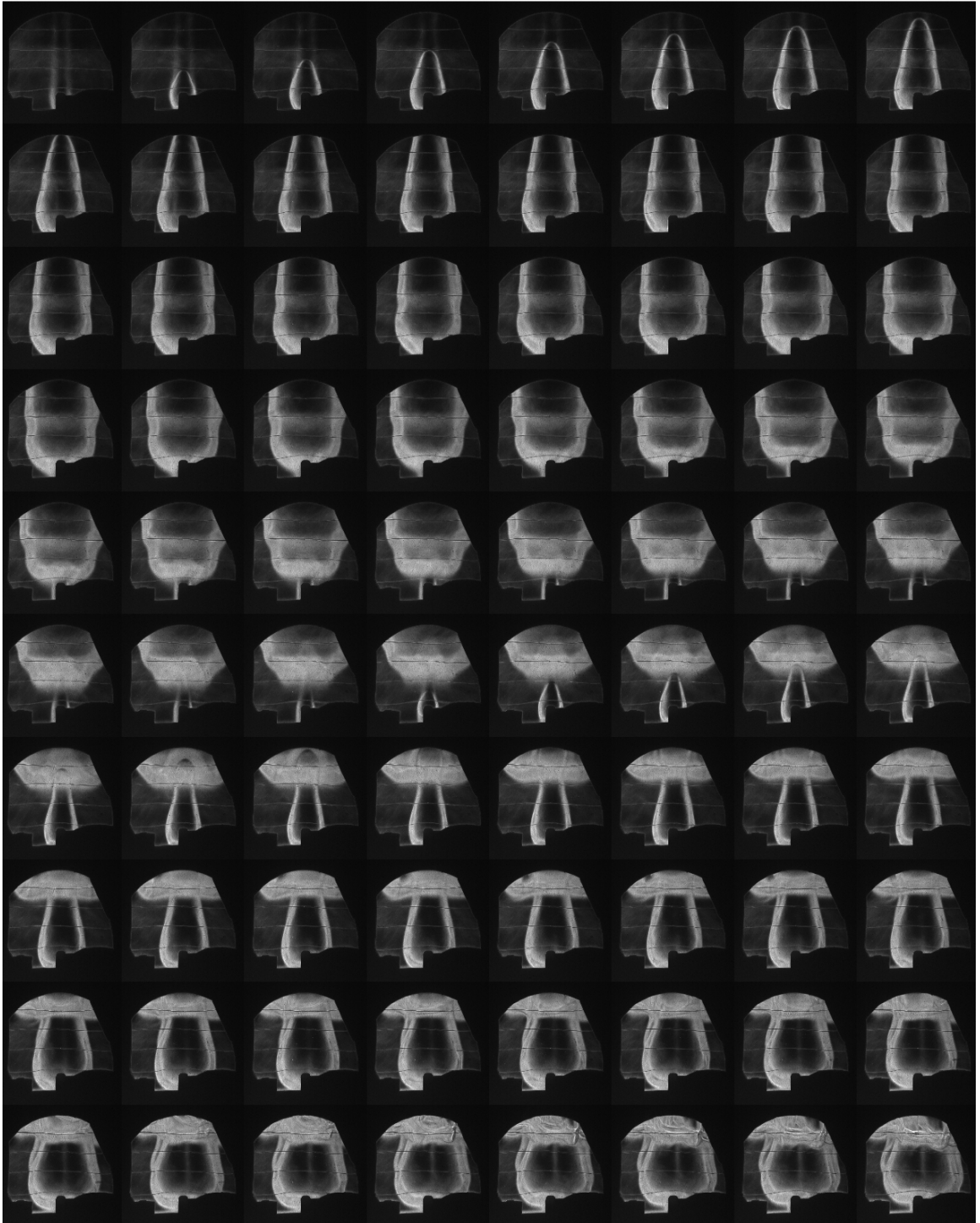


Figure K.51: Shot 58 montage ($\Delta t = 2.5$ ms between images)

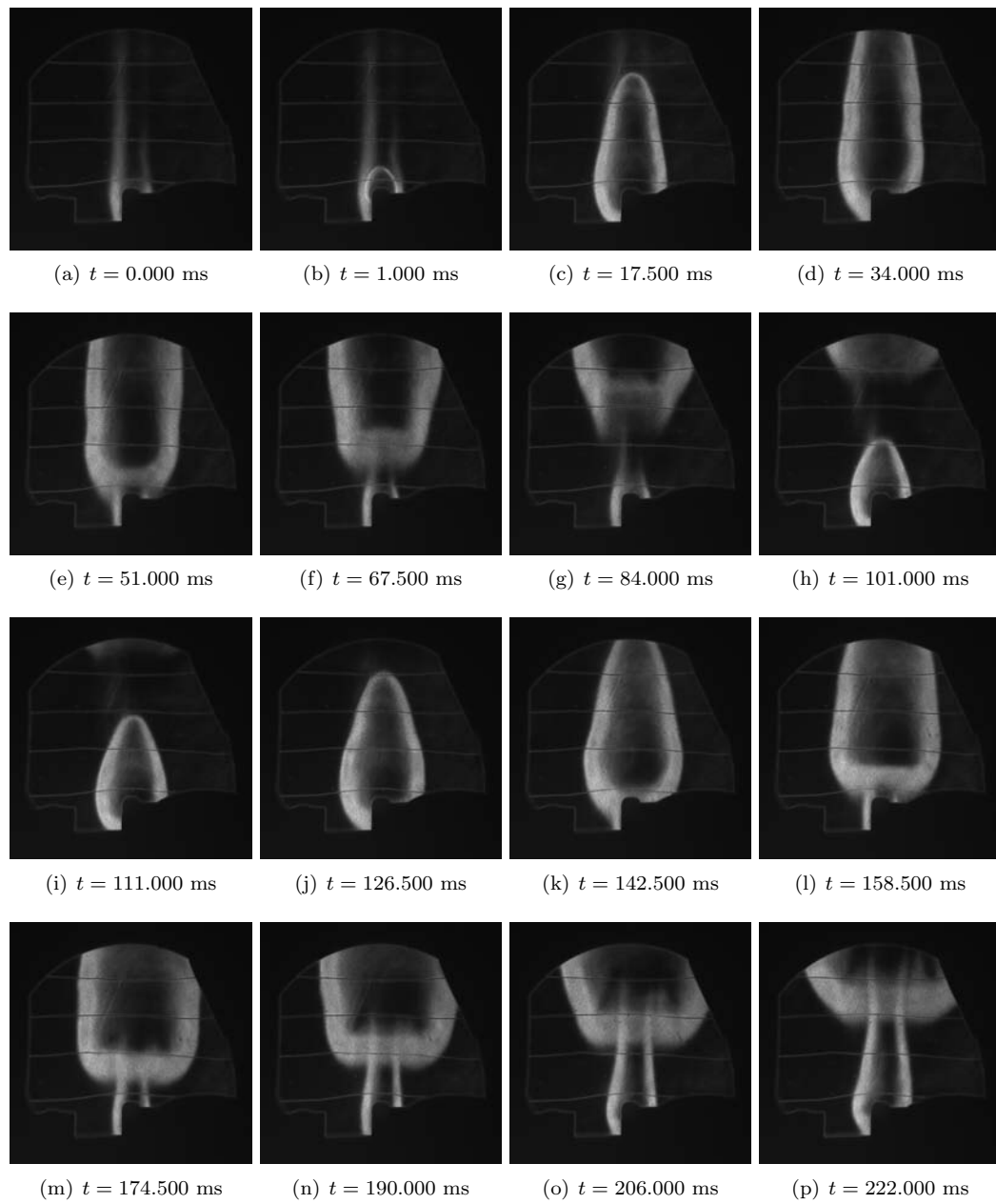


Figure K.52: Shot 60

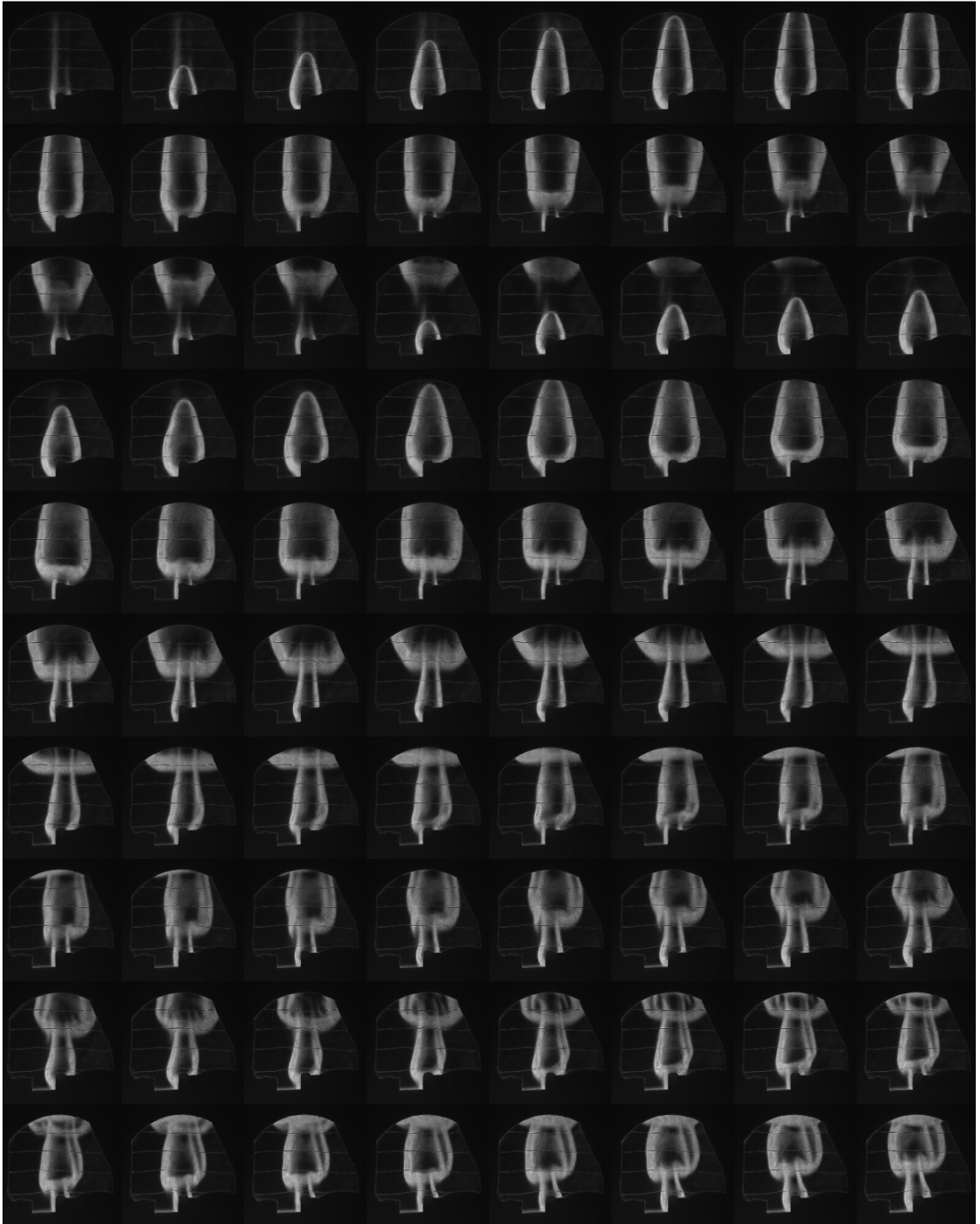


Figure K.53: Shot 60 montage ($\Delta t = 5$ ms between images)

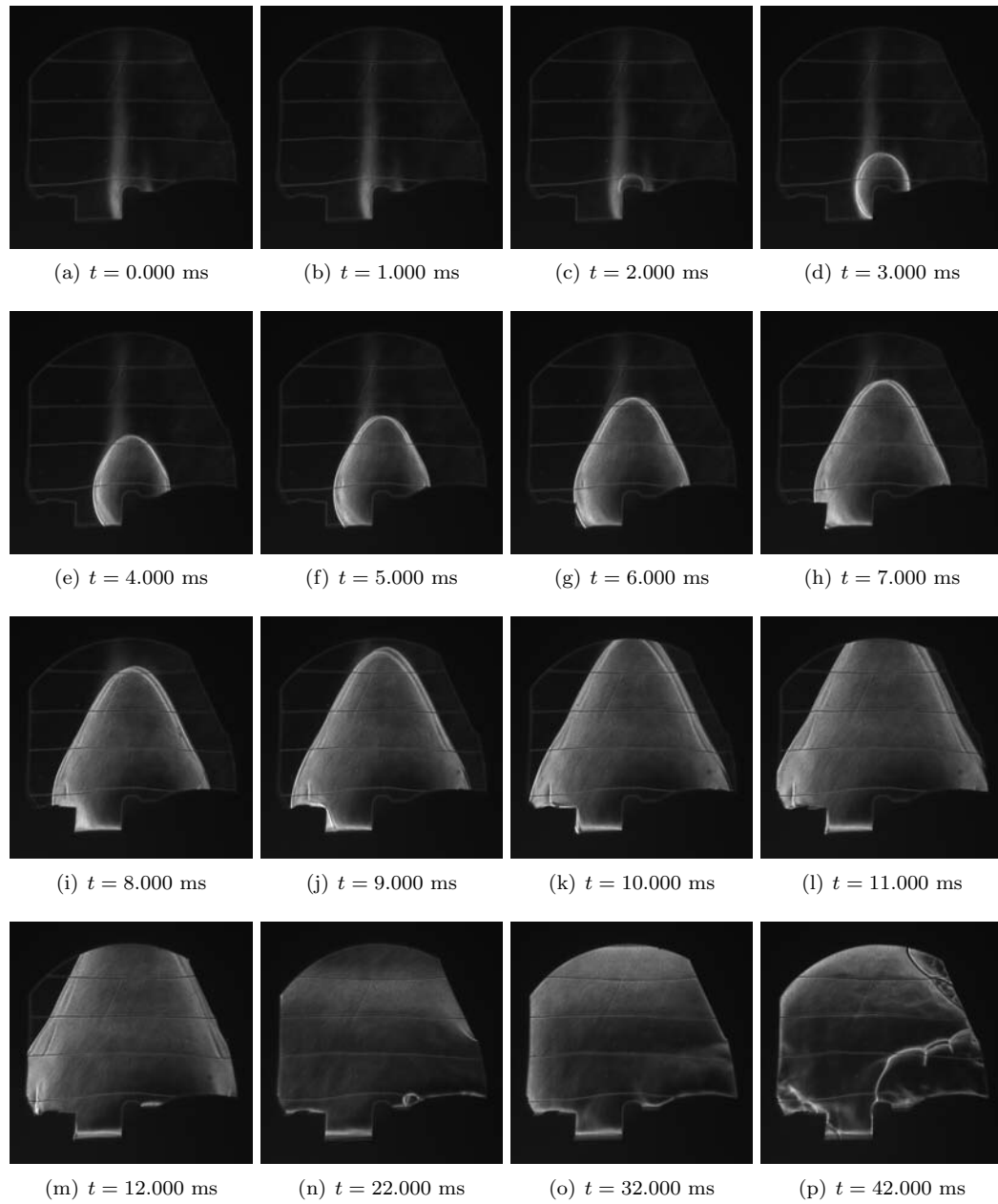


Figure K.54: Shot 61

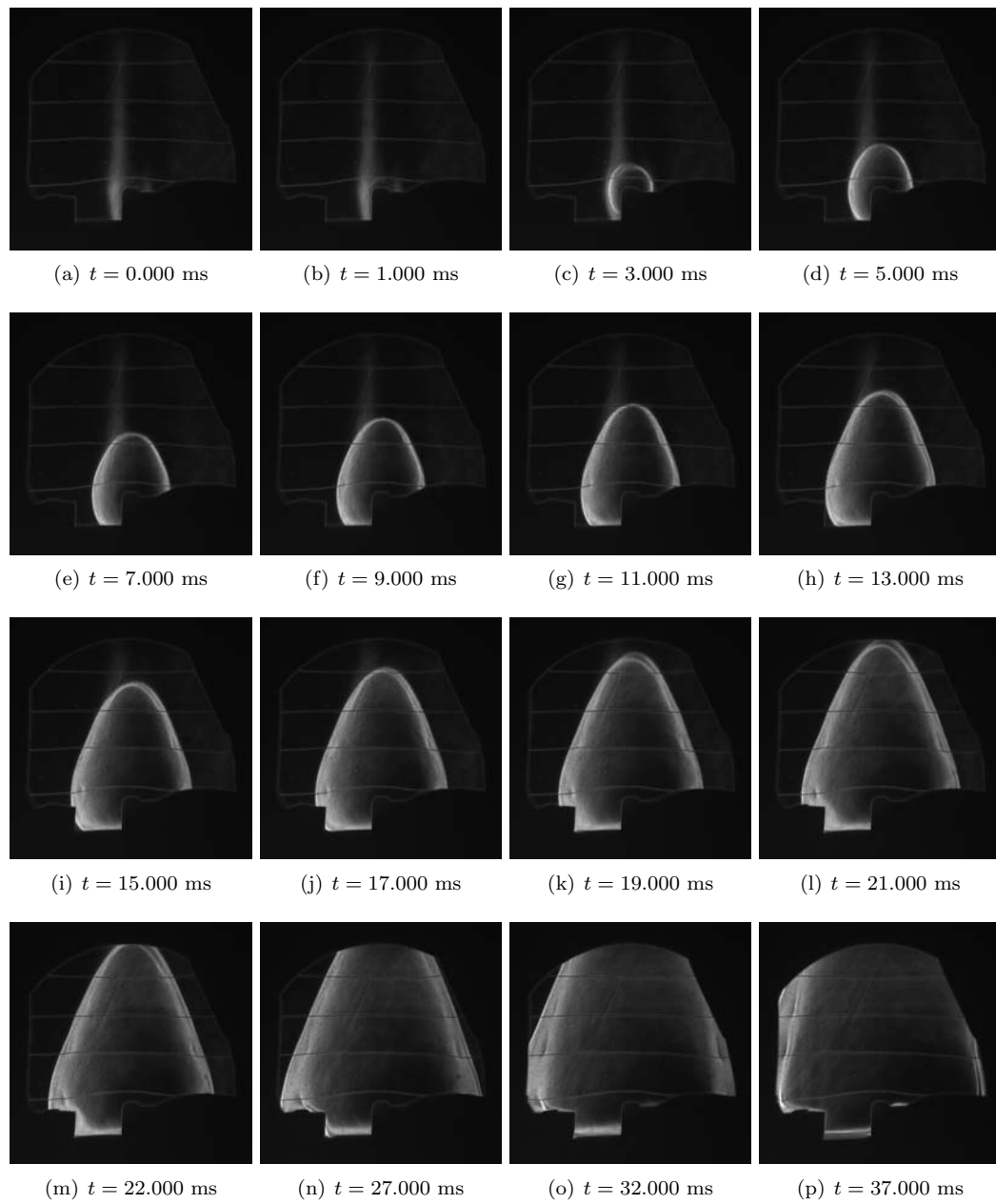


Figure K.55: Shot 64

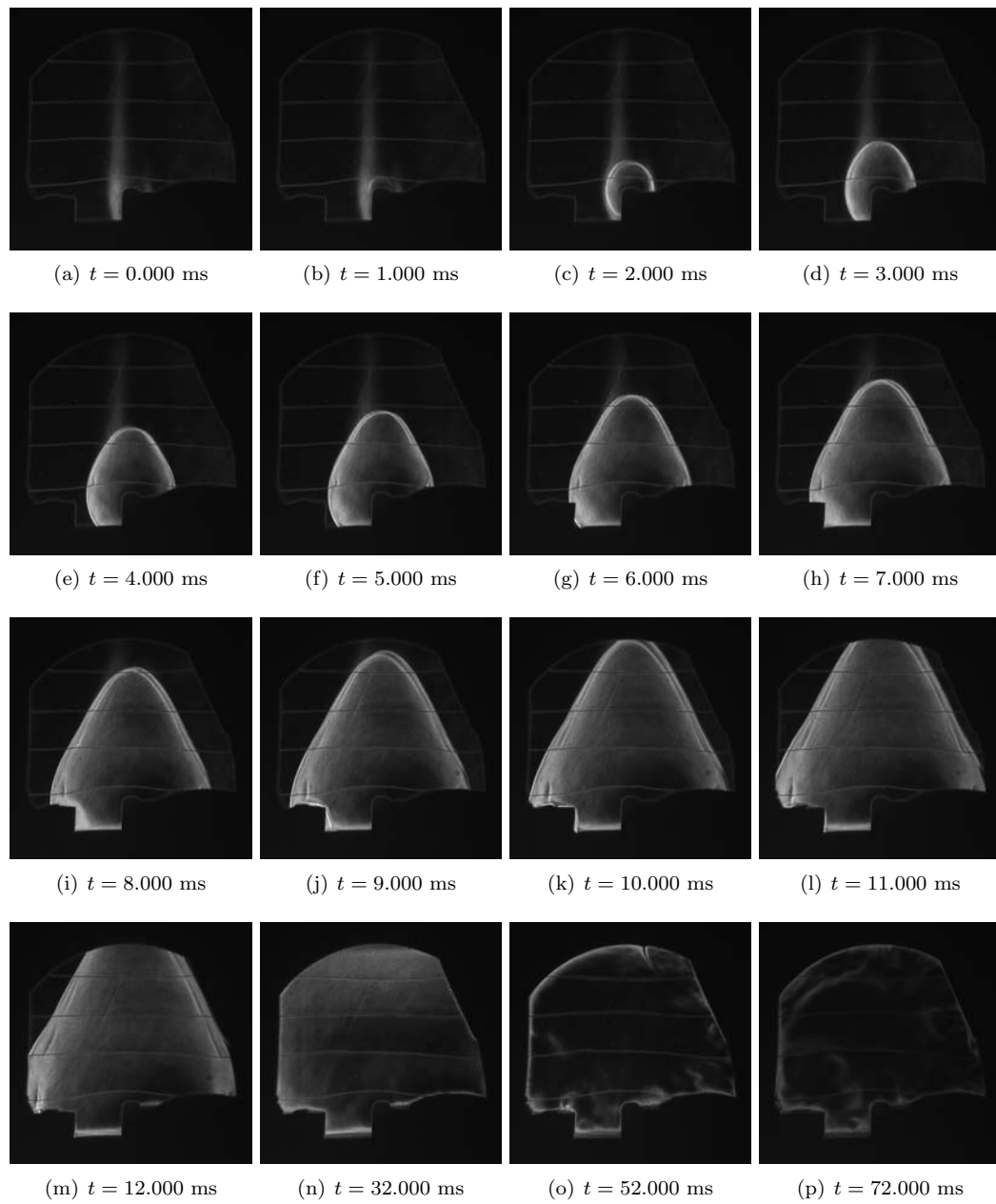


Figure K.56: Shot 65

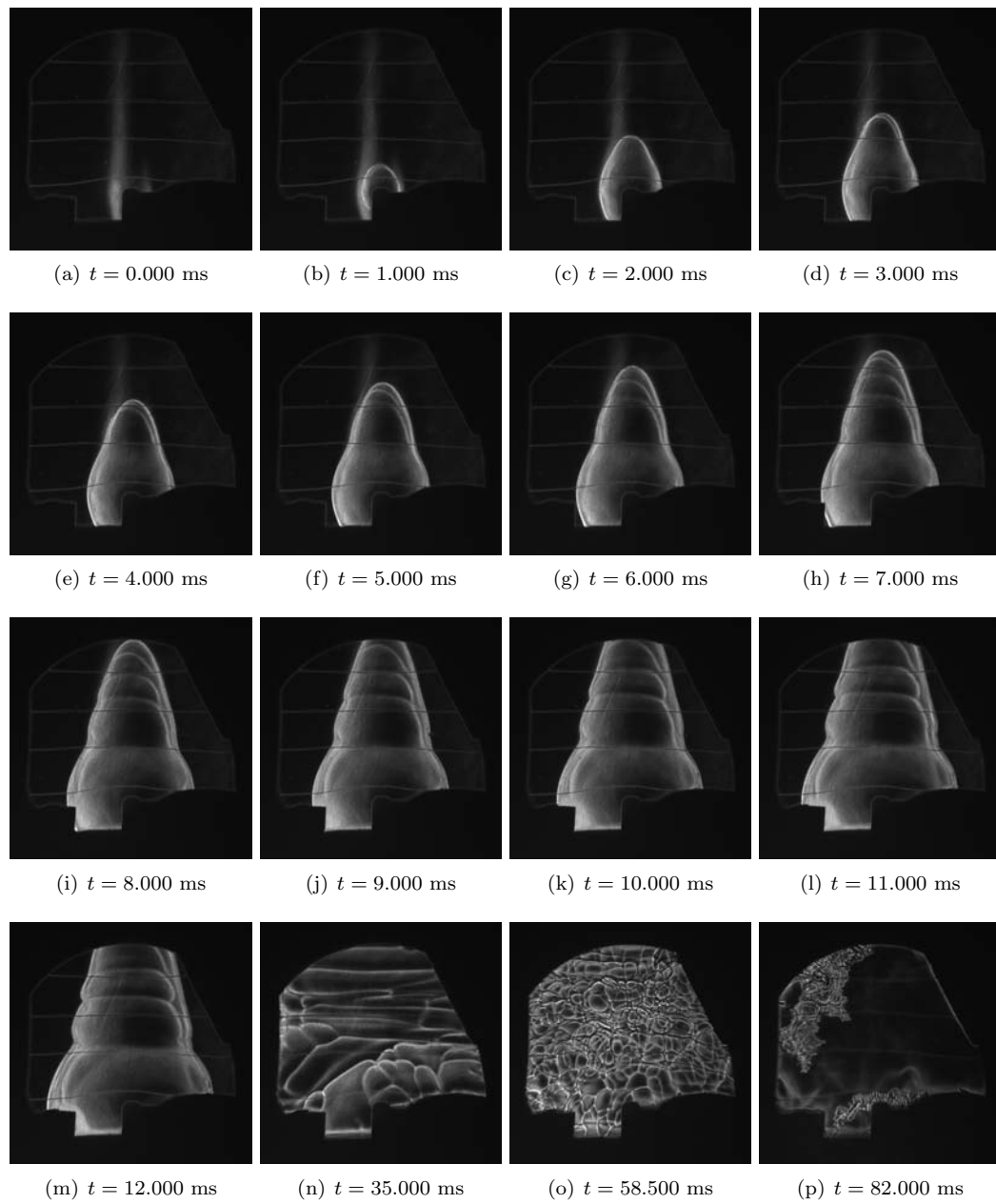


Figure K.57: Shot 66

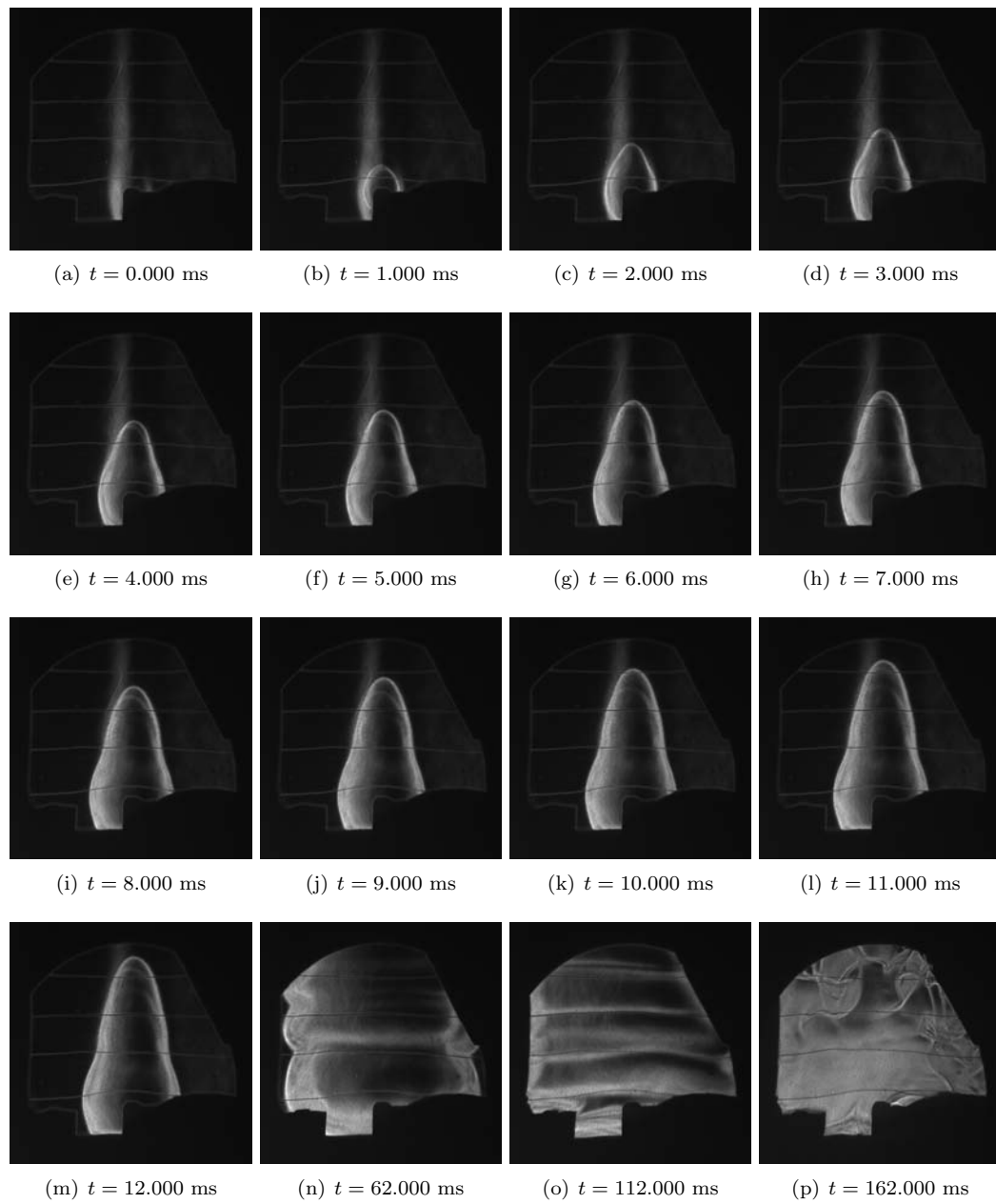


Figure K.58: Shot 68

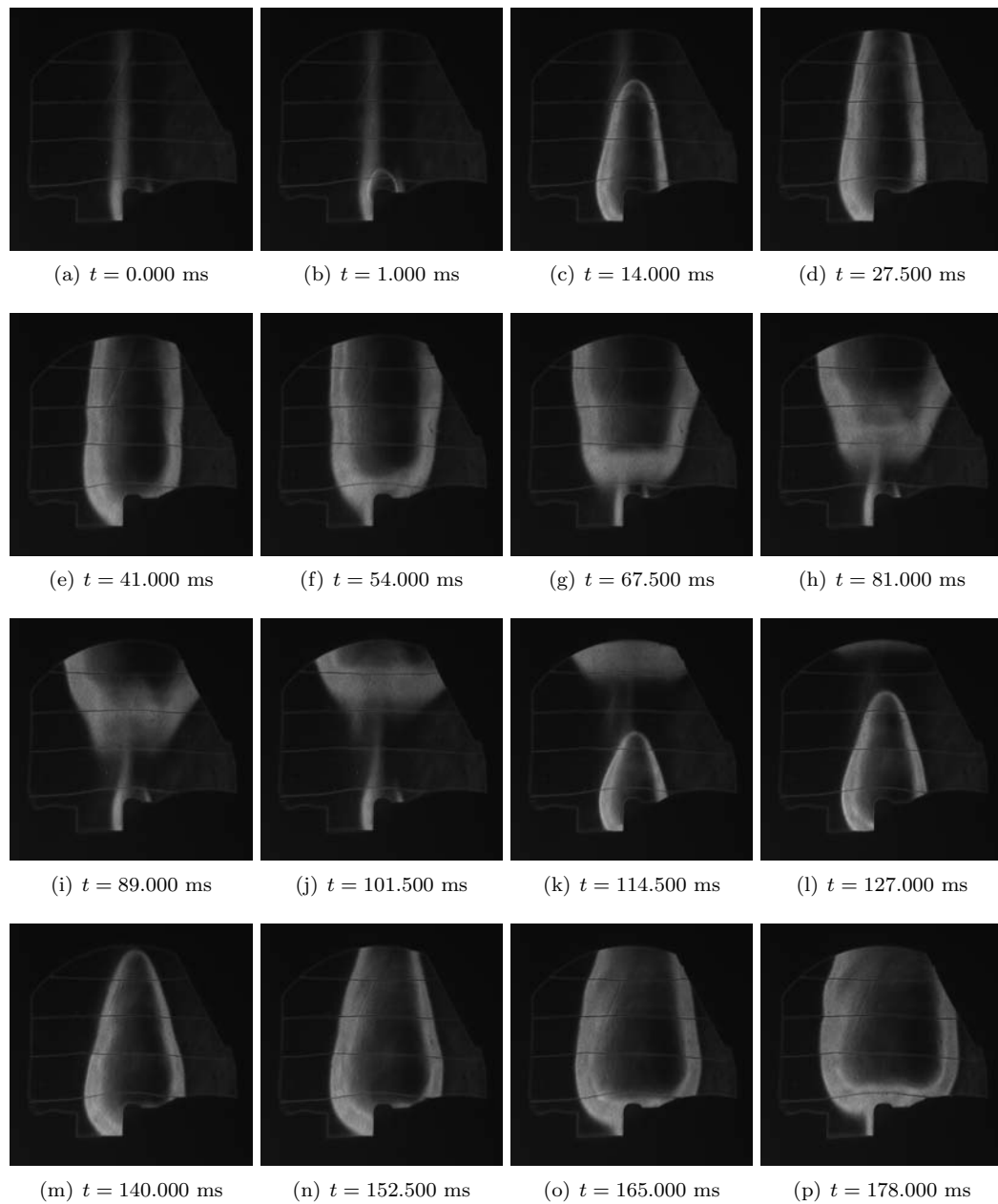


Figure K.59: Shot 69

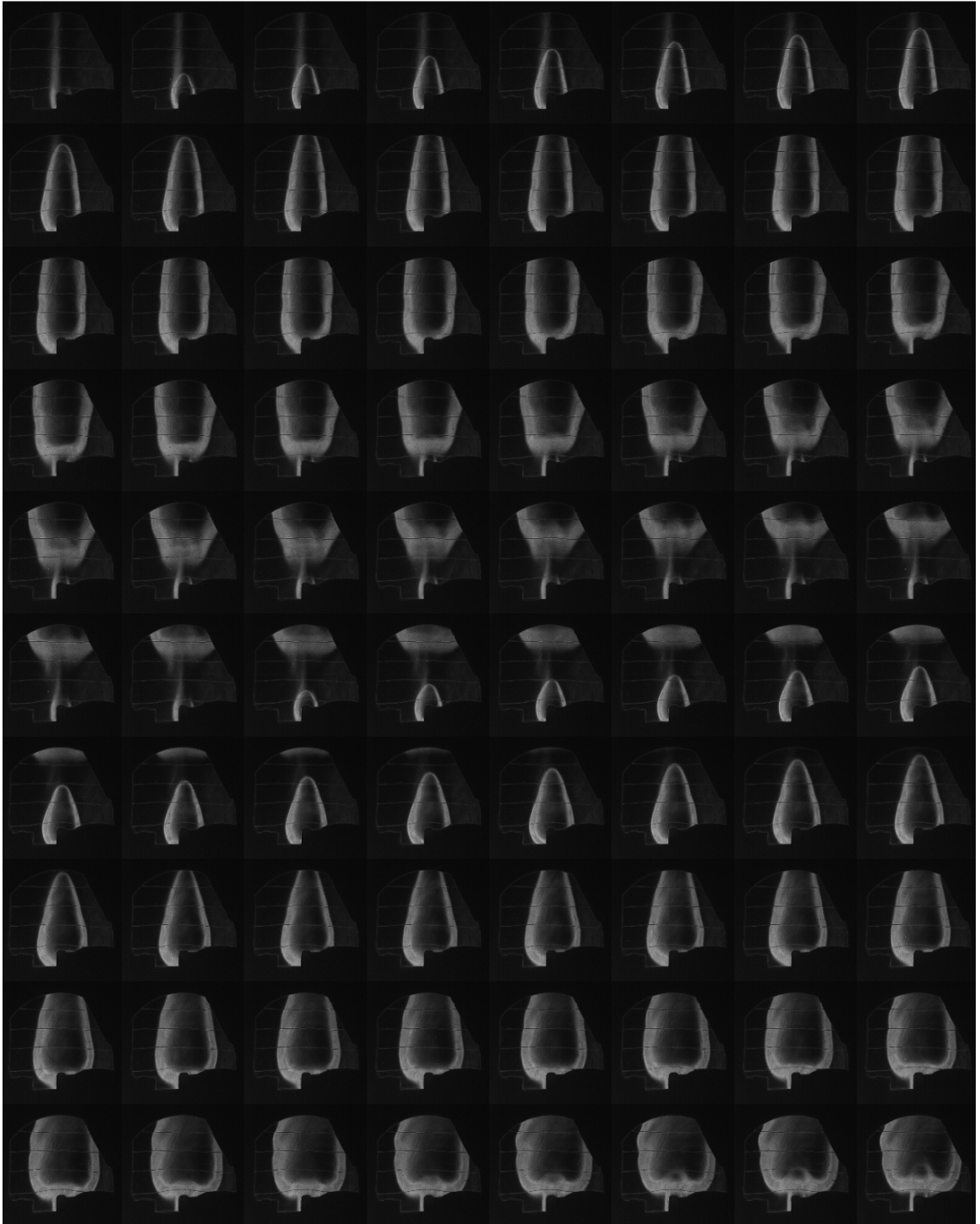


Figure K.60: Shot 69 montage ($\Delta t = 5$ ms between images)

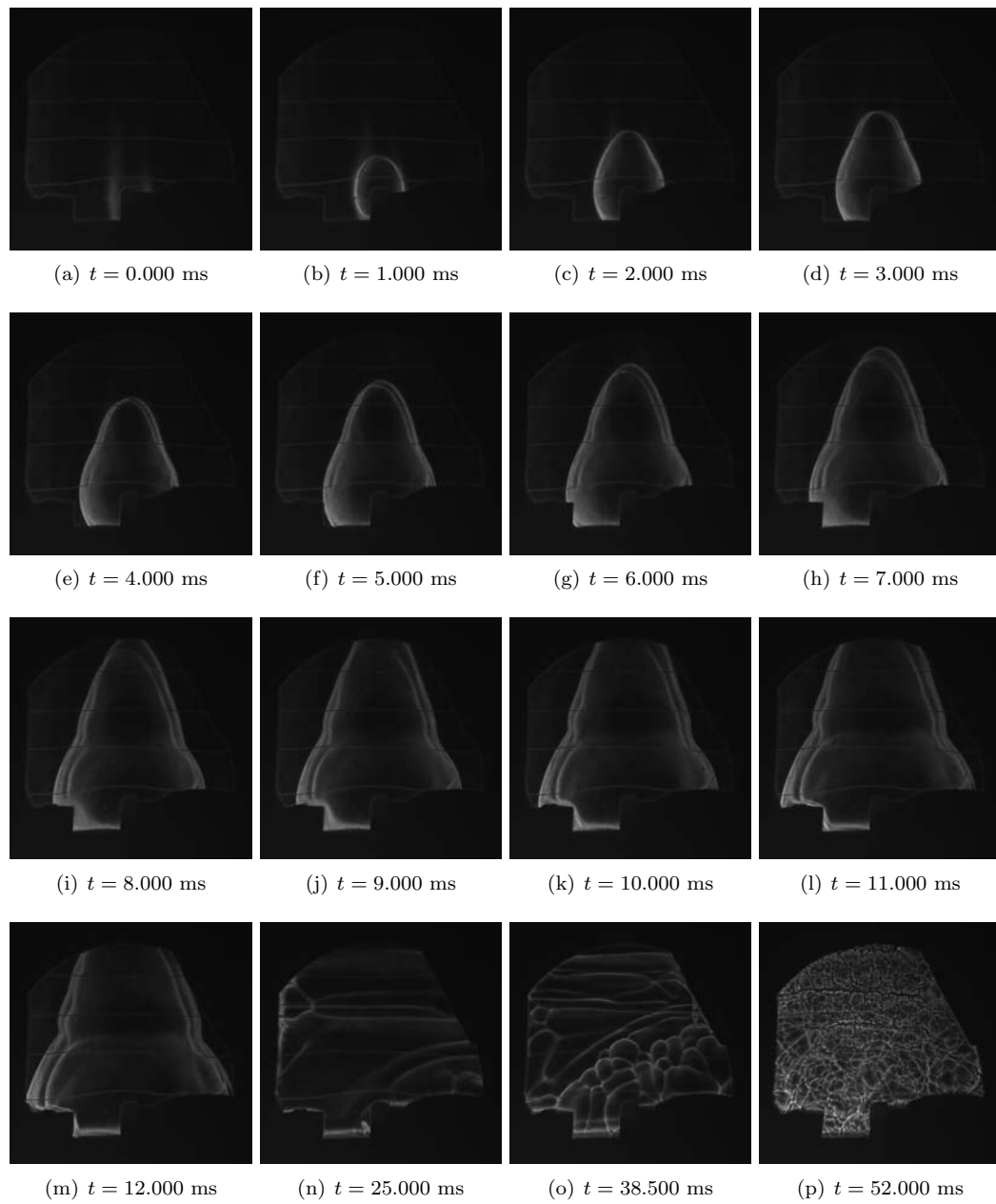


Figure K.61: Shot 70

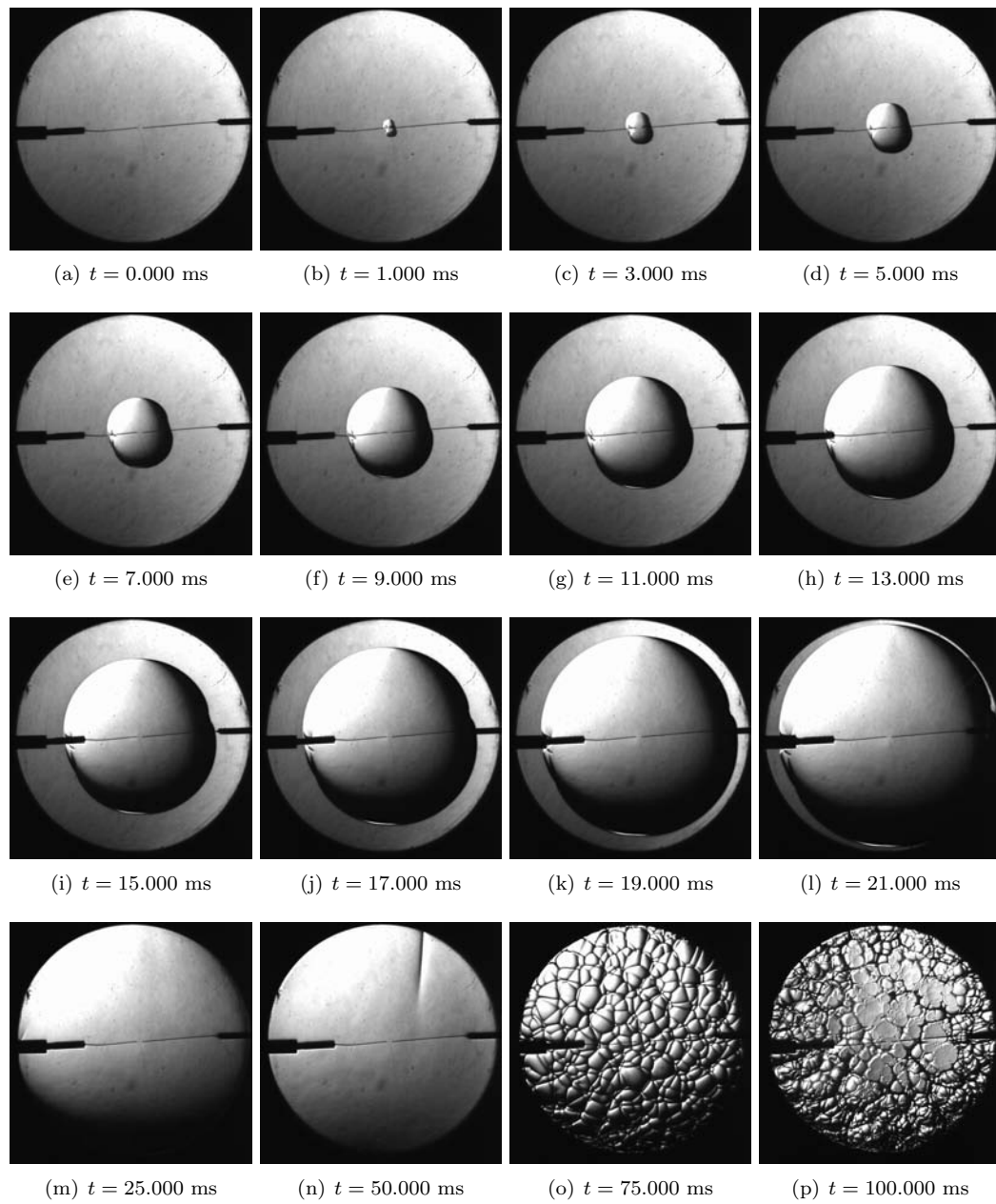


Figure K.62: Shot 73

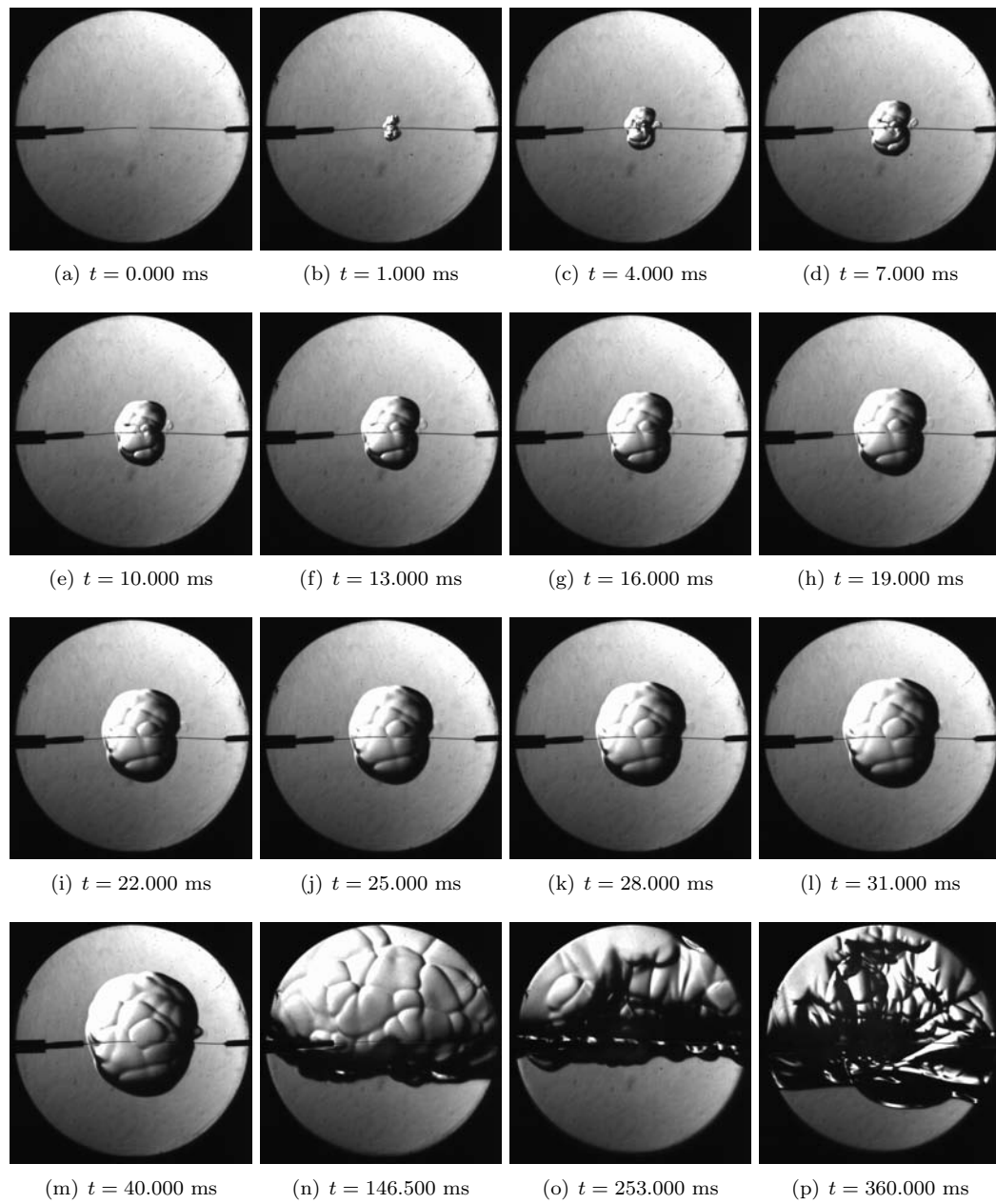


Figure K.63: Shot 76

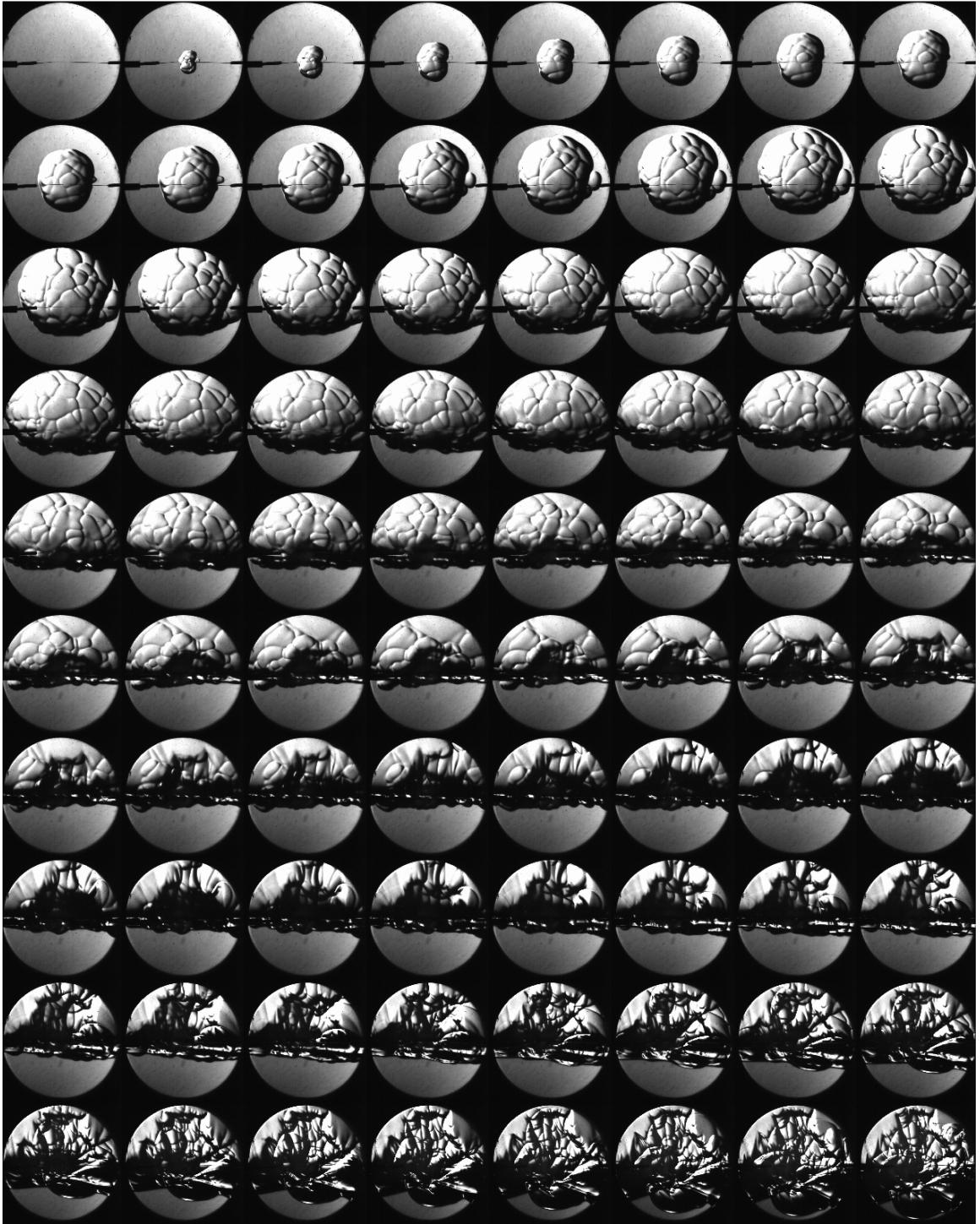


Figure K.64: Shot 76 montage ($\Delta t = 10$ ms between images)

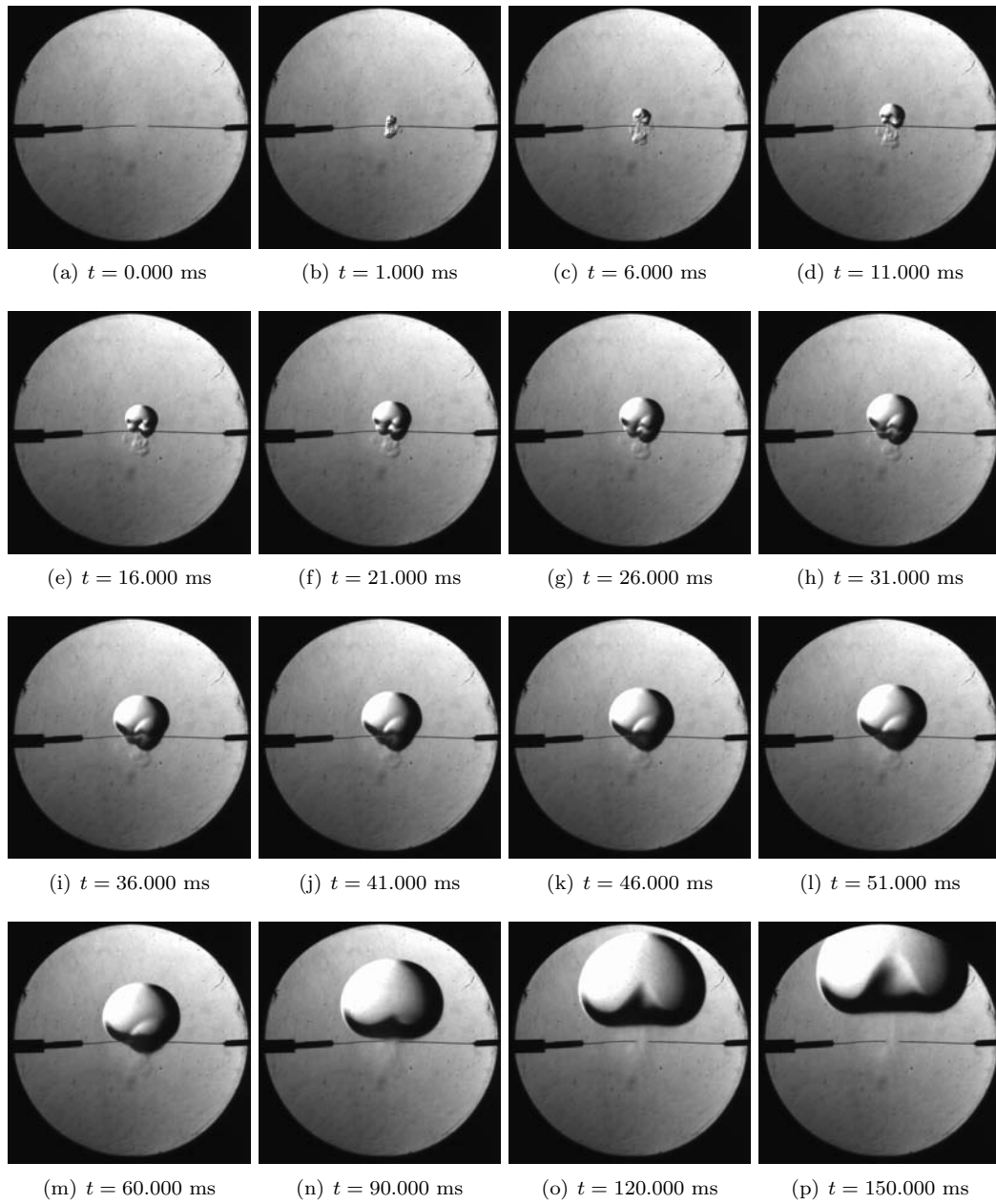


Figure K.65: Shot 77

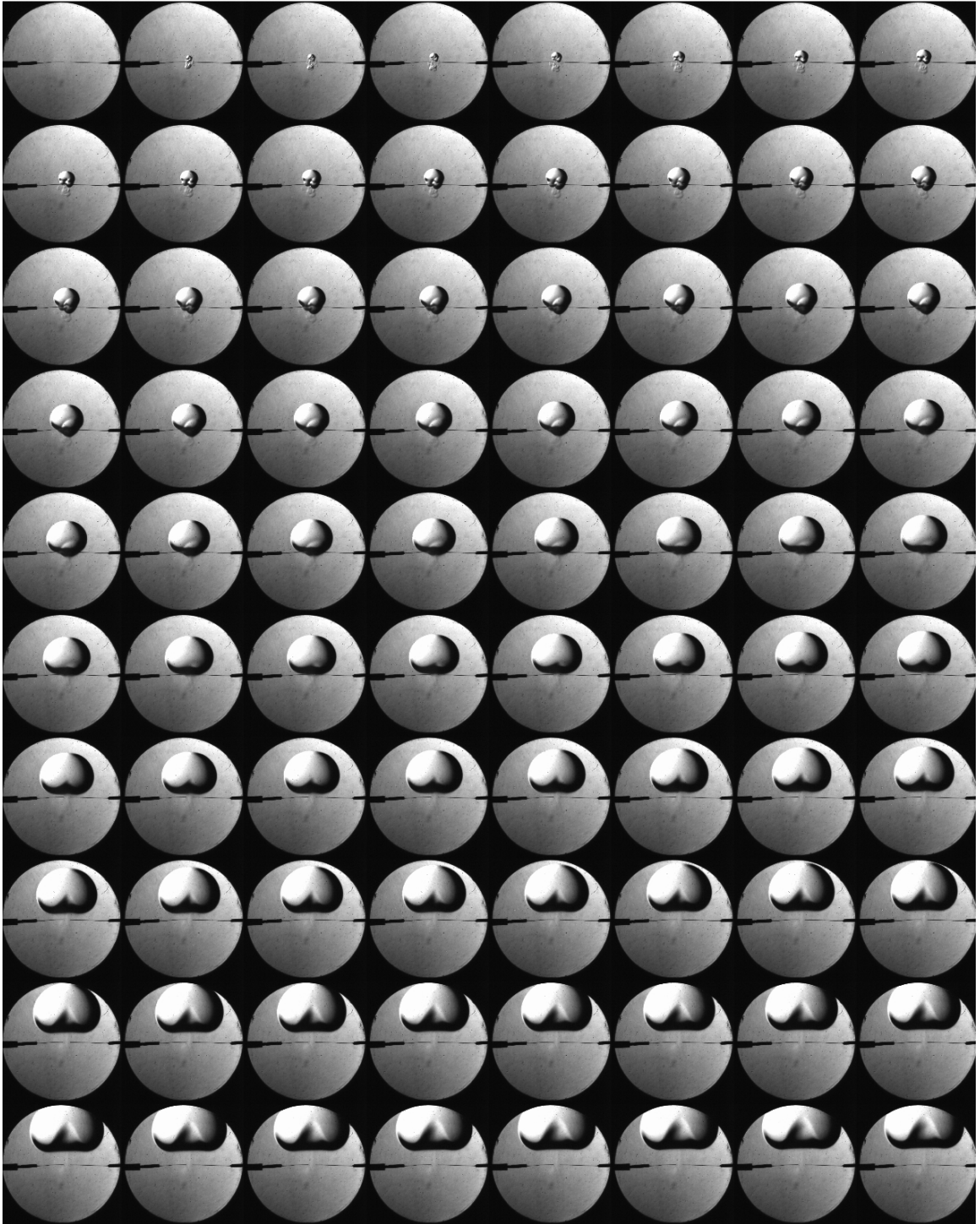


Figure K.66: Shot 77 montage ($\Delta t = 10$ ms between images)

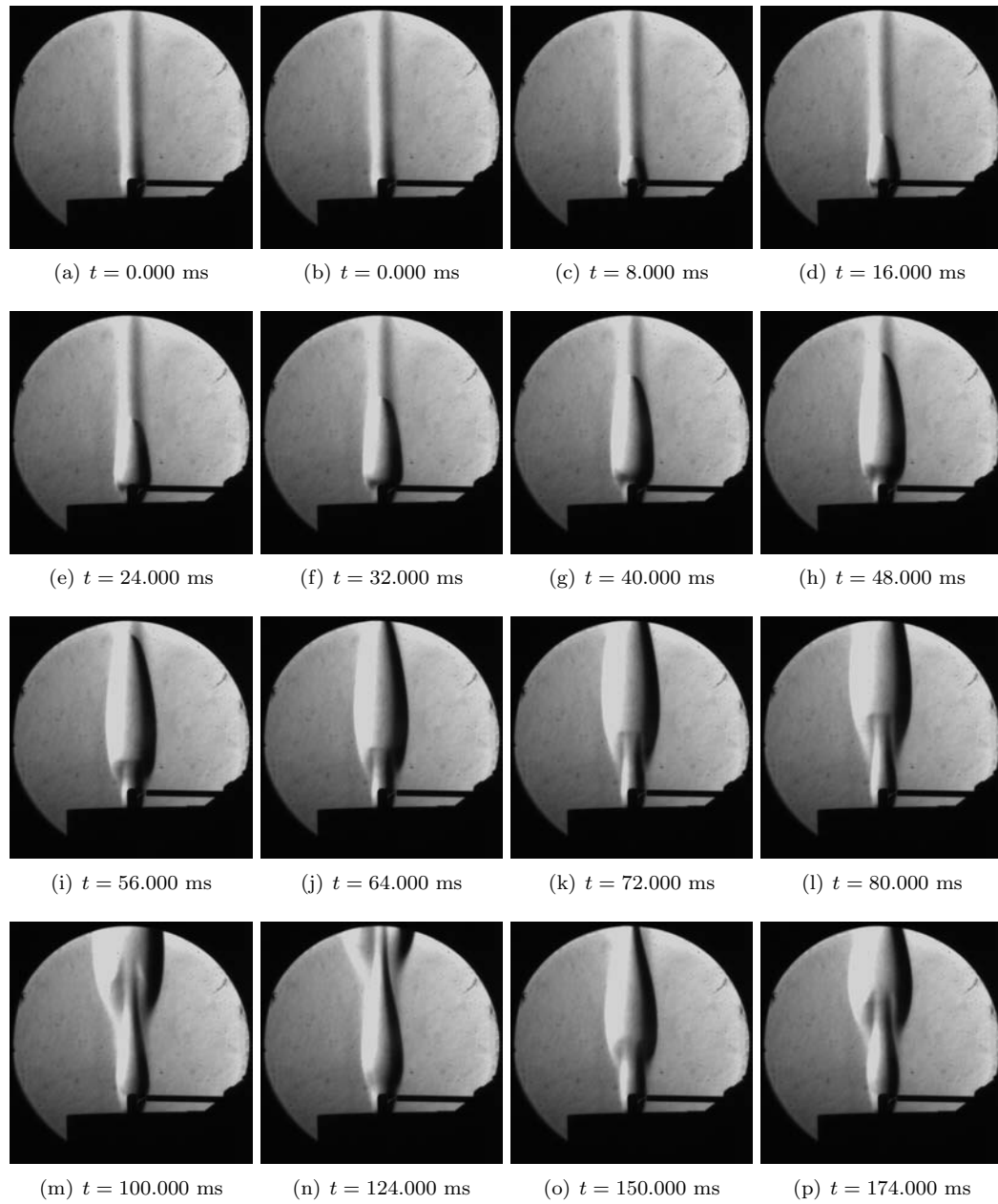


Figure K.67: Shot 80

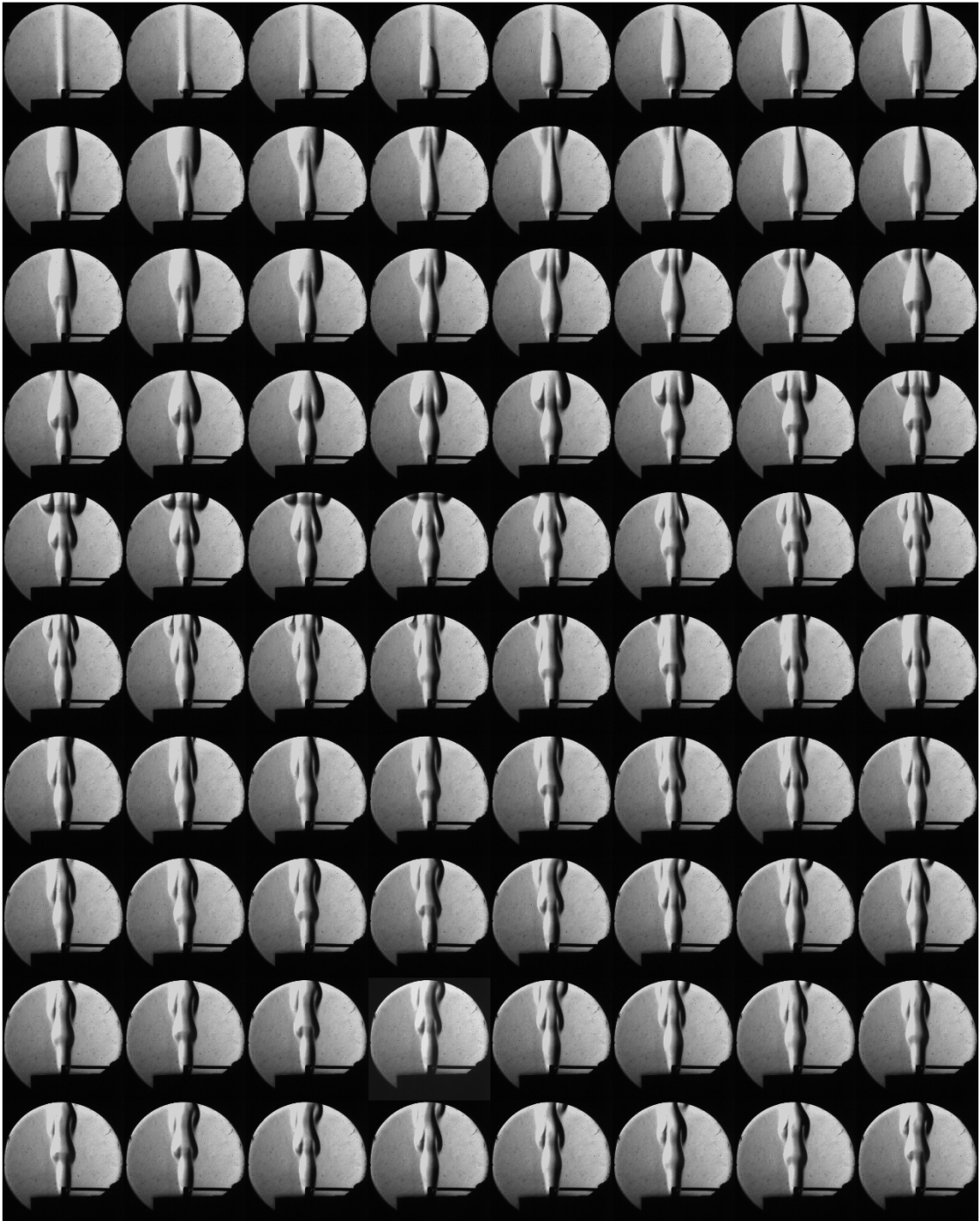


Figure K.68: Shot 80 montage ($\Delta t = 10$ ms between images)

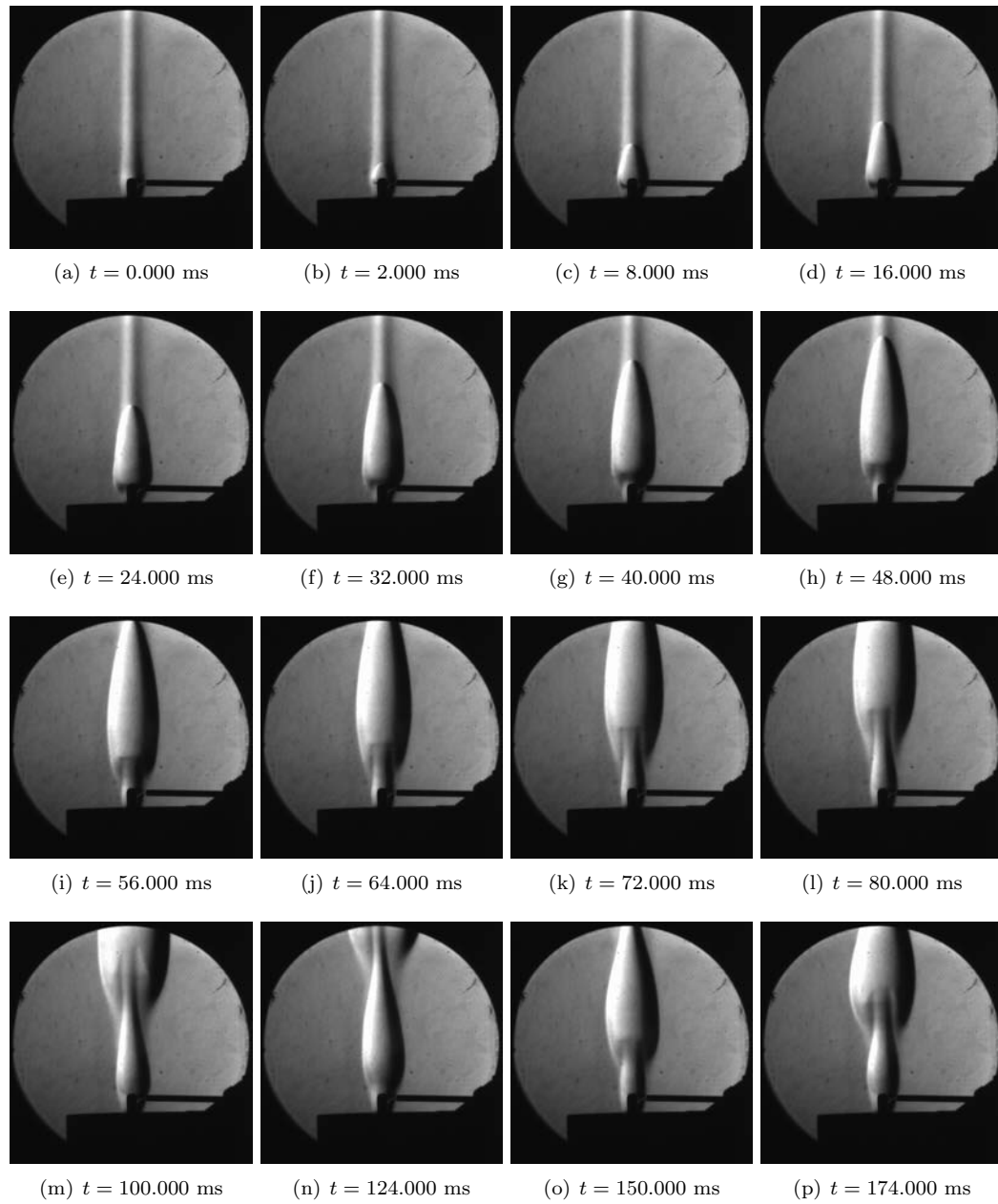


Figure K.69: Shot 81

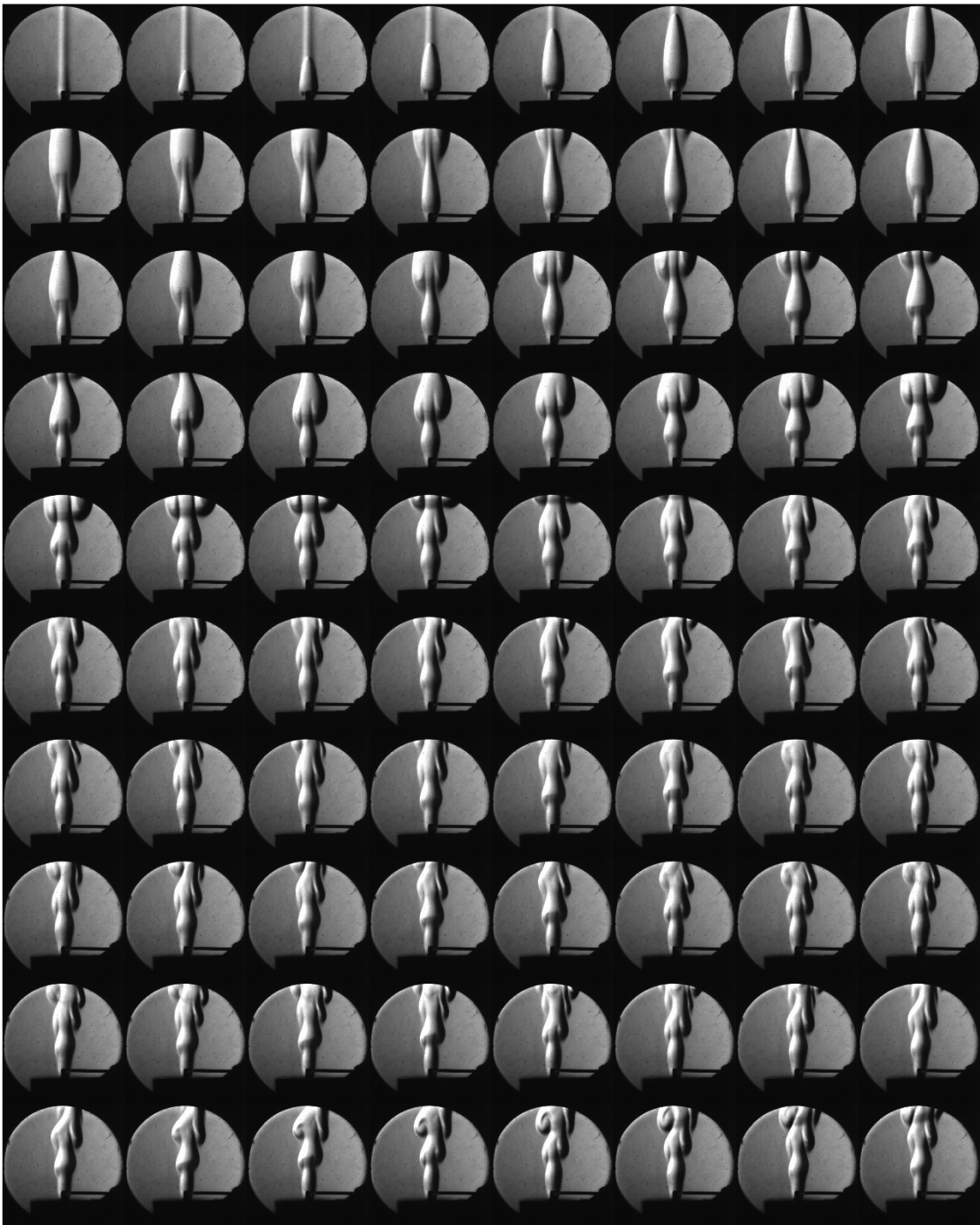


Figure K.70: Shot 81 montage ($\Delta t = 10$ ms between images)

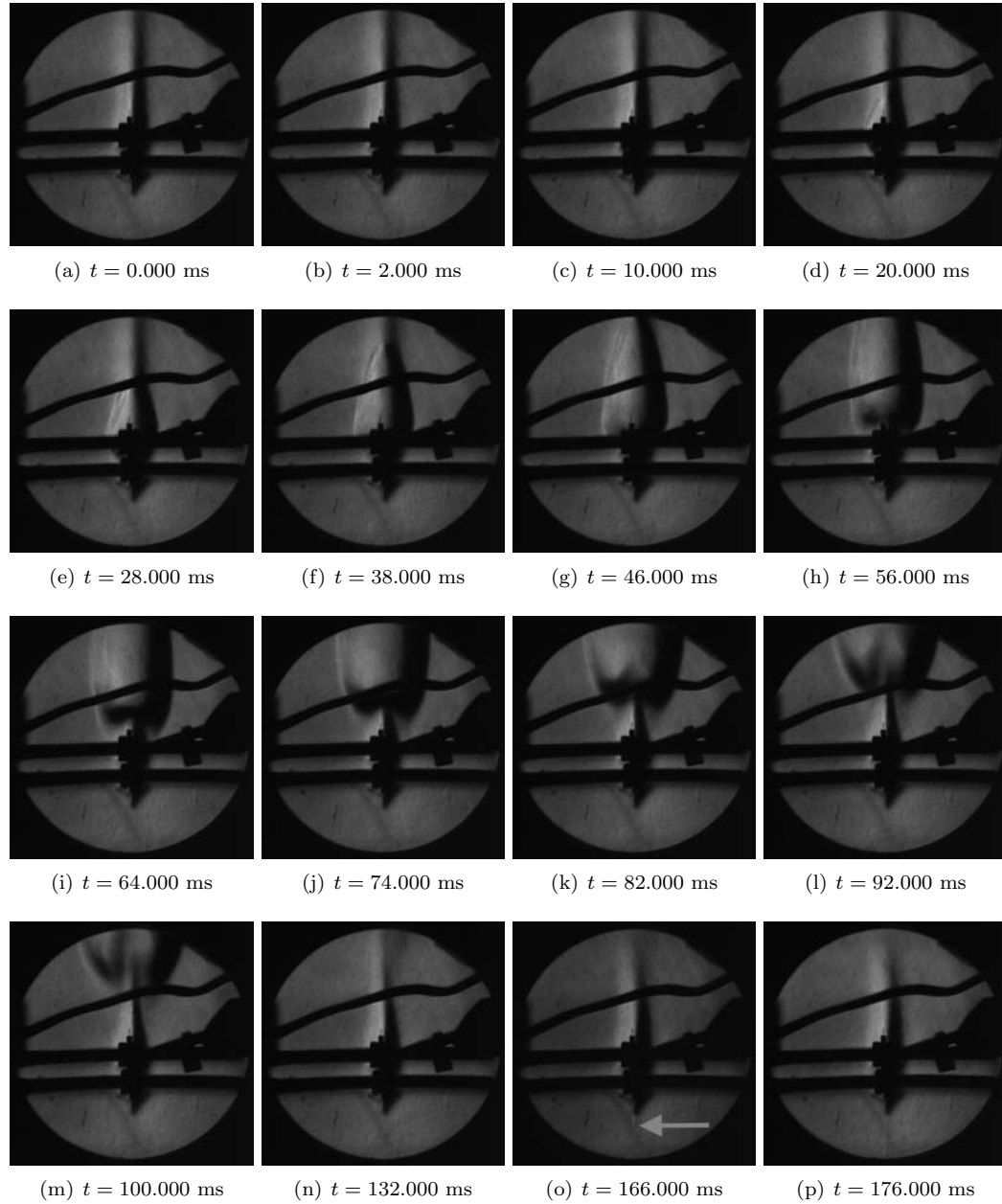


Figure K.71: Shot 85 (Note the drop of molten copper visible below the hot surface holder in the last two frames)

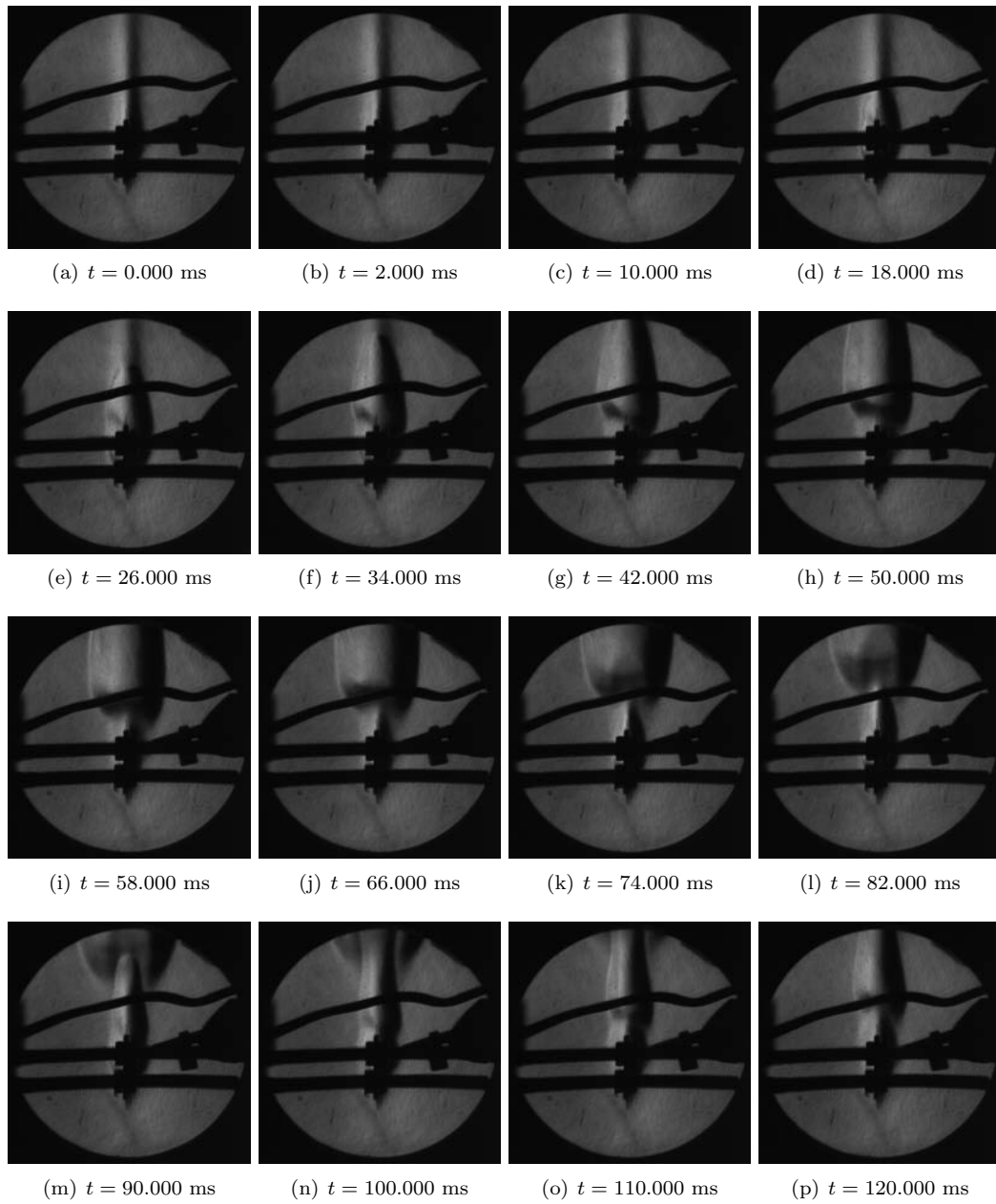


Figure K.72: Shot 86

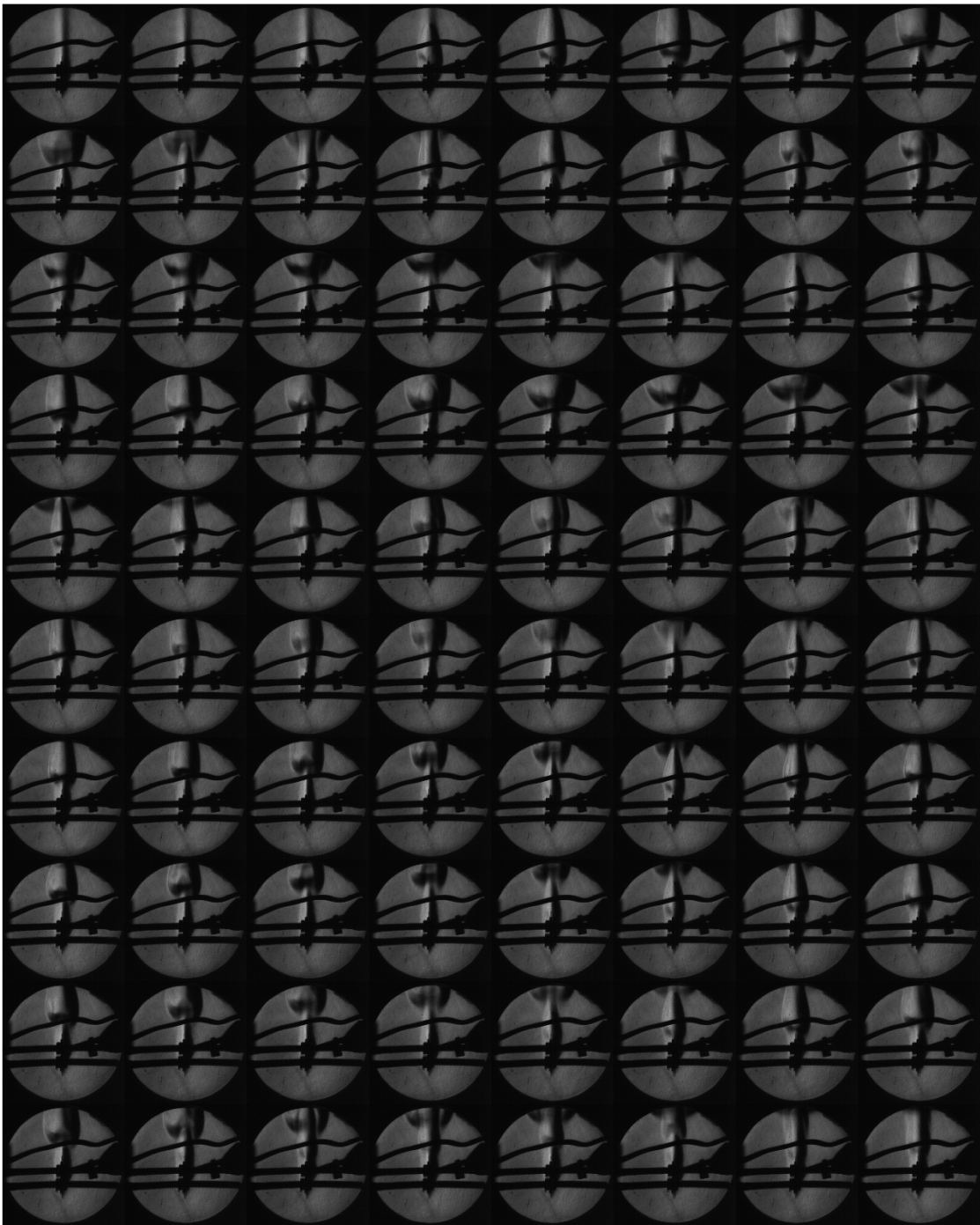


Figure K.73: Shot 86 montage ($\Delta t = 10$ ms between images)

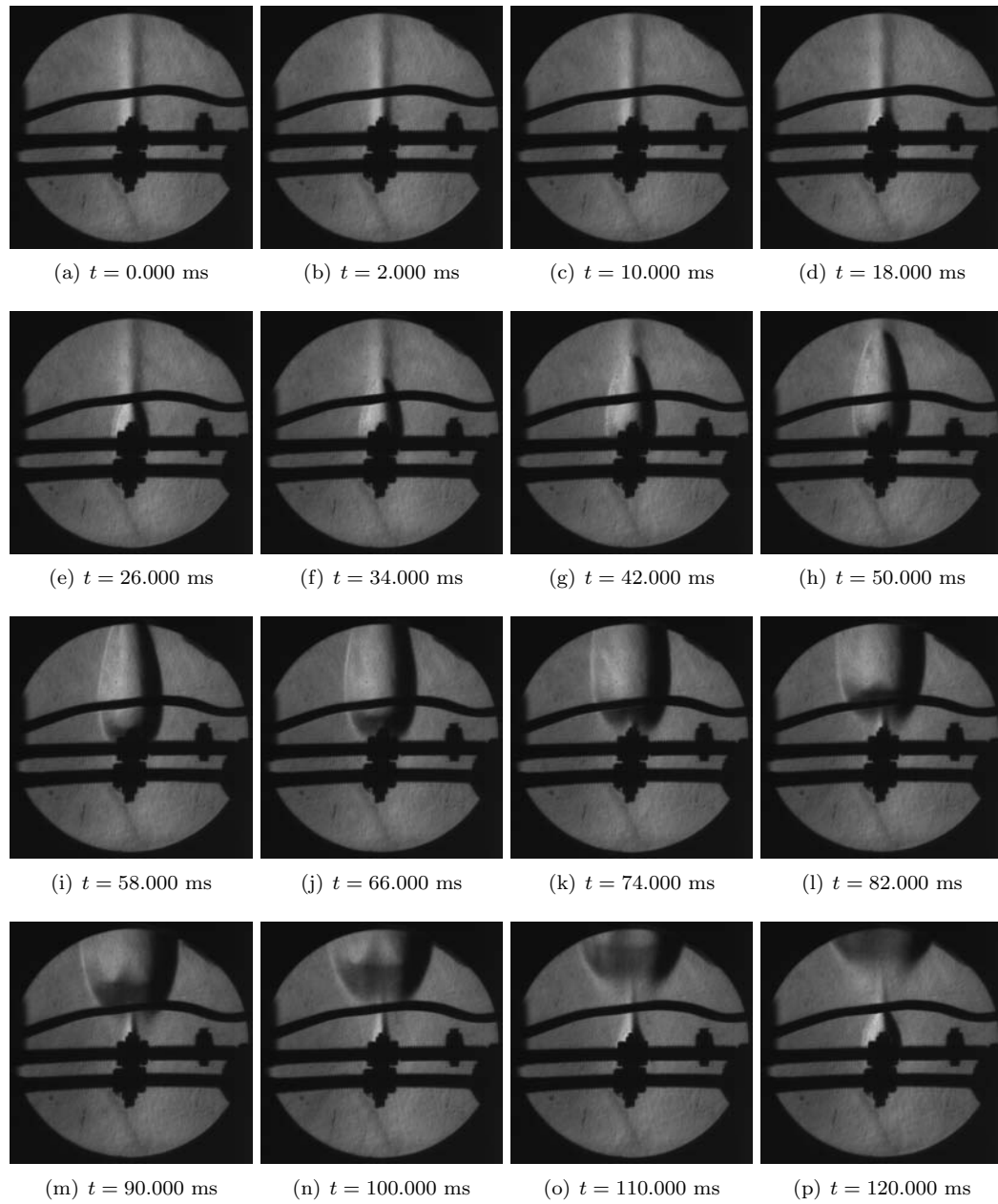


Figure K.74: Shot 87

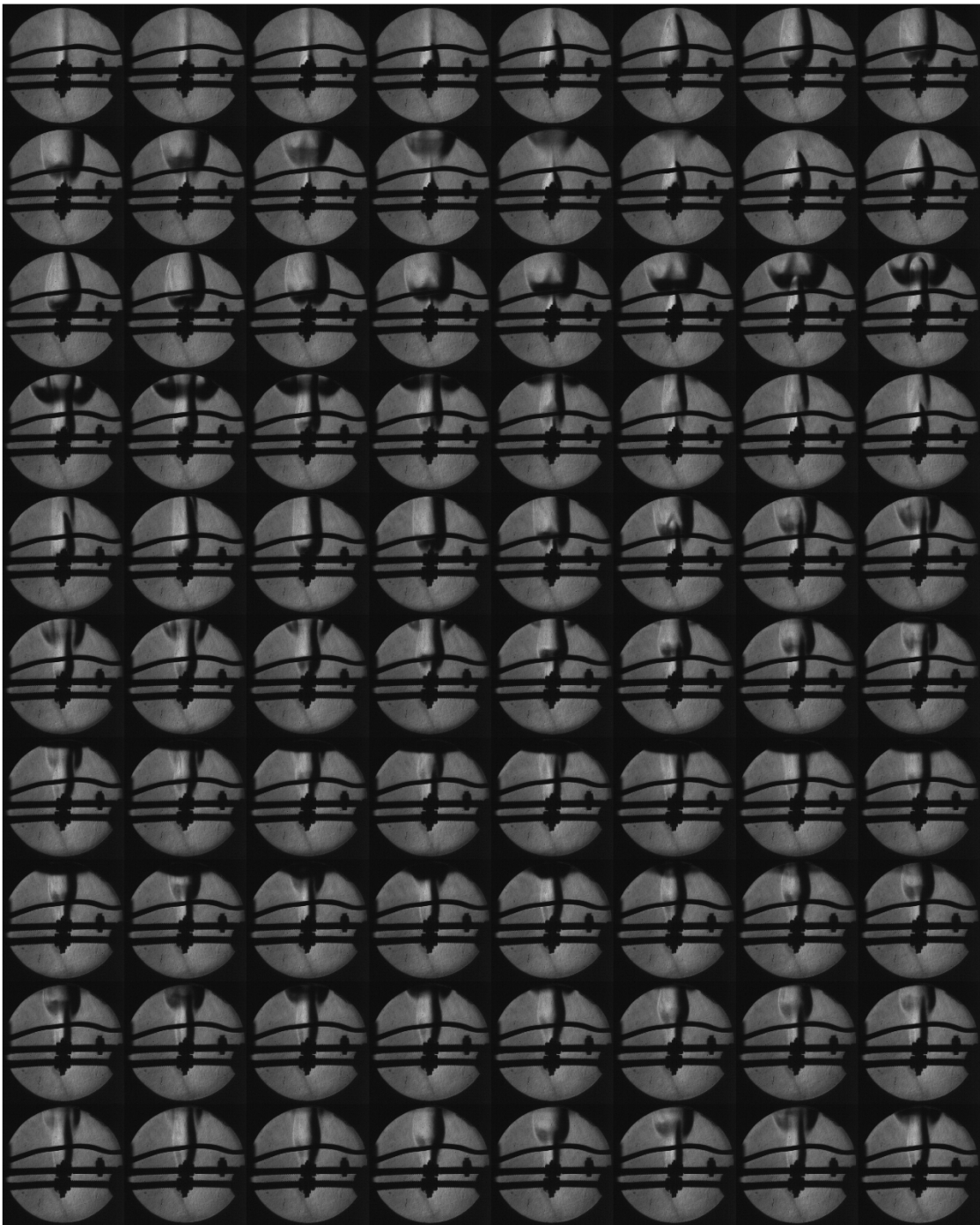


Figure K.75: Shot 87 montage ($\Delta t = 10$ ms between images)

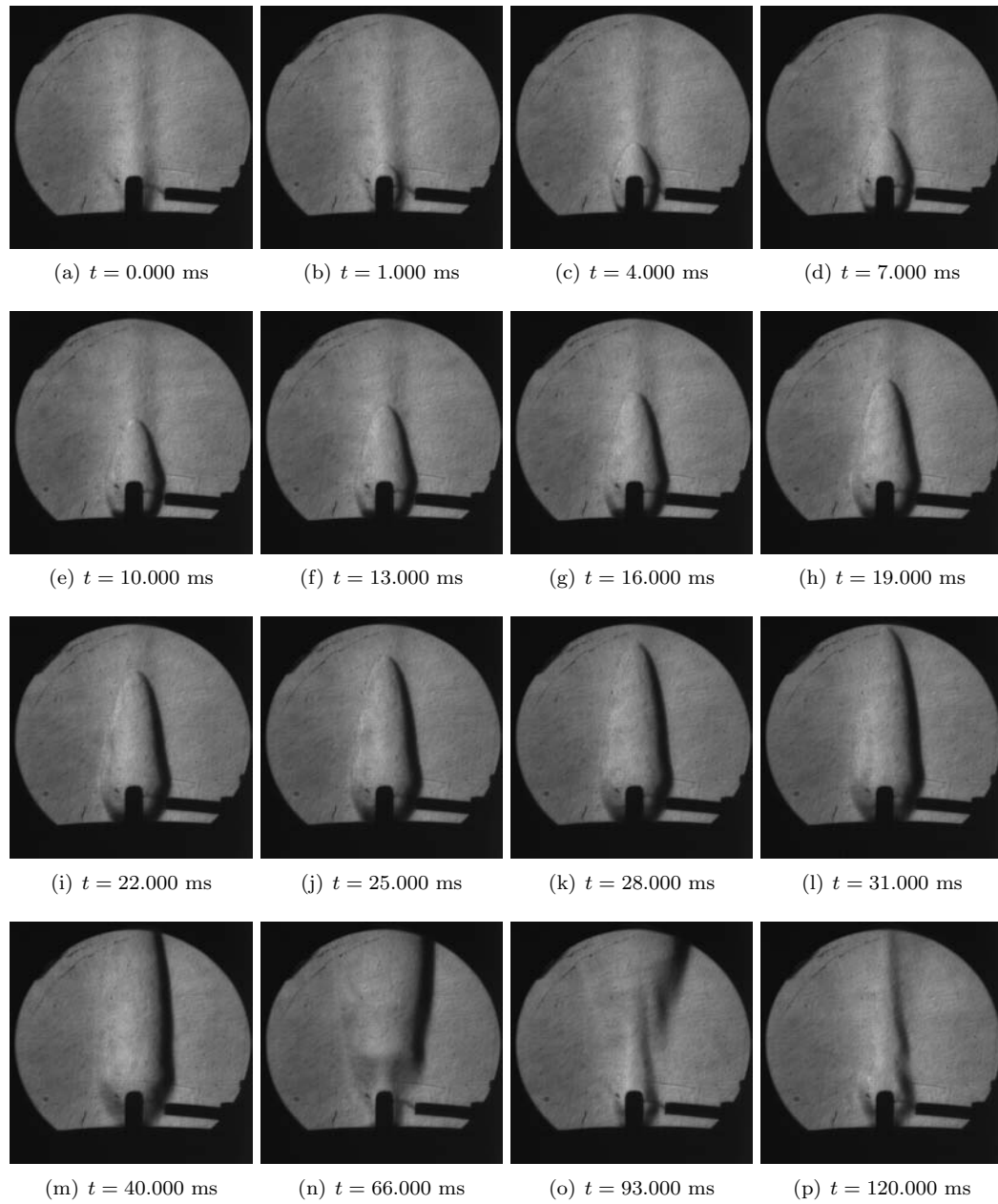


Figure K.76: Shot 90

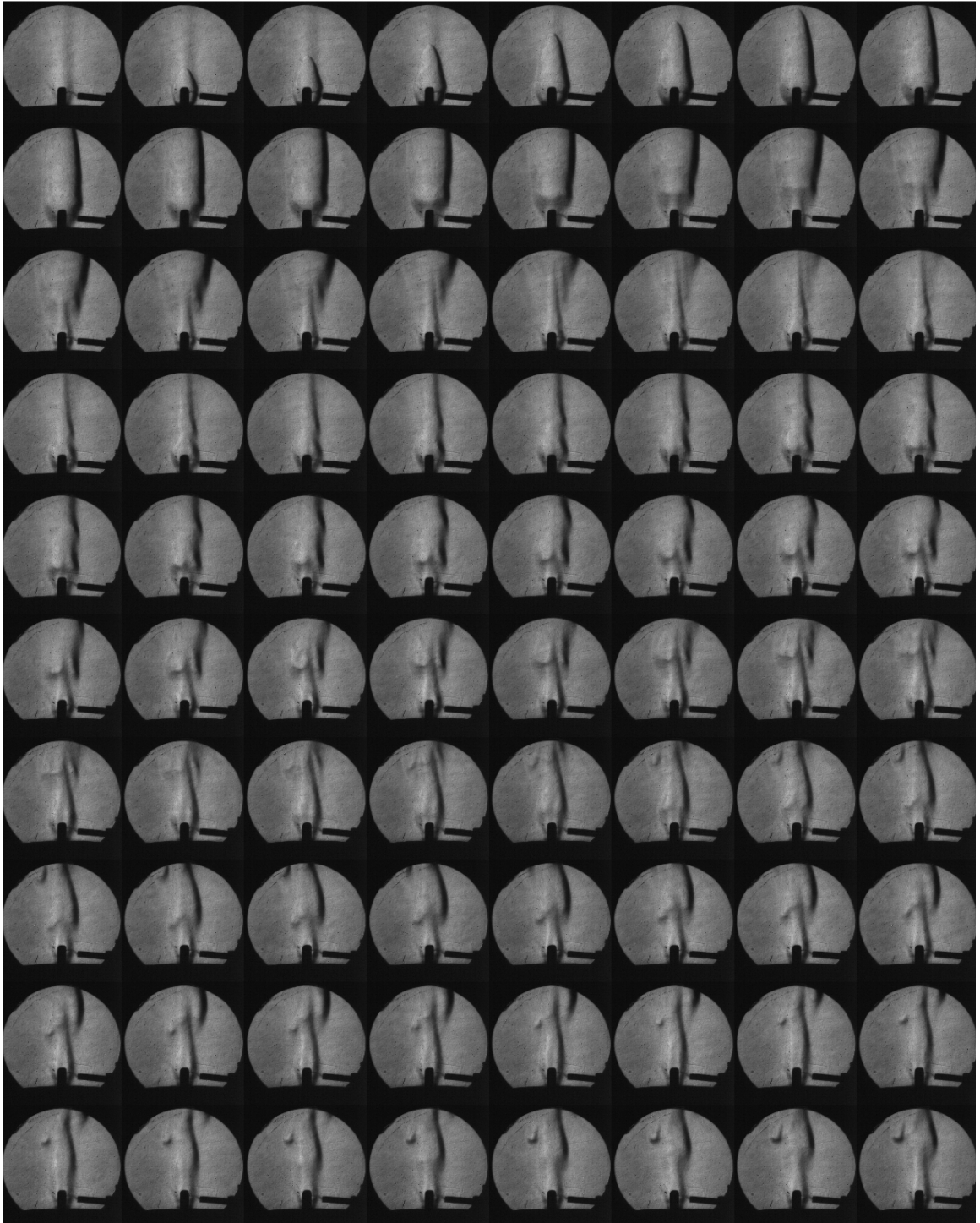


Figure K.77: Shot 90 montage ($\Delta t = 10$ ms between images)

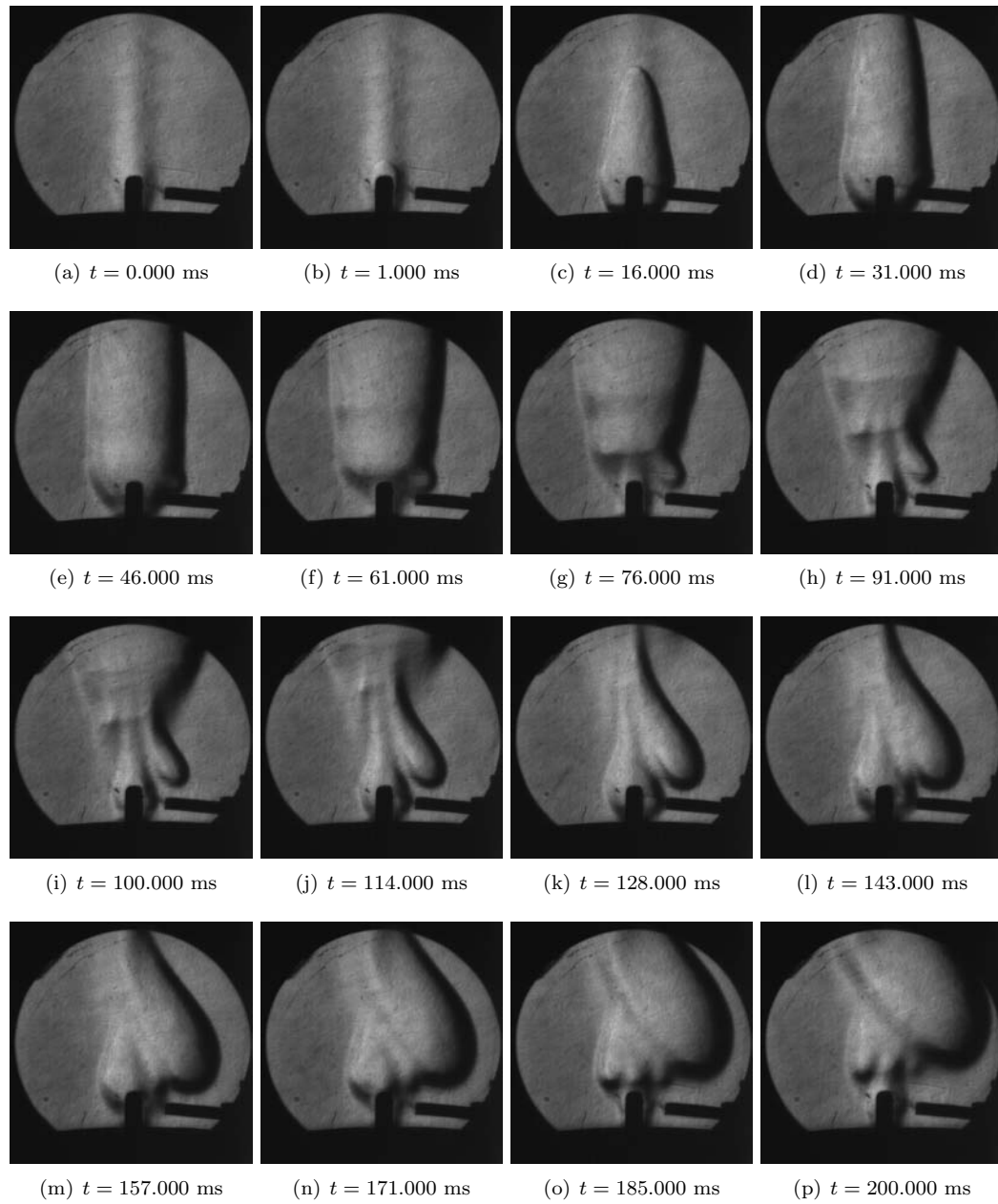


Figure K.78: Shot 91

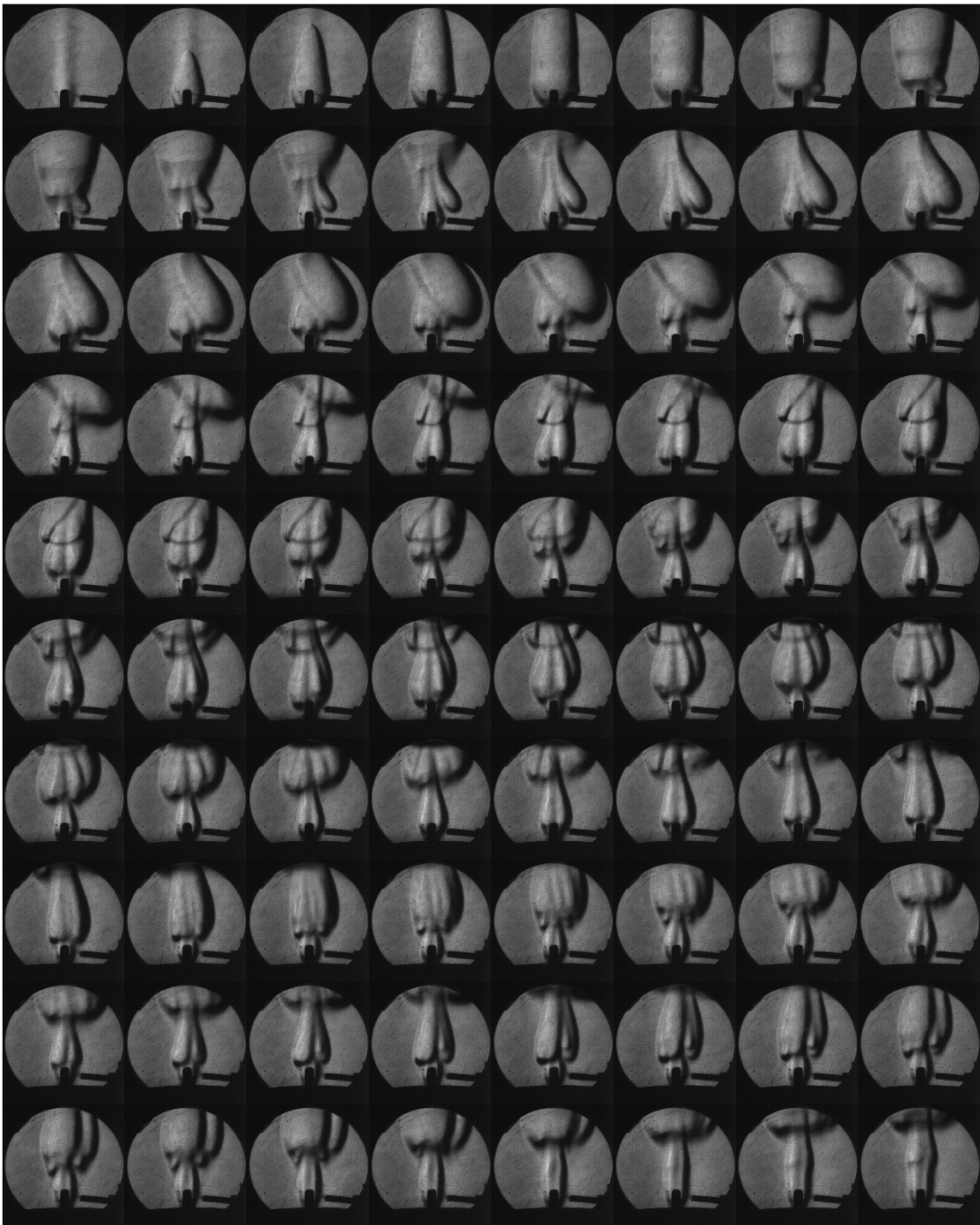


Figure K.79: Shot 91 montage ($\Delta t = 10$ ms between images)

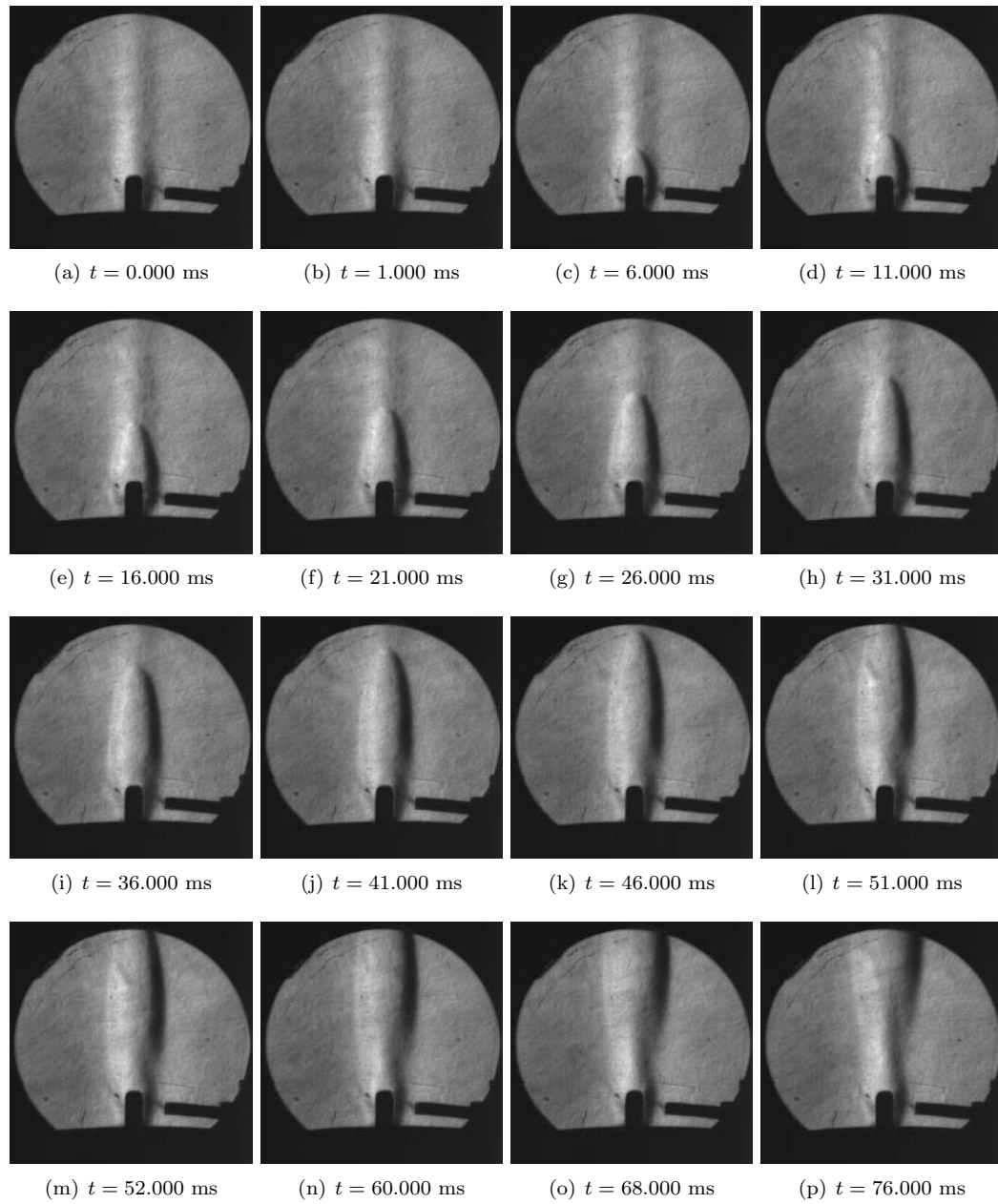


Figure K.80: Shot 92

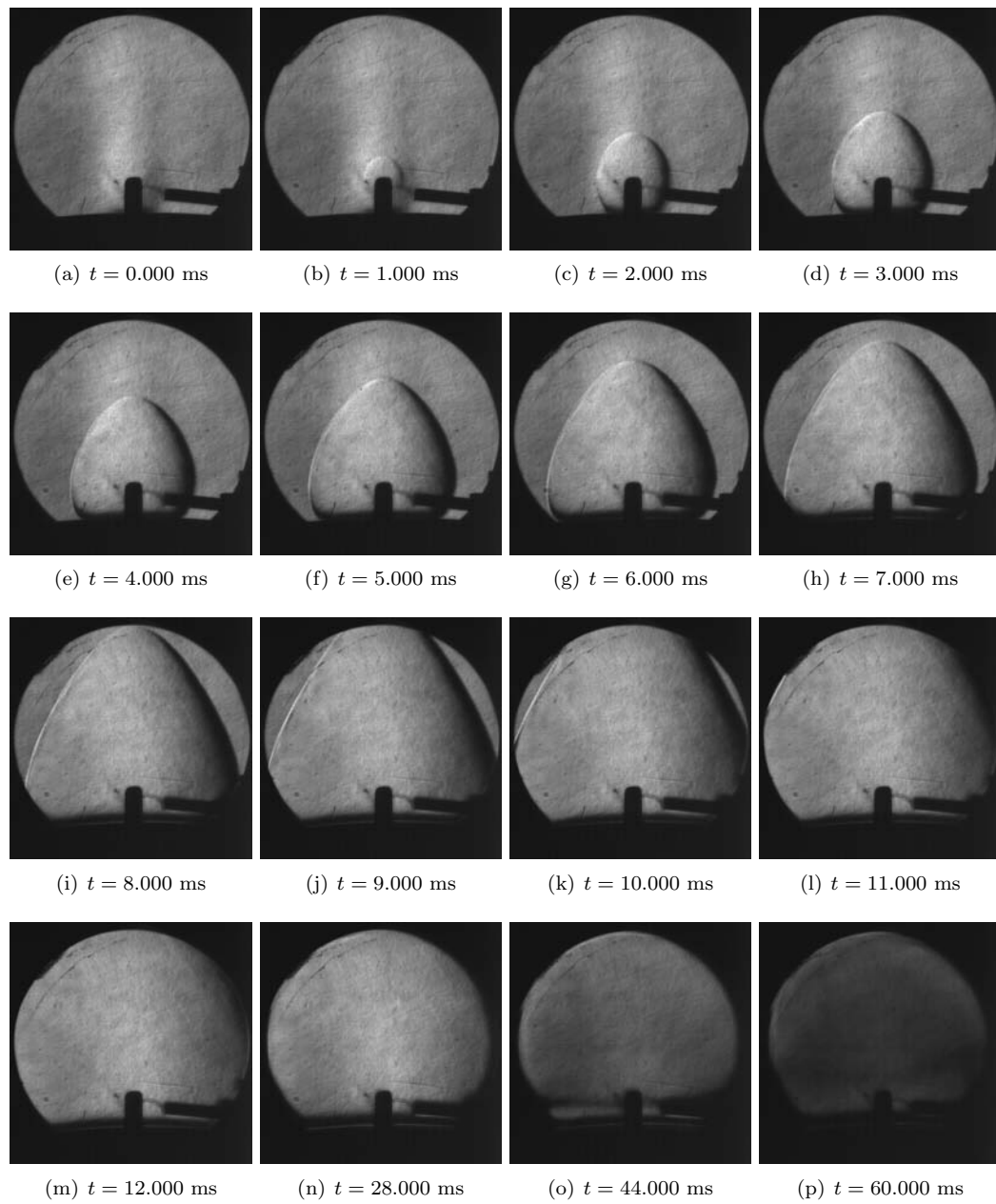


Figure K.81: Shot 93

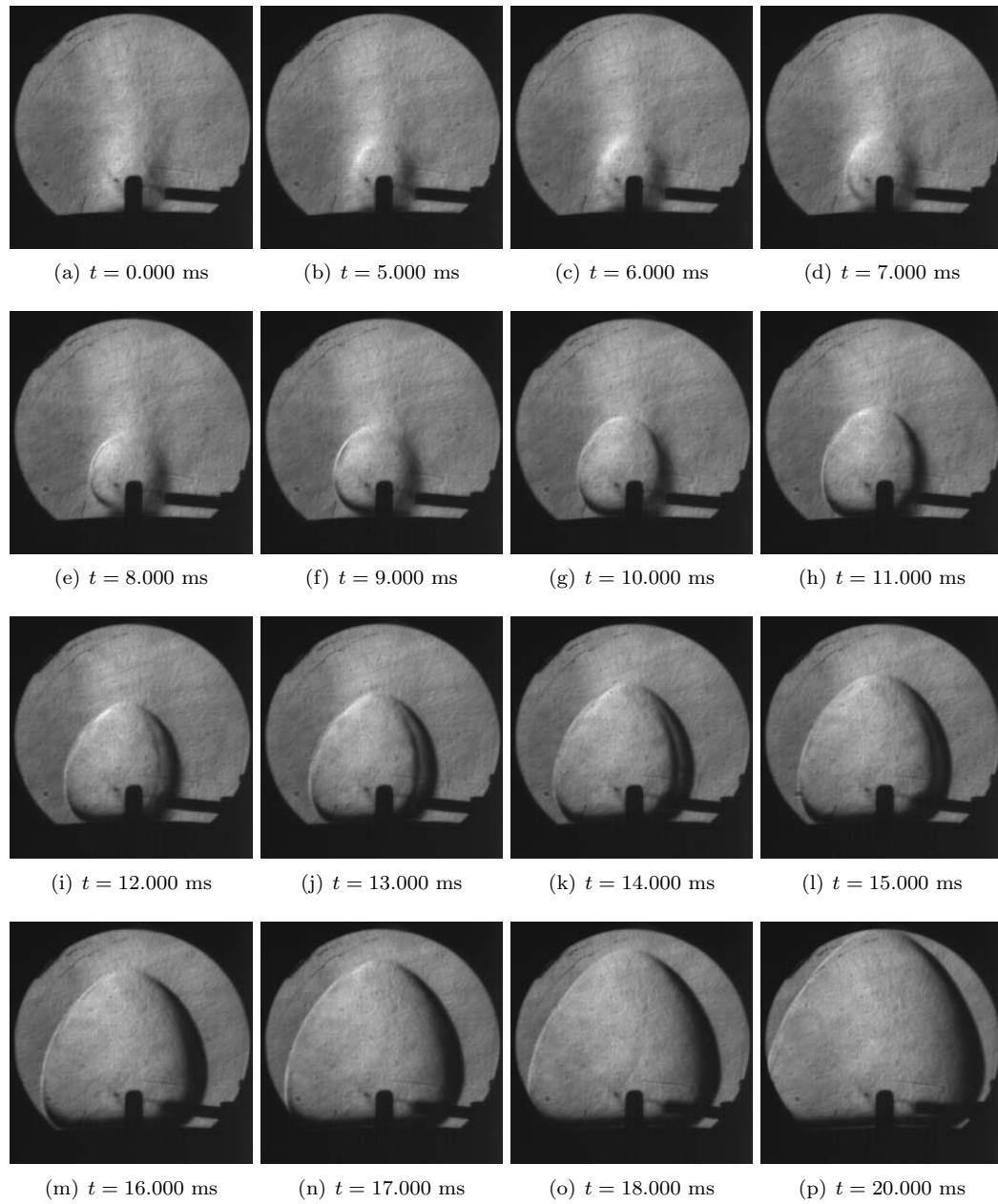


Figure K.82: Shot 94

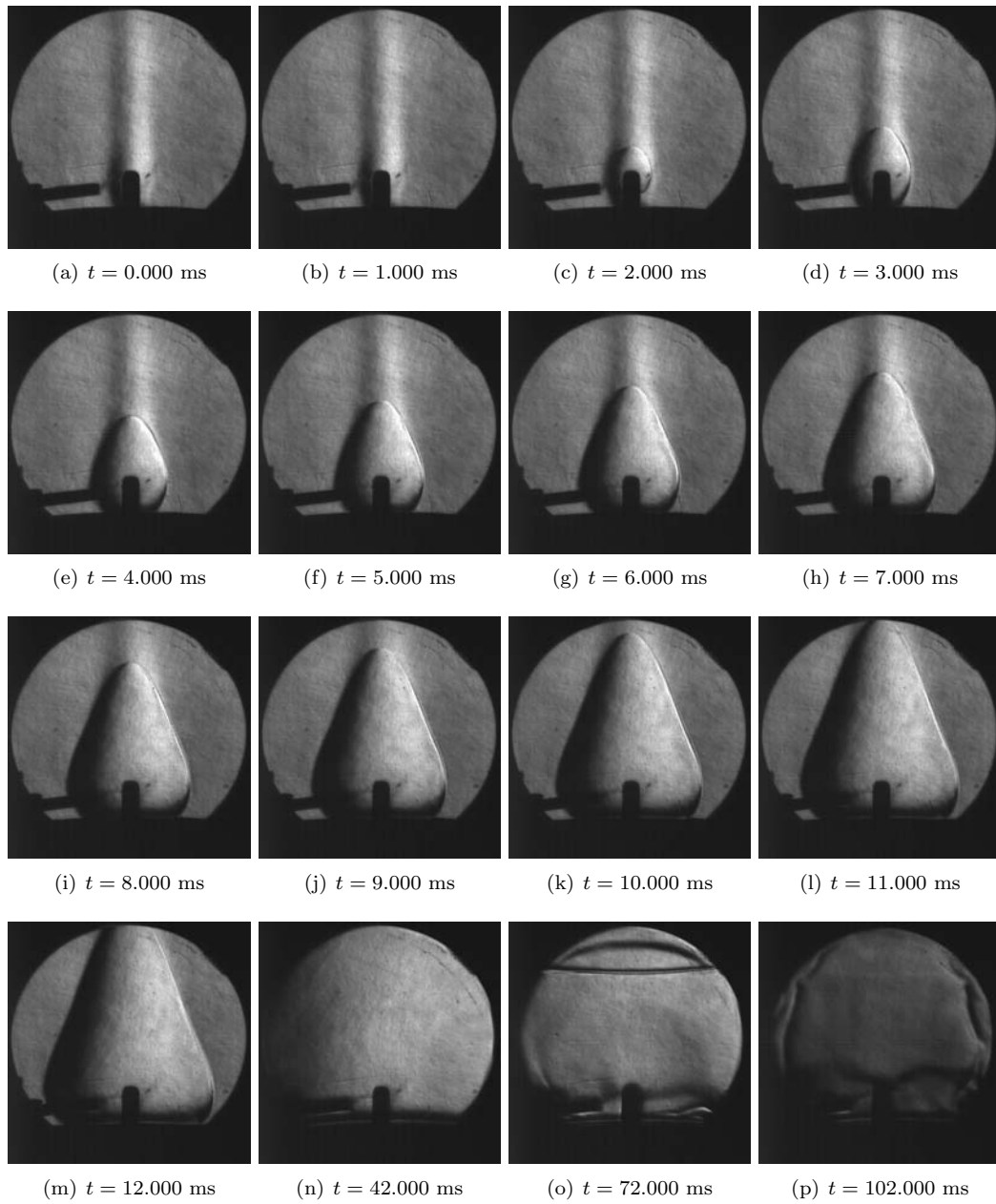


Figure K.83: Shot 97

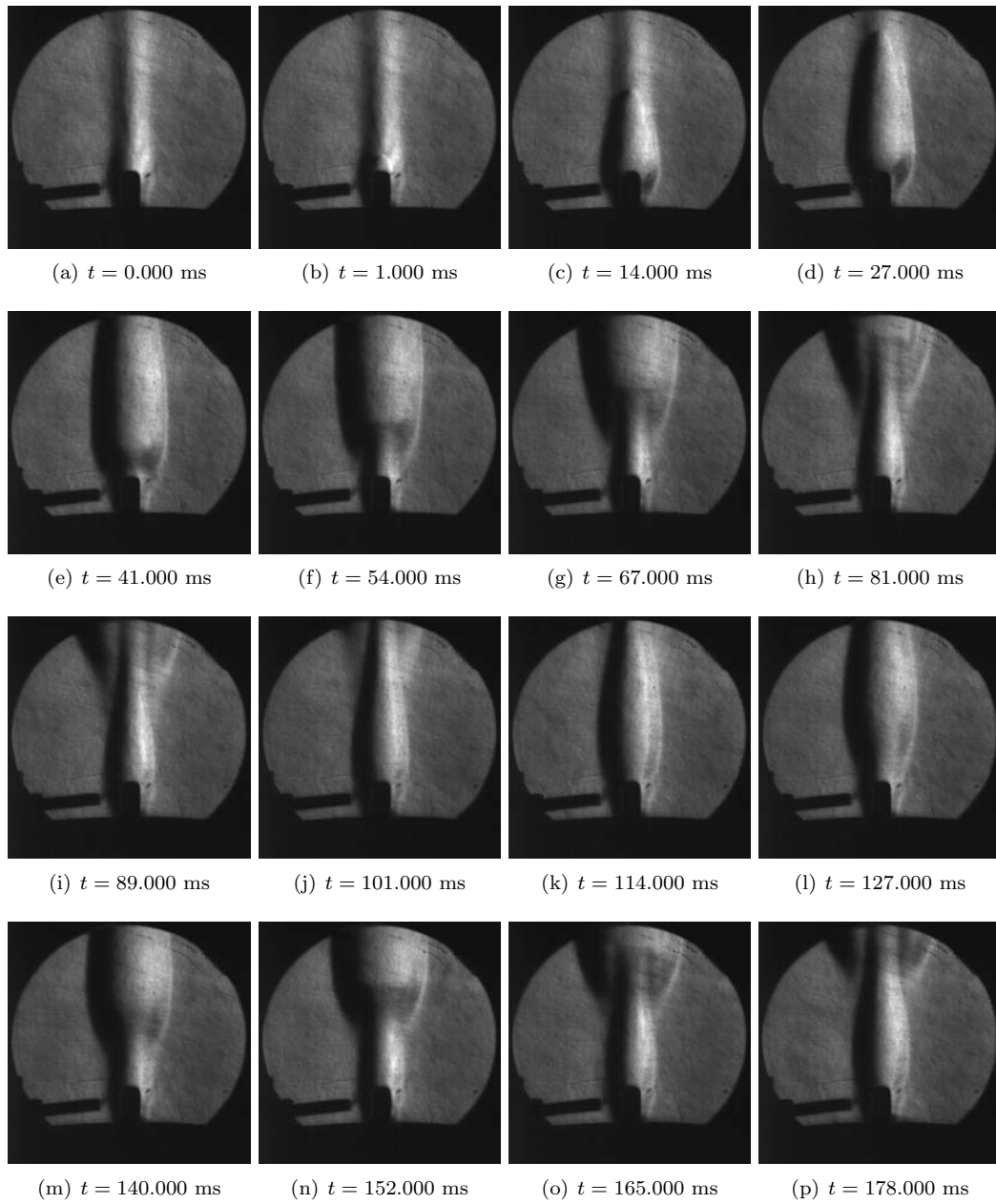


Figure K.84: Shot 98

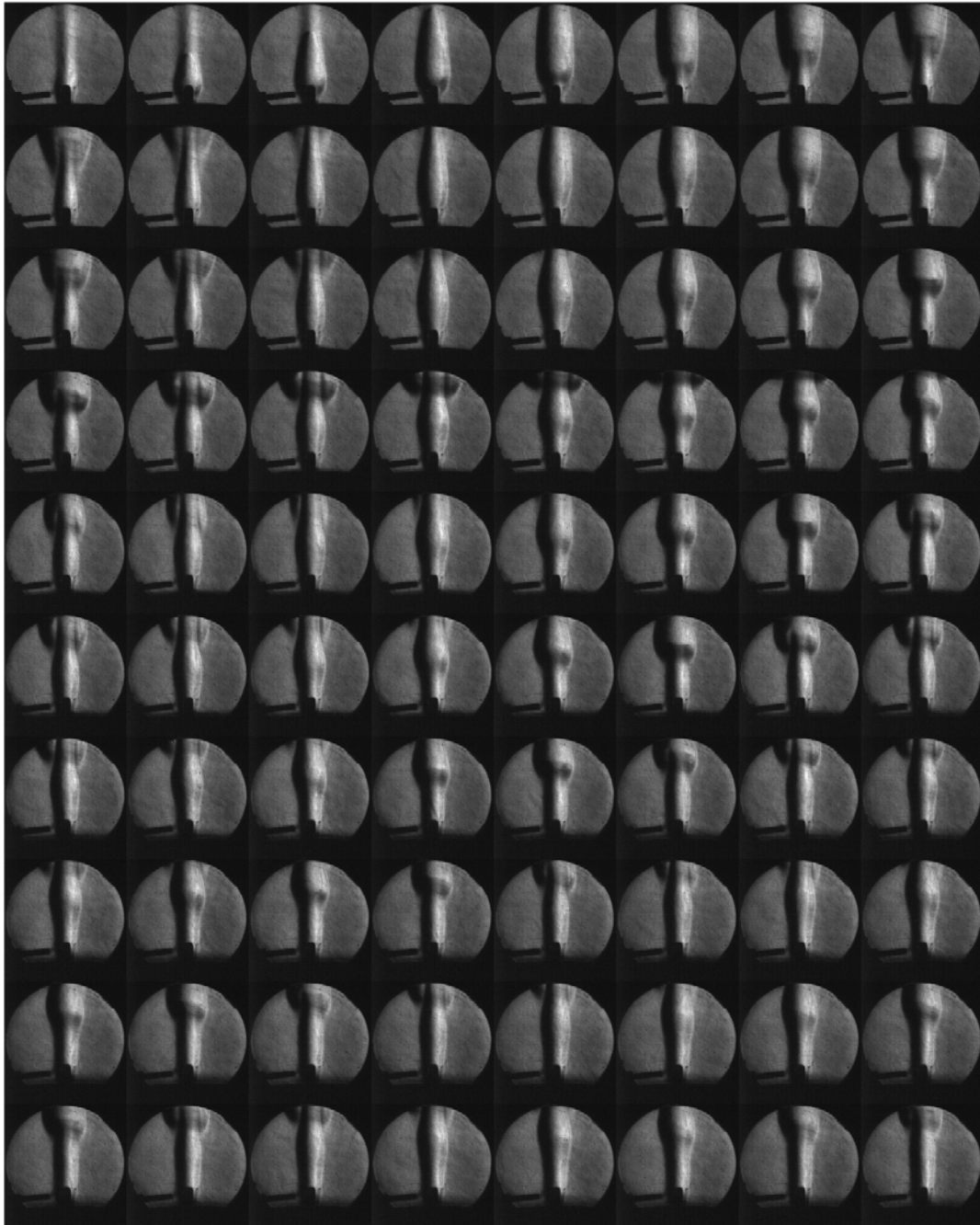


Figure K.85: Shot 98 montage ($\Delta t = 10$ ms between images)

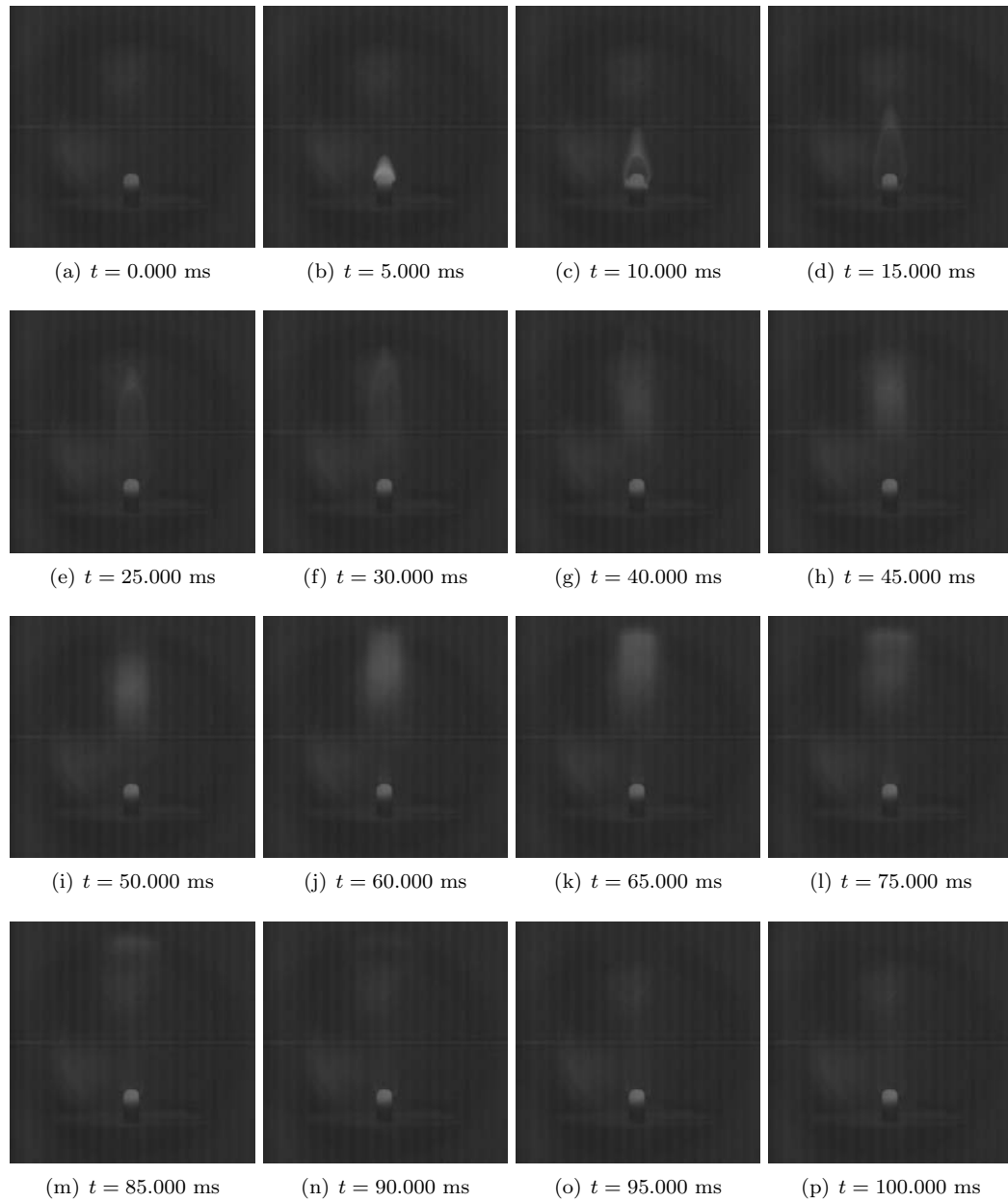


Figure K.86: Shot 100

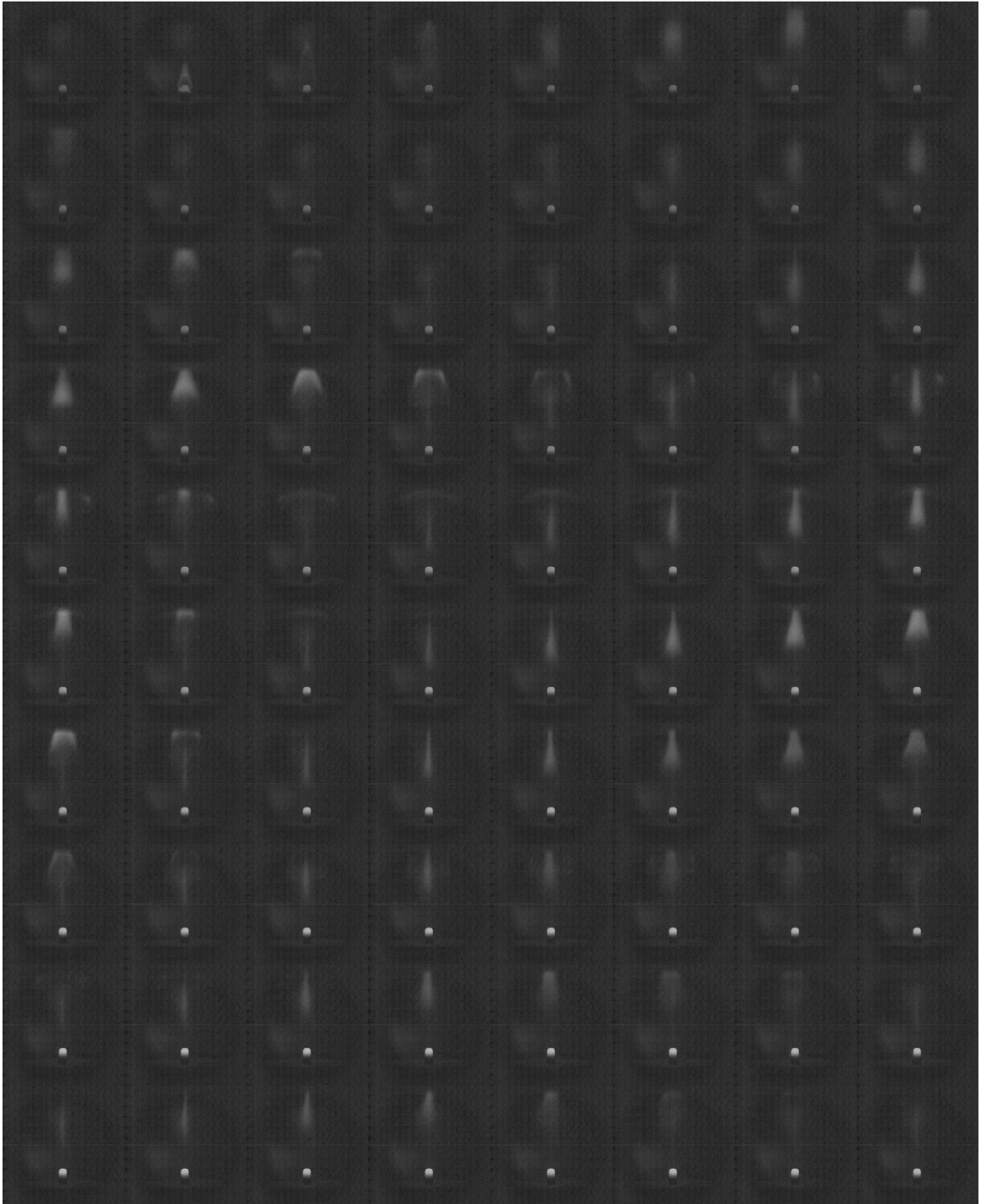


Figure K.87: Shot 100 montage ($\Delta t = 10$ ms between images)

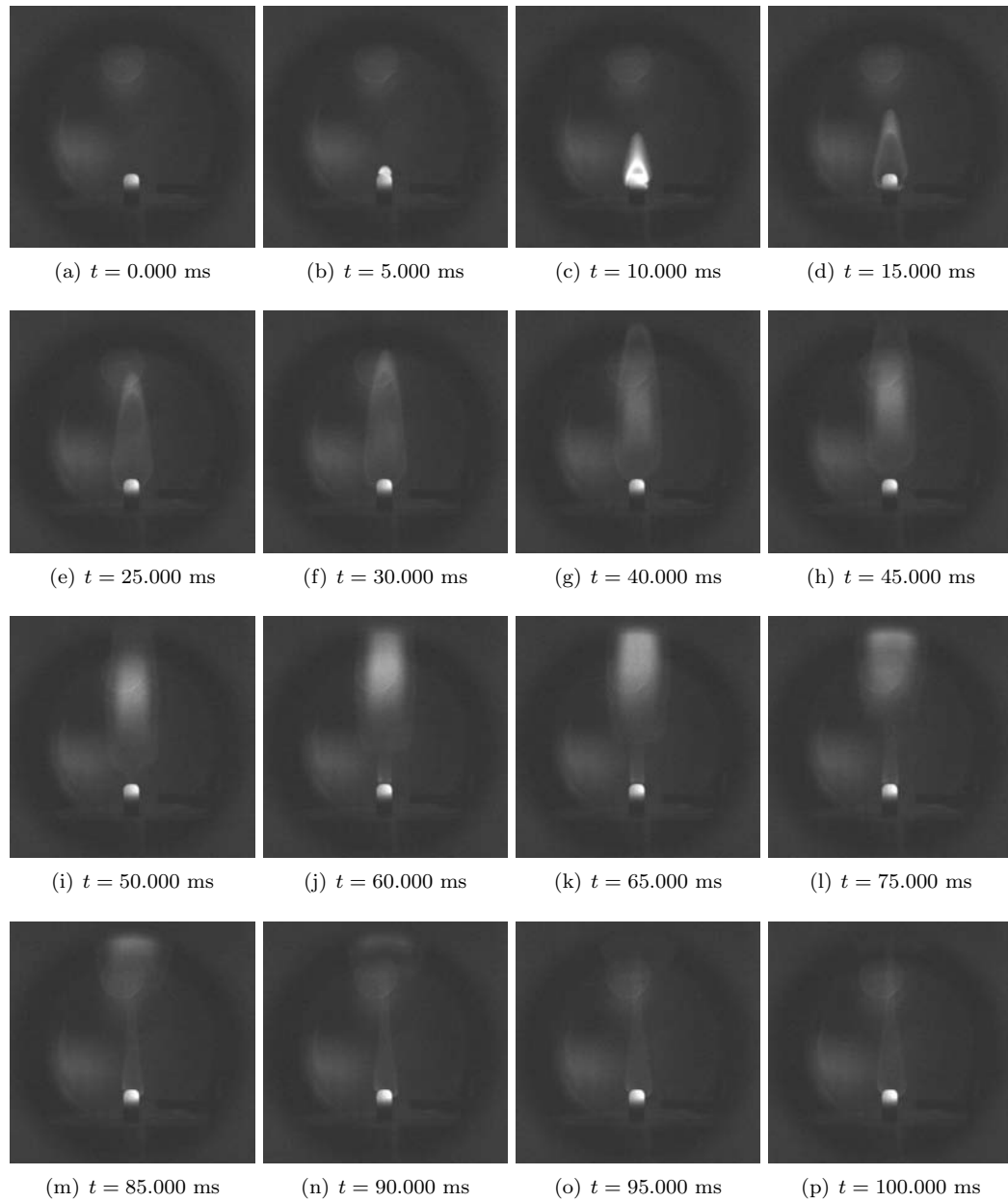


Figure K.88: Shot 101

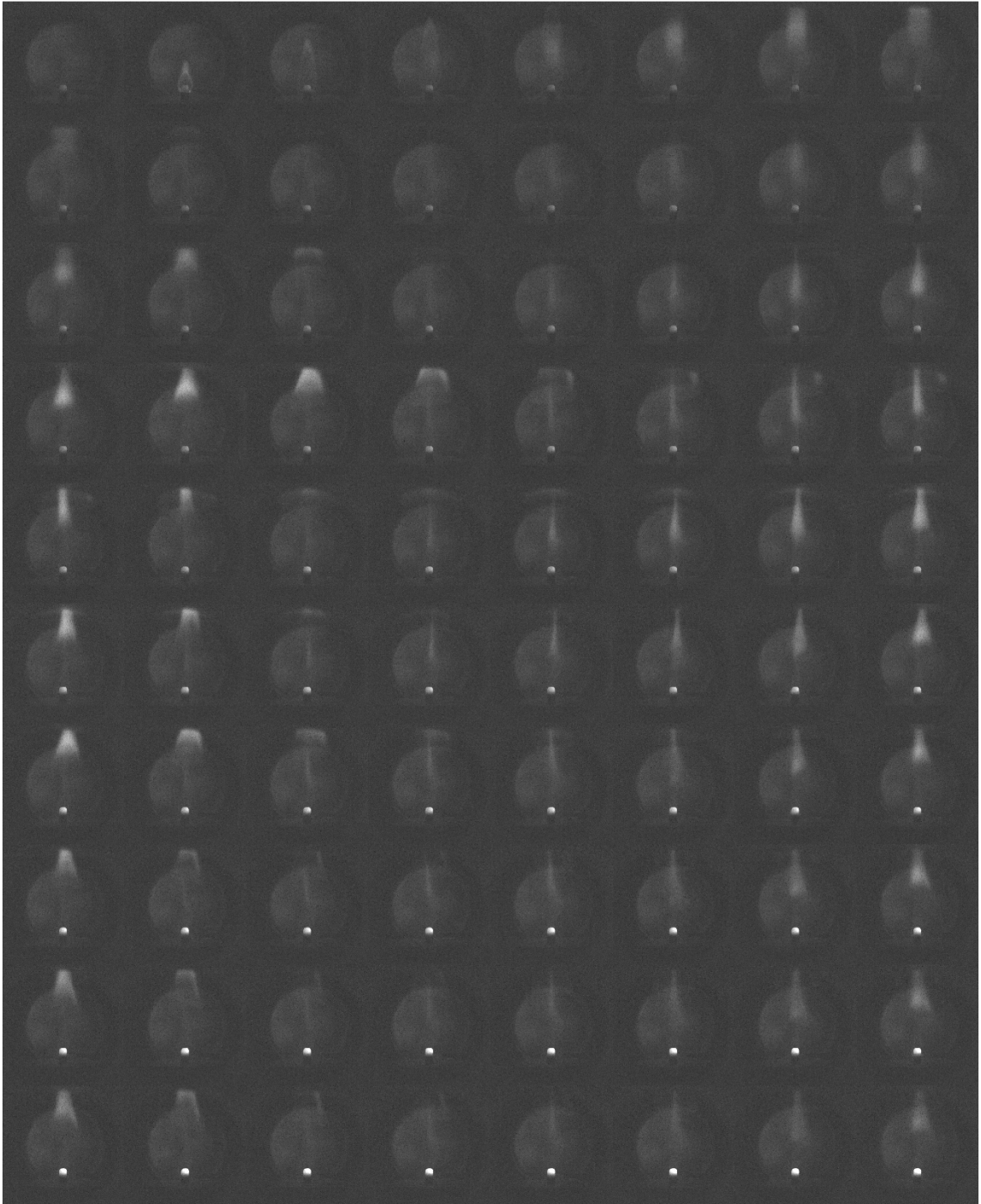


Figure K.89: Shot 101 montage ($\Delta t = 10$ ms between images)

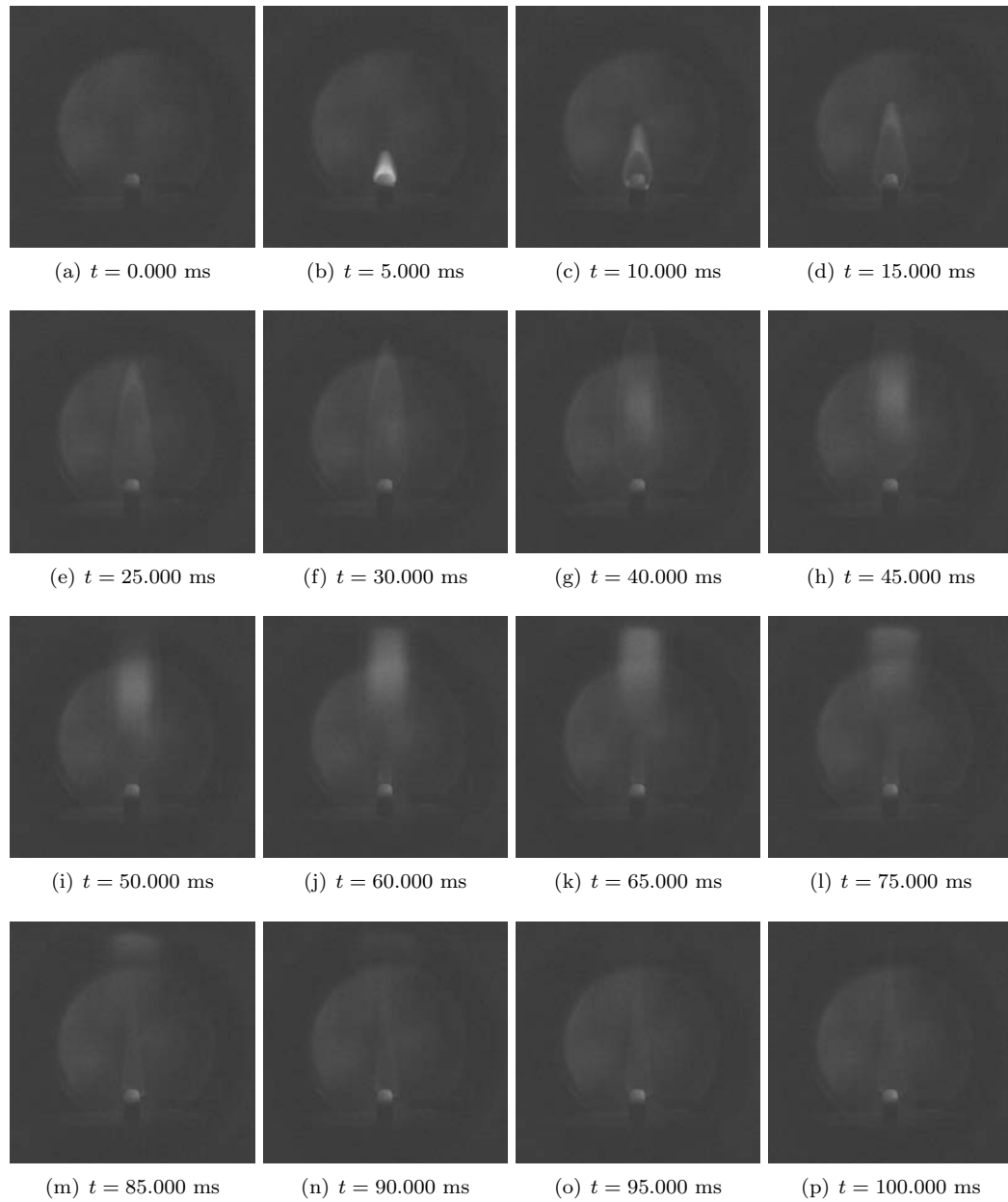


Figure K.90: Shot 102

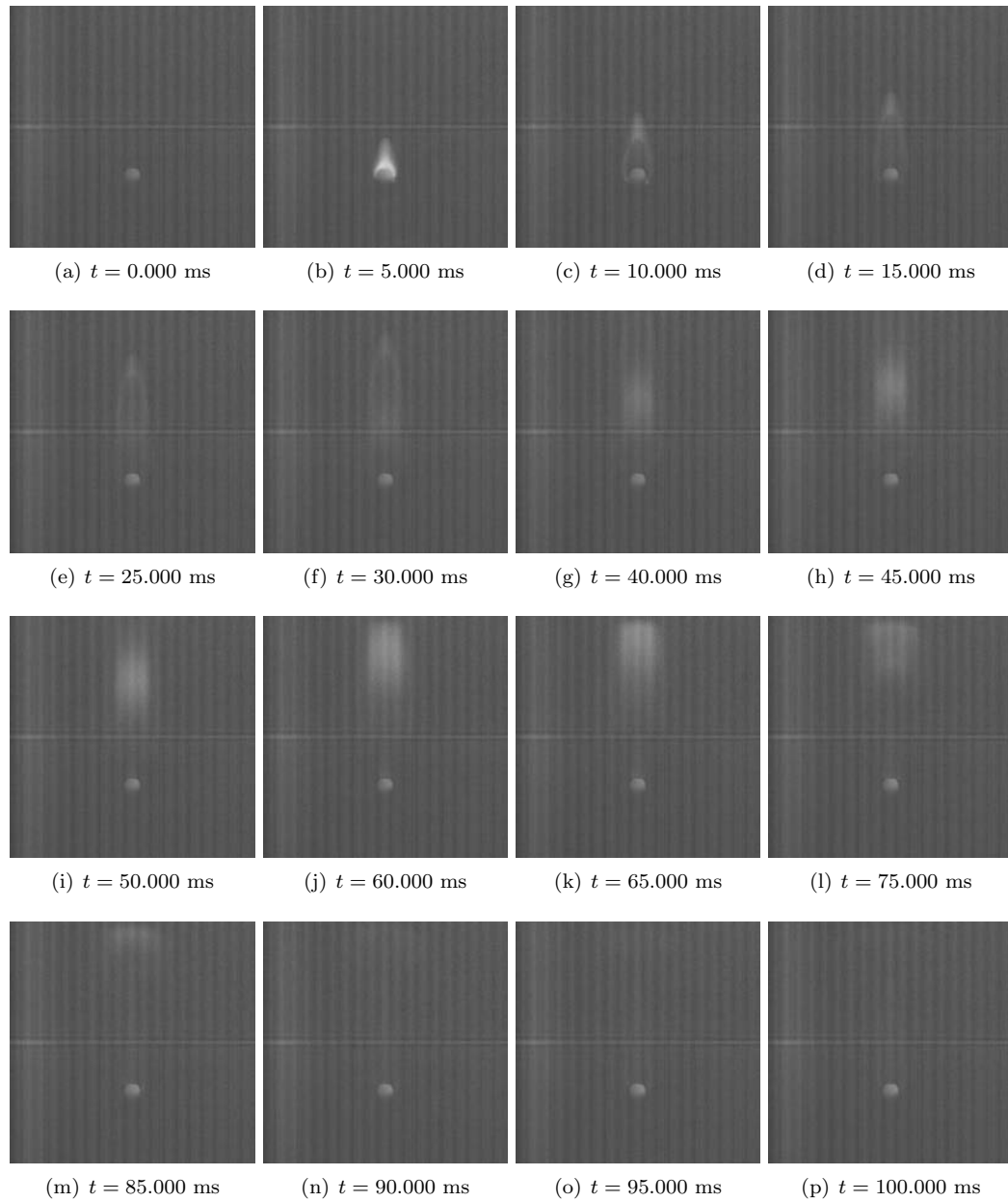


Figure K.91: Shot 103

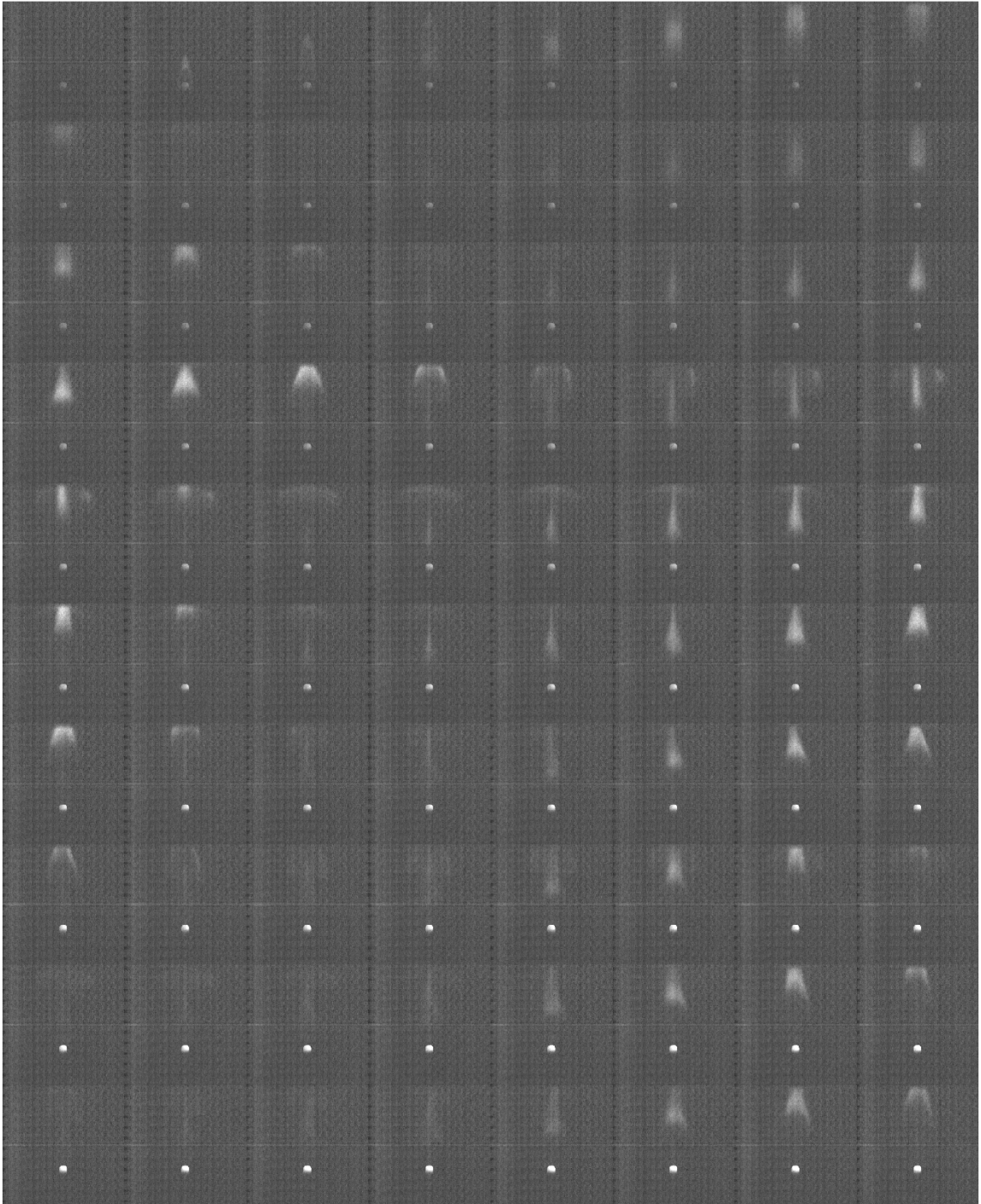


Figure K.92: Shot 103 montage ($\Delta t = 10$ ms between images)

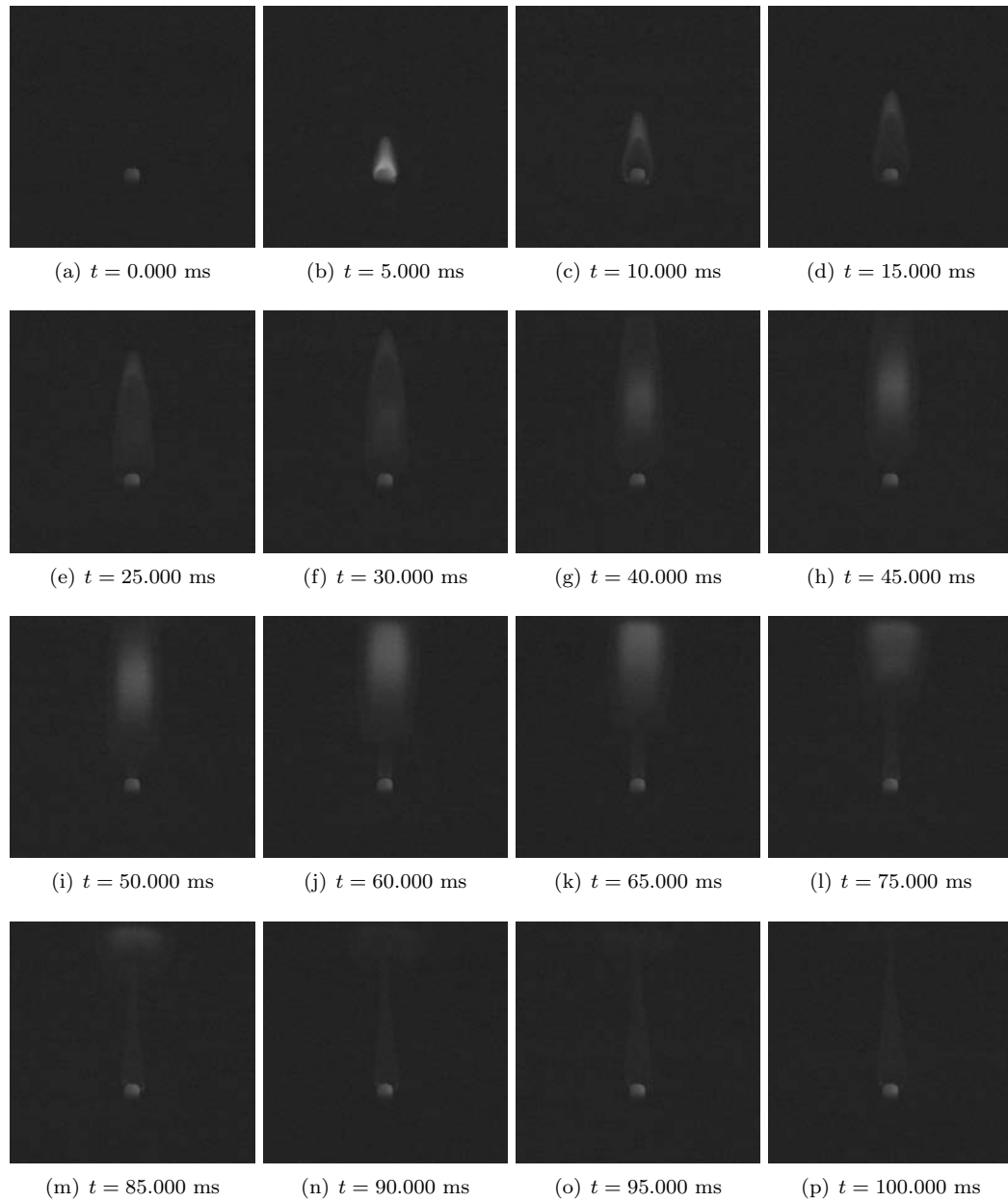


Figure K.93: Shot 104

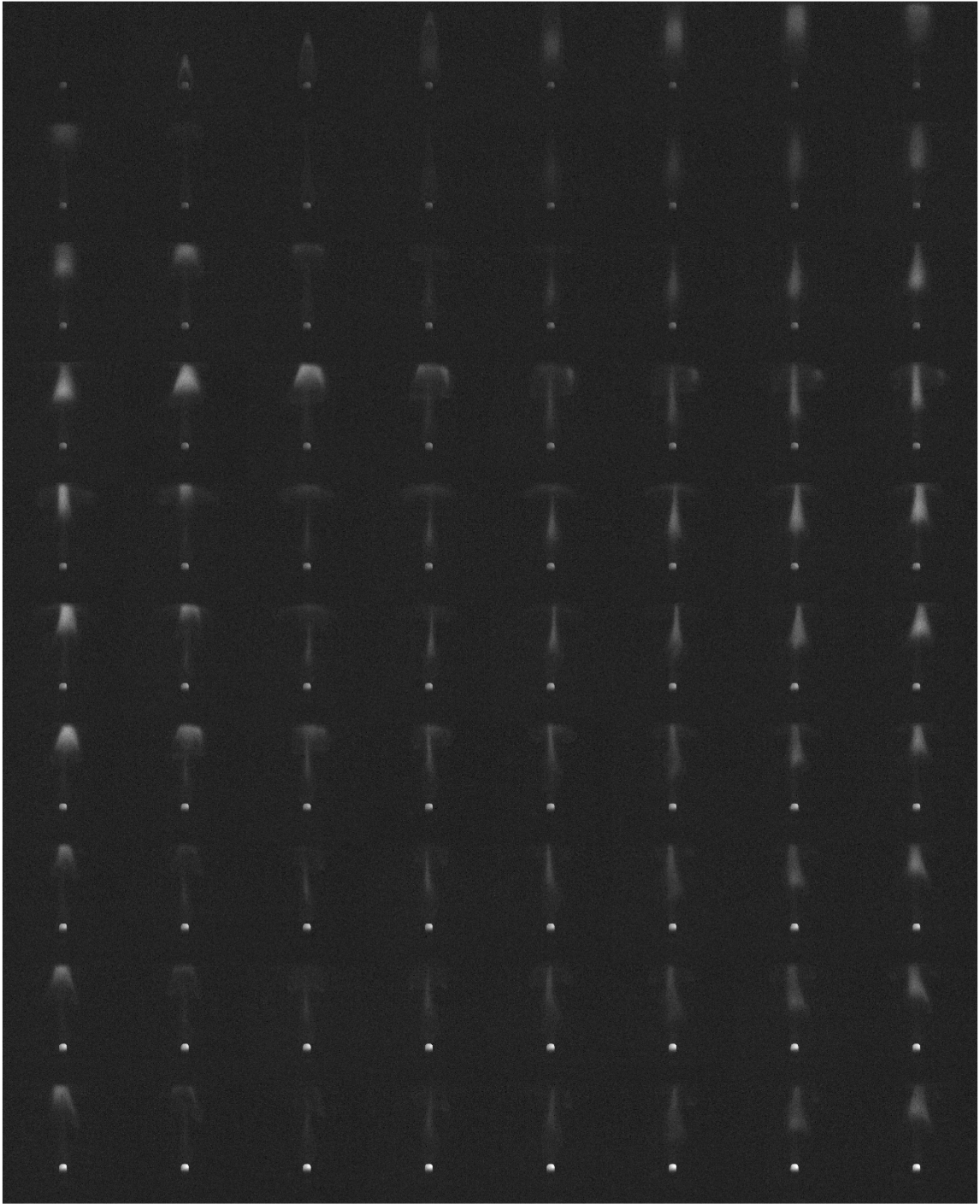


Figure K.94: Shot 104 montage ($\Delta t = 10$ ms between images)

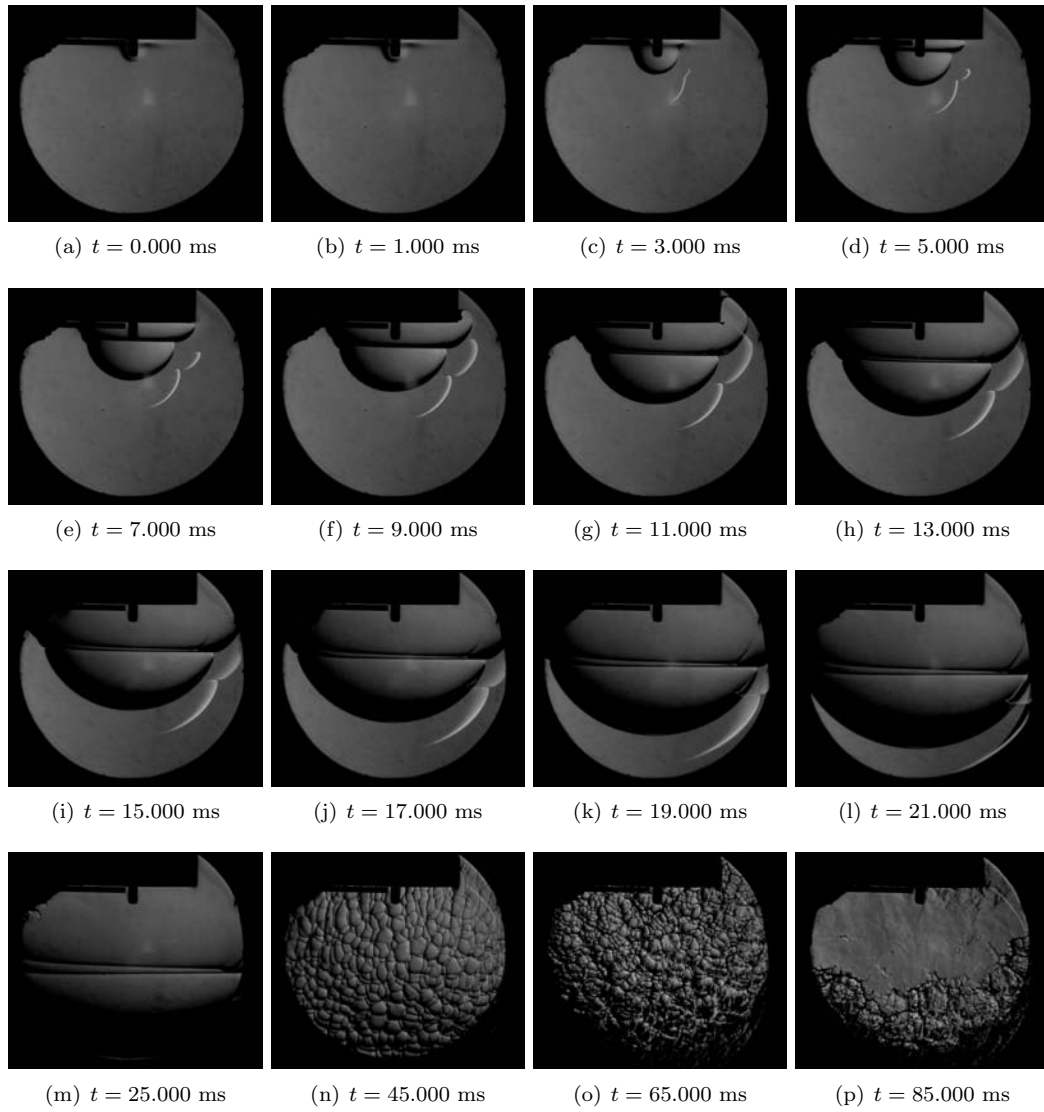


Figure K.95: Shot 110

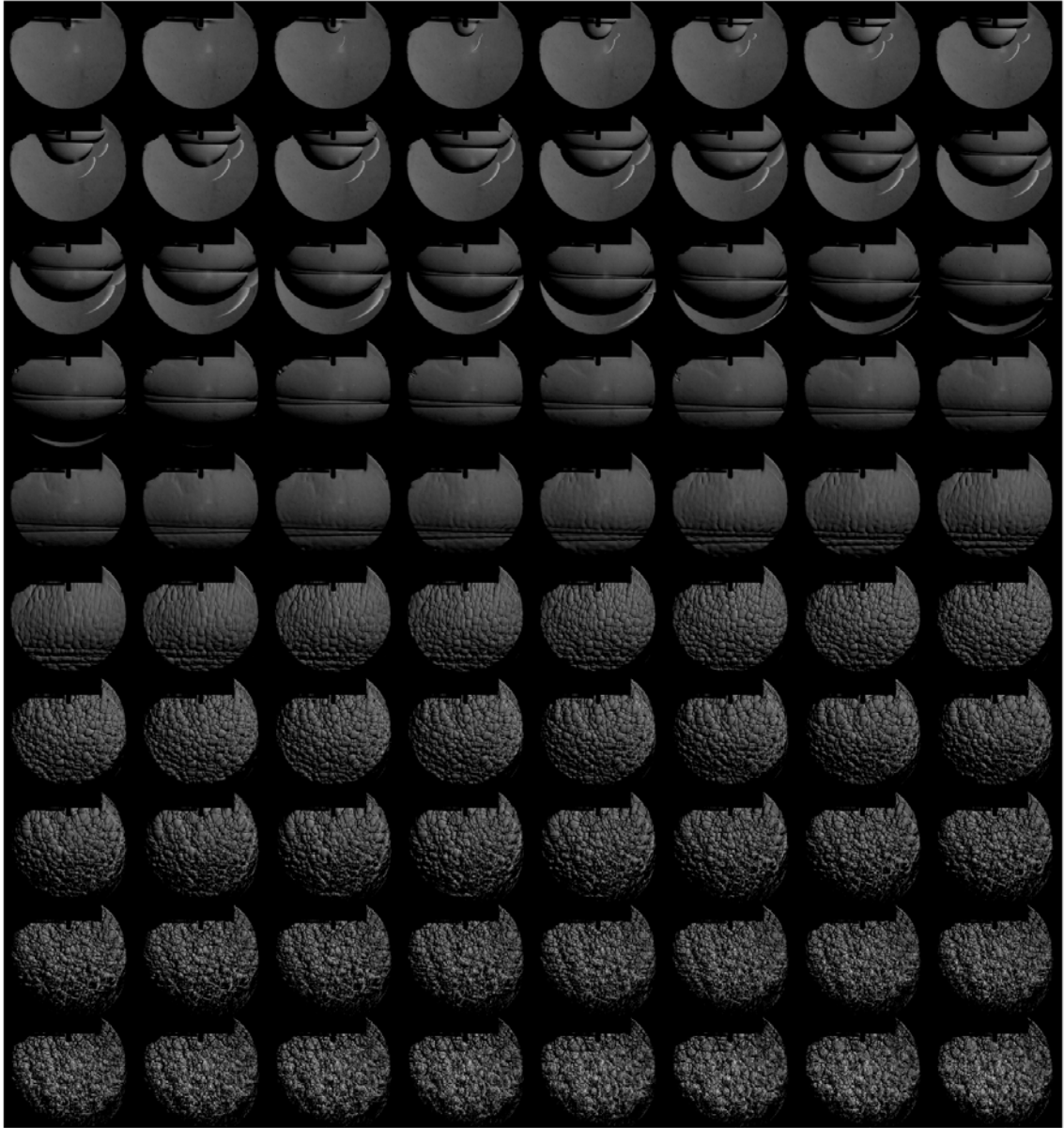


Figure K.96: Shot 110 montage ($\Delta t = 10$ ms between images)

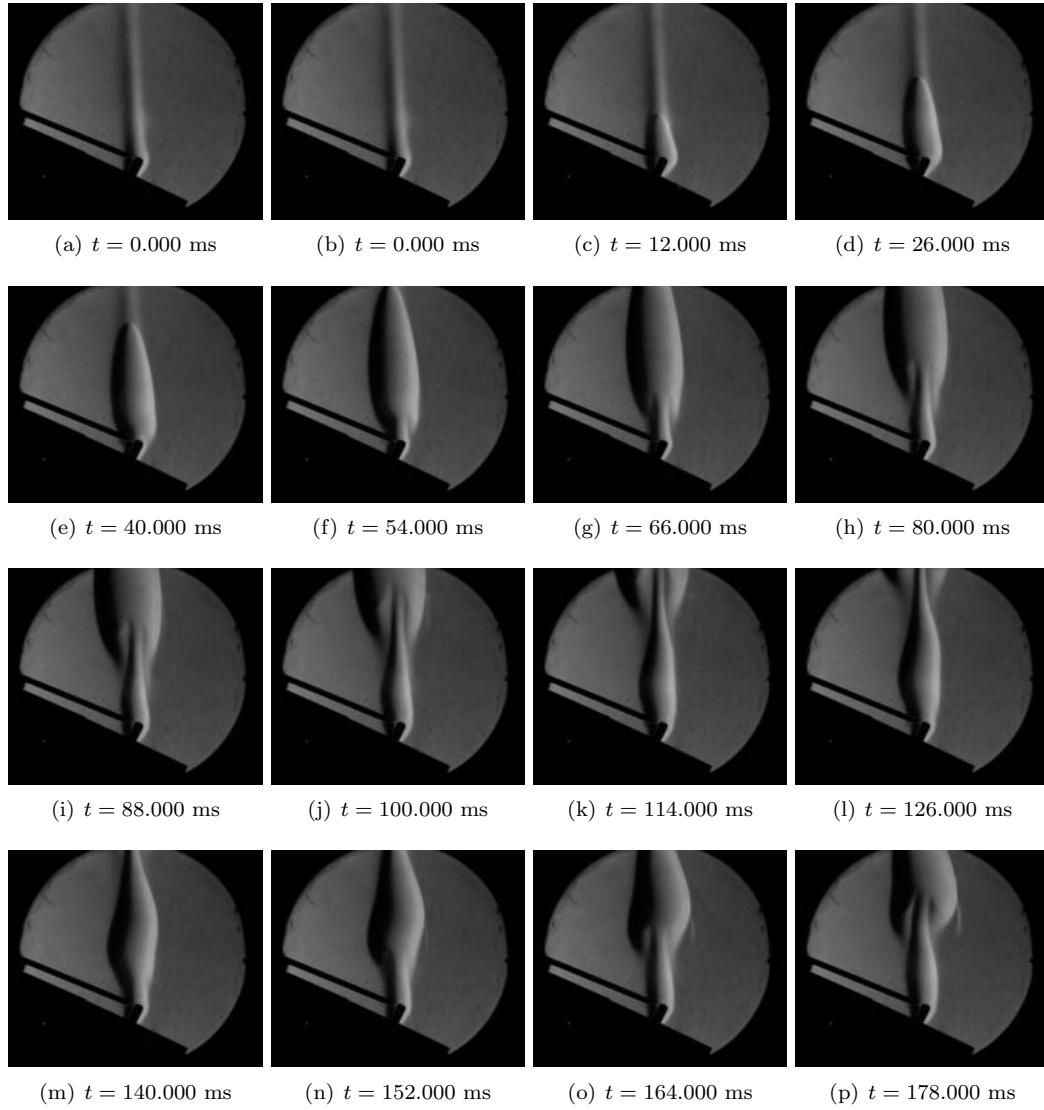


Figure K.97: Shot 112

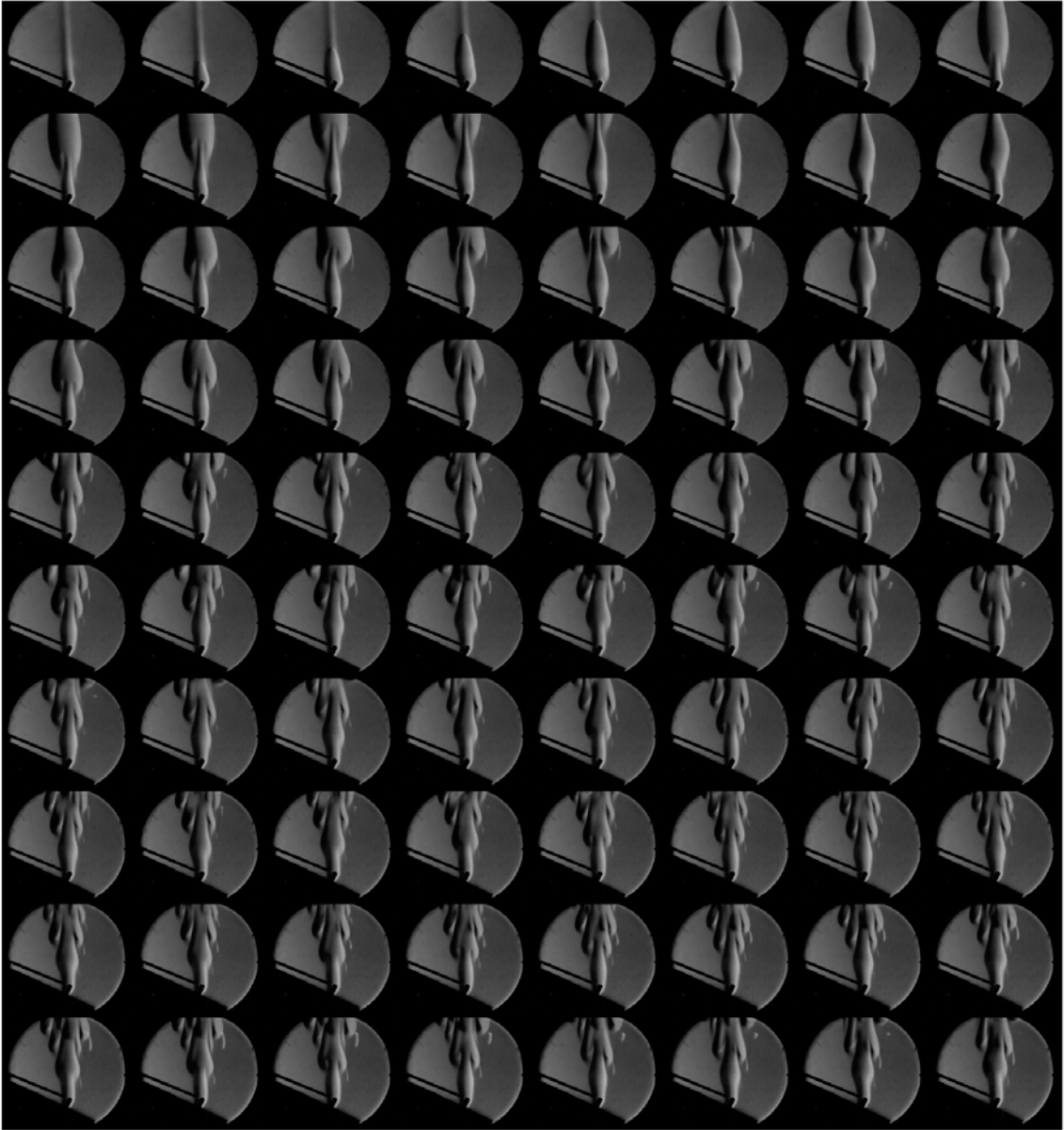


Figure K.98: Shot 112 montage ($\Delta t = 10$ ms between images)

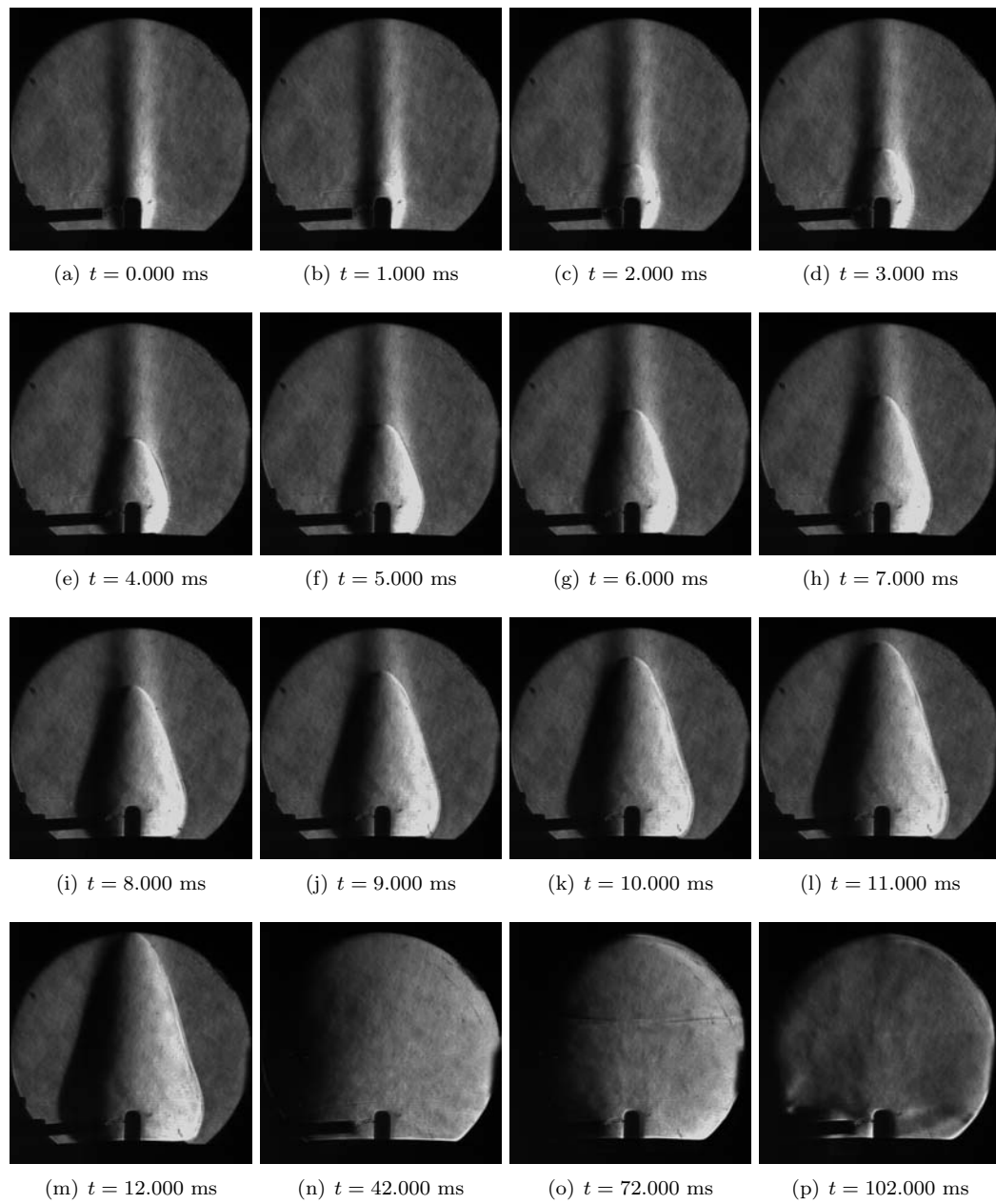


Figure K.99: Shot 115

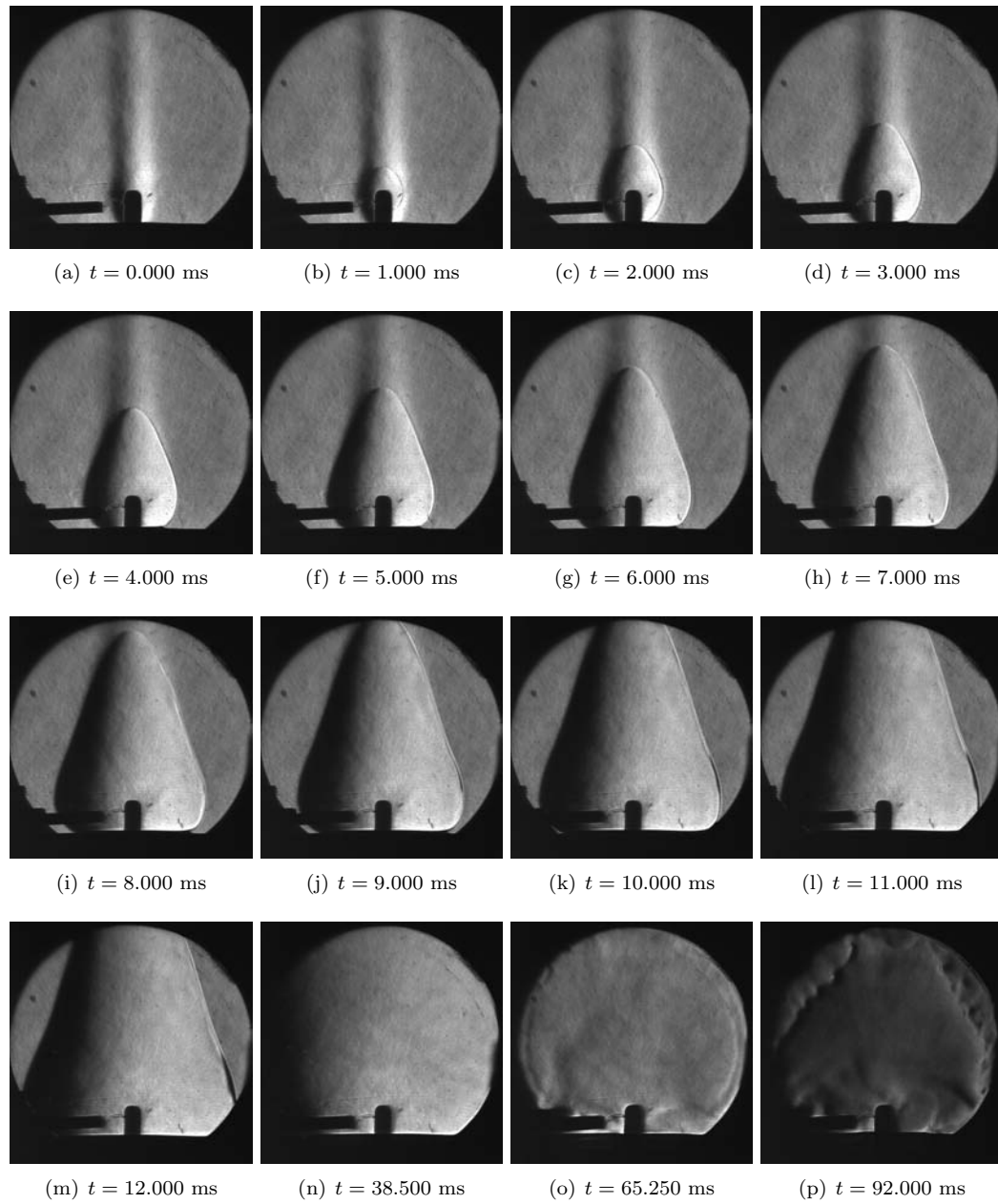


Figure K.100: Shot 116

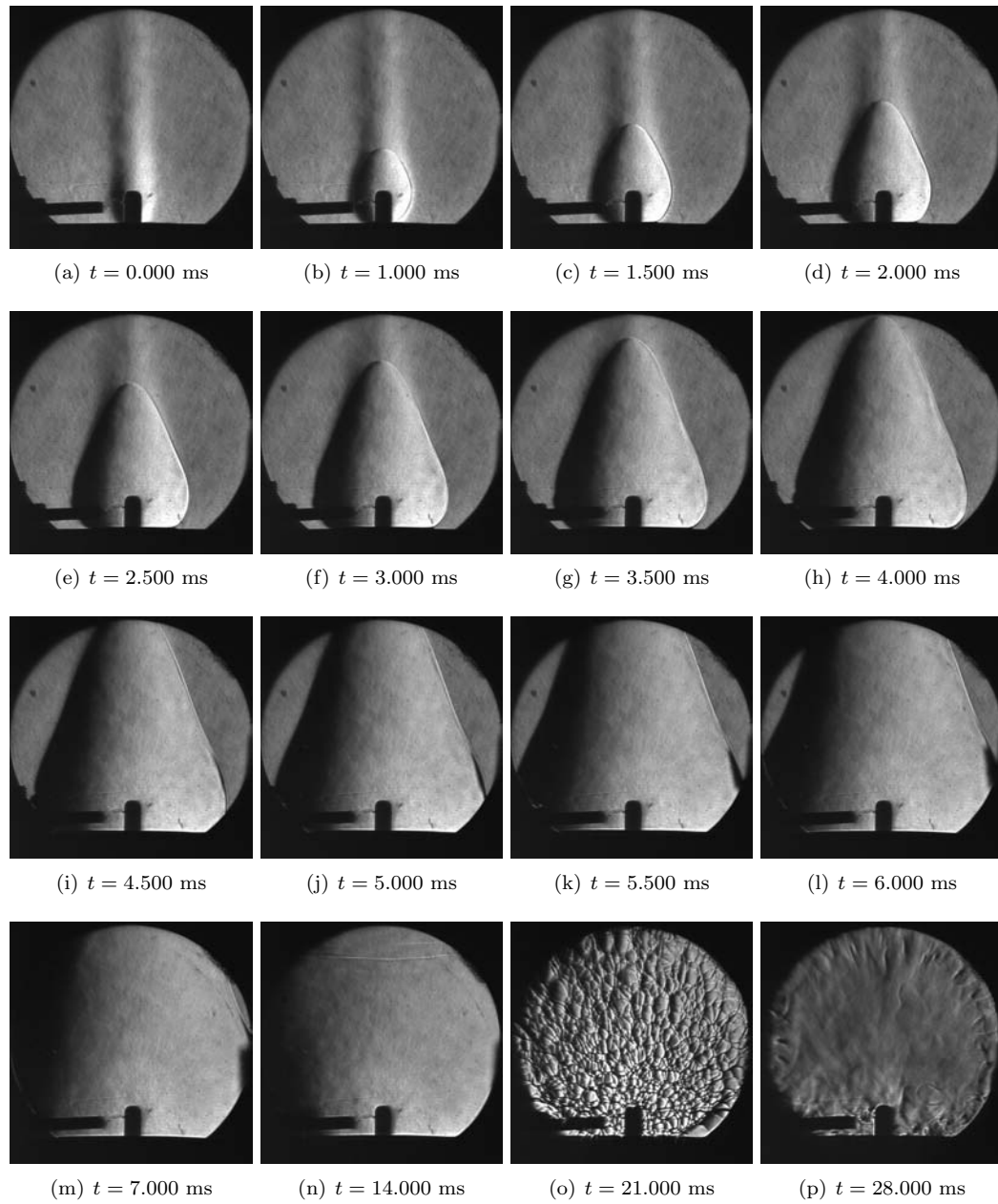


Figure K.101: Shot 117

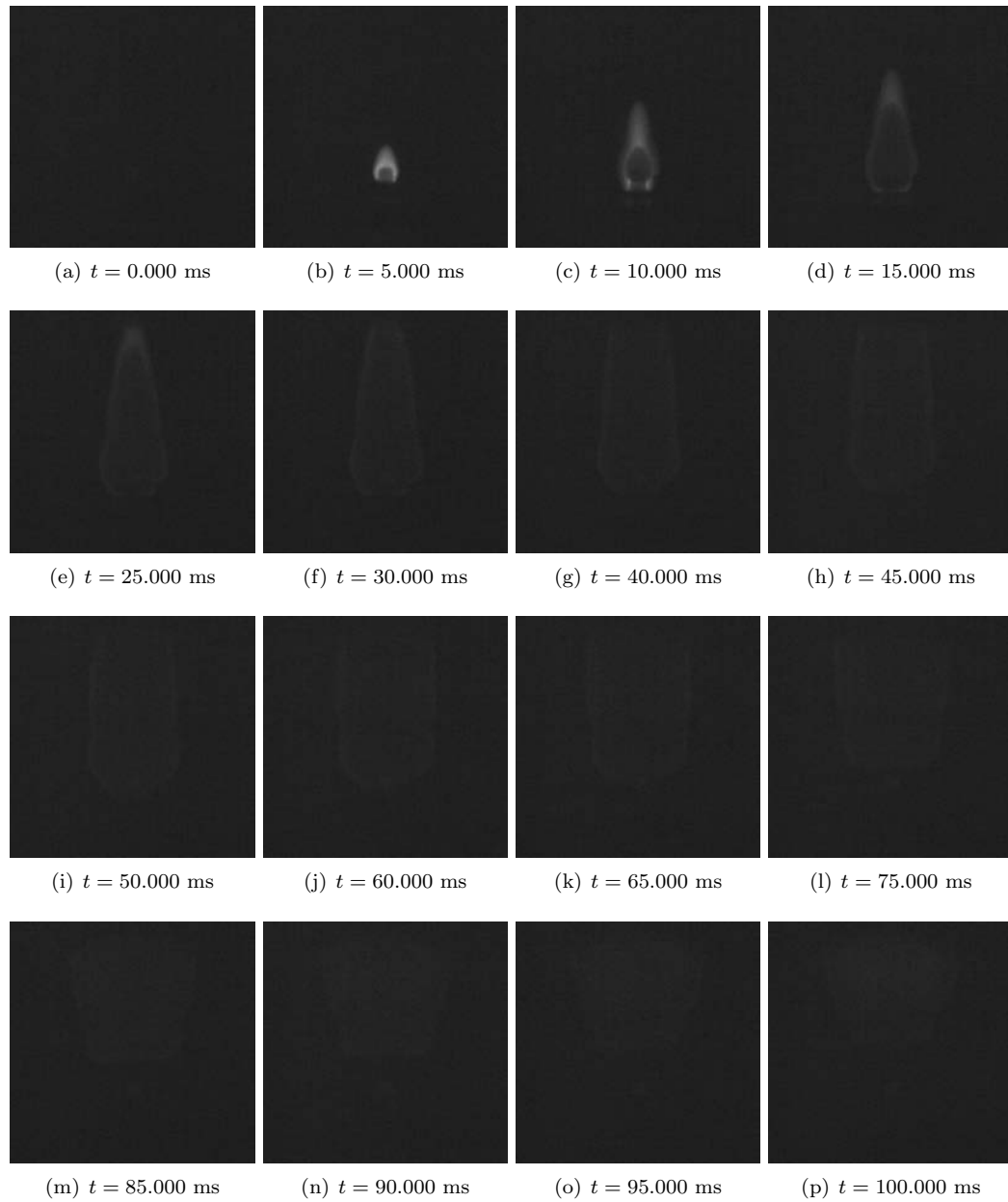


Figure K.102: Shot 118

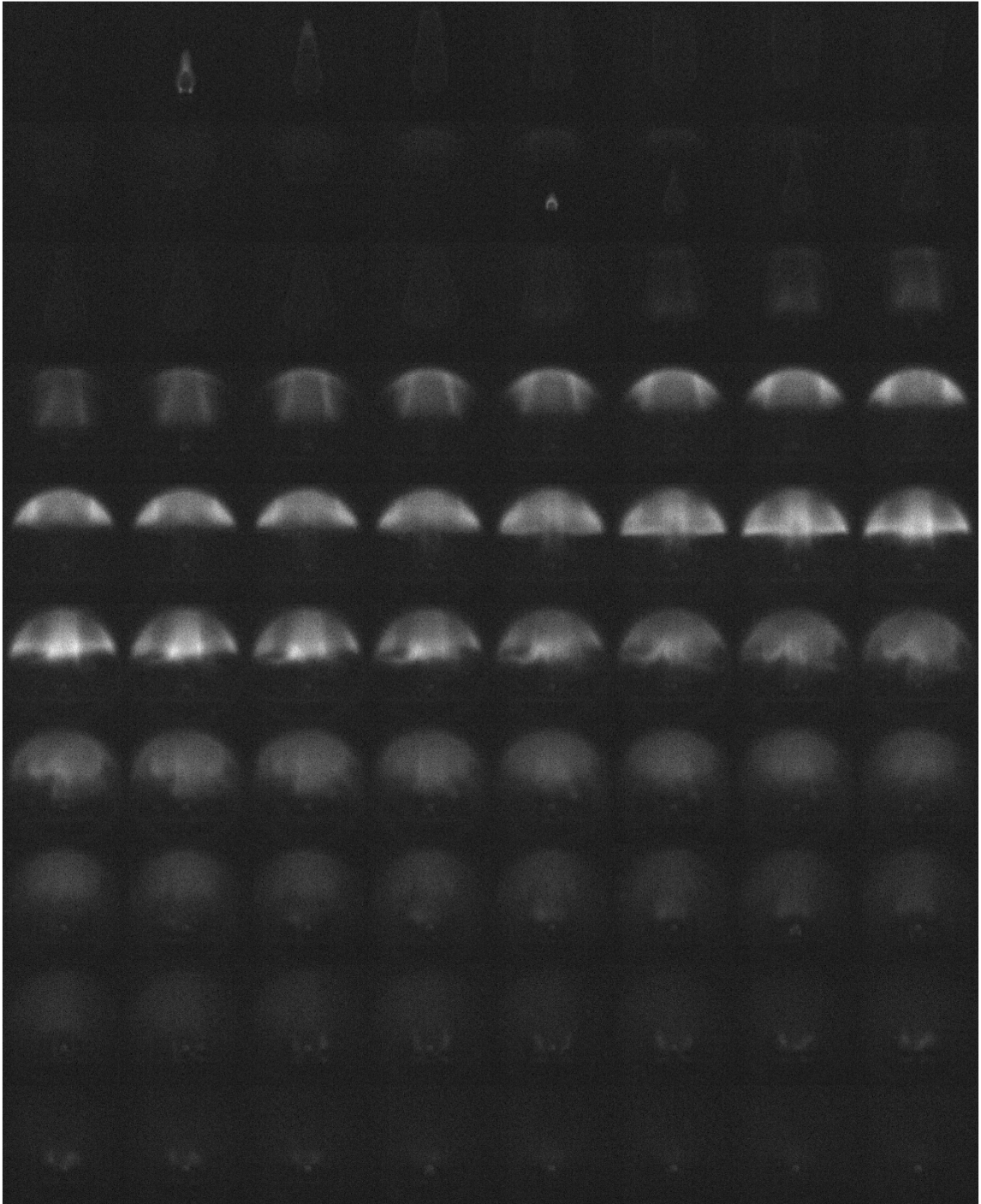


Figure K.103: Shot 118 montage ($\Delta t = 10$ ms between images)

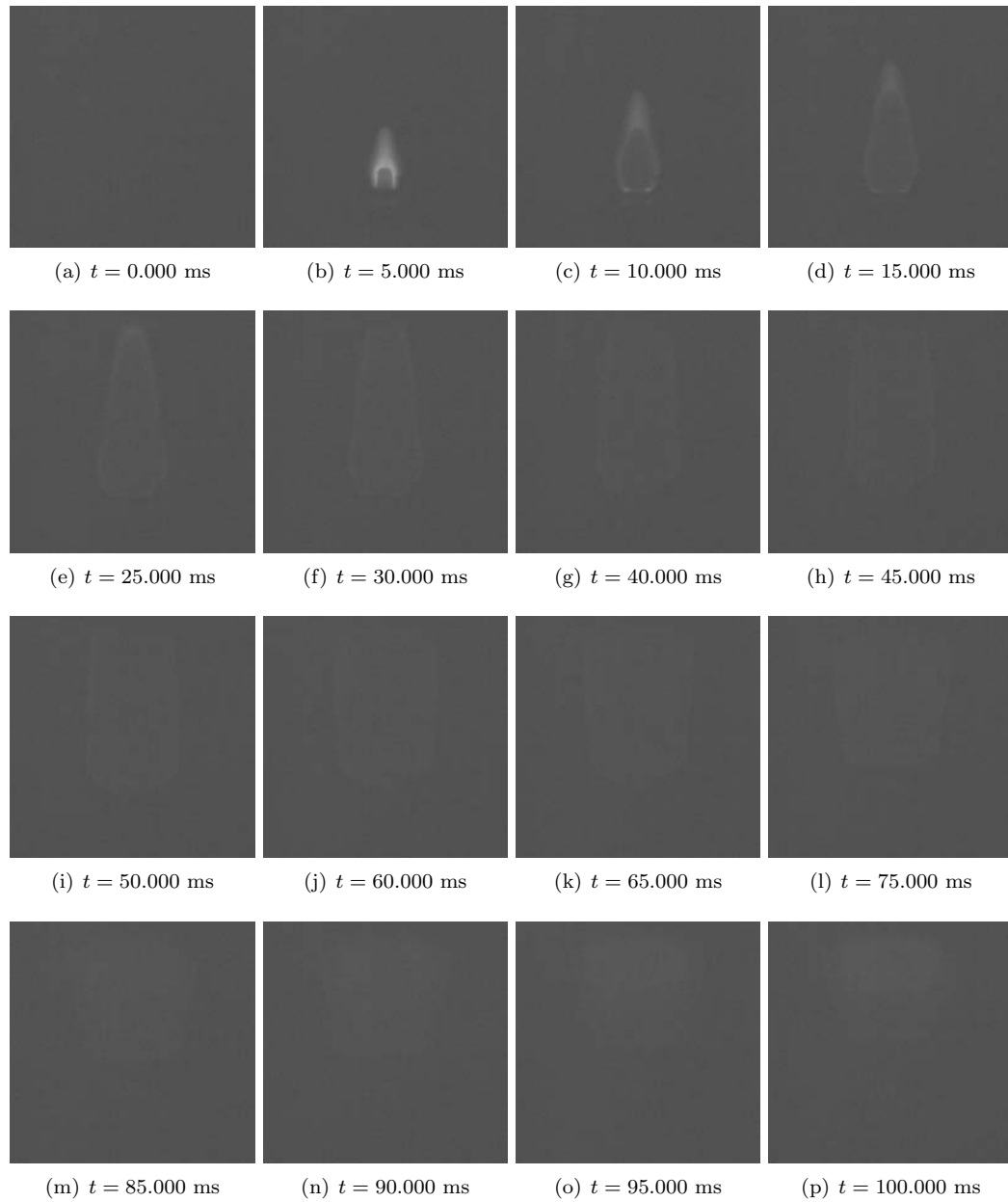


Figure K.104: Shot 119

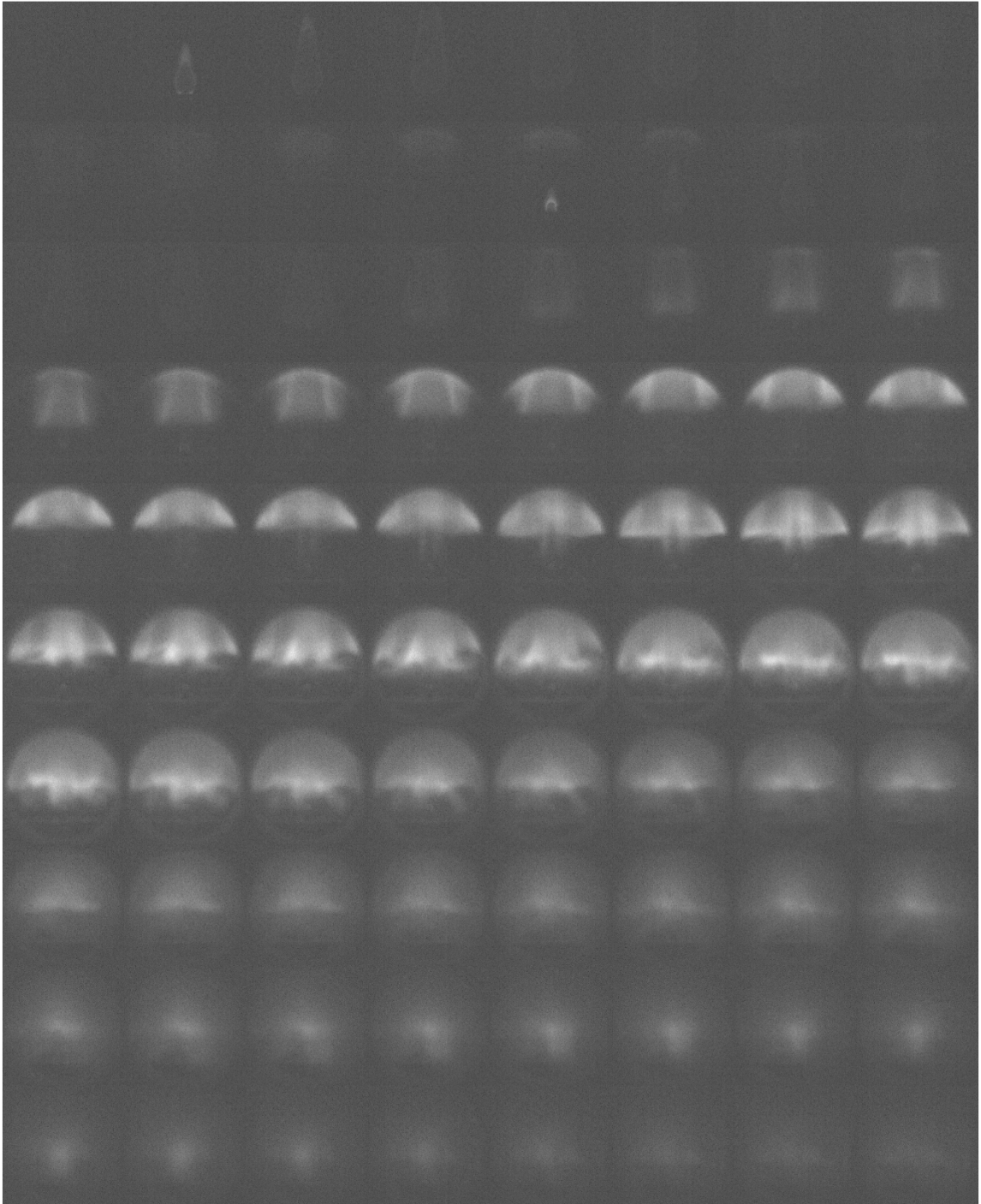


Figure K.105: Shot 119 montage ($\Delta t = 10$ ms between images)

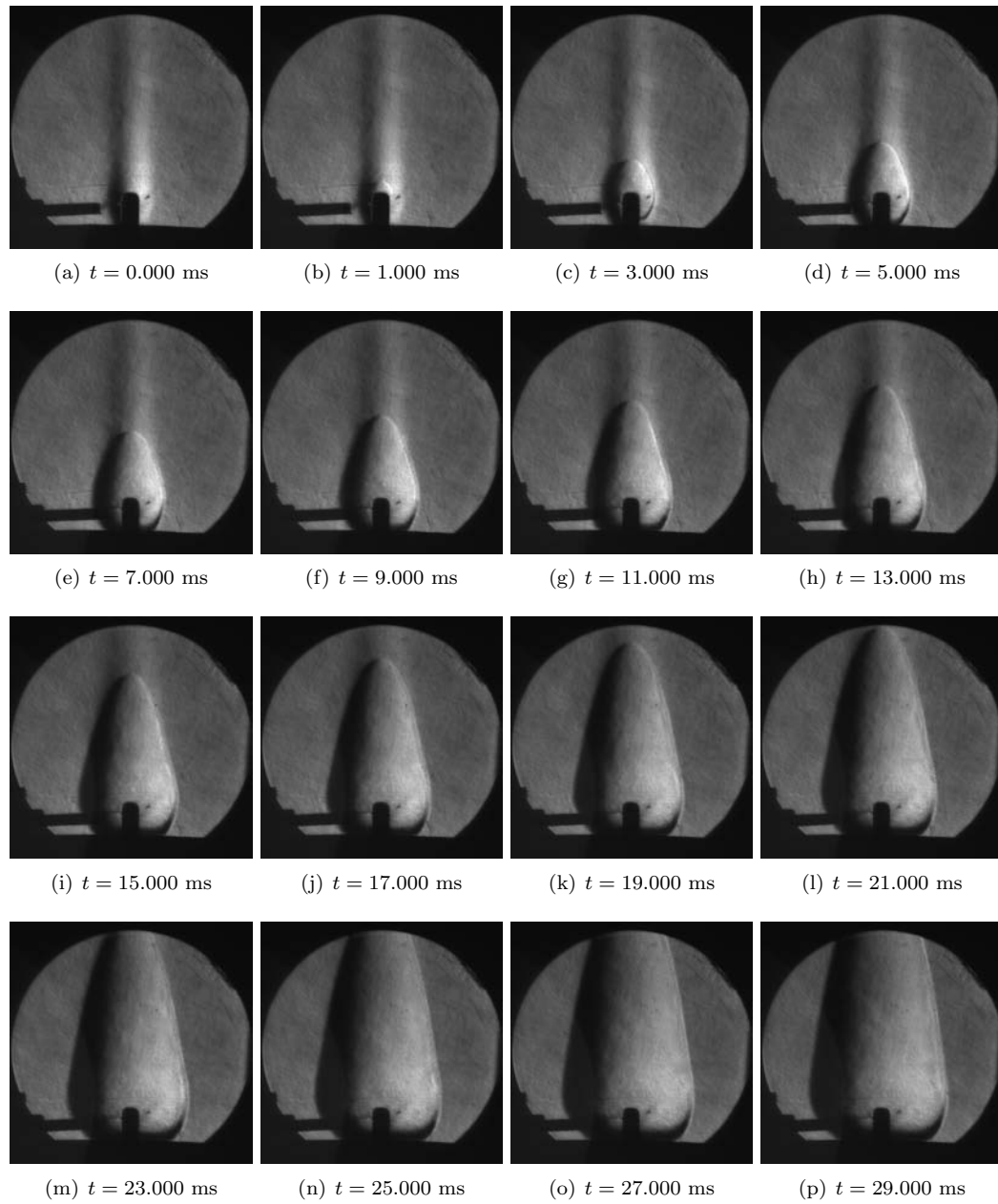


Figure K.106: Shot 121

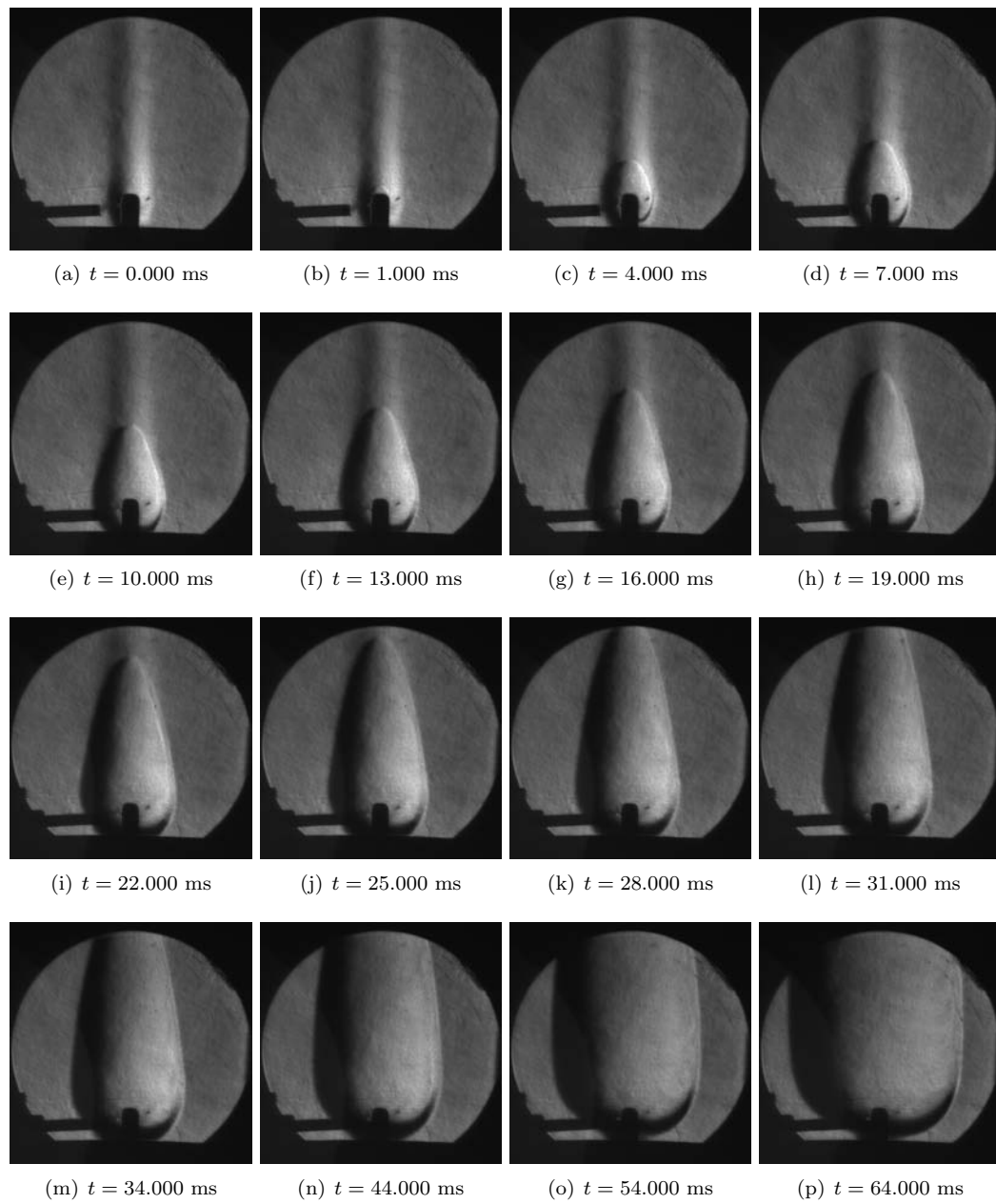


Figure K.107: Shot 122

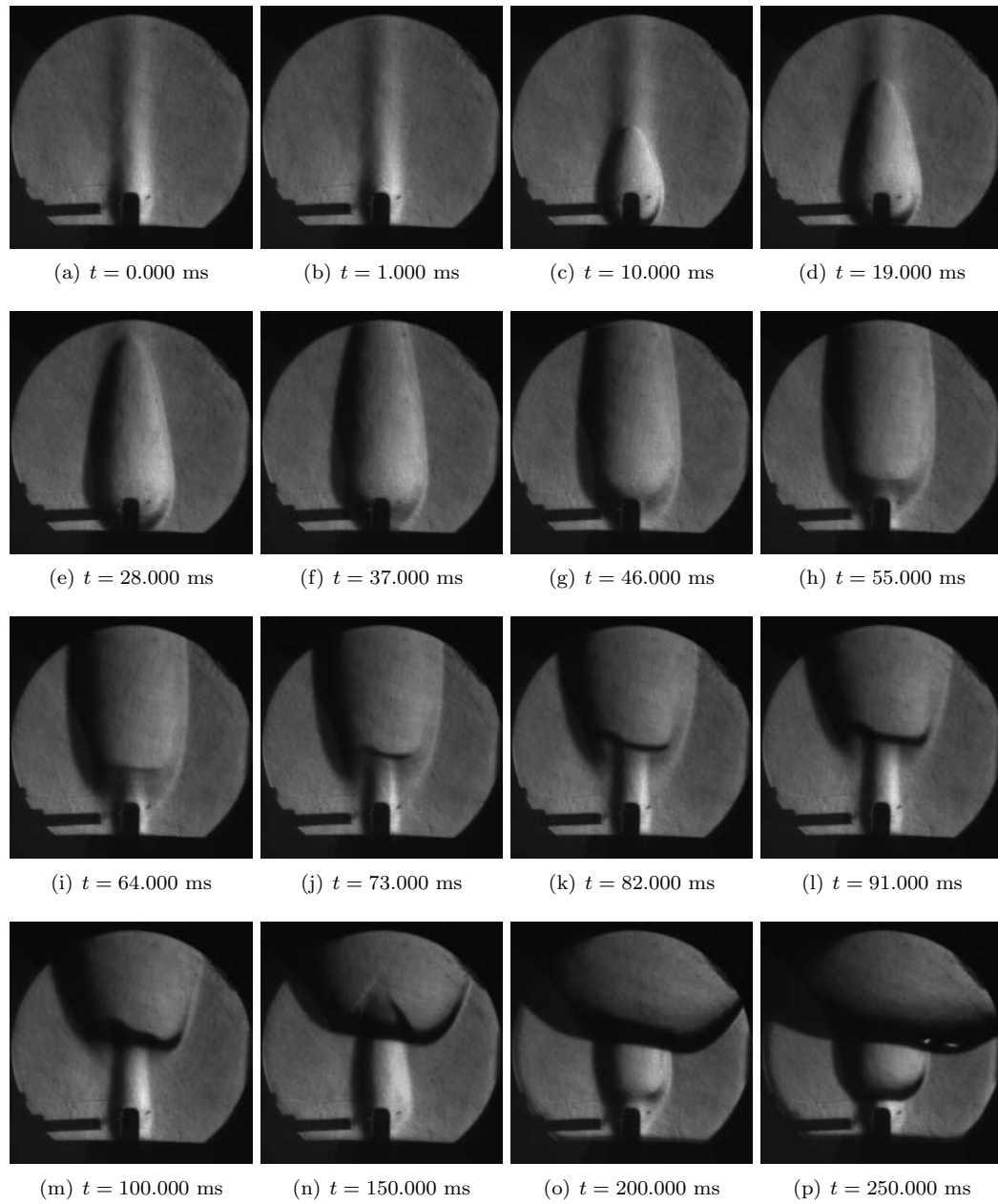


Figure K.108: Shot 123

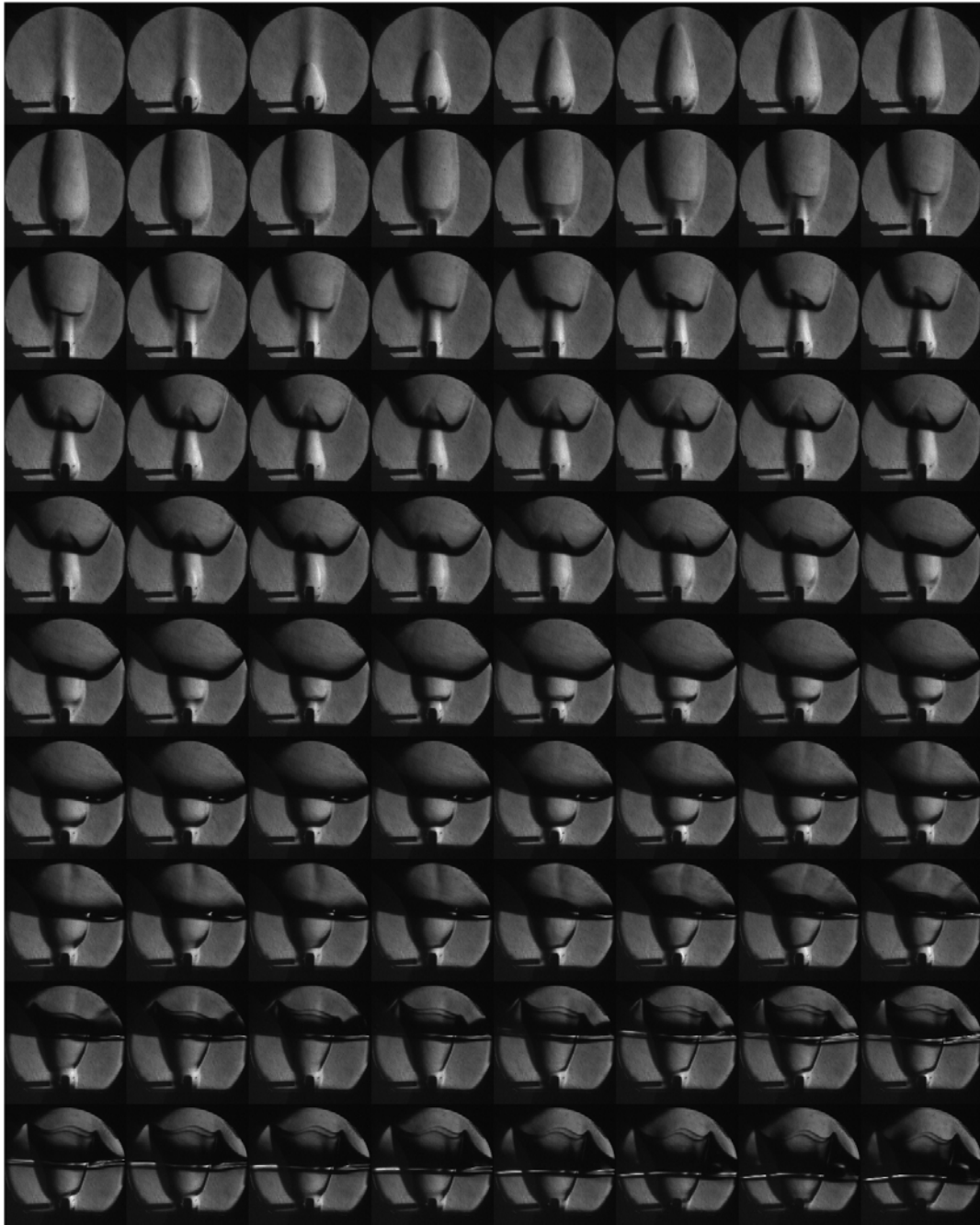


Figure K.109: Shot 123 montage ($\Delta t = 10$ ms between images)

This page intentionally left blank.

Appendix L

Selected Color Schlieren Images ¹

Color schlieren images were taken for a number of the hot surface ignition experiments. These images were obtained simultaneously with the high-speed gray-scale movies. Simultaneous capturing was achieved by splitting the beam using a 5 mm cubic beam splitter about 2.5 cm before the focal point. The color images were captured using a Nikon D200 camera.

¹All images were taken in the Explosion Dynamics Laboratory with the help of Kliulai Chow-Yee and Brian Ventura.

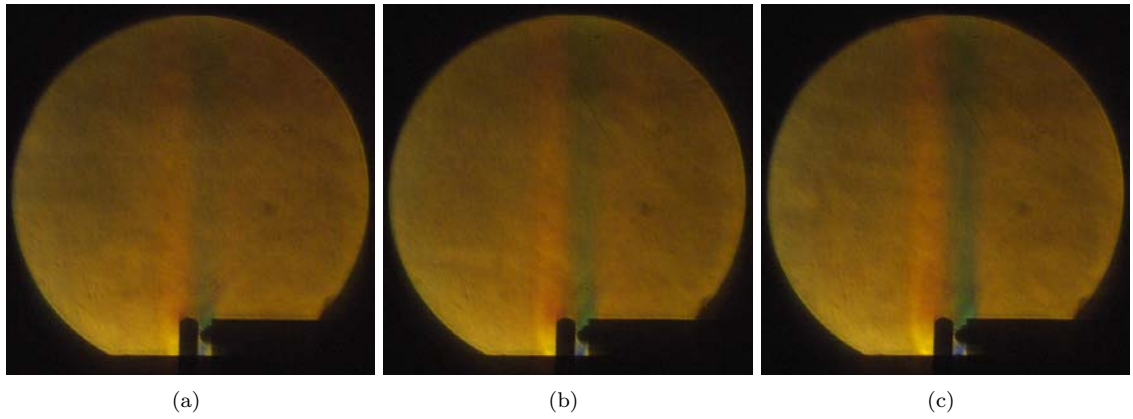


Figure L.1: Color schlieren images of the thermal plume only from shot 28

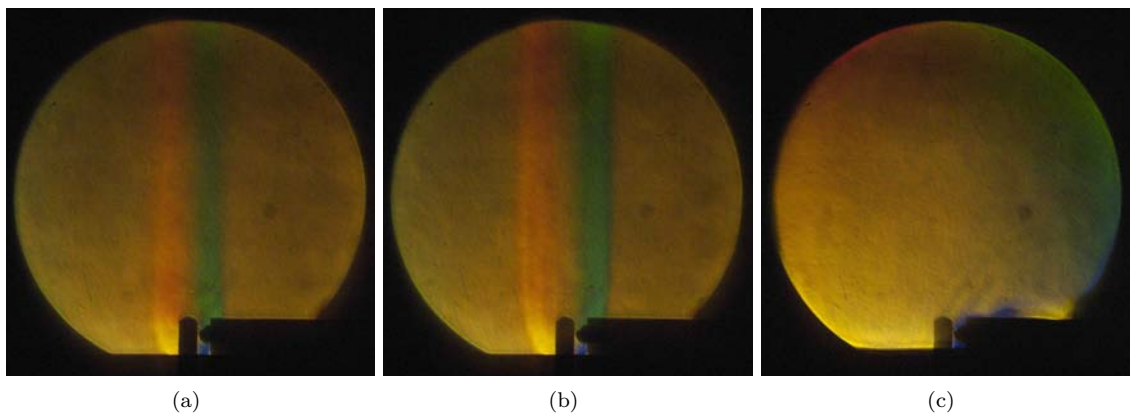


Figure L.2: Color schlieren images from shot 30

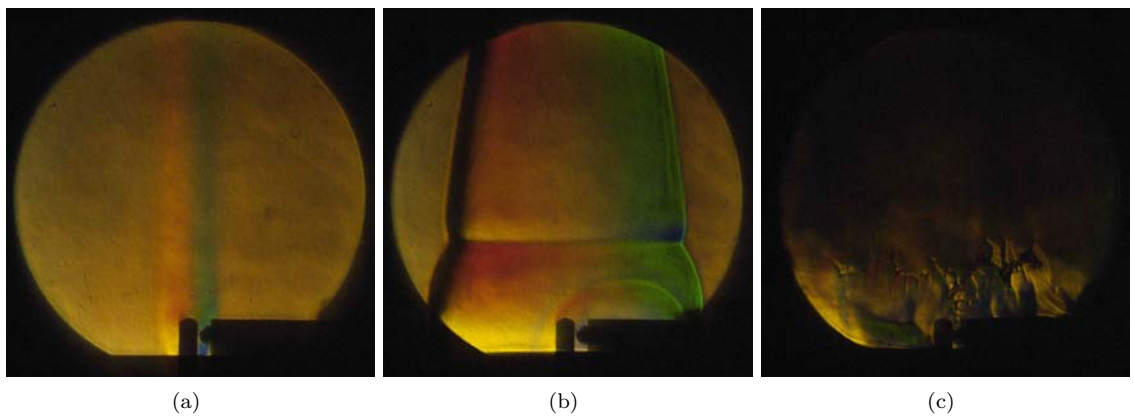


Figure L.3: Color schlieren images from shot 33

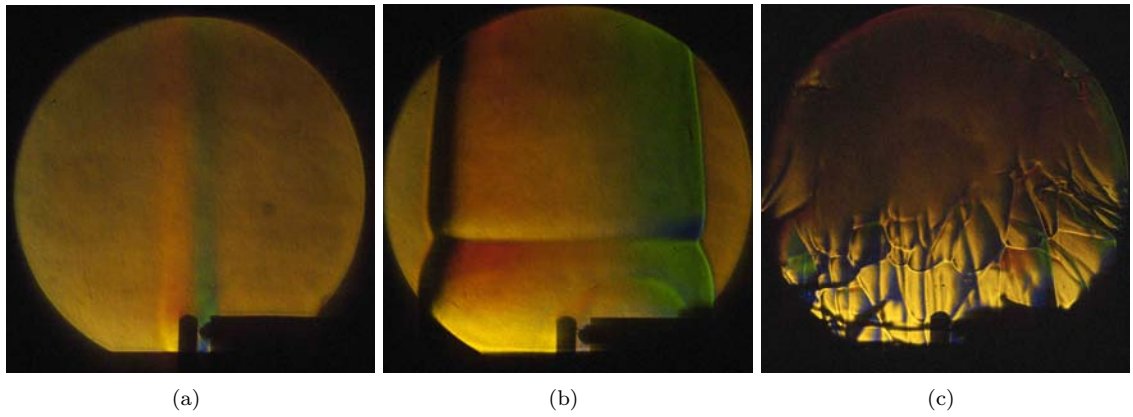


Figure L.4: Color schlieren images from shot 34

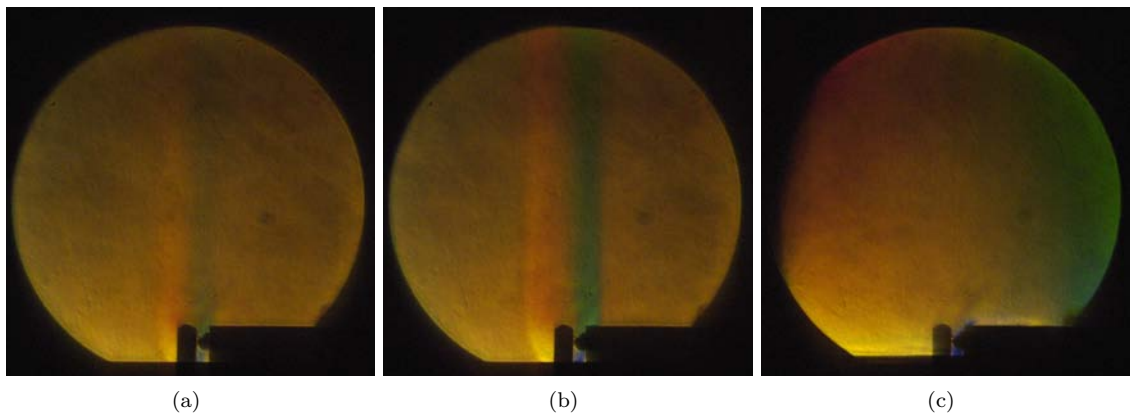


Figure L.5: Color schlieren images from shot 36

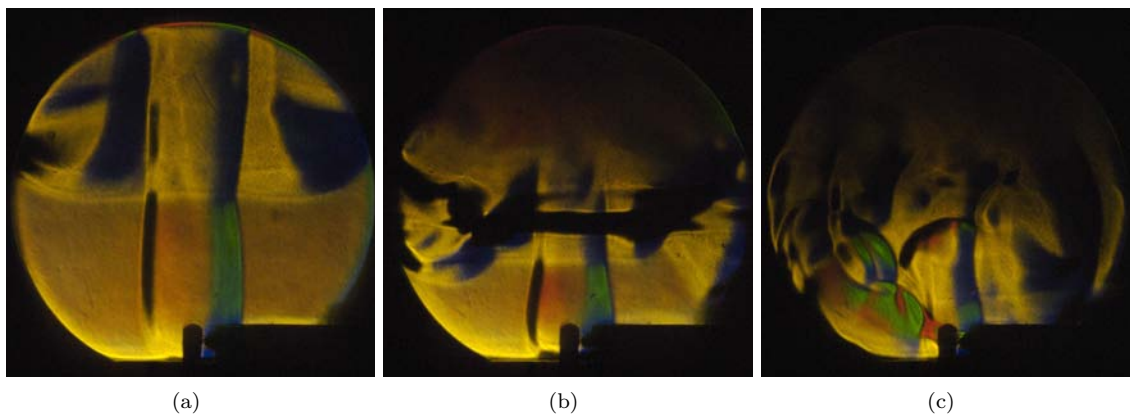


Figure L.6: Color schlieren images from shot 41

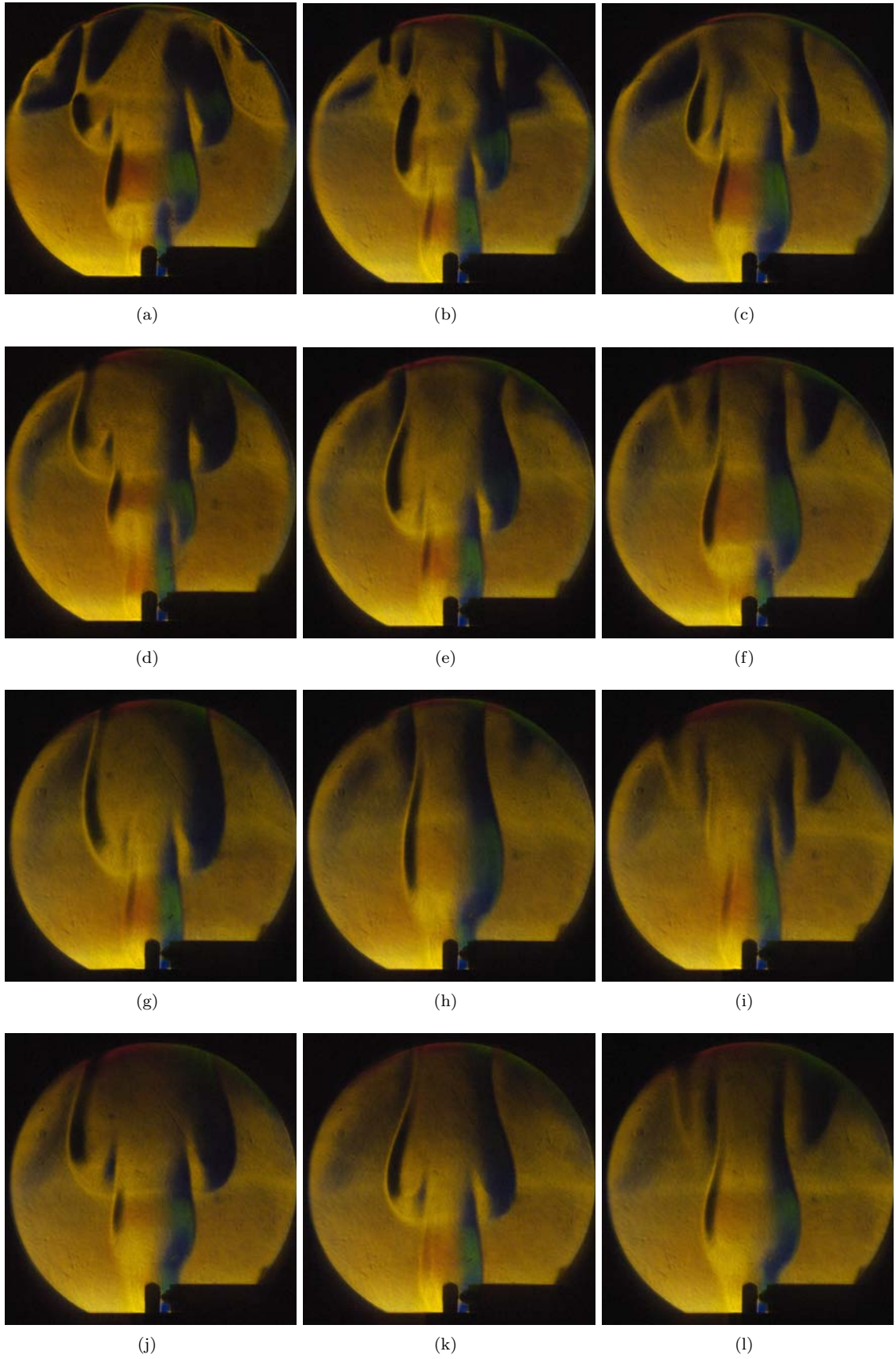


Figure L.7: Color schlieren images from shot 42

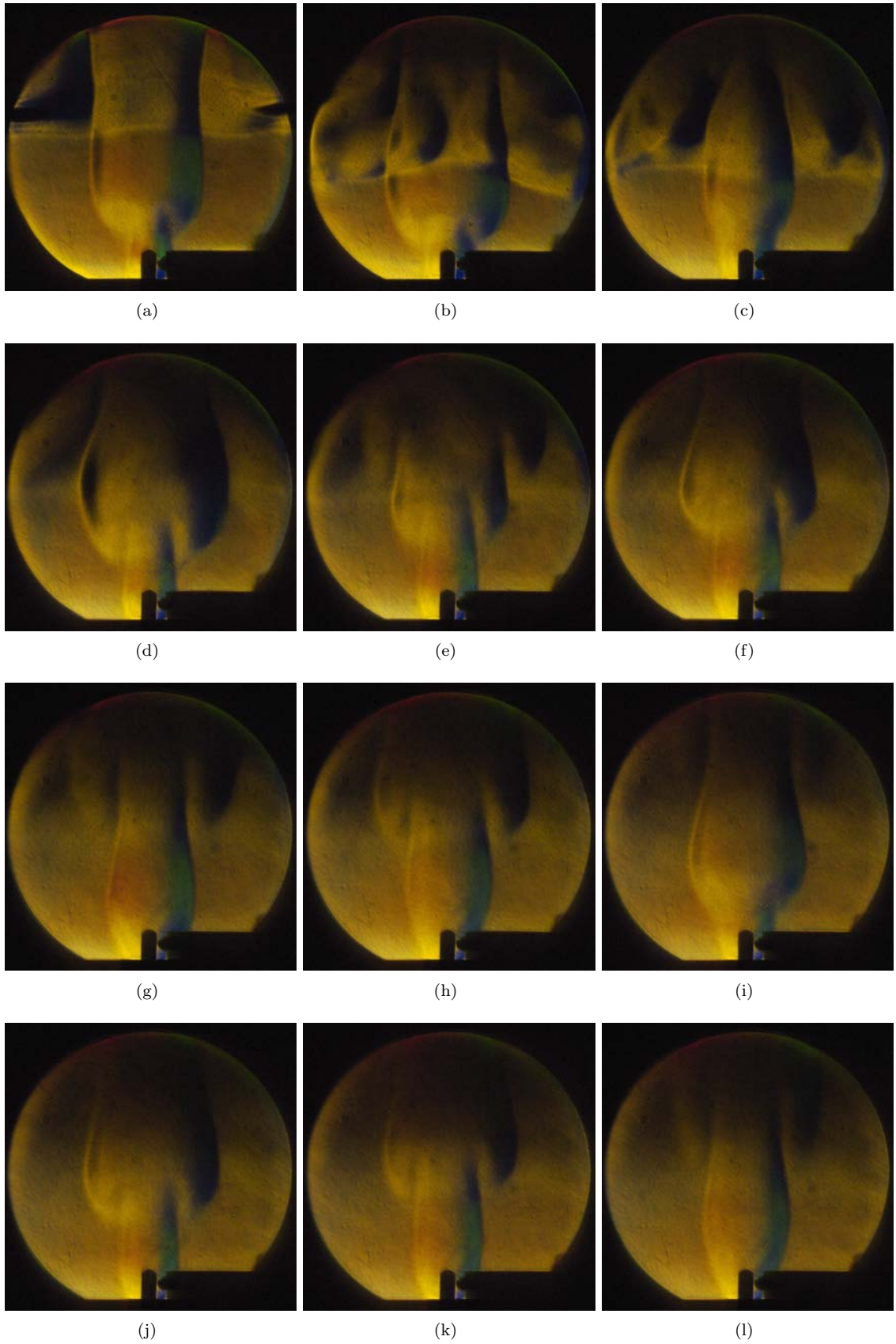


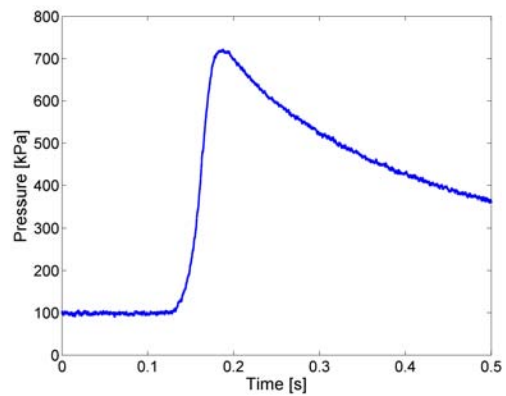
Figure L.8: Color schlieren images from shot 45

This page intentionally left blank.

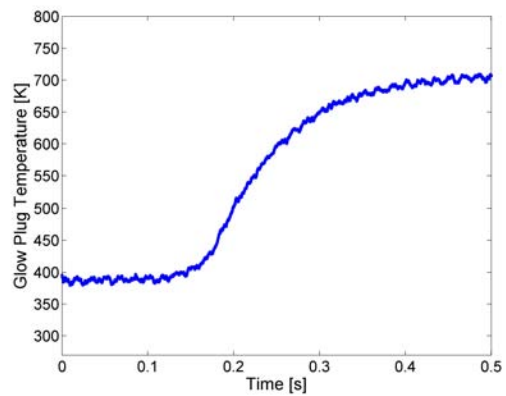
Appendix M

Hot Surface Temperature and Pressure Traces

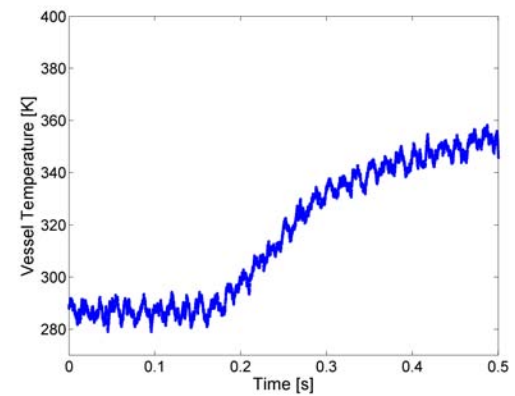
This appendix contains the temperature traces collected at the glow plug and the top of the vessel during the experiment as well as the pressure observed. Red lines indicate time of ignition from the schlieren video.



(a) Pressure

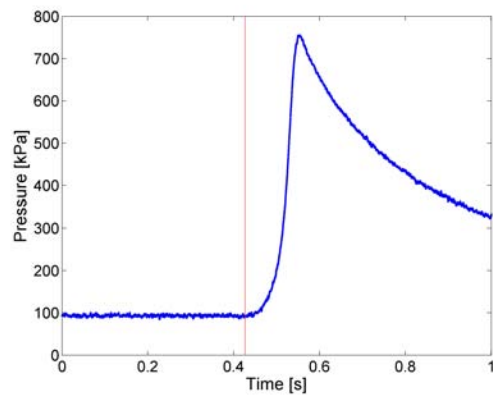


(b) Glow plug temperature

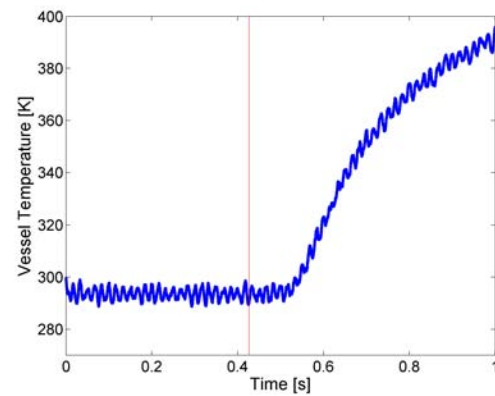


(c) Vessel temperature

Figure M.1: Experimental data from shot 7

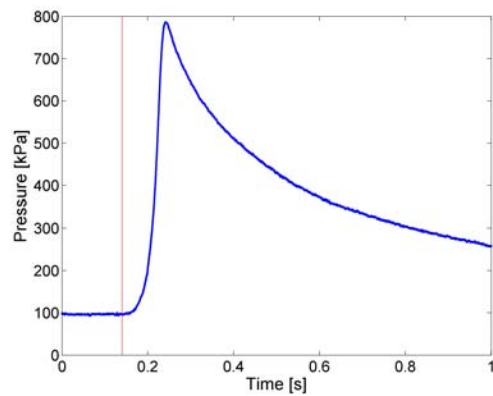


(a) Pressure

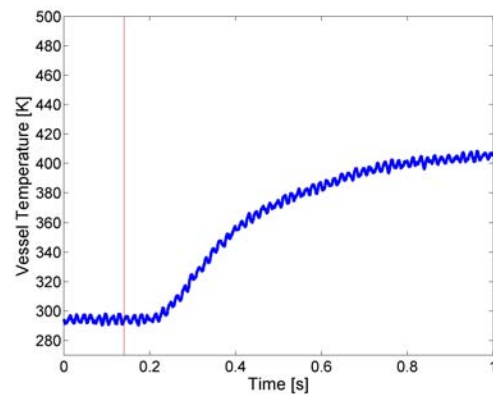


(b) Vessel temperature

Figure M.2: Experimental data from shot 8

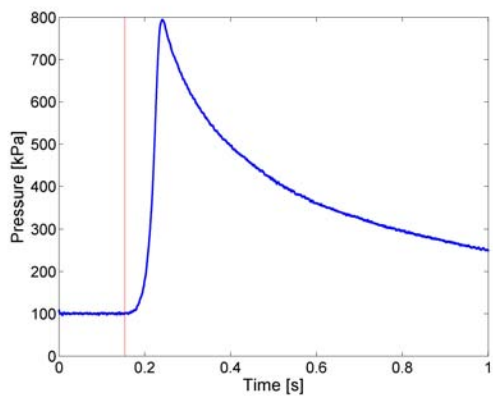


(a) Pressure

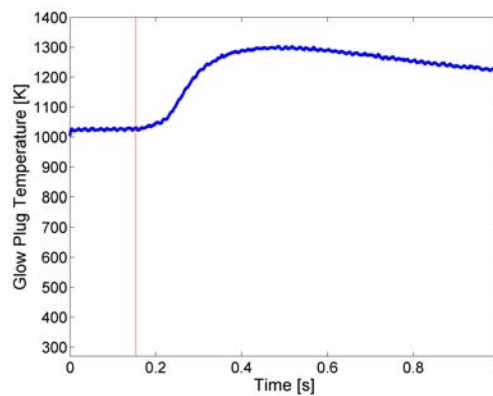


(b) Vessel temperature

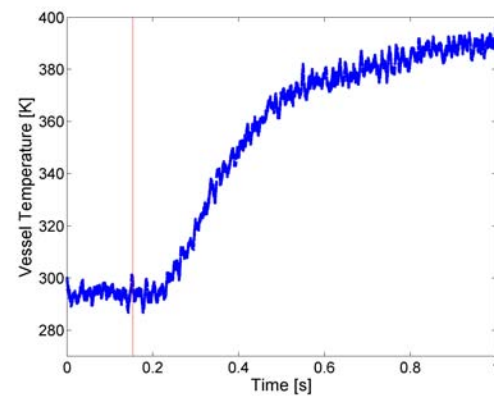
Figure M.3: Experimental data from shot 9



(a) Pressure

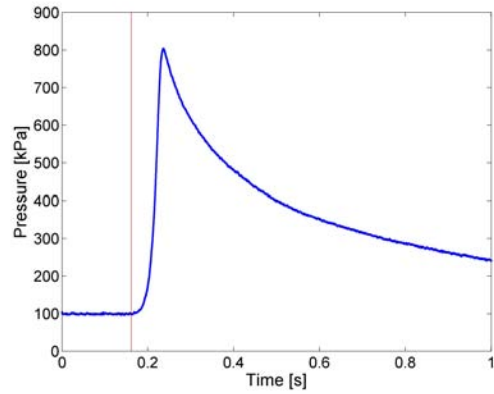


(b) Glow plug temperature

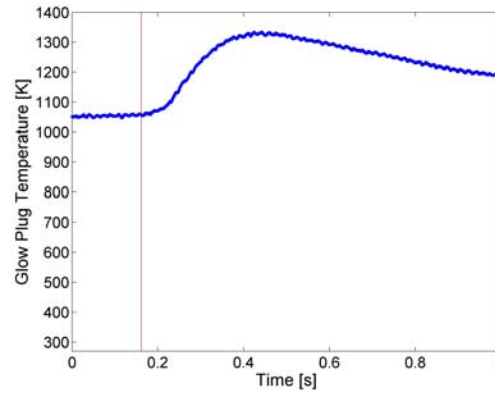


(c) Vessel temperature

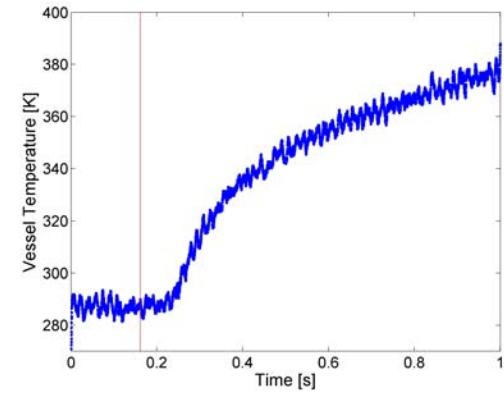
Figure M.4: Experimental data from shot 10



(a) Pressure

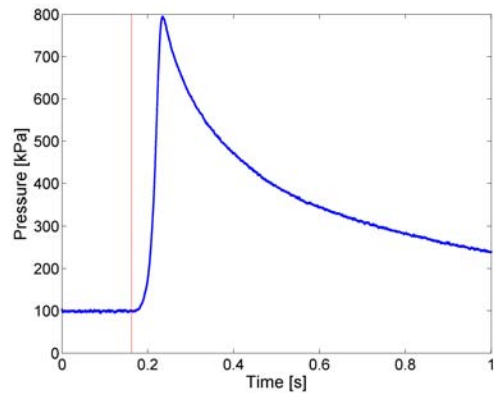


(b) Glow plug temperature

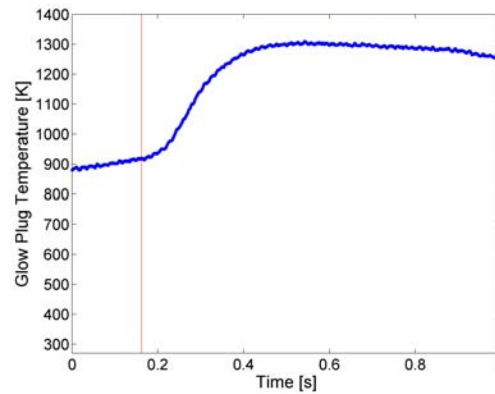


(c) Vessel temperature

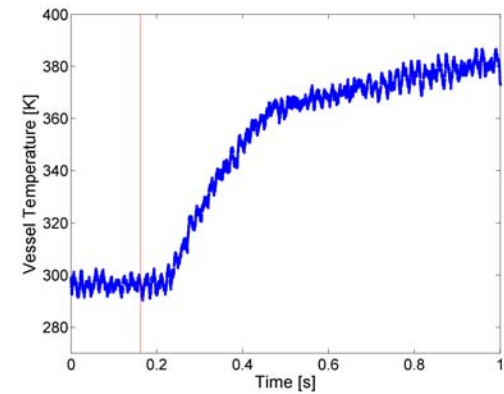
Figure M.5: Experimental data from shot 11



(a) Pressure

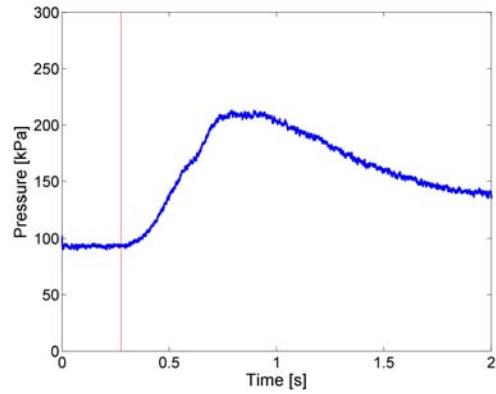


(b) Glow plug temperature

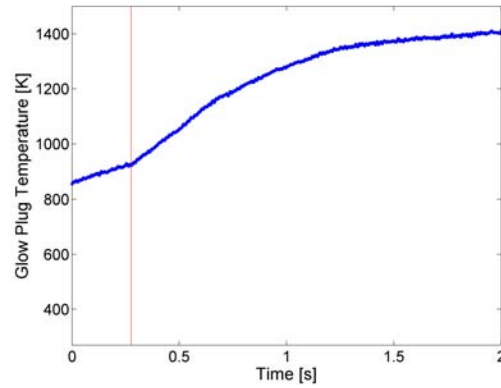


(c) Vessel temperature

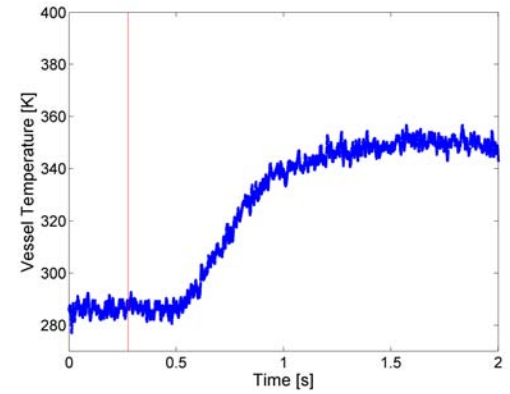
Figure M.6: Experimental data from shot 12



(a) Pressure

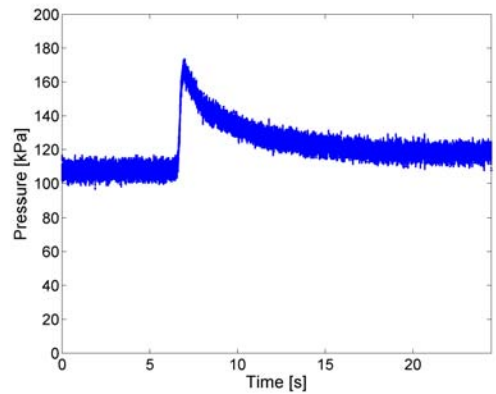


(b) Glow plug temperature

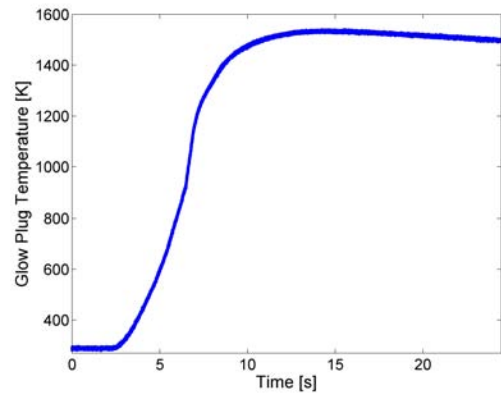


(c) Vessel temperature

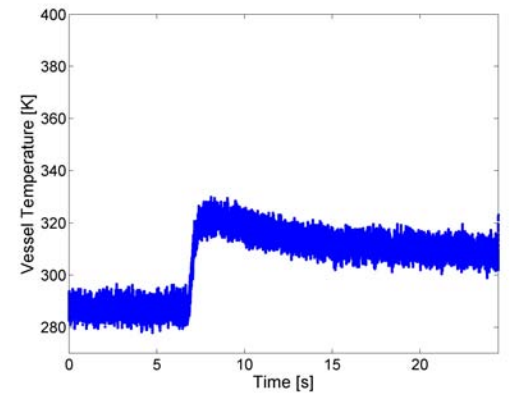
Figure M.7: Experimental data from shot 15



(a) Pressure

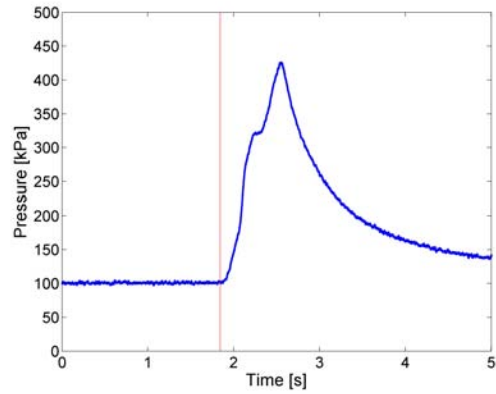


(b) Glow plug temperature

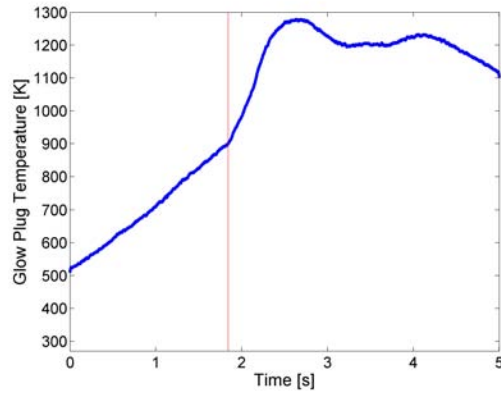


(c) Vessel temperature

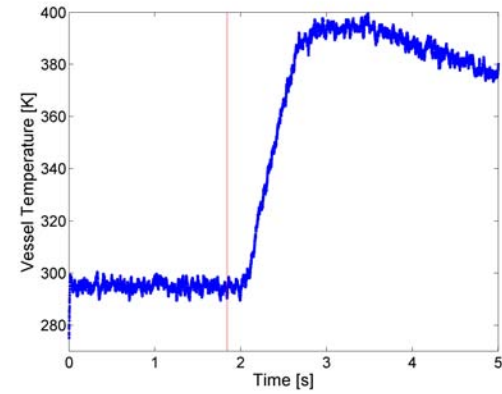
Figure M.8: Experimental data from shot 17



(a) Pressure

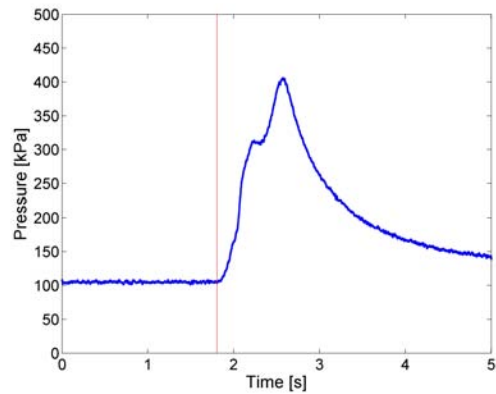


(b) Glow plug temperature

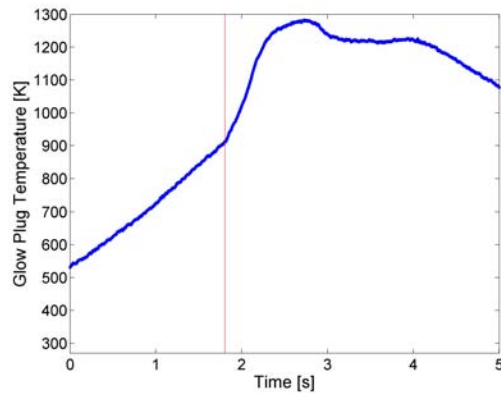


(c) Vessel temperature

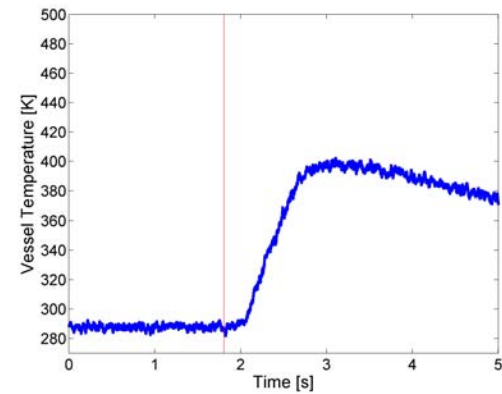
Figure M.9: Experimental data from shot 20



(a) Pressure

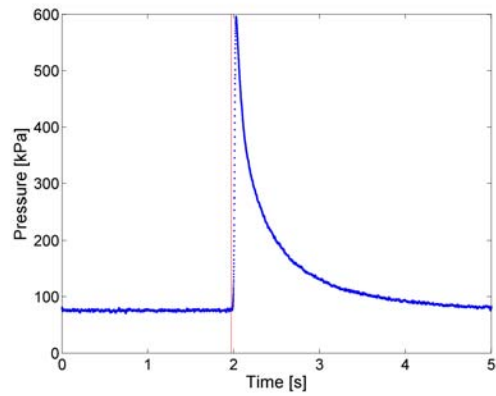


(b) Glow plug temperature

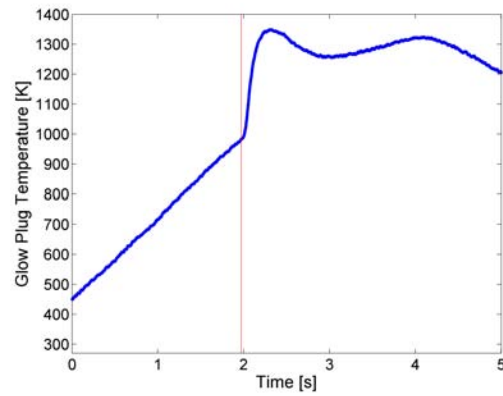


(c) Vessel temperature

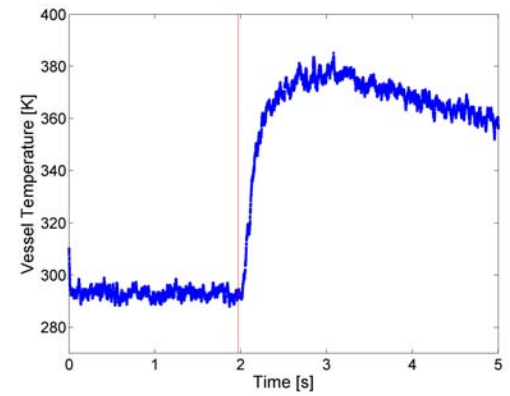
Figure M.10: Experimental data from shot 21



(a) Pressure

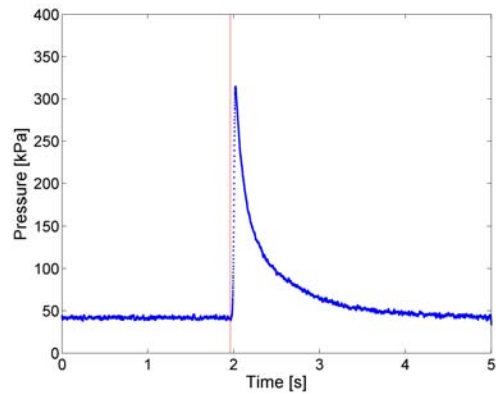


(b) Glow plug temperature

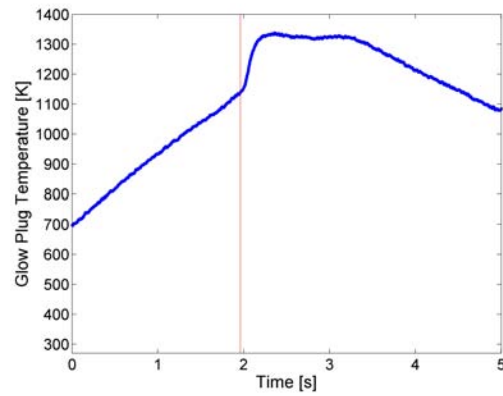


(c) Vessel temperature

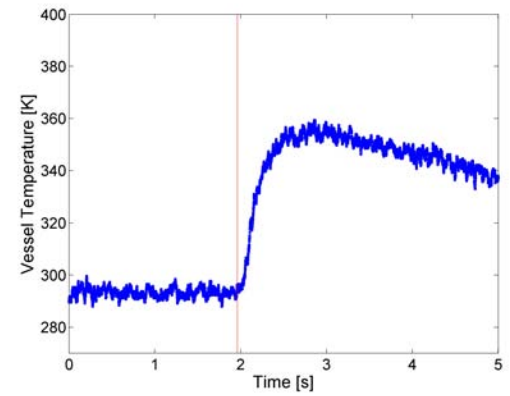
Figure M.11: Experimental data from shot 22



(a) Pressure

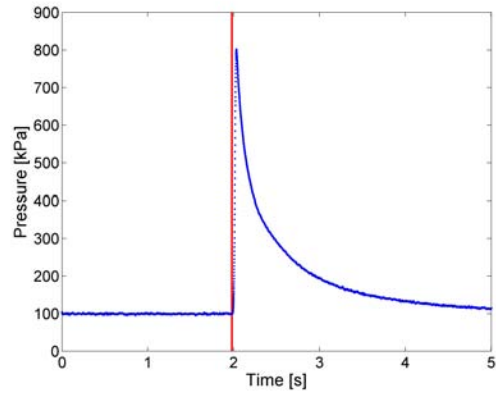


(b) Glow plug temperature

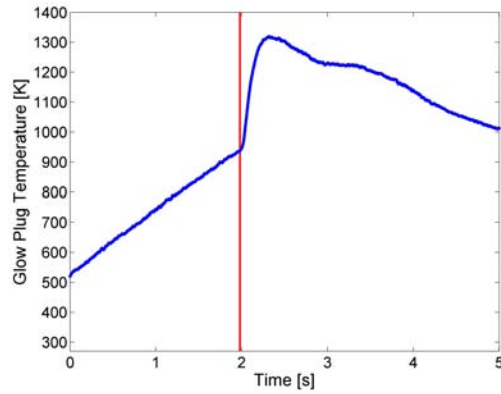


(c) Vessel temperature

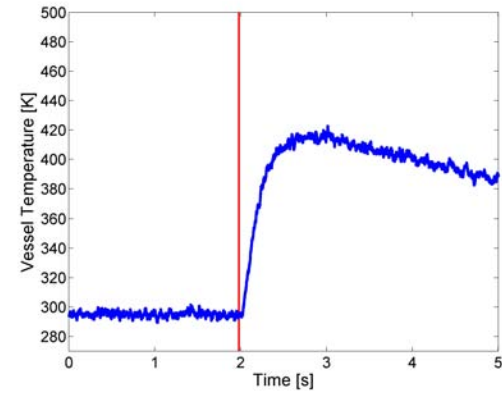
Figure M.12: Experimental data from shot 23



(a) Pressure

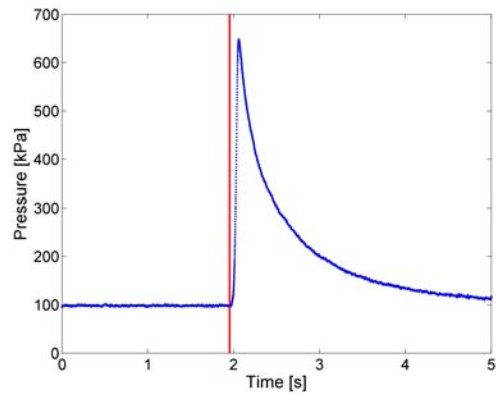


(b) Glow plug temperature

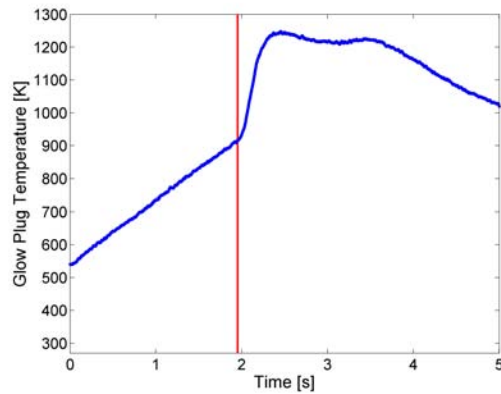


(c) Vessel temperature

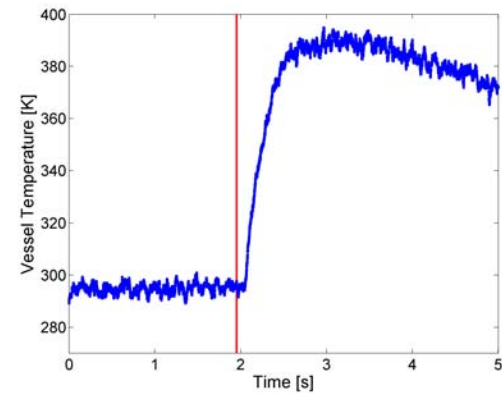
Figure M.13: Experimental data from shot 24



(a) Pressure

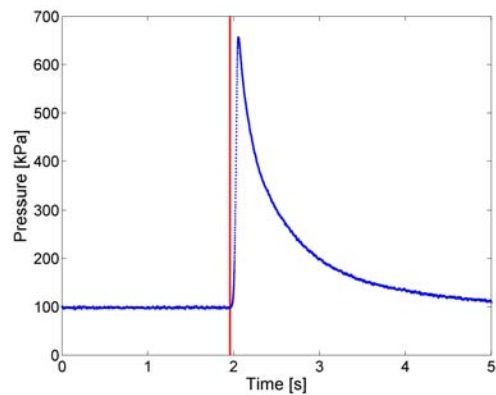


(b) Glow plug temperature

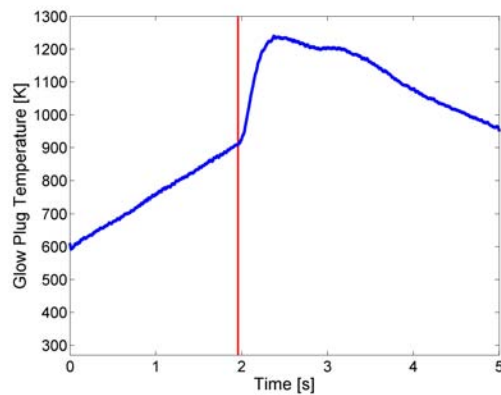


(c) Vessel temperature

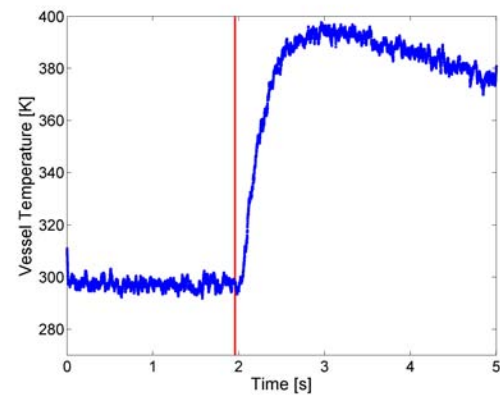
Figure M.14: Experimental data from shot 25



(a) Pressure

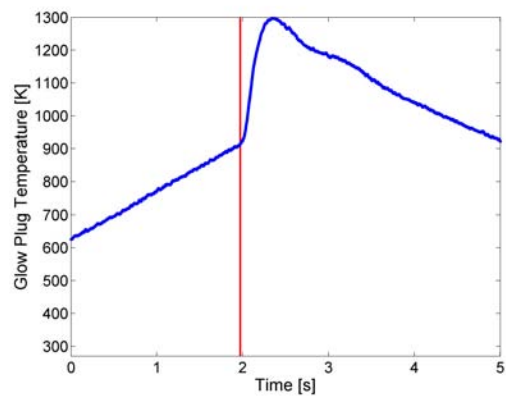


(b) Glow plug temperature

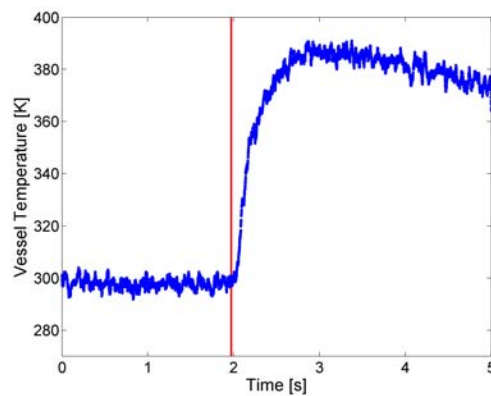


(c) Vessel temperature

Figure M.15: Experimental data from shot 26

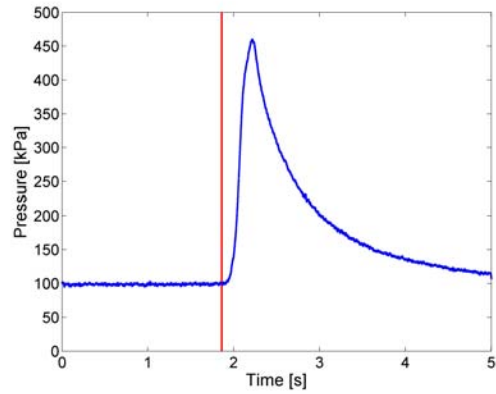


(a) Glow plug temperature

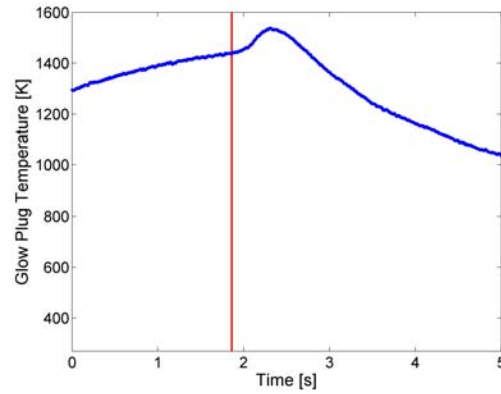


(b) Vessel temperature

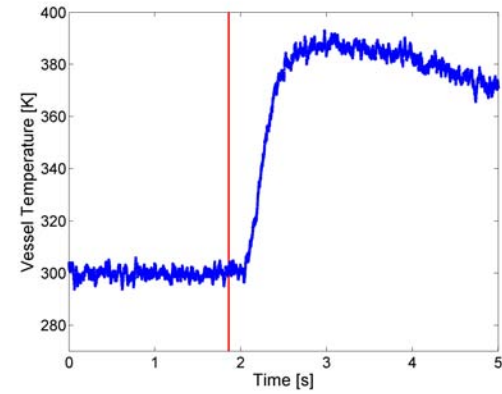
Figure M.16: Experimental data from shot 27



(a) Pressure

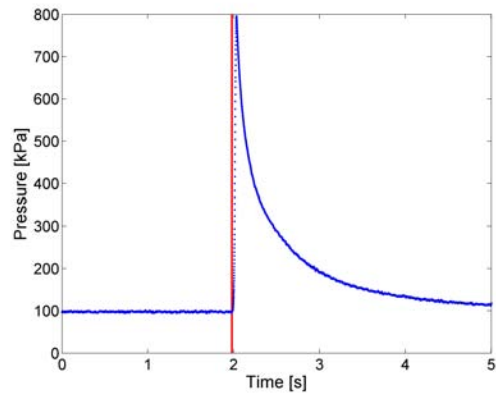


(b) Glow plug temperature

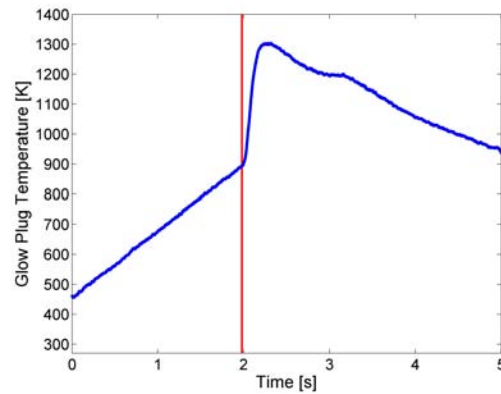


(c) Vessel temperature

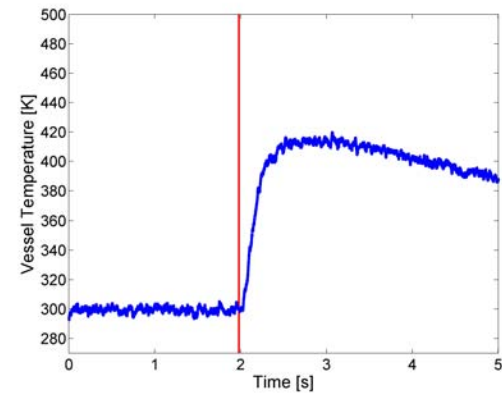
Figure M.17: Experimental data from shot 28



(a) Pressure

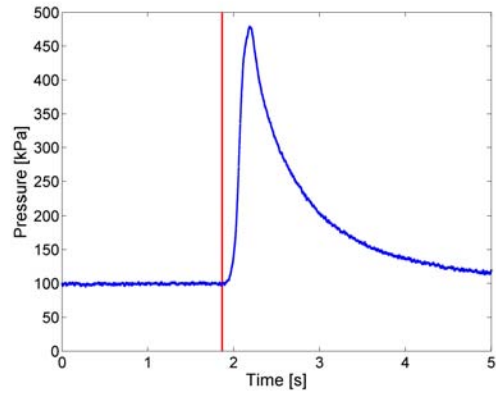


(b) Glow plug temperature

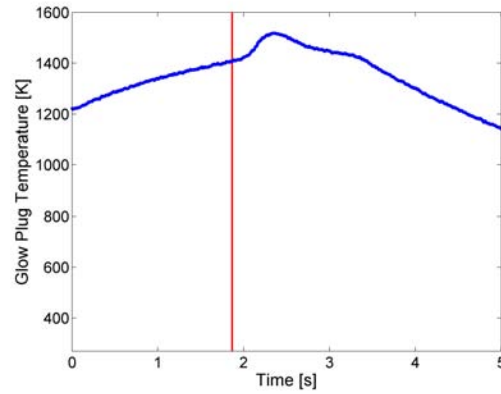


(c) Vessel temperature

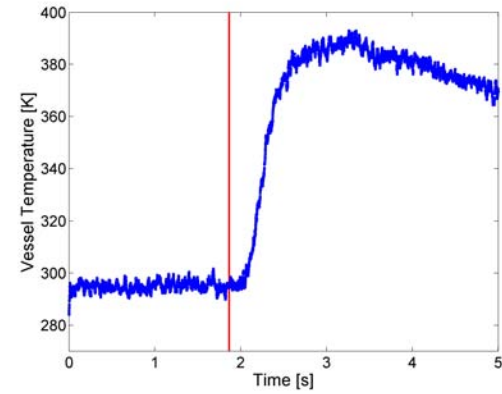
Figure M.18: Experimental data from shot 29



(a) Pressure

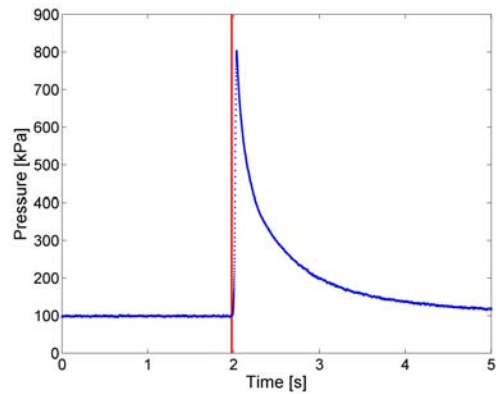


(b) Glow plug temperature

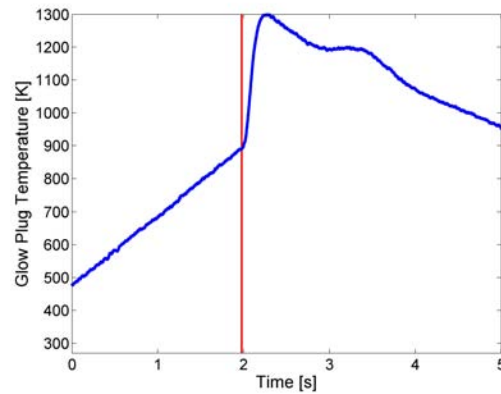


(c) Vessel temperature

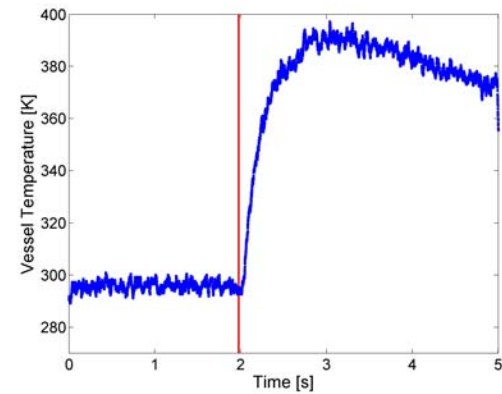
Figure M.19: Experimental data from shot 30



(a) Pressure

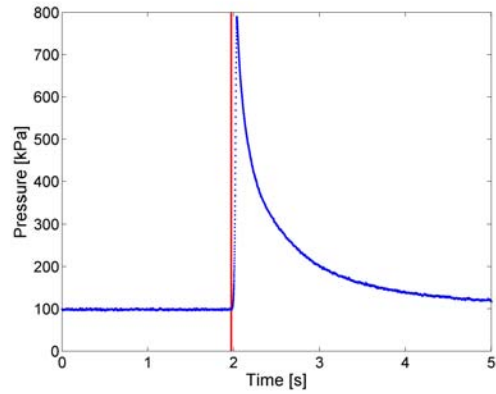


(b) Glow plug temperature

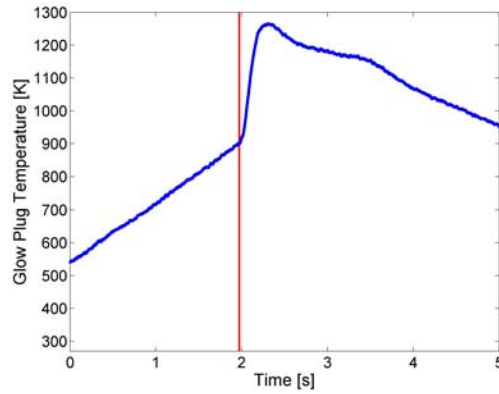


(c) Vessel temperature

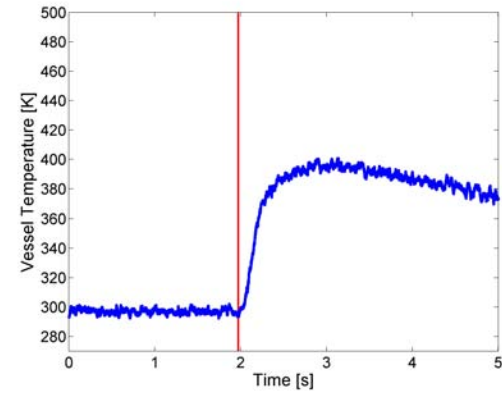
Figure M.20: Experimental data from shot 31



(a) Pressure

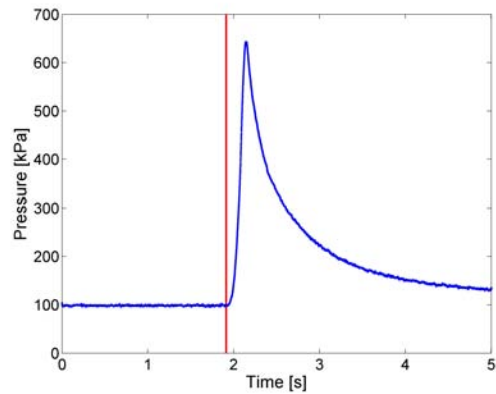


(b) Glow plug temperature

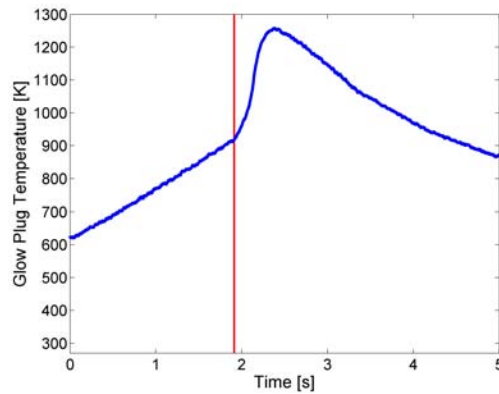


(c) Vessel temperature

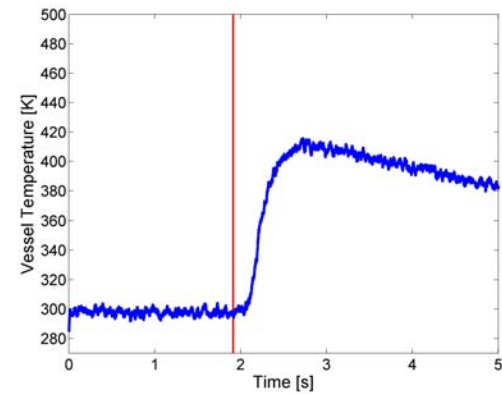
Figure M.21: Experimental data from shot 32



(a) Pressure

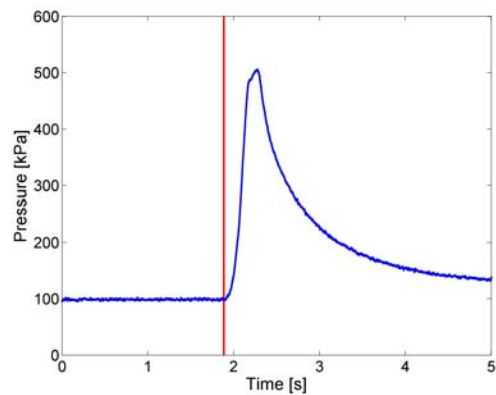


(b) Glow plug temperature

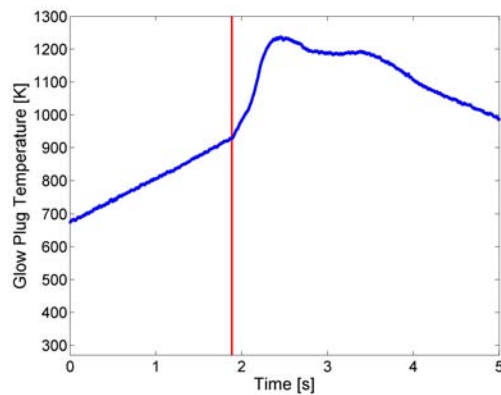


(c) Vessel temperature

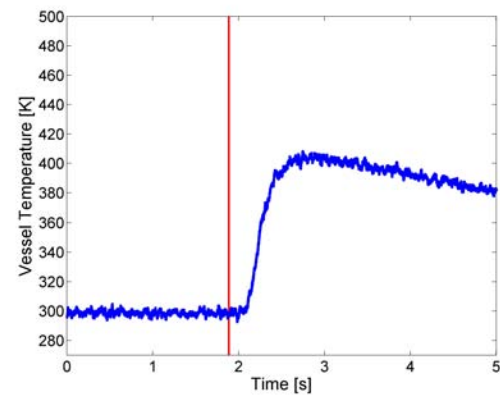
Figure M.22: Experimental data from shot 33



(a) Pressure

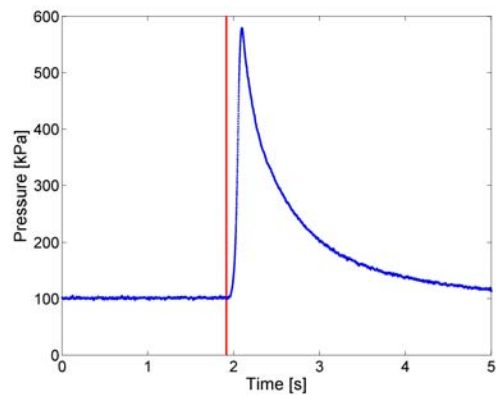


(b) Glow plug temperature

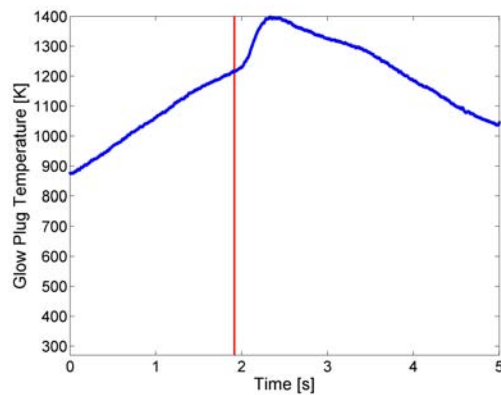


(c) Vessel temperature

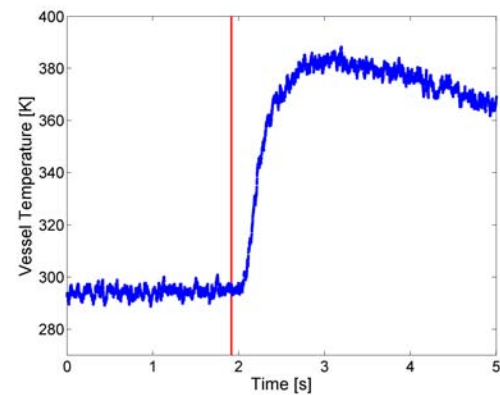
Figure M.23: Experimental data from shot 34



(a) Pressure

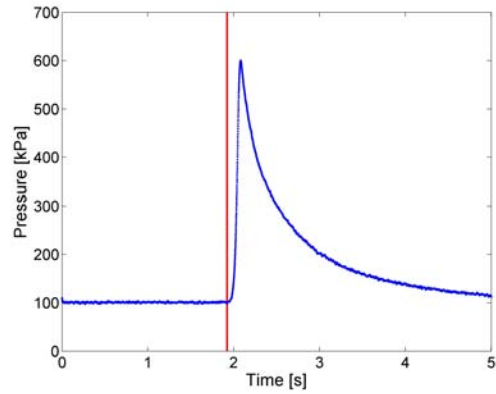


(b) Glow plug temperature

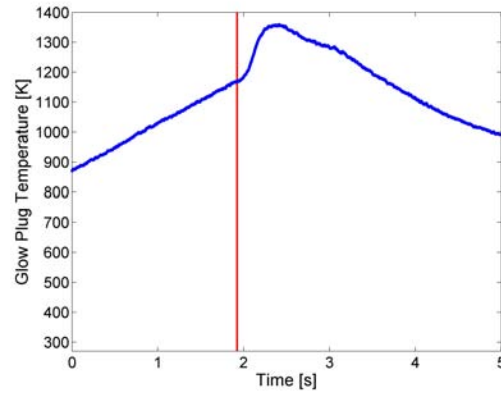


(c) Vessel temperature

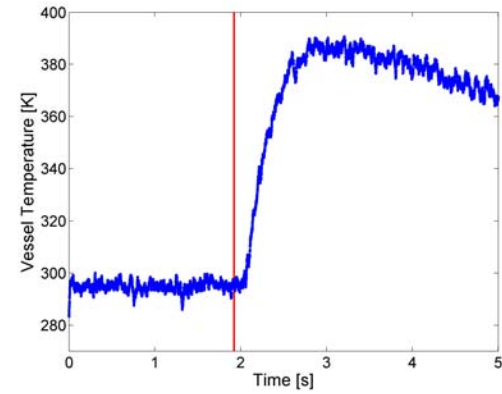
Figure M.24: Experimental data from shot 36



(a) Pressure

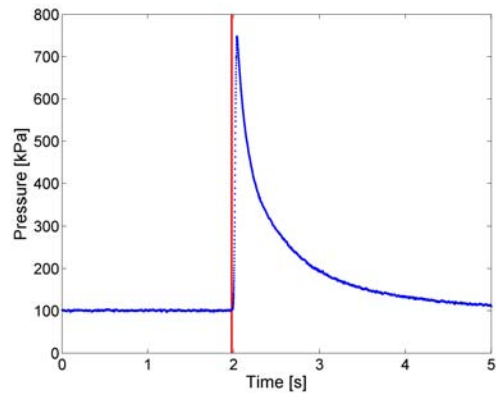


(b) Glow plug temperature

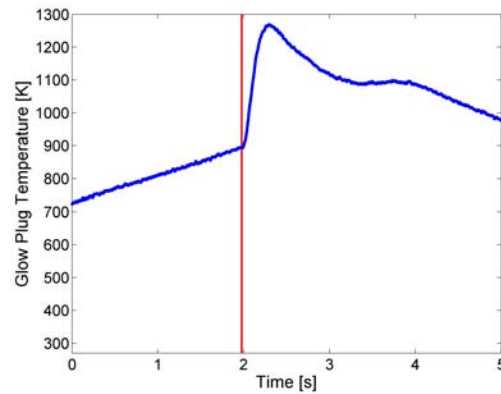


(c) Vessel temperature

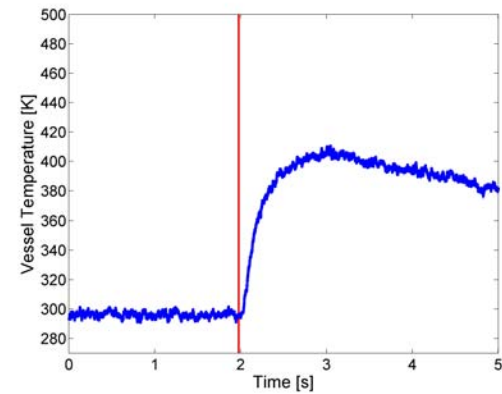
Figure M.25: Experimental data from shot 37



(a) Pressure

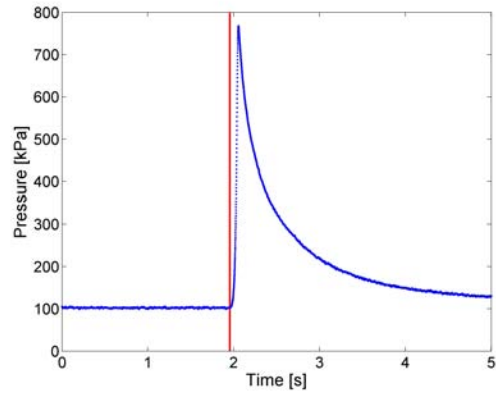


(b) Glow plug temperature

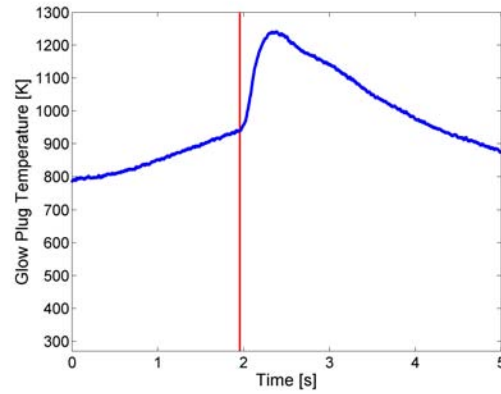


(c) Vessel temperature

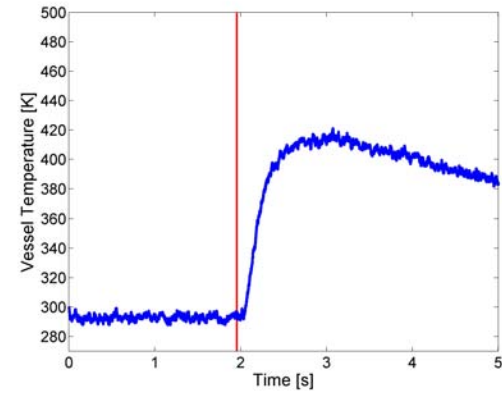
Figure M.26: Experimental data from shot 38



(a) Pressure

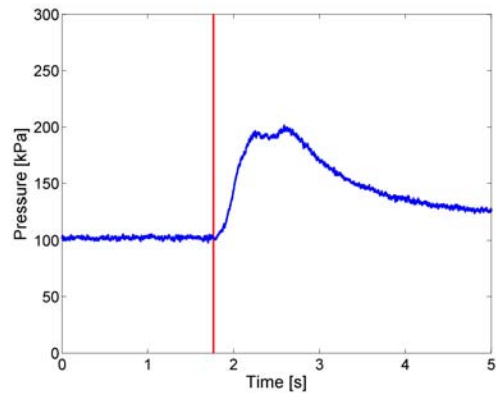


(b) Glow plug temperature

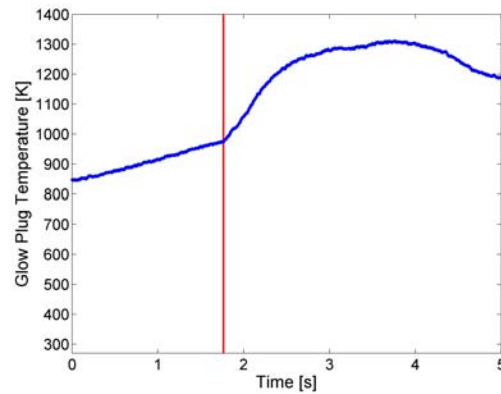


(c) Vessel temperature

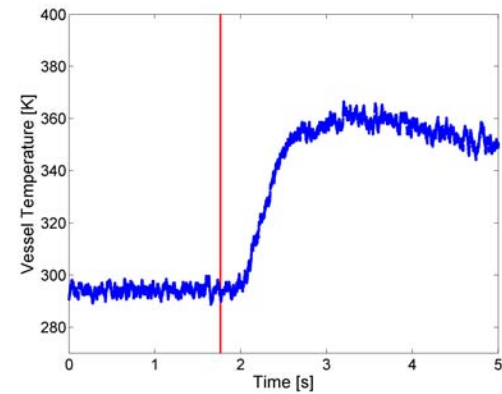
Figure M.27: Experimental data from shot 40



(a) Pressure

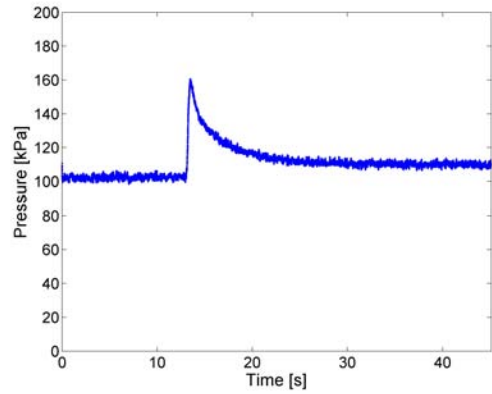


(b) Glow plug temperature

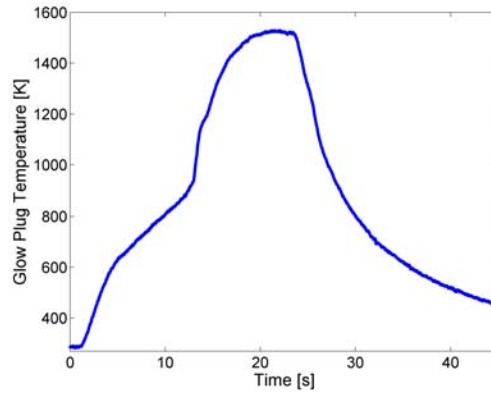


(c) Vessel temperature

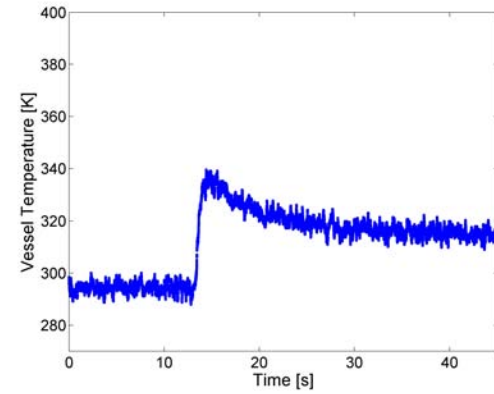
Figure M.28: Experimental data from shot 41



(a) Pressure

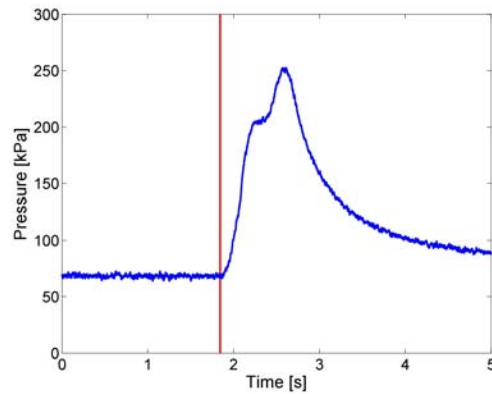


(b) Glow plug temperature

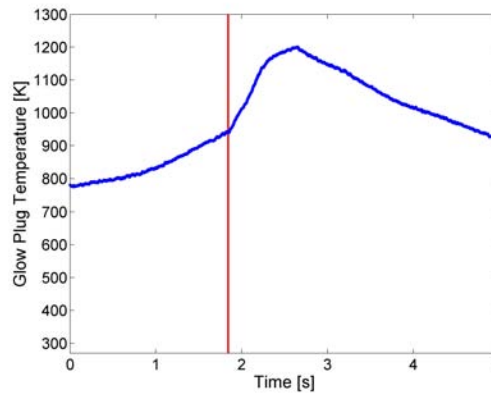


(c) Vessel temperature

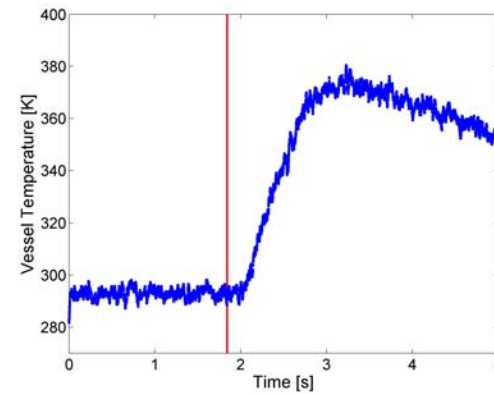
Figure M.29: Experimental data from shot 42



(a) Pressure

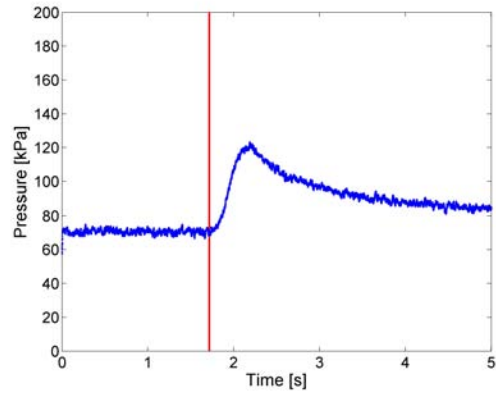


(b) Glow plug temperature

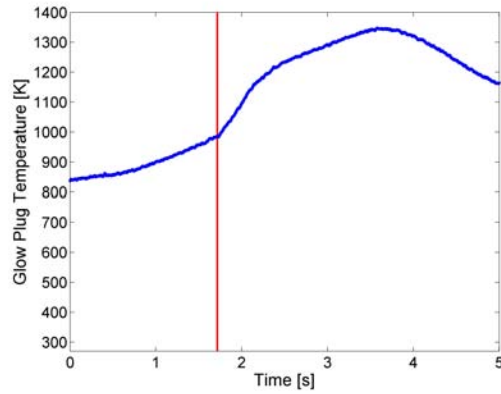


(c) Vessel temperature

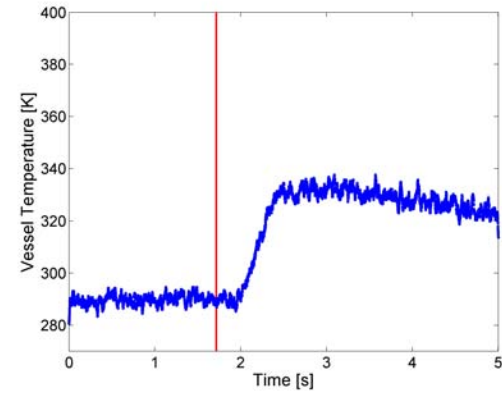
Figure M.30: Experimental data from shot 43



(a) Pressure

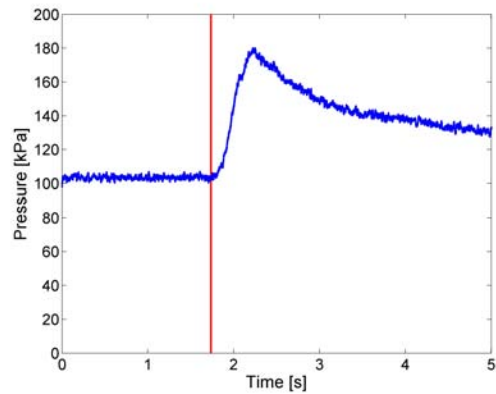


(b) Glow plug temperature

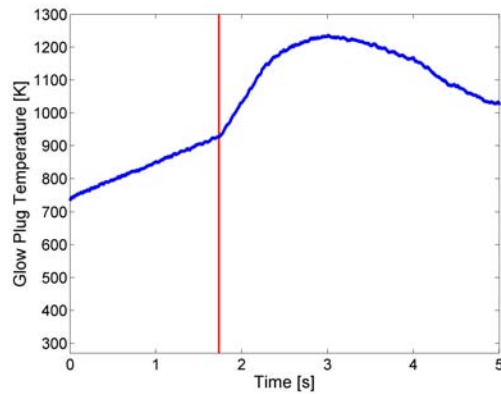


(c) Vessel temperature

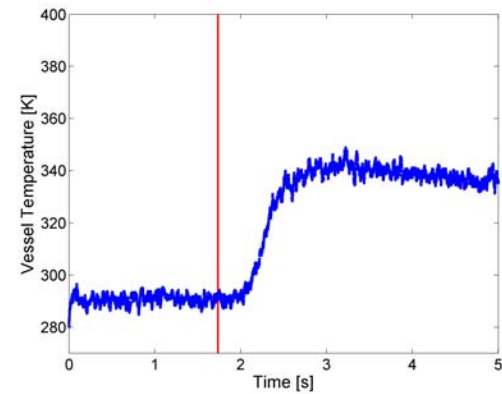
Figure M.31: Experimental data from shot 44



(a) Pressure

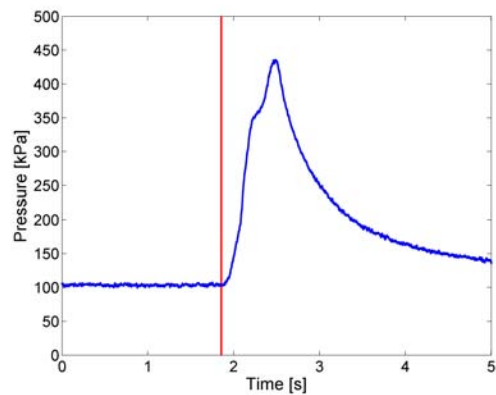


(b) Glow plug temperature

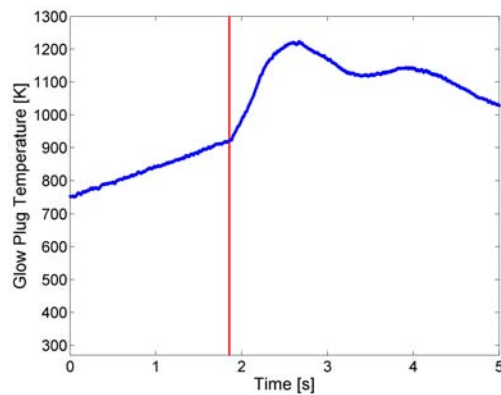


(c) Vessel temperature

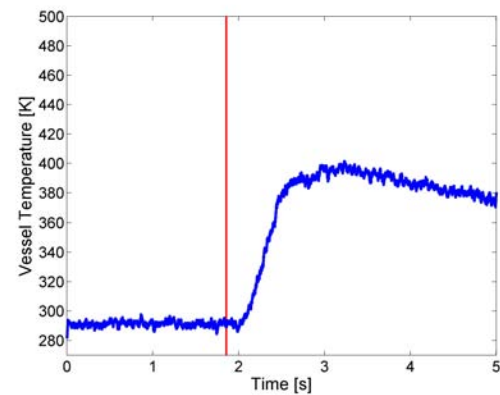
Figure M.32: Experimental data from shot 45



(a) Pressure

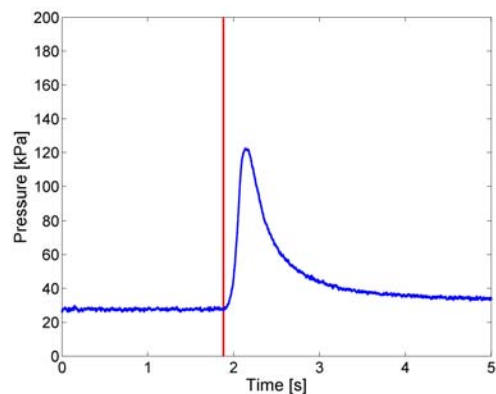


(b) Glow plug temperature

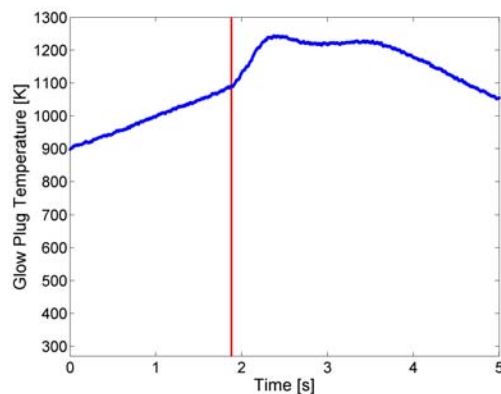


(c) Vessel temperature

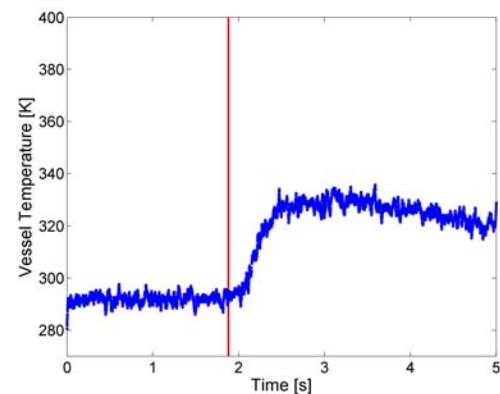
Figure M.33: Experimental data from shot 46



(a) Pressure

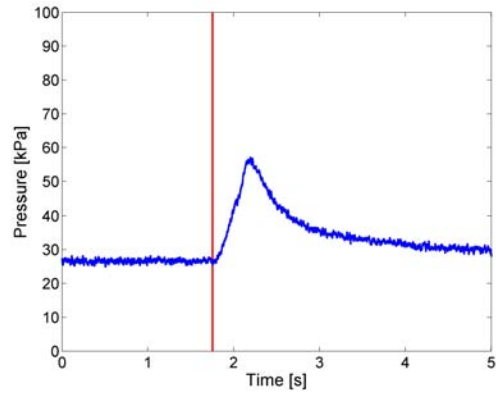


(b) Glow plug temperature

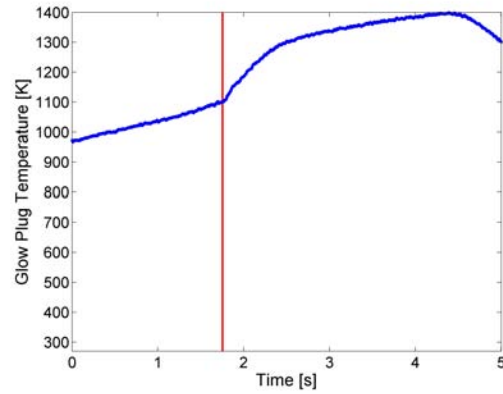


(c) Vessel temperature

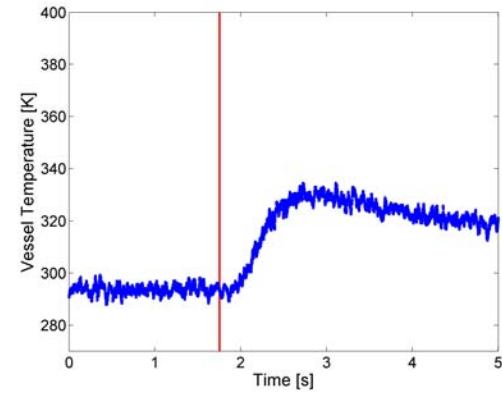
Figure M.34: Experimental data from shot 47



(a) Pressure

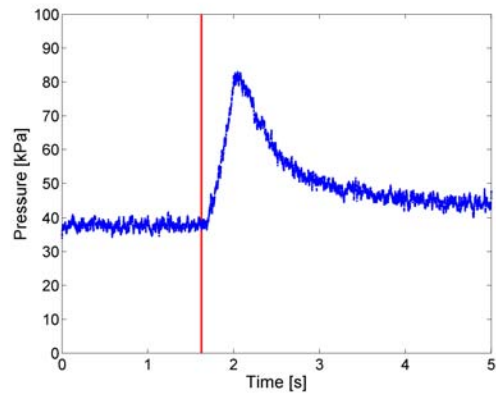


(b) Glow plug temperature

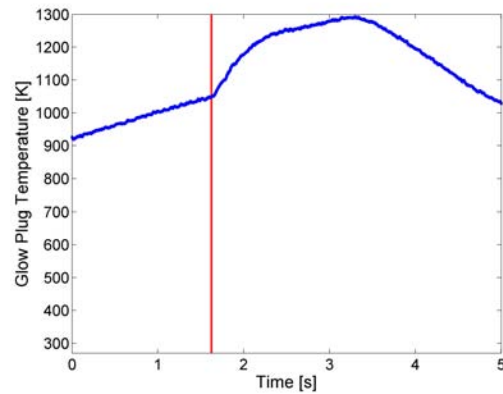


(c) Vessel temperature

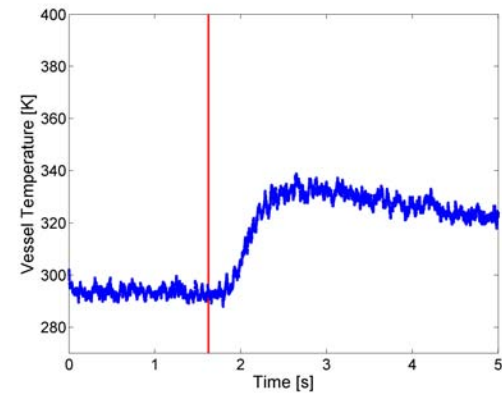
Figure M.35: Experimental data from shot 49



(a) Pressure

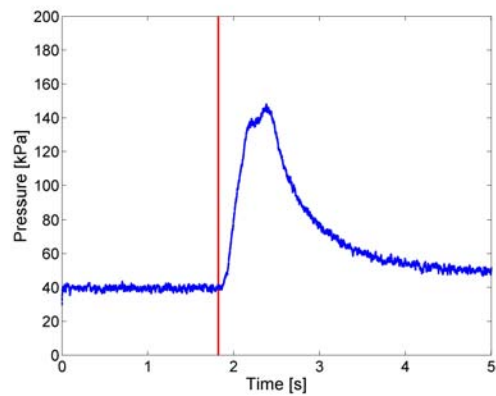


(b) Glow plug temperature

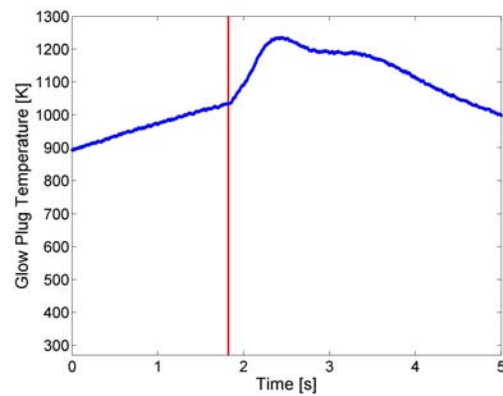


(c) Vessel temperature

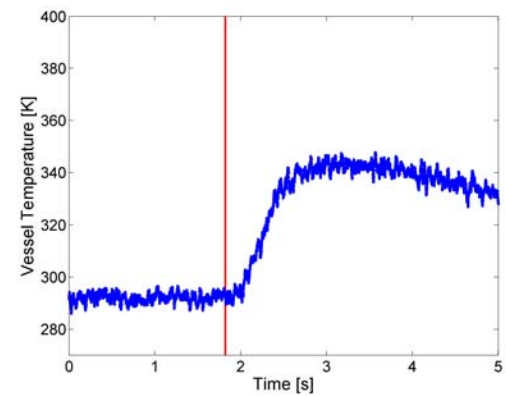
Figure M.36: Experimental data from shot 50



(a) Pressure

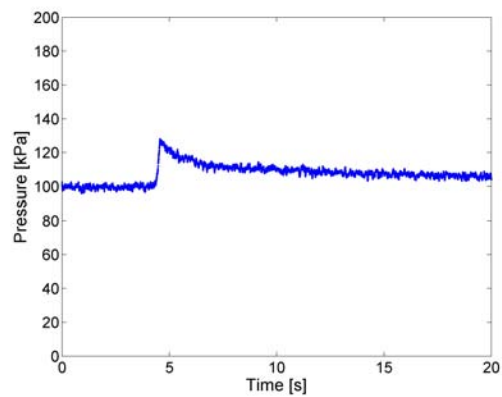


(b) Glow plug temperature

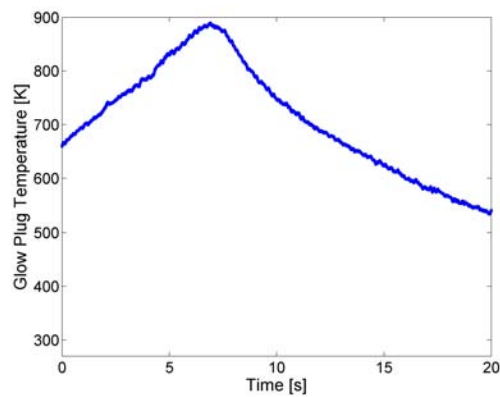


(c) Vessel temperature

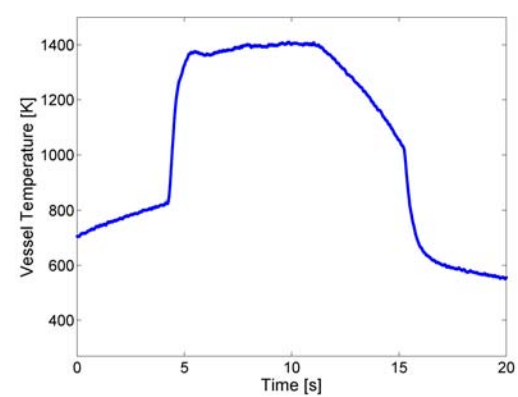
Figure M.37: Experimental data from shot 51



(a) Pressure

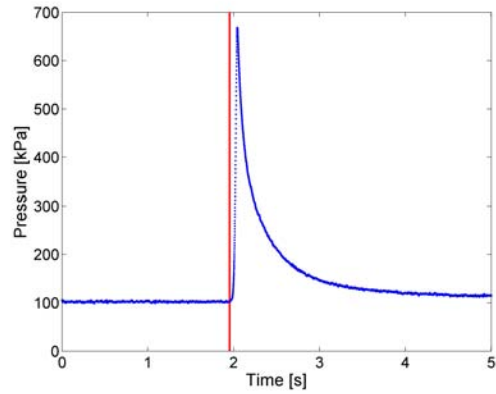


(b) Glow plug temperature

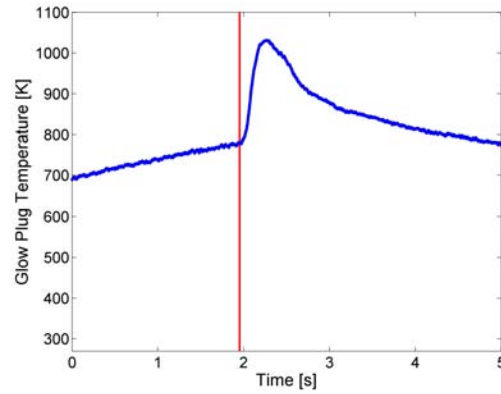


(c) Vessel temperature

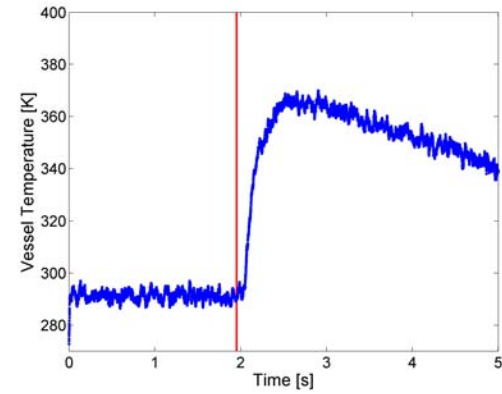
Figure M.38: Experimental data from shot 54



(a) Pressure

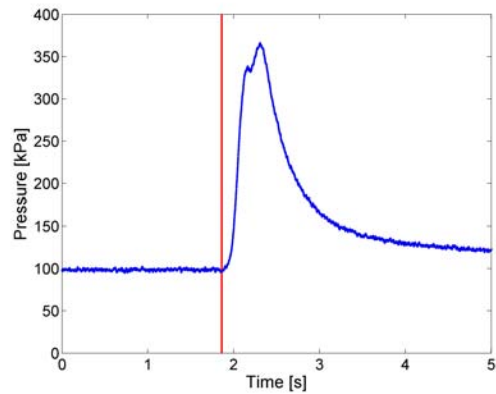


(b) Glow plug temperature

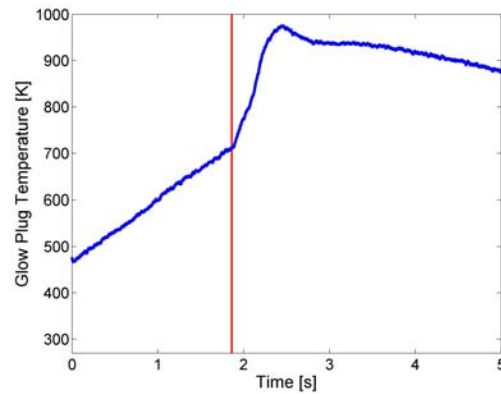


(c) Vessel temperature

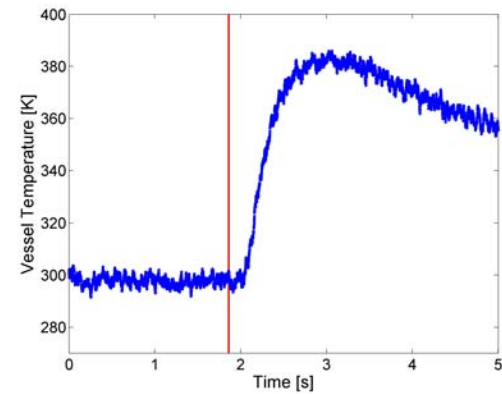
Figure M.39: Experimental data from shot 55



(a) Pressure

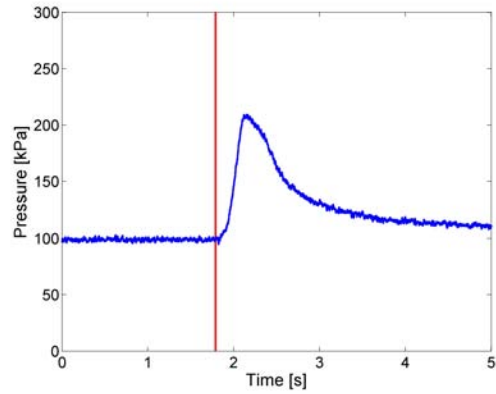


(b) Glow plug temperature

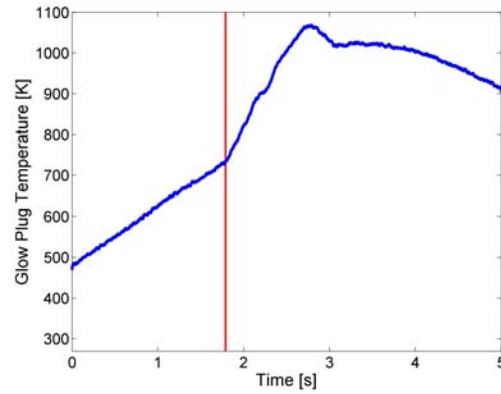


(c) Vessel temperature

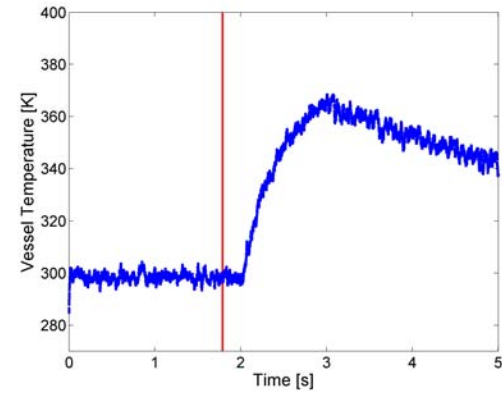
Figure M.40: Experimental data from shot 57



(a) Pressure

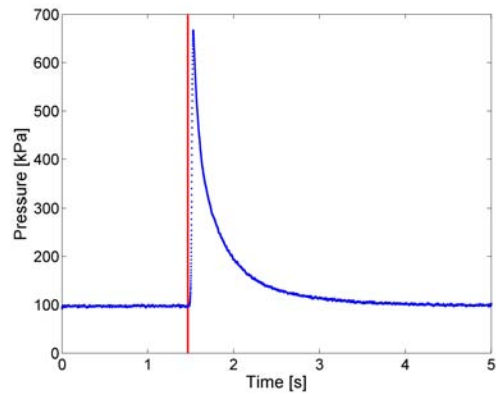


(b) Glow plug temperature

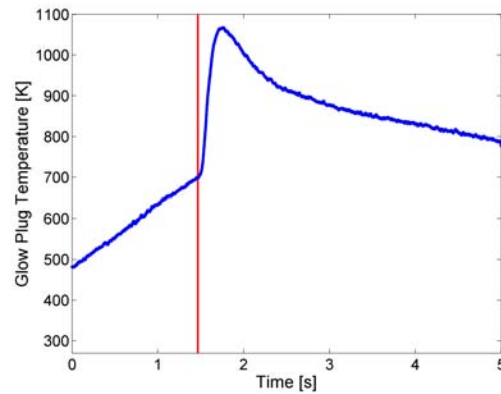


(c) Vessel temperature

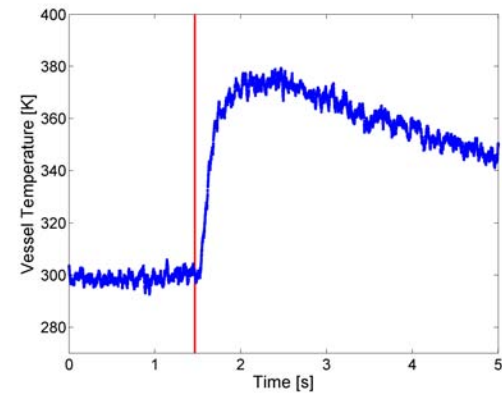
Figure M.41: Experimental data from shot 58



(a) Pressure

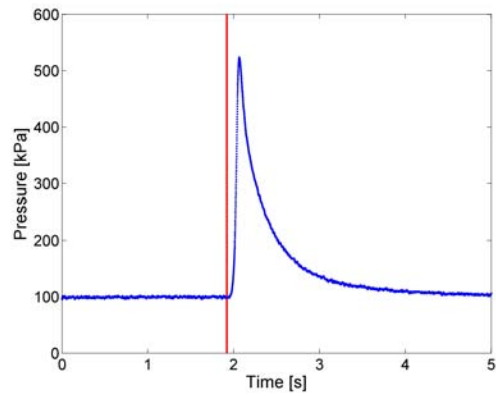


(b) Glow plug temperature

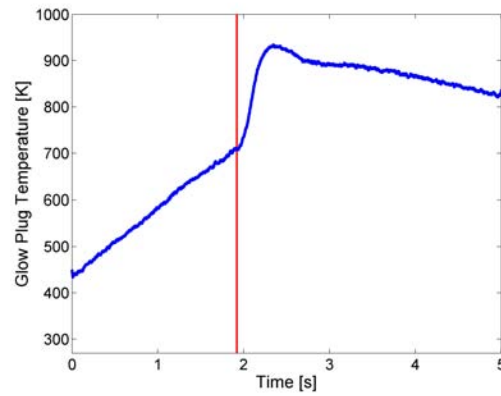


(c) Vessel temperature

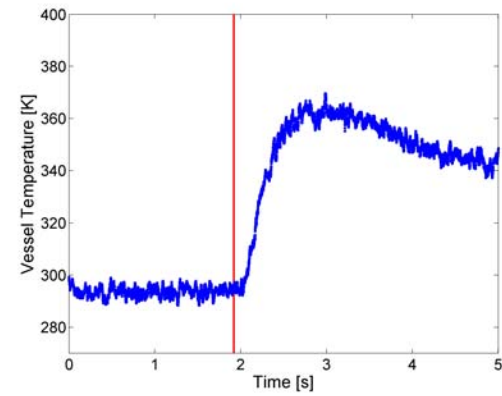
Figure M.42: Experimental data from shot 61



(a) Pressure

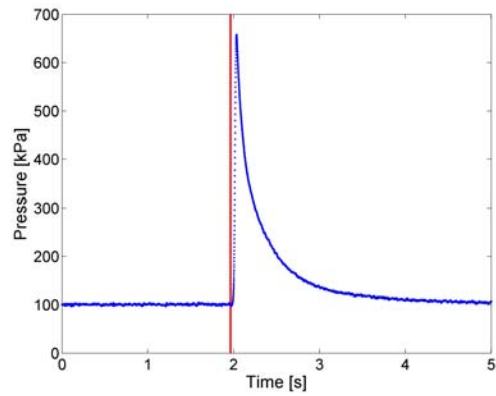


(b) Glow plug temperature

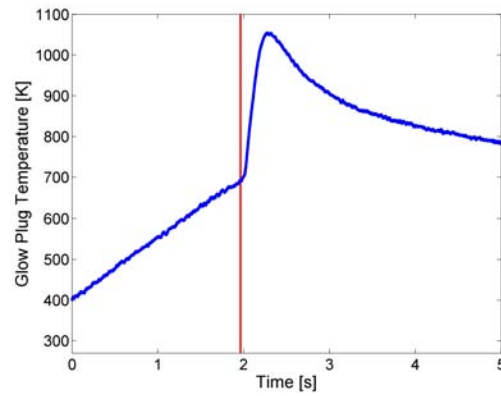


(c) Vessel temperature

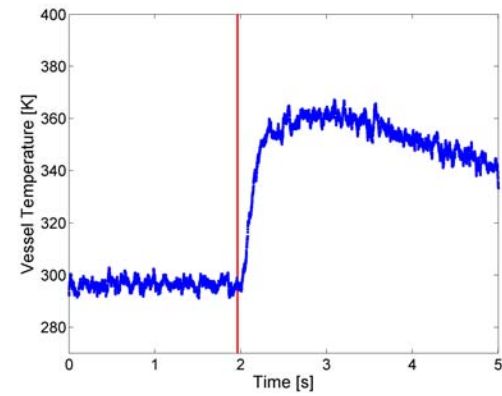
Figure M.43: Experimental data from shot 64



(a) Pressure

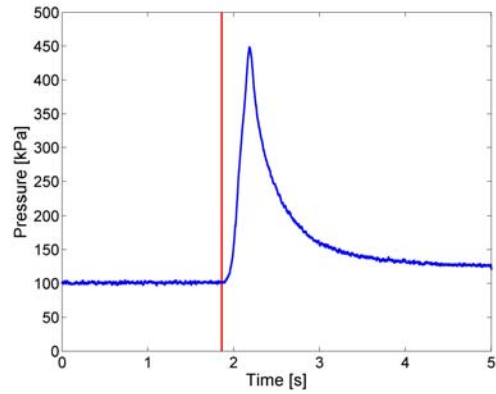


(b) Glow plug temperature

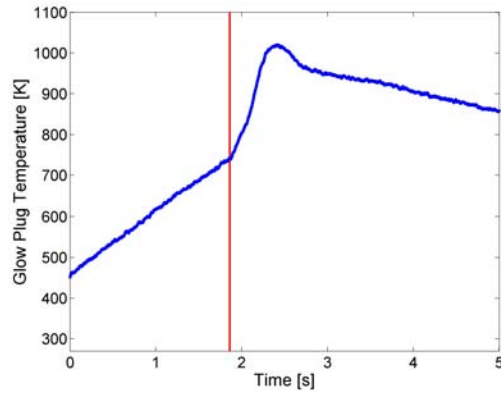


(c) Vessel temperature

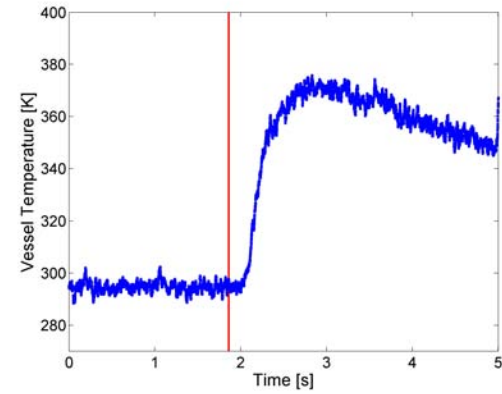
Figure M.44: Experimental data from shot 65



(a) Pressure

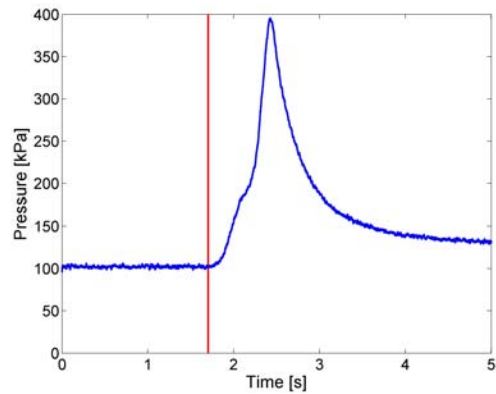


(b) Glow plug temperature

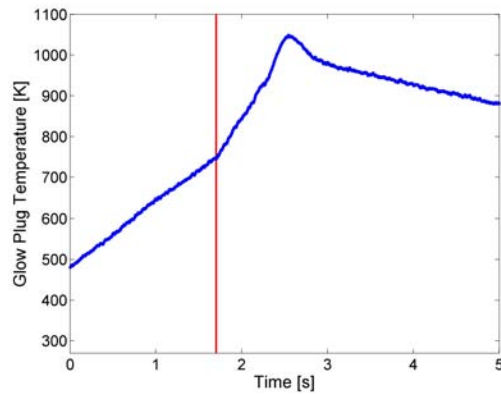


(c) Vessel temperature

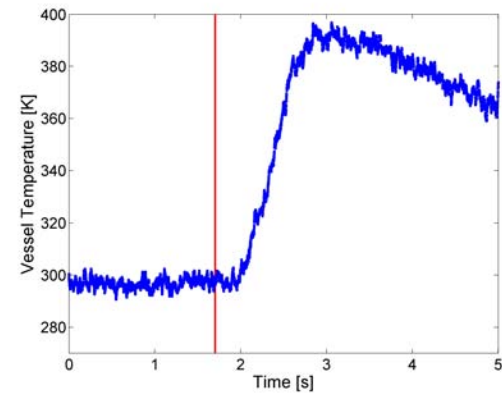
Figure M.45: Experimental data from shot 68



(a) Pressure

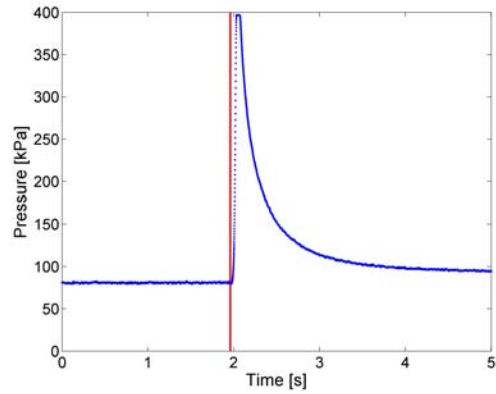


(b) Glow plug temperature

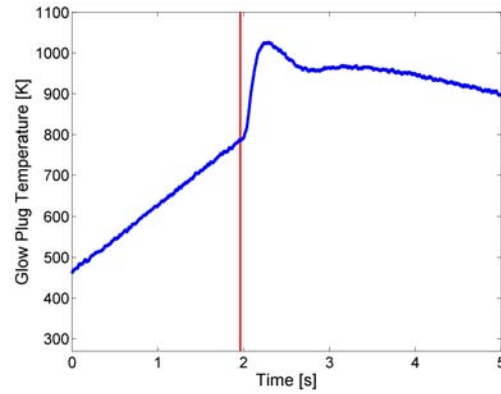


(c) Vessel temperature

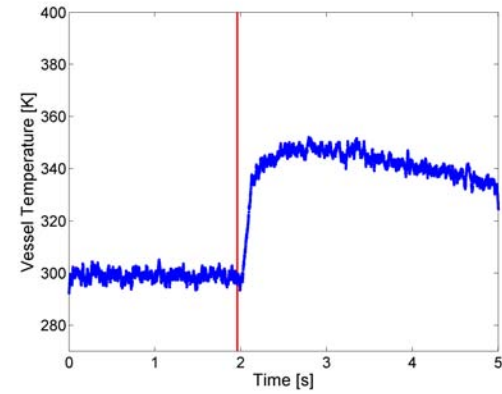
Figure M.46: Experimental data from shot 69



(a) Pressure

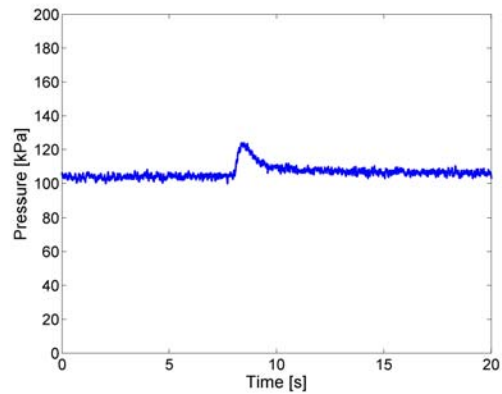


(b) Glow plug temperature

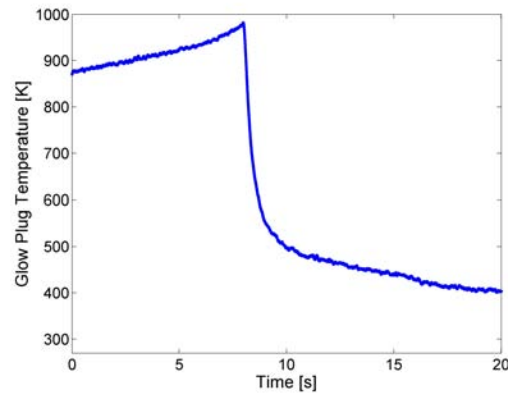


(c) Vessel temperature

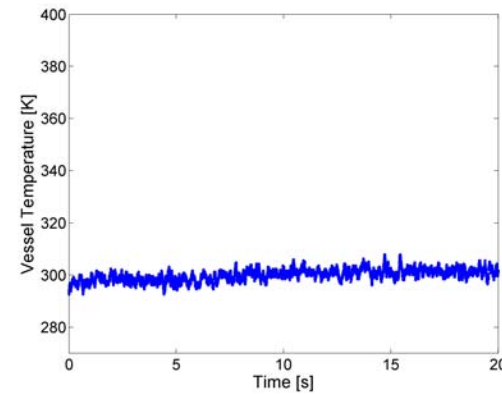
Figure M.47: Experimental data from shot 70



(a) Pressure

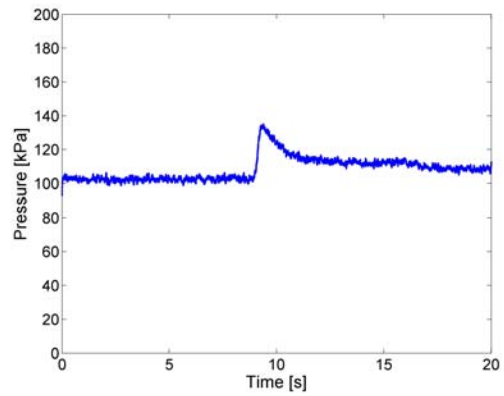


(b) Glow plug temperature

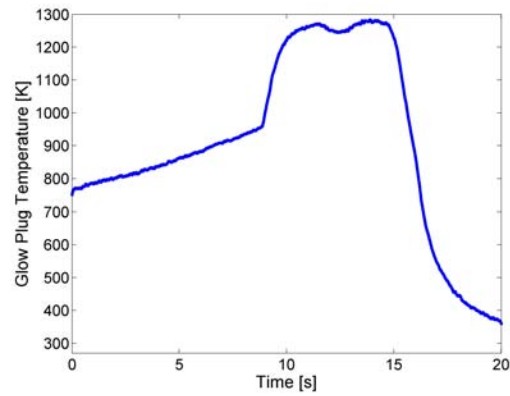


(c) Vessel temperature

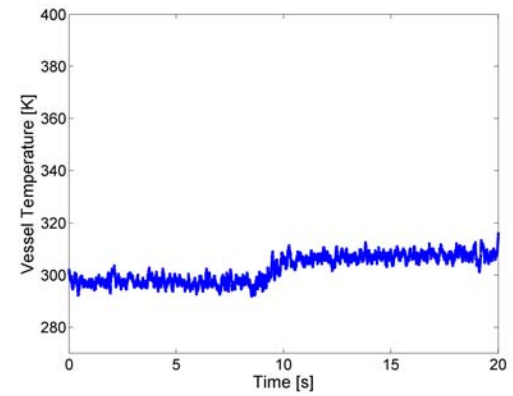
Figure M.48: Experimental data from shot 85



(a) Pressure

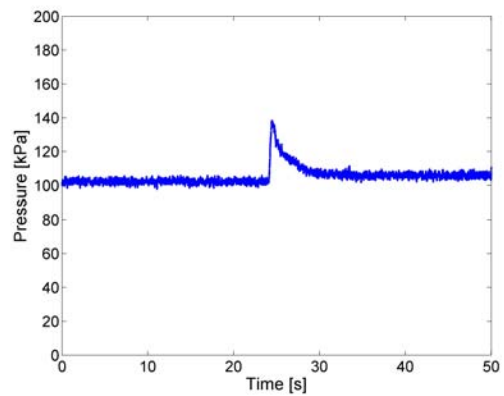


(b) Glow plug temperature

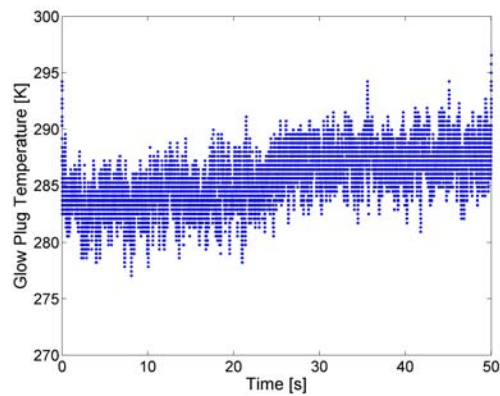


(c) Vessel temperature

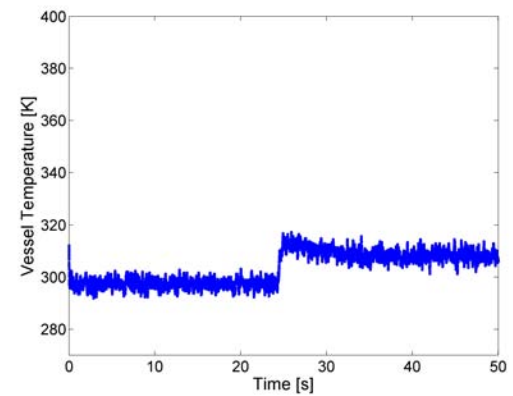
Figure M.49: Experimental data from shot 86



(a) Pressure

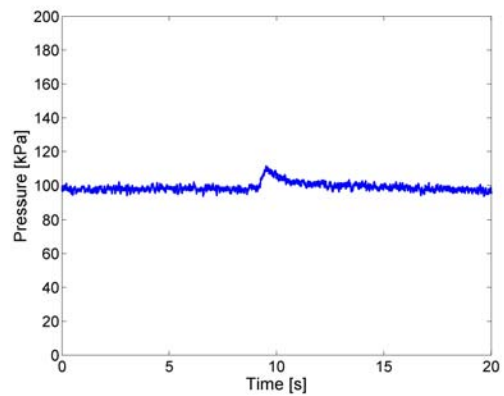


(b) Glow plug temperature

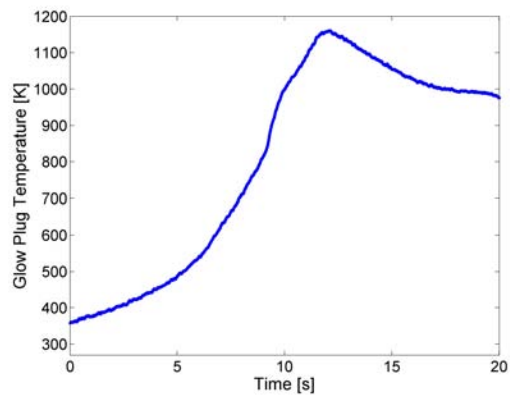


(c) Vessel temperature

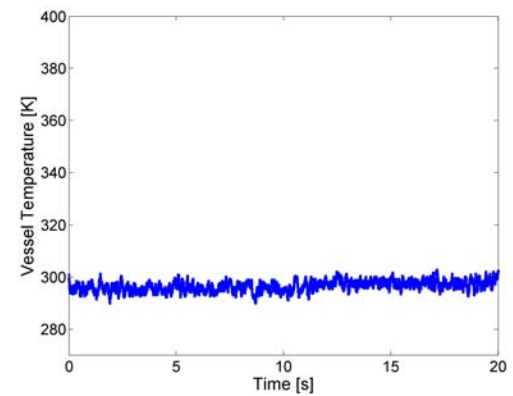
Figure M.50: Experimental data from shot 87



(a) Pressure

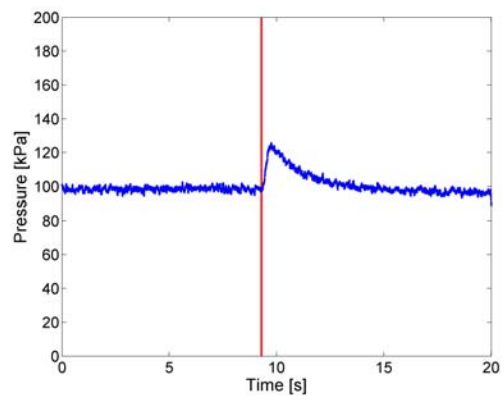


(b) Glow plug temperature

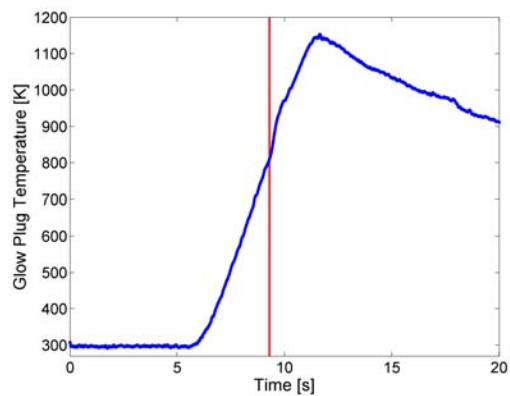


(c) Vessel temperature

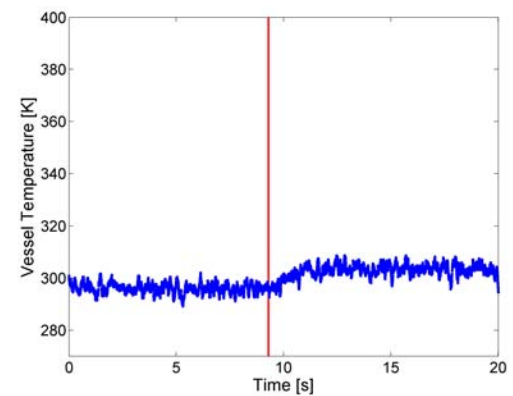
Figure M.51: Experimental data from shot 90



(a) Pressure

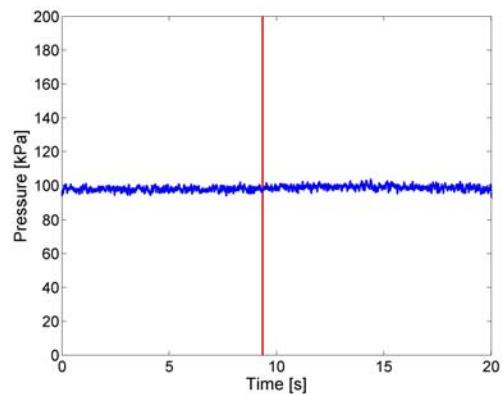


(b) Glow plug temperature

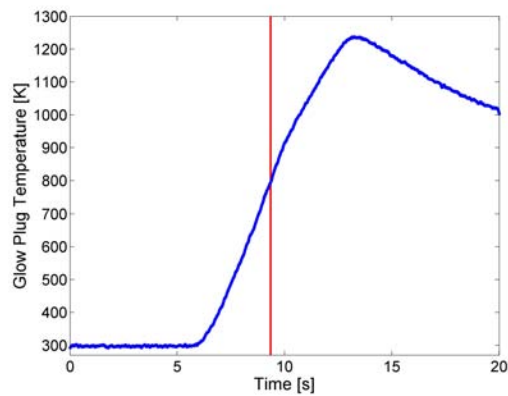


(c) Vessel temperature

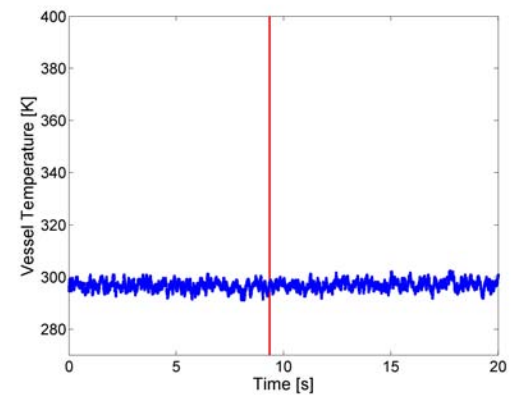
Figure M.52: Experimental data from shot 91



(a) Pressure

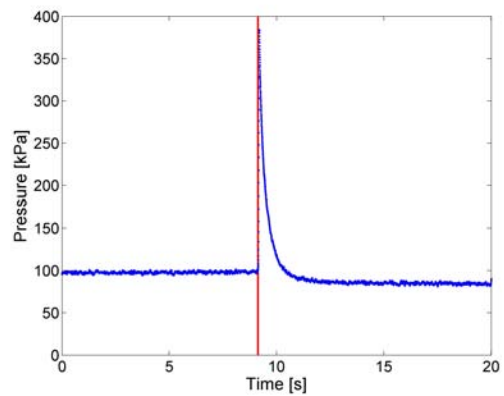


(b) Glow plug temperature

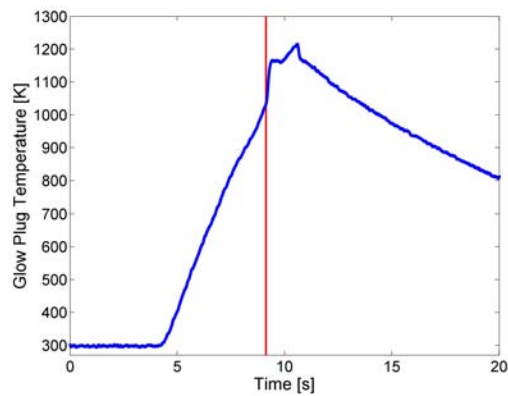


(c) Vessel temperature

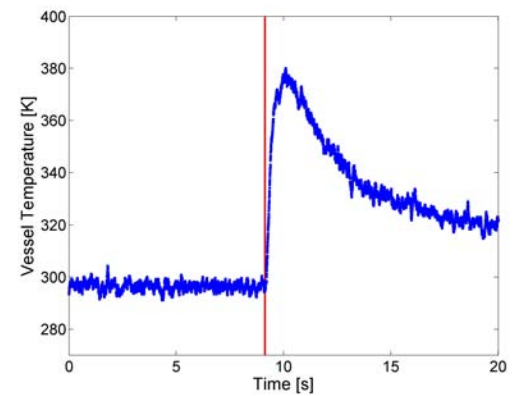
Figure M.53: Experimental data from shot 92



(a) Pressure

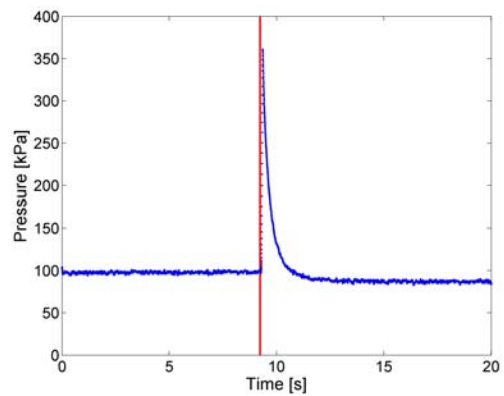


(b) Glow plug temperature

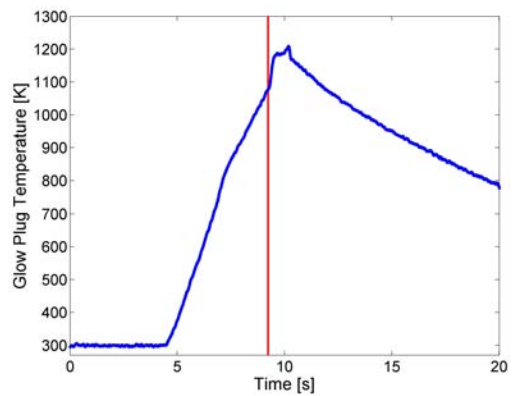


(c) Vessel temperature

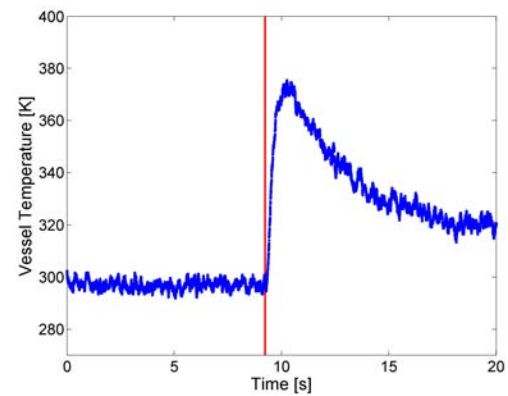
Figure M.54: Experimental data from shot 93



(a) Pressure

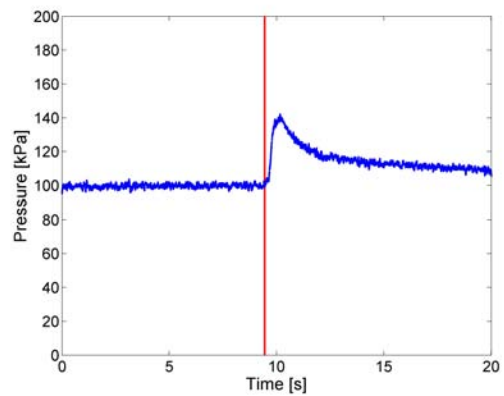


(b) Glow plug temperature

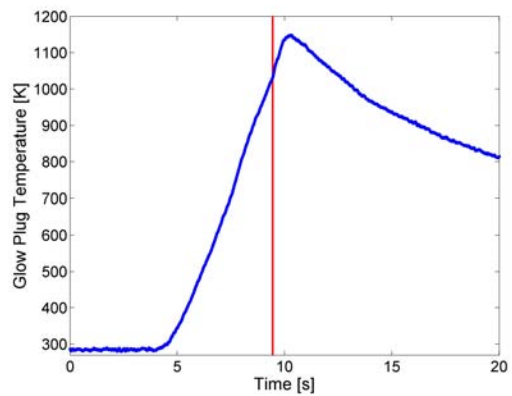


(c) Vessel temperature

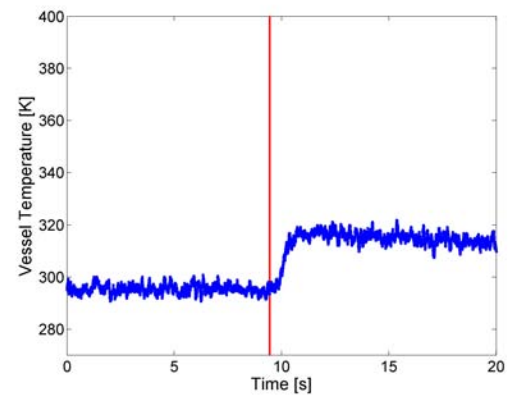
Figure M.55: Experimental data from shot 94



(a) Pressure

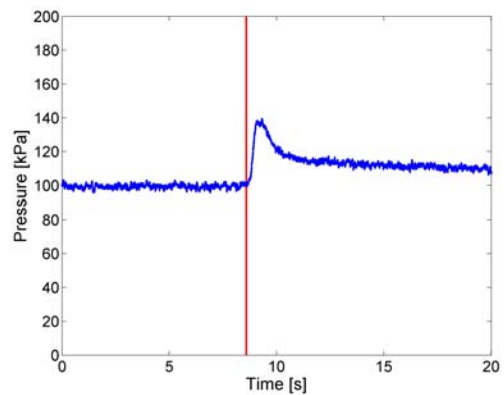


(b) Glow plug temperature

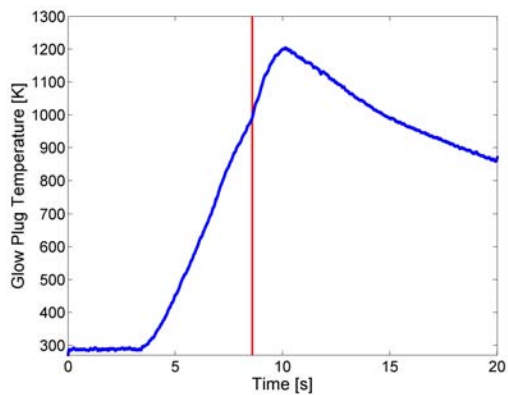


(c) Vessel temperature

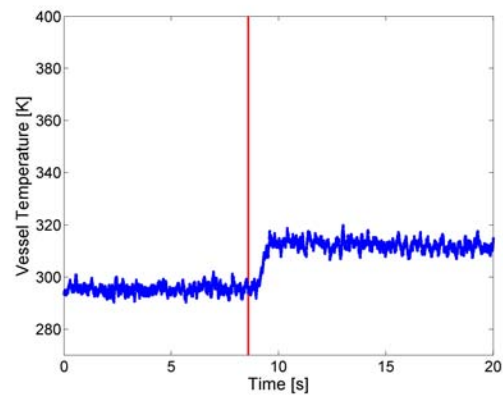
Figure M.56: Experimental data from shot 95



(a) Pressure

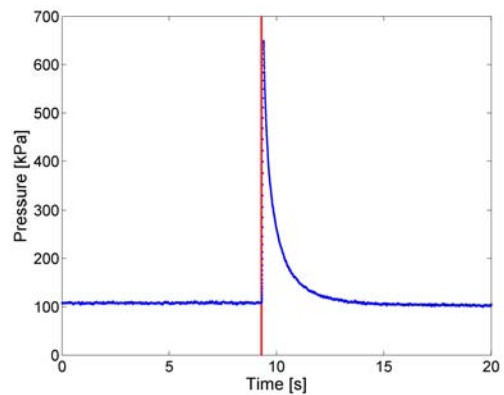


(b) Glow plug temperature

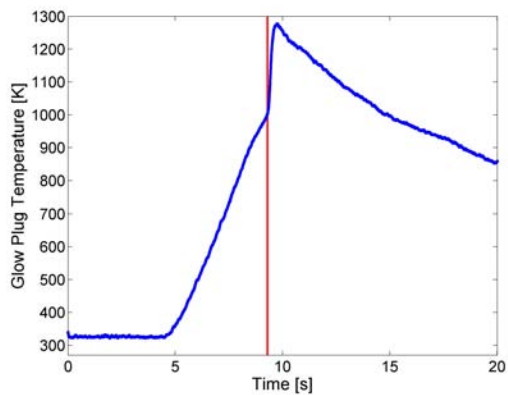


(c) Vessel temperature

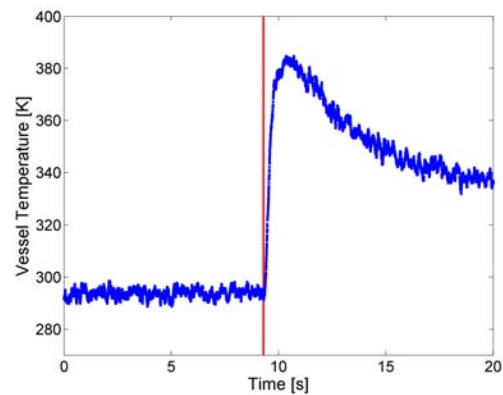
Figure M.57: Experimental data from shot 96



(a) Pressure

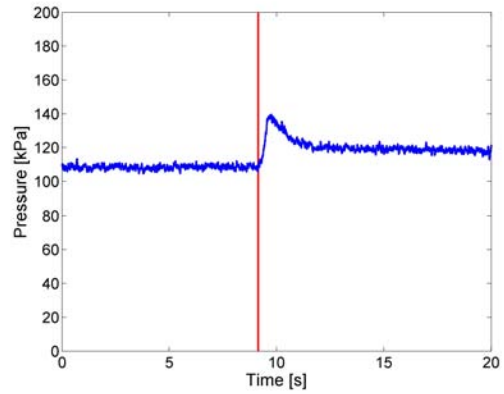


(b) Glow plug temperature

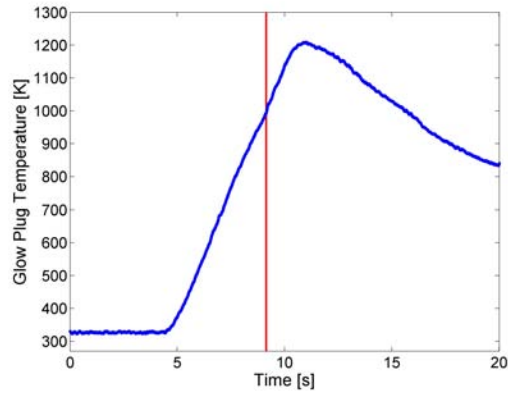


(c) Vessel temperature

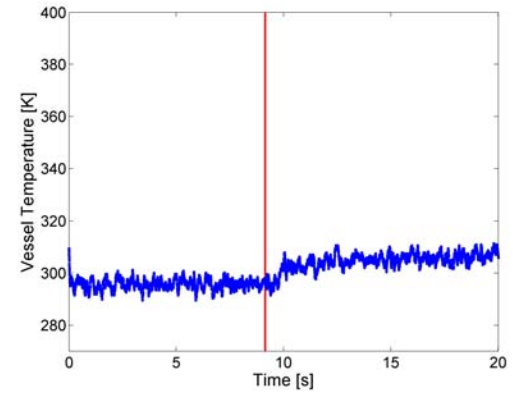
Figure M.58: Experimental data from shot 97



(a) Pressure

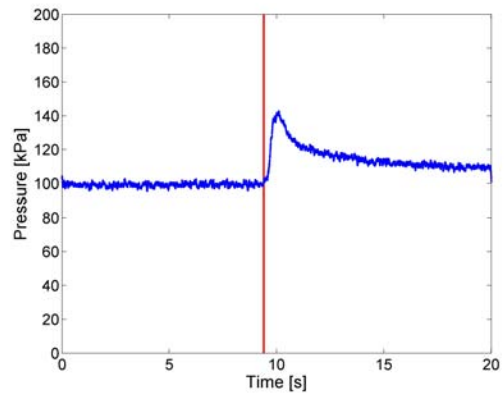


(b) Glow plug temperature

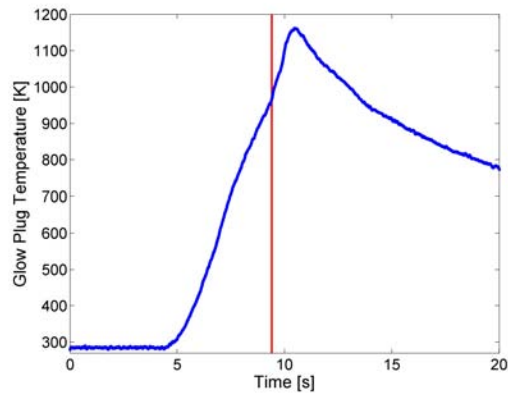


(c) Vessel temperature

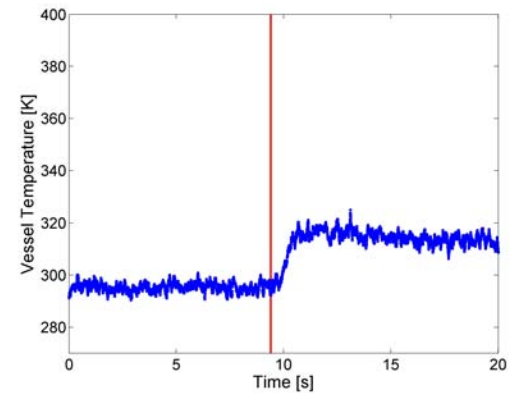
Figure M.59: Experimental data from shot 98



(a) Pressure

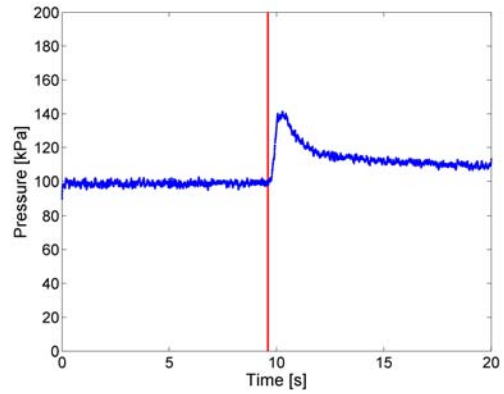


(b) Glow plug temperature

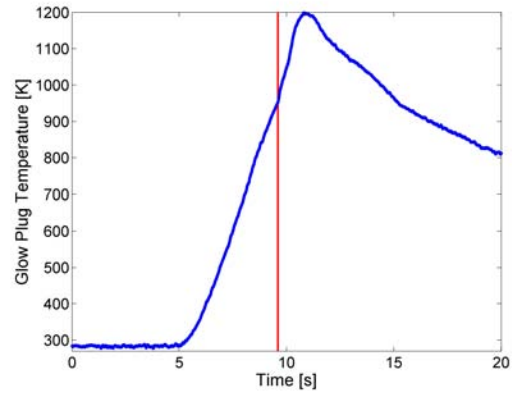


(c) Vessel temperature

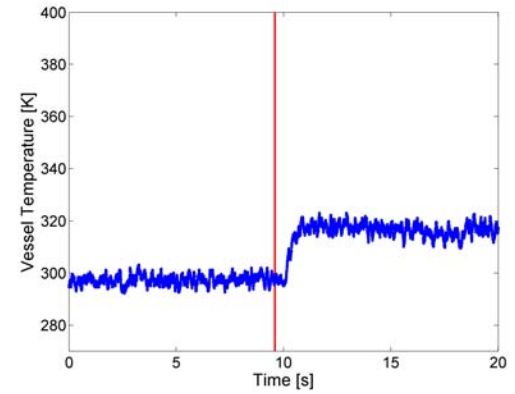
Figure M.60: Experimental data from shot 100



(a) Pressure

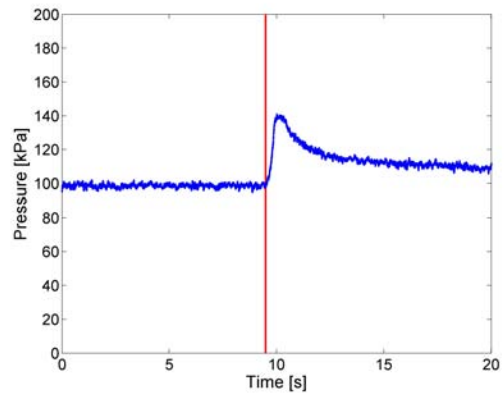


(b) Glow plug temperature

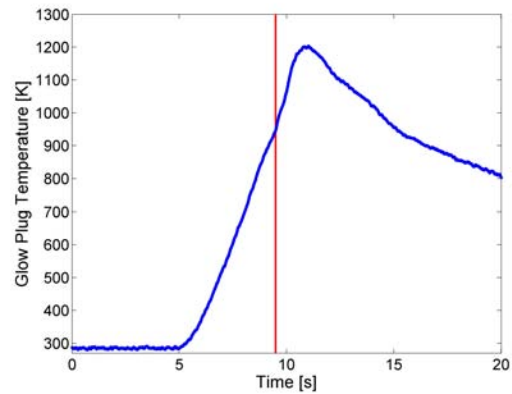


(c) Vessel temperature

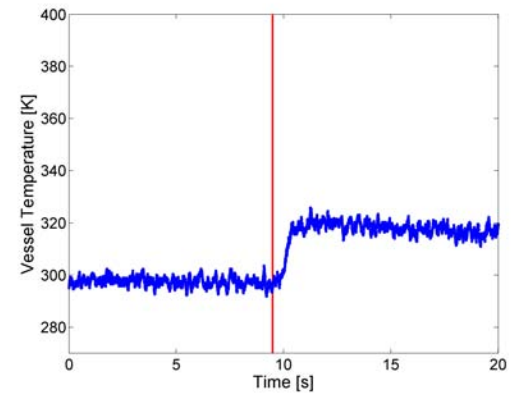
Figure M.61: Experimental data from shot 101



(a) Pressure

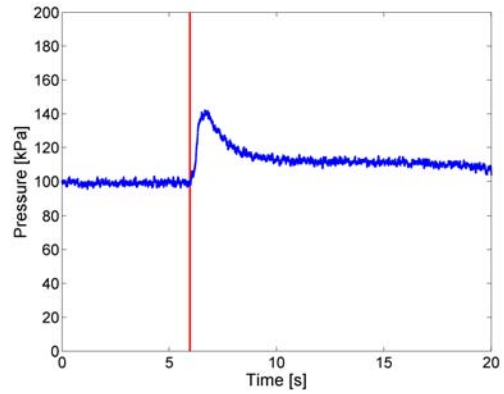


(b) Glow plug temperature

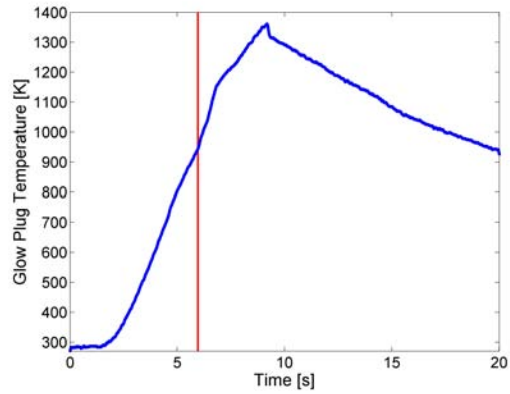


(c) Vessel temperature

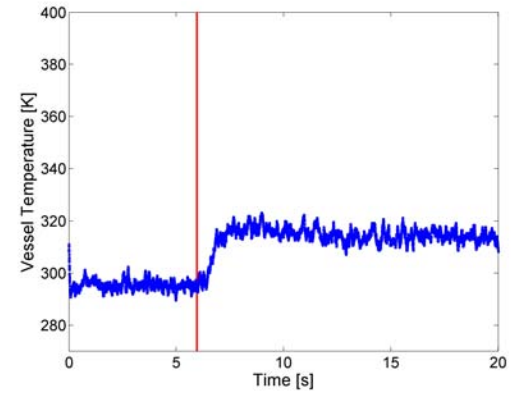
Figure M.62: Experimental data from shot 102



(a) Pressure

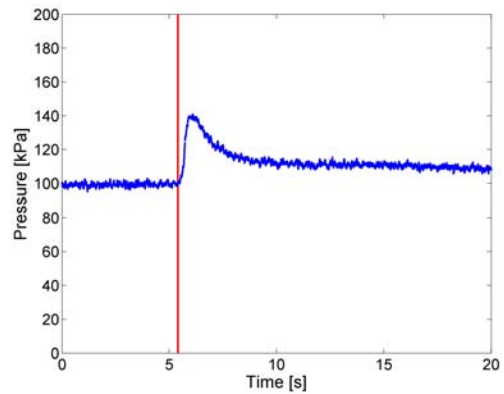


(b) Glow plug temperature

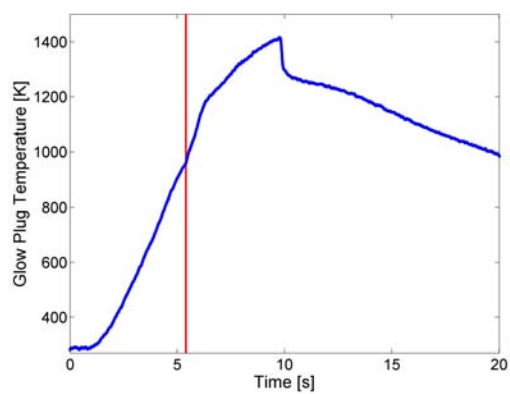


(c) Vessel temperature

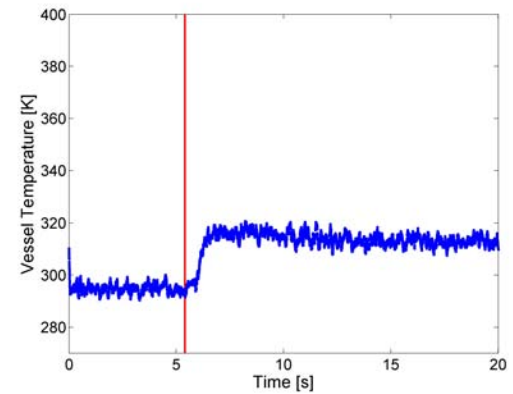
Figure M.63: Experimental data from shot 103



(a) Pressure

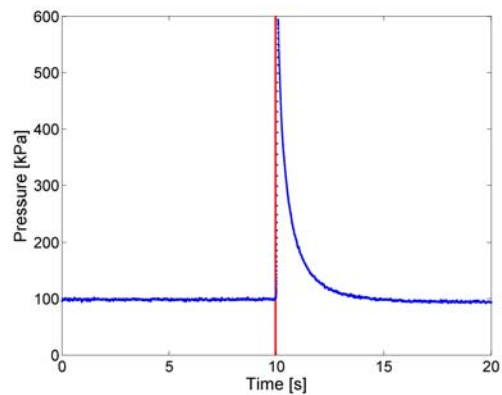


(b) Glow plug temperature

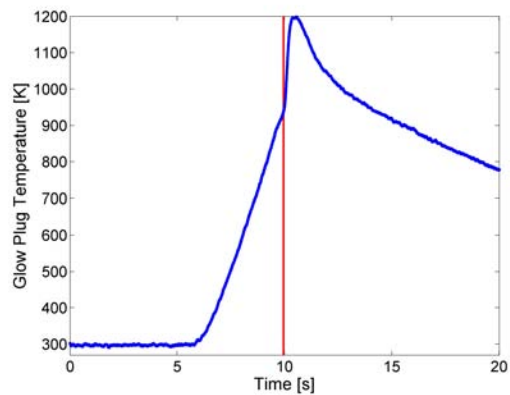


(c) Vessel temperature

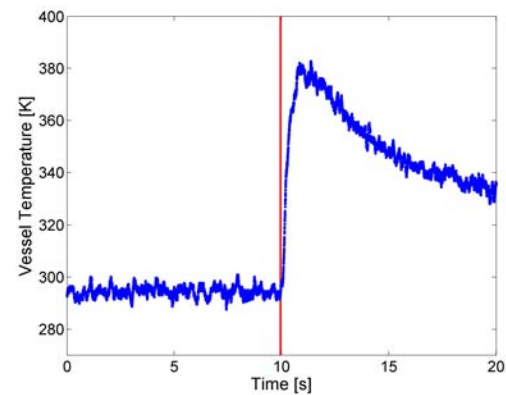
Figure M.64: Experimental data from shot 104



(a) Pressure

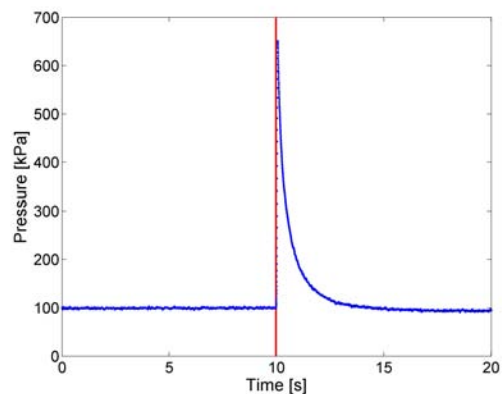


(b) Glow plug temperature

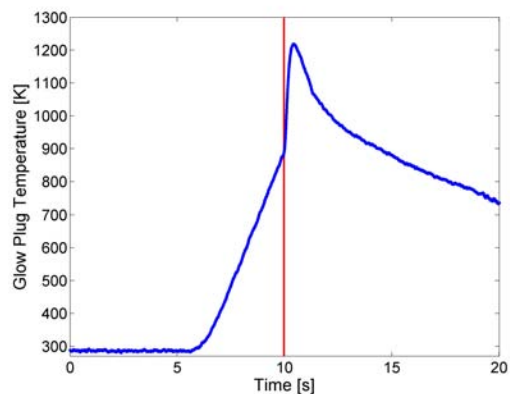


(c) Vessel temperature

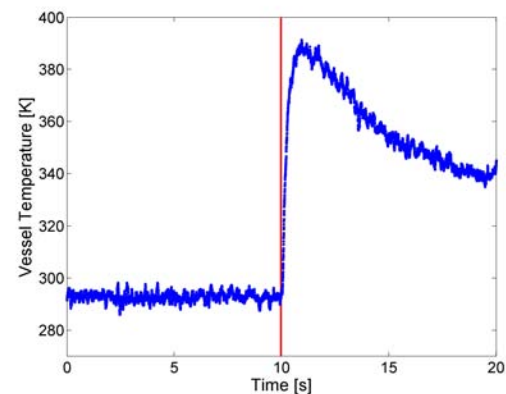
Figure M.65: Experimental data from shot 115



(a) Pressure

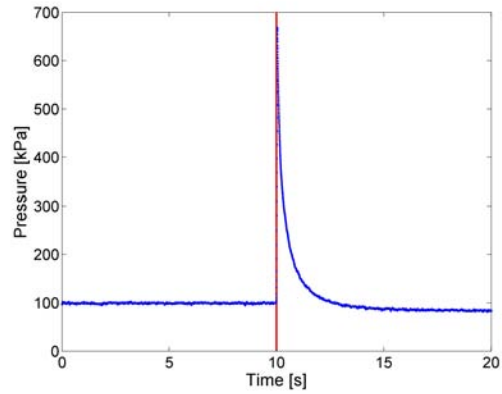


(b) Glow plug temperature

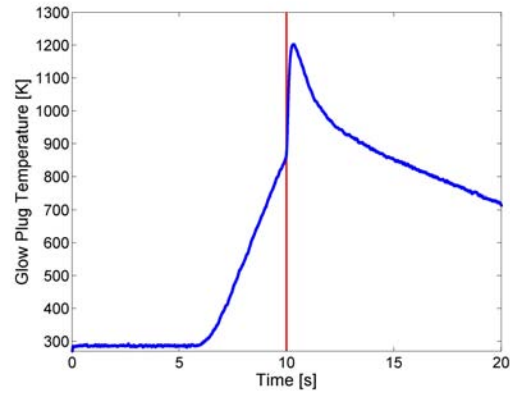


(c) Vessel temperature

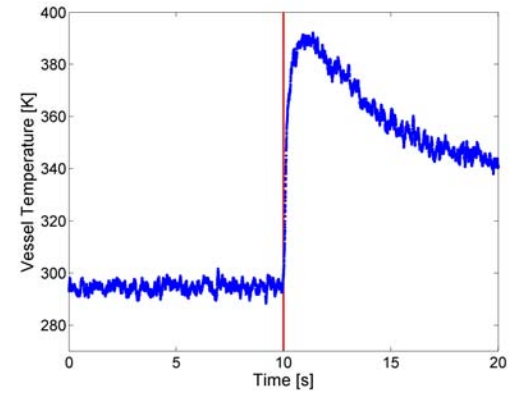
Figure M.66: Experimental data from shot 116



(a) Pressure

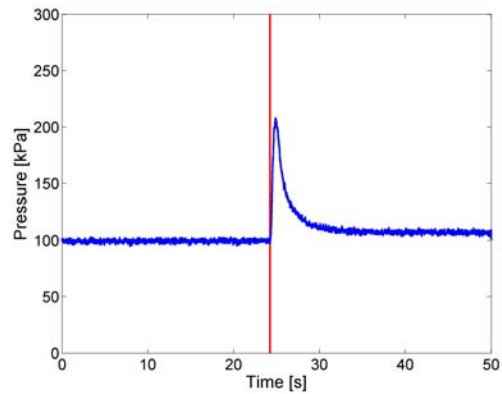


(b) Glow plug temperature

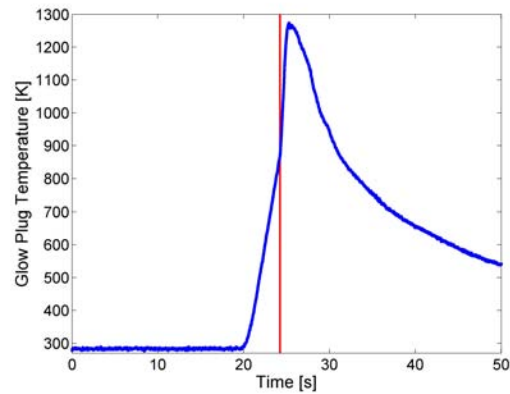


(c) Vessel temperature

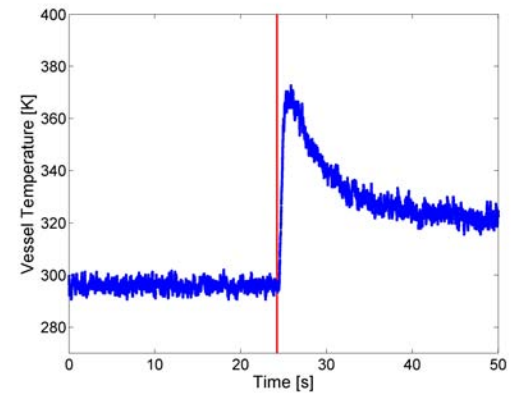
Figure M.67: Experimental data from shot 117



(a) Pressure

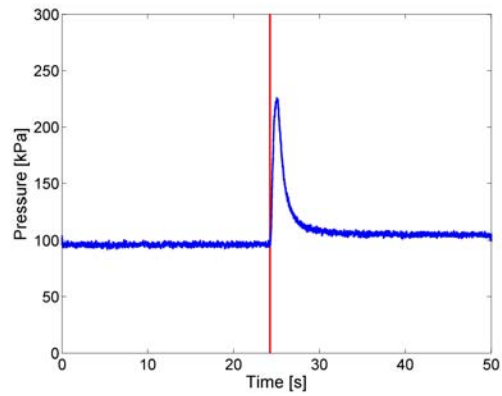


(b) Glow plug temperature

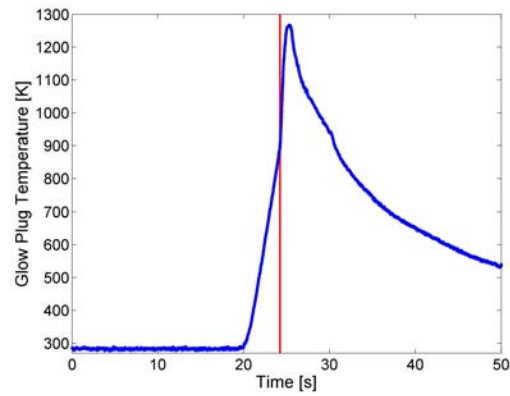


(c) Vessel temperature

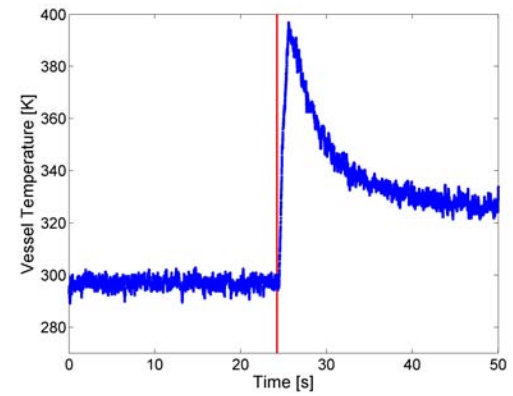
Figure M.68: Experimental data from shot 118



(a) Pressure

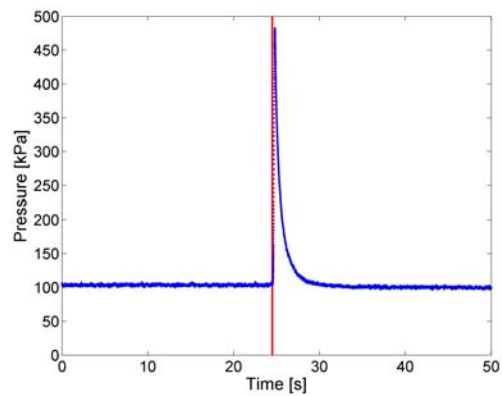


(b) Glow plug temperature

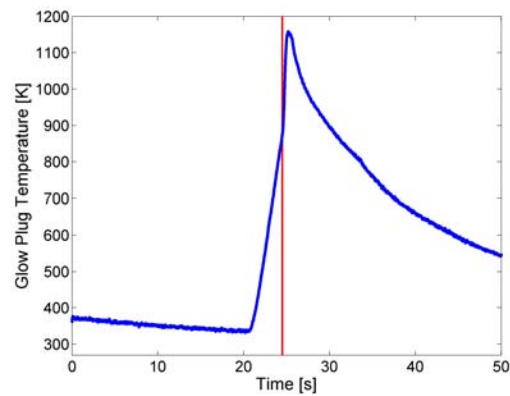


(c) Vessel temperature

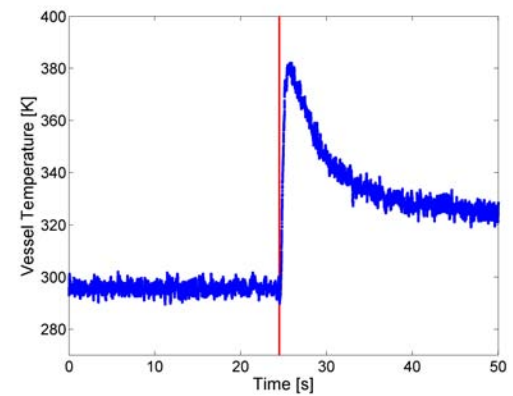
Figure M.69: Experimental data from shot 119



(a) Pressure

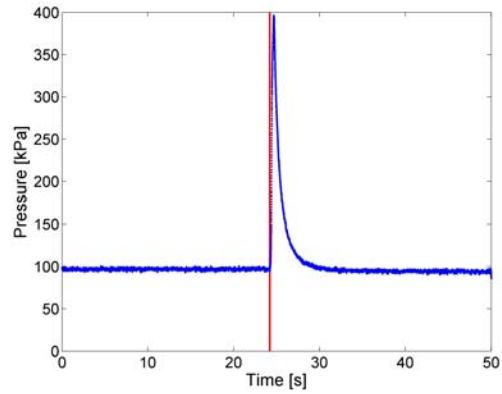


(b) Glow plug temperature

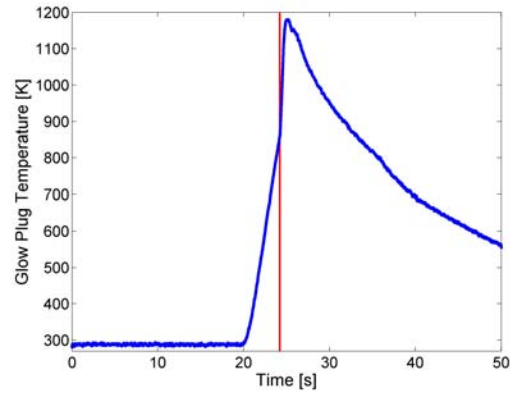


(c) Vessel temperature

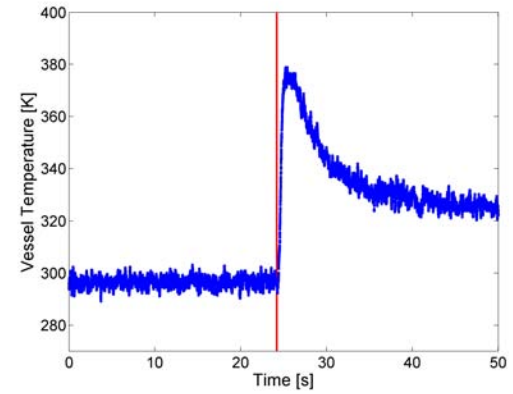
Figure M.70: Experimental data from shot 121



(a) Pressure

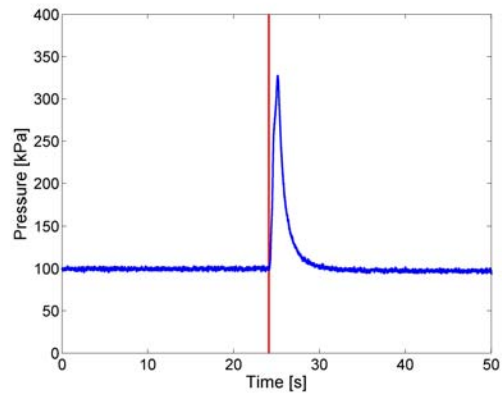


(b) Glow plug temperature

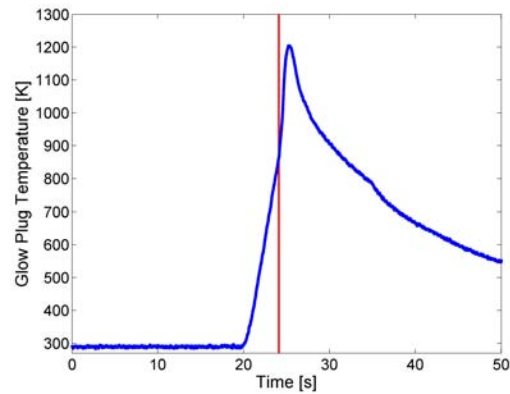


(c) Vessel temperature

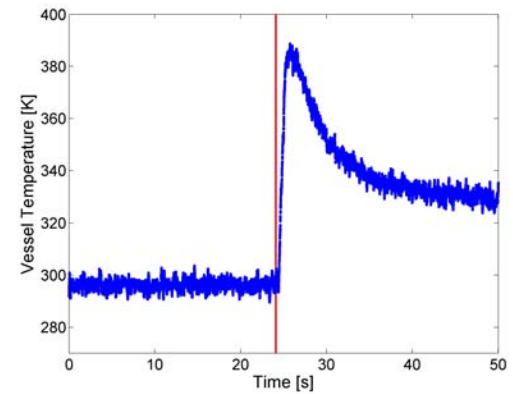
Figure M.71: Experimental data from shot 122



(a) Pressure



(b) Glow plug temperature



(c) Vessel temperature

Figure M.72: Experimental data from shot 123

This page intentionally left blank.